Technical Report

TR-12-09

Analysis of SKB MiniCan Experiment 3

Nick Smart, Andy Rance, Bharti Reddy, Paul Fennell, AMEC

Robert Winsley, NDA

November 2012

Svensk Kärnbränslehantering AB
Swedish Nuclear Fuel
and Waste Management Co

Box 250, SE-101 24 Stockholm
Phone +46 8 459 84 00

ISSN 1404-0344
SKB TR-12-09
ID 1336853

Analysis of SKB MiniCan Experiment 3

Nick Smart, Andy Rance, Bharti Reddy, Paul Fennell, AMEC

Robert Winsley, NDA

November 2012

Executive summary

To ensure the safe encapsulation of spent nuclear fuel rods for geological disposal, SKB of Sweden is planning to use a system that consists of an outer copper canister and a cast iron insert (the KBS-3 concept). In 2007 Serco[1] completed the set up of five model canister experiments at SKB's Äspö laboratory and monitoring has continued since. The original aim of the model canister experiments was to examine how corrosion of the cast iron insert inside a copper canister would evolve with time, if water ingress through a small defect in the copper canister were to occur. Serco arranged manufacture and installation of five miniature copper canisters containing cast iron inserts, with 1 mm defects deliberately machined into the copper shell. The experiments use five small-scale model canisters (300 mm long × 150 mm diameter) that simulate the main features of the SKB canister design (hence the project name, 'MiniCan'). The main aim of the work is to examine how corrosion of the cast iron insert will evolve if a leak is present in the outer copper canister. The experiments also included electrochemical equipment to monitor the corrosion behaviour of the model canisters *in situ*. In 2011 one of the experiments, Experiment 3, was removed for analysis. This report presents details of the procedures that were applied and the findings that were obtained from the analysis that was carried out on Experiment 3.

To minimise exposure to air and to keep the contents of the experiment wet until the analysis was carried out, Experiment 3 was extracted from its borehole in August 2011 directly into a transfer tank that was filled with deaerated groundwater and placed in a purpose-built, water-filled and deoxygenated transfer flask. The transfer flask was then transported to the UK for dismantling and examination in a purpose-built anoxic glovebox that contained the appropriate lifting and cutting equipment for handling and sectioning the copper canister and the cast iron insert. The report presents details of the analysis of the water samples taken from the experiment before it was removed, followed by observations of the dismantled experiment and the results from the chemical and physical analytical techniques that were subsequently applied to samples taken from the experiment. Estimates of the corrosion rates of iron and copper were made by analysis of the weight loss specimens and these have been compared and contrasted with the *in situ* corrosion rates measured during the last five years.

The water analysis showed that there had been an increase in the concentration of dissolved iron in the water inside the support cage of the experiment, accompanied by a fall in the pH of the water to approximately 6.6 and a decrease in the hydrogen concentration. Microbial analysis indicated that the surface of the canister was colonised by high concentrations of sulphate reducing bacteria (SRB). When the experiment was opened it was immediately apparent that the majority of the surfaces were covered with a layer of black deposit. The surface of the copper canister had turned black, although the coverage was not uniform. Corrosion product was visible extruding from the machined defect at the top of the canister and to a lesser extent from the machined defect at the bottom of the canister. This report presents the detailed results of the analyses.

The main conclusions from the analysis are as follows:

1. The observed corrosion behaviour in the MiniCan experiment was heavily influenced by extensive sulphate reducing bacteria activity in the groundwater-filled headspace inside the support cage but above the MiniCan. This aqueous phase is not expected to occur next to the canisters in the repository in the presence of highly compacted bentonite.
2. The concentration of dissolved iron measured in water inside the support cage had increased since 2010, leading to a concentration of several 10 s of mgL^{-1}. The concentration of both sulphate and hydrogen had decreased, with an accompanying increase in the concentrations of sulphate reducing bacteria and cultivable heterotrophic aerobic bacteria.

[1] This report presents the results of a programme of research that was carried out by Serco Technical Consulting Services in support of SKB. The Serco Technical Consulting Services business has now been transferred to AMEC plc, UK.

3. The cast iron weight loss coupon in MiniCan Experiment 3 had completely corroded, due to a graphitisation process induced by the presence of sulphate reducing bacteria. Severe corrosion was also observed on the cast iron electrodes, although some residual iron was present at the core of the specimen.
4. The corrosion rate of the cast iron was at least 500 μm yr^{-1}, based on weight loss measurements and electrochemical measurements.
5. The weight loss coupon residue was a mass of graphite and amorphous iron oxide/silicon corrosion product. This corrosion process for cast iron is commonly referred to as 'graphitisation'.
6. The iron released into the groundwater through corrosion had precipitated as a black deposit on all surfaces inside the support cage; it was predominantly amorphous iron sulphide, but it also contained graphitic carbon and a silicon rich phase.
7. The uniform corrosion rate of the copper was estimated to be 0.15 μm yr^{-1}, on the basis of weight loss measurements. This is considerably lower than the corrosion rates measured by electrochemical methods, which are considered unreliable due to the deposition of a layer of conductive iron corrosion product from the iron electrodes and the neighbouring cast iron insert. The copper corrosion product was a mixture of copper oxide and copper sulphide. There were no indications of localised corrosion (i.e. pitting or stress corrosion cracking) on the copper test specimens. Copper specimens exposed directly to the borehole water developed a predominantly copper oxide corrosion product, with only a trace of sulphide present.
8. The outer dimensions of the copper canister from MiniCan Experiment 3 were measured and no changes from the initial design dimensions were detected, indicating that no expansion had occurred due to corrosion of the cast iron insert. No expansion was observed in the copper-cast iron sandwich specimen either.
9. Non-uniform blackening of the outer surface of the copper canister had occurred and it was concentrated on areas facing the holes in the inner cylinder of the support cage. The defects in the copper canister had become blocked with corrosion product, but locally high rates of corrosion of the cast iron insert were observed opposite the machined defects in the copper canister. The corrosion process in the half-height area of the annulus was different to that opposite the defects, with the major corrosion product being an iron and chlorine-rich phase.
10. Copper sulphide crystals were observed on the surfaces of the canister. The copper and cast iron surfaces that were in close proximity (e.g. between the cast iron insert and the copper canister, and between the cast iron and copper pieces in the sandwich specimen) had corroded less than fully exposed surfaces (e.g. the weight loss specimen), suggesting no galvanic corrosion between the two materials.

Contents

1 Introduction

To ensure the safe encapsulation of spent nuclear fuel rods for geological disposal, SKB of Sweden is considering using a system that consists of an outer copper canister and a cast iron insert, commonly referred to as the KBS-3 design. In 2007 Serco completed the set up of five model canister experiments at SKB's Äspö laboratory and monitoring has continued since. The original aim of the model canister experiments was to examine how corrosion of the cast iron insert inside a copper canister would evolve with time, if leakage through a small defect in the copper canister were to occur. Serco arranged manufacture and installation of five miniature copper canisters containing cast iron inserts, with 1 mm defects deliberately machined into the copper shell. The experiments also included electrochemical equipment to monitor the corrosion behaviour of the model canisters *in situ*. The detailed design of the experiment is described in Smart et al. (2009) and the set up and results obtained to date are summarised in Smart et al. (2011a, b, 2012). This report should be read in conjunction with the most recent progress report for a summary of the experimental setup and latest data from the monitoring programme (Smart et al. 2012).

It was agreed at the expert advisory group meeting held in June 2009 that Experiment 3 should be removed for analysis and a separate planning document was prepared for the removal and analysis of this experiment. The purpose of the current document is to present and discuss the results from the analysis programme that was carried out on Experiment 3, based on the original planning document. The project plan for the removal and analysis of Experiment 3 is shown in Figure 1-1 and this report is structured around the sequence of events that was carried out in accordance with the project plan.

The overall objective of the plan was to carefully extract Experiment 3 from its borehole, whilst minimising exposure to oxygen in the air. This was achieved by extracting the experiment directly into a tank (the 'transfer' tank) of groundwater that was actively deoxygenated by sparging it with a stream of nitrogen. Whilst still underwater the experiment was then placed into a specially designed, sealed and water-filled transfer flask that was used to transport the experiment to the UK for analysis in a specially constructed inert-gas purged glovebox. Once in the glovebox the experiment was carefully dismantled and various samples were prepared for analysis without exposure to the atmosphere. A description of the designs, procedures, results and observations made at each stage of implementing the plan are presented below.

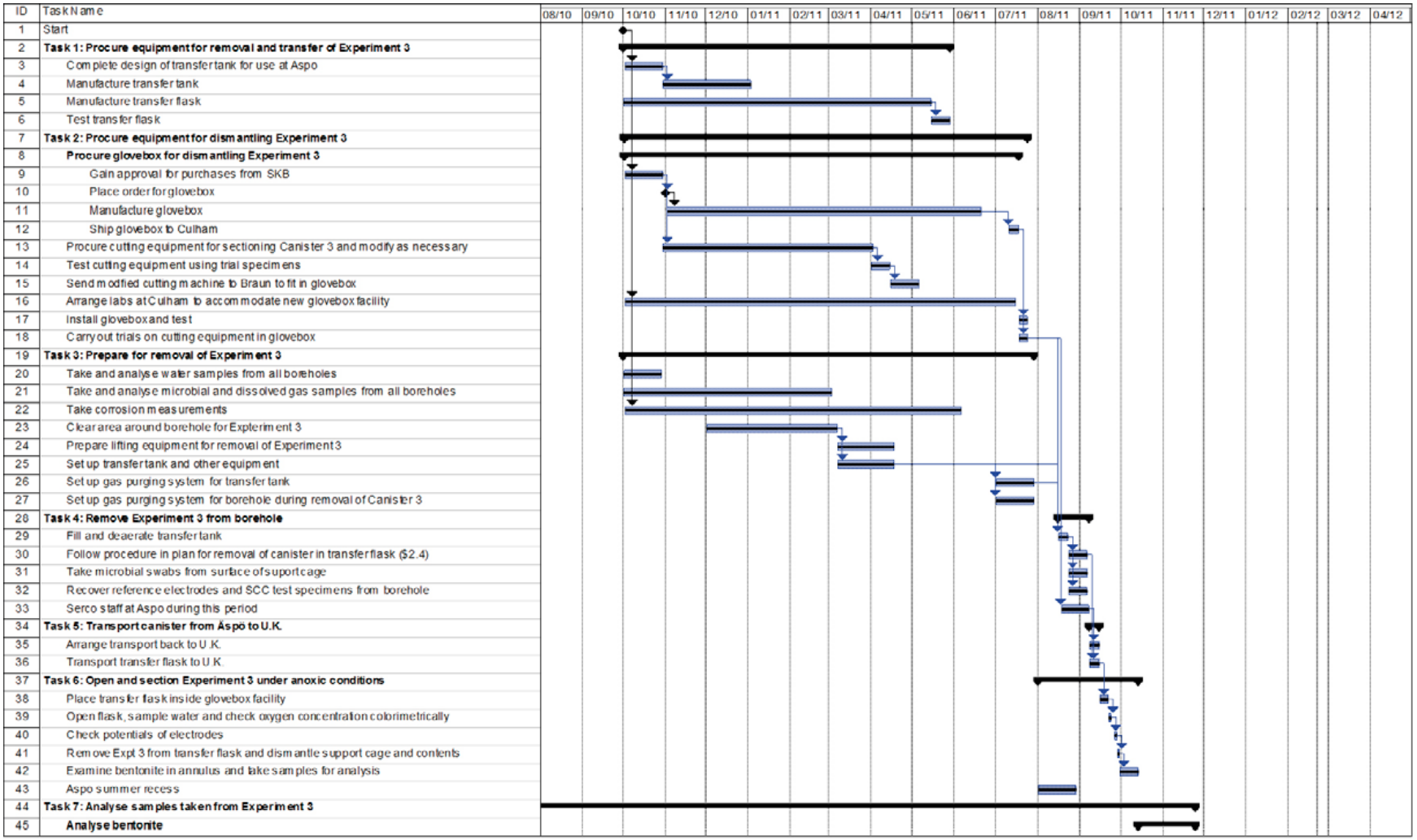

Figure 1-1. *Project plan for removal and analysis of Experiment 3 (the black bars indicate that the task is complete).*

ID	Task Name
46	Apply analytical techniques as agreed with SKB - see plan document
47	**Analyse corrosion coupons**
48	Visual examination and photography of coupons inside glovebox
49	Measure weight gain of coupons under inert gas
50	Prepare coupons for Raman analysis in glovebox
51	Analyse corrosion product by Raman analysis and XRD
52	Measure weight loss of iron and copper coupons
53	SEM examination of coupons
54	**Analyse electrodes**
55	Take microbial swabs from electrodes
56	Prepare electrodes for Raman analysis in glovebox
57	Analyse composition of surface films (Raman, SEM/EDX, XRD, etc)
58	**Examine sandwich specimens**
59	Check dimensions of sandwich specimens
60	Dismantle specimens in glovebox
61	Examine corrosion products using Raman spectroscopy
62	Section copper and cast iron specimens and check for localised corrosion
63	**Examine model canister**
64	Visual examination and photography of external surface of copper canister
65	Check dimensions of copper canister
66	Disect model canister and map distribution of corrosion product on CI insert
67	Raman analysis of samples of copper and cast iron from model canister
68	Prepare and examine metallographic samples from various locations on copper canister
69	Surface profilometry of copper surface at various locations
70	Examine lid region of cast iron insert
71	**Examine SCC specimens**
72	Visual and photographic examination of SCC test specimens
73	Mount and polish SCC test specimens for metallographic examination
74	**Task 10: Project management, preparation of status reports, reporting**

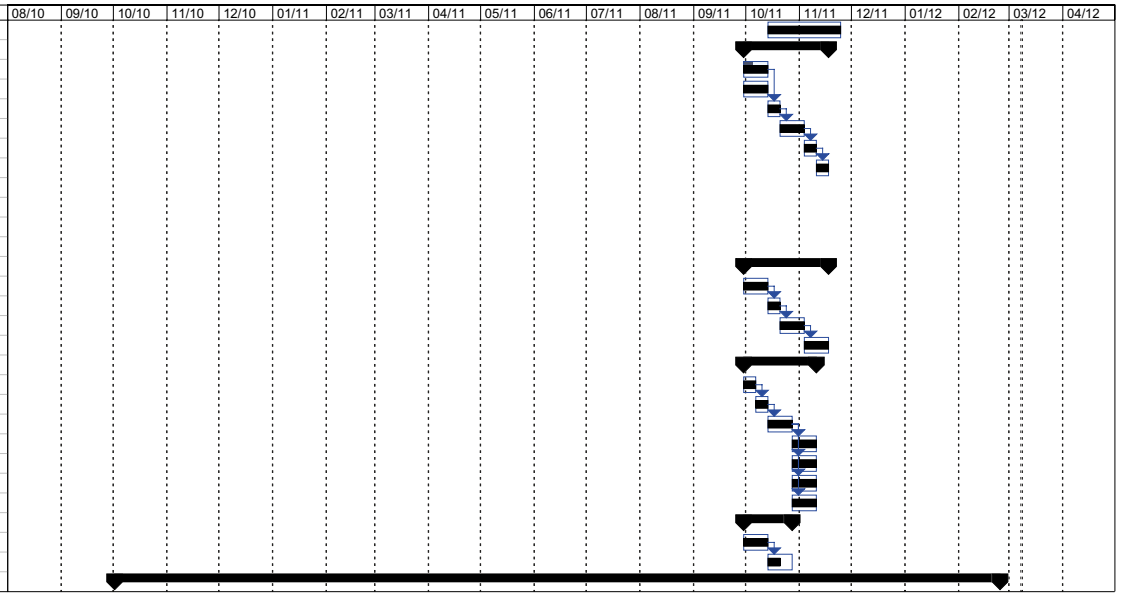

Figure 1-1 (continued). *Project plan for removal and analysis of Experiment 3 (the black bars indicate that the task is complete).*

2 Equipment for removal and transfer of Experiment 3

The transfer tank for removal of Experiment 3 was designed and manufactured by SKB (Figure 2-1 and 2-2). The stainless steel tank was attached and sealed to the borehole flange by the means shown in Figure 2-1 and 2-2. Photographs of the tank are displayed in Figure 2-3, 2-4 and 2-5. The transfer flask was designed by Serco and manufactured by SKB. The design is shown in Figure 2-6 and photographs of the flask are shown in Figure 2-7. It consisted of a stainless steel vessel with a double O-ring seal on the lid flange. The interior was also equipped with guide fins to prevent the support cage moving inside the transfer flask during transport and to allow space around the cage for the gas feed pipe and good access of groundwater to all sides of the experiment, and to aid the deaeration process. The flask was equipped with gas purging that was delivered via a $^{3}/_{8}$" (~9.5 mm) internal diameter stainless steel tube and a perforated false base. The transfer flask was tested before use by SKB's contractors to ensure leak tightness, by pressurising it to three bar pressure and monitoring the pressure for one hour.

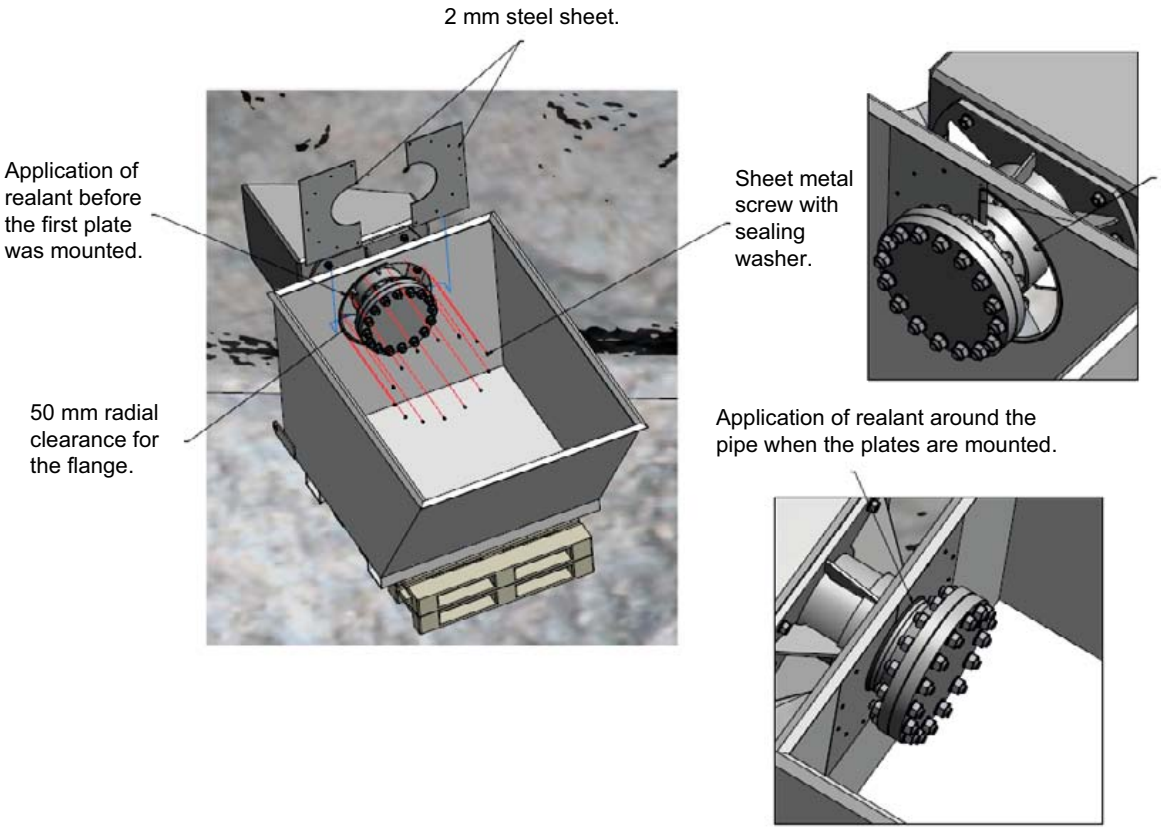

Figure 2-1. *3D CAD drawing of the transfer tank.*

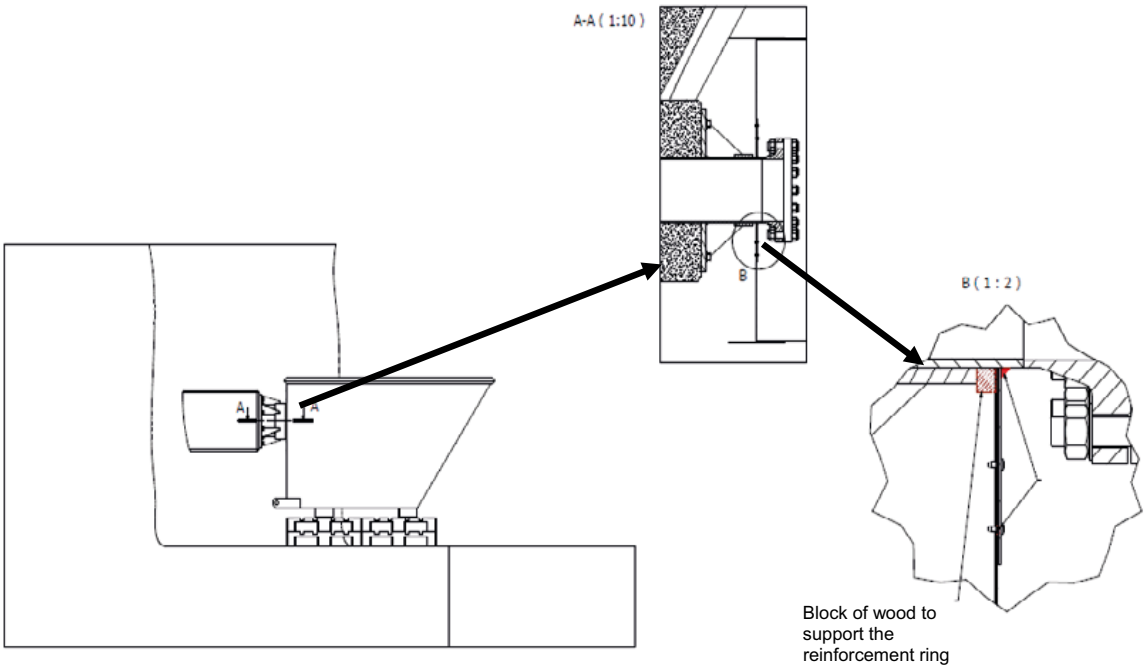

Figure 2-2. *Sealing arrangement for flange to transfer tank.*

Figure 2-3. *Photograph of transfer tank set up to enable MiniCan Experiment 3 to be removed and transferred into the transfer flask ready for transport without drying or exposure to air.*

Figure 2-4. *Photograph of transfer tank to flange coupling.*

Figure 2-5. *Photograph from above the transfer tank showing the borehole flange below the waterline.*

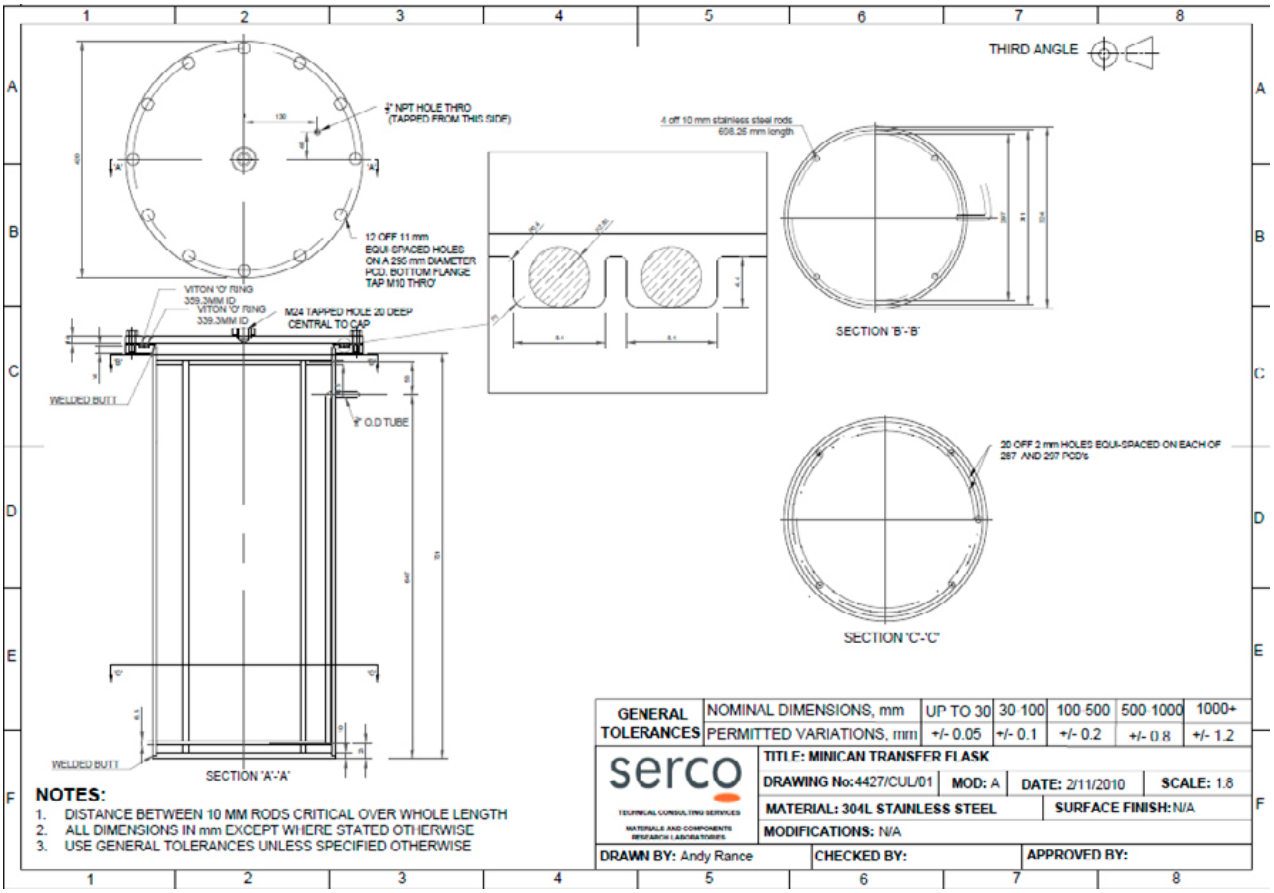

Figure 2-6. *Design of transfer flask for MiniCan Experiment 3.*

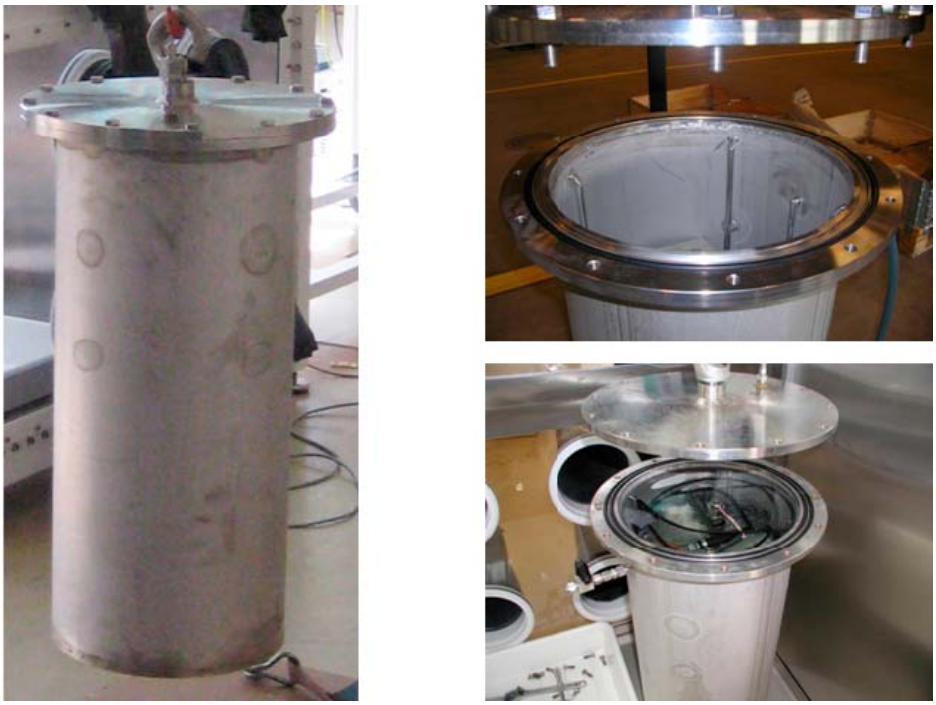

Figure 2-7. *Photograph of transfer flask used for anaerobic transport of MiniCan Experiment 3 (left hand side); (top right) view inside the flask showing two supporting fins and the purge pipe; (bottom right) opening flask inside glovebox showing the double 'O' ring seal, the electrochemical connection cables coiled on top of model canister experiment, reference electrodes, borehole specimens and ball of carbon steel wire for scavenging any residual oxygen.*

3 Equipment for dismantling Experiment 3

In order to dismantle Experiment 3 without exposure to the atmosphere it was necessary to design and procure a purpose-built glovebox that would accommodate the support cage and suitable lifting and cutting equipment. The glovebox facility was specified by Serco and manufactured by MBRAUN Intergas-Systeme GmbH (a global company specialising in glovebox technology) at their German manufacturing site in Garching, under contract to SKB. The glovebox consisted of two main compartments, one large one for conducting cutting operations, which also included a lifting system for handling the transfer flask and removing the MiniCan experiment from the transfer flask, and a smaller compartment connected to the main compartment for specimen preparation. The design of the glove box is shown in Figure 3-1 and photographs of the glovebox and the lifting and cutting equipment in the glovebox are shown in Figure 3-2 and 3-3 respectively. The rotary cutting wheel was an Evolution Rage 3 mitre saw with a base modified to include a purpose-built vice that could hold the canister in a number of orientations while cutting operations were carried out. Before sectioning the MiniCan experiment, Serco carried out trials on the cutting equipment using a dummy model canister consisting of a cylinder of cast iron mounted inside a copper cylinder, as shown in Figure 3-4.

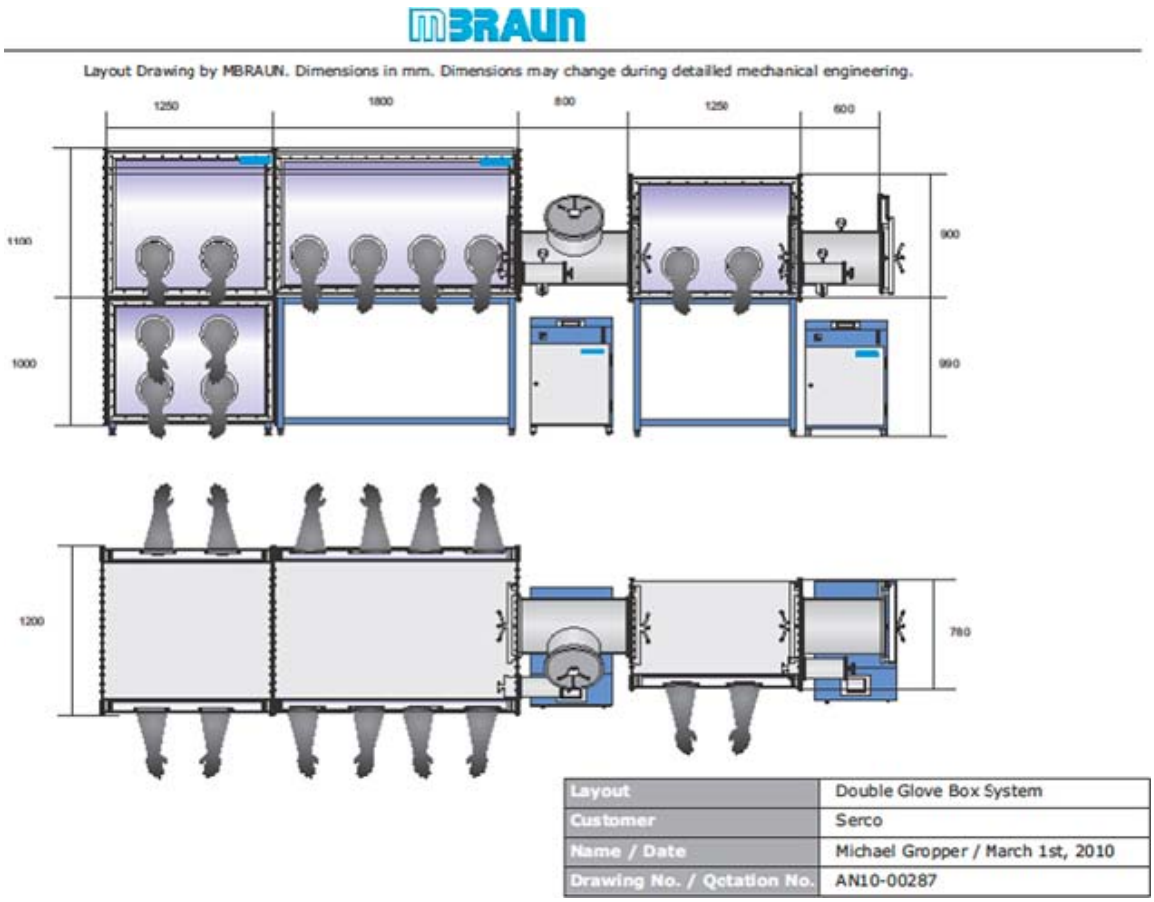

Figure 3-1. *Design of purpose-built glovebox for dismantling and analysis of Experiment 3.*

Figure 3-2. *Photographs of glovebox in operation.*

Figure 3-3. *Photograph of lifting and cutting equipment inside glovebox.*

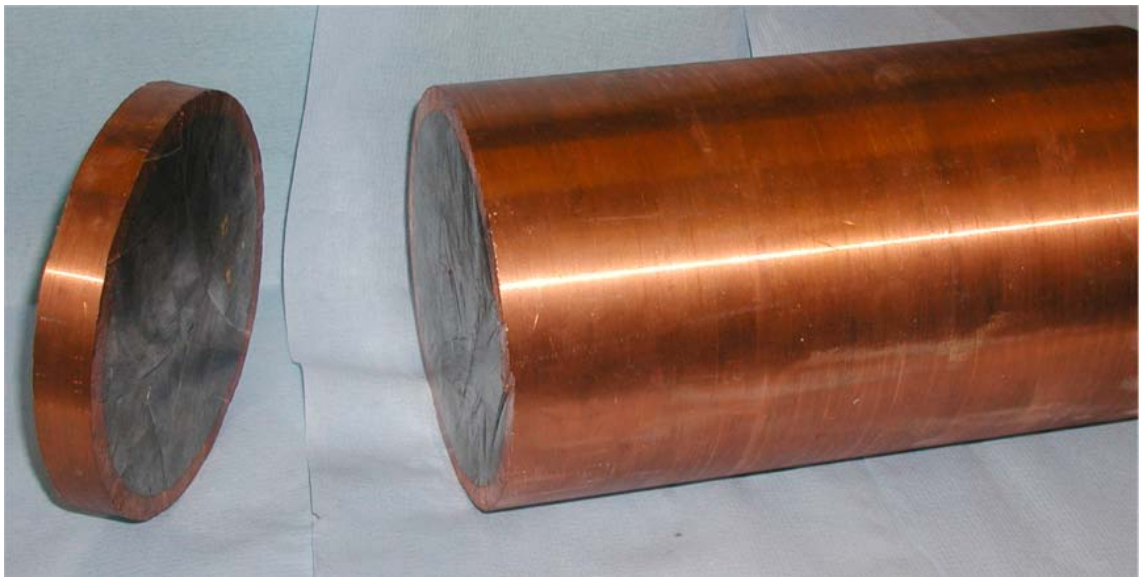

Figure 3-4. *Photograph of specimen used for cutting trials on copper canister with a cast iron insert.*

4 Preparation for removal of Experiment 3

Prior to removal of Experiment 3 from the borehole a set of water samples was collected from the headspace above the miniature canister (using the stainless steel pipe connected to the outer borehole flange) and analysed by staff at SKB using the procedures applied in previous water analysis campaigns (Smart et al. 2012). The results from these analyses are given in Table 4-1. Similarly, microbial and gas analysis was carried out on water samples taken from the Experiment 3 borehole by Microbial Analytics. The analytical techniques and the results from these analyses are presented in Hallbeck et al. (2011). Comparison of the results of the analysis with previous analyses (Smart et al. 2012) shows the following notable features:

- The sulphate concentration inside the support cage of Experiment 3 had fallen from 400 mgL^{-1} in December 2010 to 270 mgL^{-1}, suggesting that some had been consumed by sulphate reducing bacteria (SRB) activity.
- The dissolved iron (II) concentration had increased from a value of 9.91 mgL^{-1} in December 2010 to 39.17 mgL^{-1} in August 2011, indicating that the corrosion rate of the cast iron had increased. Note that differences were observed between the total amount of iron measured by ICP and by wet chemical analysis (see Table 4-1).
- The strontium concentration had increased from 41.8 mgL^{-1} to 48.8 mgL^{-1}; the reasons for this increase are not currently known, but note that the main sources of strontium in the experiment are the groundwater, which contains 40–50 mgL^{-1} and the MX-80 bentonite, which contains ~200–300 ppm by dry weight (Åkesson et al. 2012).
- The pH had fallen from 7.3 in December 2010 to 6.6–7.0 in August 2011 (two separate pH readings were provided by SKB, Table 4-1).
- There had been a marked decrease in the hydrogen concentration since December 2010 (> 54.1 μlL^{-1} to only 1.2 μlL^{-1}), suggesting that the SRB population had consumed any hydrogen produced due to iron corrosion. This would be consistent with the observation that the sulphate concentration had also decreased significantly.
- The carbon dioxide concentration had fallen to 0.4 mlL^{-1} compared to 0.68 mlL^{-1} in December 2010.
- Two values of phosphate concentration are given. The first value (0.0009 mgL^{-1}) was obtained using ion chromatography, whereas the second value (0.002 mgL^{-1}) was obtained after the sample was hydrolysed with acid. The second value was higher because groundwater can form precipitates that bind phosphate. When the water is hydrolysed the precipitate dissolves and the phosphate is released.
- The predominant organic gas was methane with trace amounts of ethylene.
- The concentration of both the SRB and the cultivable heterotrophic aerobic bacteria (CHAB) in the water from within the Experiment 3 support cage had increased since the 2010 measurement (Hallbeck et al. 2011). Both the SRB and CHAB concentrations were the highest values measured in Experiment 3 since sampling started in 2007. Further detailed analysis of the microbial species present is given in Hallbeck et al. (2011) and is not repeated here.

Electrochemical corrosion rate measurements were taken just before Experiment 3 was removed from its borehole and these are reported in Smart et al. (2012).

The area in the tunnel in which the MiniCan experiments are located was cleared of equipment and a mobile crane was commissioned for lifting the experiment out of its borehole. The transfer tank was attached to the borehole flange (Figure 2-1 to 2-4) and filled with water that was transported from a borehole on a different level at Äspö (i.e. the transfer tank was filled with groundwater, but not with water directly from the Experiment 3 borehole itself). A gas purge system, consisting of a perforated plastic pipe attached to a bank of nitrogen cylinders was set up so that the oxygen concentration in the water tank could be reduced prior to removal of the experiment.

Table 4-1. Results of water analysis for sample taken from inside the canister of Experiment 3 on 22nd August 2011.

Ion	Concentration	Species or measurement	Concentration or result
Cl (mgL^{-1}) ± 5%	8,262	Cu ($\mu g\ L^{-1}$) ± 0.67	2.3100
Ca (mgL^{-1}) ± 296	2,470	Ni ($\mu g\ L^{-1}$) ± 0.53	2.2400
Na (mgL^{-1}) ± 314	2,350	Cr ($\mu g\ L^{-1}$) ± 0.175	0.4070
SO_4 (mgL^{-1})[1] ± 12%	271	Cd ($\mu g\ L^{-1}$) ± 0.0375	0.0520
S (mgL^{-1})[2] ± 16	126	He (mlL^{-1})	7.81
Mg (mgL^{-1}) ± 8.3	67.70	Ar (mlL^{-1})	0.61
Fe (mgL^{-1})[3] ± 6.5	49.60	N_2 (mlL^{-1})	52.1
Sr (mgL^{-1}) ± 6.06	48.80	CO_2 (mlL^{-1})	0.445
Fe(tot) (mgL^{-1})[3]) ± 8%	39.88	O_2 (mlL^{-1})	Bd
Fe(II) (mgL^{-1})[3]) ± 8%	39.17	CH_4 (mlL^{-1})	0.192
Br (mgL^{-1}) ± 15%	45.27	H_2 (μlL^{-1})	1.18
HCO_3 (mgL^{-1}) ± 4%	34.20	CO (μlL^{-1})	0.82
K (mgL^{-1}) ± 1.5	12.30	C_2H_2 (μlL^{-1})	< 0.10
Si (mgL^{-1}) ± 0.70	4.83	C_2H_6(μlL^{-1})	0.26
Li (mgL^{-1}) ± 0.231	1.78	C_2H_4(μlL^{-1})	< 0.10
F (mgL^{-1}) ± 13%	0.99	C_3H_8(μlL^{-1})	< 0.10
Mn (mgL^{-1}) ± 0.172	0.794	C_3H_6(μlL^{-1})	< 0.10
Ba (mgL^{-1}) ± 0.045	0.189		
Sulphide (mgL^{-1}) ± 32%	0.045	Gas volume(mlL^{-1})[4]	61.10
Total NO_2 and NO_3 (mgL^{-1})[5] ± 0.0002	0.0022	Volume of water extracted (g)	194.00
NO_2 (mgL^{-1}) ± 0.0001	0.0012	Acetate (mgL^{-1})	3.4
NO_3[6] (mgL^{-1})	0.0011	pH ± 0.10	6.62/6.96
PO_4 (mgL^{-1}) ± 0.0005	0.0009	Conductivity mS/m ± 5%	2,210/2,270
PO_4 (mgL^{-1})[7] ± 0.0005	0.0020		

[1] Ion chromatography measurement.

[2] Inductively Coupled Plasma Discharge spectroscopy analysis for sulphur.

[3] Fe is measured by Inductively Coupled Plasma Discharge spectroscopy by ALS Scandinavia, Sweden with the other metals; Fe(tot) and Fe(II) are measured at Äspö URL by wet chemical colorimetric methods (To et al. 1999).

[4] Details of the methods used for the gas analysis are given in Lydmark and Hallbeck (2011).

[5] This refers to the combined concentration of nitrite and nitrate.

[6] Calculated from the difference between total NO_2 and NO_3, and NO_2.

[7] An alternative analytical method was used for this result. The value was obtained after the sample had been "acid hydrolysed".

5 Removal of Experiment 3 from Äspö URL

In summary, the main steps concerning removal of MiniCan Experiment 3 from its borehole, after attachment of the transfer tank to the borehole flange, and its transfer to Serco's Culham Laboratories are listed below. Serco staff visited Äspö URL on 22nd August 2011 and the sequence of events for removing the canister is listed below. Figure 5-1 shows a photograph of the MiniCan being extracted from its borehole into the water-filled transfer tank.

1. On Monday 22nd August 2011 the transfer tank was filled using three 1 m^3 loads of groundwater that were taken from elsewhere in the URL. The reason for this was that the rate of water supply from the Experiment 3 borehole was believed to be too slow to fill the transfer tank to the required level in the time available. The tank was filled to a height such that the flange on the borehole was submerged, as shown in Figure 2-5.
2. The water in the transfer tank was sparged with nitrogen in order to reduce the concentration of dissolved oxygen in the water to which the experiment was exposed when it was withdrawn from the borehole. The concentration of dissolved oxygen was measured with an oxygen probe (Cole-Parmer dissolved Oxygen meter cat No: RZ-53014-65). The tank was purged overnight with a tarpaulin covering the tank. By the morning the dissolved oxygen concentration had reduced to 0.00 ppm. The tarpaulin cover was removed and operations on removing Experiment 3 commenced at 10.14 am on 23rd August 2011. After this the dissolved oxygen concentration slowly increased to approximately 1 ppm while operations were underway. This was unavoidable because of the need for workers to be present in the tanks.
3. Microbial Analytics took some water samples from the transfer tank, so that the microbial activity could be assessed (Hallbeck et al. 2011). It was necessary to reduce the water level in the tank to allow man-access by siphoning some water out of the tank. Two workers then entered the tank, equipped with full-length waders and personal low oxygen alarms (Figure 5-1). By ~11.00 am the bolts holding the flange to the entrance to the borehole had been removed and the tubes and cables passing into the experiment were cut. It was necessary to remove some more water from the tank because of the additional water entering the tank from the opened borehole.
4. The MiniCan assembly was then withdrawn from the borehole using the pull rod that was already attached to the top lid of the support cage. As the pull rod was withdrawn into the tank it was cut twice using a pipe cutter, because the pull rod was longer than the length of the tank. The SCC test specimens, the Silvion reference electrode and the metal oxide E_h probe that were suspended from the pull rod were recovered.
5. When the support cage assembly reached the mouth of the borehole a strop suspended from a crane was used to take the weight of the support cage. At this stage microbial swabs were taken from the surface of the support cage using swabs supplied by staff from Microbial Analytics (Hallbeck et al. 2011). There were no obvious signs of corrosion, biofilms or extruded bentonite on any of the stainless steel components (i.e. the support cage, or any of the pipes or fittings).
6. The support cage assembly was then lowered deeper into the tank using the strop and slid into the transfer flask, which had been pre-positioned at a suitable angle underwater in the transfer tank. The oxygen concentration inside the transfer flask at this point was 1.4 ppm, but the interior was then purged at a high flow rate using nitrogen.
7. The transfer tank was allowed to fill to a higher level, using water from the borehole, and the transfer flask was then turned to the vertical position. The E_h probe and SCC test specimens were placed into groundwater-filled plastic bottles and placed into the transfer flask for transport to the UK for analysis, together with the Silvion reference electrode and a coil of steel wire to act as an oxygen getter during transport. The lid of the transfer flask was then loosely bolted on and rapidly purged with nitrogen for ten minutes before the lid was tightened and the flask was then further purged at a slower rate for a period of two hours before the flask was sealed. The transfer flask was then placed into a wooden crate for transport to the UK by a specialist transport company and it was delivered to Serco's Culham laboratories on 31st August 2011.

8. The transport flask was transferred into the operating purpose built glove-box at Culham laboratories in UK on 1st September 2011, together with the equipment necessary for taking samples from the canister, including microbial swab equipment provided by Microbial Analytics. A small mobile hydraulic crane was used to lift the transfer flask into the large port at the end of the glovebox (Figure 5-2).

Figure 5-1. *Removal of Experiment 3 from its borehole at Äspö URL.*

Figure 5-2. *Transfer flask for MiniCan experiment being lifted into glovebox for dismantling and analysis. The right hand photograph shows the transfer flask inside the glovebox, the control for the lifting equipment and the sampling equipment for the microbial analyses in the background.*

6 Dismantling Experiment 3

The next stage of the programme was to remove the MiniCan experiment from the transfer flask and examine and analyse samples taken from the experiment under anoxic conditions to ensure that the samples were not affected by exposure to air. This section describes the steps taken and the observations made while the experiment was dismantled. All operations were recorded by still photography and/or video recording.

Opening of the transfer flask (Figure 6-1) and dismantling the experiment commenced on 2nd September 2011 when the oxygen concentration in the glovebox had reduced to less than 0.1 ppm by volume. The support cage was lifted out of the transfer flask using the overhead crane in the glovebox (see Figure 6-2). When the support cage was extracted from the transfer flask it was seen to have a shiny appearance, indicating that the external surface of the stainless steel support cage had not suffered from significant corrosion, although some black deposit was observed around the Swagelok fittings in the lid of the support cage. The water inside the transport flask was clear and the steel wire that had been placed in the flask as an oxygen getter was still shiny (Figure 6-1), indicating that there had not been a significant amount of oxygen ingress into the water during transport. This was confirmed by measuring the oxygen concentration in the water using the portable oxygen probe that had been used at Äspö URL for monitoring the oxygen concentration in the transfer tank. The dissolved oxygen level indicated immediately upon opening the flask was 0.04 ppm. The oxygen concentration was also checked colorimetrically using a CHEMetrics dissolved oxygen comparator C-7511 with a range of 0 to 20 ppb. The level indicated by this technique was 0 ppb.

Before opening the support cage the external surfaces were swabbed for microbial activity by Microbial Analytics (Hallbeck et al. 2011). The results from analysis of the swabs taken from the support cage at Äspö are described in detail in (Hallbeck et al. 2011) and are not repeated here. A layer of green deposit was observed on the upper surface of the support cage lid and this was removed using swabs (see Figure 6-3).

The oxygen level in the glovebox was less than 0.1 ppm (by gas volume) when the transfer flask was opened. On opening the transfer flask potentials of the various sensor electrodes were measured against the Silvion reference electrode recovered from Experiment 3 borehole and a Hg/HgO master reference electrode stored at Culham. The results from these measurements are given in Table 6-1; they show good agreement between the measurements made in the laboratory compared to the measurements made at Äspö URL.

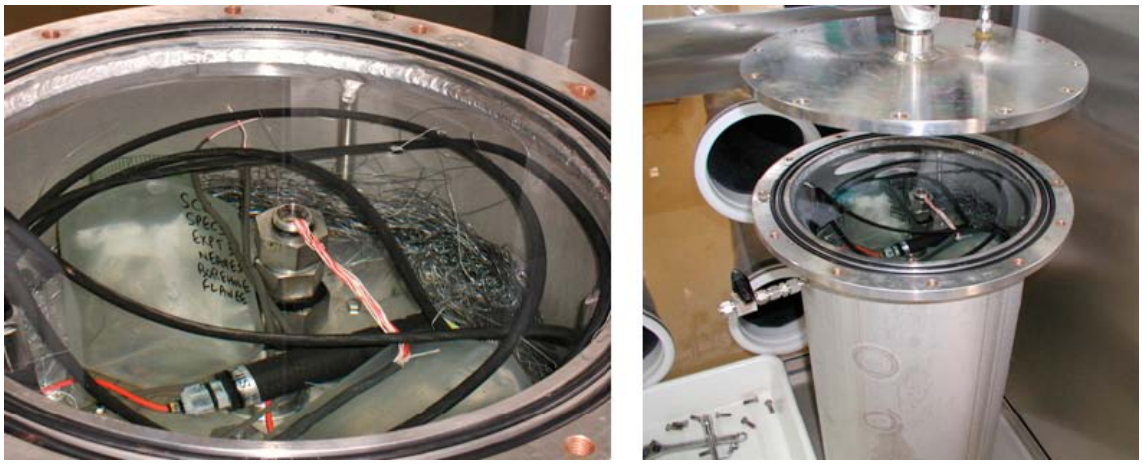

Figure 6-1. *Photographs of the inside of the groundwater-filled transfer flask, showing the Silvion reference electrode, Eh probe, packaged stress corrosion test pieces and steel wire oxygen getter resting on the top of the support cage.*

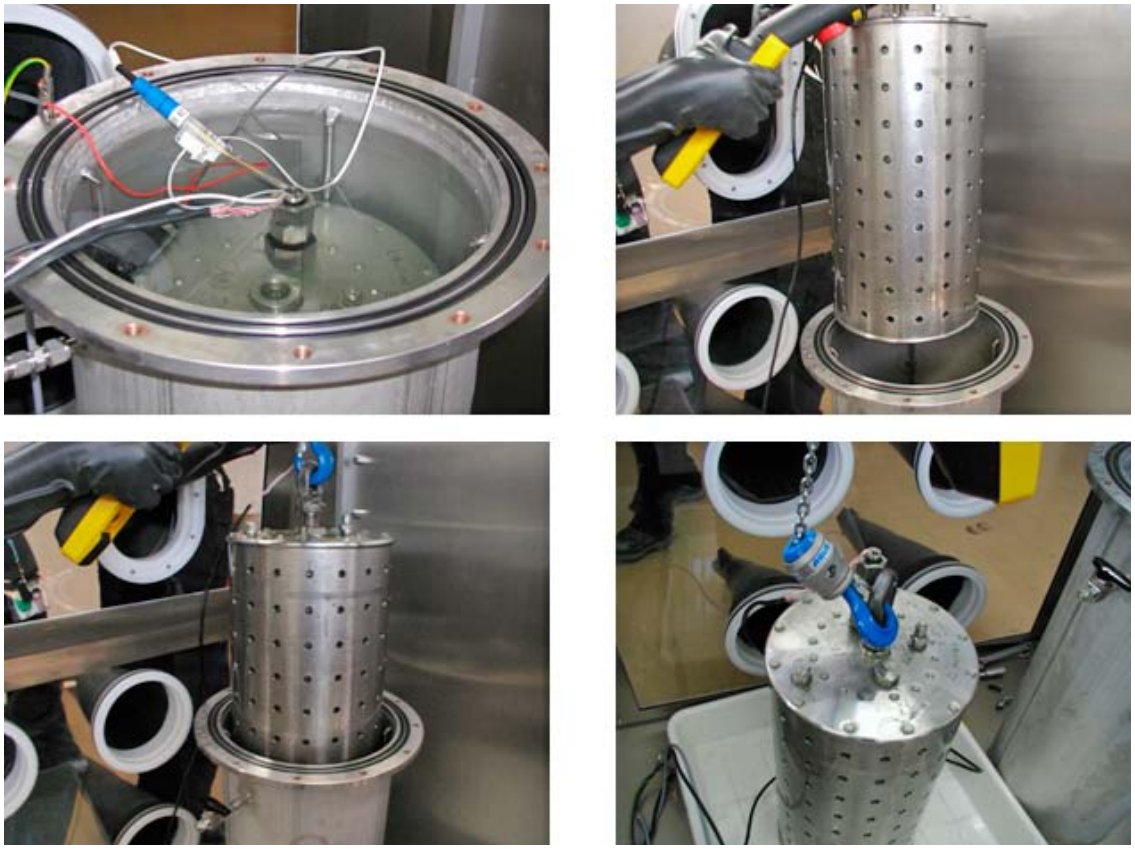

Figure 6-2. *Removing the support cage from transfer flask. The top left hand photograph shows measurements in progress to check the potential values of the electrodes and sensors.*

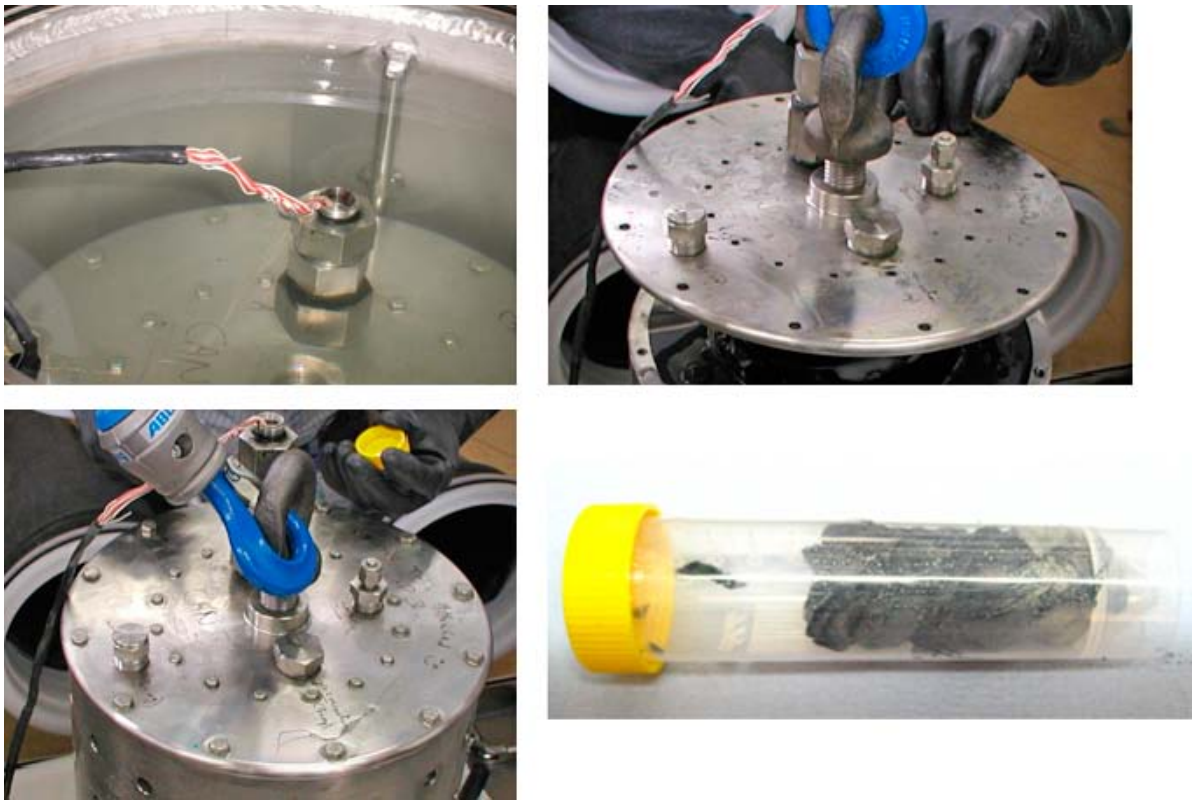

Figure 6-3. *Photographs of lid of support cage when it was removed from the transfer flask showing: presence of thin patchy film on surface, black deposit around the stainless steel fitting where it enters the lid (top left hand photo) and swabs taken from surface.*

Table 6-1. Electrode potential measurements taken on opening transfer flask in glovebox, with respect to the Silvion electrode recovered from the Experiment 3 borehole and with respect to a Hg/HgO master reference held at Culham laboratory, UK. Final readings from the in situ monitored data are also included. The Silvion reference electrode from Experiment 3 appears to have failed in the removal process. All data have been adjusted to vs standard hydrogen electrode, SHE, as shown in parentheses.

Electrode	Wire colour	Electrode Potential (mV vs Silvion recovered from Experiment 3[1], vs SHE in brackets)	Electrode Potential at Culham (mV vs Hg/HgO[2], vs SHE in brackets)	Final electrode potential reading at Äspö (mV vs Silvion, vs SHE in brackets)
Cu 1	Blue	27.5 (284.5)	–645.0 (–487.0)	–627 (–370.0)
Cu 2	Light blue	11.3 (268.3)	– 649.4 (–491.4)	NA
Fe 1	Orange	14.0 (271.0)	– 646.2 (–488.2)	–653 (–396.0)
Fe 2	Mauve	14.4 (271.4)	– 644.0 (–486.0)	NA
Pt	White	7.2 (264.2)	– 648.2 (–490.2)	–624 (–367.0)
Can	Yellow	47.6 (304.6)	– 615.3 (–457.3)	–578 (–321.0)
Au	Black	11.6 (268.6)	– 645.5 (–487.5)	–640 (–383.0)
RE 1	Red	5.1 (262.1)	– 647.1 (–489.1)	NA
RE 2	Green	5.7 (262.7)	– 652.7 (–494.7)	NA

Note: NA = Not Applicable (Cu 2 and Fe 2 were only used for electrochemical noise measurements and were not routinely monitored. RE1 and RE2 were not functioning properly during the in situ experiment at Äspö).

[1] Silvion reference electrode recovered from Experiment 3. Measured against Hg/HgO: –656 mV. Calibrated against new Silvion before removal from borehole :+60 mV.

[2] Hg/HgO master reference electrode at Culham laboratory.

For comparison with later photographs of the MiniCan experiment the original condition of the components of the experiment are shown in Figure 6-4 and 6-5. The lid on the support cage was unbolted and slowly lifted using the overhead crane (see Figure 6-6). The striking feature about the appearance of all the components inside the support cage when the lid was removed was that they were all covered in a layer of black deposit. The bentonite in the annulus of the support cage, which had originally been present in pellet form (see Figure 6-4), had become a homogeneous mass, formed by swelling of the bentonite, with no indications of the original boundaries between the bentonite pellets (see Figure 6-7) or channeling in the bentonite. No further analysis of the bentonite was carried out, but samples were removed by Microbial Analytics for microbial analysis (Figure 6-7), as reported in Hallbeck et al. (2011). The bentonite had the consistency of butter, with some reddish staining in the bentonite and a black ring on the inner and outer surfaces of the bentonite. The support cage containing the bentonite mass was returned to SKB for storage and/or further analysis. Microbial Analytics also took swabs from the surface of the copper canister and the results are given in Hallbeck et al. (2011).

The photographs in Figure 6-8 and 6-9 show the appearance of the sensors and electrodes on the nylon support rack that was located on top of the copper canister inside the support cage. It can be clearly seen that all the surfaces were covered with a layer of black material. The iron surfaces appeared to have a thicker layer of black material on them than the copper surfaces. The nylon support rack was disconnected from the lid of the support cage and placed on a supporting rack inside the glovebox for future dismantling and analysis. It had some bare patches, where the black material had not adhered to the surface.

Figure 6-4. *For comparison with later photographs, these photographs show the original condition of the support cage, bentonite pellets and copper canister in 2006 before the start of the experiment in the Äspö URL.*

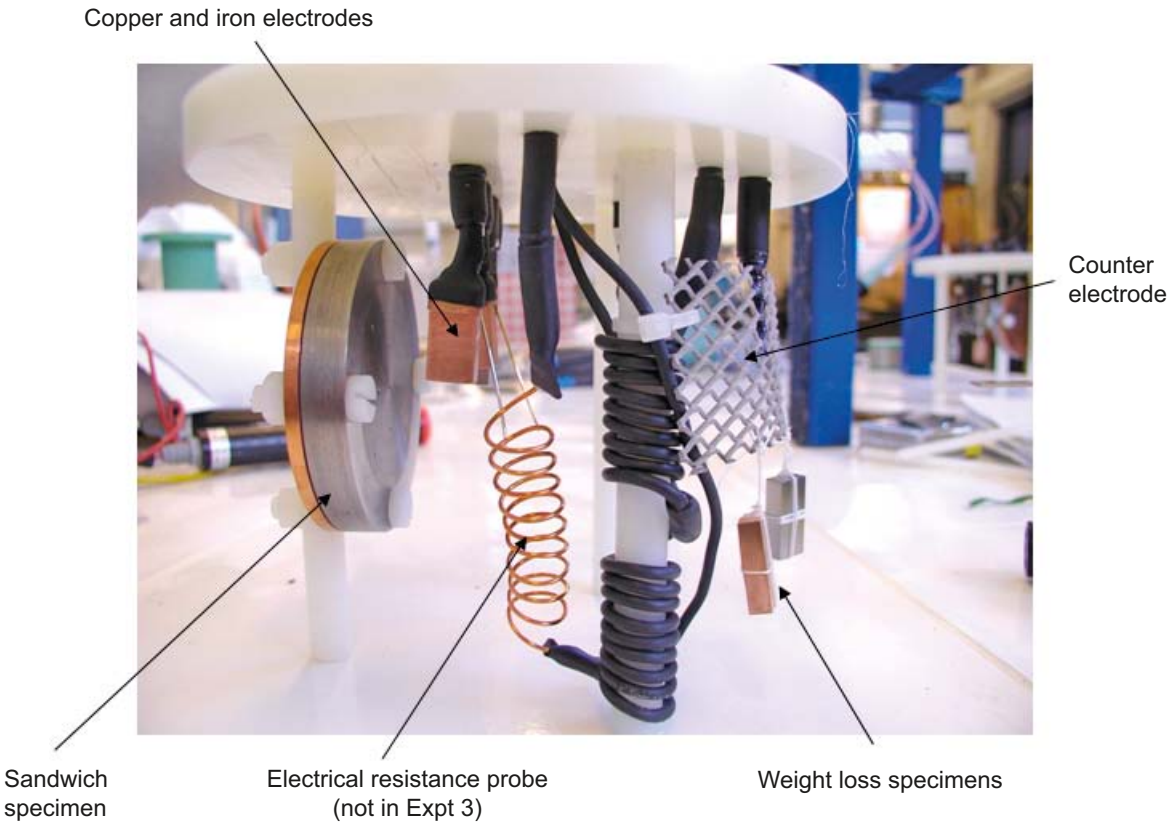

Figure 6-5. *For comparison with later photographs, these photographs show the original condition of the sensors on the support rack above the copper canister in 2006 before the start of the experiment in the Äspö URL.*

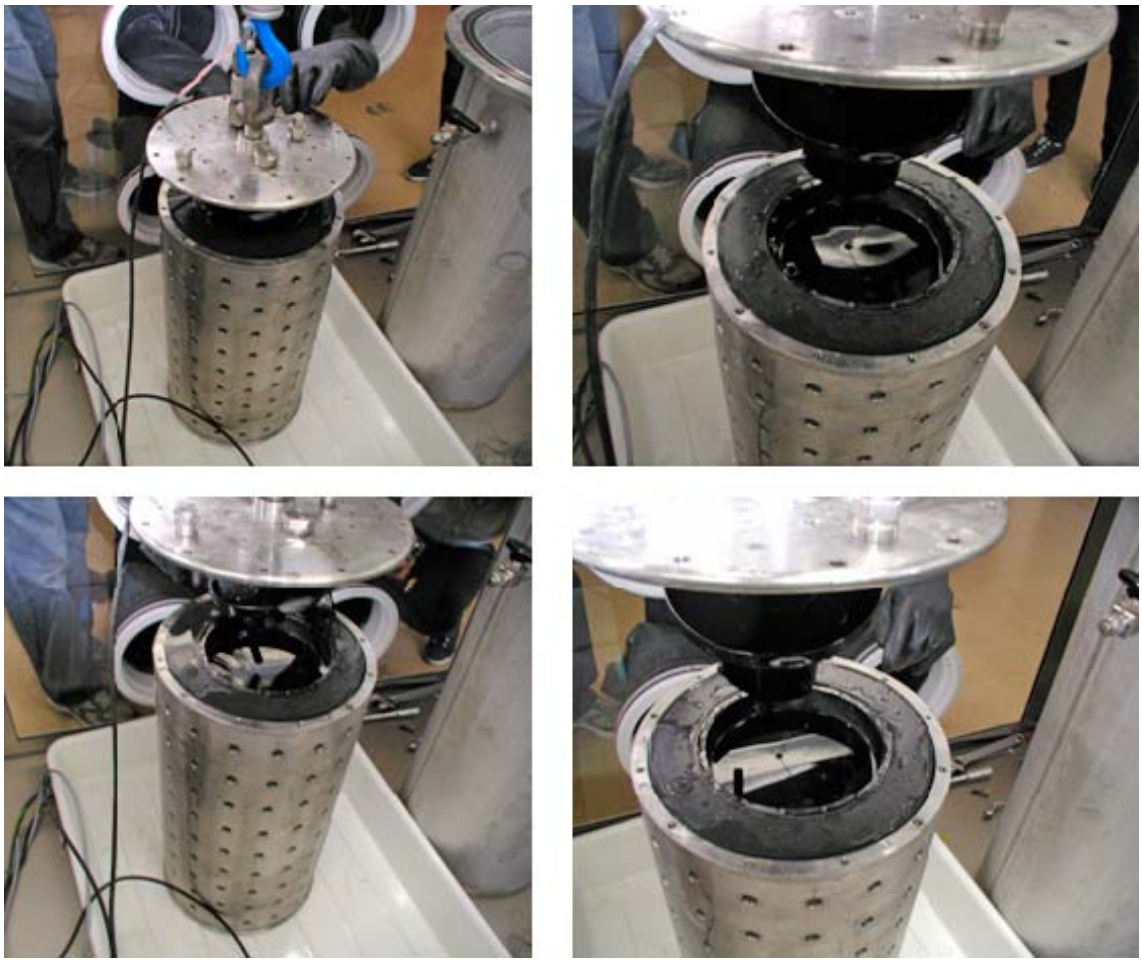

Figure 6-6. *Opening the support cage inside the anoxic glovebox.*

Figure 6-7. *Photographs of the bentonite in the annulus of the support cage. The right hand photograph shows a sample of bentonite being taken for analysis by Microbial Analytics.*

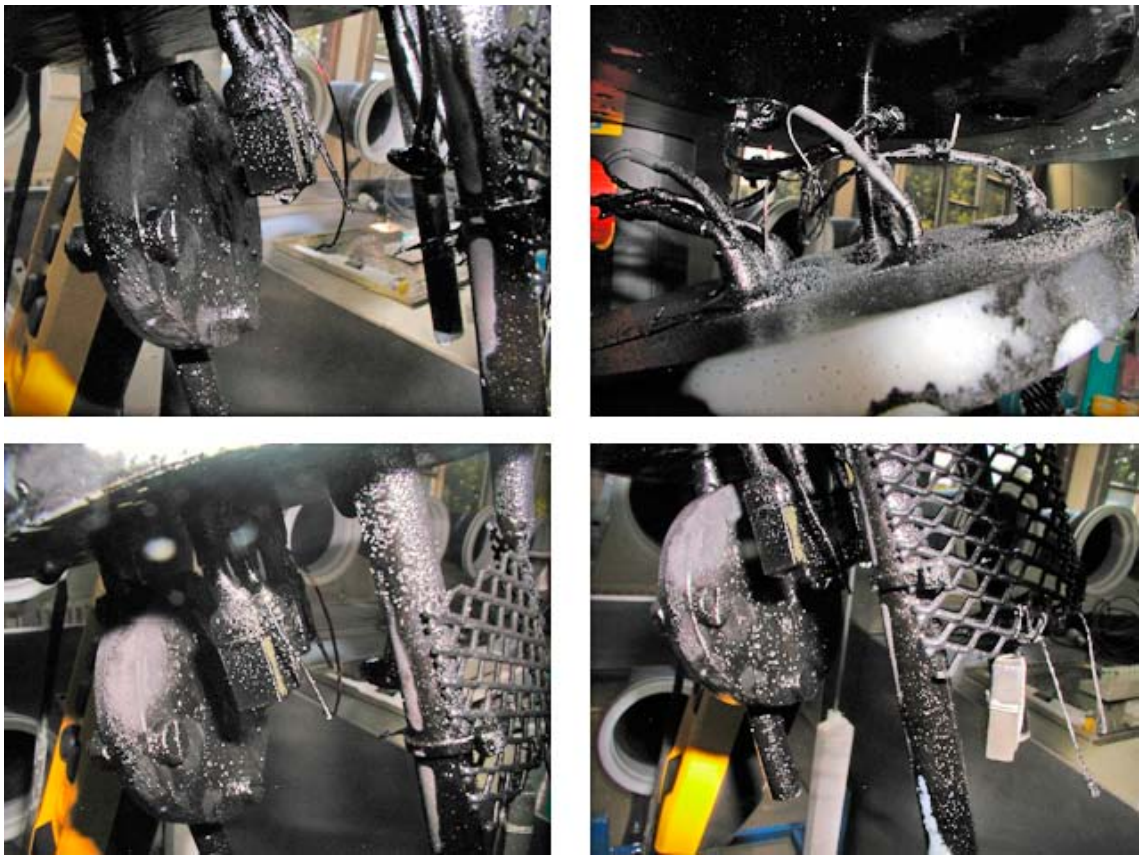

Figure 6-8. *Appearance of sensors and electrodes supported on nylon table.*

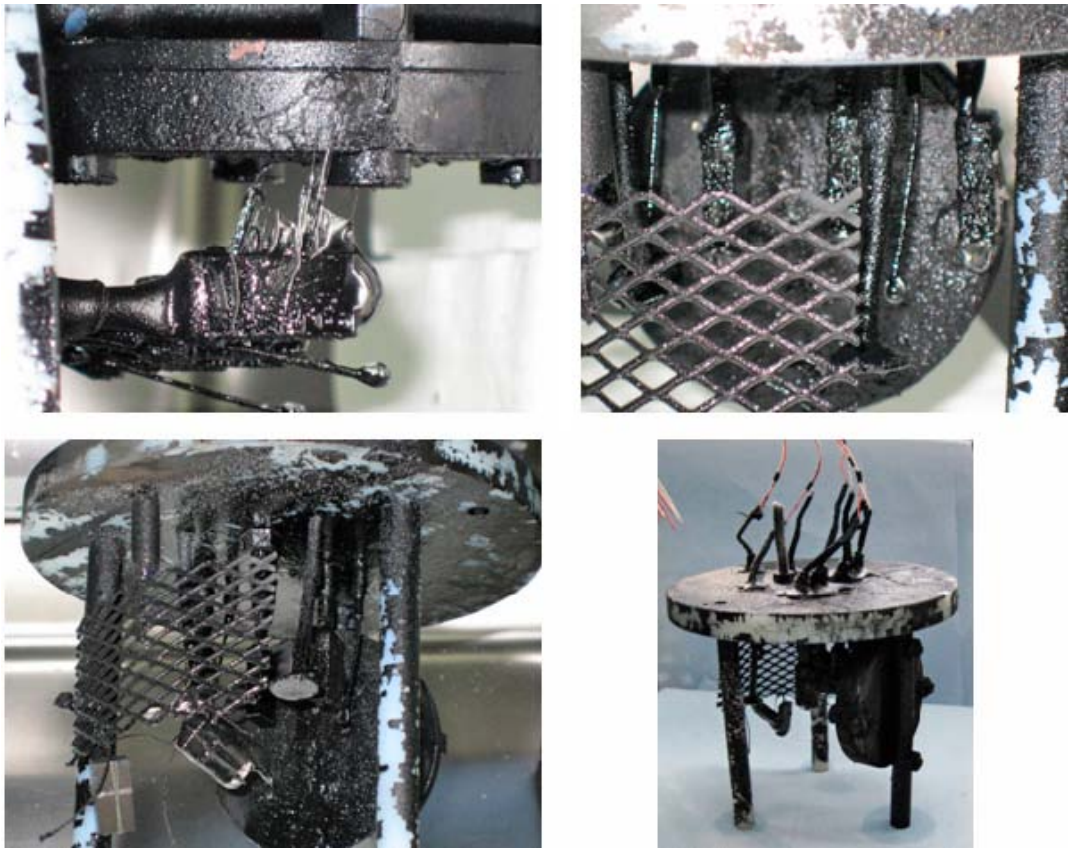

Figure 6-9. *Appearance of sensors and electrodes supported on nylon table.*

The copper MiniCan was then removed from the support cage using the overhead crane, as shown in Figure 6-10 and close up photographs of the surface of the copper canister at various locations are shown in Figure 6-11 to 6-14. It can be seen that there was significant, non-uniform blackening of the surface of the canister and that the blackening was concentrated on areas facing the holes in the inner cylinder of the support cage (see Figure 6-4). Other notable features of the appearance of the canister were as follows:

- The top 1 mm defect which was located near to the top weld appeared to have a black volcano-shaped extruberance emerging from it. The thickest layer of black deposit on the canister surface was around the hole, suggesting that it was due to material that had extruded out of the defect.
- The bottom 1 mm defect showed signs of a black layer around it, which was flaking off as the can dried, leaving a comparatively clean area (Figure 6-11). There was a ring around the bottom hole, which was probably an artefact caused when the defect was drilled before the canister was placed in the support cage (see also Section 7.3.12).
- There were areas with a green tinge around the black areas on the surface of the copper canister.
- There was a clear 'chain-like' pattern on the surface, which corresponded with the plastic insulator that was placed around the copper canister to prevent electrical contact between the copper canister and the support cage. This would suggest that the insulator material had screened the surface for material deposited from the groundwater, or that it had prevented access of the substances that caused development of the black layer.

It should be noted that when the various components were exposed to the atmosphere inside the glovebox they dried out quite rapidly, due to the very low humidity. The components were therefore stored in plastic containers of groundwater taken from the transfer flask when they were not being examined. When the surface of the canister dried, black flakes fell away from it.

The following section presents the results of detailed analyses that were carried out on each of the component parts of the experiment.

Figure 6-10. *Extraction of the copper canister from the support cage.*

Figure 6-11. *Appearance of copper canister after removal from support cage, showing condition of holes at top and bottom of the copper canister. Note that the surface had dried in the glovebox due to the very low humidity.*

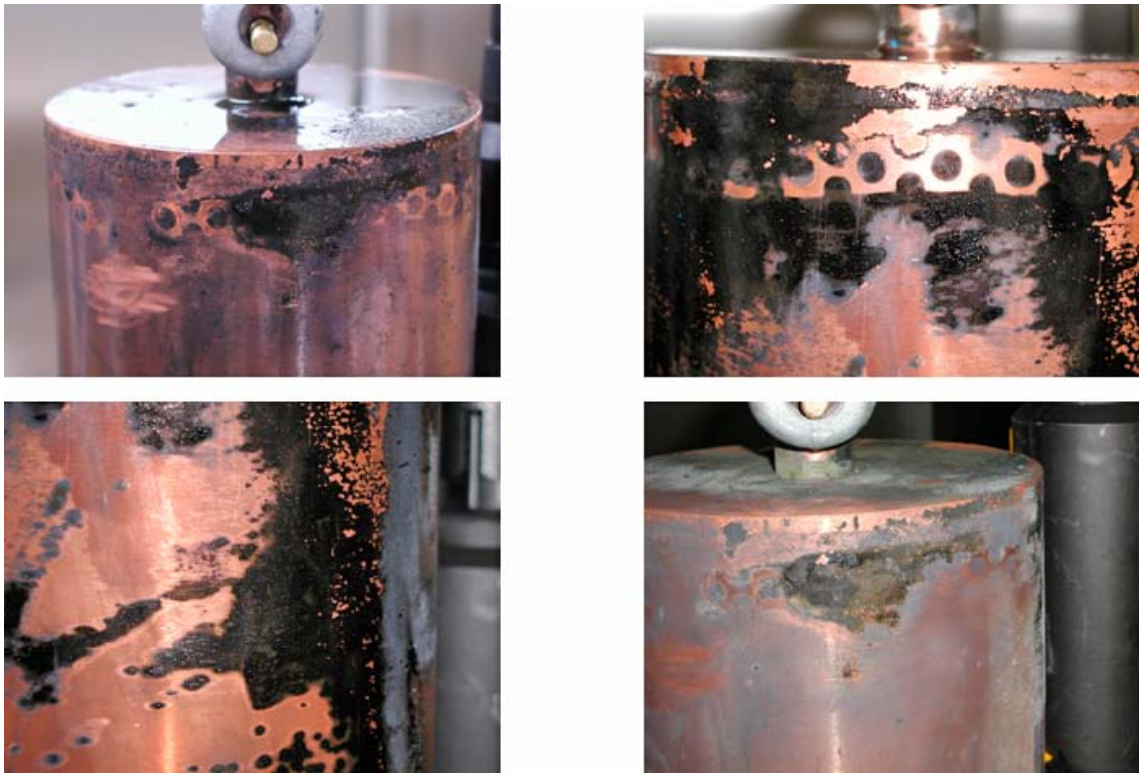

Figure 6-12. *Appearance of the surface of the copper canister. The chain-like pattern on the surface at the top of the canister corresponds to the contact area with the strip of plastic insulator that was placed between the copper canister and the inner surface of the support cage.*

Figure 6-13. *Appearance of the surface of the copper canister, showing location of defects at top of canister.*

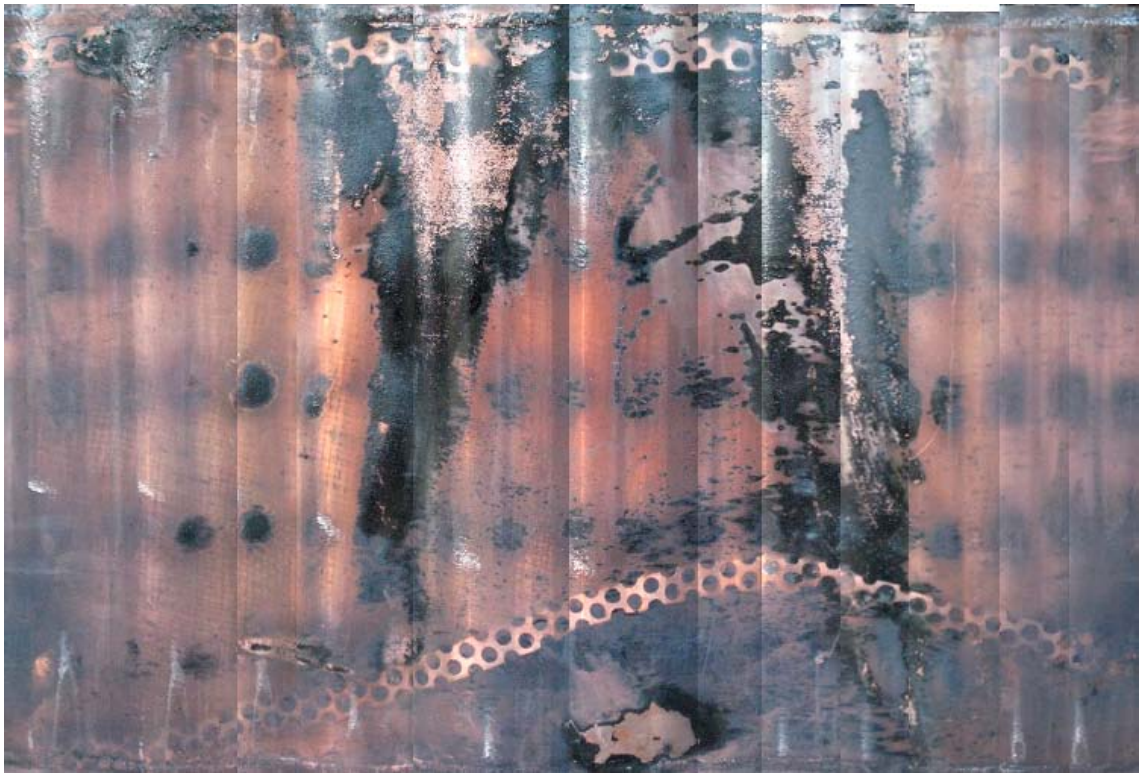

Figure 6-14. *Panoramic photo-montage of surface of copper canister on removal from support cage.*

7 Analysis of samples from Experiment 3

This section describes the analyses that were carried out on the various components of the MiniCan experiment and presents the observations and results for each sample. The analysis carried out on each specimen is summarised in Table 7-1. The following analytical techniques were applied to the various specimens:

- Visual observation and photography, to assess the extent of any corrosion.
- Raman analysis, to identify mineral phases.
- X-ray Diffraction analysis, to identify crystalline mineral phases.
- Scanning electron microscopy (SEM) and Energy dispersive X-ray analysis (EDX), to examine the morphology of any deposits and to determine the elemental composition of materials at a microscopic level of detail (but not the chemical state).
- X-ray photoelectron spectroscopy, to measure the composition of very thin films on the surface of specimens, with a surface sensitivity of a few atomic layers.
- Fourier transform Infra-red spectroscopy (FTIR), to identify chemical bonds and chemical groups in the materials.

In addition the following measurements were carried out:

- Profilometry, to determine the extent of any localised corrosion of the copper canister surfaces.
- Dissolved hydrogen analysis of a copper sample, to determine whether any hydrogen produced by corrosion had entered the material.
- Weight gain and weight loss measurements to determine the integrated corrosion rate of the metal coupons.

Details of the preparation techniques and the analytical equipment used for these various techniques are given in Appendix 1. The results from the analysis from each component are considered in turn below.

Table 7-1. Summary of analyses carried out on samples from Experiment 3.

	Sample	Visual	Raman	XRD	SEM/ EDAX	XPS	FTIR	Weight loss	Profilometry	Hydrogen analysis
Table Items	Copper electrode 1	√	√		√					
	Copper electrode 2	√								
	Copper weight loss	√	√		√			√		
	Iron electrode 1	√			√					
	Iron electrode 2	√	√	√	√					
	Iron weight loss	√	√	√	√		√	√		
	Whisker samples	√		√	√					
	Gold electrode	√	√							
	Platinum electrode	√								
	Pt-Ti gauze	√								
	Sandwich specimen	√	√							
	Ag/AgCl disc 1	√			√					
	Ag/AgCl disc 2	√								
	Black flakes from table	√	√	√	√		√			
Other Items	U-bend 1	√				√	√			
	U-bend 2	√								
	Silvion	√								
	Eh probe	√								
	Swabs from outer surface of stainless cage	√								

Table 7-1 (contd). Summary of analyses carried out on samples from MiniCan canister from Experiment 3.

	Sample	Visual	Raman	XRD	SEM/ EDAX	XPS	FTIR	Weight loss	Profilometry	Hydrogen analysis
MiniCan	Black flakes from outer surface	√		√	√					
	Cu can inner surface around the top hole	√	√		√					
	Cu can outer surface green areas around the top hole	√			√			√		
	Cu can outer surface area around bottom hole	√			√					
	Cu can inner surface area around bottom hole	√			√					
	Welds	√								
	Inner surface of copper canister	√	√		√					
	Outer surface of copper canister	√	√		√		√		√	√
	Outer surface of cast iron insert	√	√		√					
	Cast Iron insert pitted area	√	√		√					

7.1 Items mounted on support table

7.1.1 Copper electrodes

The appearance of the copper electrode 1 is shown in Figure 7-1 and 7-2 and that of copper electrode 2 is shown in Figure 7-3. It can be seen that the electrodes were covered with a blotchy, non-uniform black deposit and that some loose black non-adherent material flaked off the electrodes when they were stored in water (see Figure 7-1). When the electrically insulating PTFE heat shrink was removed from copper electrode 2 a shiny metallic surface was visible indicating that crevice corrosion had not occurred beneath the sheathing (see right hand side images in Figure 7-2). The surface of copper electrode 1 was analysed by Raman spectroscopy and the results from the analysis are shown in Figure 7-4. These results indicate that the material was predominantly non-crystalline, with possible indications of graphitic carbon and mixed oxide/sulphide species. The SEM/EDX (Appendix 2) analysis for copper electrode 1 identified the following main features (note that all results refer to the elements detected and that EDX does not provide any information about the chemical state of the material analysed):

- EDX analysis of apparently clean areas on the electrode surface showed the presence of mainly copper with small quantities of iron, chlorine, calcium, carbon, oxygen, silicon and sulphur.
- Analysis of a number of dark areas showed high concentrations of iron, silicon and sulphur with small quantities of chlorine, calcium, carbon, oxygen and copper. Note that the end of this sample was contaminated with a layer of epoxy resin while mounting the specimen for Raman analysis (shown in the SEM results as a dark film across the tip of the specimen with a high concentration of carbon, sulphur and oxygen).
- Some deposits had high concentrations of calcium.
- Beneath the sheathing the surface was predominantly copper.

These features are consistent with the copper surfaces being covered with a thin film of copper sulphur/oxygen superimposed in some areas with a layer rich in iron, sulphur and silicon. The chlorine and calcium are probably residues from the groundwater, since the specimens were not washed in pure water before analysis.

Figure 7-1. *Copper electrode 1 in water, showing loose deposit that washed off electrode.*

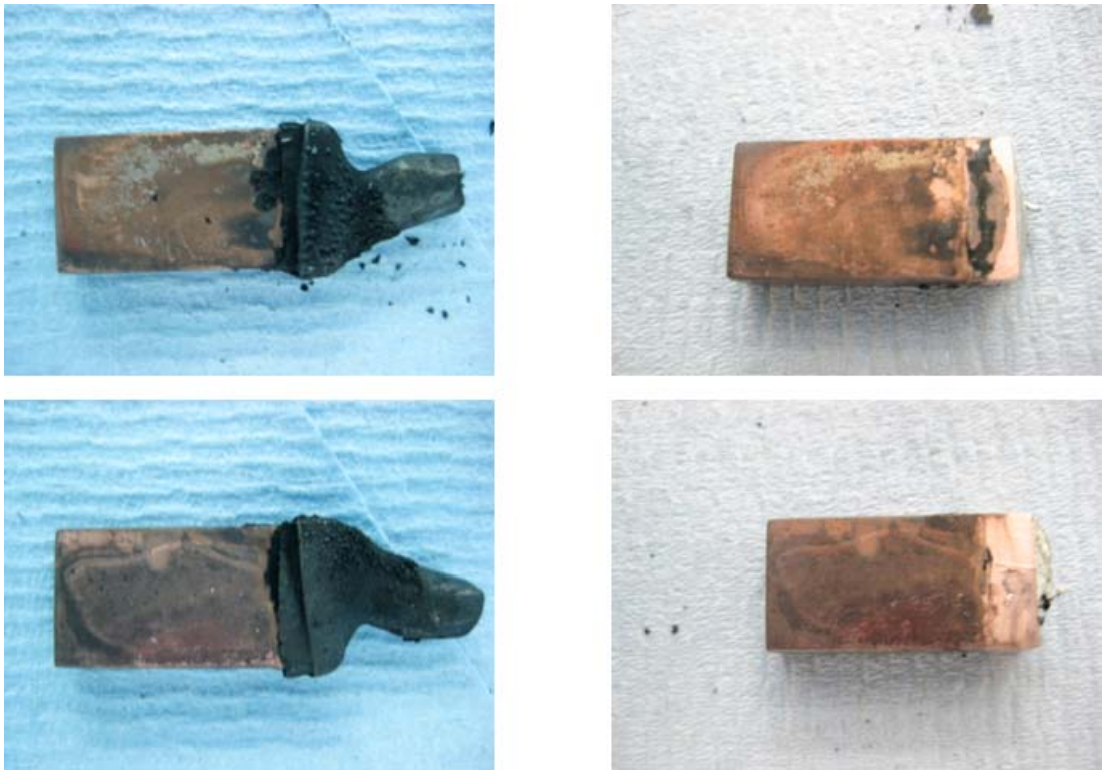

Figure 7-2. *Copper electrode 1 showing both sides, before and after removal of sheathing. Note that the surface had dried out in the glovebox when these photographs were taken. The specimens were 10 mm wide.*

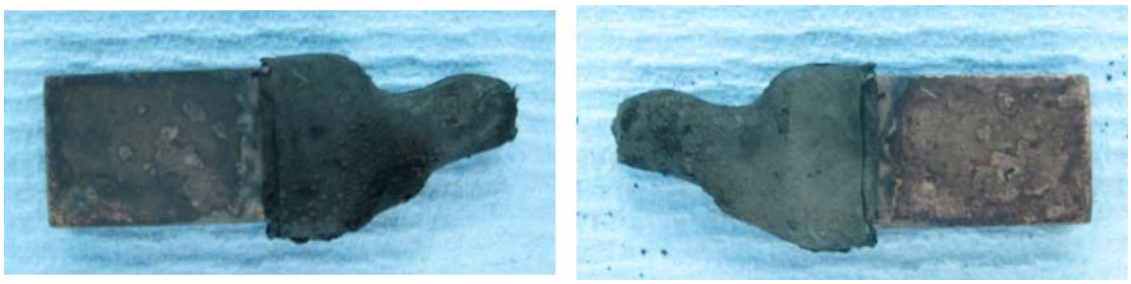

Figure 7-3. Copper electrode 2 showing both sides, before removal of sheathing. Note that the surface had dried out in the glovebox when these photographs were taken. The specimens were 10 mm wide.

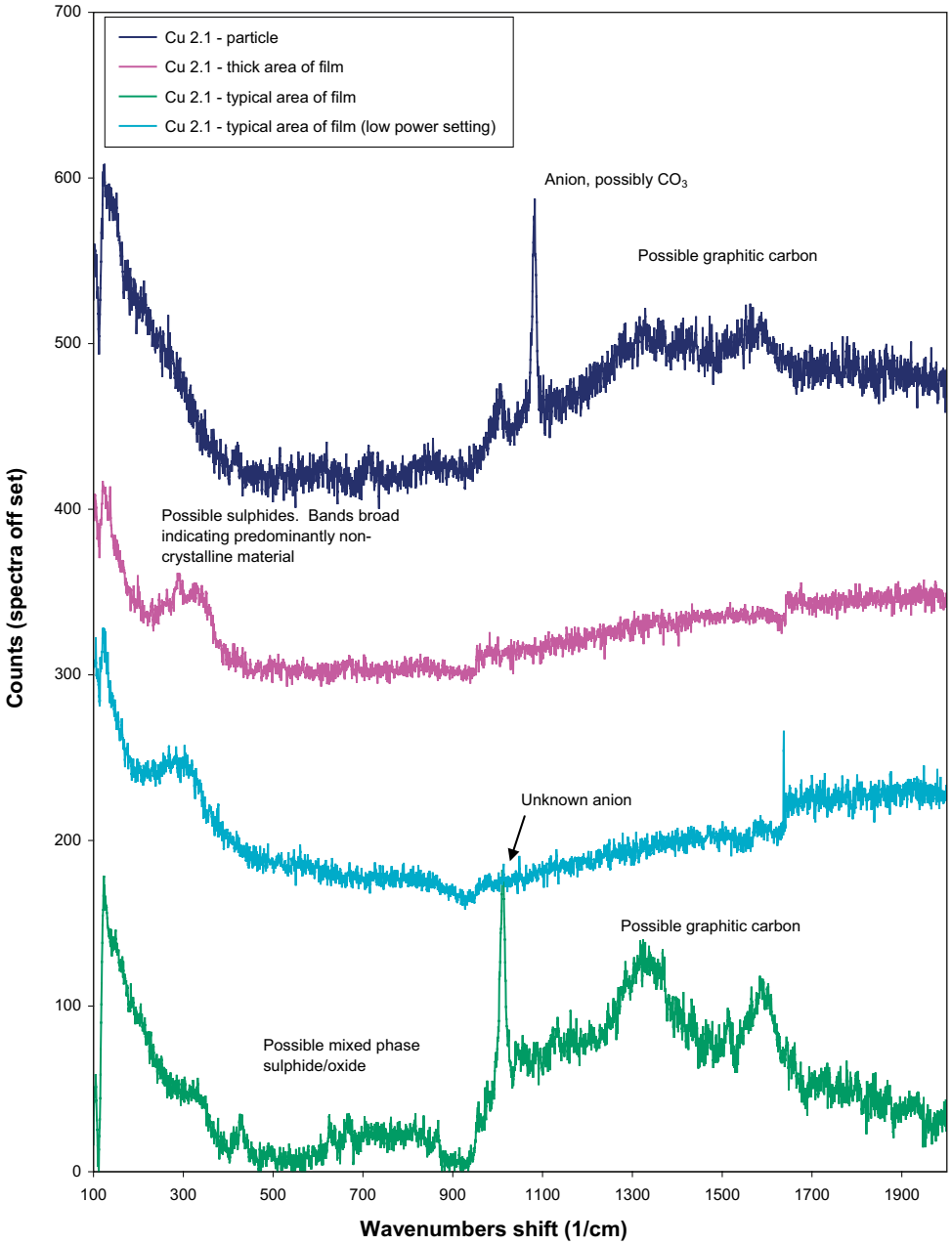

Figure 7-4. Raman spectra for four areas on surface of copper electrode 1.

7.1.2 Copper weight loss specimen

Photographs of the copper weight loss sample are shown in Figure 7-5, which shows that the specimen was covered in a layer of black deposit. Raman analysis of the surface was carried out by sealing the specimen in a gas-tight Perspex holder and obtaining the spectra through a glass slide (see Appendix 1 for details). The results from the Raman analysis are shown in Figure 7-6, which shows that the surface deposit was mainly amorphous and that it was not possible to identify any specific materials, although the sample had some low wavenumber shift bands which may be attributable to a mixed $CuFeS_2$ phase. Three different spots on the sample were measured. All the spectra showed the same similar structure with a broad multiple peaked band at ca. 450 cm^{-1} shift, another broad band at ca. 800 cm^{-1} shift (attributable to scattering from the glass lid) and a smaller broad band at ca. 1,050 cm^{-1} shift (attributable to carbonate or sulphate species). A Raman spectrum from crystalline pyrites[2] (FeS_2) is shown overlaid on the spectrum. The broad composite band at ca. 450 cm^{-1} shift can be fitted with three bands at 350, 450 and 490 cm^{-1} shift as shown in Figure 7-7. Although the peak positions do not match exactly those of the crystalline pyrites (350, 390 and 430 cm^{-1} shift), Raman bands tend to broaden and the peak centres can shift as materials become less crystalline. The breadth of the bands observed in the sample spectra would suggest that the sulphide phase, if present, was tending towards amorphous.

Copper sulphide can take a variety of forms. CuS_2 presents a band in a similar position to those for FeS_2. The Raman spectrum from the copper sample displays a definite Raman band at ca. 140 cm^{-1} (possibly as a doublet), which may be indicative of a mixed copper/iron sulphide.

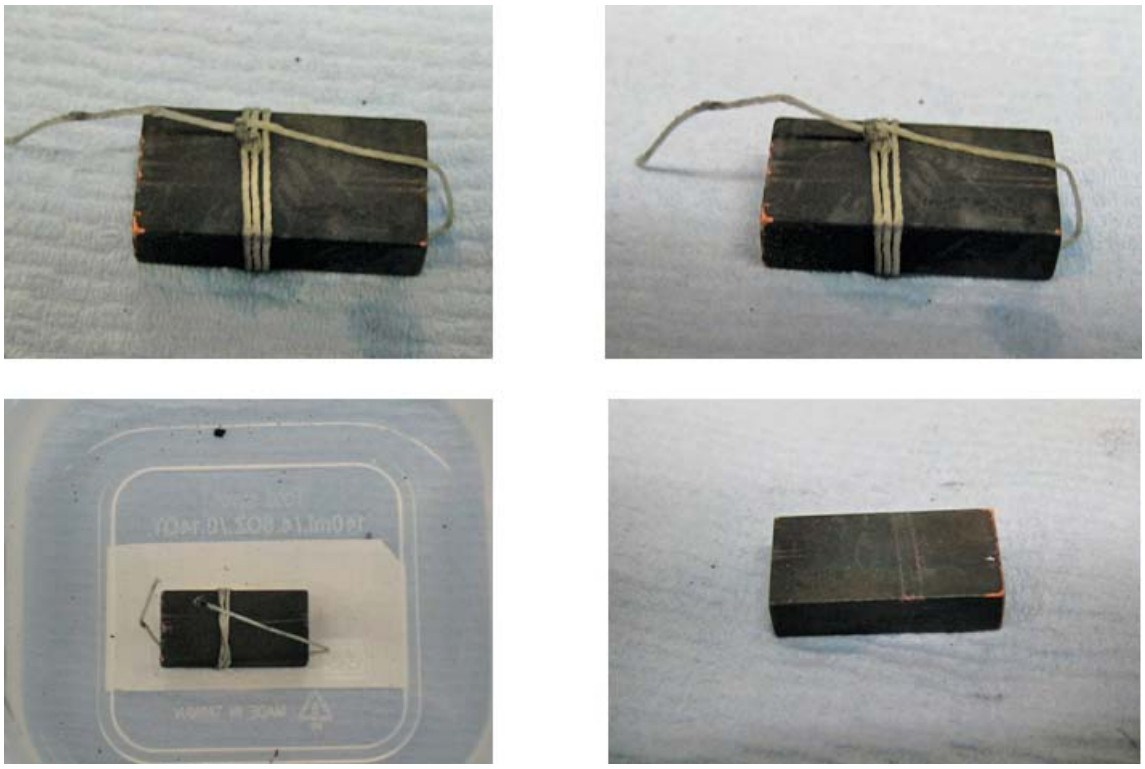

Figure 7-5. *Copper weight loss specimen after removal from MiniCan Experiment 3. The polypropylene thread was used to suspend the specimen from the nylon support rack. The bottom left hand photograph shows the specimen immersed in groundwater taken form the transfer flask. The specimen had original dimensions of 5·10·20 mm.*

[2] RRUFF™ Project
FeS_2 http://rruff.info/pyrite/display=default/R050190
CuS_2 http://rruff.info/chem=Cu,S/display=default/R060514
$CuFeS_2$ http://rruff.info/chem=Cu,S/display=default/R050018

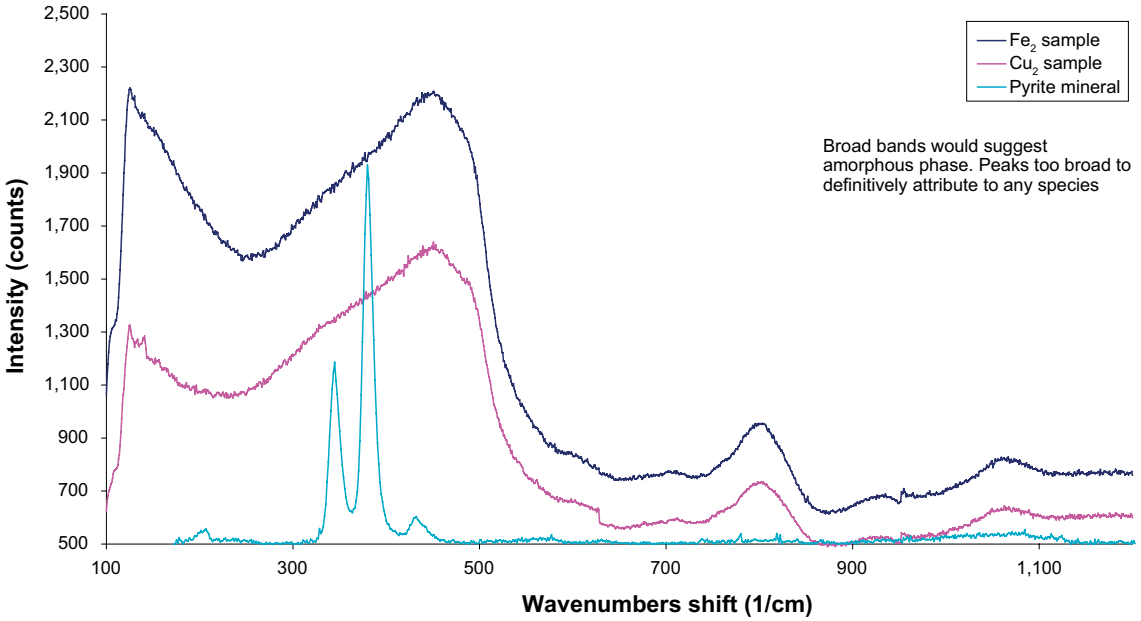

Figure 7-6. *Raman spectra for copper and iron weight loss specimens.*

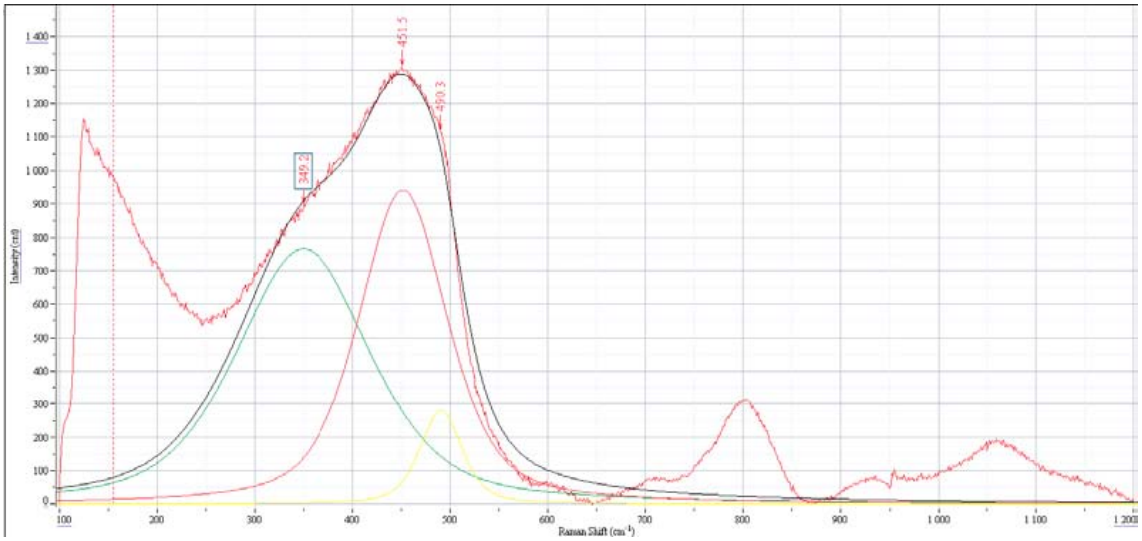

Figure 7-7. *Peak fitting to the broad composite band at ca. 450 cm^{-1} shift.*

The SEM/EDX analysis of this specimen (Appendix 2) showed the presence of a uniform coating of very small particles (typically < 5 µm) which were predominantly composed of copper and sulphur, with a small quantity of iron, silicon, calcium, oxygen, carbon and chlorine.

A weight loss measurement was obtained for this sample, using a method which was finalised after carrying out some trial tests with a range of possible cleaning reagents based on recommendations in the appropriate ASTM standard (ASTM 1999) (sulphuric acid, chromic acid and hydrochloric acid). On the basis of these trials it was decided to use 10% sulphuric acid as the cleaning medium, combined with ultrasonic cleaning. The cleaning procedure was selected with the aim of removing any accumulated corrosion product, whilst minimising any dissolution of the base metal. The sequence of cleaning operations is given below and the weights at each stage of the weight loss measurements are shown graphically in Figure 7-8 and the raw data are given in Table 7-2. The steps in the cleaning procedure were as follows:

1. Sample weighed before mounting in Experiment 3 (to an accuracy of 1 mg).
2. Sample weighed after removal from Experiment 3 inside glovebox.
3. Sample reweighed after range of analyses had been carried out. It was necessary to stick the sample to an SEM stub which resulted in some adhesive residue being present on the surface and therefore the weight increased. The sample was stored in groundwater in a plastic container. There was a decrease in weight as the sample dried out. The weight measurements were carried out at least three times after each treatment and an average weight was taken.
4. The surface was cleaned by gentle rubbing of the surface with a swab wetted in solvent. This removed most of the visible adhesive on the surface.
5. The sample was exposed to 10% sulphuric acid for 90 seconds, twice, without any ultrasonic cleaning. At this stage some black deposit was still visible on the surface so the intensity of the cleaning was increased by applying ultrasonic cleaning.
6. The ultrasonic cleaning was carried out five times with a five minute exposure period in 10% sulphuric acid. After the second treatment the slope in the weight loss curve changed and this was taken at the point at which all the surface deposit had been removed. The surface appeared clean at this stage (see Figure 7-8). All subsequent treatments corresponded to a small amount of metal loss and this was taken into account in the calculation of the corrosion rate (see Table 7-2), using the formula:

$$\text{Corrosion Rate} = (K \cdot W)/(A \cdot T \cdot D)$$

where:

K = a constant

T = time of exposure in hours

A = area in cm^2

W = mass loss in grams, and

D = density in gcm^{-3}.

There were no indications of localised corrosion on the cleaned surface and in calculating the corrosion it was therefore assumed that uniform corrosion had occurred. As Table 7-2 shows, the calculated corrosion rate, based on the weight loss measurements, was 0.15 μm yr^{-1}. The biggest source of error is in the initial start weight, which was only measured to an accuracy of 1 mg. The maximum initial weight would have been 8.8575 and the minimum would have been 8.8565. The final weight was measured to an accuracy of 0.01 mg. Sensitivity analysis shows that the corrosion rate based on the possible range in the starting weight was 0.15 ± 0.02 microns/year.

7.1.3 Iron electrodes

The iron electrodes were black in appearance with whiskers hanging vertically down, apparently due to gravitational effects (Figure 7-9). Iron electrode 2 was analysed by Raman analysis (Figure 7-10), XRD (Figure 7-11) and SEM/EDX (Appendix 2). The Raman analysis showed the presence of graphitic carbon and possible weak sulphide peaks, and the XRD analysis showed that the material was amorphous. The SEM examination of both iron electrodes clearly shows the presence of spheroidal graphite nodules in the parent material. In the EDX analysis the main elements detected were iron, silicon, sulphur and oxygen, with small amounts of calcium, sodium, zinc and chloride. The corroded areas were mainly covered with flaky layers of iron sulphide. Iron electrode 1 was cross-sectioned using

a rotary diamond cutting wheel and then mounted in epoxy resin (Araldite) with a screw connection to the back of the specimen to provide an electrical connection to the stage (to prevent charging of the specimen in the SEM) and ground to a 800 grit finish (see Figure 7-12).

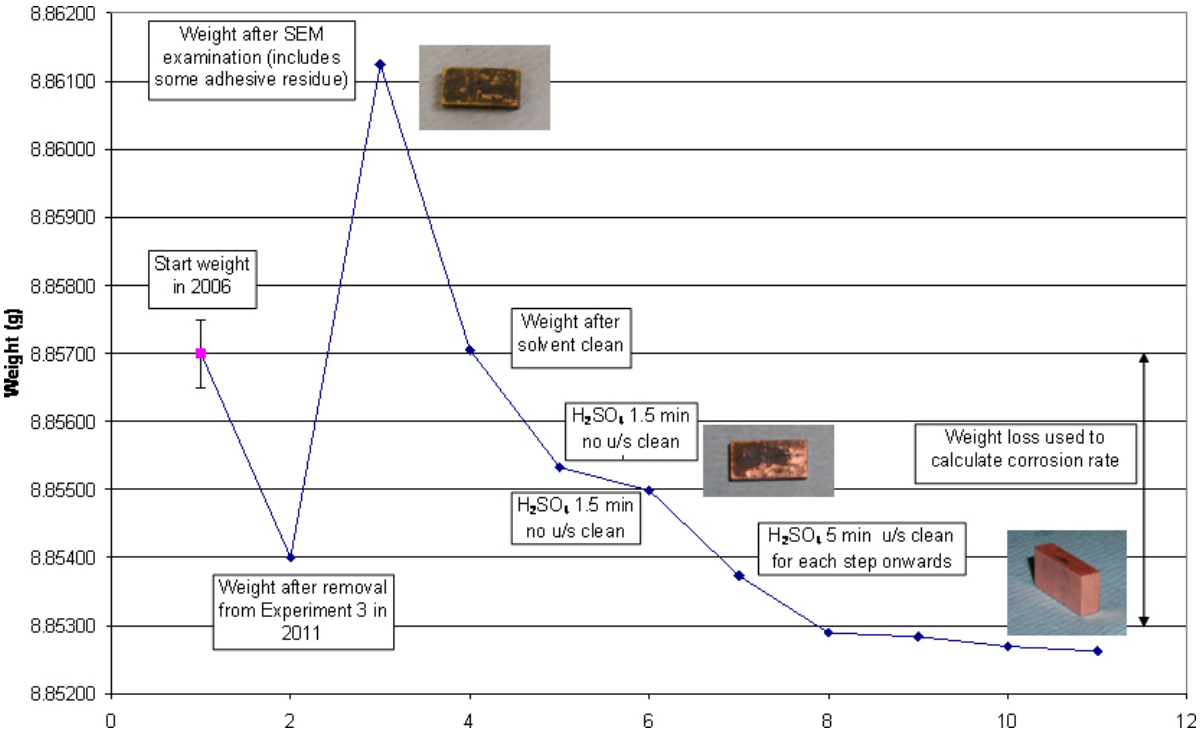

Figure 7-8. Results of successive weight loss measurements on copper weight loss specimen.

Table 7-2. Results from weight loss measurements for copper weight loss specimen from MiniCan Experiment 3 and summary of corrosion rate calculation.

Weight loss measurements.

	Mo	Rinse Wt	After Analysis	Solvent clean	1st H_2SO_4	2nd H_2SO_4	3rd H_2SO_4	4th H_2SO_4	5th H_2SO_4	6th H_2SO_4	7th H_2SO_4
Grams		**In glovebox**	**SEM etc**	**1**	**2**	**3**	**4**	**5**	**6**	**7**	**8**
	8.857	8.854	8.86135	8.85720	8.85509	8.85499	8.85397	8.85293	8.85281	8.85275	8.85263
			8.86124	8.85707	8.85541	8.85497	8.85362	8.85286	8.85291	8.85266	8.85262
			8.86115	8.85702	8.85547	8.85500	8.85372	8.85289	8.85279	8.85267	8.85262
				8.85691			8.85362				
Averaged weight	8.85700	8.854	8.86125	8.85705	8.85532	8.85499	8.85373	8.85289	8.85284	8.85269	8.85262

Assumed constants in corrosion rate calculation.

Width (cm)	Height (cm)	Thickness (cm)	Surface area (cm^2)	Density of iron ($g\ cm^{-3}$)	Density of copper ($g\ cm^{-3}$)
2	1	0.5	7	7.8	8.94

Corrosion rate calculation.

Initial Wt. (M_0) (g)	Rinse Wt (g)	M_1 (g)	M_2 (g)	Lg (g)	Lg/Area g/cm^2	Lg/Area/yr $g/cm^2/yr$	Calculated corrosion rate $\mu m\ yr^{-1}$
8.8570	8.8540	8.8529	8.8526	0.00384	0.0005	0.000132	0.15

Figure 7-9. *Iron electrode 2 from MiniCan Experiment 3, showing presence of whiskers of iron sulphide.*

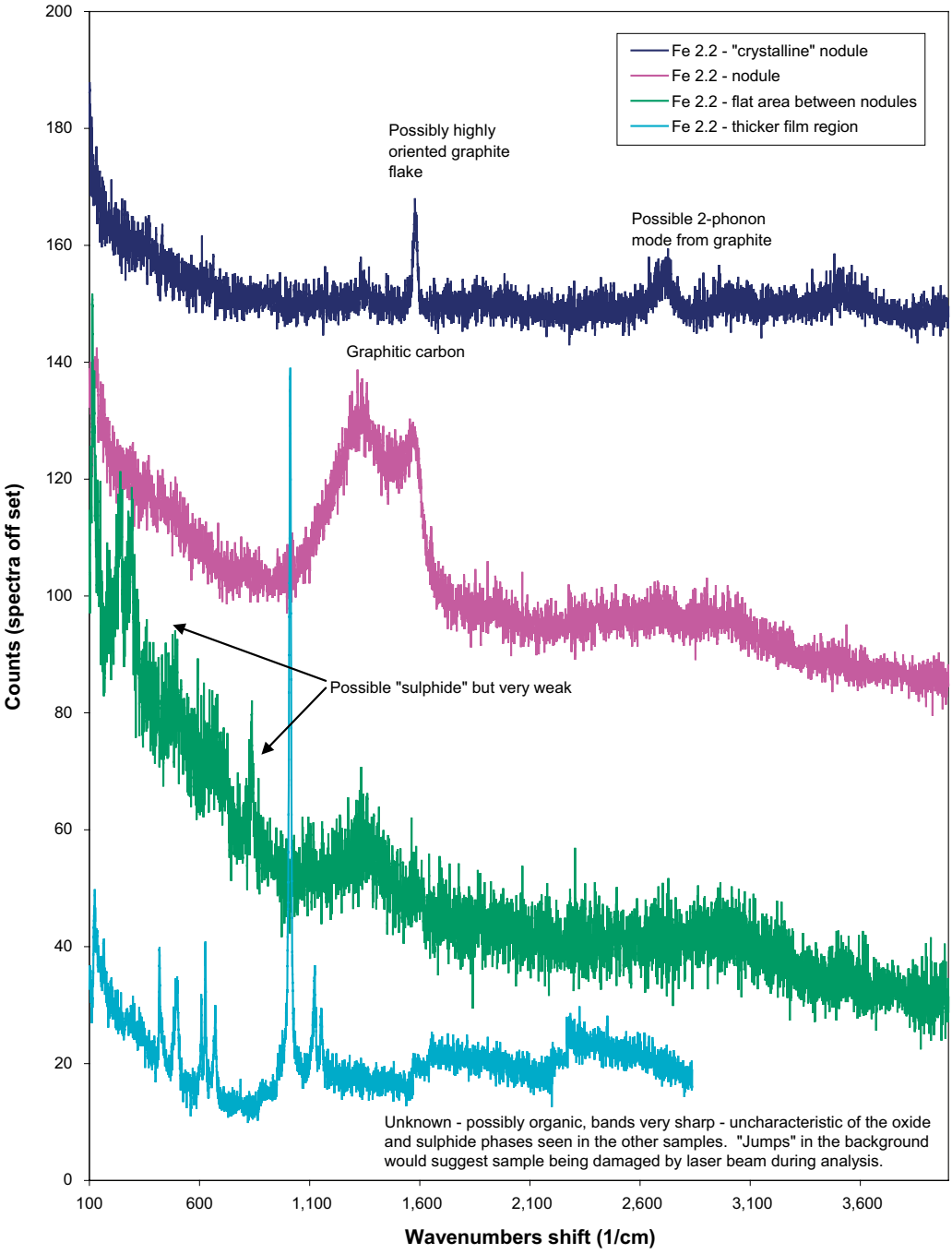

Figure 7-10. *Raman analysis of iron electrode 2 from MiniCan experiment 3.*

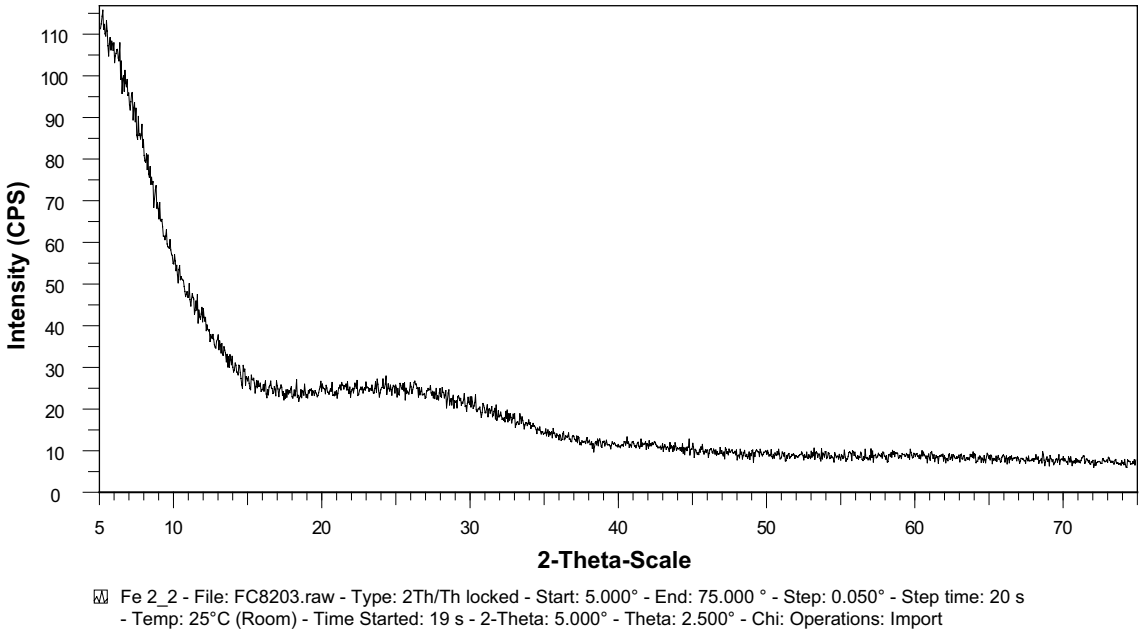

Figure 7-11. *XRD pattern for iron electrode 2 from MiniCan Experiment 3.*

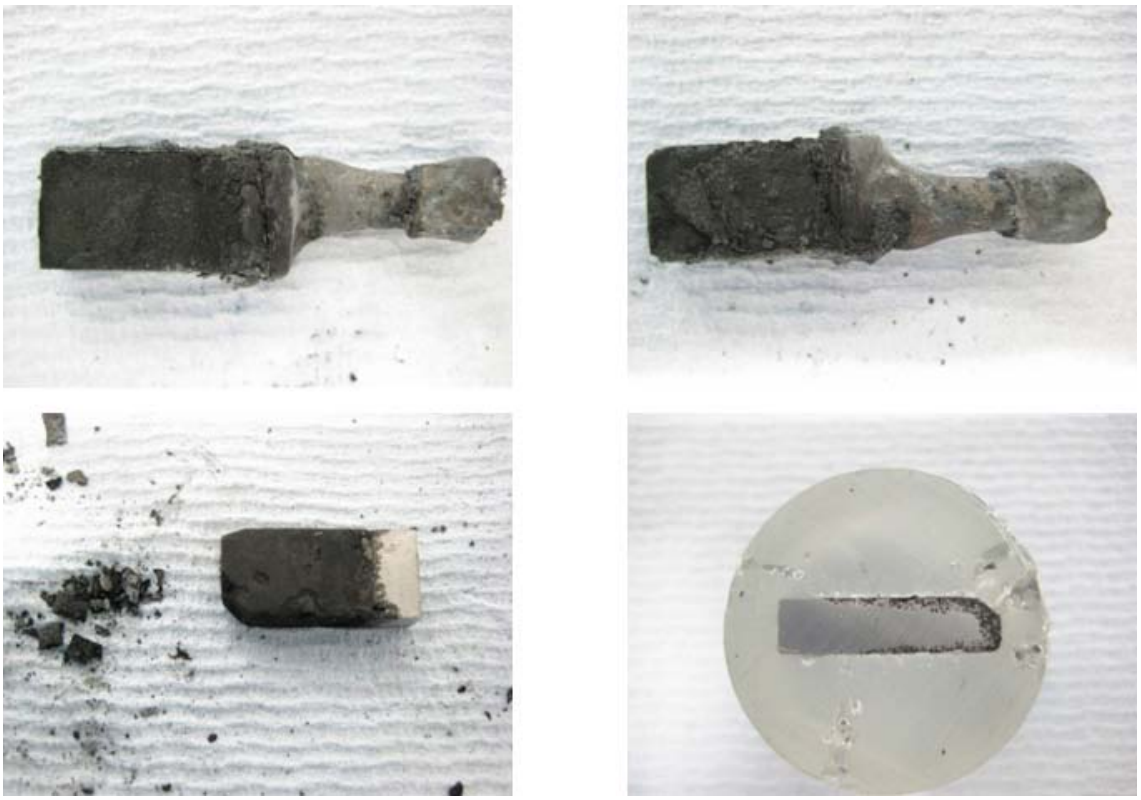

Figure 7-12. *Iron electrode 1 from MiniCan Experiment 3. The specimen was mounted in cross-section for SEM/EDX examination.*

7.1.4 Iron weight loss specimen

When the experiment was opened the iron weight loss specimen was seen to be black, with whiskers of material hanging down (Figure 6-8). The appearance of the specimens is shown in more detail in Figure 7-13 and 7-14. These photographs show the crumbly, cracked, uneven nature of the surface and that loose flaky material was easily separated from the sample. The specimen was weighed in the glovebox and the mass was 1.4207 g, compared to a starting weight of 6.558 g. This final weight corresponds to the weight after the suspending thread had been removed, but it should be noted that a significant amount of flaky deposit fell from the specimen while the thread was being removed. All the deposit was collected and weighed along with the specimen and deposit that was scraped from the thread, but not the thread itself. The deposit also dried out while it was being weighed, due to the dry atmosphere in the glovebox.

Raman analysis of the weight loss coupon was carried out through the window of a sealed Perspex holder. A representative Raman spectra is shown in Figure 7-6. As for the copper sample (see Section 7.1.2), the observed Raman bands were very broad indicating that the material was tending towards the amorphous phase. It was not possible to make an exact match to iron sulphide, although the bands did overlap with those of crystalline FeS_2 (a Raman spectrum from crystalline pyrites (FeS_2) is shown overlaid on the spectrum). There was no evidence from the Raman spectra to suggest the presence of Fe_3O_4, Fe_2O_3 or $Fe_{3-x}M_xO_4$ (spinel) on the sample surfaces.

The iron weight loss sample was removed from the Perspex holder used for the Raman analysis and a fragment of the black surface removed and placed in a sealed capillary tube for analysis by XRD. When the sample was ground up for analysis it was found that it was easily broken up using a mortar and pestle, indicating a low mechanical strength. The XRD pattern (Figure 7-15) showed that the only crystalline phase present was graphite, showing that all the metallic iron phase had completely corroded away.

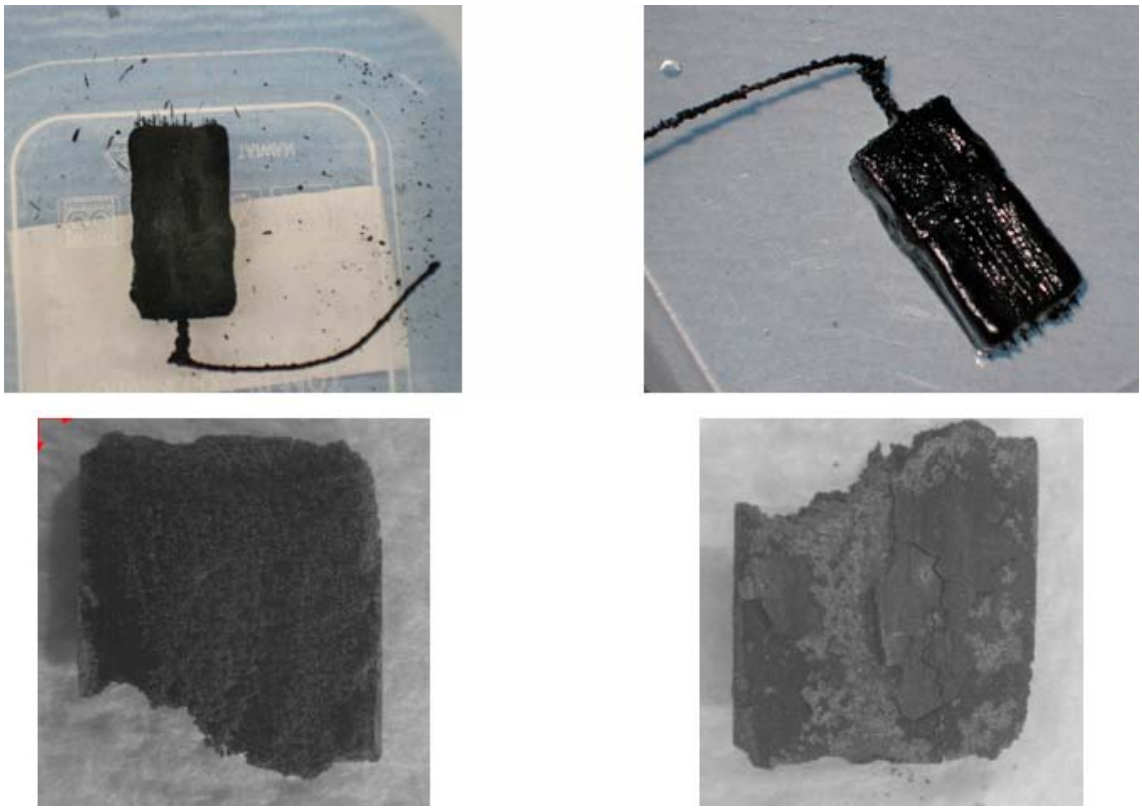

Figure 7-13. *Iron weight loss specimen after removal from Experiment 3.*

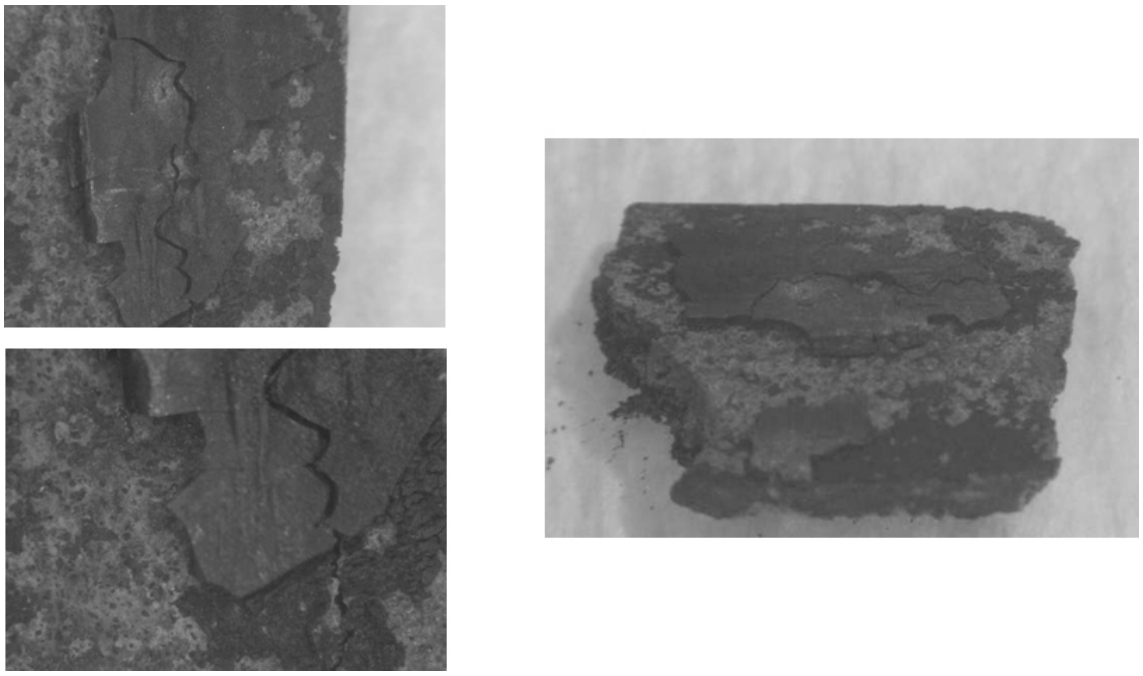

Figure 7-14. Iron weight loss specimen after removal from Experiment 3.

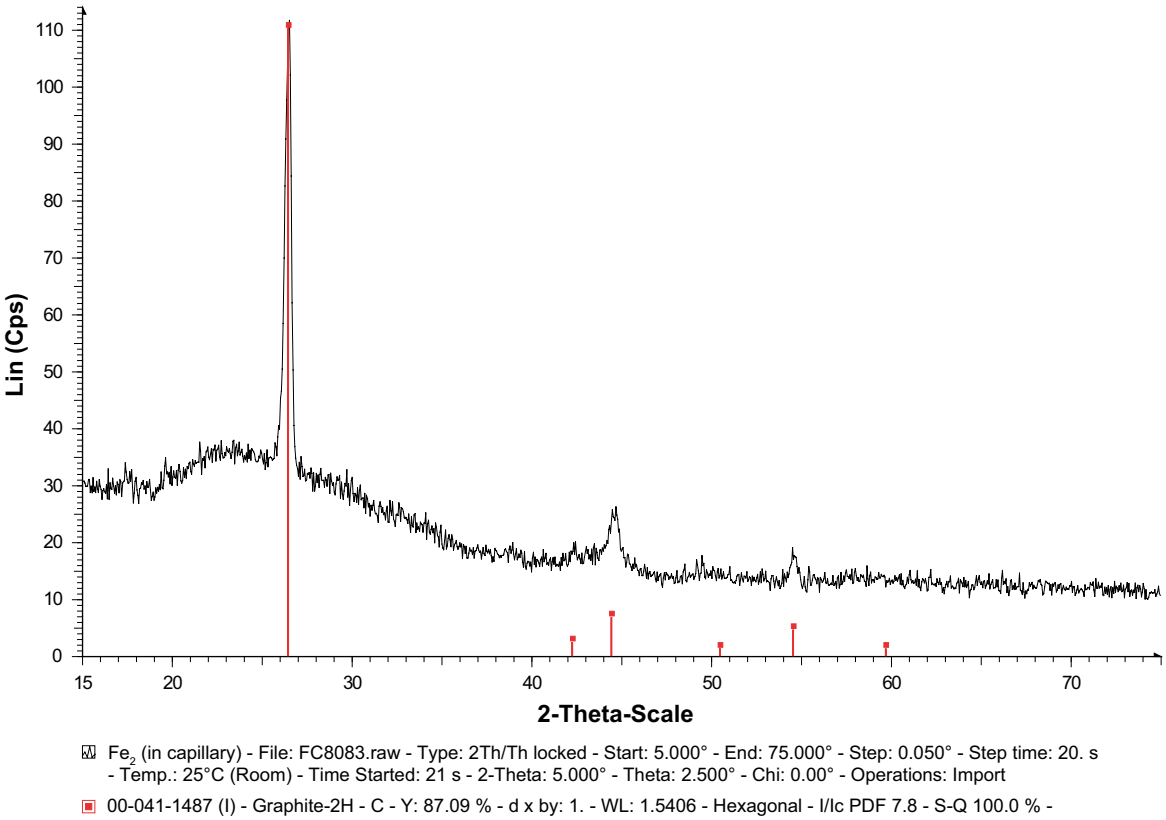

Figure 7-15. XRD analysis of iron weight loss specimen removed from Experiment 3. The red stick pattern corresponds to graphite.

SEM/EDX analysis of the iron weight loss coupon (Appendix 2) showed that:

- The residue is predominantly composed of iron, silicon, oxygen and carbon, with traces of chlorine, phosphorus and aluminium.
- Nodules of residual graphite are clearly visible within a porous structure composed of iron, silicon and oxygen.

FTIR analysis was carried out on a number of samples, including two specimens removed from the iron weight loss specimen. The spectra, shown in Figure 7-16, indicate the presence of OH, carbonate and metal-oxygen bonds.

The weight loss on this sample was very large compared to the starting weight, with the weight reducing to a value which was ~22% of its original value. When all the other analyses had been completed a sample of the weight loss coupon was placed into Clarke's reagent (inhibited hydrochloric acid (1 litre SG 1.18 HCl, 50 g $SnCl_2$, 20 g Sb_2O_3) to determine whether the residue would dissolve. It was noted that when the sample was placed into the reagent a smell of hydrogen sulphide was released, but the sample did not dissolve even after a period of several weeks' exposure, indicating that the material was not a typical iron oxide, which would have dissolved rapidly. The initial composition of the original cast iron would have been typically (wt%): C 3.52; Si 2.66, Mn 0.092, S 0.006; P 0.037; Mg 0.067; Cu 0.006, Fe bal. The smell of hydrogen sulphide indicates that iron sulphide was present in the material, even though very little sulphur was observed in the EDX analysis. This suggests that the sulphur was concentrated deeper into the specimen, which would have been beyond the sampling depth of the EDX analysis, of a few microns.

The sample had retained its original dimensions but the metallic iron had been dissolved. This indicates that on average the corrosion rate was at least 500 μm yr^{-1} and possibly higher, since it was not known at what point during the test period complete dissolution of the sample had occurred.

7.1.5 Whisker samples

Samples of the whiskers attached to iron electrode 2 (Figure 7-9) were analysed by XRD (Figure 7-17) and SEM/EDX (Appendix 2). The XRD analysis shows that the material was amorphous and the SEM/EDX analysis showed that the whiskers were composed of predominantly iron and sulphur with small amounts of calcium, chlorine and silicon. Discrete crystals with a high concentration of calcium, oxygen and carbon (assumed to be calcium carbonate) were seen on the surface of a porous mass of very small crystals of iron sulphide.

7.1.6 Gold and platinum electrode

The appearance of the platinum and gold wires following removal from Experiment 3 is shown in Figure 7-18. A mass of black deposit had formed at the tip of the electrodes. The deposit on the gold wire was analysed by Raman spectroscopy (Figure 7-19) and the dark areas were found to contain a sulphide species, with indications of graphitic carbon on the clean areas.

7.1.7 Platinised titanium gauze

The appearance of the Pt-Ti gauze counter electrode is shown in Figure 6-9, which shows that it was covered by a layer of black material that is assumed to have had the same composition as the material on the gold and platinum electrodes, namely iron sulphide. It was not analysed separately.

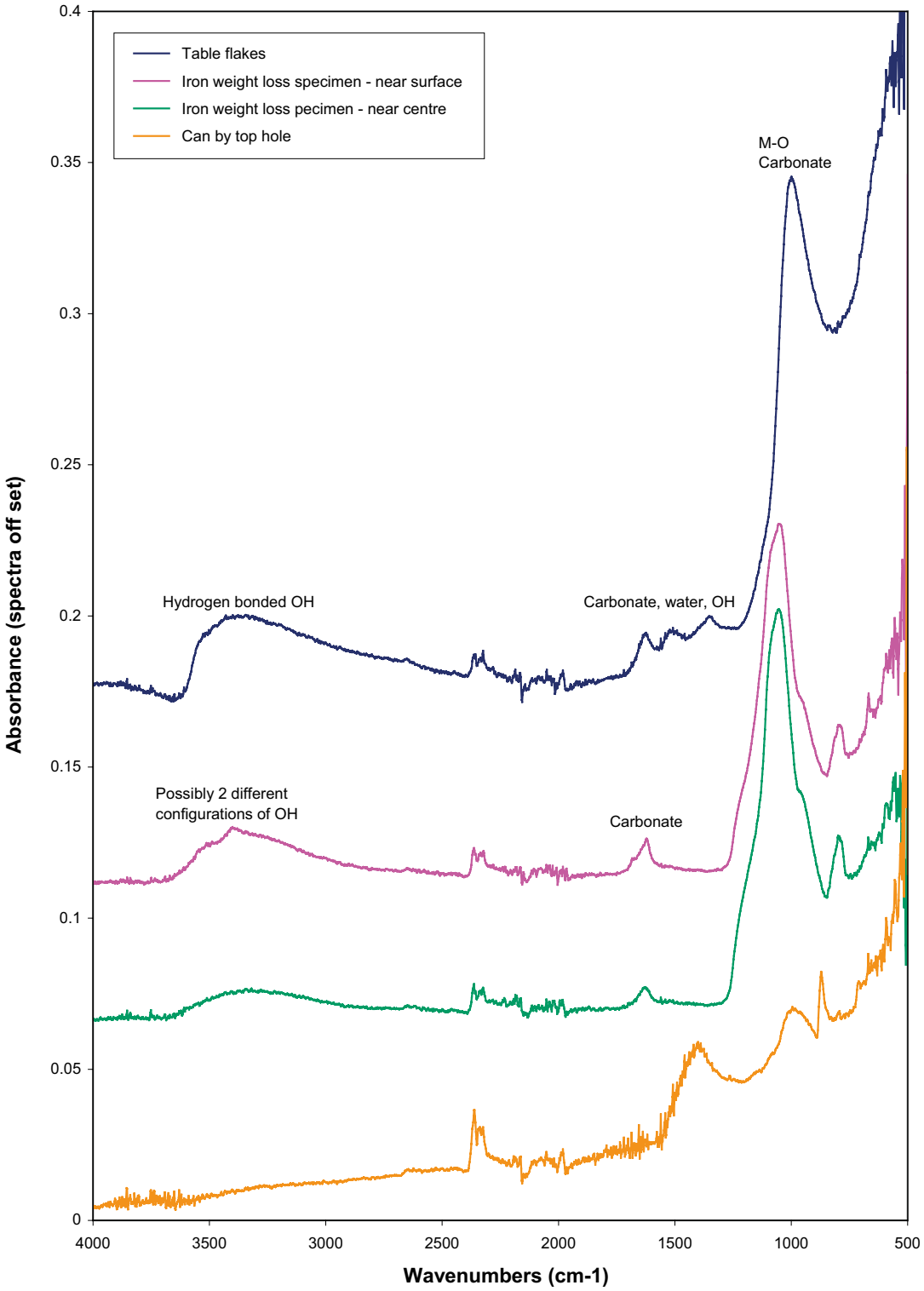

Figure 7-16. *Results from FTIR analysis of samples from Experiment 3.*

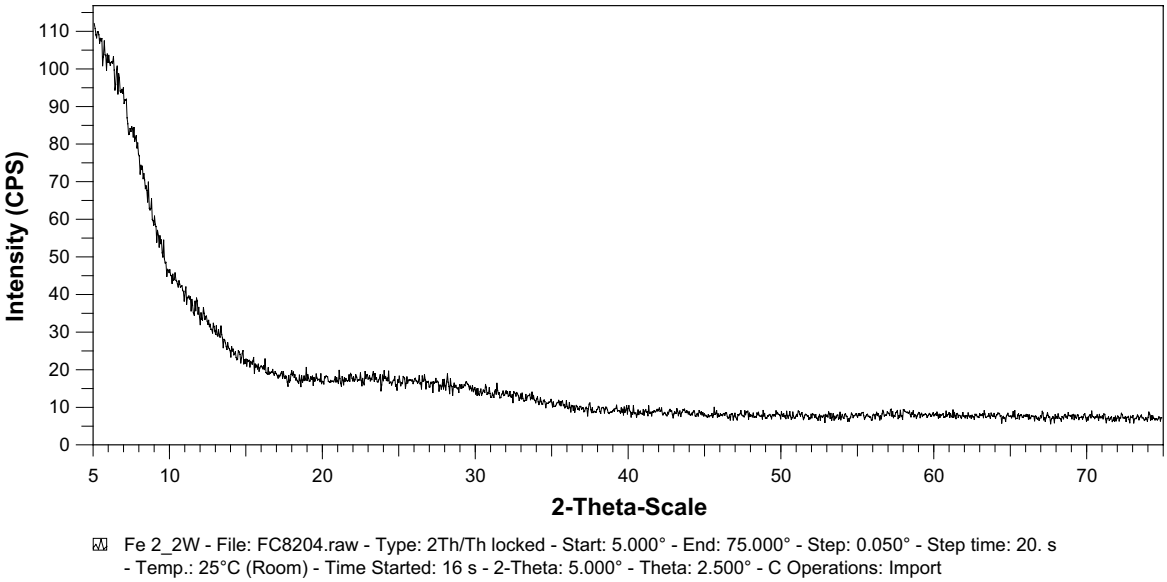

Figure 7-17. *XRD pattern for whiskers taken from iron electrode 2.*

Figure 7-18. *Platinum (top) and gold (bottom) electrodes removed from MiniCan Experiment 3. The insulating sheathing is still present at the left hand end of the wires.*

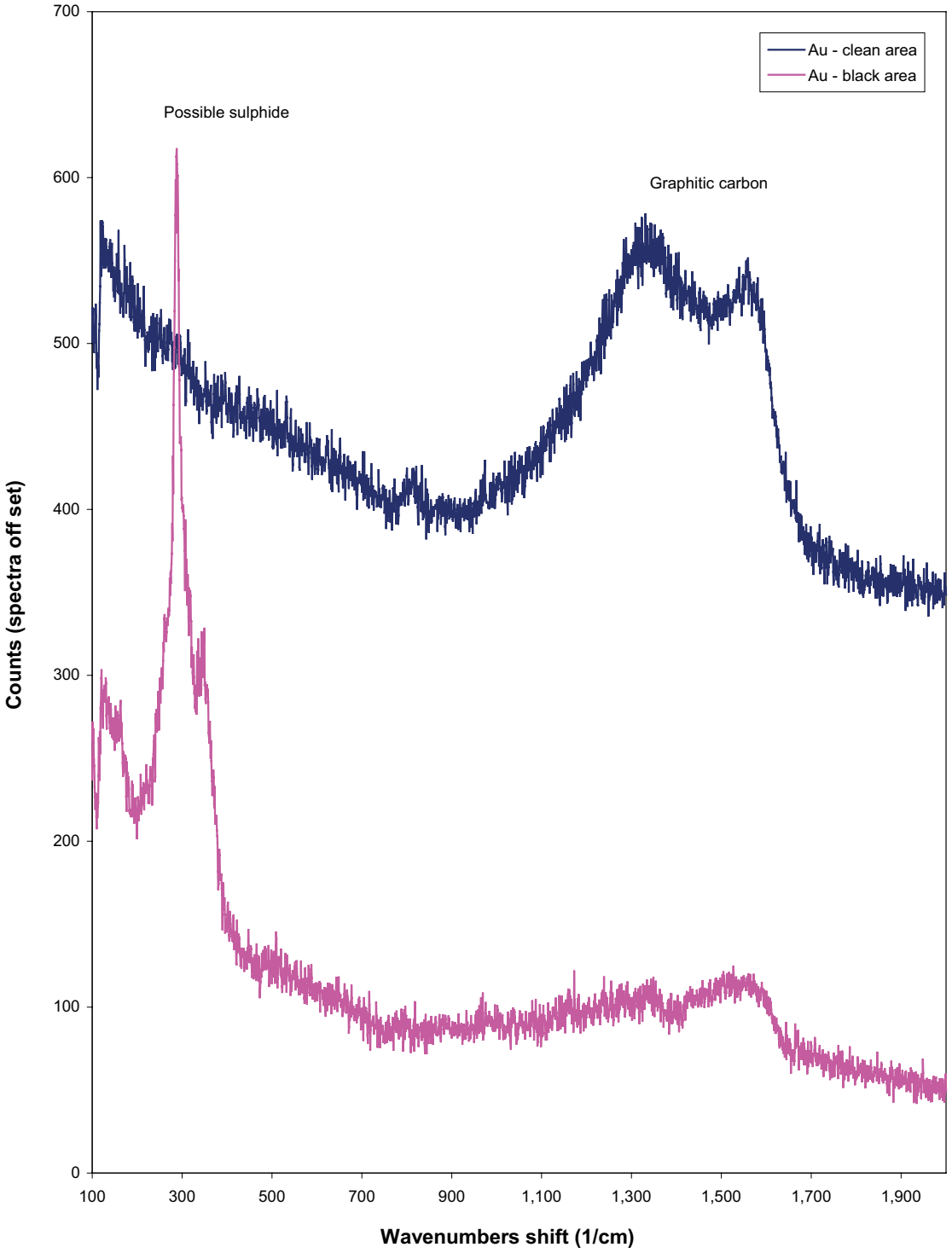

Figure 7-19. *Raman analysis of surface of gold electrode removed from MiniCan Experiment 3.*

7.1.8 Sandwich specimen

The condition of the sandwich specimen can be seen in Figure 6-9, 7-20 and 7-21. No expansion of the sandwich specimen was observed, as shown by Figure 7-22. The inner surfaces were relatively clean and uncorroded, whereas the outer cast iron surface had a thick black flaky layer of material. The dimensional measurements indicate that the layer was approximately 1 mm thick. Raman analysis was performed by encasing the samples in custom-built Perspex specimen holders fitted with optical glass windows (see Appendix 1 for details) and the results of the Raman analysis are shown in Figure 7-23 and 7-24, for the iron surfaces (outer and inner surfaces respectively), and Figure 7-25 and 7-26, for the copper surfaces (outer and inner surfaces respectively). The main features of the analysis of the sandwich specimen are as follows:

- The cast iron outer surface of the cast iron component of the sandwich specimen was predominantly graphitic.
- The inner surface of the cast iron component was composed of a mixture of spinel type materials, such as magnetite, Fe_3O_4, as well as iron sulphide, including FeS_2, graphite and amorphous carbon. There were variations between different areas on the surface.
- The outer surface of the copper component had a composition that varied at different locations, but showed signs of sulphides, including copper sulphide, Cu_2S.
- The inner surface of the copper component showed variations in composition at different locations, with indications of crystalline copper sulphide Cu_2S and an unidentified amorphous phase.

Figure 7-20. *Appearance of sandwich specimen when removed from MiniCan Experiment 3.*

Figure 7-21. *Appearance of sandwich specimen when removed from MiniCan Experiment 3. The lower two photographs show the interior surfaces of the specimen.*

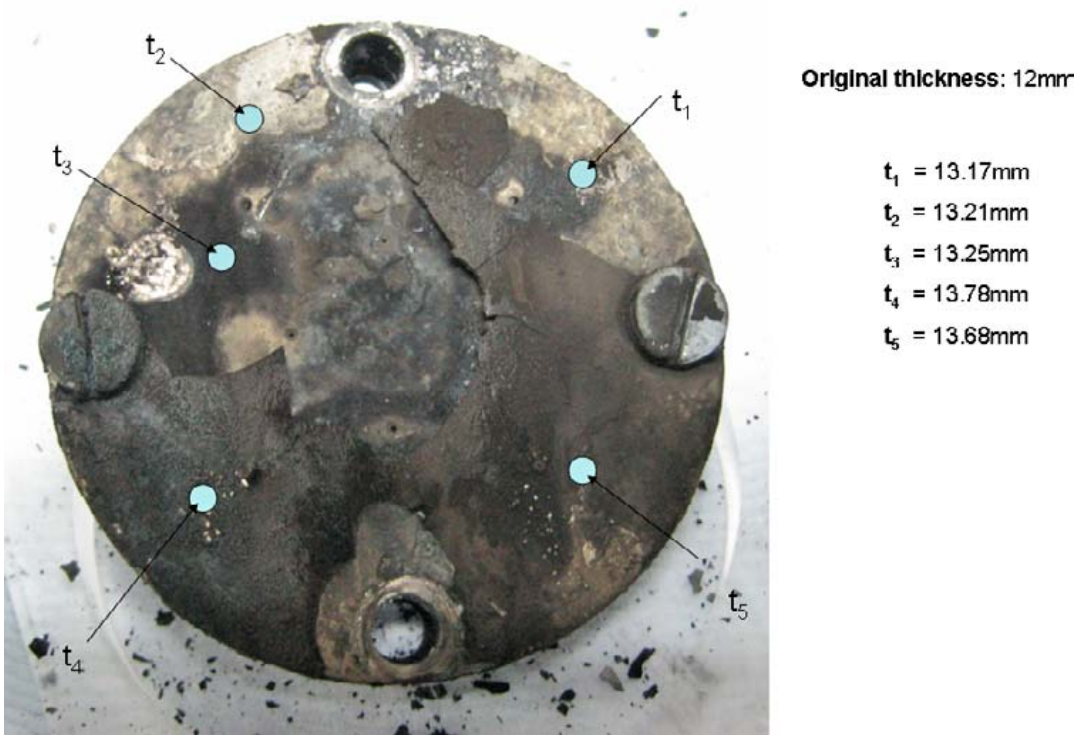

Figure 7-22. *Thickness of sandwich specimen at various locations.*

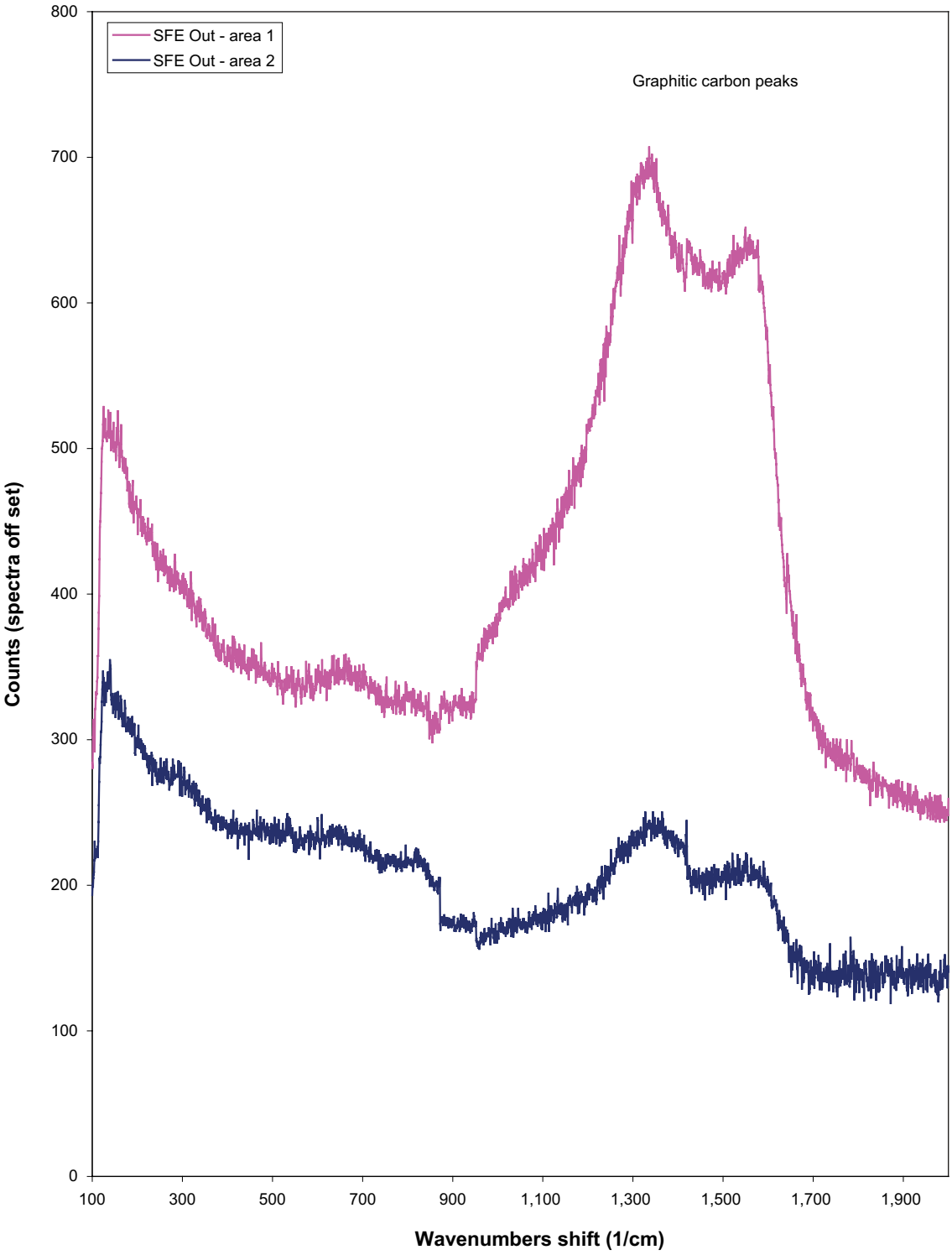

Figure 7-23. *Raman analysis of outer iron surface of sandwich specimen.*

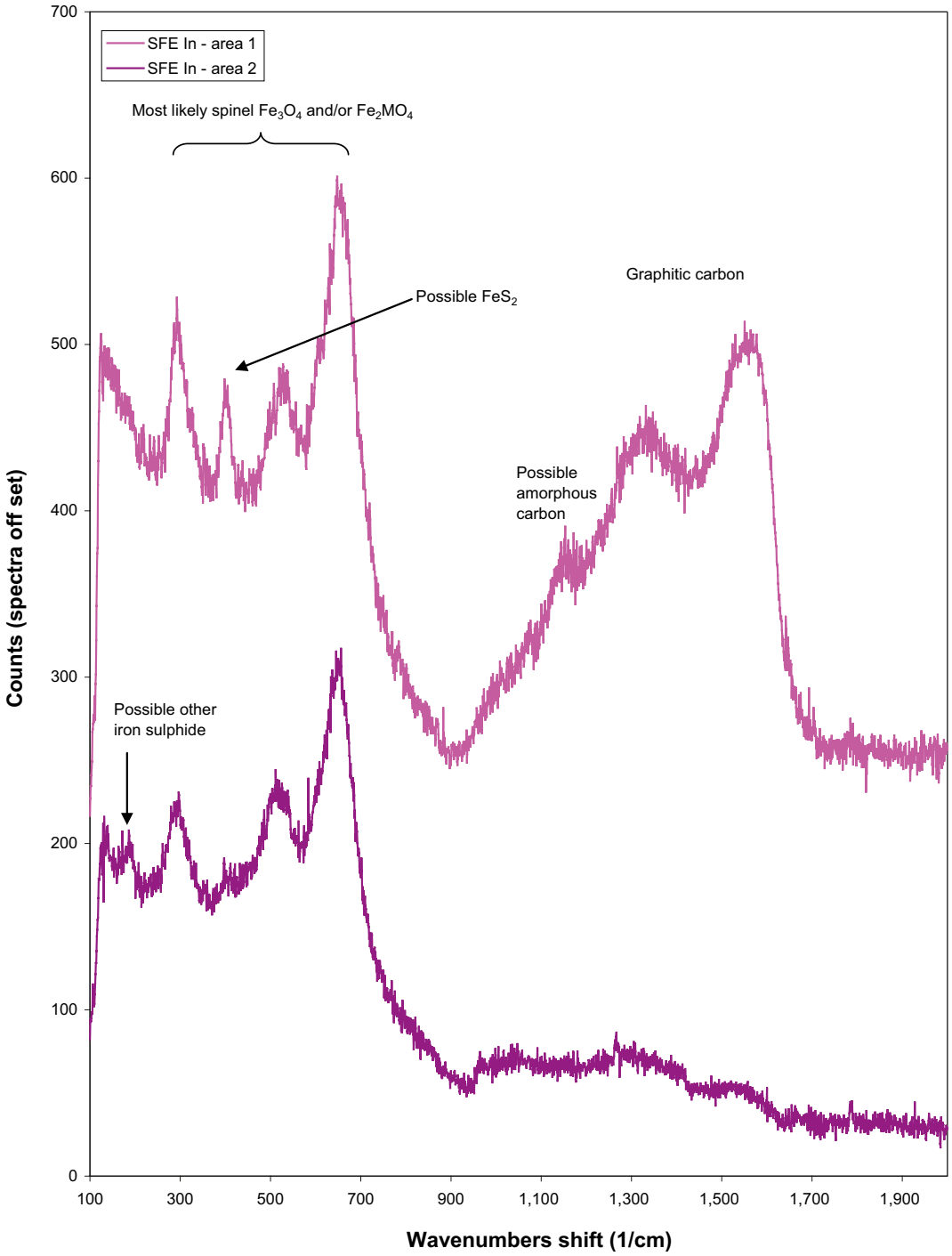

Figure 7-24. *Raman analysis of inner iron surface of sandwich specimen.*

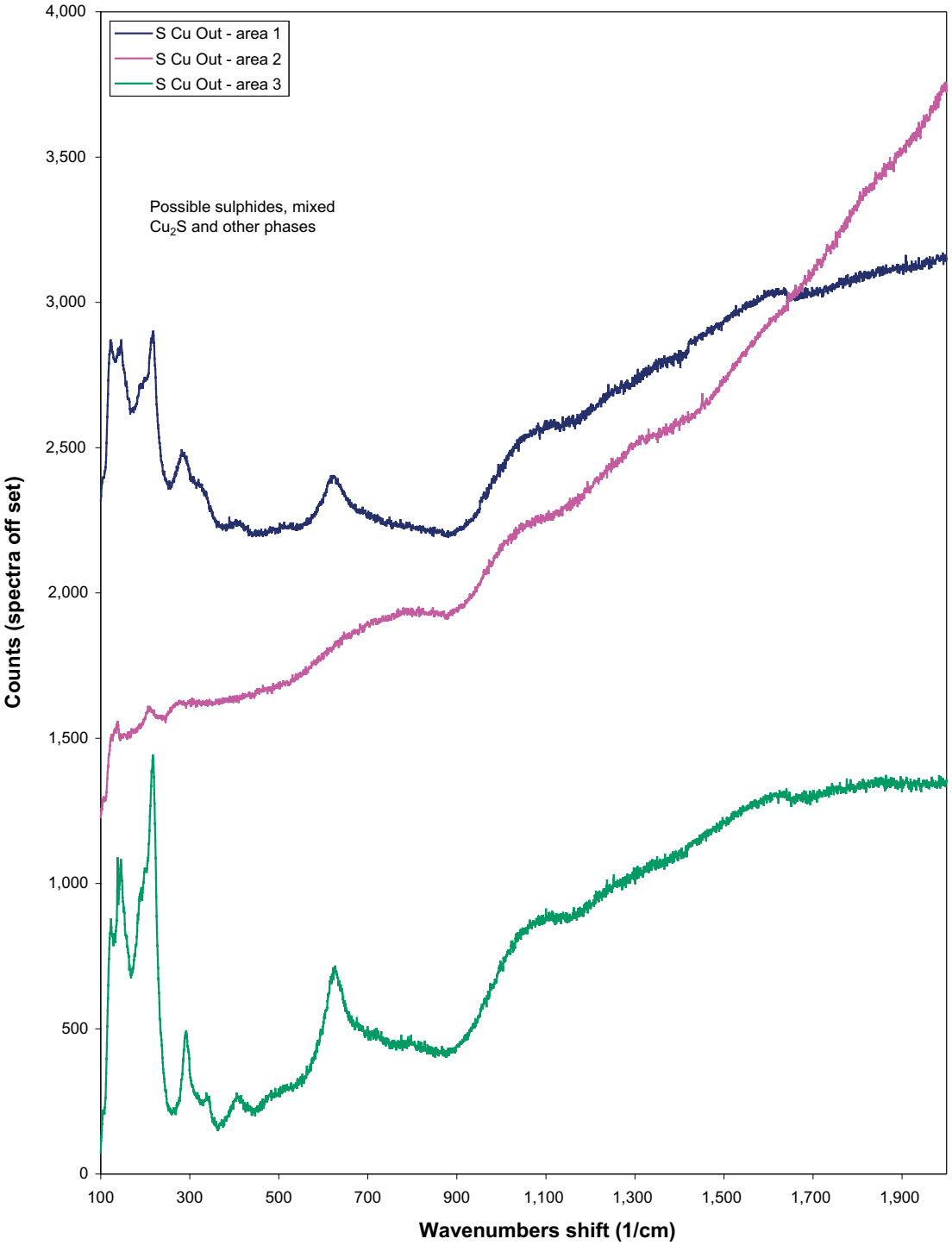

Figure 7-25. *Raman analysis of outer copper surface of sandwich specimen.*

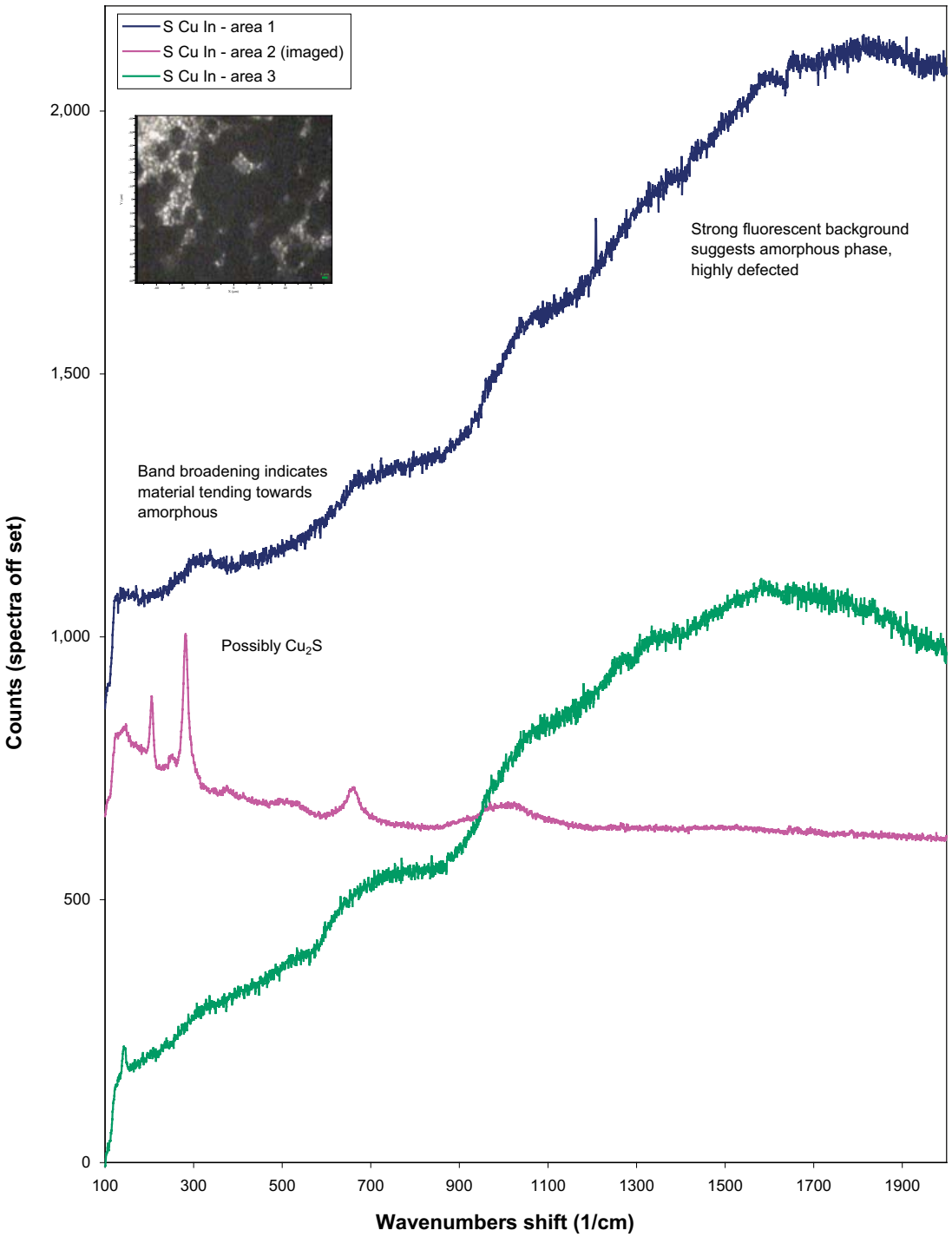

Figure 7-26. *Raman analysis of inner copper surface of sandwich specimen.*

7.1.9 Ag/AgCl disc reference electrodes

The silver-silver chloride disc electrodes had become covered in a layer of black deposit as shown in Figure 7-27. SEM/EDX analysis of the material on the reference electrodes (Appendix 2) showed the black material on the surface was predominantly composed of iron, sulphur, carbon and oxygen with small amounts of calcium, silicon, magnesium, sodium and aluminium. It is noteworthy that no silver was detected, indicating that the whole surface had become sealed with a layer of deposit. This explains why the electrodes no longer functioned as reference electrodes (Smart et al. 2012). It is also possible that some of the deposit is of organic origin (e.g. microbial material).

7.1.10 Black flakes from table

As the support table dried out, the black coating material started to flake off. Examples of the appearance of this material are shown in Figure 7-28 and 7-29. In close up it can be seen that the surface had dried to leave some white fluffy material on the surface. Raman analysis of flakes from the table (Figure 7-30 and 7-31) gave indications of Fe_2O_3, carbonate, graphitic carbon and iron sulphide, and generally the material was amorphous.

X-ray diffractograms for the material (Figure 7-32 and 7-33) show that it was predominantly amorphous with some unidentified peaks in one analysis (Figure 7-32) and no peaks at all in the other analysis (Figure 7-33). SEM/EDX analysis (Appendix 2) shows that the material consists of a mass of closely compacted small crystallites (< 5 µm) with a high concentration of iron, sulphur, silicon and oxygen. Crystals with a different morphology, with a high concentration of calcium, carbon and oxygen are superimposed on the top surface of the iron-sulphur rich layer. This probably accounts for the fluffy white material visible in Figure 7-29 and is likely to be calcium carbonate. FTIR analysis (Figure 7-16) of the material shows the presence of metal-oxide bonds, carbonate and OH bonds. SEM images of the edge of a flake show that it was approximately 0.1 mm thick (Appendix 2).

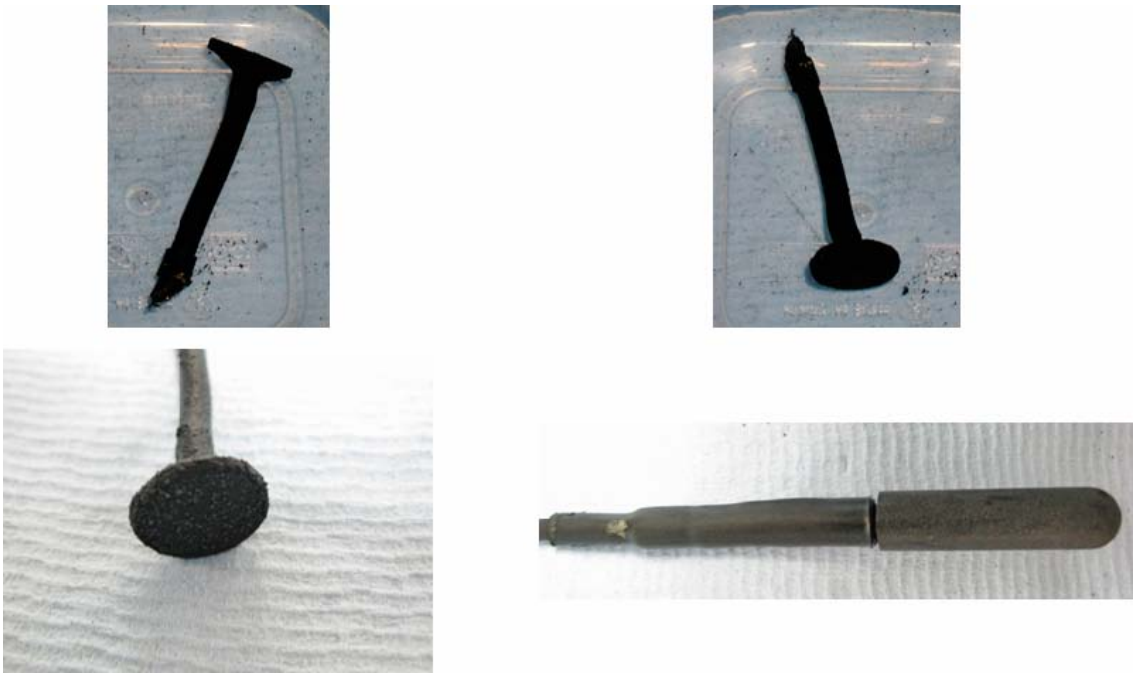

Figure 7-27. *Appearance of silver-silver chloride electrodes and metal oxide E_h probe (bottom right hand corner) after removal from MiniCan Experiment 3. The top two photographs show the disc electrodes submerged in groundwater.*

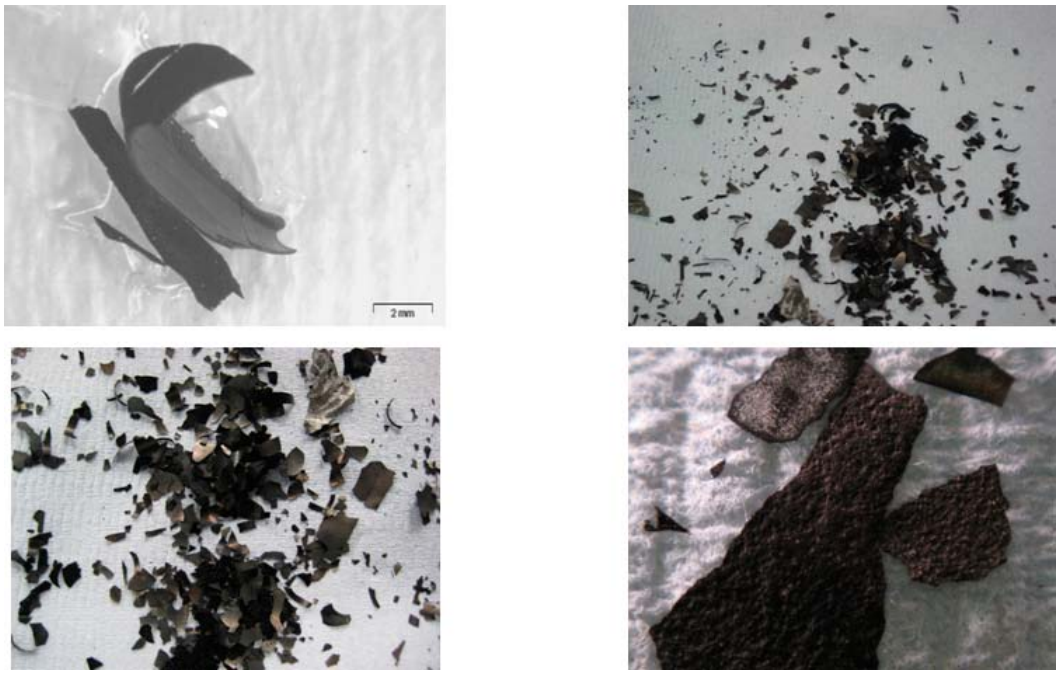

Figure 7-28. *Black flakes from support table.*

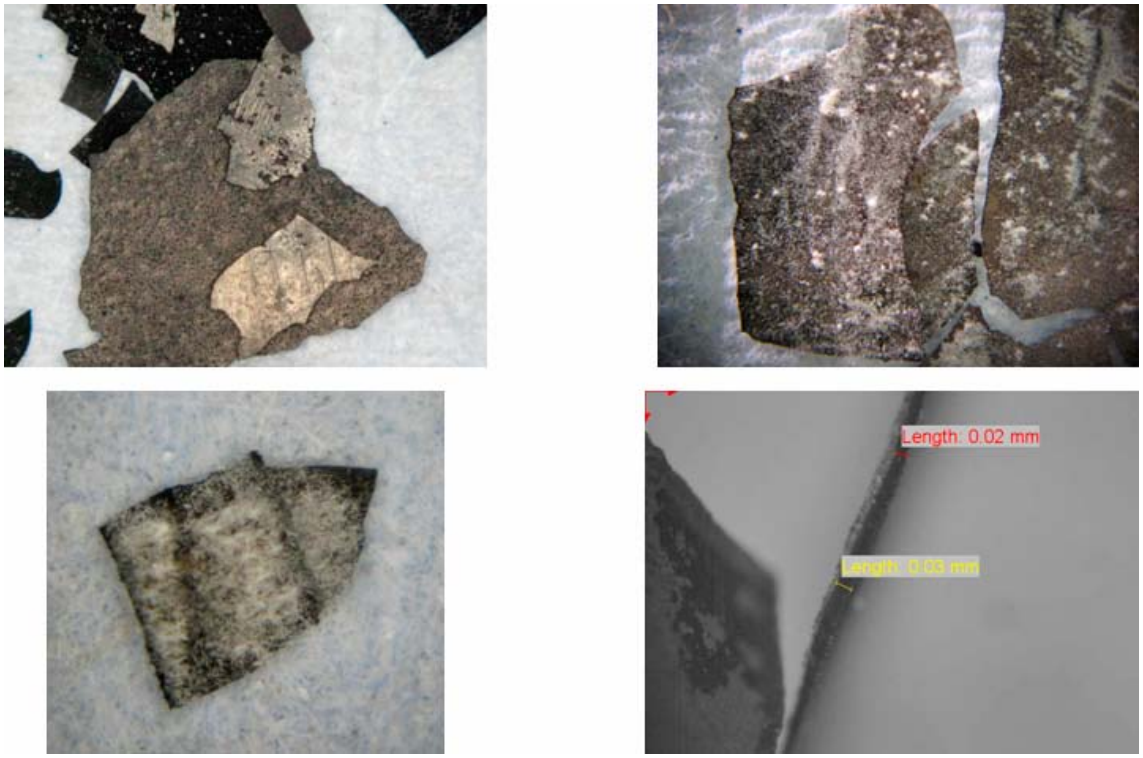

Figure 7-29. *Black flakes from support table.*

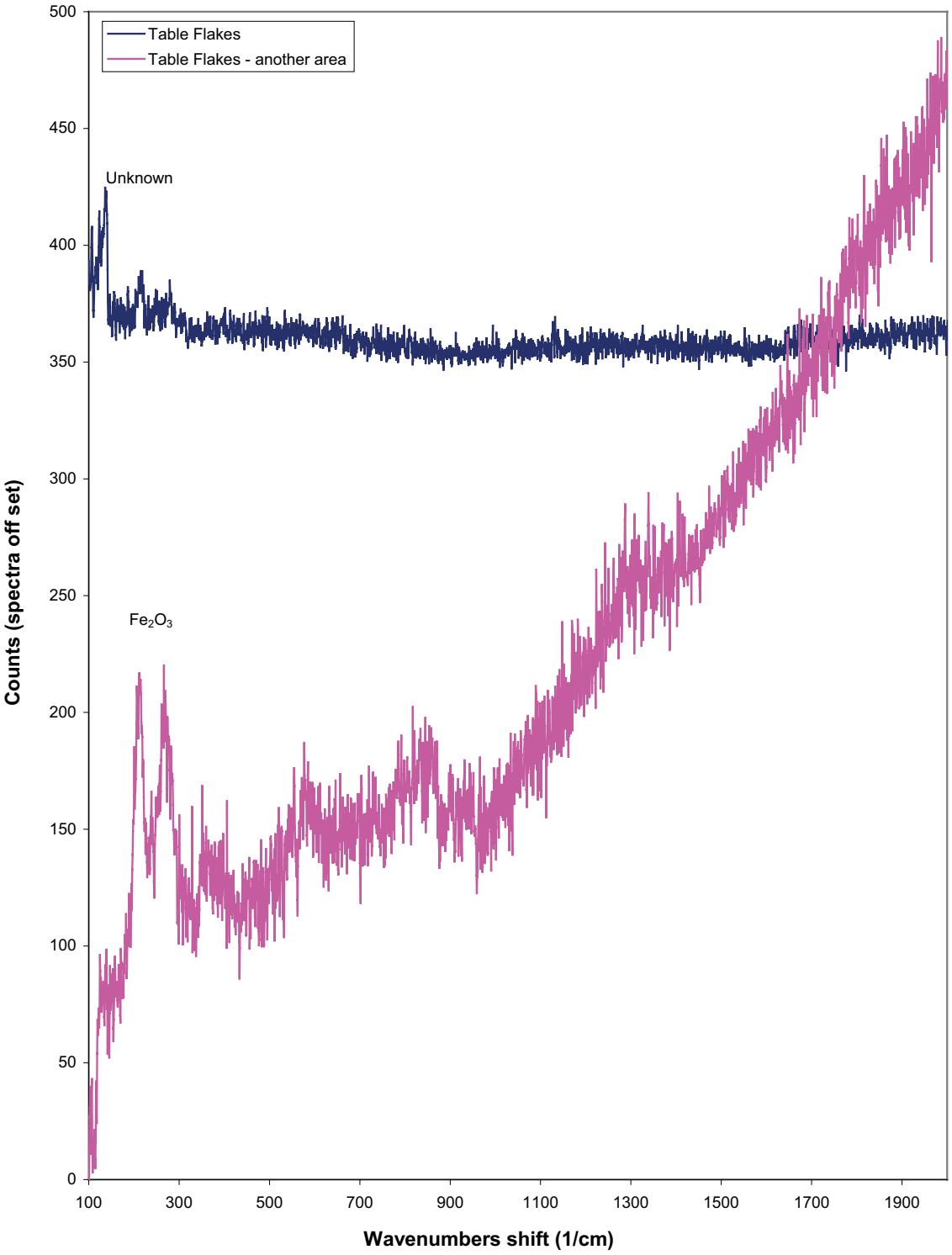

Figure 7-30. *Raman analysis of flakes from support table (1).*

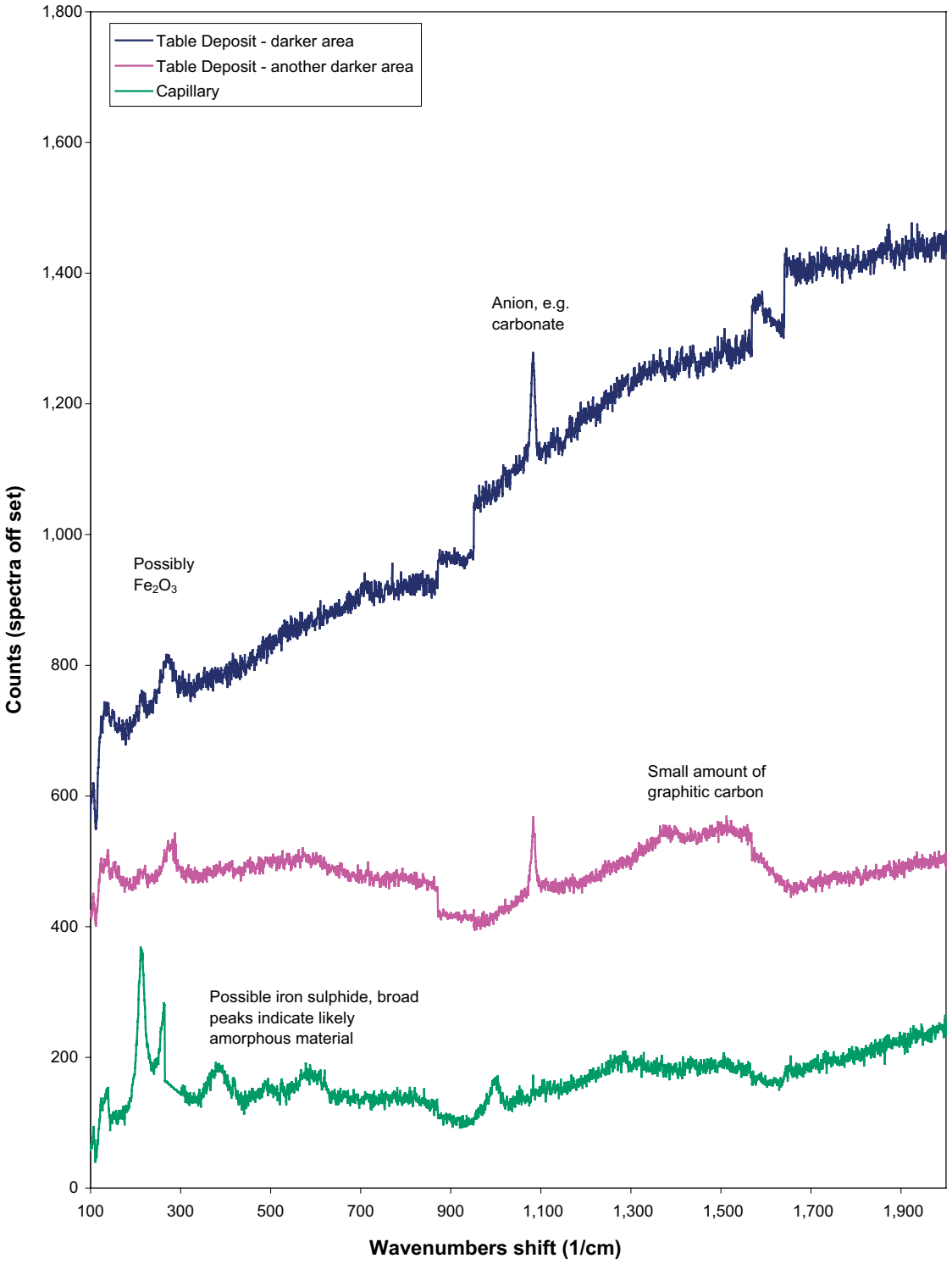

Figure 7-31. *Raman analysis of flakes from support table (2).*

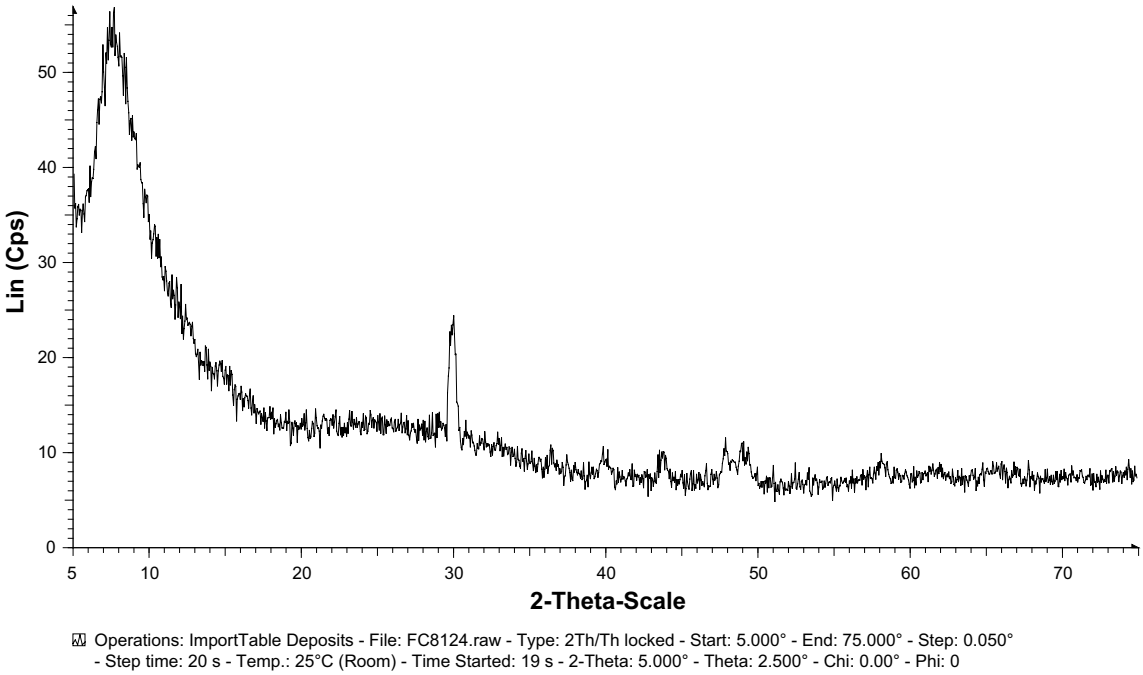

Figure 7-32. *X-ray diffractogram for black flake (1) from surface of support table in MiniCan Experiment 3.*

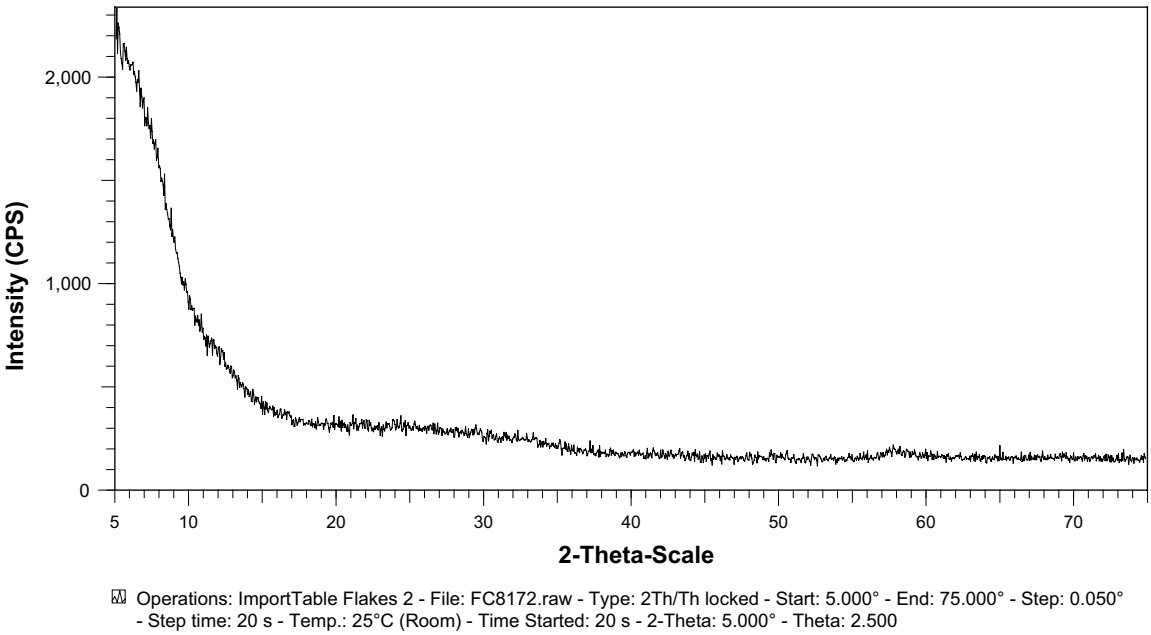

Figure 7-33. *X-ray diffractogram for black flake (2) from surface of support table in MiniCan Experiment 3.*

7.2 Other items

7.2.1 U-bend specimens

Two copper U-bend specimens were removed from Experiment 3; one was suspended on the pull rod attached to the support cage near the support cage and the other was suspended on the pull rod near the flange on the borehole. Photographs of both specimens are shown in Figure 7-34 and 7-35. Both specimens had a dark appearance due to the formation of a surface film. The black tape on the specimens was present when they were inserted into the borehole; the tape was placed on the surface when the specimens were manufactured and it was mistakenly left in place. The surface film was analysed using X-ray Photoelectron Spectroscopy (XPS) and FTIR and the results of this examination are shown in Figure 7-36 and 7-37. The analysed sample was cut from the unstressed section of the specimen (i.e. a flat section). The XPS analysis shows that the main components of the top layer of the film (a few nm or atomic layers sampling depth) were copper, carbon and oxygen, with a trace of sulphur. The composition from the XPS analysis was (at%) C 41.8; O 39.7; Cu 14.6; S 3.9. The FTIR analysis (Figure 7-37) showed peaks that can be attributed to hydrocarbons C-H bonds, aromatic C-H bonds, metal-oxygen bonds, water and OH groups. Note that this sample was only exposed to groundwater, rather than water conditioned by bentonite, since it was mounted in the borehole water rather than inside the support cage. No indications of stress corrosion cracking were observed in the U-band specimens using optical microscopy, although further metallurgical analysis is planned to confirm this.

7.2.2 Silvion and E_h probe

The Silvion reference electrode (not shown), which was mounted in the borehole outside the support cage, was not covered with black deposit and the sintered disc at the tip of the electrode remained relatively clean, apart from a few black spots. The E_h probe, which was also mounted outside the support cage, showed no signs of degradation (Figure 7-27). Both electrodes functioned satisfactorily during the test period.

Figure 7-34. *Photographs of U-bend SCC specimens from near the support cage removed from borehole Experiment 3.*

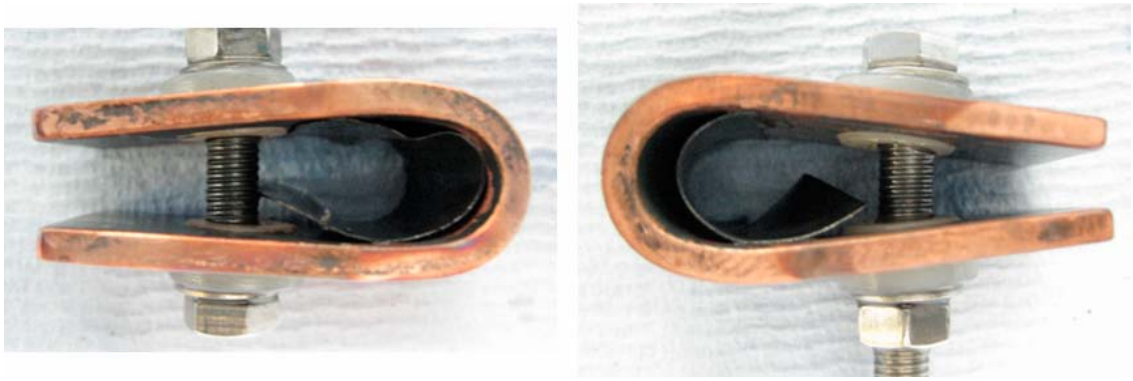

Figure 7-35. Photographs of U-bend SCC specimens from near the flange end of the borehole removed from Experiment 3.

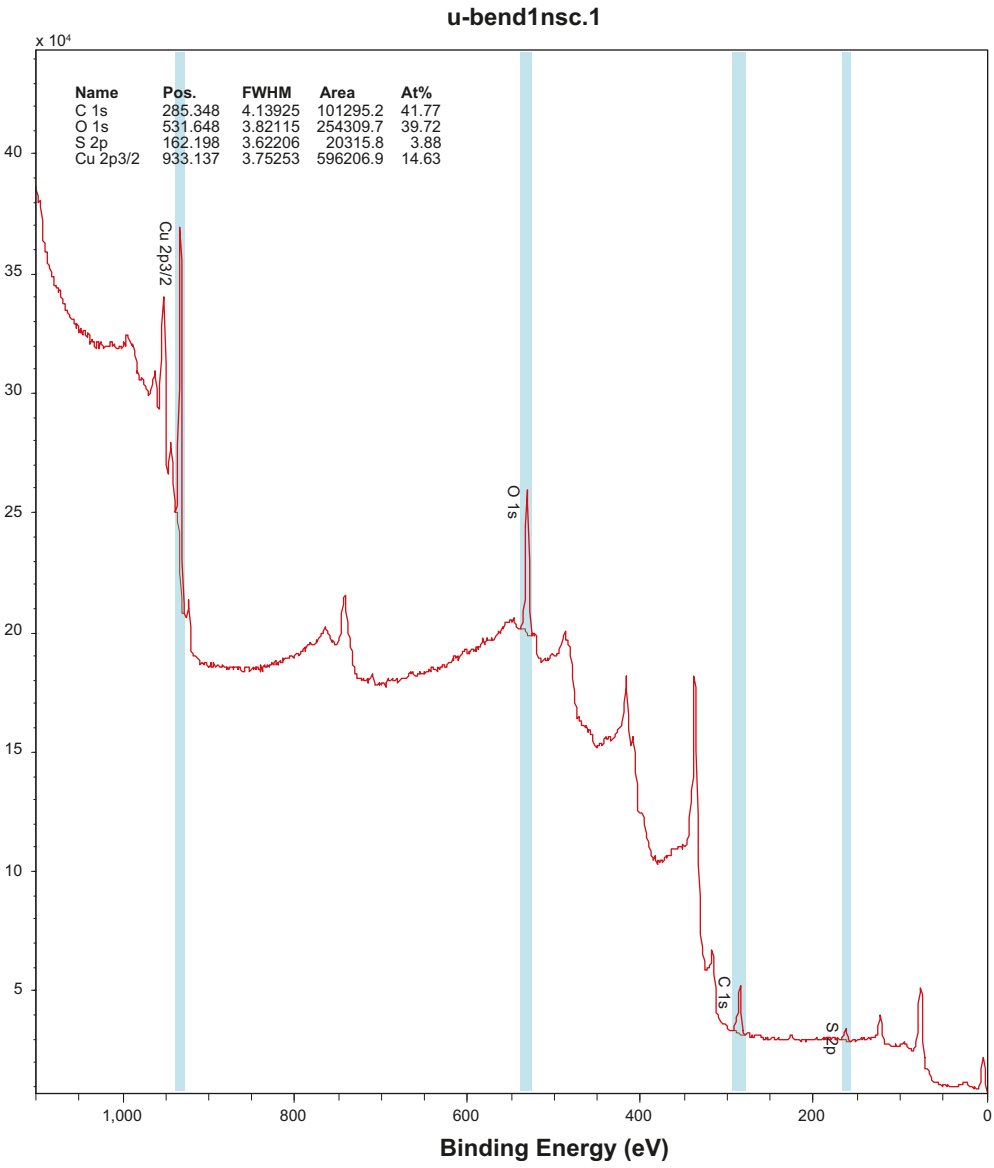

Figure 7-36. XPS results for U-Bend specimen removed from Experiment 3 borehole.

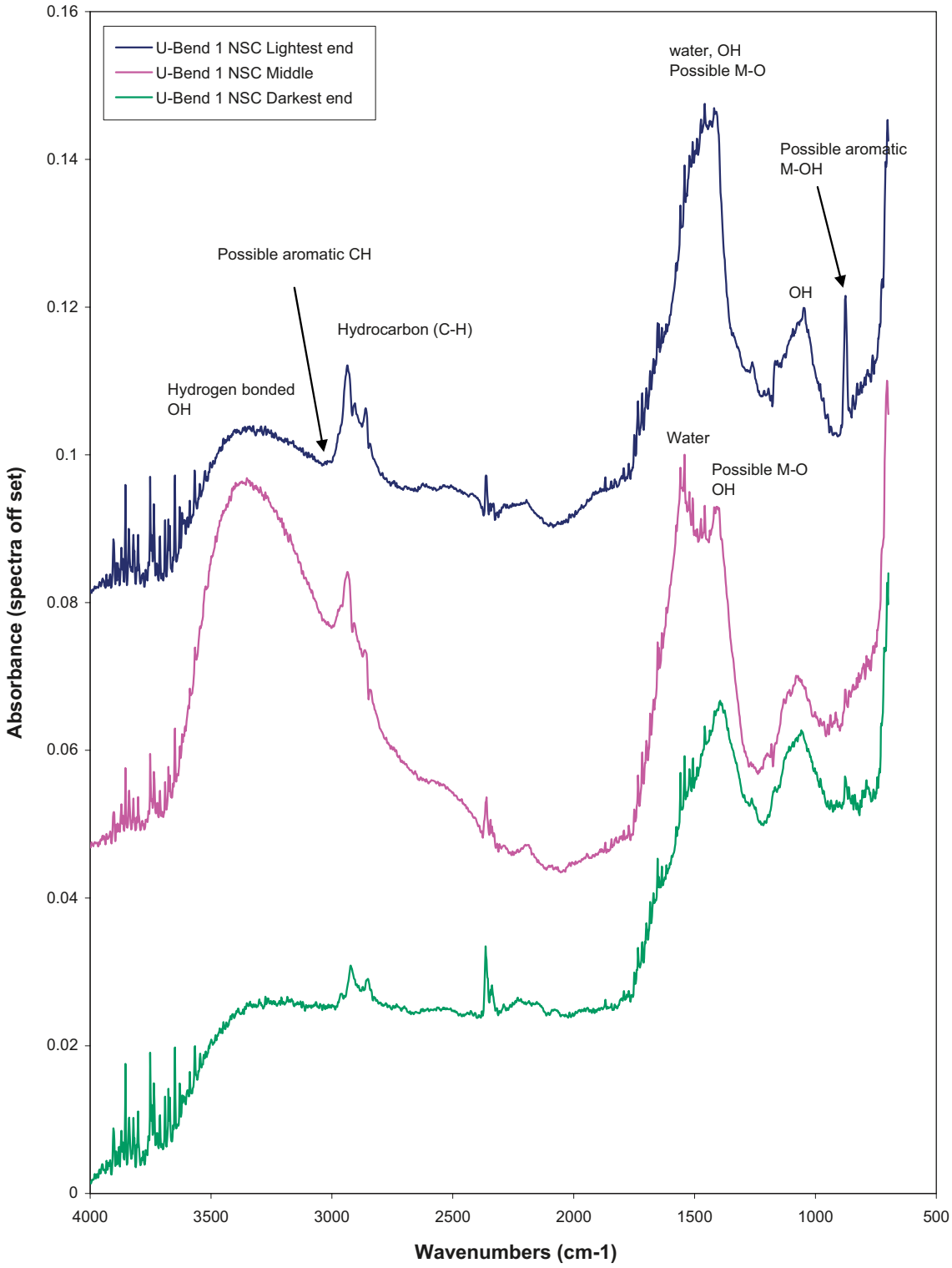

Figure 7-37. *FTIR spectra for U-Bend specimen removed from Experiment 3 borehole.*

7.2.3 Swabs from outer surface of stainless cage

When the support cage was removed from the transfer flask there were indications of thin green-black films on the surface of the stainless steel lid (Figure 6-3). Swabs of the surface were taken by Microbial Analytics and the results of the analysis are presented in Hallbeck et al. (2011) and are not reported here. Figure 6-3 also shows a photograph of swabs taken from the surface of the lid, indicating the presence of dark material removed from the surface of the cage.

7.3 Canister

After a thorough visual examination of the intact canister, including accurate measurement of the outer dimensions to check for any expansion or contraction, the outer copper canister was carefully cut using a mechanical saw mounted in the custom-built glovebox.

Using the rotary cutting disc the canister was cut across the diameter into three sections. With the top two sections the copper was cut vertically to give three equal segments so that it could be peeled away from the cast iron insert to reveal the distribution of the corrosion product around the annulus in relation to the position of the defect in the copper container. The bottom section of the canister was cut vertically and completely into four segments, again allowing the pieces of copper canister to be peeled away from the cast iron insert. The distribution of corrosion product in the annulus was photographed and documented. A number of samples were removed for analysis and the results are presented below.

7.3.1 Dimensional measurements

The dimensions of the copper canister were measured using a vernier caliper gauge inside the glovebox, by measuring the diameter of the copper cylinder across four diameters at 45° intervals and 20 mm steps in height. The results are tabulated in Table 7-3. These show that within the accuracy of the measurements (± 0.05 mm) there was no increase in the dimensions of the canister, compared to the original ‘as machined’ diameter of 145 ± 0.5 mm.

7.3.2 Observations when canister was sectioned

The copper canister was sectioned using the rotary saw in the glovebox, by cutting it in to three equal lengths, then cutting longitudinally through the copper walls of the canister. Photographs of the cutting operation and the appearance of the various components are shown in Figure 7-38 to 7-46.

The lid region of the cast iron insert was carefully dismantled and examined for any signs of crevice corrosion around the gasket material. The appearance of these components is shown in Figure 7-43. No corrosion was observed below the level of the O-ring seal, whereas tarnishing of the iron surface was visible above the level of the O-ring and on the top surface of the lid. The simulated fuel channels inside the cast iron insert were dry and uncorroded (Figure 7-43).

Analyses of the various samples taken from the copper canister and the cast iron insert are described in the following sections.

Table 7-3. Summary of measurements of diameter of copper canister from Experiment 3, measured in the anoxic glovebox using a vernier calliper (height accuracy ± 2 mm; diameter accuracy ± 0.05 mm). The hole in the canister was located at the top of the canister on the Position 3 diameter. The original permitted variation in diameter was ± 0.5 mm on a machined diameter of 145 mm.

Distance from top of canister that measurement was taken at (mm)	Position 1 Canister diameter (mm)	Position 2 Canister diameter (mm)	Position 3 Canister diameter (mm)	Position 4 Canister diameter (mm)
0	145.40	145.06	145.17	145.35
20	144.98	145.10	145.10	145.36
40	145.10	145.06	145.16	145.12
60	145.20	145.06	144.98	145.16
80	144.97	145.17	145.20	145.06
100	145.23	145.28	145.15	145.24
120	145.18	144.97	145.11	145.15
140	145.44	145.24	145.13	145.17
160	145.16	144.98	145.02	145.05
180	145.11	144.97	144.99	144.94
200	144.99	145.19	144.96	145.15
220	144.97	144.93	144.98	145.02
240	144.99	144.94	145.13	144.99
260	145.15	145.01	145.05	145.02
280	145.06	144.90	145.12	144.92

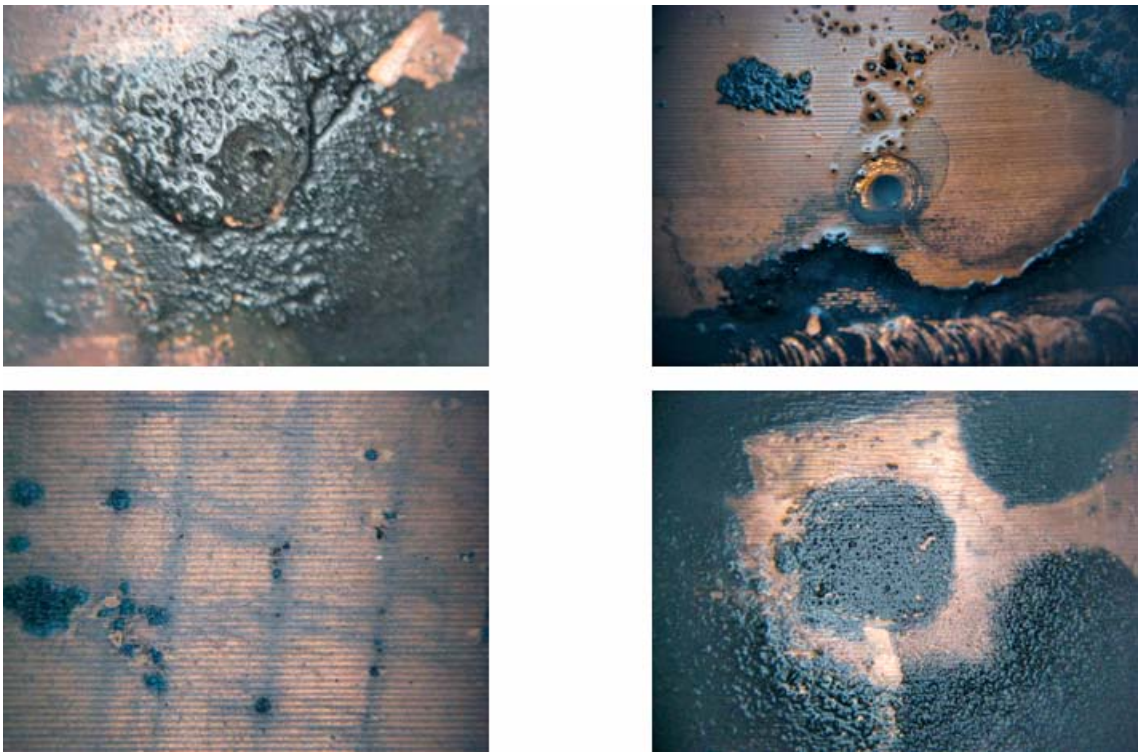

Figure 7-38. *Appearance of features on surface of copper canister from Experiment 3: top left – top defect in copper canister; top right – bottom defect in copper canister; bottom left – machining marks in copper and areas of dark deposit; bottom right – details of 'chain' pattern from under plastic insulator.*

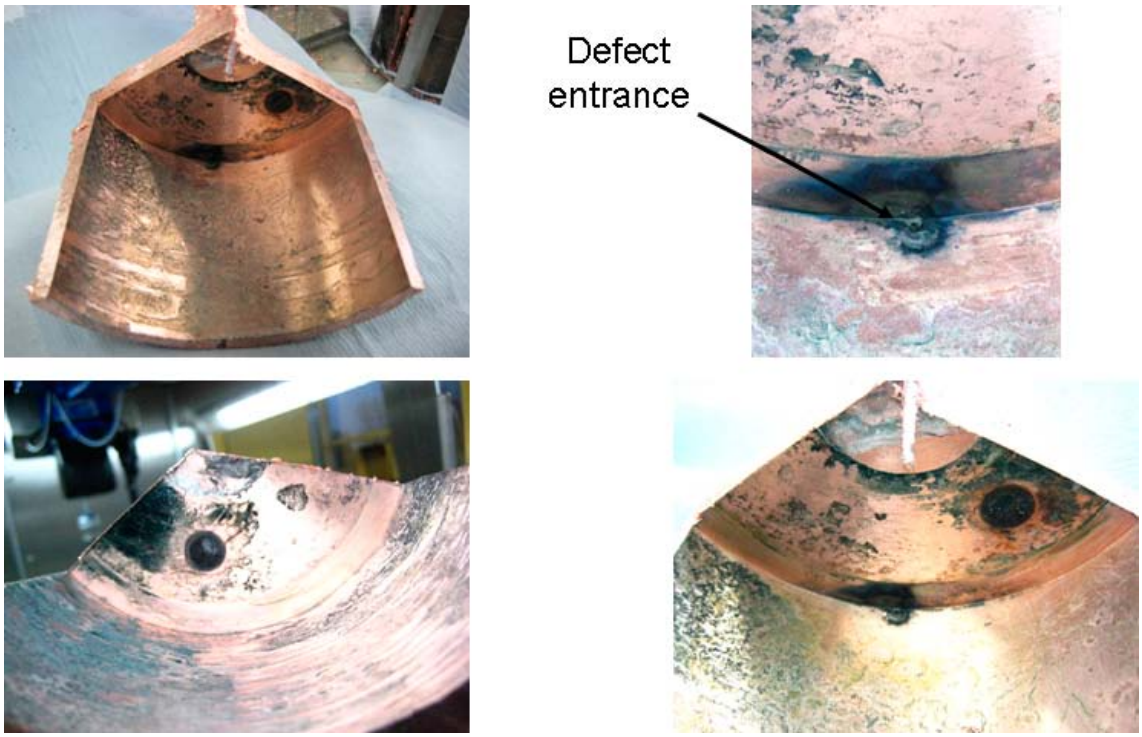

Figure 7-39. *Appearance of inner surface of copper canister – top section. The entrance of the defect can be seen.*

Figure 7-40. *Appearance of outer surface of cast iron insert – top section (1).*

Figure 7-41. *Appearance of outer surface of cast iron insert – top section (2).*

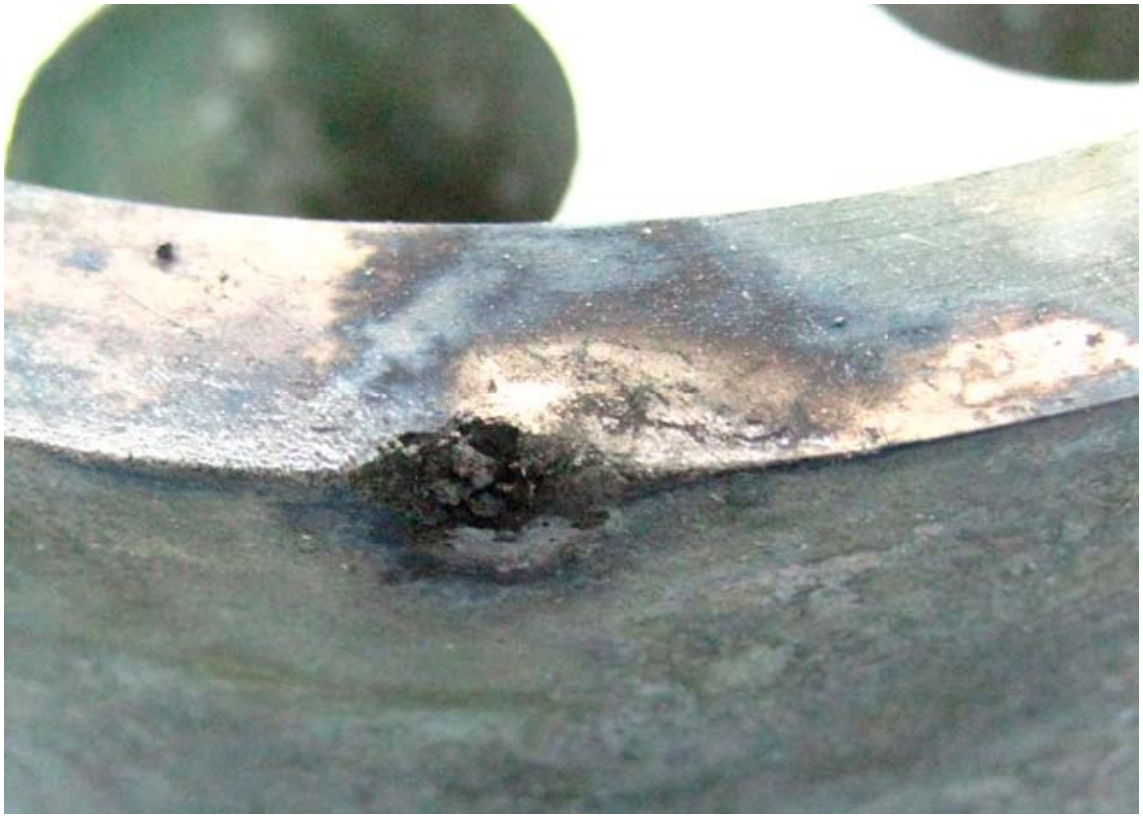

Figure 7-42. *Top of cast iron insert showing attack of iron opposite defect in copper.*

Figure 7-43. *Lid of cast iron insert removed from Experiment 3 in an anoxic glovebox.*

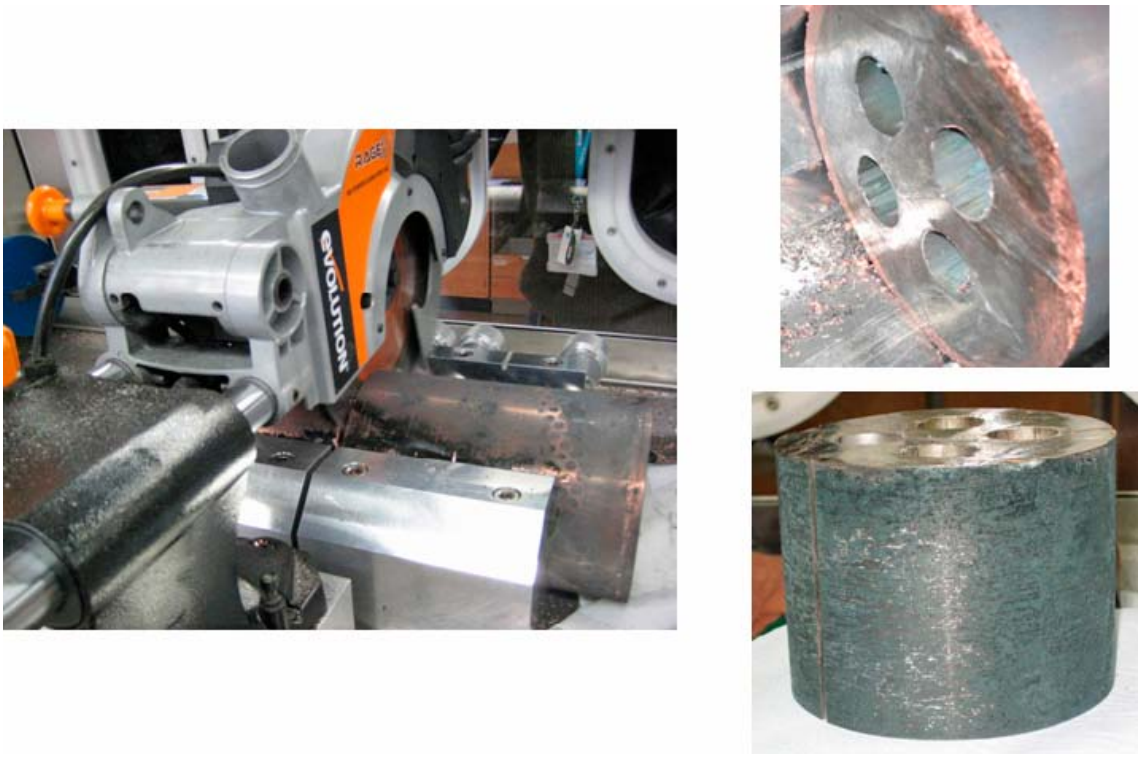

Figure 7-44. *Cutting mid section of Experiment 3 inside an anoxic glovebox.*

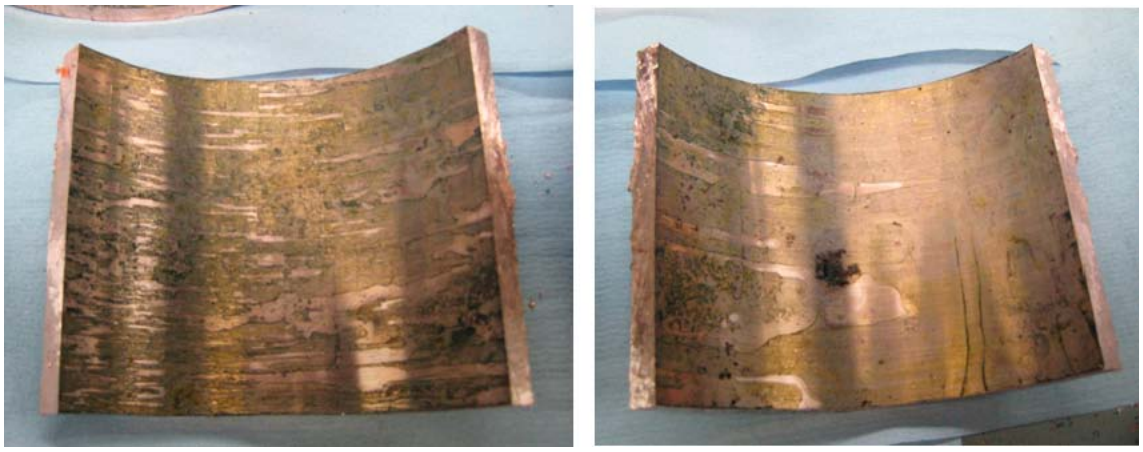

Figure 7-45. *Sections of copper from centre section of canister.*

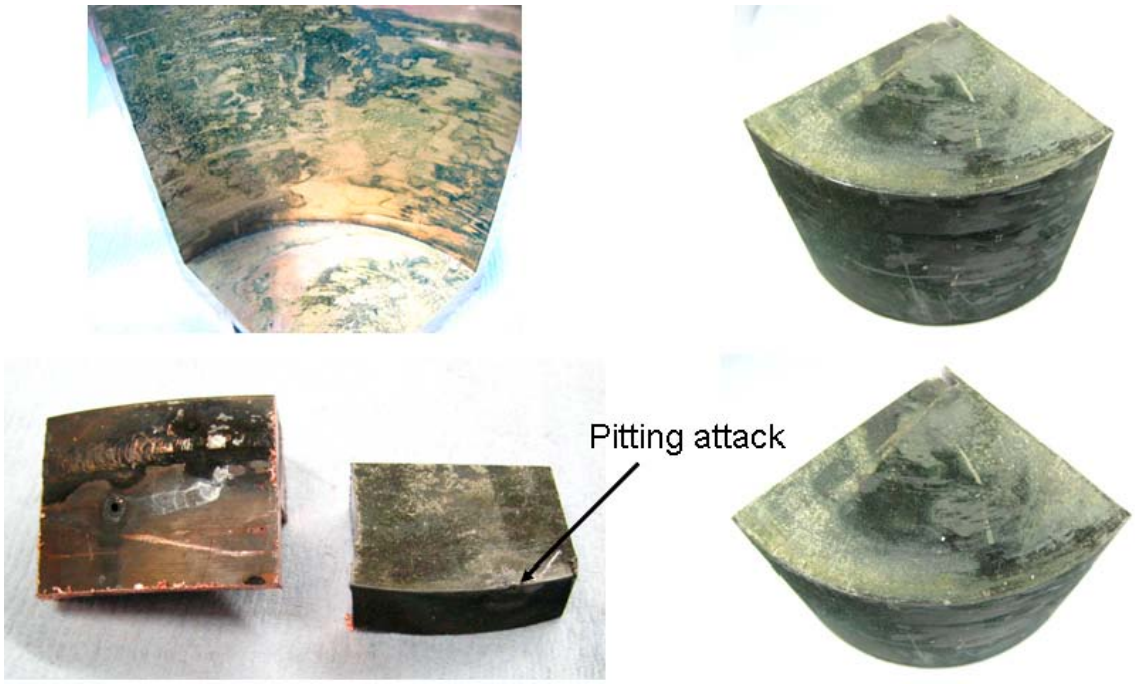

Figure 7-46. *Appearance of inner surface of copper canister and outer surface of cast iron insert – bottom section.*

7.3.3 Black flakes from outer surface of canister

The X-ray diffraction pattern for scrapings of black material taken from the outside surface of the copper canister is shown in Figure 7-47. This shows that the material was predominantly amorphous with a trace of FeS (troilite) or $CuFeS_2$ (chalcopyrite); the XRD peak positions were the same as the flakes from the support table (Figure 7-37). SEM/EDX analysis showed that the surface of the material was covered with a variety of particles with a range of sizes and shapes, including threads and larger crystals masses. It is likely that the threads are residues from the swabs that were used to take samples for microbial analysis or from the tissue that was used to collect the scrapings before they were sprinkled on to the top of an adhesive carbon disc on an SEM stub.

- The composition of the large crystallites was predominantly copper, zinc, iron, calcium, chlorine, sulphur, oxygen and silicon, with small amounts of aluminium. The proportions of these elements in the large crystals varied between particles.
- Some crystals had a high concentration of magnesium.
- The composition of the flakes was different to that of the flakes on the table, which were predominantly composed of iron, sulphur, silicon and oxygen (Section 7.1.10).
- Some crystals appeared to be mainly calcium carbonate.
- Some spherical particles, which were ~5 µm in diameter were predominantly iron, sulphur and silicon.
- Some flakes were almost entirely iron, sulphur and oxygen.
- Fine structure in the morphology of the crystals can be seen at the sub-micron level.

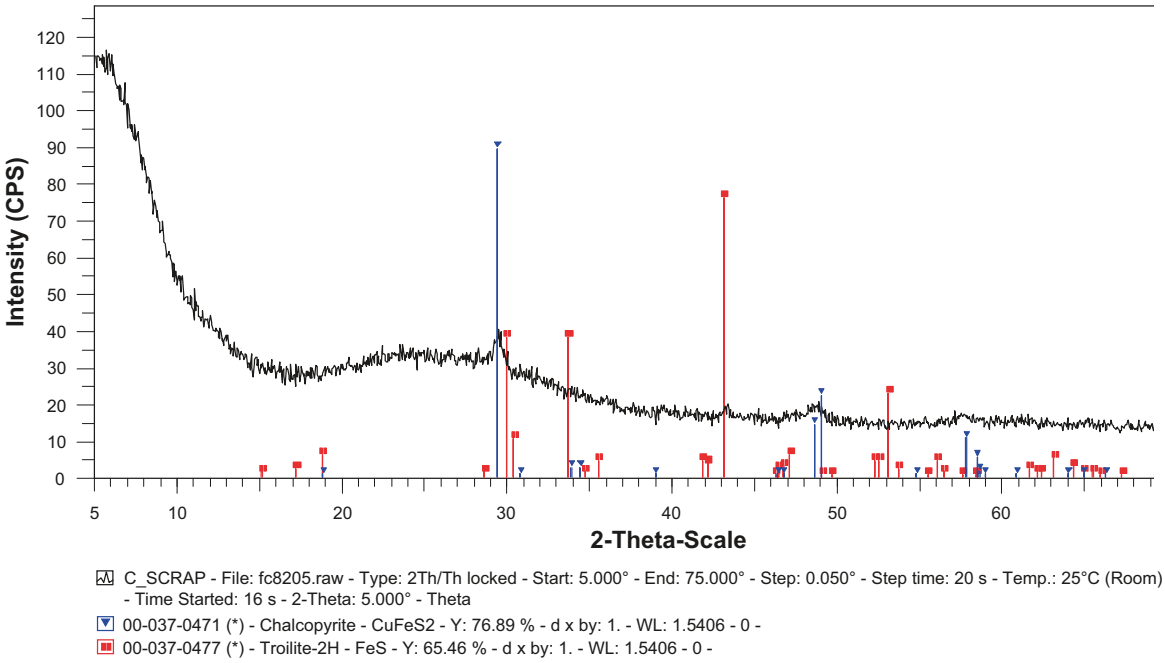

Figure 7-47. *XRD pattern for scrapings of black material from outer surface of copper canister.*

7.3.4 Copper canister: inner surface around the top hole

The area on the inner surface of the copper canister near the top defect is shown in Figure 7-39, which shows discoloration on the copper surface. SEM/EDX analysis (Appendix 2) shows a mixture of different crystal morphologies. The analysis identified the following main types of material:

- Flower-shaped crystalline material with high levels of calcium, sulphur and oxygen, suggesting the presence of calcium sulphate (one source of this may be gypsum from the bentonite in the annulus of the support cage).
- Sodium chloride crystals.
- Iron, copper, sulphur, silicon, chlorine, sodium, oxygen-rich particles.
- Crystals of copper sulphide, approximately 10 μm long.
- Filamentous strands composed of copper, which are believed to be swarf from cutting the specimen for analysis.
- Small spherical particles (~7 μm diameter) that appear to be rich in iron, copper, zinc, calcium, chlorine, sulphur, silicon and oxygen.
- Unusual concertina shaped crystals composed of copper which are most likely to be swarf from cutting operations.
- Elemental maps show that calcium, sulphur and oxygen correlate (probably calcium sulphate), and sodium and chlorine correlate (probably sodium chloride).
- Iron and silicon were concentrated around the entrance to the hole.
- High copper, iron and sulphur concentrations. This indicates that some residue of iron sulphide had transferred from the surface of the cast iron insert.
- There was a mixture of materials on the surface and it is not possible to distinguish them from the elemental analysis.

7.3.5 Copper canister: outer surface green areas around the top hole

The SEM/EDX analyses of this area (Appendix 2) exhibited the following features:

- In the elemental maps there is a correlation in the concentration of copper and sulphur, and sodium and chlorine around the entrance to the hole, with a correlation between iron and sulphur further away from the hole.
- The elemental maps show clear layers rich in copper, iron and sulphur on the copper substrate.
- The mouth to the hole shows areas rich in sulphur, chlorine and calcium, with some oxygen. The exact composition varies with location on the surface, indicating the presence of a number of different phases, including a calcium-rich phase.
- One area shows a thin flaky layer composed predominantly of iron and sulphur on the surface of the copper.

7.3.6 Copper canister: inner surface area around bottom hole

Note that the specimens from around the bottom hole were prepared in air (~0.5 hours of exposure). The SEM/EDX analysis of the inner surface area around the bottom hole shows the following key features:

- The presence of flaky deposits composed predominantly of iron, copper, sulphur, chlorine and oxygen. This indicates that there was some transfer of material from the surface of the cast iron insert to the inner surface of the copper canister.
- Discrete flower-like crystals with a high concentration of calcium, silicon, sulphur, chlorine and sodium.
- Very small crystals (< 2 μm) composed of copper, iron and sulphur.
- Some calcium and sulphur rich crystals.

- Some areas rich in copper, others rich in iron, suggesting patchy deposits of iron rich sulphide material on a copper sulphide coated surface.
- Silicon correlates with a high oxygen concentration, suggesting the presence of silicate; calcium, sulphur and oxygen correlate, suggesting the presence of calcium sulphate; iron correlates with oxygen suggesting the presence of iron oxide; sodium correlates with chlorine suggesting the presence of sodium chloride.
- Small crystallites (< 1 μm) rich in copper, chlorine, sulphur and oxygen.

7.3.7 Copper canister: outer surface area around bottom hole

The outer surface of the canister around the bottom defect (Figure 6-11) was examined by SEM/EDX and the results are presented in Appendix 2. The key features from the analysis are as follows:

- Sulphur is concentrated around the mouth of the hole and it correlates with an increased concentration in oxygen and calcium, suggesting deposition of calcium sulphate.
- There is a uniform low-level coverage of iron.
- Analysis of discrete particles shows the presence of particles containing iron, copper, calcium, chlorine, sulphur, silicon, sodium, calcium, chlorine in various proportions.
- Some particles had particularly high concentrations of calcium, carbon and oxygen, indicating the presence of calcium carbonate particles.
- Sodium chloride residue was present.
- Areas rich in iron, copper, chlorine, sulphur and oxygen, suggesting mixed metal oxide-chloride phases.
- Hemi-spherical and fine feathery sub-micron deposits, rich in copper and oxygen.
- SEM examination of the electron beam weld area did not show any signs of localised corrosion, such as pitting or stress corrosion cracking.

7.3.8 Inner surface of copper canister

Raman analysis for the inner surface of the copper canister at approximately half-height (Figure 7-48) is inconclusive but gave indications of graphitic carbon, an oxide phase with a spinel structure and amorphous material. The SEM/EDX analysis (Appendix 2) shows a fairly clean surface, with the machining marks visible, with the following key features:

- No indications of sulphur on the surface.
- Traces of chlorine, iron and silicon.
- Sodium chloride crystals.
- Iron, copper, oxygen, chlorine-rich sub-micron sized crystals.

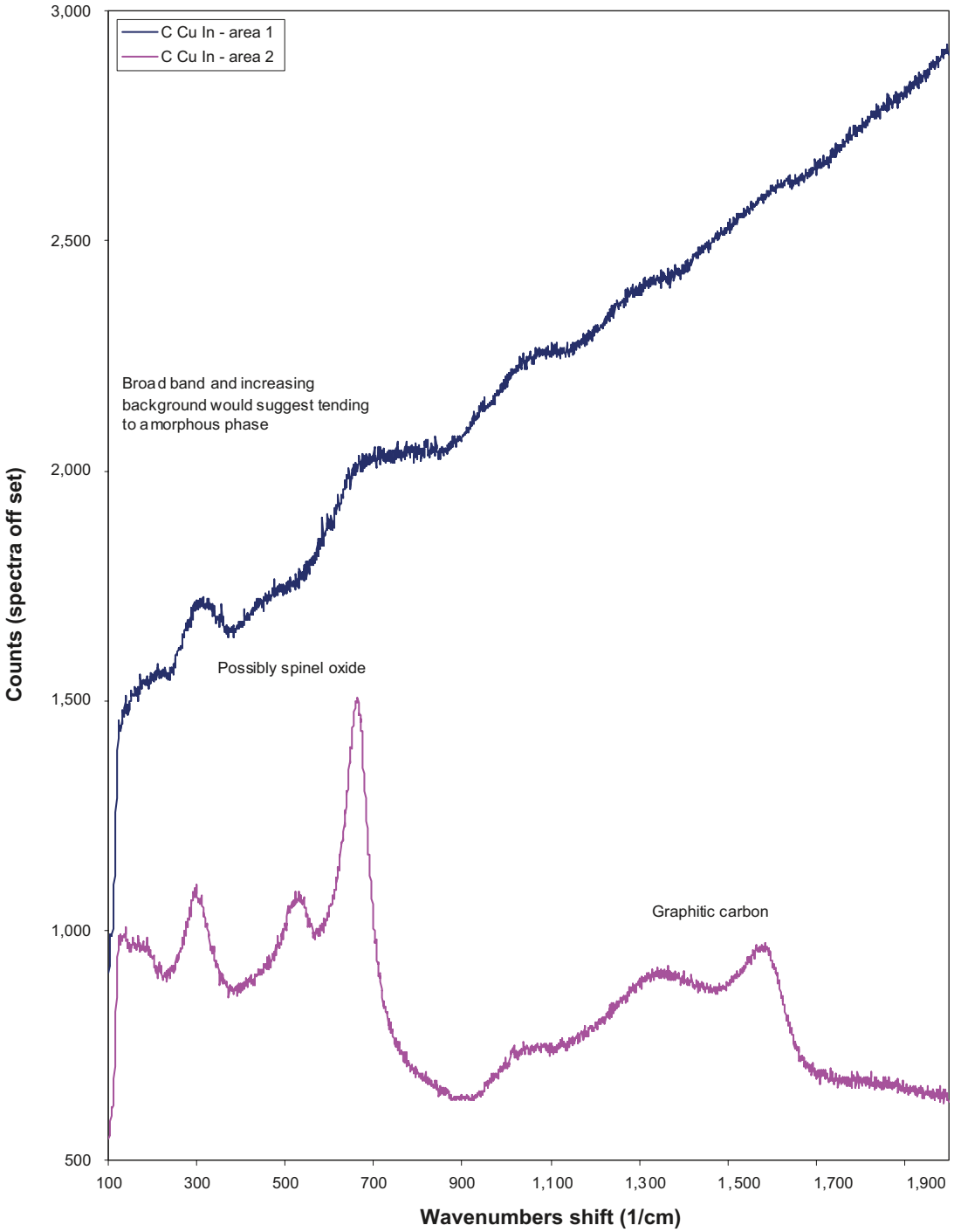

Figure 7-48. *Raman spectra for the inner surface of the copper canister surface at approximately half-height.*

7.3.9 Outer surface of copper canister

The Raman analysis of a sample removed from half-height on the outer surface of the copper canister (Figure 7-49 and 7-50) shows the possible presence of copper sulphide, graphitic carbon, carbonate and other anions in the form of white crystals. The FTIR of the surface near the top defect is shown in Figure 7-16. There were indications of the presence of carbonate-containing species. The SEM/EDX analysis (Appendix 2) shows:

- The presence of copper, iron, calcium, sulphur, silicon, aluminium, chlorine, oxygen and carbon in various proportions depending on the exact location.
- Thin layers with different compositions were present; some areas were rich in iron, copper and sulphur.
- Some areas seemed to show localised attack of the base metal (Figure 7-51), but it is not clear whether these were due to damage caused during machining or whether these areas were caused by corrosive attack. There are no indications of corrosion product within the pitted areas, so it appears more likely that they were due to machining damage.
- A particle rich in magnesium, silicon, aluminium and titanium was embedded in the surface; one possible source is bentonite from the support cage annulus.
- Some areas rich in iron, sulphur, silicon and oxygen, suggesting the possibility of a deposited layer, similar to the black flakes of material removed from the support table and other specimens inside the support cage.
- Some areas rich in copper and sulphur with small crystallites (< 5 μm).

The hydrogen content of the walls of the copper canister was measured using a fusion technique; details of the measurements are given in Appendix 1. A section was cut from the canister wall approximately one third height of the can from the bottom and this was split longitudinally into two sections to provide a sample from the inner and outer surface of the canister wall. From these two pieces, two samples measuring 25 mm × 10 mm × 5 mm were prepared; one of each pair was used as a backup sample for calibration purposes. The results of the analyses on two samples were 0.594 ppm for a section cut from the inner surface of the copper canister and 0.536 ppm for the outer surface. It is not currently known how this value compares to the concentration of hydrogen that would be expected in copper that has not been exposed to a corrosive environment.

7.3.10 Outer surface of cast iron insert

Raman analysis of the outer surface at half-height of the cast iron insert is shown in Figure 7-52 and 7-53. This analysis was inconclusive, with indications that the surface material was mainly amorphous, with the possible presence of some haematite (Fe_2O_3). The latter indicates that the surface had experienced oxidising conditions at some point in its history, such as during manufacture and before it was placed inside the copper canister. SEM/EDX analysis (Appendix 2) shows the following key features:

- Flaky surface deposit with a high concentration of iron and chlorine, suggesting the presence of ferrous chloride, $FeCl_2$, since chemical analysis of the aqueous phase (Smart et al. 2012) showed a high proportion of Fe^{2+}.
- A flattened surface where it had been in contact with the inner surface of the copper canister.
- Occasional larger crystals (> 50 μm) containing iron, calcium, silicon, magnesium, oxygen, titanium.
- Particles rich in magnesium, aluminium, silicon, titanium, calcium and sulphur, which may have originated from the bentonite in the annulus.

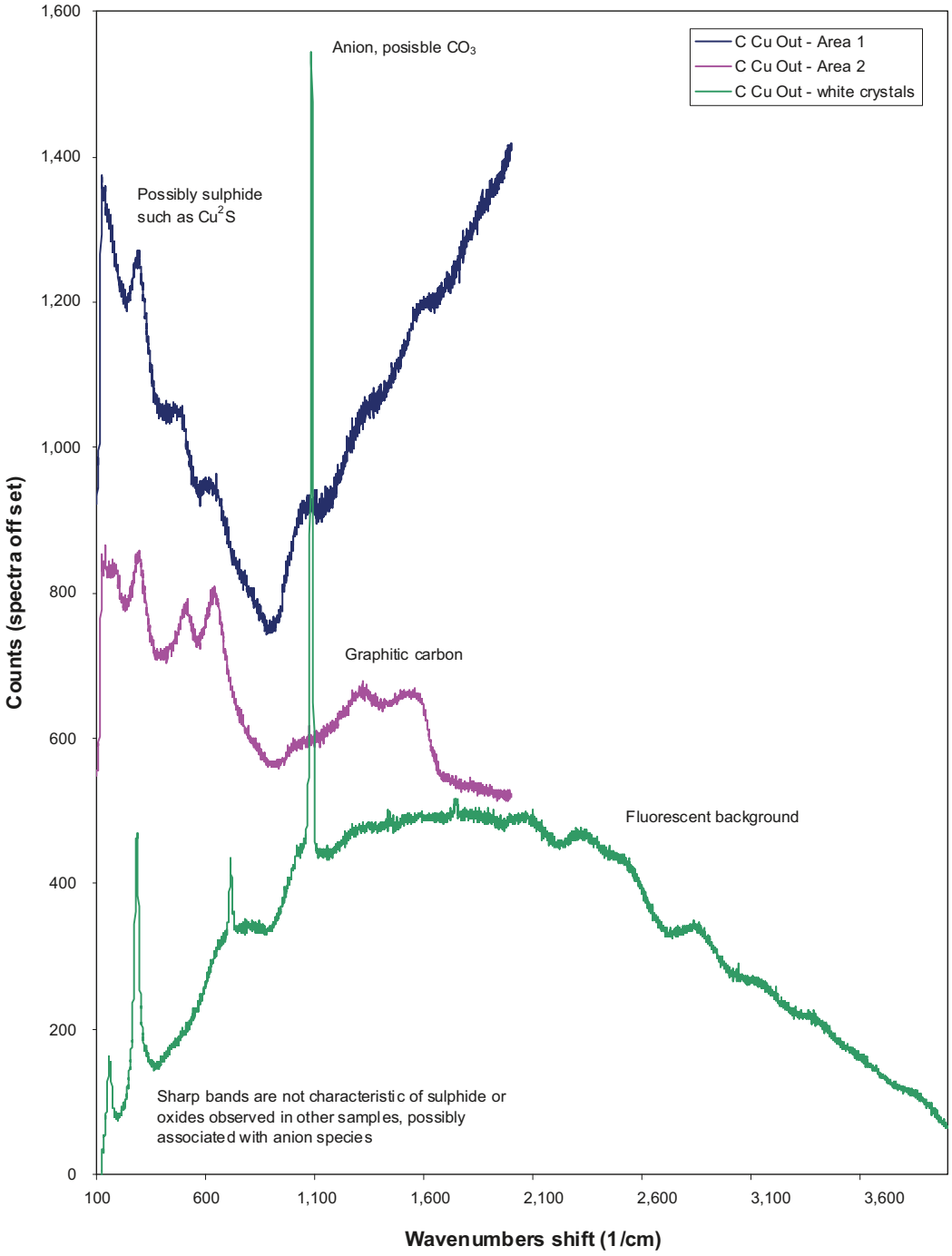

Figure 7-49. *Raman spectra for the outer surface of the copper canister surface at approximately half-height.*

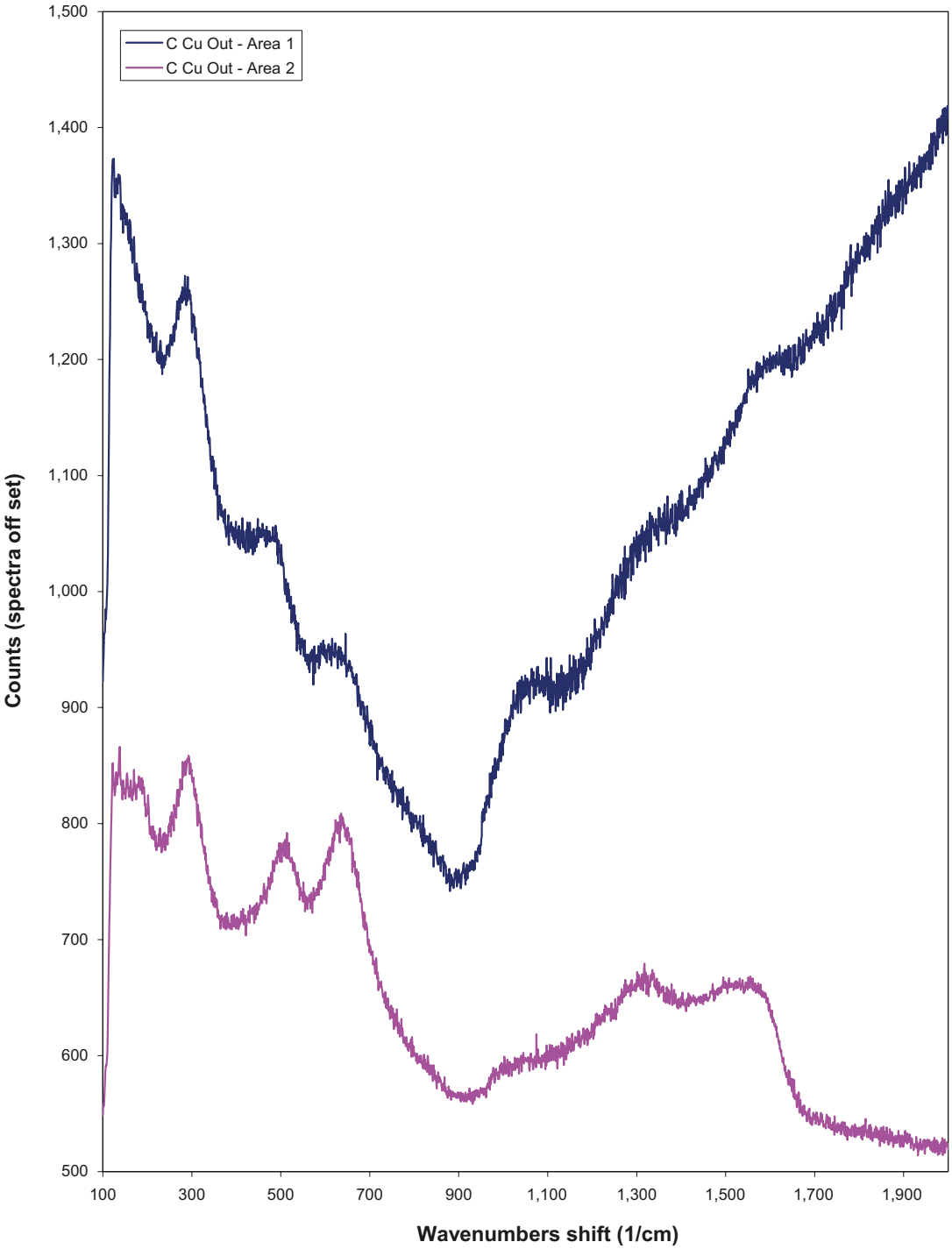

Figure 7-50. *Raman spectra for the outer surface of the copper canister surface at approximately half-height (expanded scale for results in Figure 77).*

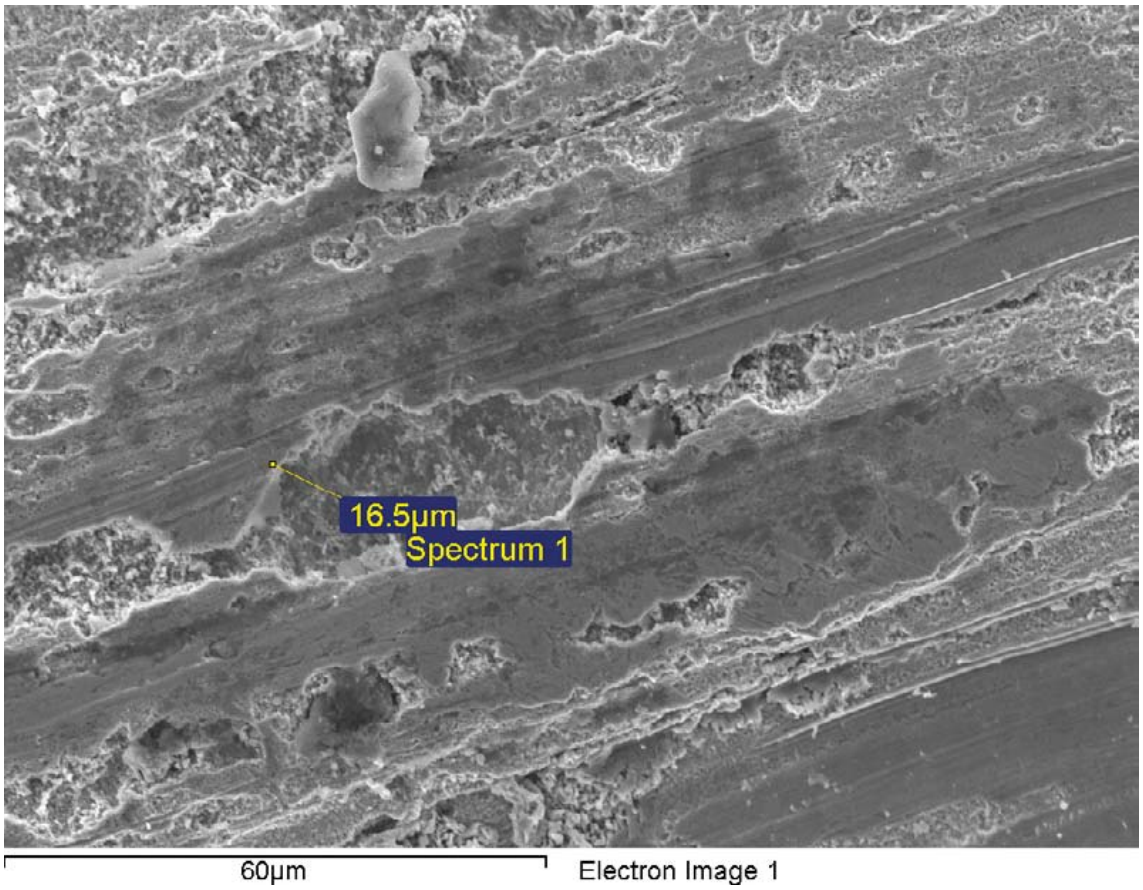

Figure 7-51. *Area on outer surface of copper canister at approximately half height, showing machine marks and areas of surface damage.*

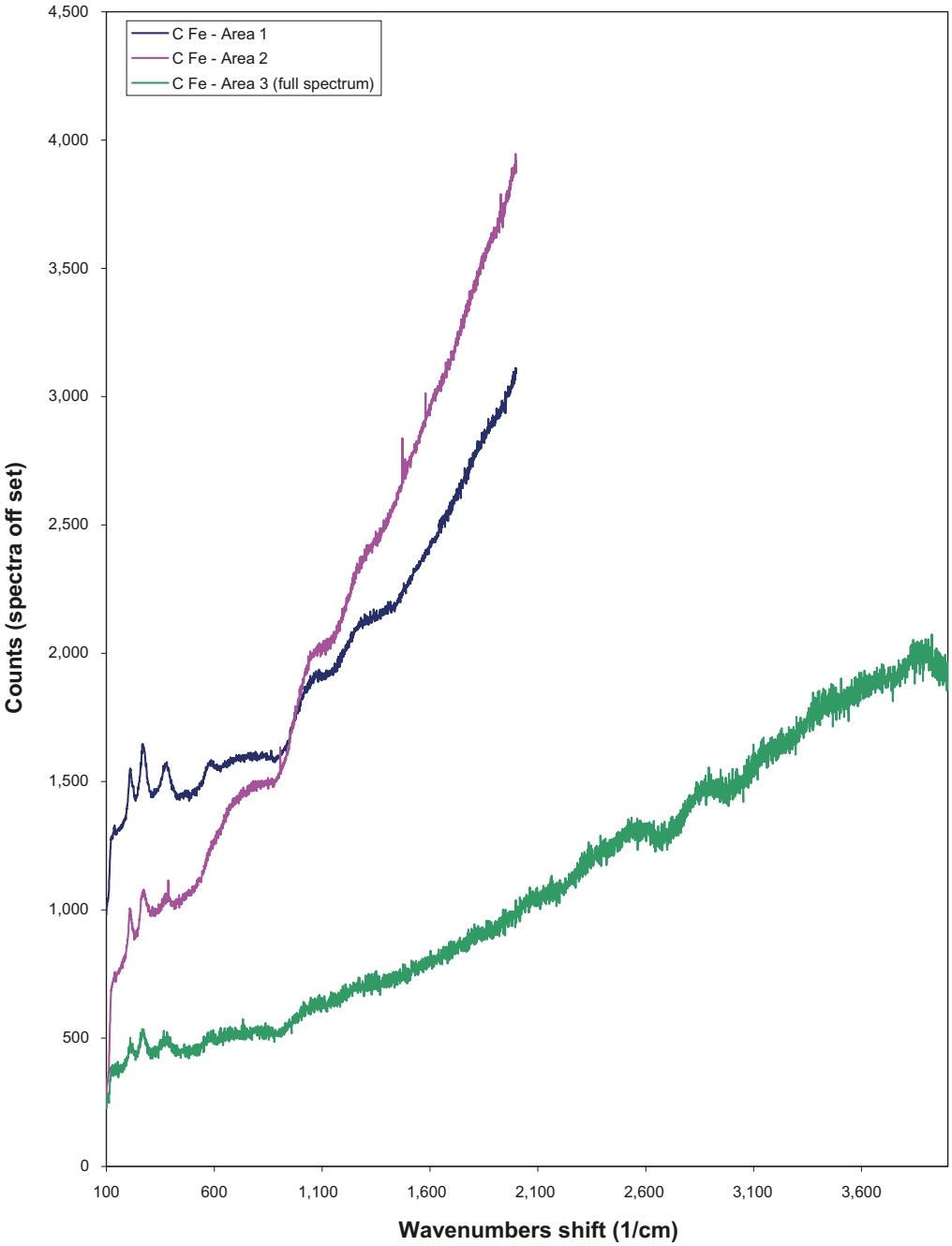

Figure 7-52. *Raman spectra for the outer surface of the cast iron at approximately half-height.*

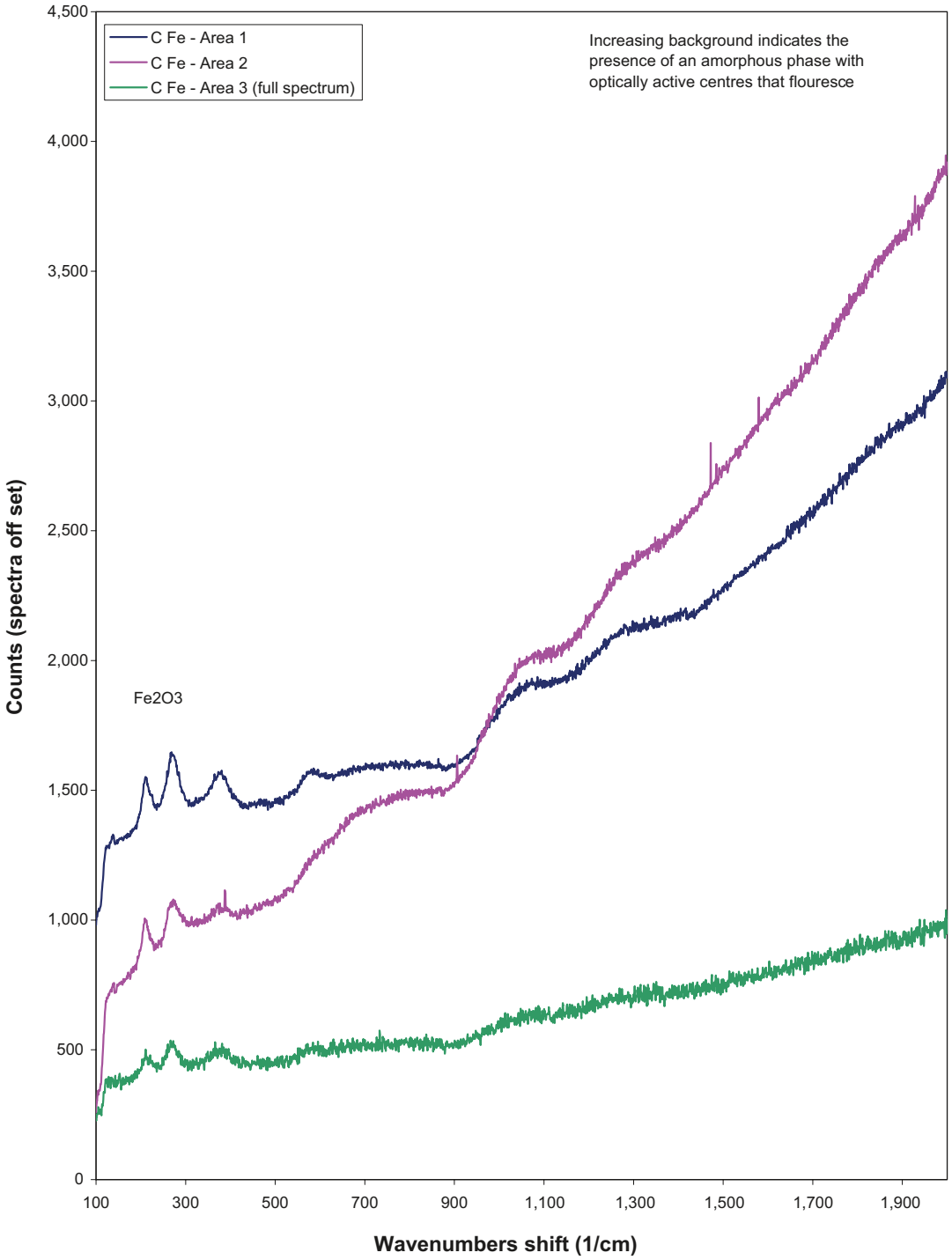

Figure 7-53. *Raman spectra for the outer surface of the cast iron at approximately half-height – same as previous spectrum (Figure 80) but expanded wavenumber scale.*

7.3.11 Cast iron insert pitted area

Raman analysis of the pitted area in the cast iron insert (Figure 7-42) opposite the top defect is shown in Figure 7-54. This showed the presence of graphitic carbon, in contrast to the surface of the cast iron further down the insert (see Figure 7-52 and 7-53). This suggests that the environment at the mid-height of the insert was different to that near the top, where localised attack occurred on the edge of the specimen. SEM/EDX analysis (Appendix 2) exhibited the following main features:

- The diameter of the attacked area was 2–3 mm and it had a very rough, porous appearance.
- The inner surface of the attacked area was mainly composed of iron and silicon, with small quantities of sulphur, chlorine, phosphorus, calcium, copper, carbon and oxygen. This elemental signature is similar to that of the weight loss specimen (see Section 7.1.4).
- The surface is composed of small crystals (< 10 μm) rich in iron and silicon.
- Discrete crystals of carbon are visible; these are assumed to be the remains of the spheroidal graphite from the cast iron.
- In some locations areas with high concentrations of iron, sulphur and silicon were detected. A spherical particle (~1 μm diameter) rich in iron, silicon and sulphur was identified.
- Some areas had a more complex mixture of elements including iron, calcium, chlorine, sulphur, silicon, magnesium, sodium and oxygen.
- Other areas were virtually pure cast iron (i.e. iron, carbon, silicon, manganese).

A smaller pitted area was also observed on the bottom edge of the lower part of the cast iron insert (Figure 7-46) opposite the bottom defect, but this was not examined using SEM/EDX. It was smaller than the pit on the top edge of the cast iron insert.

7.3.12 Profilometry measurements on canister surfaces

Profilometry measurements were carried out to characterise the roughness of a number of different areas of the copper surface to determine whether any corrosion of the copper surface had taken place. The results are shown in Figure 7-55 to 7-60. These show the regular pattern on the surface due to the machining marks, but no indications of localised corrosion attack. Some localised mechanical damage was detected around the bottom hole (Figure 7-58 and 7-59), which is attributed to local damage when the defects were drilled into the walls of the MiniCan.

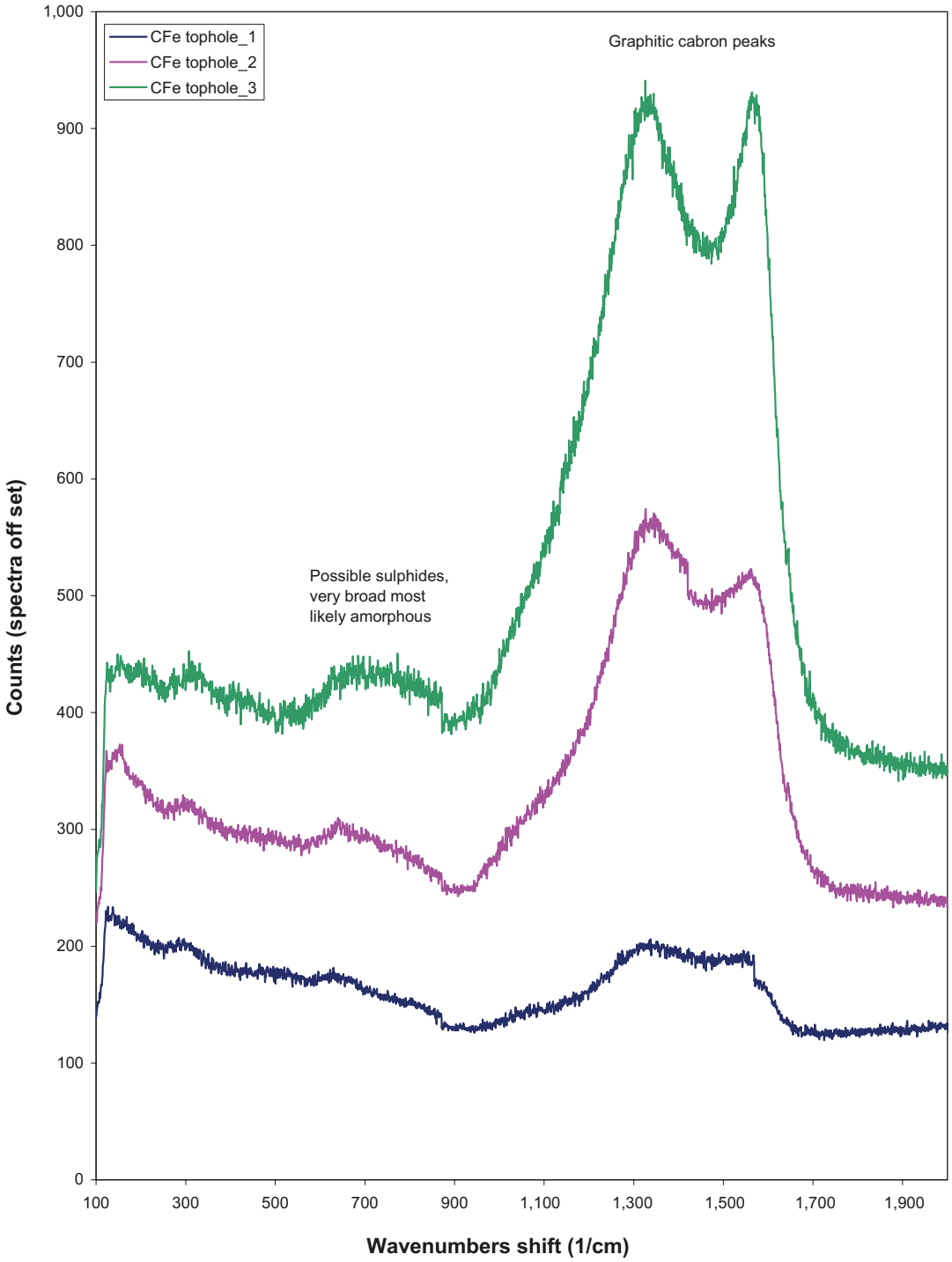

Figure 7-54. *Raman spectra for the outer surface of the cast iron insert in the pit formed opposite the top defect in the canister.*

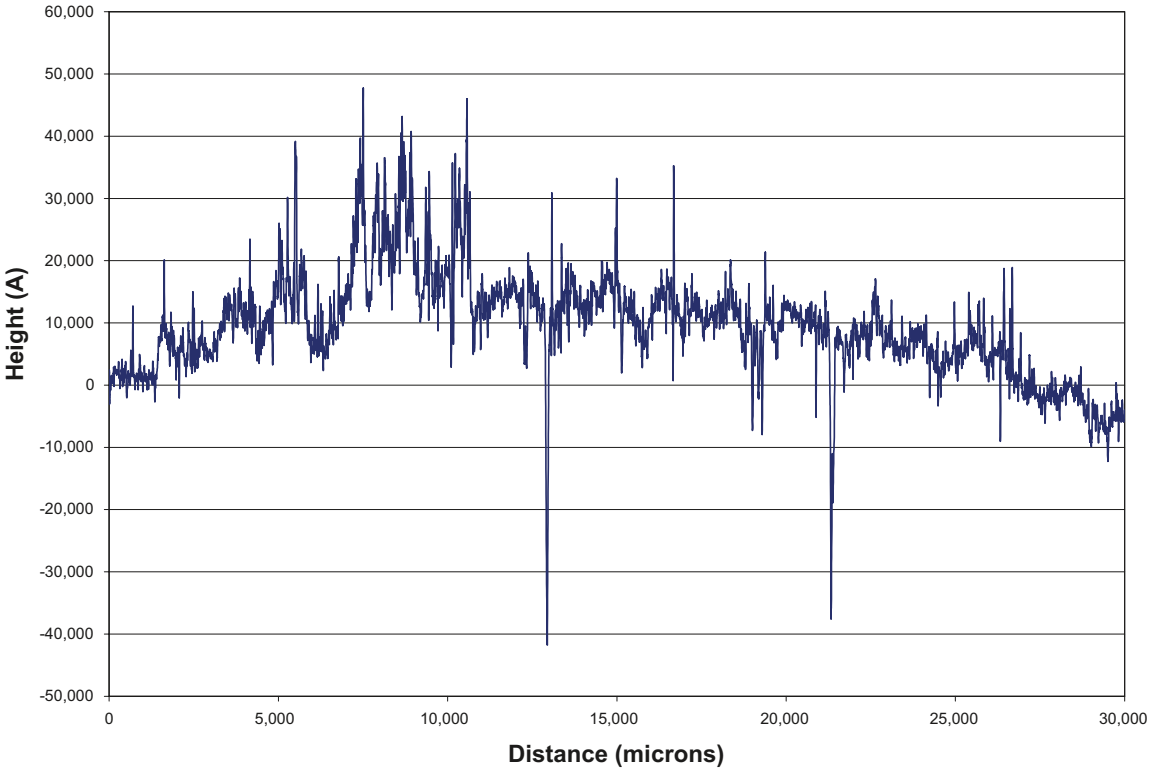

Figure 7-55. *Profilometry measurements on inner surface of middle section of canister.*

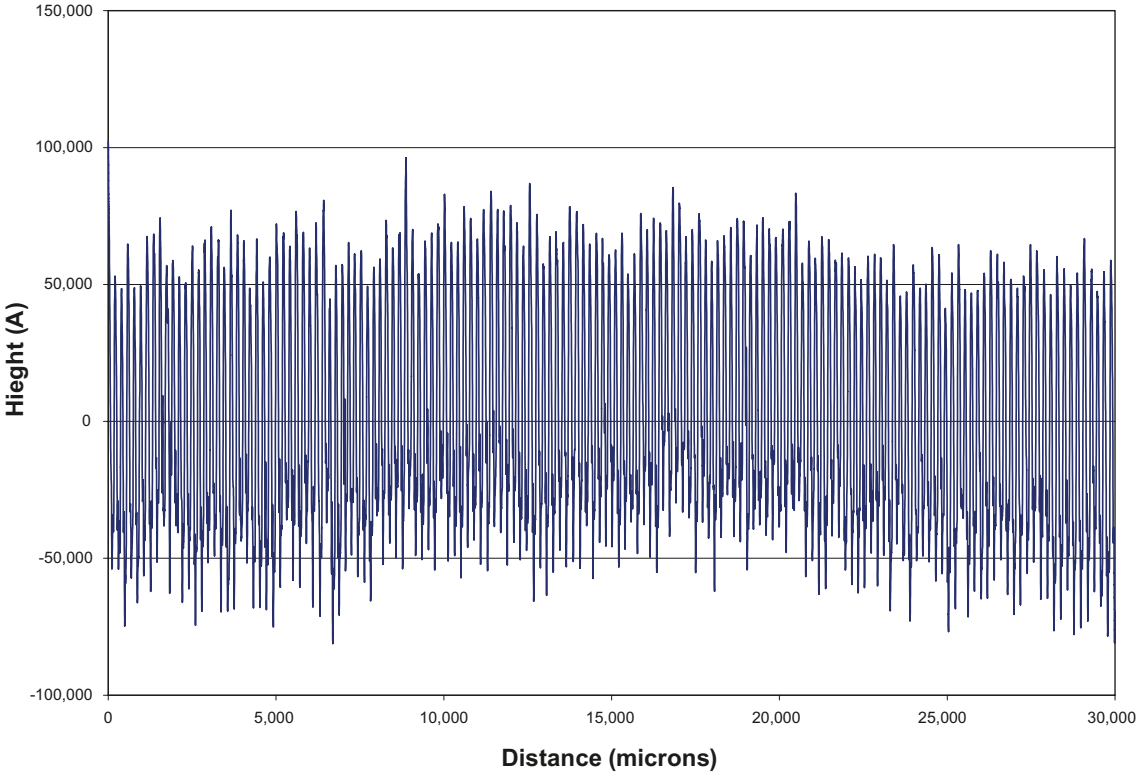

Figure 7-56. *Profilometry measurements on outer surface of middle section of canister.*

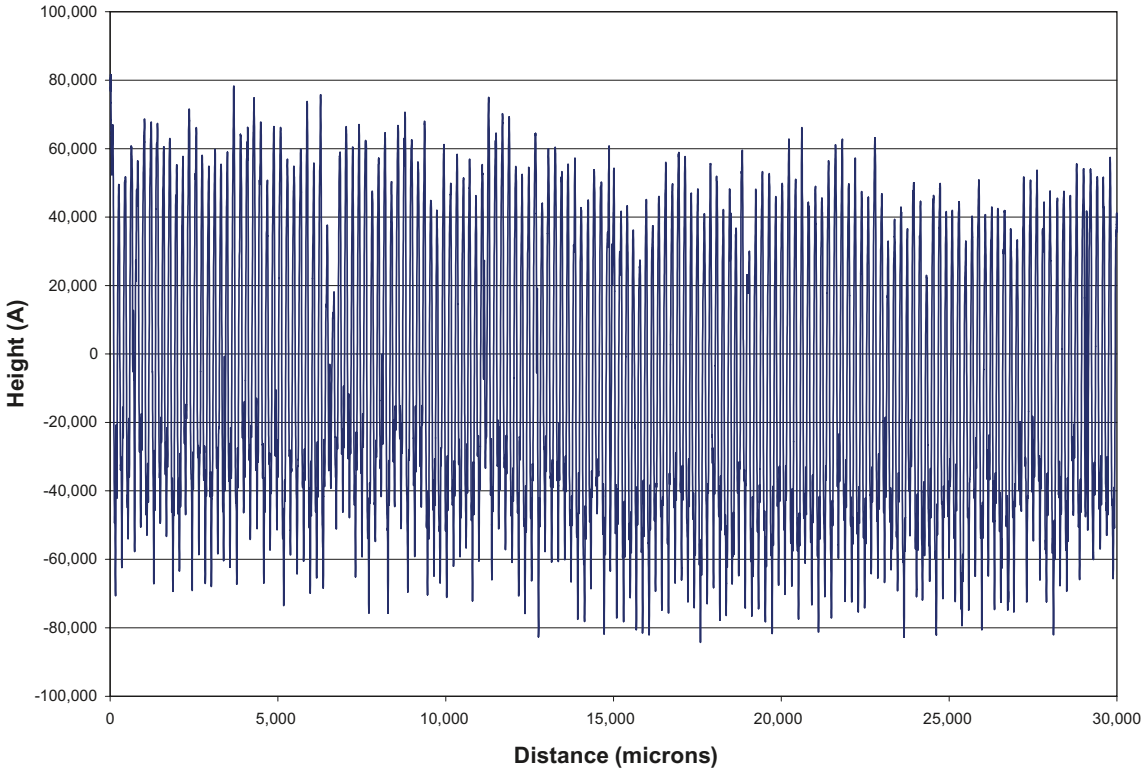

Figure 7-57. *Profilometry measurements on outer surface of middle section of canister.*

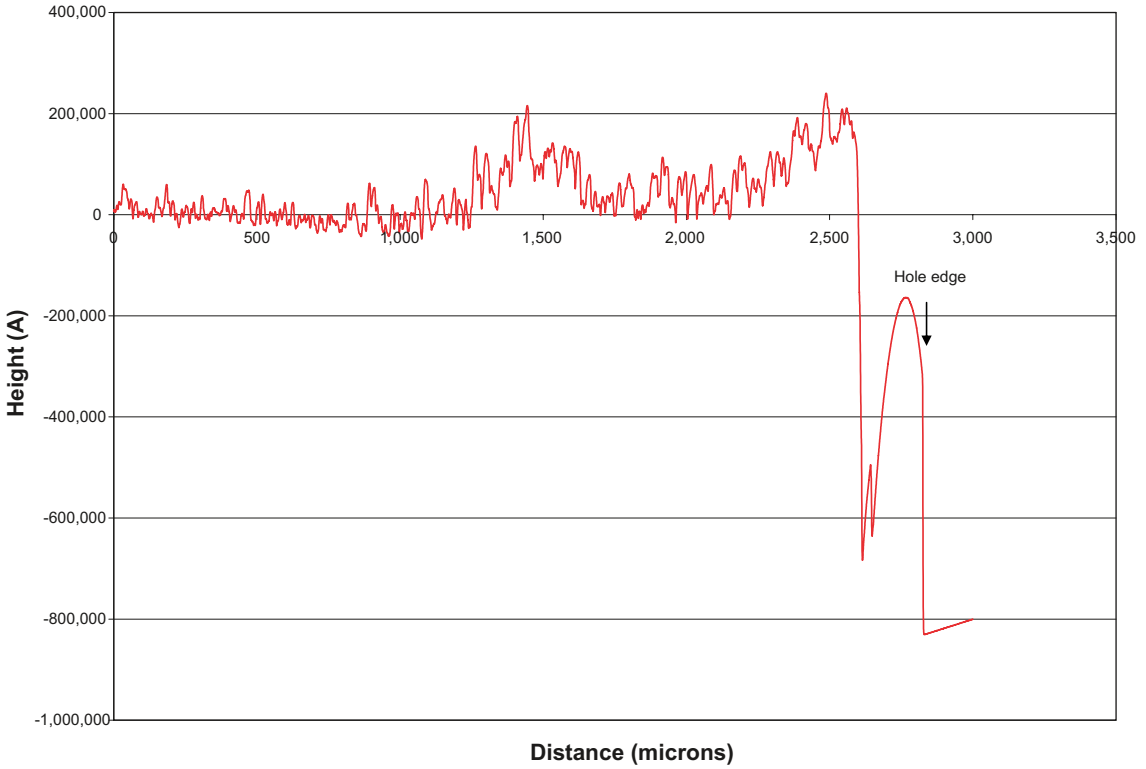

Figure 7-58. *Profilometry measurements on inner surface of canister near bottom defect.*

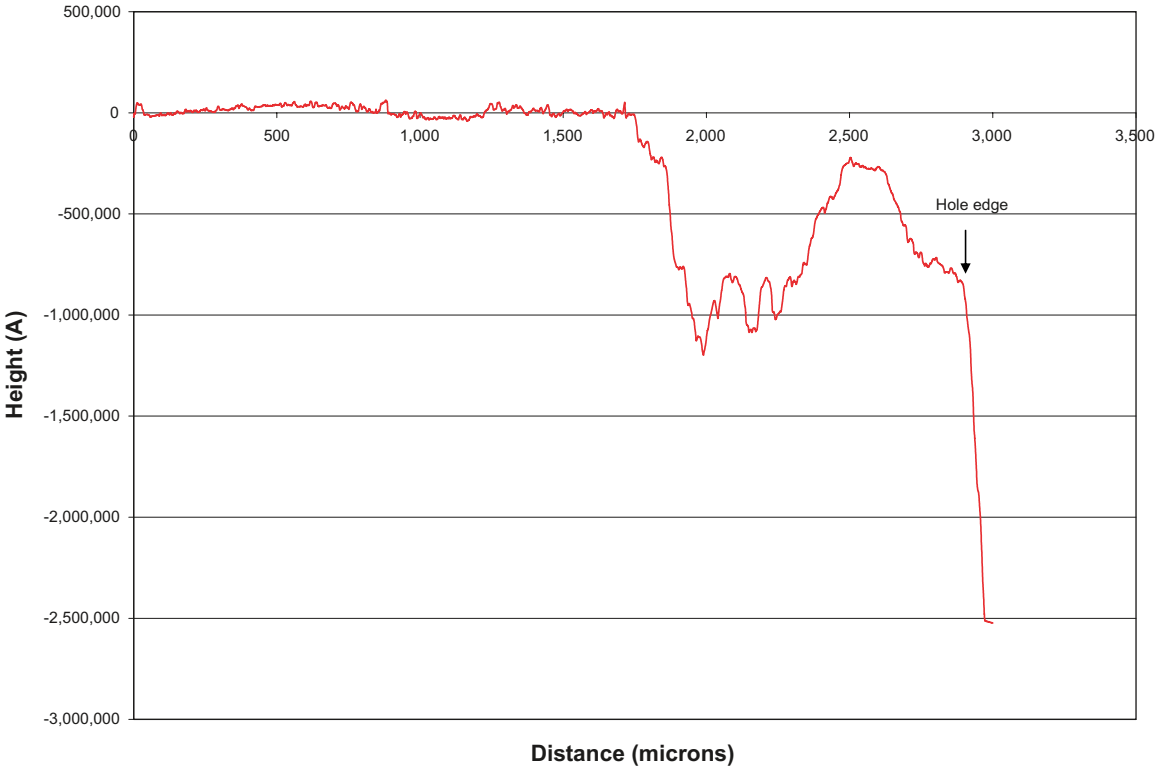

Figure 7-59. *Profilometry measurements on outer surface of canister near bottom defect.*

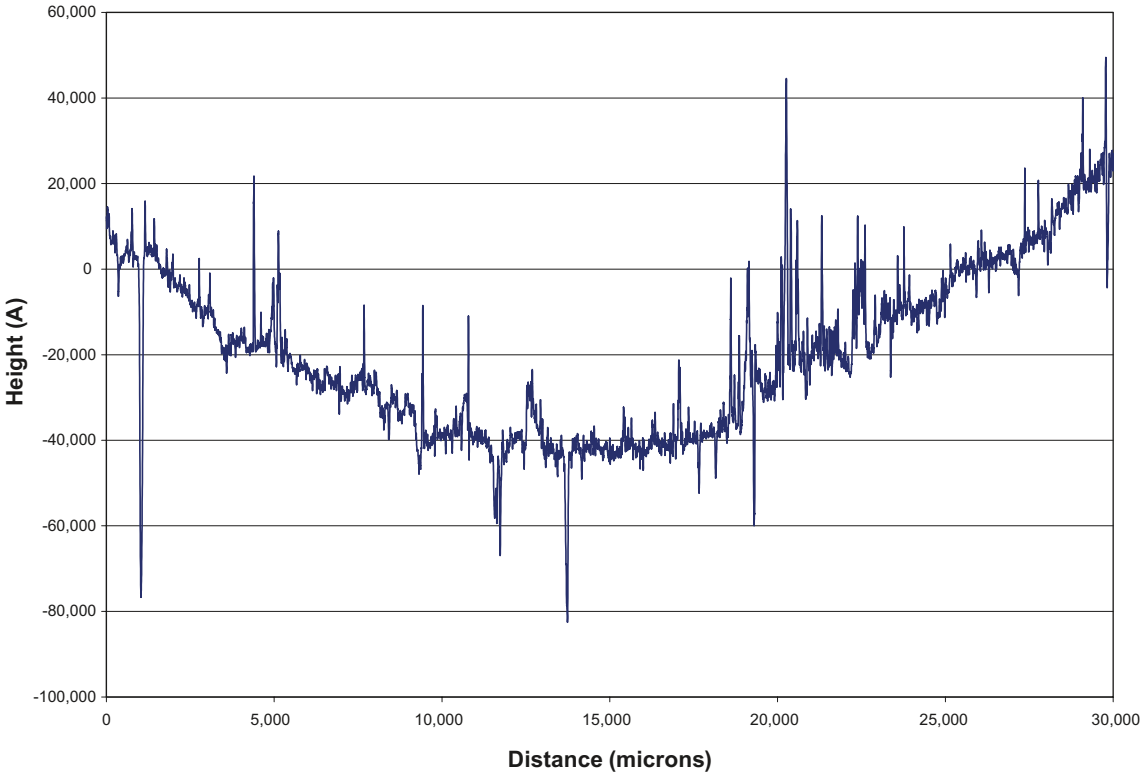

Figure 7-60. *Profilometry measurements on inner surface of middle section of canister – second profile.*

8 Discussion

8.1 Environment inside MiniCan Experiment 3

The results from the microbial analysis (Hallbeck et al. 2011) shows that there was a significant difference between the microbial populations on the outer surface of the support cage, which was exposed to the borehole water, compared to the population on the surface of the copper canister, which was exposed to the water inside the support cage. The outer surface of the support cage had a higher concentration of CHAB activity than the surface of the copper canister, whereas the surface of the copper canister had a very high concentration of SRB and a low concentration of CHAB. Both types of bacteria were detected in the groundwater sampled from within the Experiment 3 support cage, although the SRB concentration was higher.

The main feature of the water analysis was the large increase in the concentration of dissolved ferrous ions (Fe^{2+}) compared to the 2010 analysis (Smart el al. 2012), suggesting that the corrosion rate of the iron components of the experiment, namely the electrodes and the cast iron insert of the canister, had increased. This was accompanied by a small fall in the pH of the groundwater inside the support cage. However, the increase in iron concentration may also have been a result of the extended exposure period and the fall in pH, which may have affected the solubility of the iron-containing materials present.

8.2 Corrosion of copper and iron coupons

8.2.1 Copper coupons

The copper electrodes were covered with a black material, which appears to have originated from corrosion of the iron components in the experiment (i.e. an iron-sulphur-silicon, graphitic carbon phase), but the underlying copper surfaces were covered in a thin film of an unidentified mixed copper oxide-sulphide. The copper weight loss sample appeared to be coated with a layer of small (i.e. < 5 μm) crystals of copper sulphide, or a mixed iron-copper sulphide. The formation of a layer of copper sulphide on the surface of copper in the presence of SRB is well documented in the literature (Little and Lee 2007).

The weight loss measurement on the copper sample gave a corrosion rate of 0.15 μm yr^{-1}, which is several orders of magnitude lower than that measured using electrochemical means (Smart et al. 2012), but close to the value measured using the electrical resistance technique in other MiniCan experiments. The overestimate of the corrosion rate by electrochemical methods is probably related to the surface coating of material released by corrosion of the neighbouring mass of iron, which consisted mainly of iron sulphide. It should be noted that the copper was exposed to an aggressive environment due to the high concentrations of SRB in the groundwater inside the support cage and to that extent the experiment represents a severe corrosion test for the copper, which may not be representative of conditions for a copper canister surrounded by highly compacted bentonite in the repository. In this respect model canister Experiment 4 is more representative.

The copper surfaces that were exposed to the borehole water rather than the water inside the support cage (i.e. the U-bend specimens) developed a surface oxide layer with only a trace of sulphur, whereas the copper surfaces inside the support cage had a higher surface concentration of sulphur and crystals of copper sulphide were observed in the SEM/EDX analyses. Raman and FTIR analysis of the copper coupons and electrodes from inside the support cage also suggested the presence of copper sulphide.

8.2.2 Iron coupons

All the iron specimens that were mounted in the void above the copper canister had a very black appearance. The corroded surface of the electrodes consisted of graphitic carbon, which originated as graphite nodules in the cast iron, and an amorphous mass composed of iron, silicon, sulphur and oxygen. Flaky layers of iron sulphide were present on the surface.

The cast iron weight loss sample was completely corroded and no metallic iron was detected in the XRD analysis. No residual metallic iron was visible in the sample when it was broken open and no metallic iron was detected in the sample used for the XRD analysis. The remaining mass consisted of a crumbly material with no mechanical strength, which retained its initial shape and dimensions. The metallic component of the specimen had corroded leaving a skeleton of amorphous iron oxide, graphite particles and an unidentified silicon-rich phase. From weight loss testing, the corrosion rate of the iron coupon was shown to be at least as high as 500 μm yr^{-1}, based on the assumption that a material 5 mm thick had completely corroded from both sides in a period of approximately five years duration. This value agrees well with the corrosion rates measured using electrochemical techniques and reported in Smart et al. (2012). Whiskers, or 'tubercles', composed predominantly of iron and sulphur, had grown under the influence of gravity from the iron electrodes, and to a lesser extent from the weight loss specimen.

Anaerobic corrosion experiments for iron in the laboratory, using simulated groundwater compositions, have shown that the abiotic anaerobic corrosion rate will be of the order of < 1 μm yr^{-1} (Smart et al. 2002a, b). However, the corrosion rates measured in the MiniCan programme are approximately three orders of magnitude higher and the inevitable conclusion is that this increase in corrosion rate is due to the high concentrations of sulphate reducing bacteria present inside the support cage of the experiment. SRB are well known to cause accelerated corrosion rates (Little and Lee 2007) of iron-based alloys, with the end product being sulphide films. SRB are able to metabolise hydrogen to reduce sulphate to sulphide (Caffrey et al. 2008). The hydrogen may be generated by the anaerobic corrosion of iron, so that a synergistic process ensues (Smart 2011) in which the generation of hydrogen by anaerobic corrosion sustains SRB activity that leads to further corrosion. A recent study (Enning et al. 2012) has shown that some strains of lithotrophic SRB can metabolise iron directly, without the need for a source of hydrogen. These strains were detected in the MiniCan experiment (Hallbeck et al. 2011). The exact mechanism of SRB attack is still a matter of investigation and debate.

The form of attack of cast iron observed in the MiniCan experiment is an example of 'graphitisation' (LaQue 1975), which is common in the water industry where cast iron pipes are used to transport water supplies. In slightly acidic waters both flake graphite (grey) and nodular graphite (ductile) irons are corroded due to the anodic behaviour of the matrix with respect to the cathodic graphite. This results in the conversion of the structure to a weak porous mass of corrosion product and graphite residue. However, there is often little sign of the extent of this damage from the outward appearance of the material, since the original shape and dimensions of components remain unaffected.

The conditions inside the MiniCan support cage are conducive to SRB growth, because of the presence of plenty of water, an abundant supply of sulphate and hydrogen, the absence of oxygen and traces of organic material in the bentonite. The conditions within compacted bentonite, as would be used in the KBS-3 concept, would be less conducive to SRB activity because of the lower water activity (King et al. 2010).

8.2.3 Other components

The other components inside the support cage were covered by a layer of black deposit (e.g. the gold, platinum, platinised titanium gauze counter electrode, silver-silver chloride disc electrodes and support table). Analysis strongly suggests that the layer, which is up to ~0.1 mm thick, consists of closely compacted small crystallites of iron sulphide, with a component of graphite, silicon and oxygen. This layer appears to have precipitated from the bulk water phase and then become compacted, since it was present on surfaces that could not have produced it as a primary corrosion product (i.e. non-ferrous materials).

8.2.4 SCC test specimens

None of the SCC test specimens (i.e. the U-bend specimens) showed any signs of stress corrosion cracking when examined in an unsectioned state using optical microscopy, although further metallurgical analysis on mounted and polished specimens is required to confirm this.

8.3 Miniature canister

One of the main objectives of the programme was to investigate the evolution of corrosion around the annulus between the cast iron insert and the outer copper canister. The questions raised at the outset of the project are listed below, together with some responses based on the results presented in this report:

- Does water penetrate into the annulus through a small defect?

It is clear that water was able to penetrate into the inner annulus in Experiment 3. However it should be noted that this canister had a machined defect at the top and bottom, whereas the other canisters only had one defect near the top of the canister and this may affect the ease with which water can penetrate into the annulus. In fully compacted bentonite the water supply would be restricted by passage through the bentonite.

- How does corrosion product spread around the annulus from the leak point?

The whole surface of the iron canister was covered with a corrosion product layer, but the composition of the corrosion product was different in different locations. The corrosion product at the half height location was predominantly iron chloride, but near the defect severe corrosion (graphitisation) of the cast iron insert had occurred, leaving a skeleton structure of iron, oxygen, silicon and carbon. The depth of the pit at the top edge was approximately 2.5 mm, corresponding to an average corrosion rate of ~500 μm yr^{-1}, the same value that was estimated from the weight loss coupon.

- Does the formation of corrosion product in a constricted annulus cause any expansive damage to the copper canister?

There were no indications of expansive damage to the copper canister. The severely corroded section of the cast iron insert had released material out through the defect rather than forming an expansive corrosion product. Corrosion was concentrated near the defect in the copper canister. This indicates that the conditions at this point were particularly aggressive. One possible explanation for this is that SRB activity was concentrated at this location, possibly because there would have been a good supply of hydrogen emanating from corrosion of the cast iron insert. An alternative explanation is that corrosion was concentrated near the defect mainly because of mass-transport limitations from the bulk solution phase outside of the MiniCan where the corrosive agent (sulphide) was produced, to the surfaces of the cast iron insert. It is possible that the corrosion product produced at the entrance to the defect impeded the passage of water and microbial activity further into the annulus. However, over the very long timescales involved in geological disposal it is possible that if there were a defect in the copper canister graphitisation of the insert would penetrate further along the annulus and eventually lead to the complete degradation of the cast iron insert.

- What is the effect of water penetration on the insert lid seal?

The Viton O-ring appeared to have functioned well, since the interior of the cast iron insert remained dry and there were no indications of corrosion inside the simulated fuel channels.

- Is there any detectable corrosion at the copper welds?

There were no indications of corrosion in the weld areas by visual examination, or SEM examination of selected areas. No indications of stress corrosion were detected in the walls of the copper canister or in the electron beam welds (from SEM examination). Further metallographic analysis would be beneficial.

- Are there any deleterious galvanic interactions between copper and cast iron?

There were no specific indications of enhanced corrosion at contact points between the cast iron insert and the copper canister. This is in agreement with other studies of the galvanic corrosion of copper-cast iron couples under anoxic conditions (Smart et al. 2005).

- Does corrosion lead to failure of the lid on the iron insert?

The lid of the insert had fulfilled its function but there were signs of corrosion and discolouration on the lid.

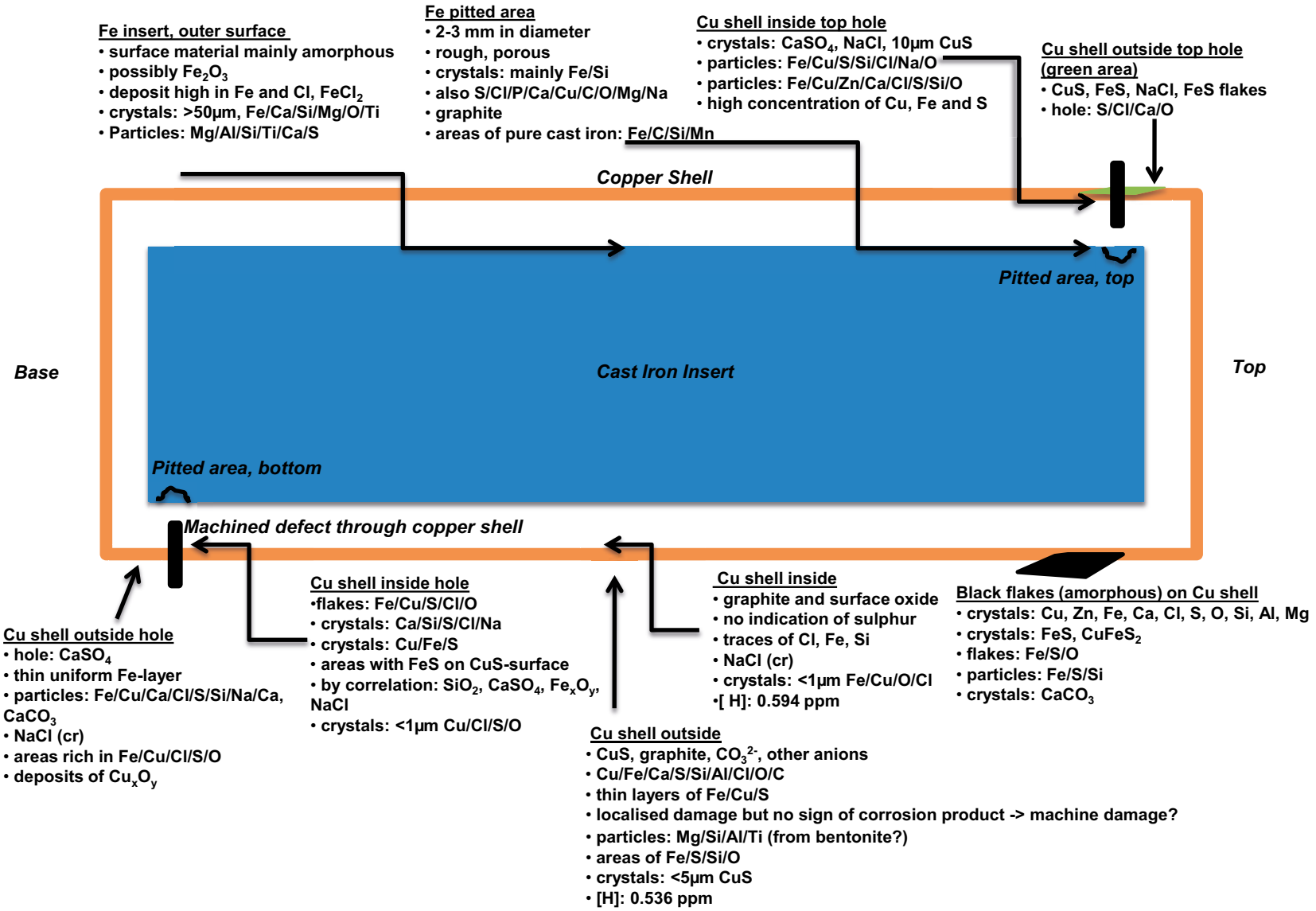

Figure 8-1. Summary of observations of corrosion product on surfaces of miniature canister.

8.3.1 Corrosion products on miniature canister

A summary of the observations of corrosion products present on the surfaces of the miniature canister is presented in Figure 8-1. The analysis of components cut from the copper canister showed the presence of a range of materials, including crystals with a high concentration of copper and sulphur (e.g. on the inner surface around the top hole, see Section 7.3.4). It is not possible to discern from the analysis the stoichiometry of the crystals because the analytical technique is semi-quantitative.

The naturally occurring mineral binary compounds of copper and sulphur are listed below:

- CuS_2, villamaninite[3] or $(Cu,Ni,Co,Fe)S_2$[4]
- CuS, covellite[3], copper monosulphide
- Cu_9S_8 ($Cu_{1.12}S$), yarrowite[5]
- $Cu_{39}S_{28}$ ($Cu_{1.39}S$) spionkopite[5]
- Cu_8S_5 ($Cu_{1.6}S$), geerite[6]
- Cu_7S_4 ($Cu_{1.75}S$), anilite[3]
- Cu_9S_5 ($Cu_{1.8}S$), digenite[3]
- $Cu_{31}S_{16}$ ($Cu_{1.96}S$), djurleite[3]
- Cu_2S, chalcocite[3]

from which it can be seen that there is a range of stoichiometric and non-stoichiometric copper sulphides that could be present on the surface of the canister and it is not possible to determine the exact mineral composition from the current dataset. The compositions of sulphides formed on copper by microbial activity are reviewed in Little and Lee (2007); the presence of dissolved iron can also affect the composition of the copper sulphides formed (Little and Lee 2007). The wide range of solids present is a reflection of the complex nature of the environment within the experiment, which is an inevitable consequence of carrying out experiments in natural waters and a natural environment, rather than a controlled laboratory environment.

The majority of the iron sulphide deposited in the void inside the MiniCan experiment appears to have originated from dissolution and precipitation of iron from the iron corrosion coupons, since the volume of the holes made by corrosion in the iron insert can be estimated as ~20 mm^3 (0.02 cm^3), compared to the volume of the weight loss specimen which was ~1 cm^3, meaning that roughly 98% of the iron in the iron sulphide phase must have originated from outside the canister. In addition, the sandwich specimen had exposed a heavily corroded cast iron surface of 60 cm^2 to the environment.

[3] **RRUFF™ Project, 2005.** Villamanínite. Available at: http://rruff.info/doclib/hom/villamaninite.pdf

[4] **RRUFF™ Project, 2005.** Villamanínite. Available at: http://rruff.info/doclib/hom/villamaninite.pdf

[5] **Goble R J, 1980.** Copper sulfides from Alberta: yarrowite Cu_9S_8 and spionkopite $Cu_{39}S_{28}$. Canadian Mineralogist 18, 511–518.

[6] **Goble R J, Robinson G, 1980.** Geerite, $Cu_{1.60}S$, a new copper sulfide from Dekalb Township, New York. Canadian Mineralogist 18, 519–523.

8.4 Application of results to SKB safety case

The results reported in this report show that in an underground repository in a granitic environment, the development of colonies of sulphate reducing bacteria can lead to rapid corrosion of cast iron ($\geq$ 500 μm yr^{-1}). The expansion of such colonies would be supported by the presence of low density bentonite, but the extent of microbial growth may be restricted by the use of compacted bentonite which will reduce the availability of water, an essential requirement for the proliferation of bacteria. If a copper canister were to develop a defect that allowed penetration of liquid water into the annulus of a canister, it is likely that eventually the annulus would be colonised by SRB, since spores of SRB are likely to be present in the bentonite, and complete graphitisation of the cast iron insert could eventually occur. The insert would probably retain its original dimensions, but it would lose its mechanical strength hence raising the possibility that the canister could collapse under the local hydrostatic pressure.

Copper has been shown to suffer from a corrosion rate of the order of 0.15 μm yr^{-1} under severely corrosive conditions with a high SRB activity. In the real disposal situation the presence of compacted bentonite will restrict the extent of SRB activity and the corrosion rate of the copper will be limited by mass transport considerations, which will restrict the availability of water and the rate of passage of sulphide ions and/or sulphate ions through the bentonite.

It should be noted that this assessment refers to processes at ambient temperature and does not take any account of elevated temperature effects, such as increased corrosion rates, or the potential effects on microbial growth.

9 Conclusions

A detailed analysis of MiniCan Experiment 3 has been conducted under carefully controlled conditions and the main conclusions from the investigation are as follows:

1. The observed corrosion behaviour in the MiniCan experiment was heavily influenced by extensive sulphate reducing bacteria activity in the groundwater-filled headspace inside the support cage but above the MiniCan. This aqueous phase is not expected to occur next to the canisters in the repository in the presence of highly compacted bentonite.
2. The concentration of dissolved iron measured in water inside the support cage had increased since 2010, leading to a concentration of several 10 s of mgL^{-1}. The concentration of both sulphate and hydrogen had decreased, with an accompanying increase in the concentrations of sulphate reducing bacteria and cultivable heterotrophic aerobic bacteria.
3. The cast iron weight loss coupon in MiniCan Experiment 3 had completely corroded, due to a graphitisation process induced by the presence of sulphate reducing bacteria. Severe corrosion was also observed on the cast iron electrodes, although some residual iron was present at the core of the specimen.
4. The corrosion rate of the cast iron was of at least 500 $\mu m\ yr^{-1}$, based on weight loss measurements and electrochemical measurements.
5. The weight loss coupon residue was a mass of graphite and amorphous iron oxide/silicon corrosion product. This corrosion process for cast iron is commonly referred to as ‘graphitisation’.
6. The iron released into the groundwater through corrosion had precipitated as a black deposit on all surfaces inside the support cage; it was predominantly amorphous iron sulphide, but it also contained graphitic carbon and a silicon rich phase.
7. The uniform corrosion rate of the copper was estimated to be 0.15 $\mu m\ yr^{-1}$, on the basis of weight loss measurements. This is considerably lower than the corrosion rates measured by electrochemical methods, which are considered unreliable due to the deposition of a layer of conductive iron corrosion product from the iron electrodes and the neighbouring cast iron insert. The copper corrosion product was a mixture of copper oxide and copper sulphide. There were no indications of localised corrosion (i.e. pitting or stress corrosion cracking) on the copper test specimens. Copper specimens exposed directly to the borehole water developed a predominantly copper oxide corrosion product, with only a trace of sulphide present.
8. The outer dimensions of the copper canister from MiniCan Experiment 3 were measured and no changes from the initial design dimensions were detected, indicating that no expansion had occurred due to corrosion of the cast iron insert. No expansion was observed in the copper-cast iron sandwich specimen either.
9. Non-uniform blackening of the outer surface of the copper canister had occurred and it was concentrated on areas facing the holes in the inner cylinder of the support cage. The defects in the copper canister had become blocked with corrosion product, but locally high rates of corrosion of the cast iron insert were observed opposite the machined defects in the copper canister. The corrosion process in the half-height area of the annulus was different to that opposite the defects, with the major corrosion product being an iron and chlorine rich phase.
10. Copper sulphide crystals were observed on the surfaces of the canister. The copper and cast iron surfaces that were in close proximity (e.g. between the cast iron insert and the copper canister, and between the cast iron and copper pieces in the sandwich specimen) had corroded less than fully exposed surfaces (e.g. the weight loss specimen).

10 Acknowledgements

The authors gratefully acknowledge assistance provided by the following during the course of this work:

- SKB: Mats Lundqvist, Siren Bortelid Moen, Johannes Johansson (who prepared Figure 8-1) and various SKB support staff at Äspö.
- Microbial Analytics Sweden AB.
- University of Oxford Materials Characterisation Services.

The authors also gratefully acknowledge financial support provided by SKB for conducting this project.

11 References

SKB's (Svensk Kärnbränslehantering AB) publications can be found at www.skb.se/publications.

ASTM, 1999. ASTM G1-90(1999): Standard practice for preparing, cleaning, and evaluating corrosion test specimens. West Conshohocken, PA: ASTM International.

Briggs D, Seah M P (eds), 1990. Practical surface analysis. Vol. 1, Auger and X-ray photoelectron spectroscopy. 2nd ed. Chichester: Wiley.

Caffrey S M, Park H-S, Voordouw G, Been J, 2008. Gene array analysis of sulfate-reducing bacteria grown on an iron electrode under conditions of cathodic protection. Paper 08653, NACE Corrosion 2008, New Orleans, Louisiana, 16–20 March 2008.

Enning D, Venzlaff H, Garrelfs J, Dinh H T, Meyer V, Mayrhofer K, Hassel A W, Stratmann M, Widdel F, 2012. Marine sulfate-reducing bacteria cause serious corrosion of iron under electro-conductive biogenic mineral crust. Environmental Microbiology 14, 1772–1787.

Hallbeck L, Edlund J, Eriksson L, 2011. Microbial analyses of groundwater and surfaces during the retrieval of experiment 3, A04, in MINICAN. SKB P-12-01, Svensk Kärnbränslehantering AB.

King F, Lilja C, Pedersen K, Pitkänen P, Vähänen M, 2010. An update of the state-of-the-art report on the corrosion of copper under expected conditions in a deep geologic repository. SKB TR-10-67, Svensk Kärnbränslehantering AB.

LaQue F L, 1975. Marine corrosion: causes and prevention New York: Wiley.

Little B J, Lee J S, 2007. Microbiologically influenced corrosion. Hoboken, NJ: Wiley.

Lydmark S, Hallbeck L, 2011. Results report. Sampling and analyses of gases and microorganisms in the water from MINICAN in 2007, 2008 and 2010. SKB P-11-32, Svensk Kärnbränslehantering AB.

Shirley D A, 1972. High-resolution x-ray photoemission spectrum of the valence bands of gold. Physical Review B 5, 4709–4714.

Smart N R, 2011. The anaerobic corrosion of carbon steel and the potential influence of sulphur species. Presented at the SACNUC workshop, Brussels, 21–23 October 2008. In Féron D, Kursten B, Druyts F (eds). Sulphur-assisted corrosion in nuclear disposal systems. Leeds: Maney. (EFC 59).

Smart N R, Rance A P, 2009. Miniature canister corrosion experiment – results of operations to May 2008. SKB TR-09-20, Svensk Kärnbränslehantering AB.

Smart N R, Blackwood D J, Werme L, 2002a. Anaerobic corrosion of carbon steel and cast iron in artificial groundwaters: Part 1 – Electrochemical aspects. Corrosion 58, 547–559.

Smart N R, Blackwood D J, Werme L, 2002b. Anaerobic corrosion of carbon steel and cast iron in artificial groundwaters: Part 2 – Gas generation. Corrosion 58, 627–637.

Smart N R, Rance A P, Fennell P A H, 2005. Galvanic corrosion of copper-cast iron couples. SKB TR-05-06, Svensk Kärnbränslehantering AB.

Smart N R, Reddy B, Rance A P, 2011a. Miniature canister (MiniCan) corrosion experiment progress report 3 for 2008–2010. SKB P-11-40, Svensk Kärnbränslehantering AB.

Smart N R, Rance A P, Reddy B, Lydmark S, Pedersen K, Lilja C, 2011b. Further studies of *in situ* corrosion testing of miniature copper-cast iron nuclear waste canisters. Presented at the 4th International Workshop on Long-Term Prediction of Corrosion Damage in Nuclear Waste Systems, Bruges, June 2010. Corrosion Engineering, Science and Technology 46, 142–147.

Smart N R, Reddy B, Rance A P, 2012. Miniature canister (MiniCan) corrosion experiment progress report 4 for 2008–2011. SKB P-12-13, Svensk Kärnbränslehantering AB.

To T B, Nordstrom D K, Cunningham K M, Ball J W, McCleskey R B, 1999. New method for the direct determination of dissolved Fe(III) concentration in acid mine waters. Environmental Science & Technology 33, 807–813.

Åkesson M, Olsson S, Dueck A, Nilsson U, Karnland O, Kiviranta L, Kumpulainen S, Lindén J, 2012. Temperature buffer test. Hydro-mechanical and chemical/mineralogical characterizations. SKB P-12-06, Svensk Kärnbränslehantering AB.

Appendix 1

Details of analytical techniques

Laser Raman spectroscopy

The samples for examination were mounted into a Perspex sample holder, whilst within the purpose-built anoxic glovebox. Examples of mounted Raman samples are shown below. The sample of interest was placed in the holder and a thin glass cover slip was fixed over the top with epoxy resin (Araldite), sealing the sample in the holder, so that the Raman spectra could be obtained without exposing the samples to air.

A Horiba JY LabRam Aramis confocal Raman microscope was used to examine the samples. The exciting laser wavelength was 532 nm. A×50 extra long working distance objective lens was used to collect the 180° backscattered light.

X-ray diffraction

X-ray diffraction (XRD) analysis was carried out using a fully automated Siemens D5000 powder diffractometer employing copper kα radiation (λ=0.15406 nm) and a secondary monochromator. The sample which was supported on a single crystal of silicon, was continuously spun during data collection and scanned using a step size of 0.05°2θ between the range of 5°–75°2θ and a count time of 30 seconds per step.

Phase identification using XRD is achieved by comparing the diffraction pattern obtained from the unknown, to a standard data base that is compiled by the International Centre for Diffraction Data (ICDD). If and when a positive identification is made, the constituent is indicated by a stick pattern that is superimposed on the XRD diffractogram.

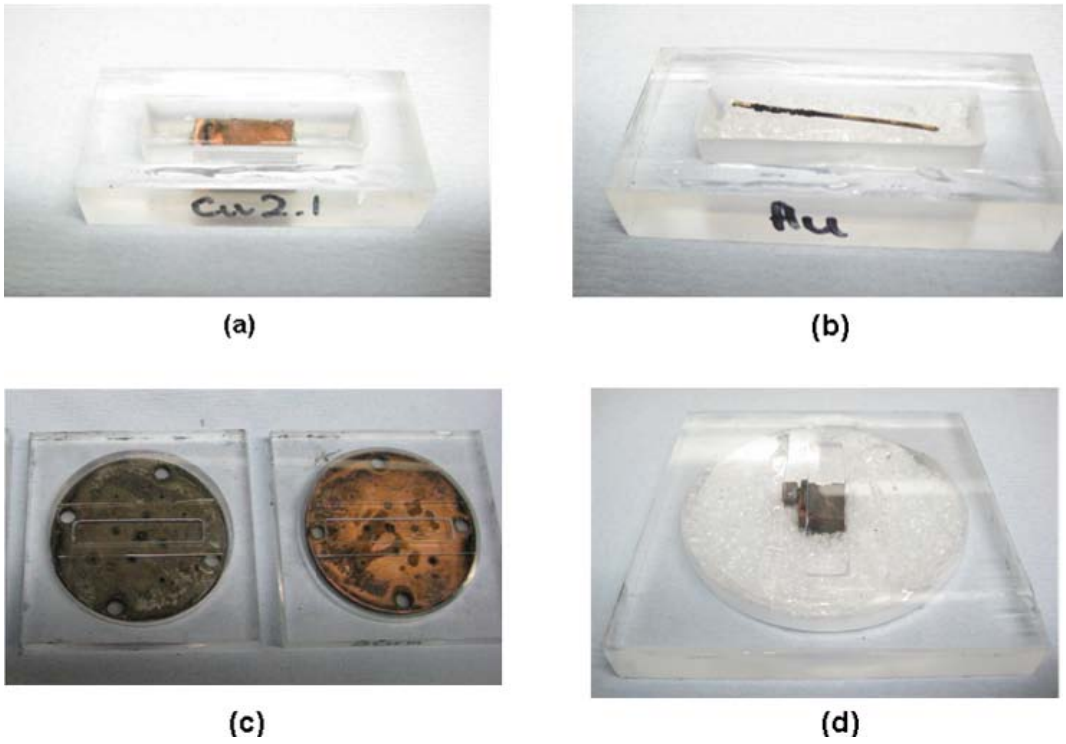

Figure A-1. *Examples of Perspex sample holders used for Raman spectroscopy analysis: (a) copper electrode 1 in Perspex holder; (b) gold electrode in Perspex holder (c) sandwich specimen halves in Perspex holder, internal surface of cast iron on the left, internal surface of copper on the right; (d) same specimen holder containing WOL specimen. The specimen holders in (c) and (d) have a Perspex cover with a rectangular window, over which a glass cover slip was attached using epoxy resin.*

SEM/EDX

A JEOL 6480 LV SEM linked to an Oxford Instruments X-MAX80 SD X-ray detector and INCA x-ray analysis system was used to image the samples and perform the compositional analysis. EDX analyses the characteristic X-rays produced by the interaction between the primary electron beam and the sample. The technique identifies all elements present with atomic numbers of 5 and greater (boron) with a detection limit of approximately 0.1 weight %. The measurements are semi-quantitative. EDX analyses were carried out at single points (i.e. the electron beam was not rastered) or over defined areas, which are shown by pink boxes superimposed on the SEM images in Appendix 2. A 'Sum' spectrum refers to an analysis of the whole area shown in the SEM image.

XPS

Samples for analysis by X-ray photoelectron spectroscopy (XPS) were supported on carbon pads adhered to standard stubs, which were introduced into the instrument via a turbo molecular pumped entry lock. The entry lock was pumped for about 15 minutes before the sample was introduced into the analysis chamber. XPS was performed in an ion pumped VG Microtech CLAM 4 MCD analyser system. 200 Watt unmonochromated Mg X-ray excitation was used. The analyser was operated at constant pass energy of 100 eV for wide scans and 20 eV for detailed scans setting the C1s peak at BE 284.8 eV to overcome any sample charging. Data was obtained using the SPECTRA version 8 operating system. Data processing was performed using CASAXPS. Peak areas were measured after satellite subtraction and background subtraction (either a linear background or following methods of Shirley (1972).

The area under the principal peak of each element in the spectrum, divided by an empirically derived sensitivity factor (see Briggs and Seah 1990), is proportional to the concentration of that element on the surface (approximately the top 10 nm). The sensitivity of the technique is about 0.1 atomic percent, depending on the element.

FTIR

Fourier transform infrared spectroscopy (FTIR) analysis was performed on a Varian Digilab Excalibur imaging FTIR UMA 600 microscope with single point MCT detector equipped with Micro Ge ATR accessory.

Profilometry

A Veeco DekTak 6M was used for all profilometry measurements reported within this work programme. The profile from a 9.0 kÅ ± 5% standard (SN85140) was also measured.

Hydrogen analysis

Hydrogen analysis of the copper was carried out by Sci-Lab Analytical Ltd, UK, using an Eltra H-500 Hydrogen Determinator. The samples were heated to release the trapped hydrogen which was then detected by means of a dual range thermal conductivity cell, with auto zero control. Four samples were prepared, all approximately 25 mm × 10 mm × 5 mm. These were cut from a section of the canister wall approximately one third height of the can from the bottom. The section was then sliced vertically to provide separate samples of the inner wall and the outer wall. From these two pieces two samples of each were cut to the above dimensions to provide a sample of inner and outer wall with back up samples. The detection limit of this technique is 0.001 ppm hydrogen in the test metal, with an accuracy of ± 1%.

Appendix 2

Results from SEM/EDX analysis

Copper electrode 1

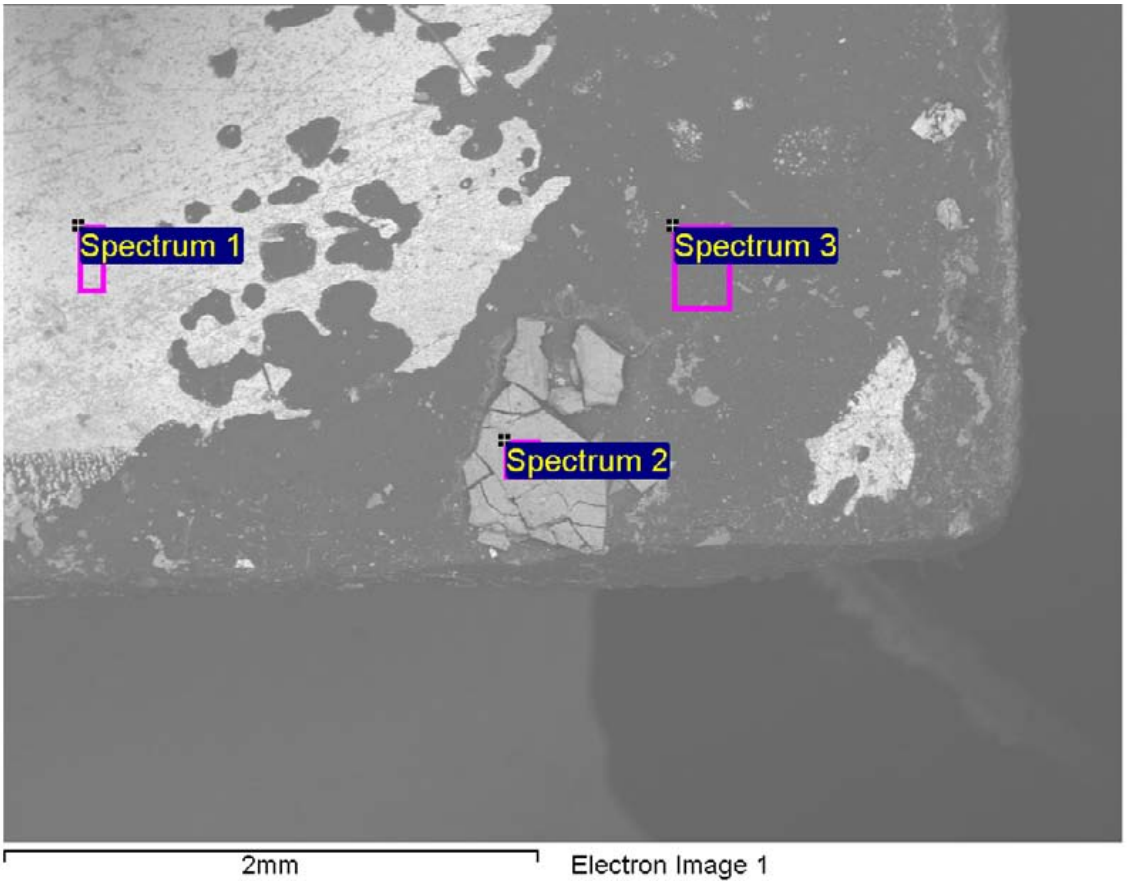

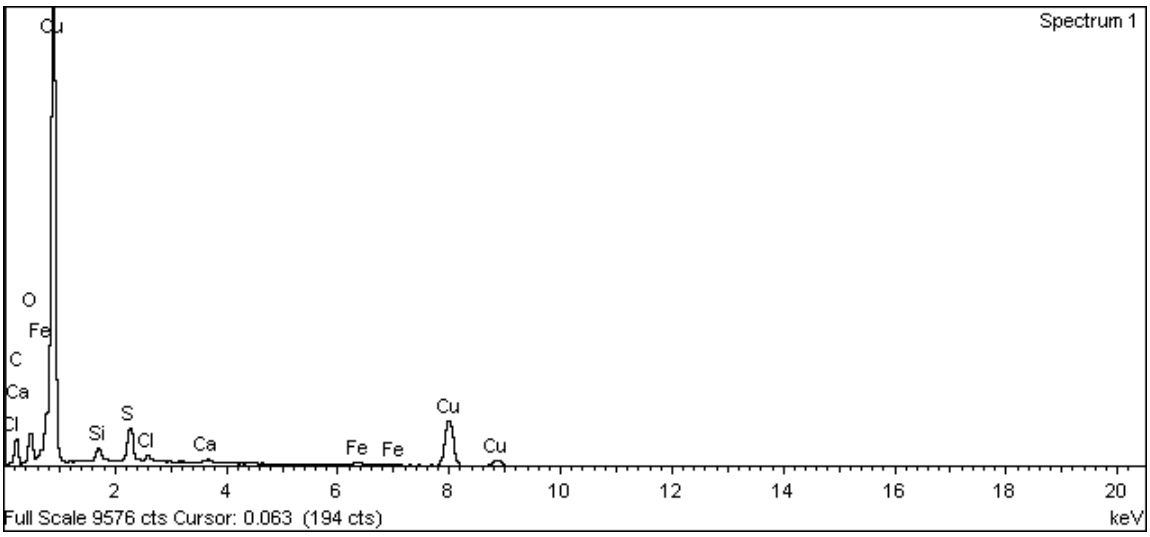

Figure A-2. Surface of copper electrode 1 and EDX analysis at position of Spectrum 1

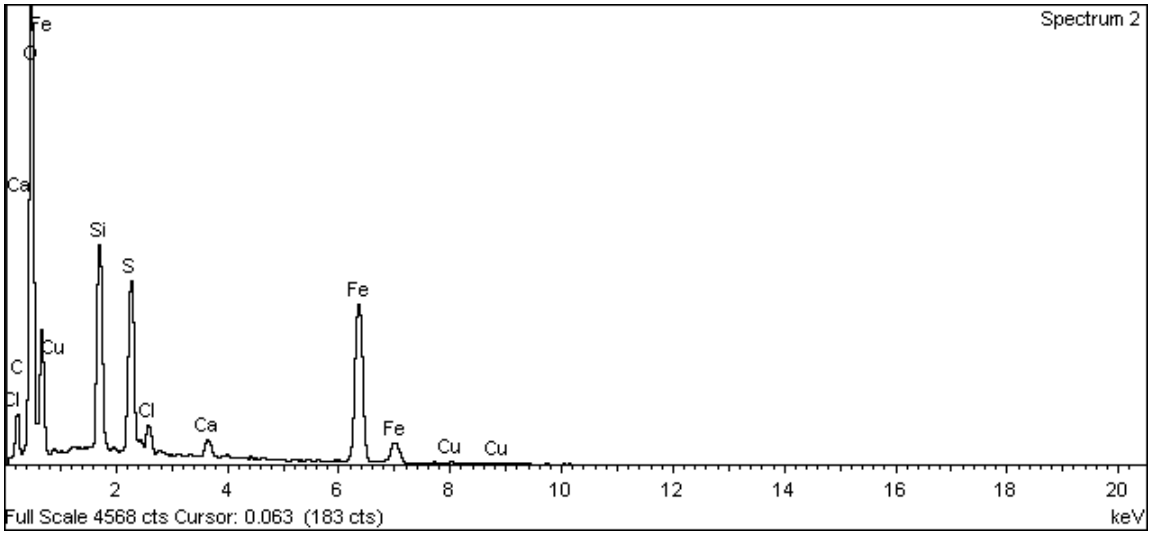

Figure A-3. Surface of copper electrode 1 and EDX analysis at position of Spectrum 2

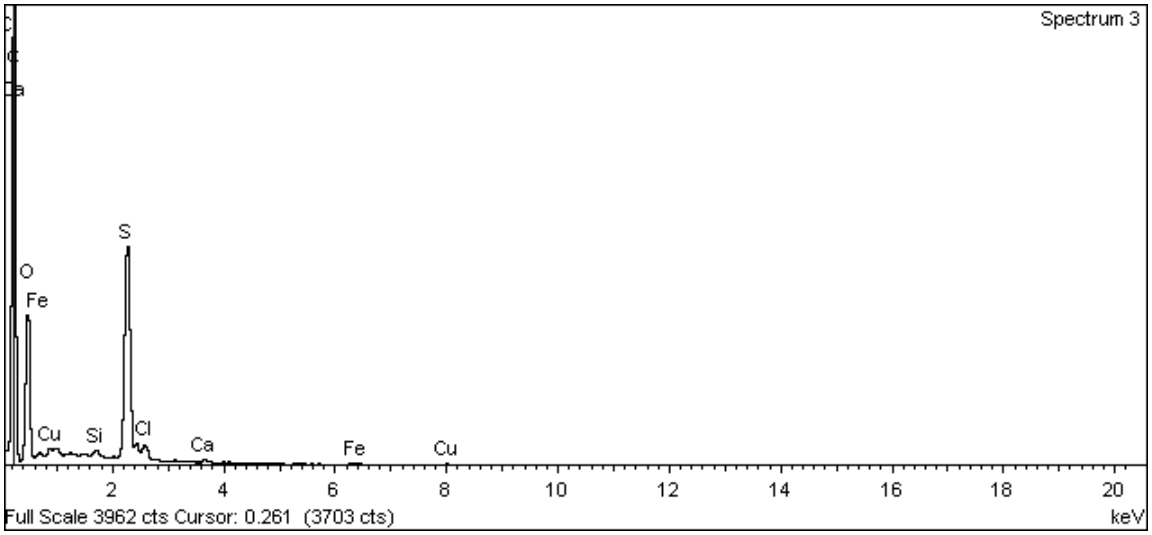

Figure A-4. Surface of copper electrode 1 and EDX analysis at position of Spectrum 3

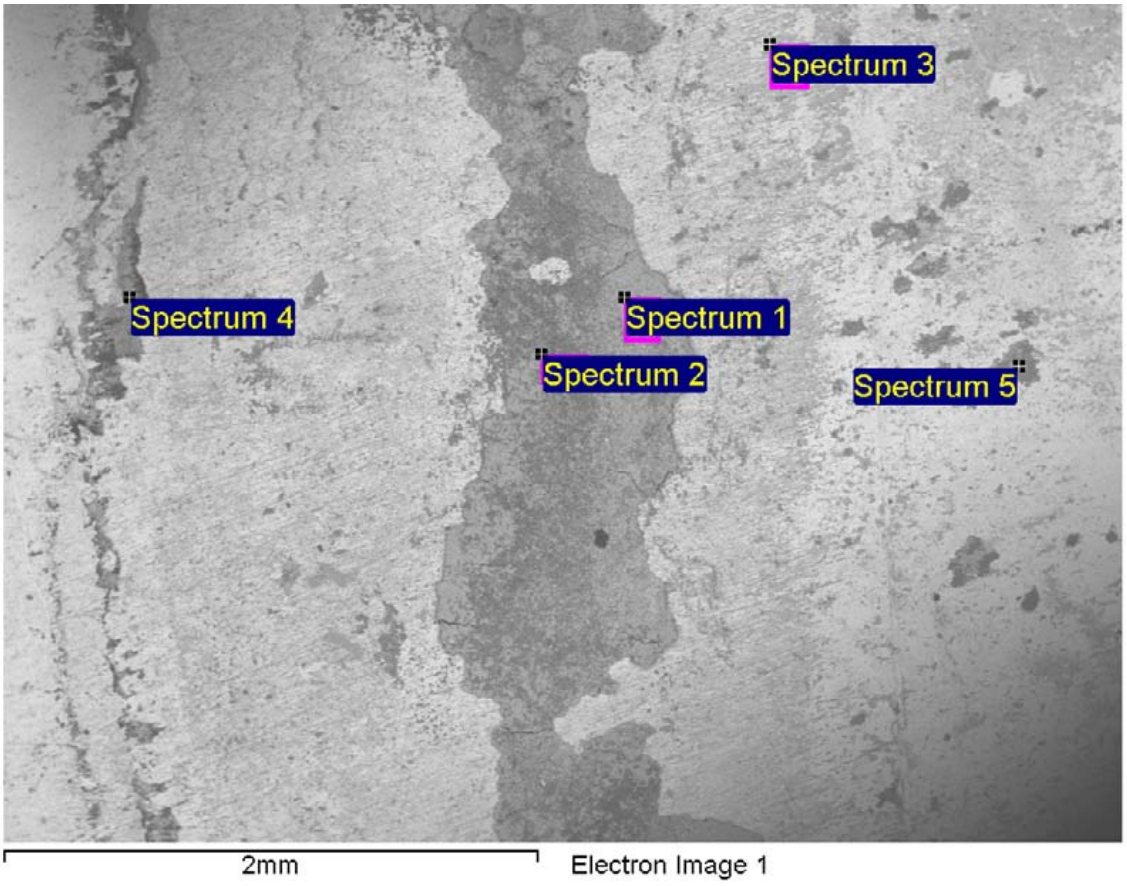

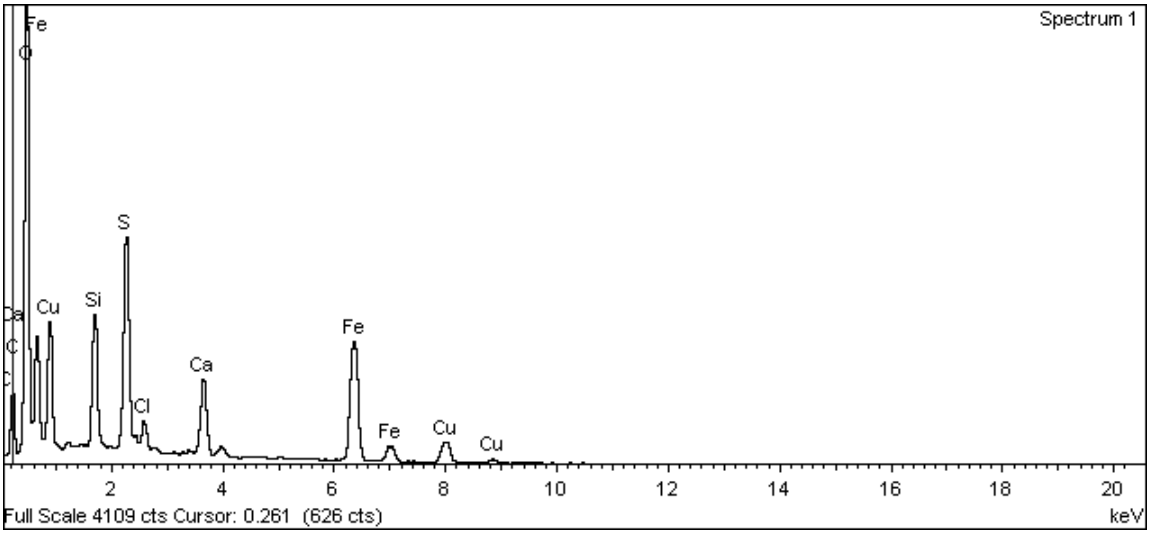

Figure A-5. Surface of copper electrode 1 and EDX analysis at position of Spectrum 1

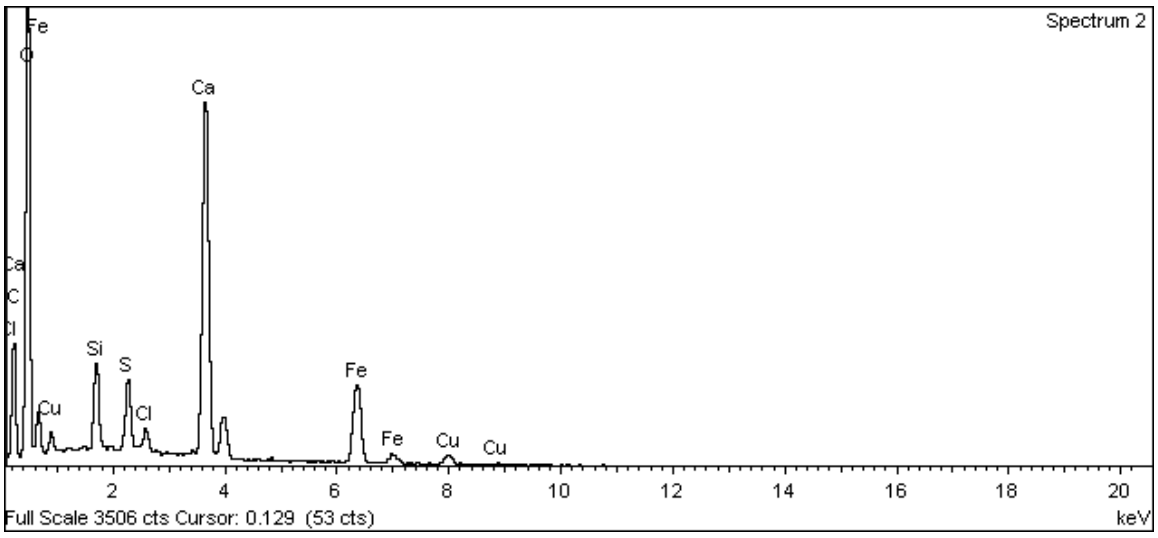

Figure A-6. Surface of copper electrode 1 and EDX analysis at position of Spectrum 2

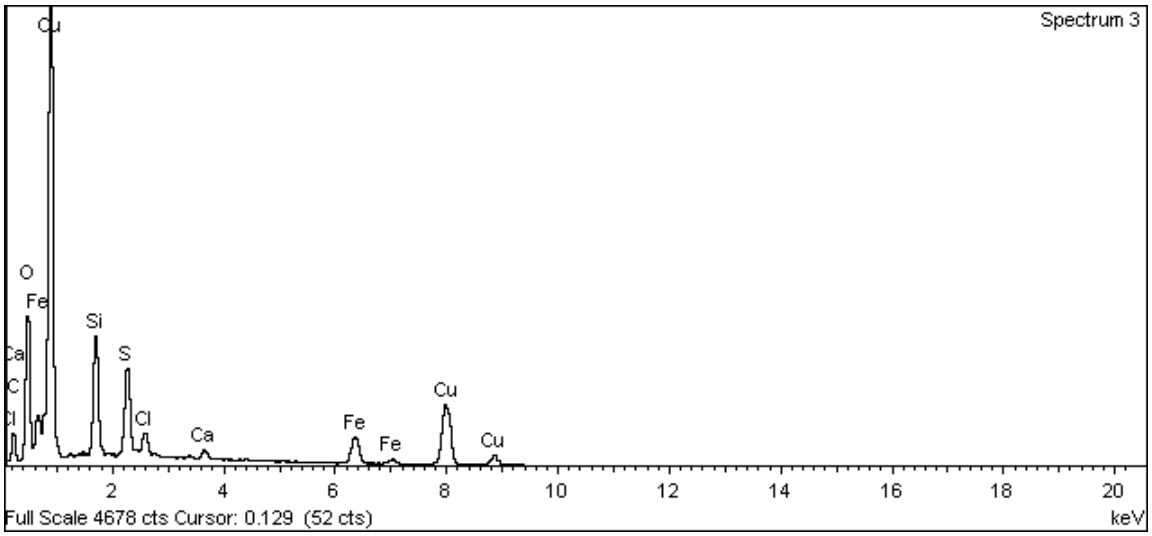

Figure A-7. Surface of copper electrode 1 and EDX analysis at position of Spectrum 3

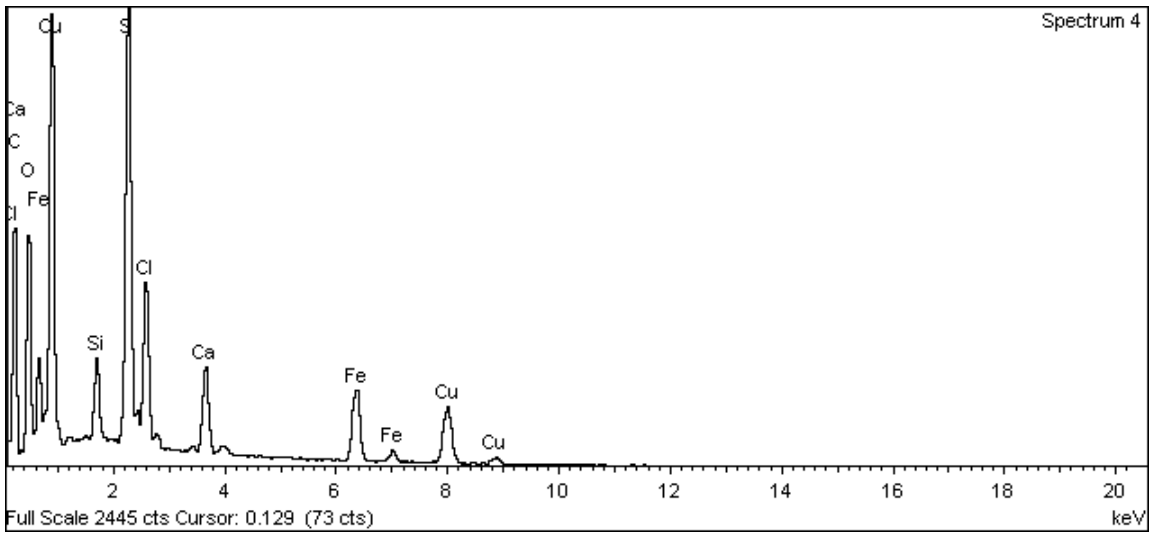

Figure A-8. Surface of copper electrode 1 and EDX analysis at position of Spectrum 4

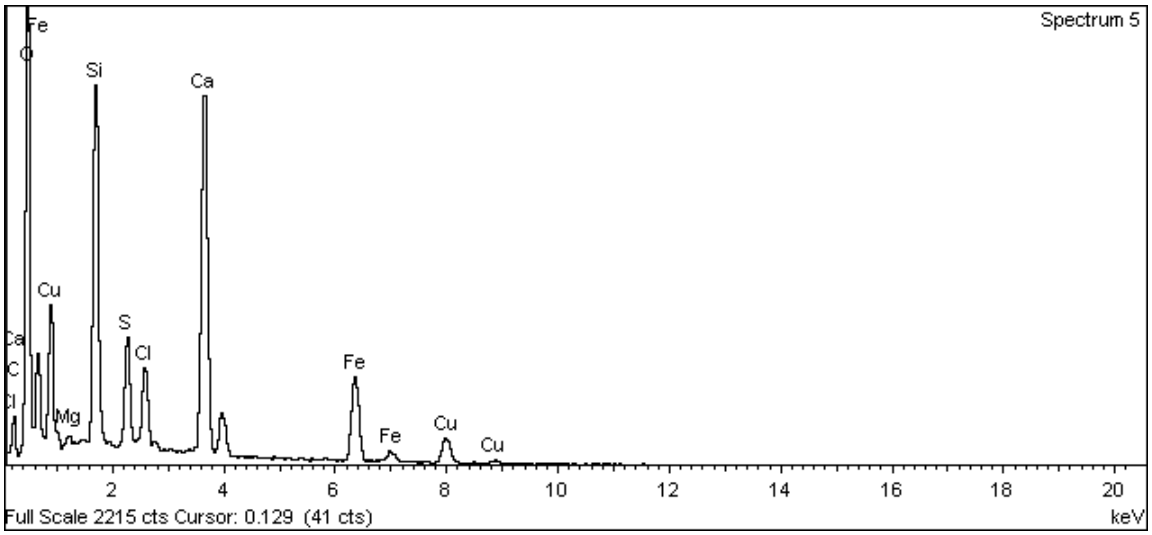

Figure A-9. Surface of copper electrode 1 and EDX analysis at position of Spectrum 5

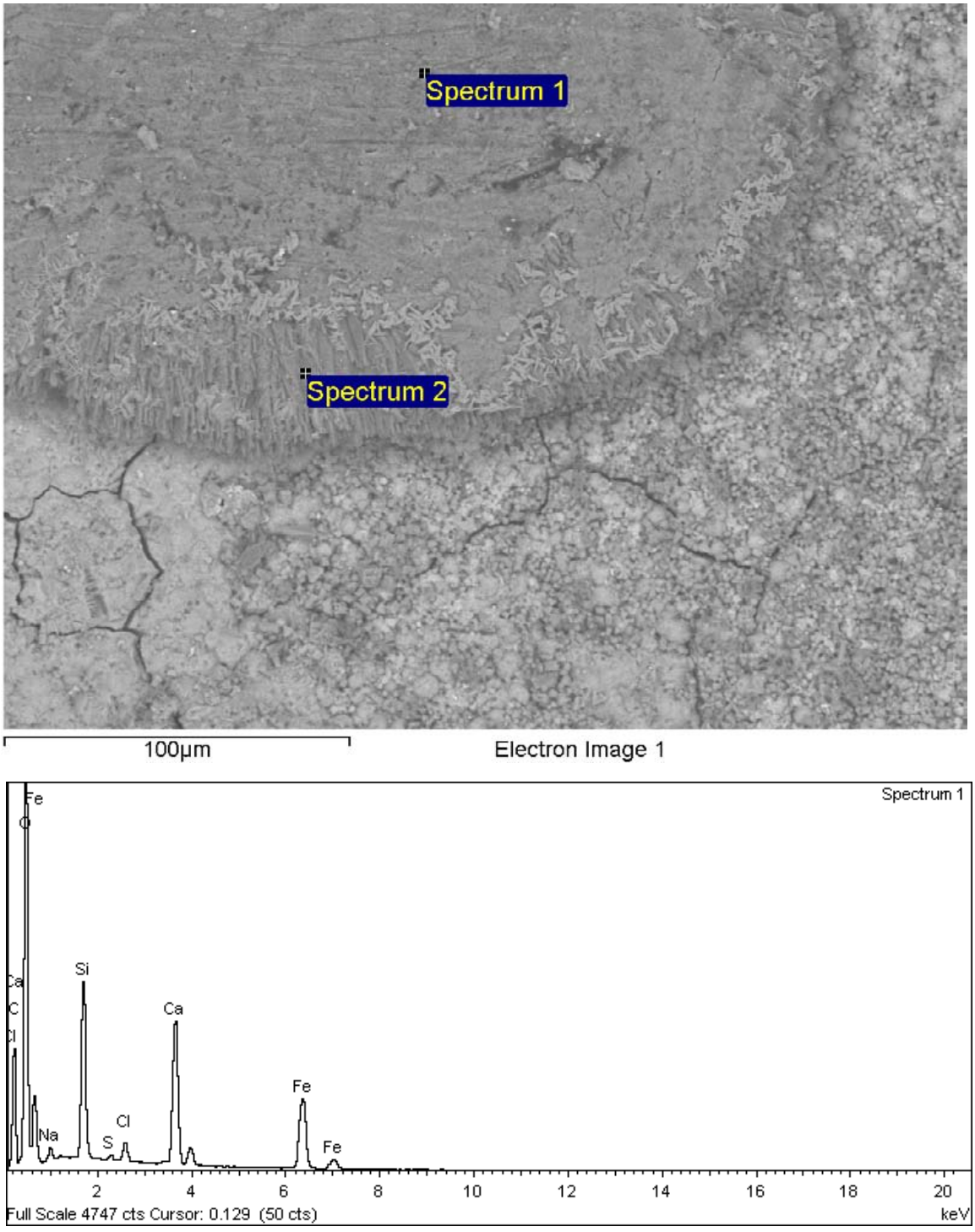

Figure A-10. Surface of copper electrode 1 and EDX analysis at position of Spectrum 1

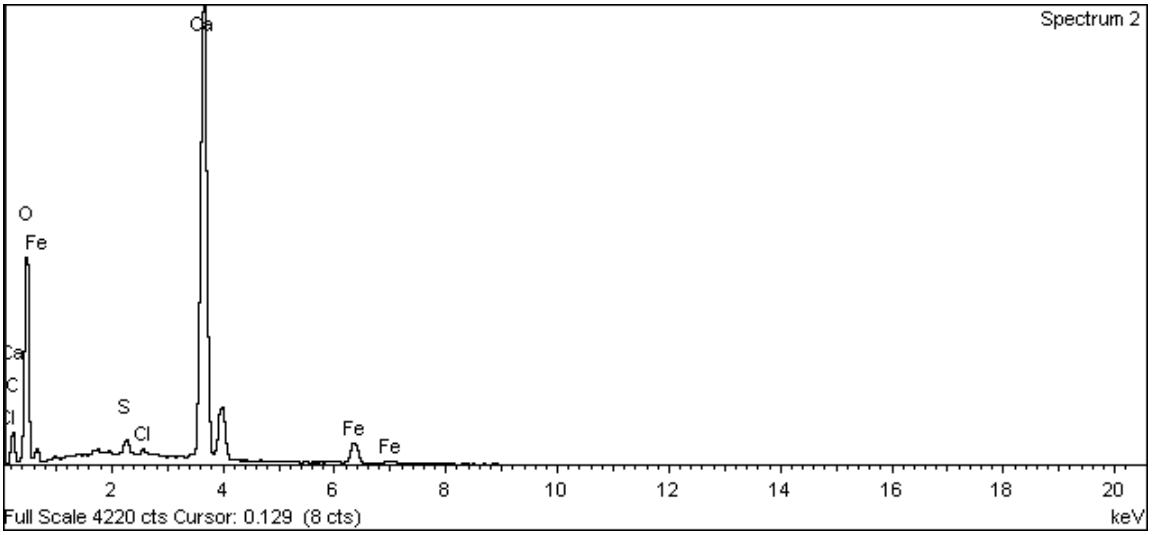

Figure A-11. Surface of copper electrode 1 and EDX analysis at position of Spectrum 2

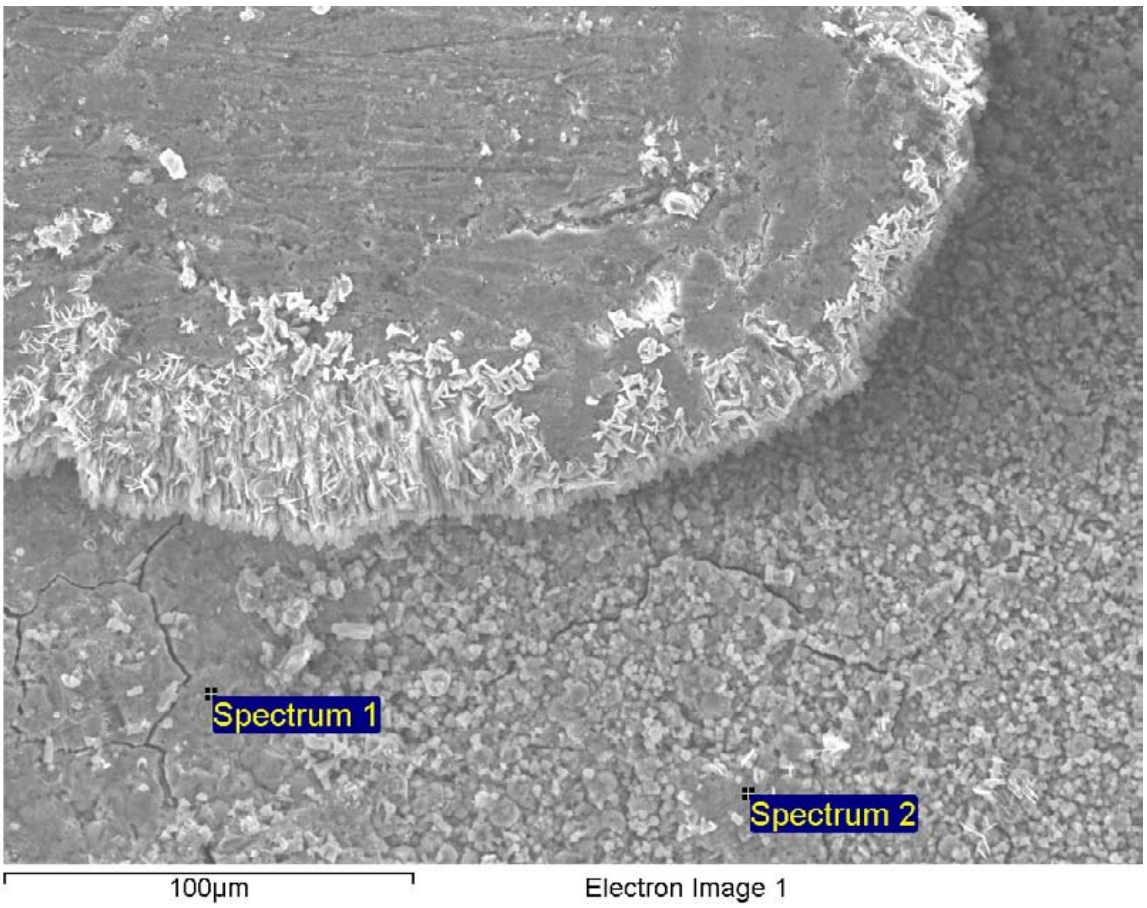

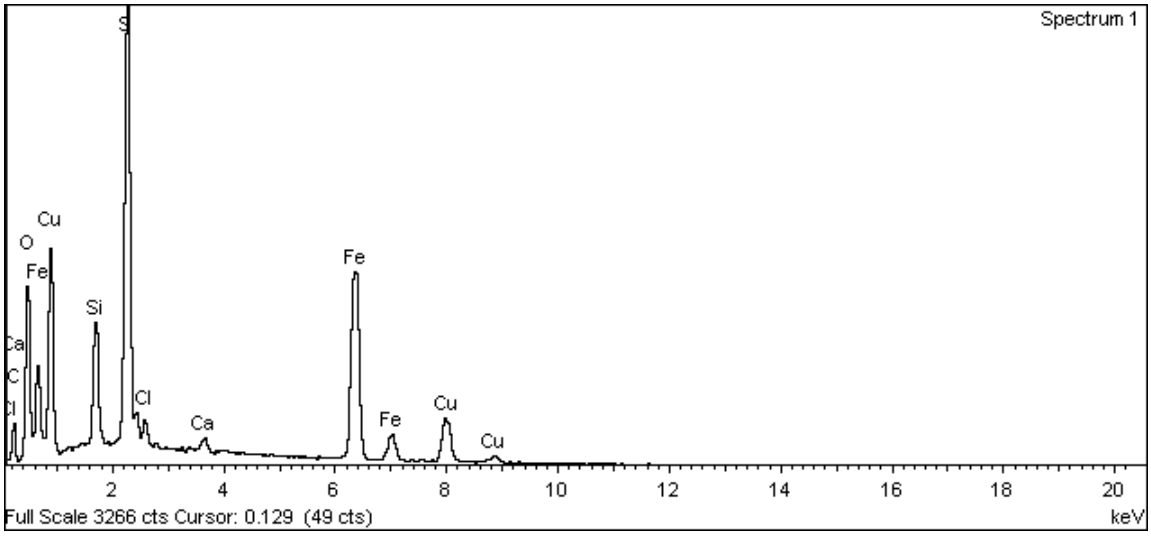

Figure A-12. Surface of copper electrode 1 and EDX analysis at position of Spectrum 1

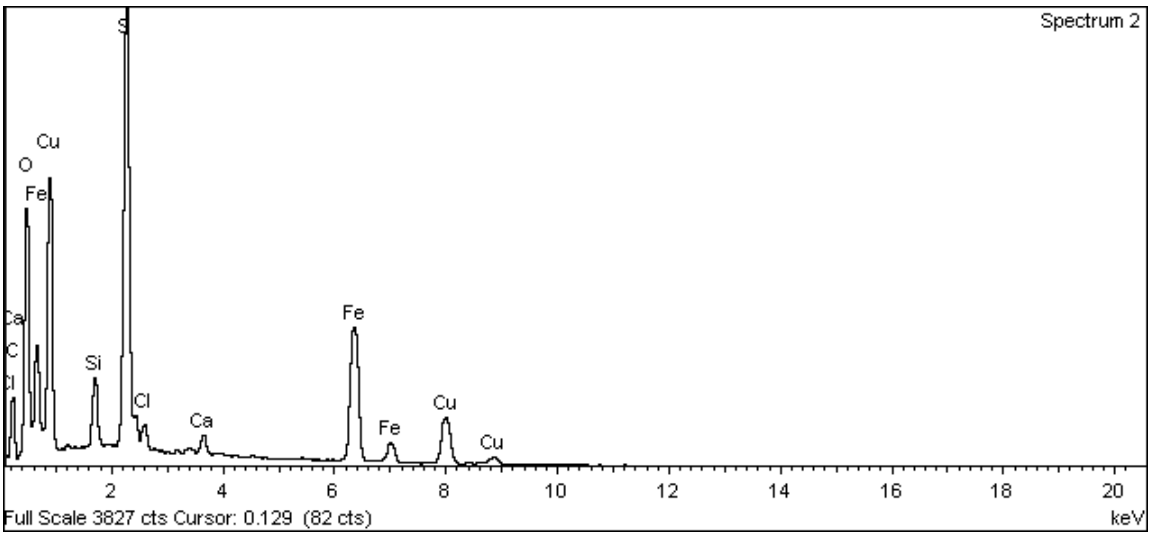

Figure A-13. Surface of copper electrode 1 and EDX analysis at position of Spectrum 2

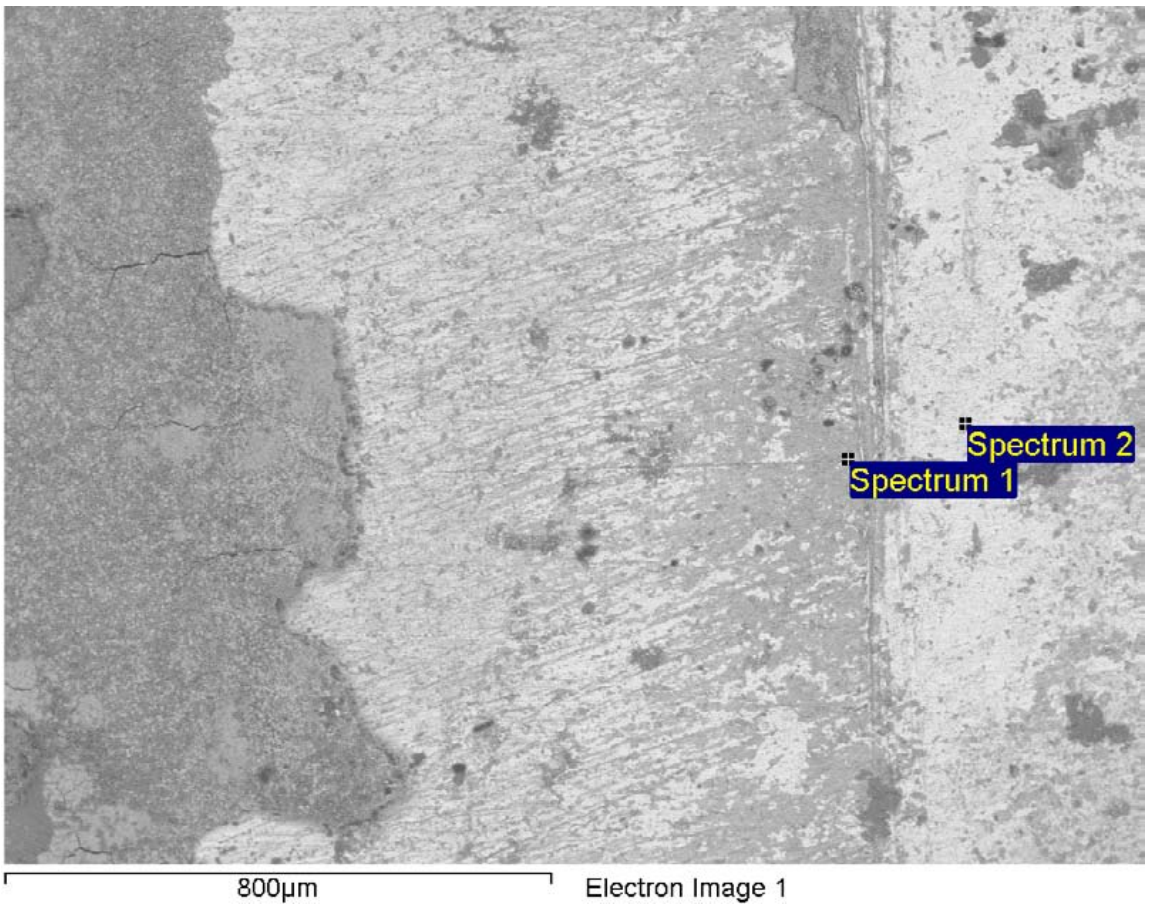

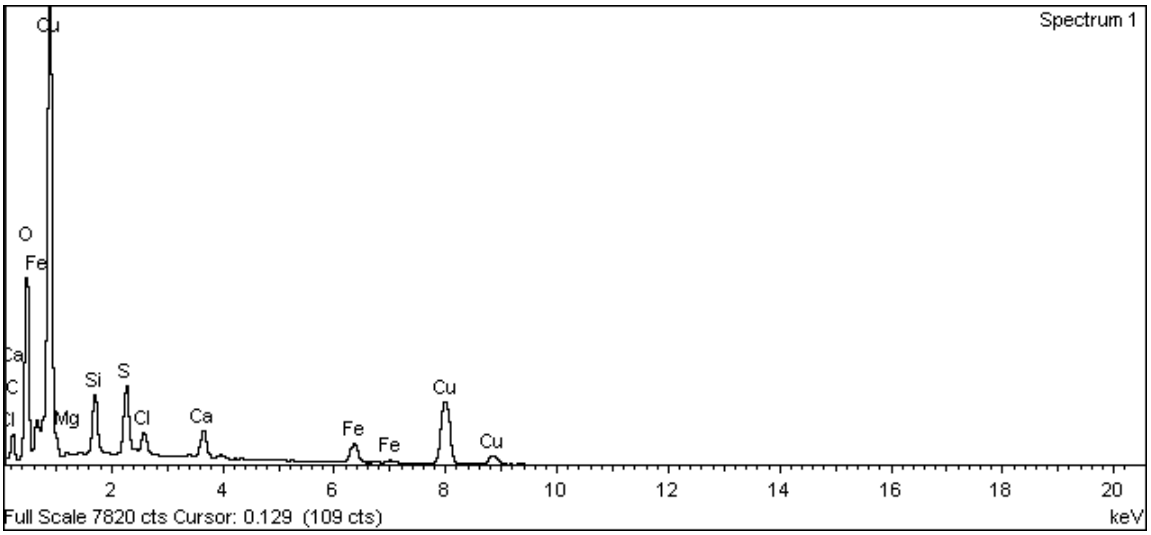

Figure A-14. Surface of copper electrode 1 and EDX analysis at position of Spectrum 1

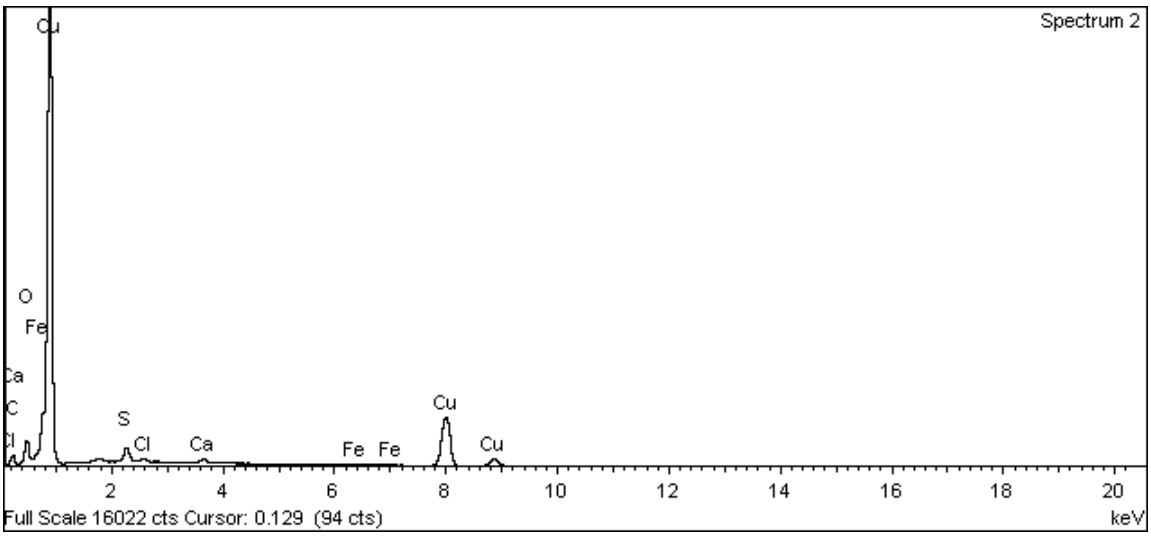

Figure A-15. Surface of copper electrode 1 and EDX analysis at position of Spectrum 2

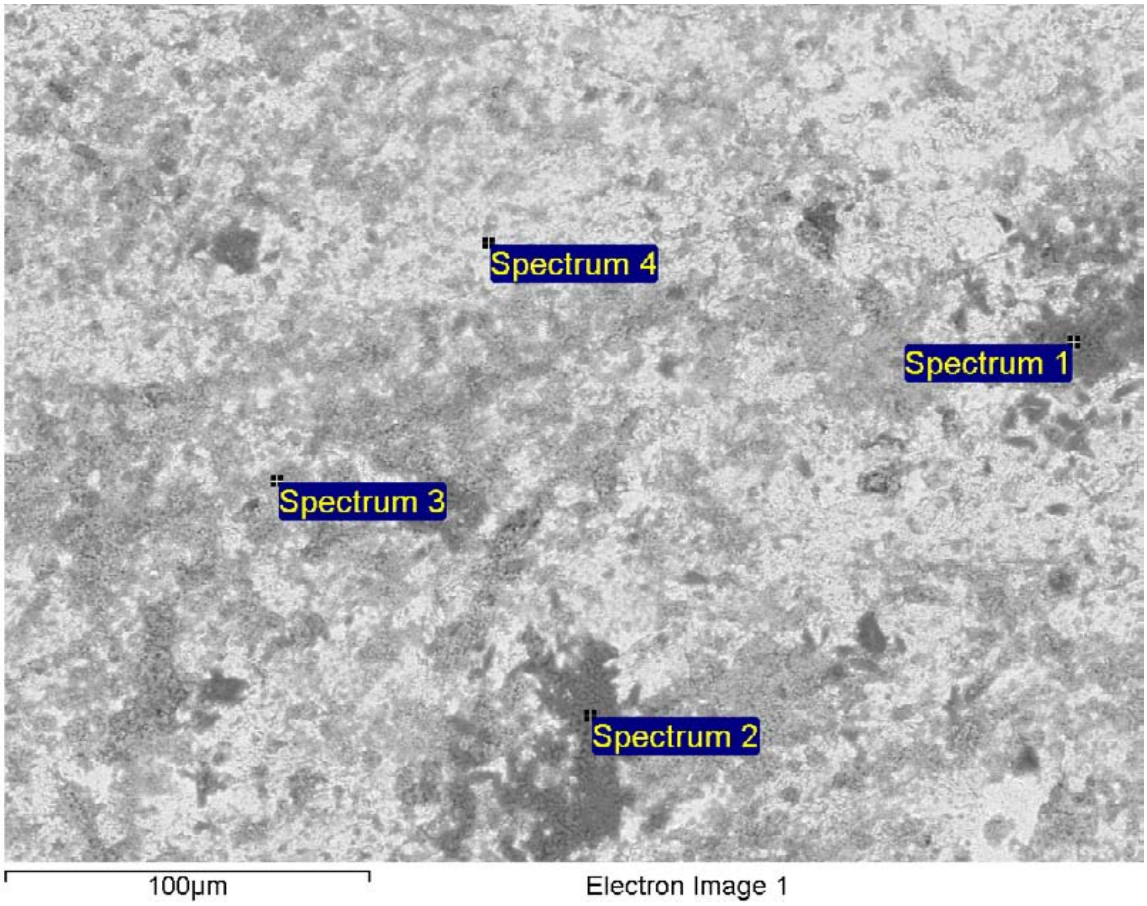

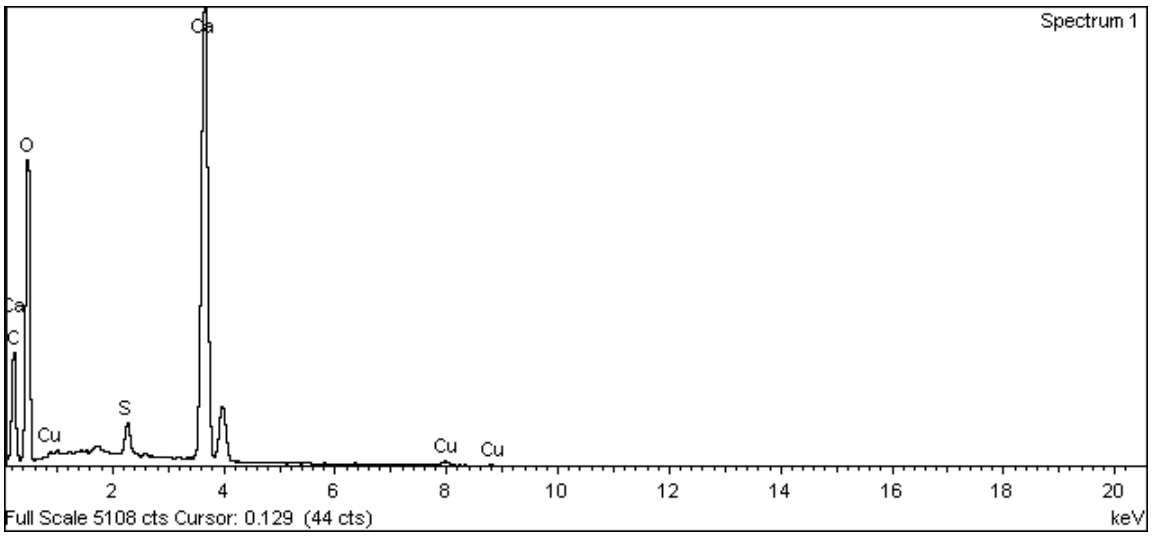

Figure A-16. Surface of copper electrode 1 and EDX analysis at position of Spectrum 1

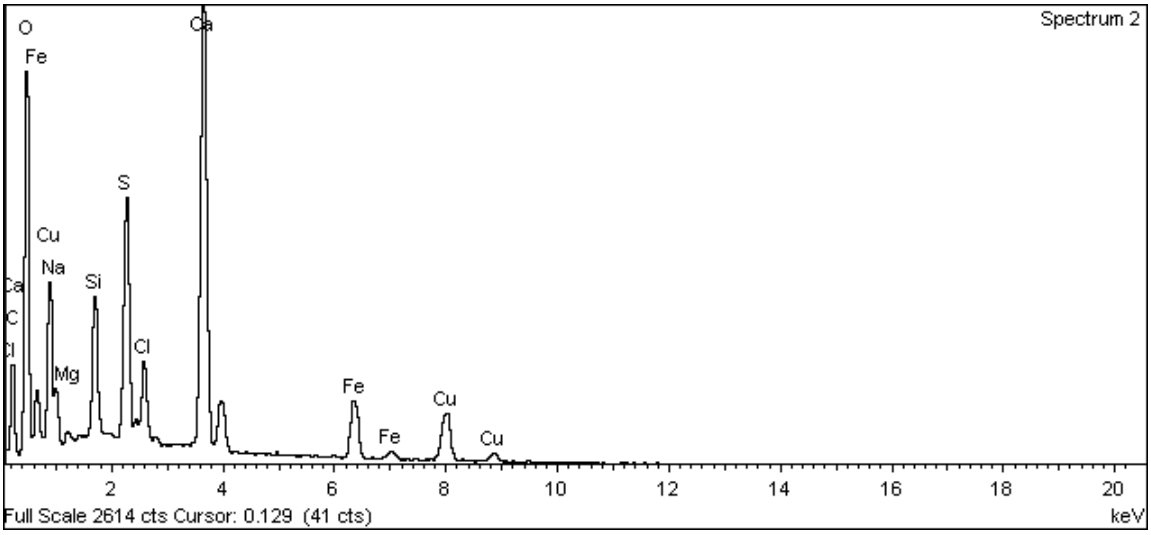

Figure A-17. Surface of copper electrode 1 and EDX analysis at position of Spectrum 2

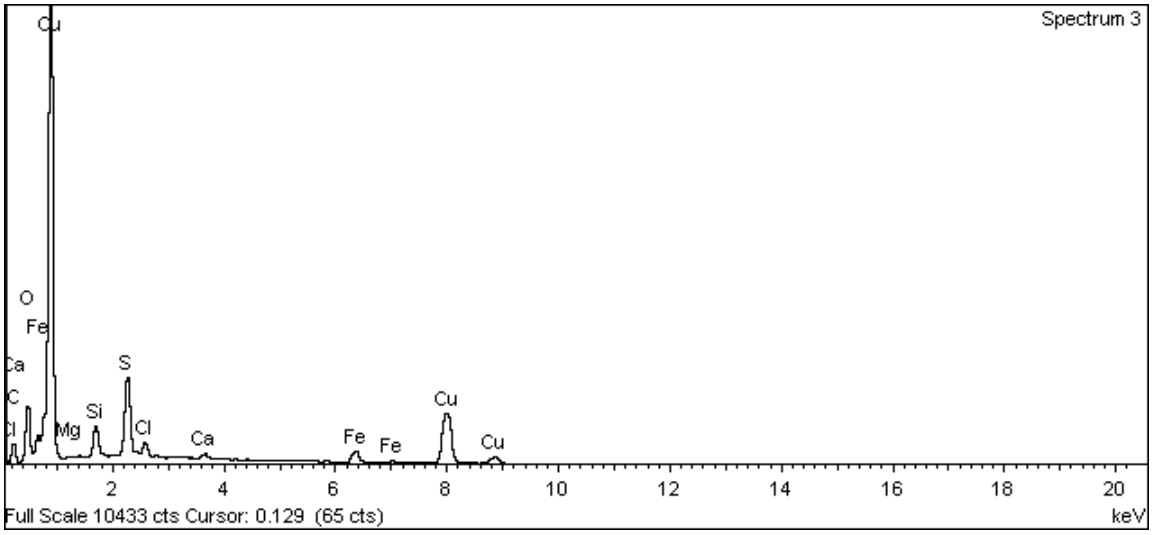

Figure A-18. Surface of copper electrode 1 and EDX analysis at position of Spectrum 3

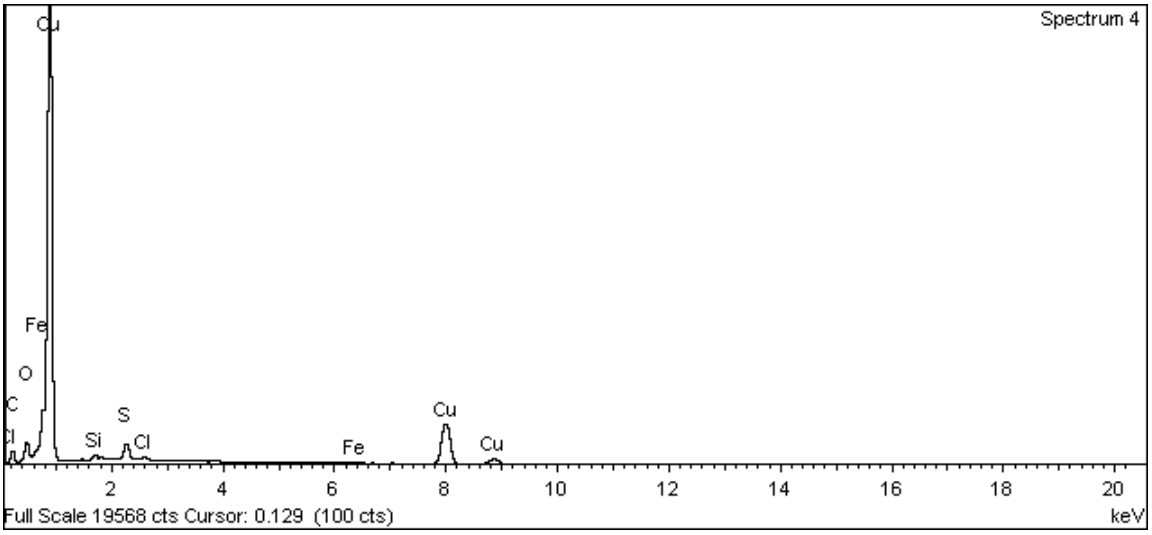

Figure A-19. Surface of copper electrode 1 and EDX analysis at position of Spectrum 4

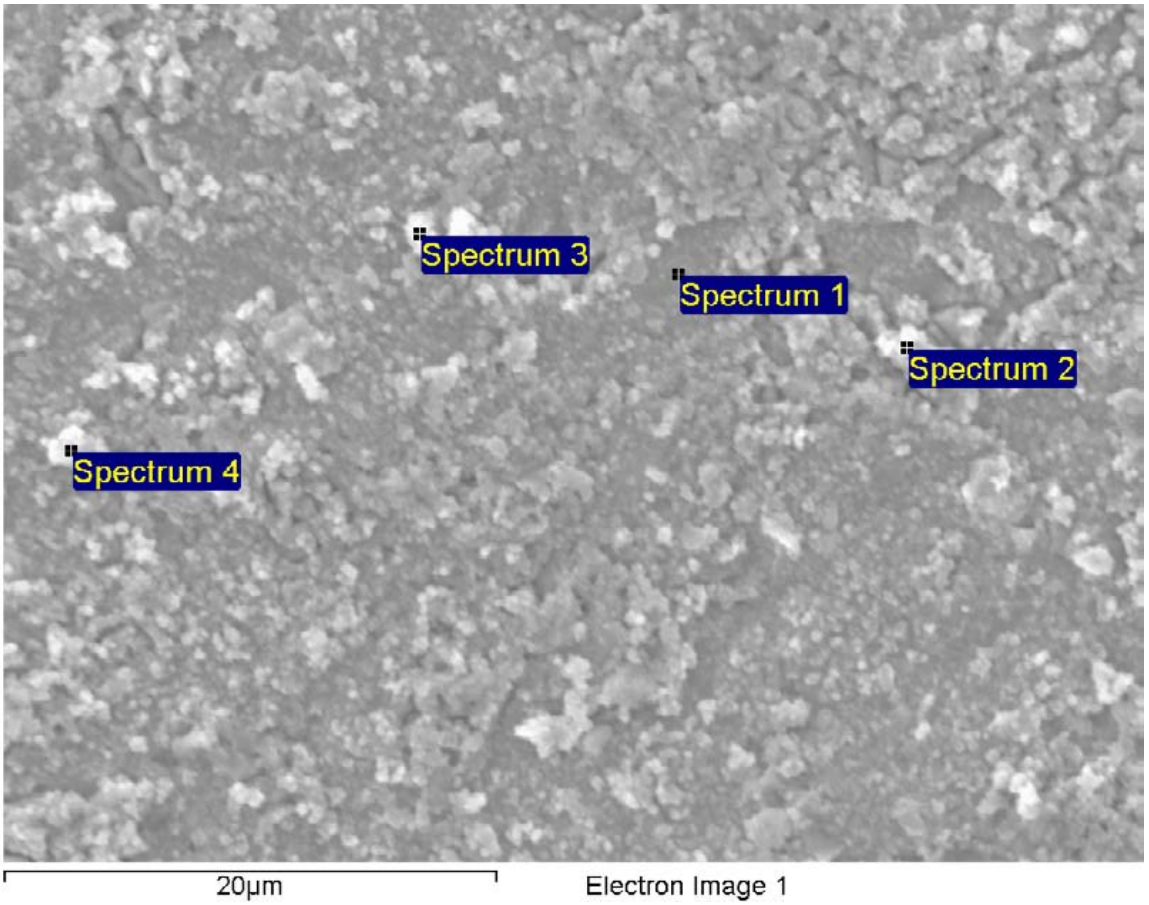

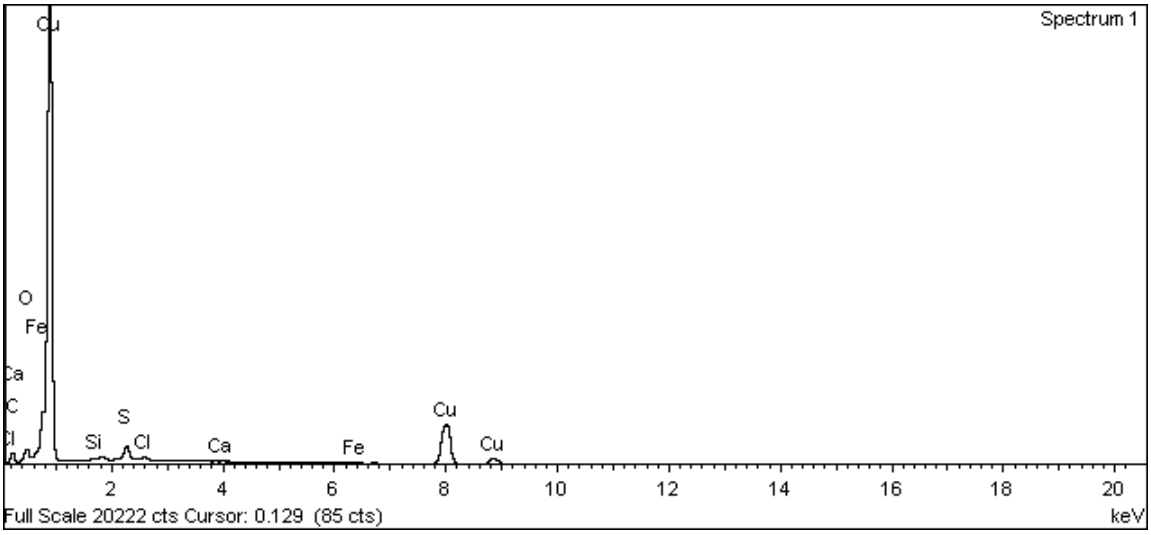

Figure A-20. Surface of copper electrode 1 and EDX analysis at position of Spectrum 1

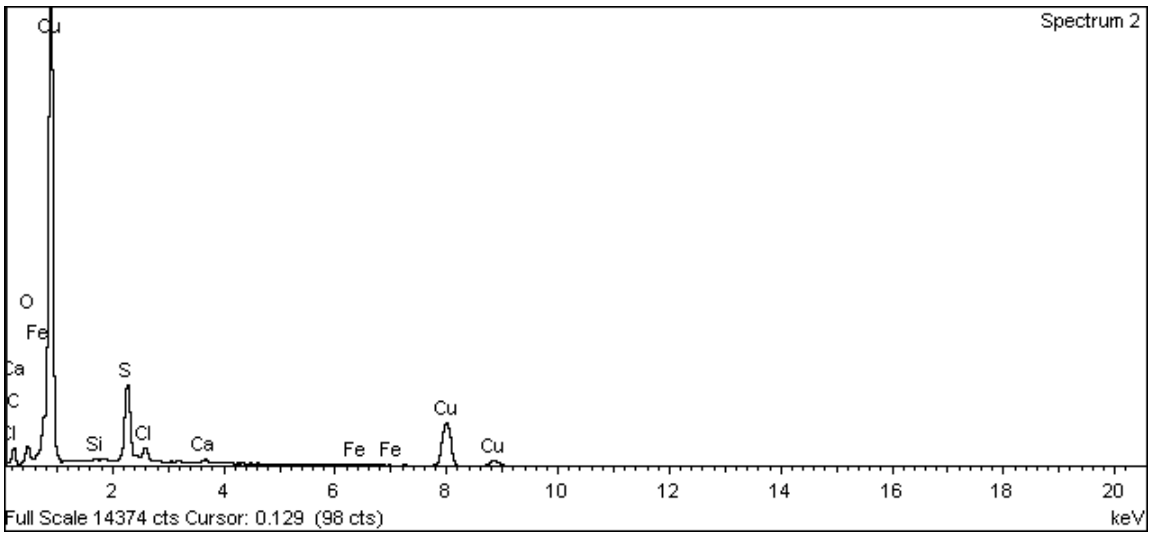

Figure A-21. Surface of copper electrode 1 and EDX analysis at position of Spectrum 2

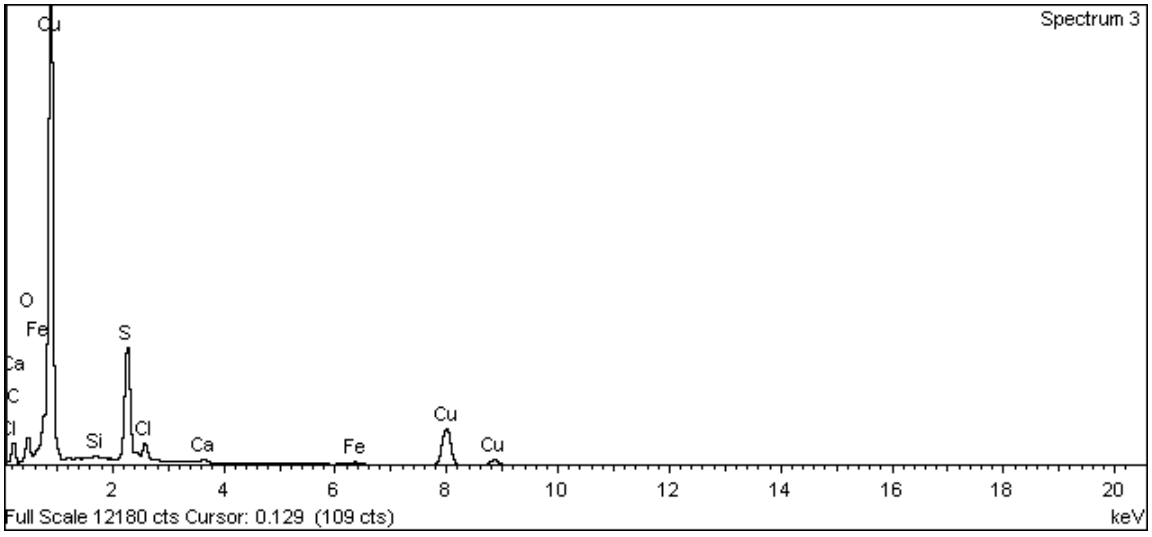

Figure A-22. Surface of copper electrode 1 and EDX analysis at position of Spectrum 3

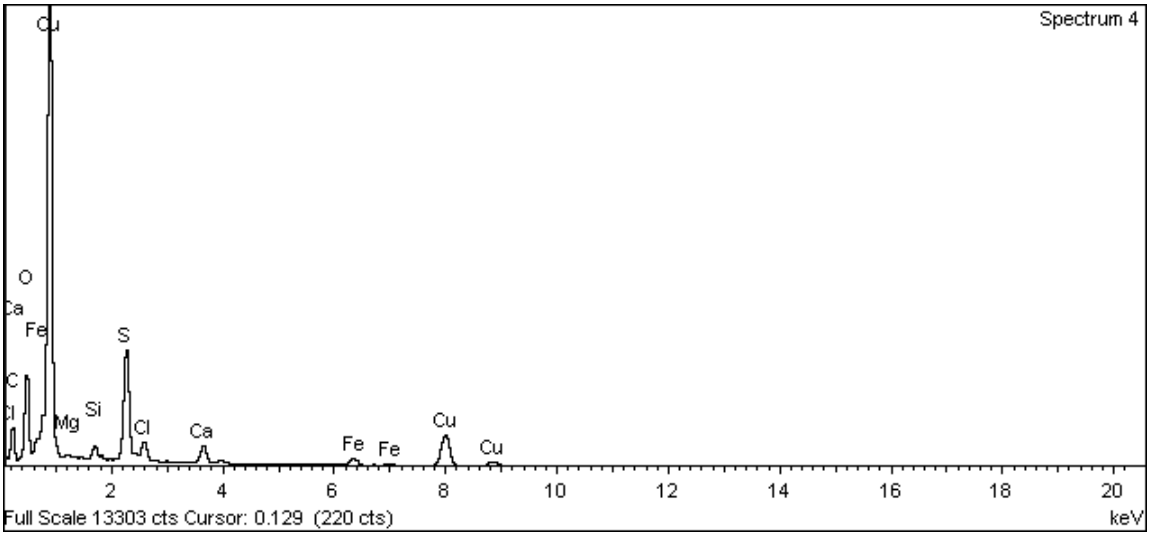

Figure A-23. Surface of copper electrode 1 and EDX analysis at position of Spectrum 4

Copper weight loss specimen

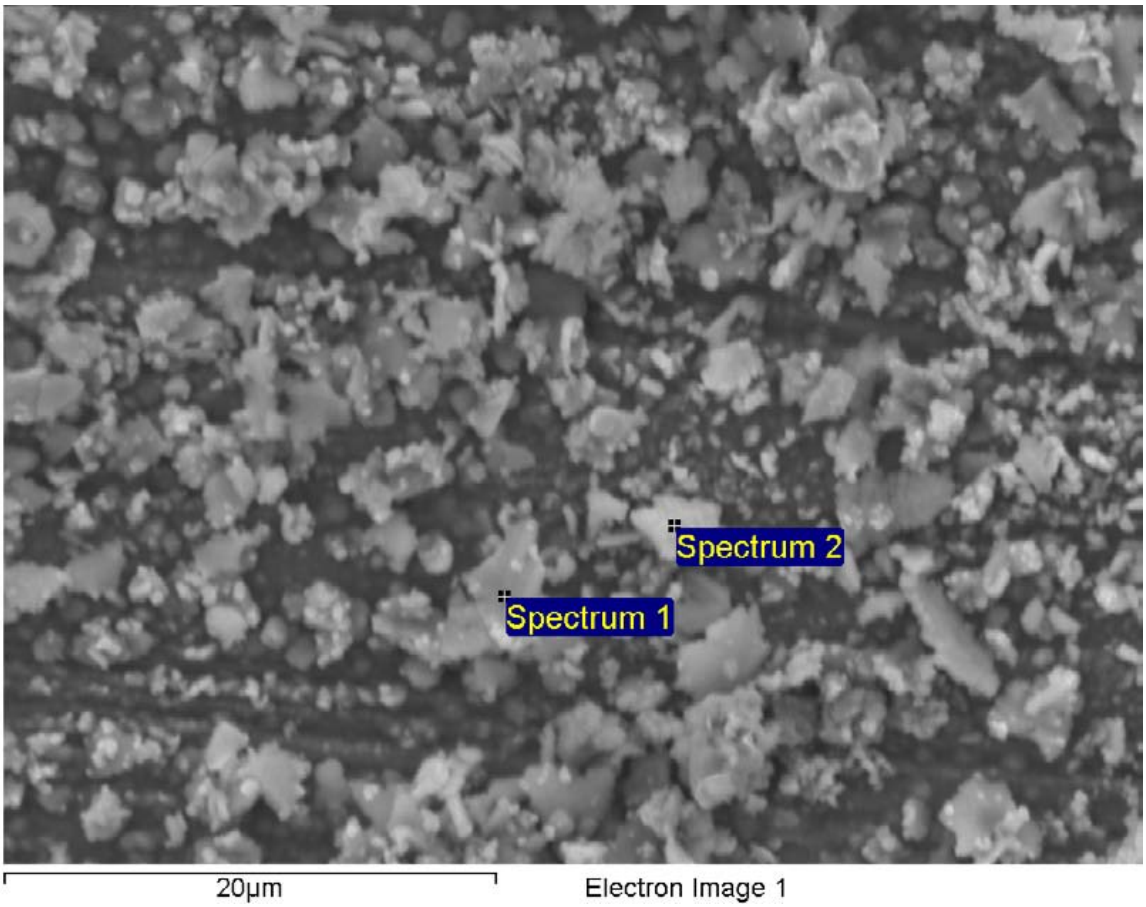

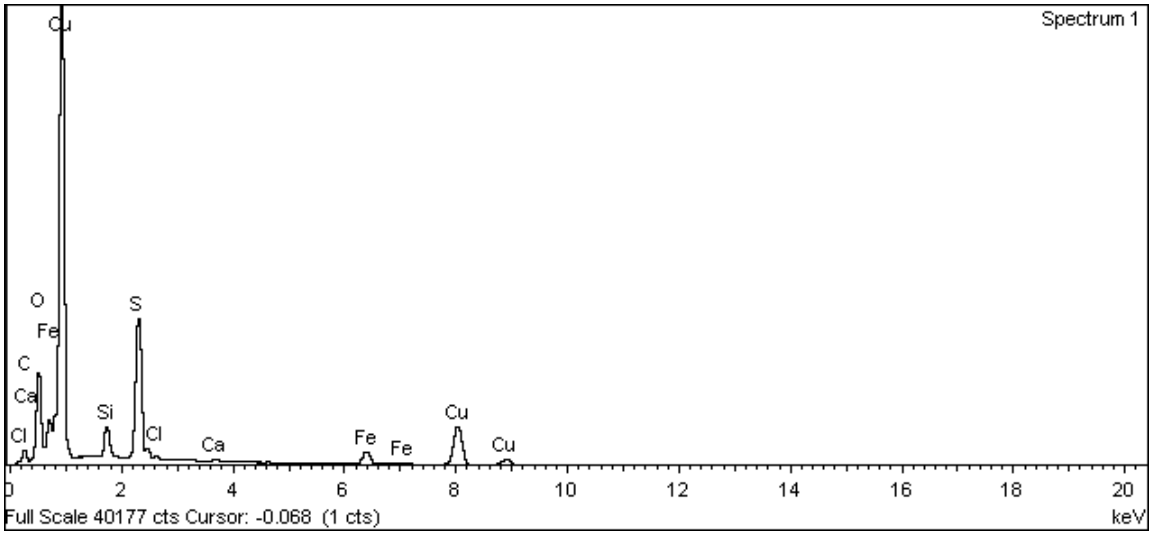

Figure A-24. Surface of copper weight loss specimen and EDX analysis at position of Spectrum 1

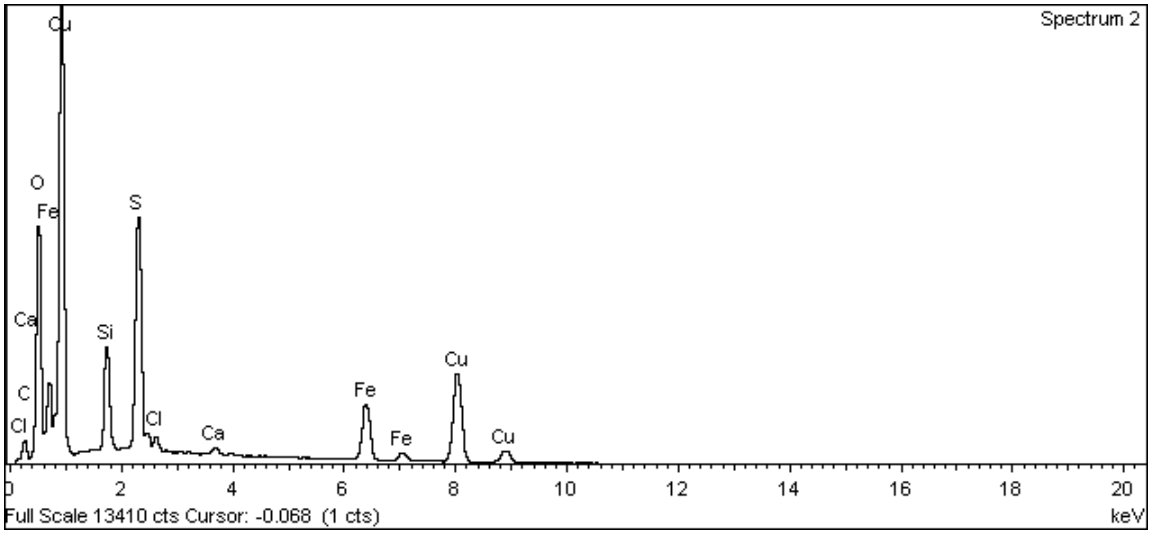

Figure A-25. Surface of copper weight loss specimen and EDX analysis at position of Spectrum 2

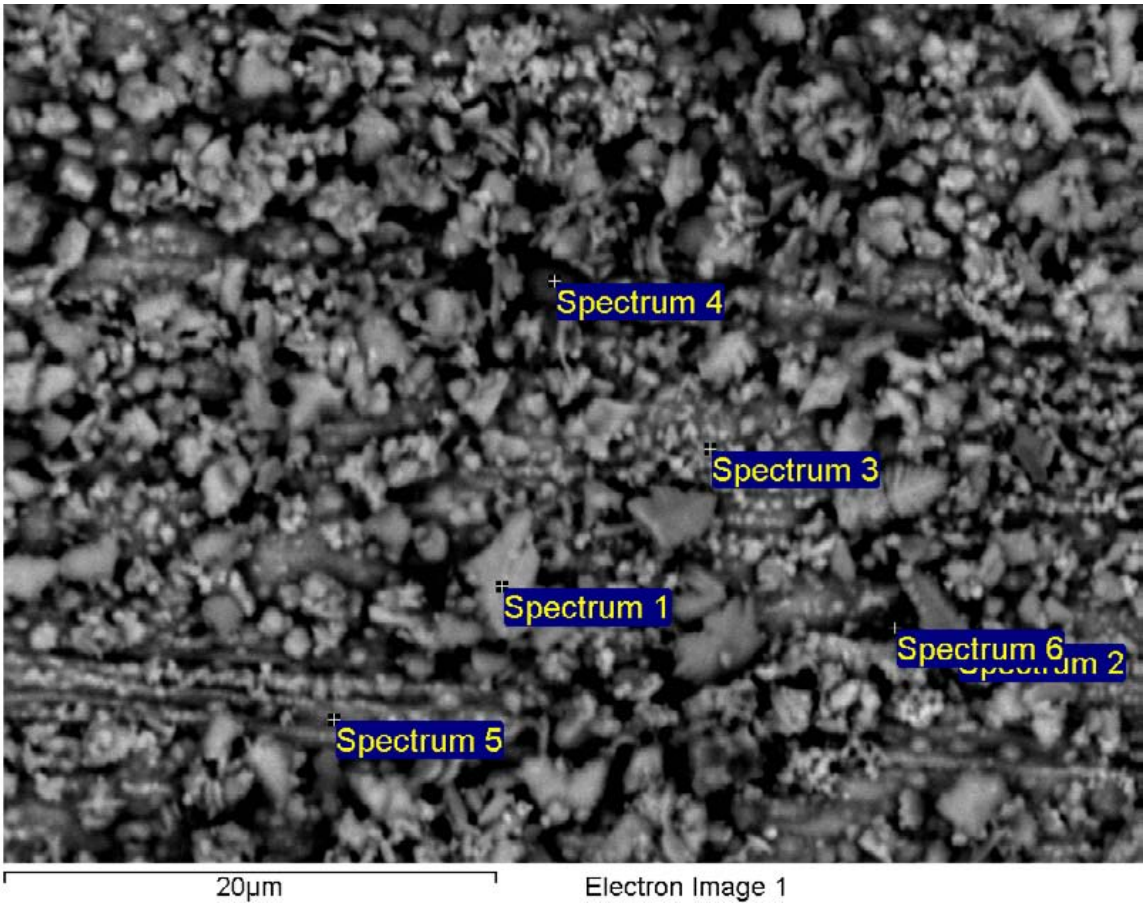

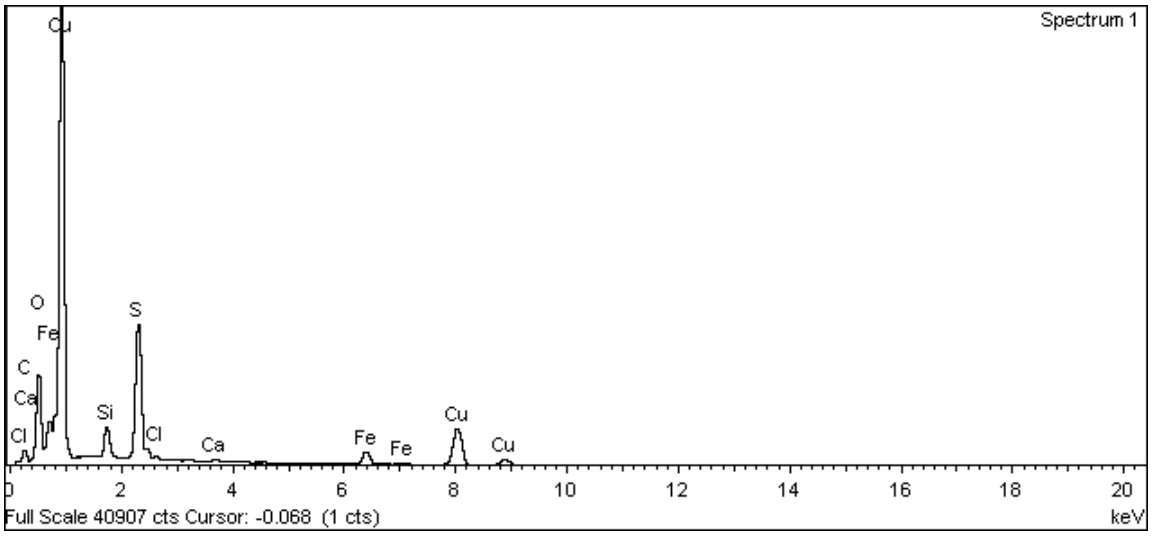

Figure A-26. Surface of copper weight loss specimen and EDX analysis at position of Spectrum 1

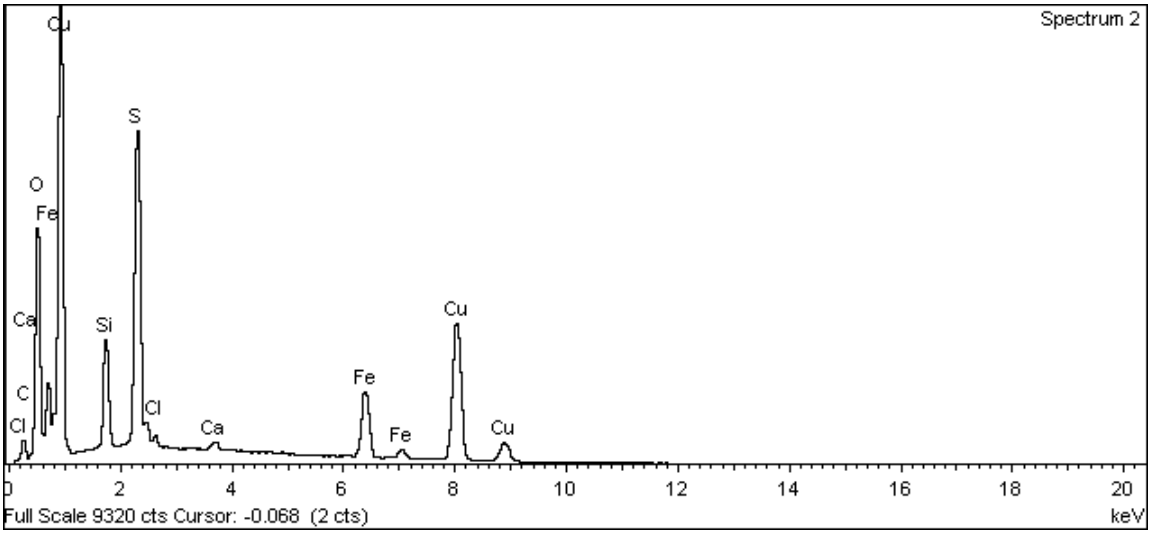

Figure A-27. Surface of copper weight loss specimen and EDX analysis at position of Spectrum 2

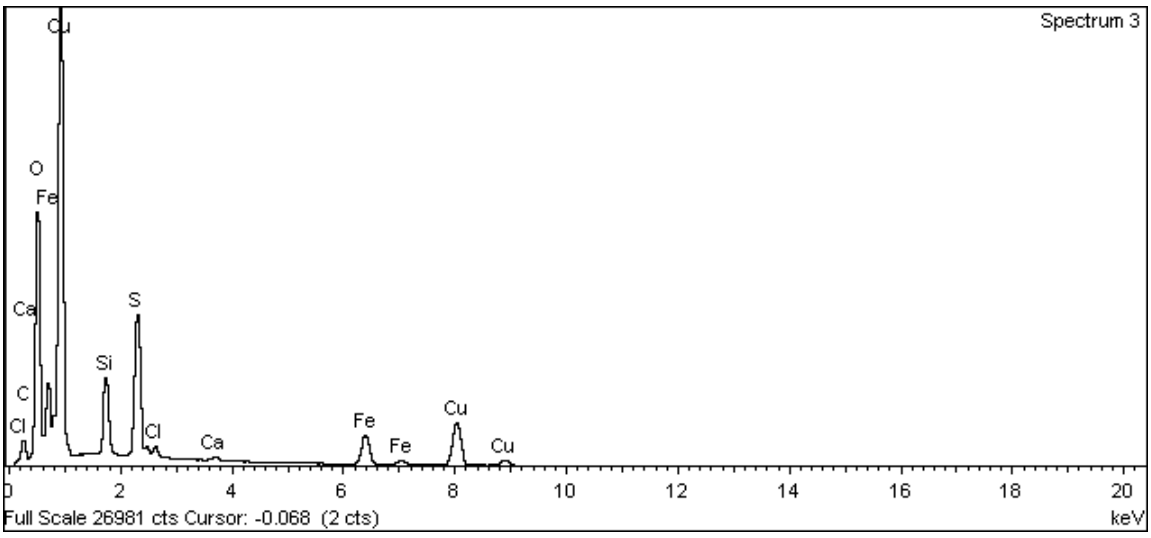

Figure A-28. Surface of copper weight loss specimen and EDX analysis at position of Spectrum 3

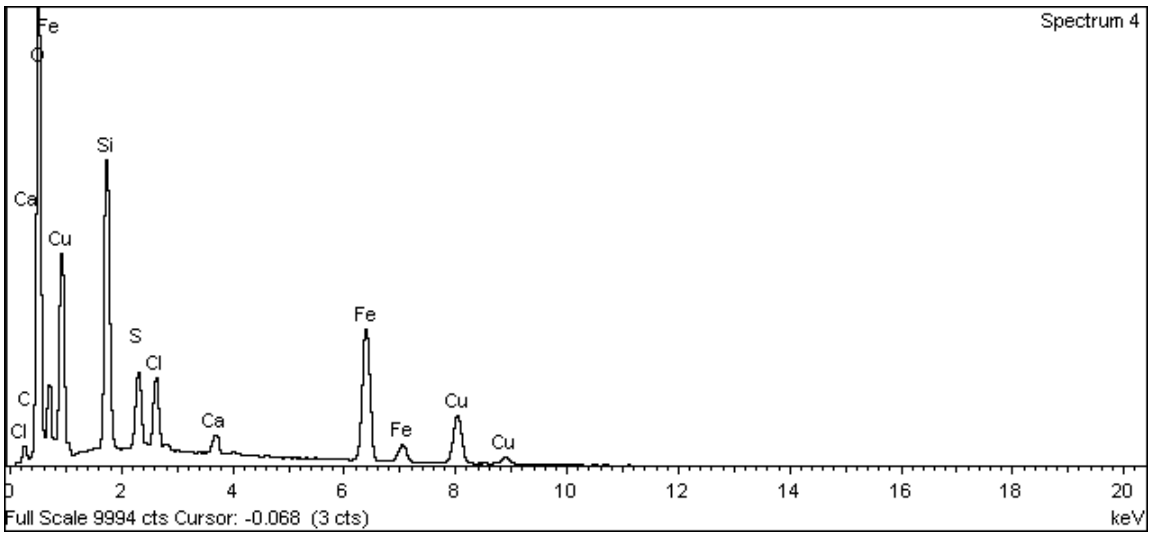

Figure A-29. Surface of copper weight loss specimen and EDX analysis at position of Spectrum 4

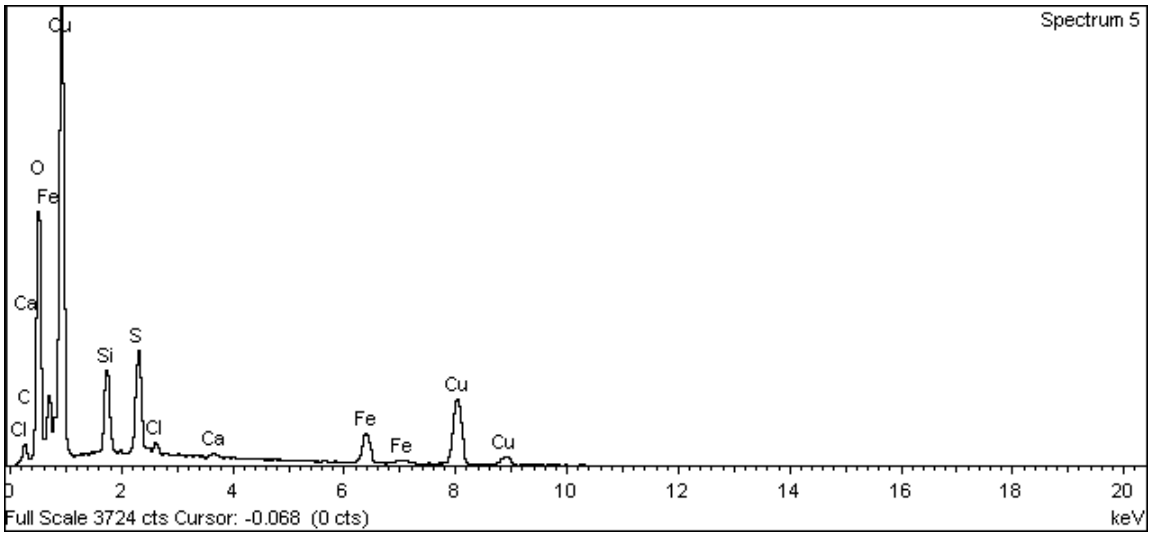

Figure A-30. Surface of copper weight loss specimen and EDX analysis at position of Spectrum 5

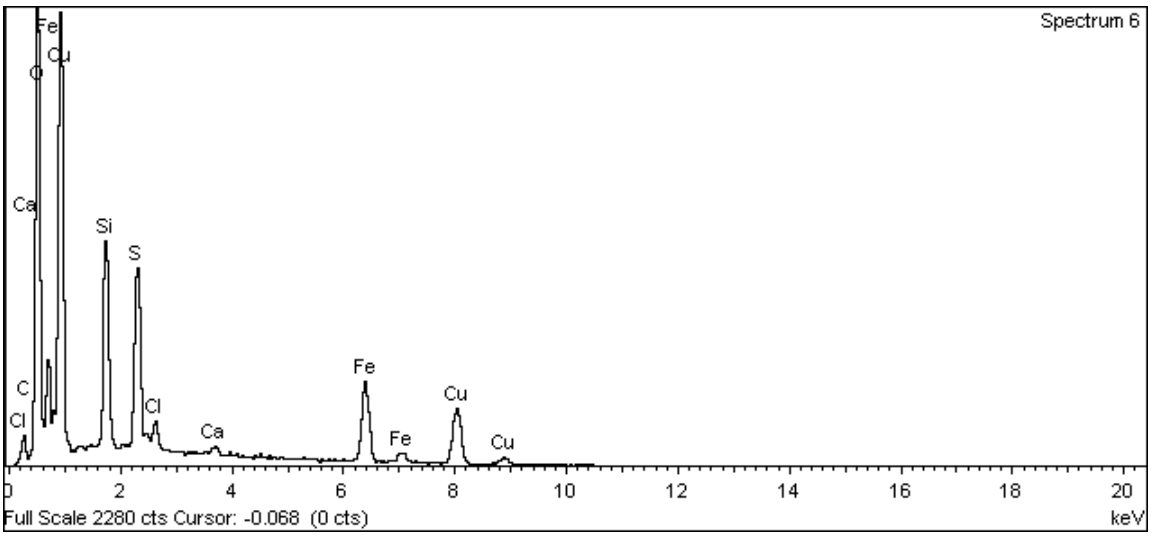

Figure A-31. Surface of copper weight loss specimen and EDX analysis at position of Spectrum 6

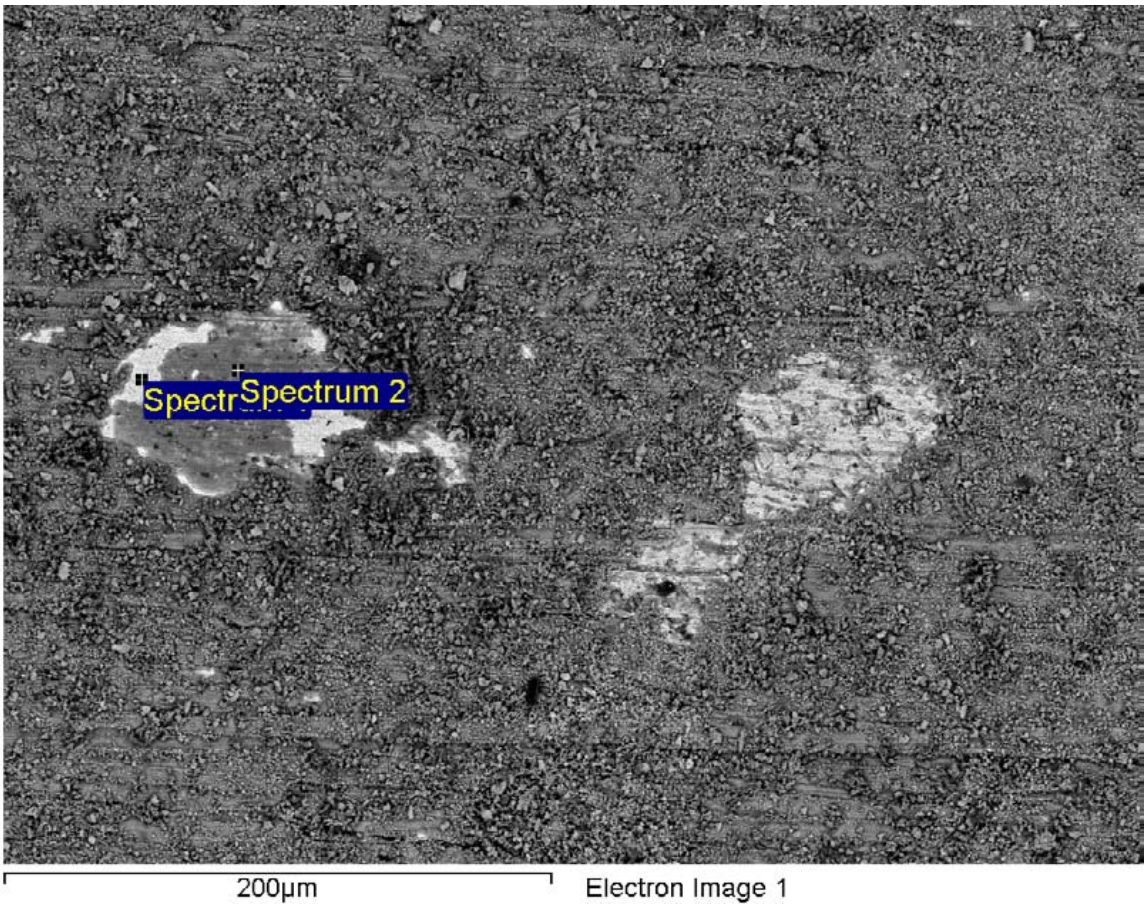

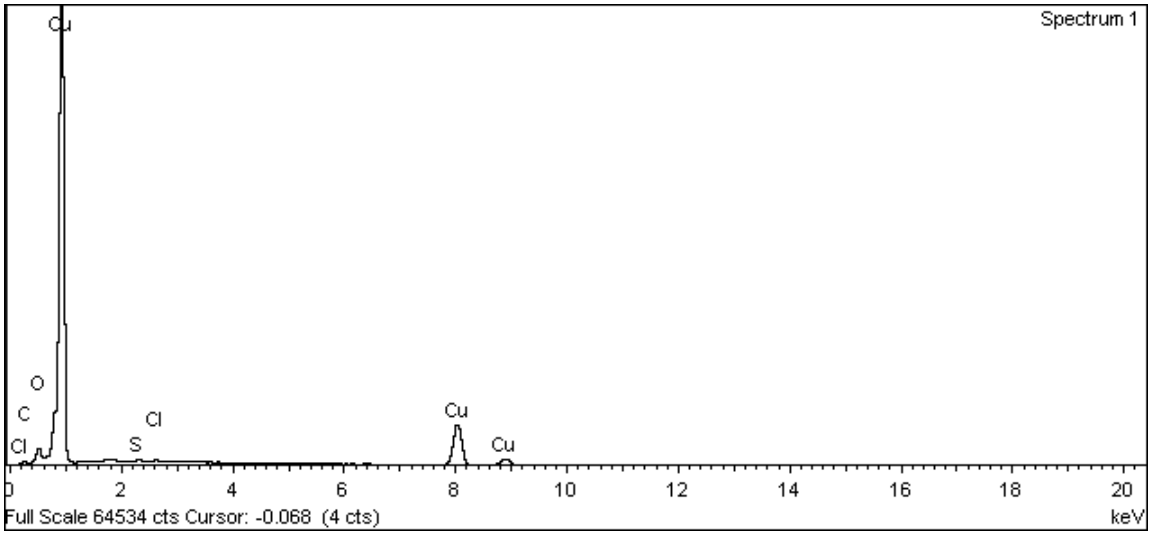

Figure A-32. Surface of copper weight loss specimen and EDX analysis at position of Spectrum 1

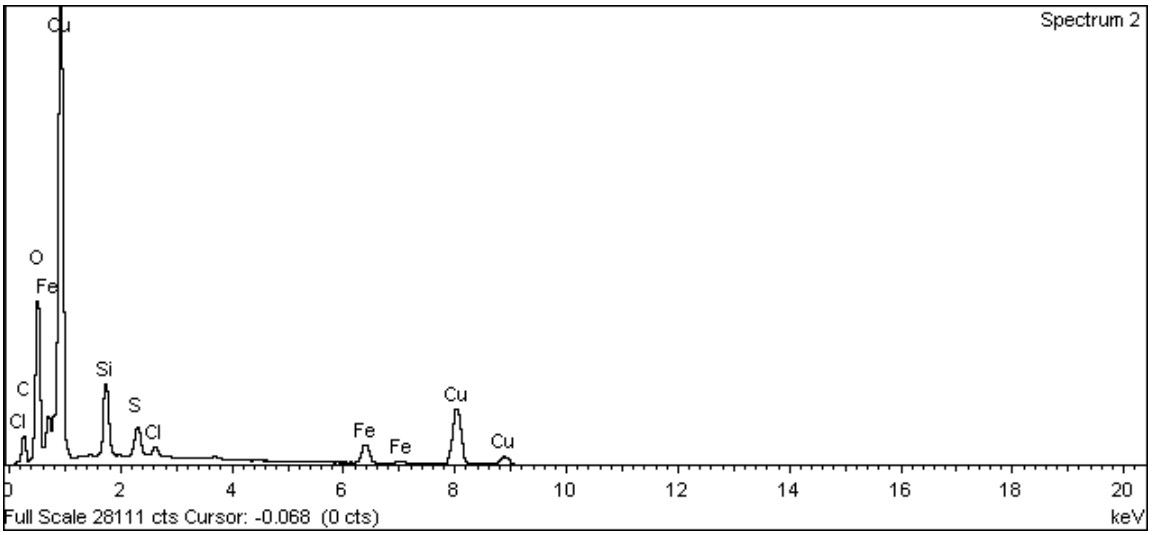

Figure A-33. Surface of copper weight loss specimen and EDX analysis at position of Spectrum 2

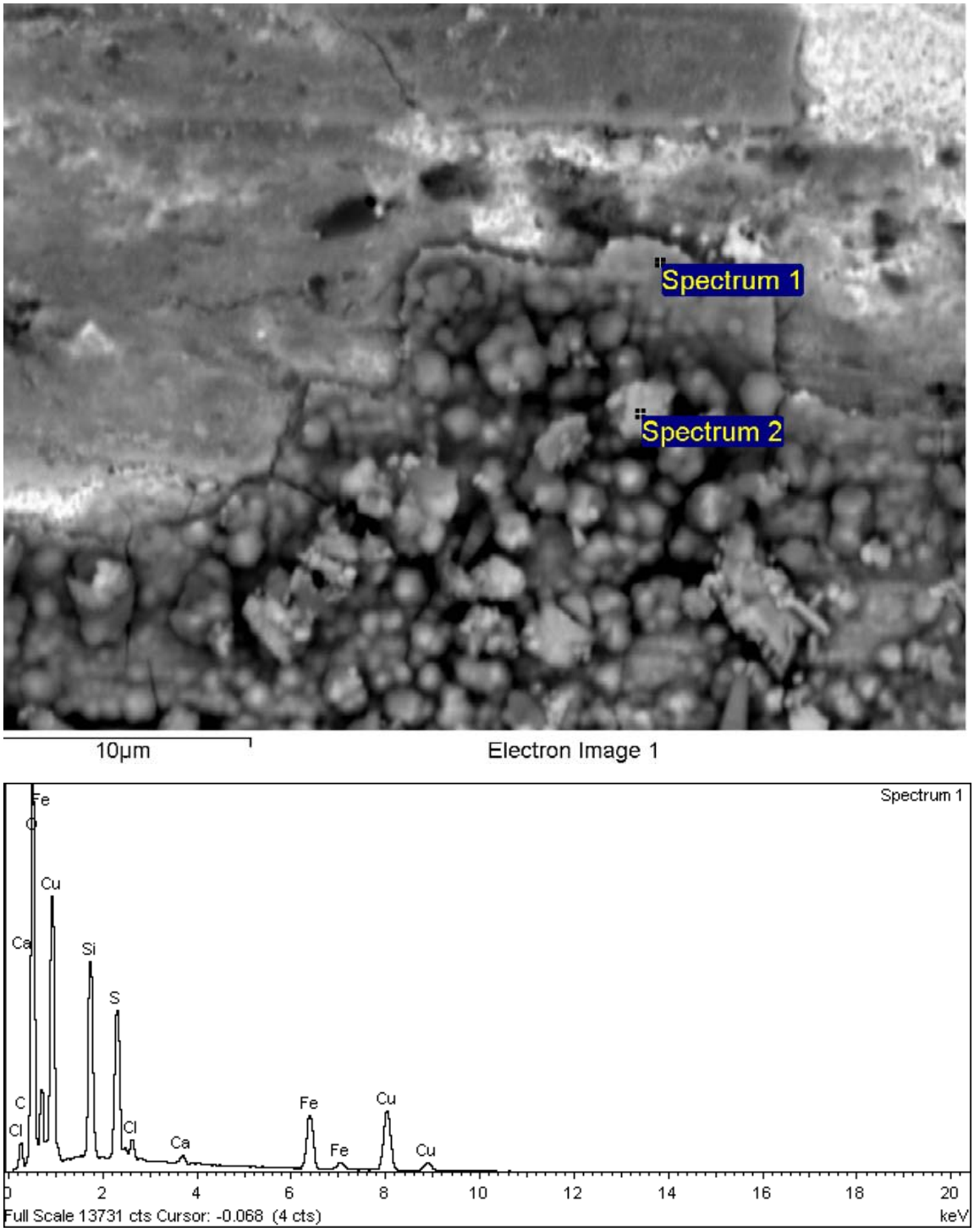

Figure A-34. Surface of copper weight loss specimen and EDX analysis at position of Spectrum 1

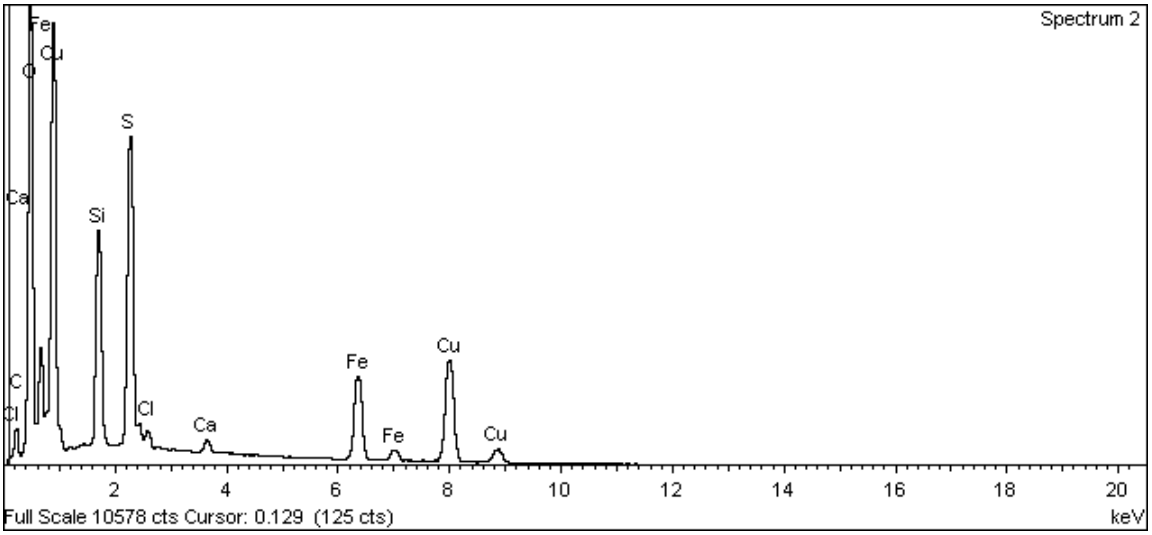

Figure A-35. Surface of copper weight loss specimen and EDX analysis at position of Spectrum 2

Iron electrode 1

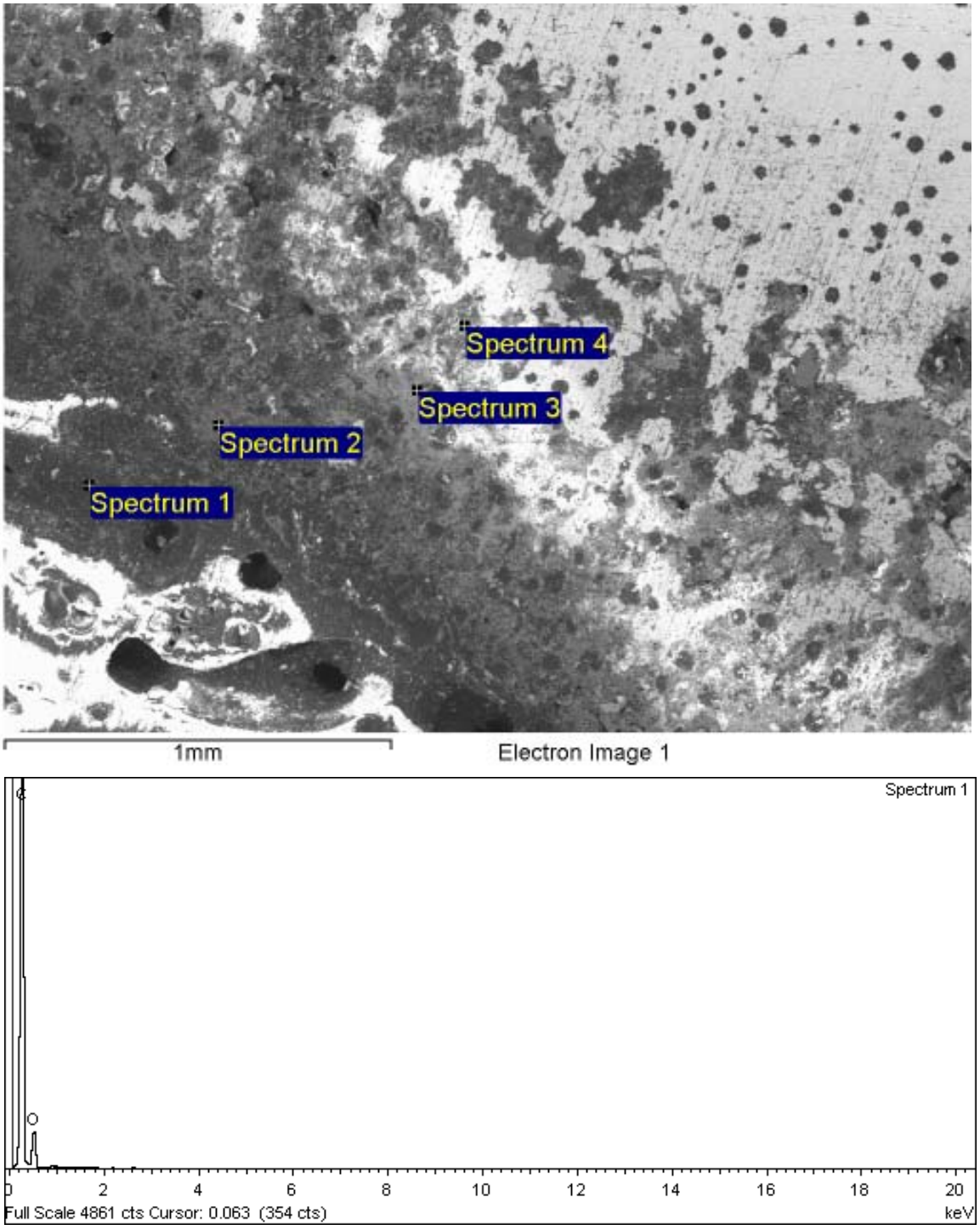

Figure A-36. Surface of iron electrode 1 and EDX analysis at position of Spectrum 1

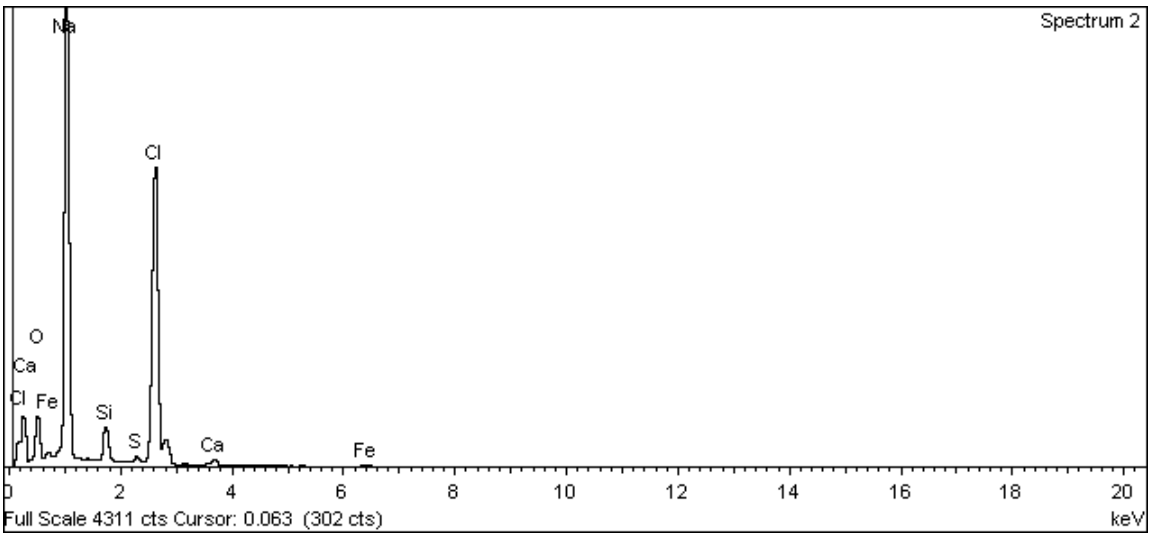

Figure A-37. Surface of iron electrode 1 and EDX analysis at position of Spectrum 2

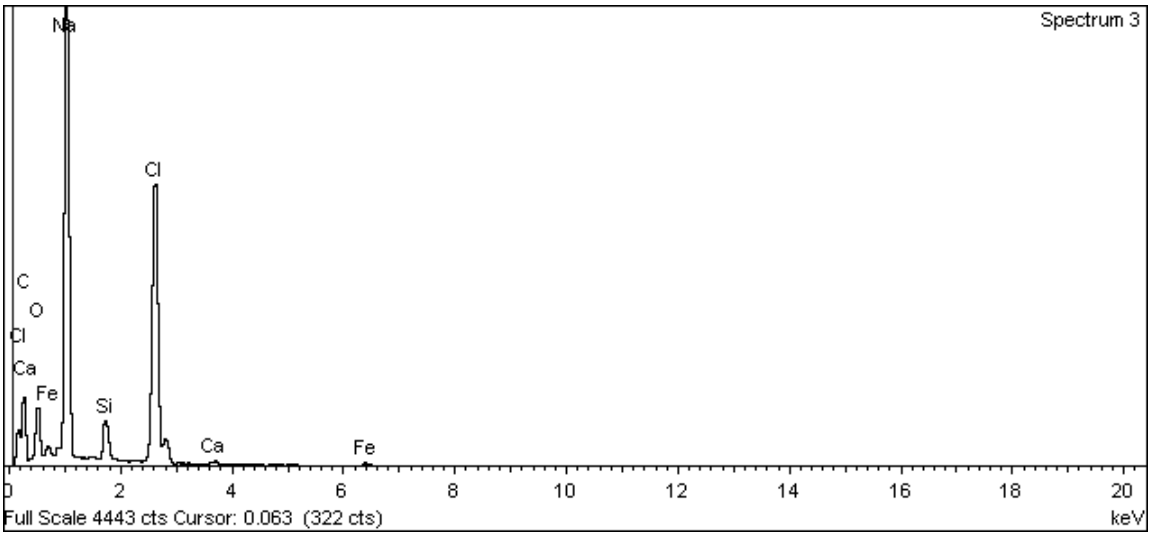

Figure A-38. Surface of iron electrode 1 and EDX analysis at position of Spectrum 3

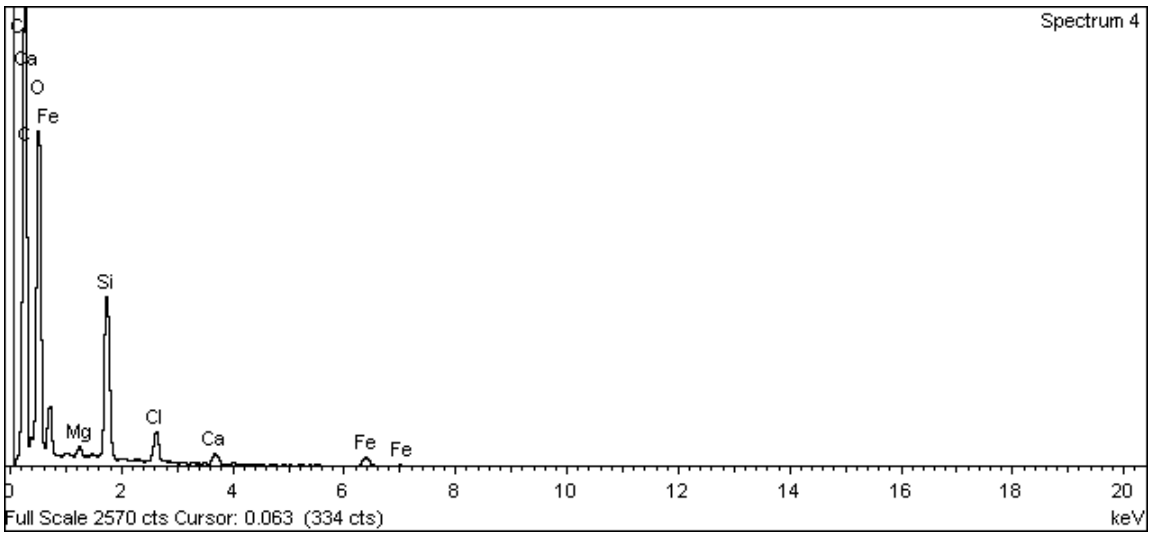

Figure A-39. Surface of iron electrode 1 and EDX analysis at position of Spectrum 4

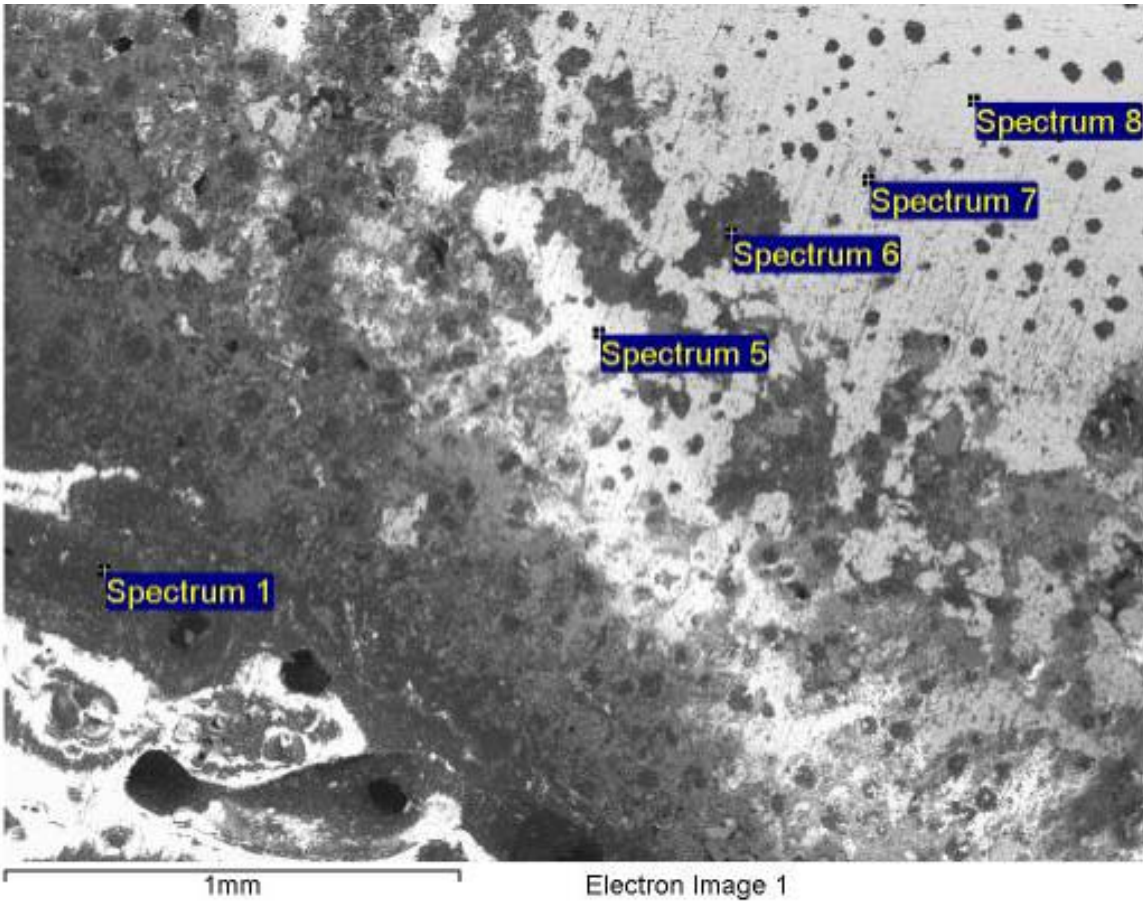

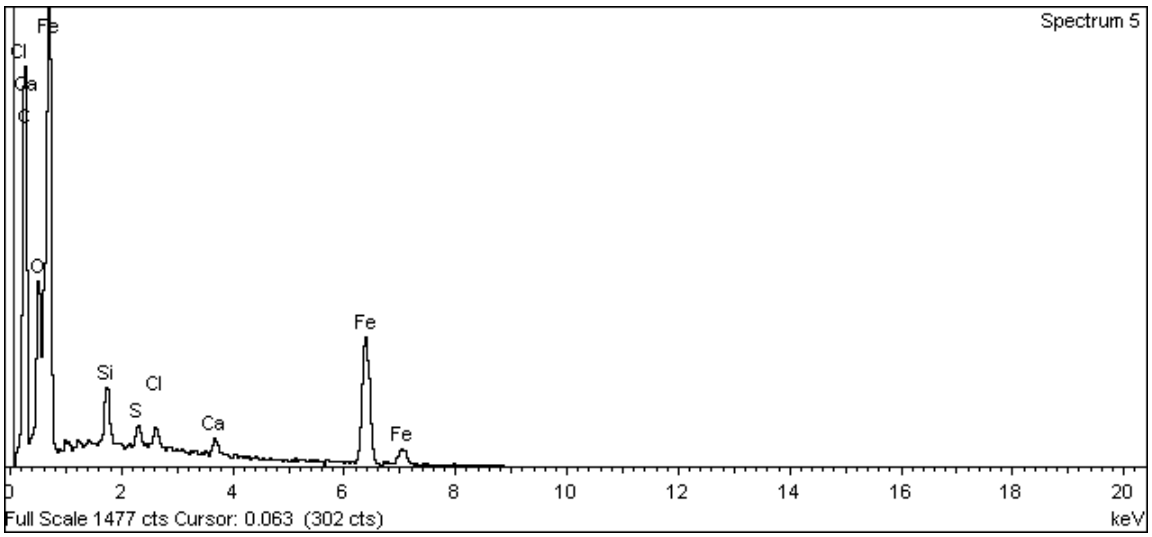

Figure A-40. Surface of iron electrode 1 and EDX analysis at position of Spectrum 5 (Spectrum 1 is shown in Figure A-36)

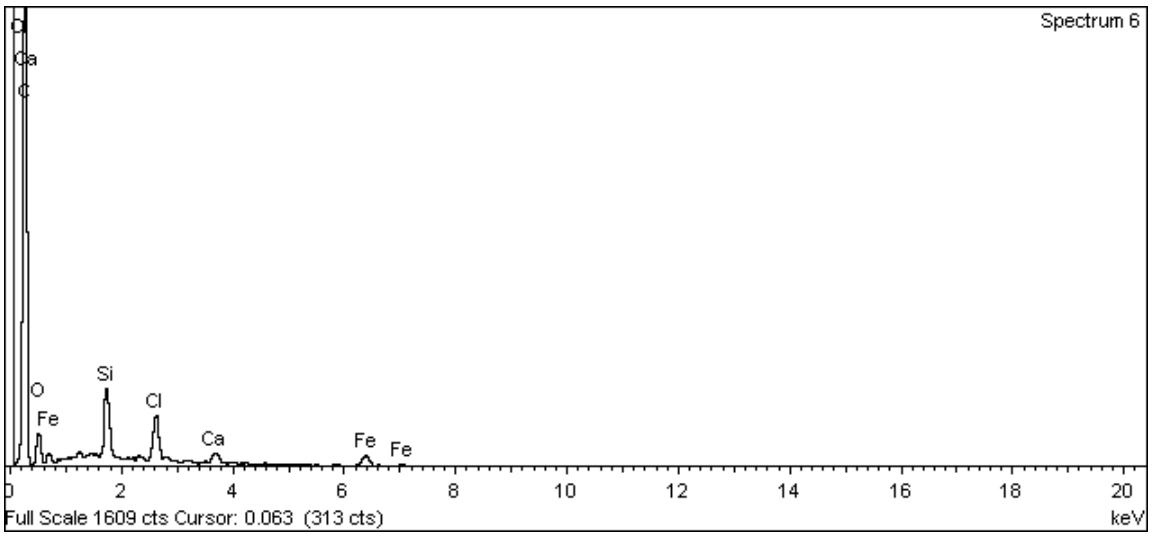

Figure A-41. Surface of iron electrode 1 and EDX analysis at position of Spectrum 6

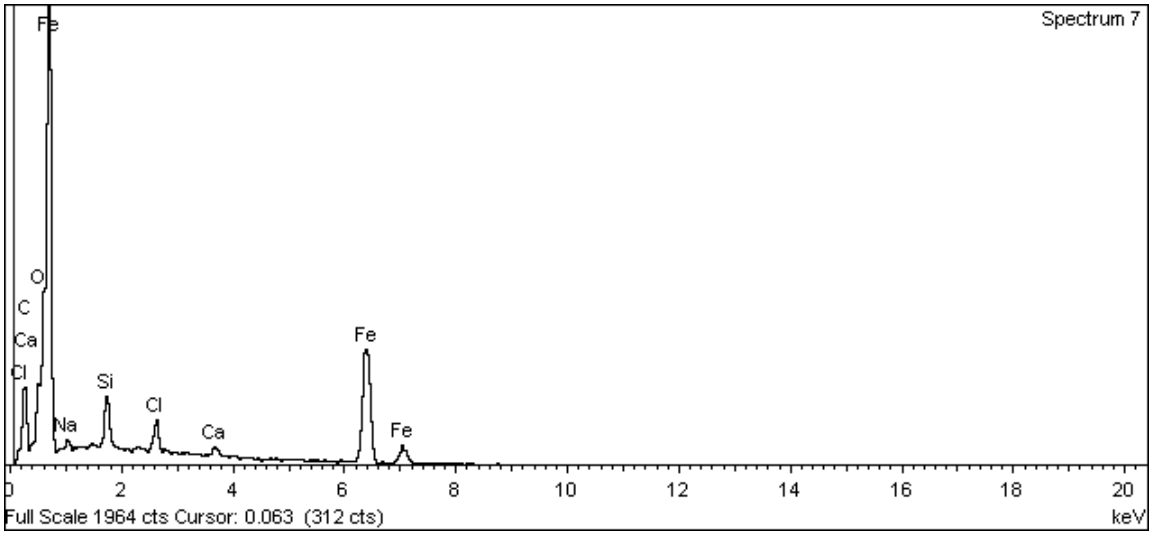

Figure A-42. Surface of iron electrode 1 and EDX analysis at position of Spectrum 7

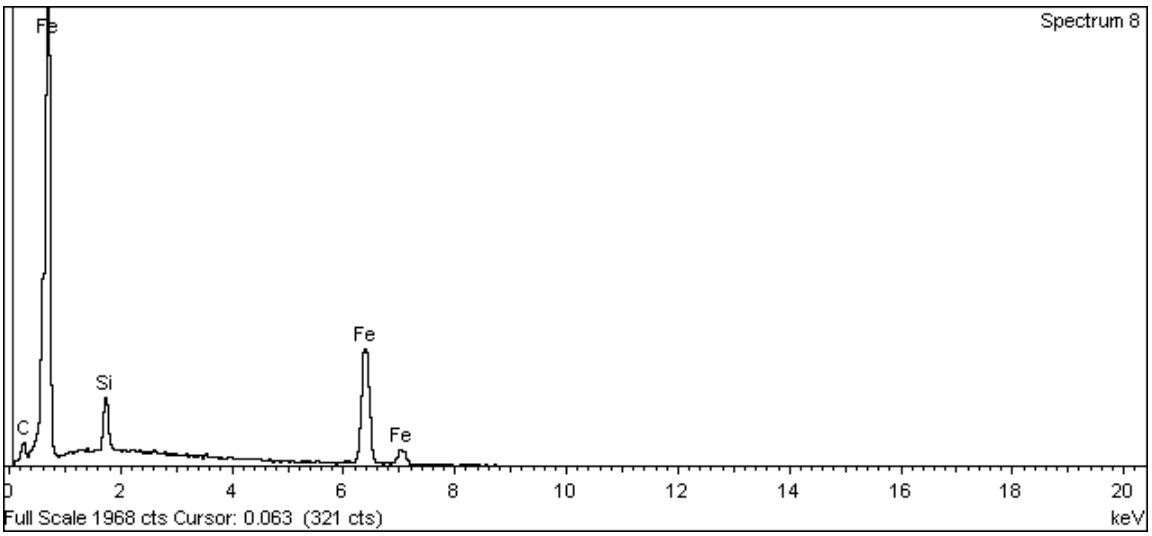

Figure A-43. Surface of iron electrode 1 and EDX analysis at position of Spectrum 8

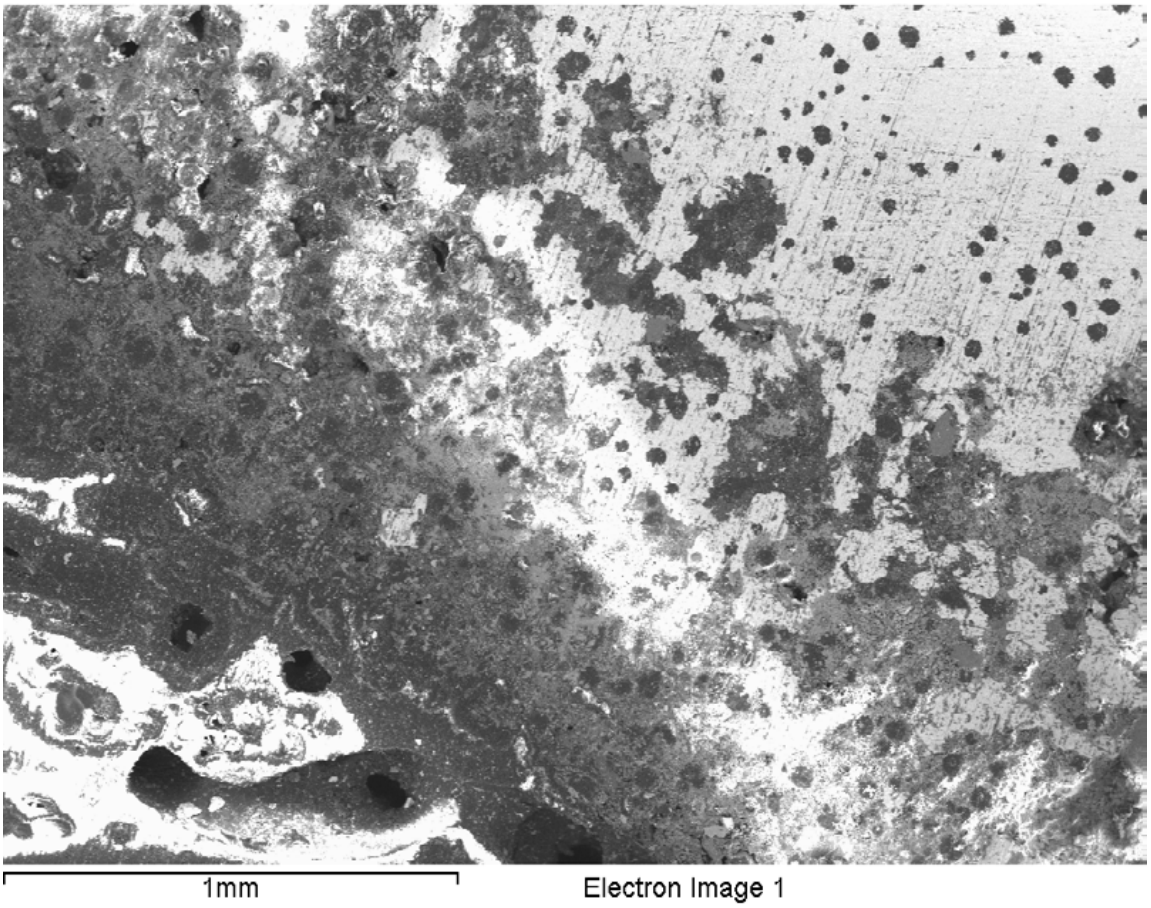

Figure A-44. Surface of iron electrode 1 and EDX analysis – Sum Spectrum

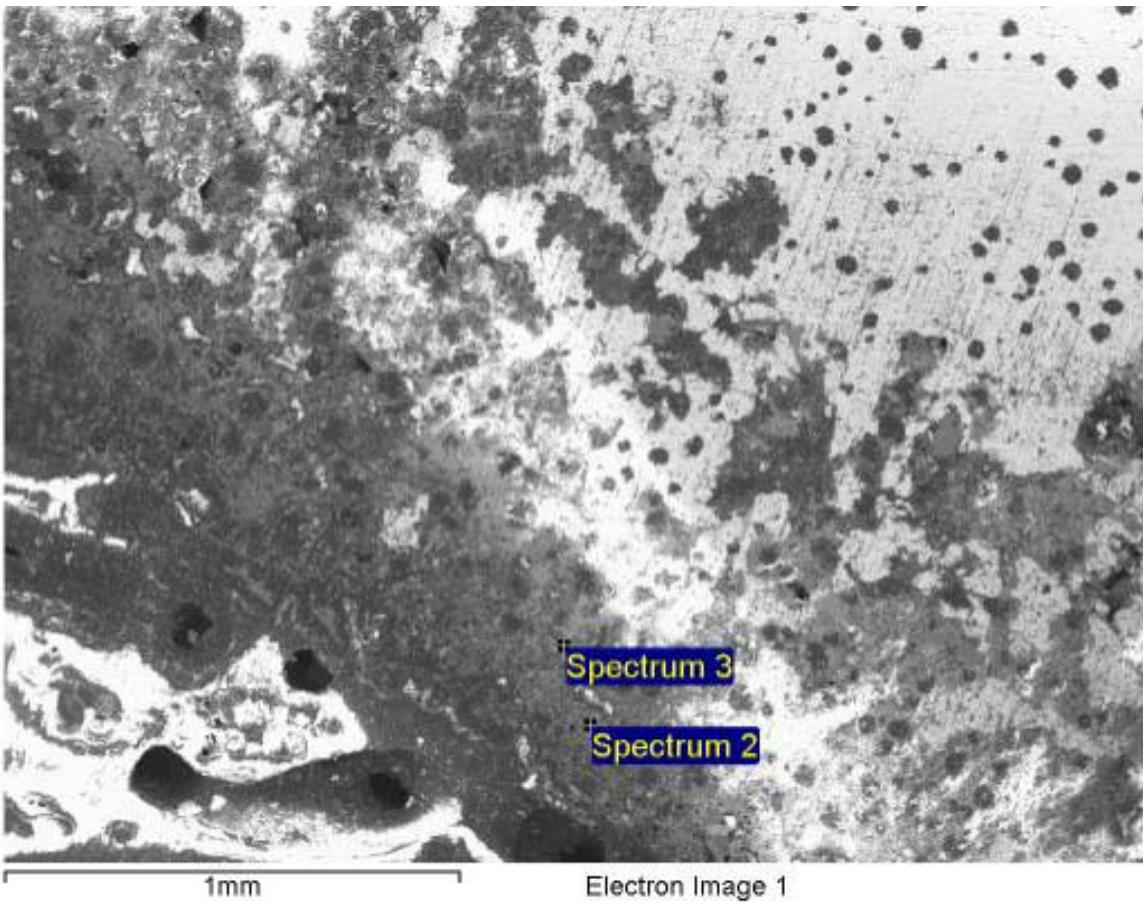

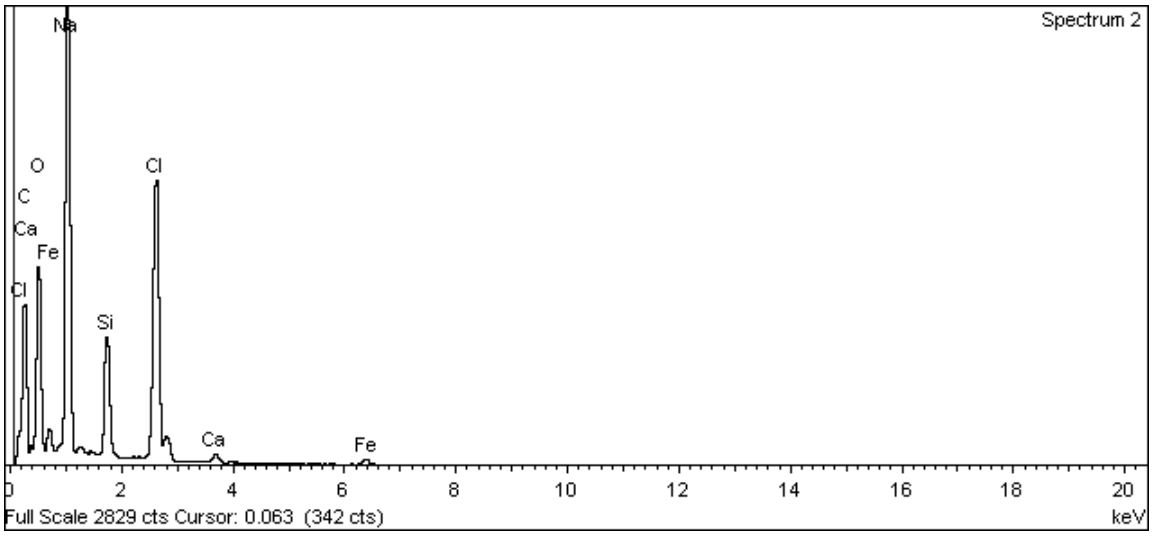

Figure A-45. Surface of iron electrode 1 and EDX analysis at position of Spectrum 2

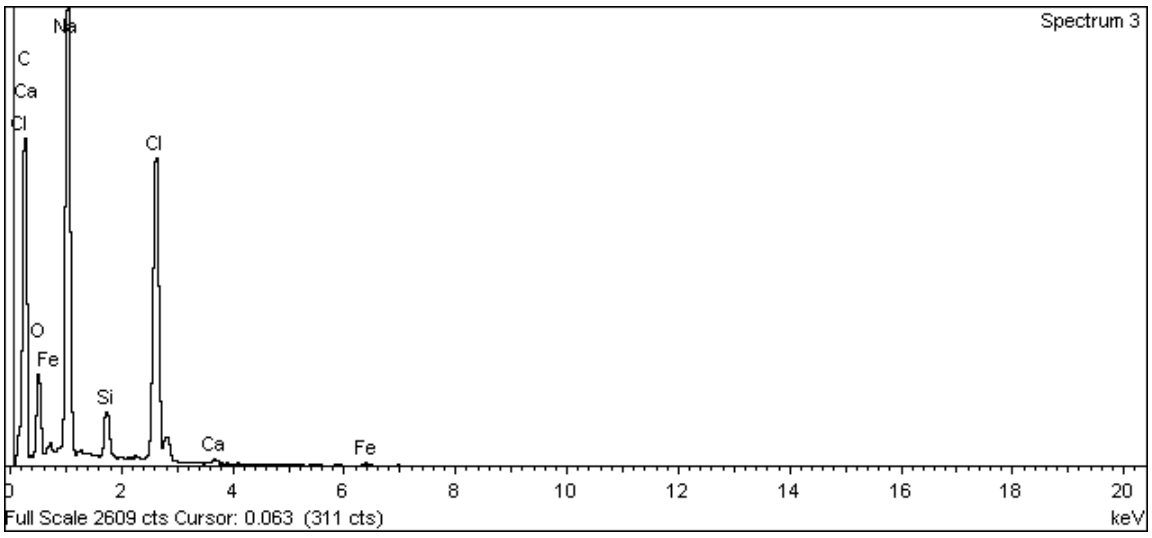

Figure A-46 Surface of iron electrode 1 and EDX analysis at position of Spectrum 3

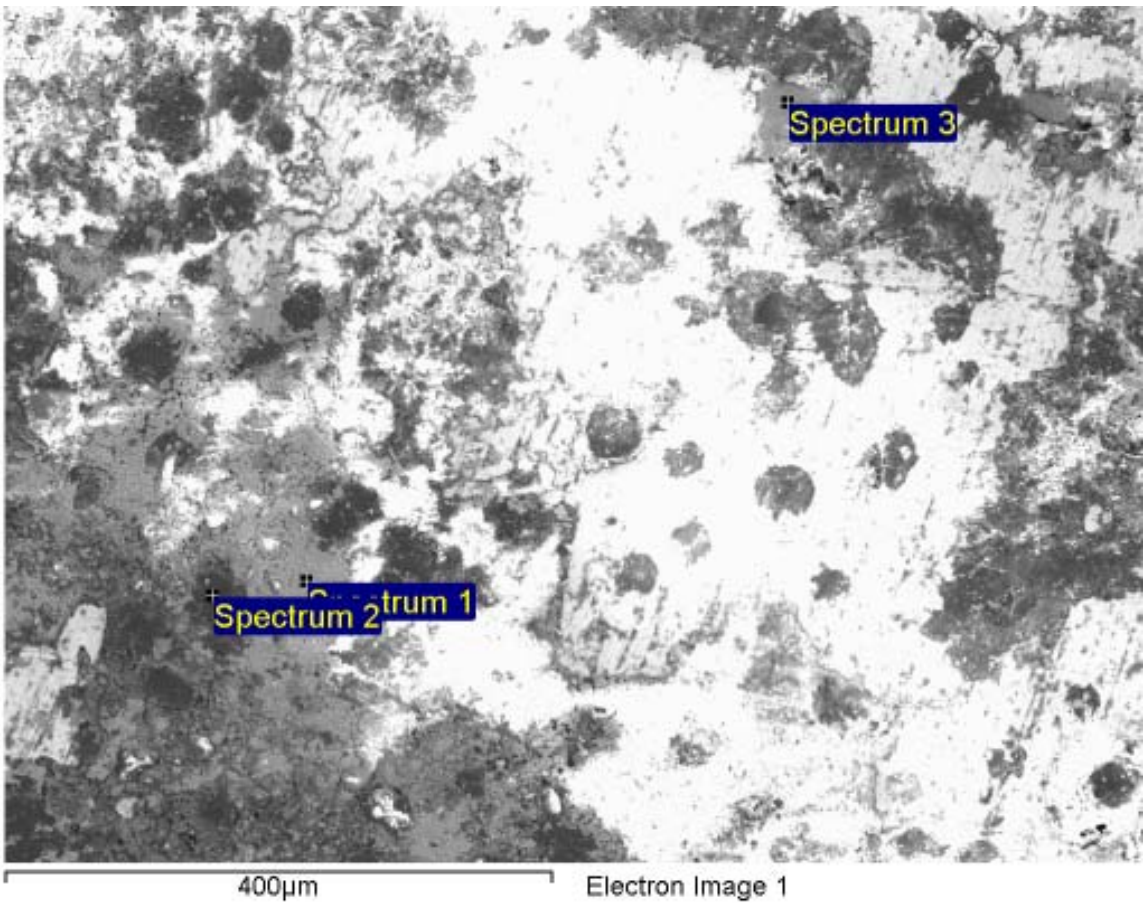

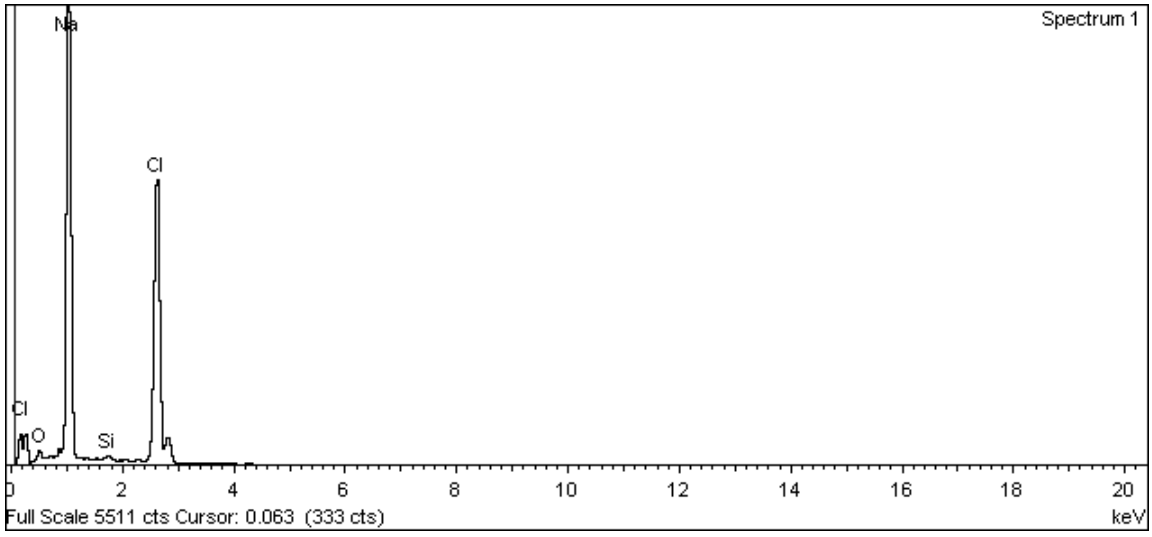

Figure A-47. Surface of iron electrode 1 and EDX analysis at position of Spectrum 1

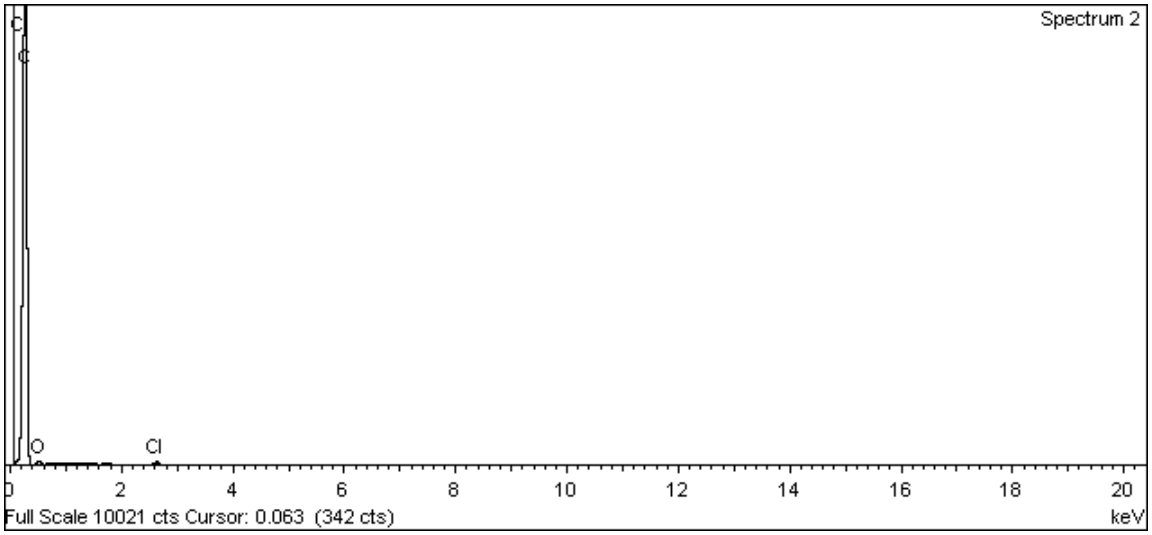

Figure A-48. Surface of iron electrode 1 and EDX analysis at position of Spectrum 2

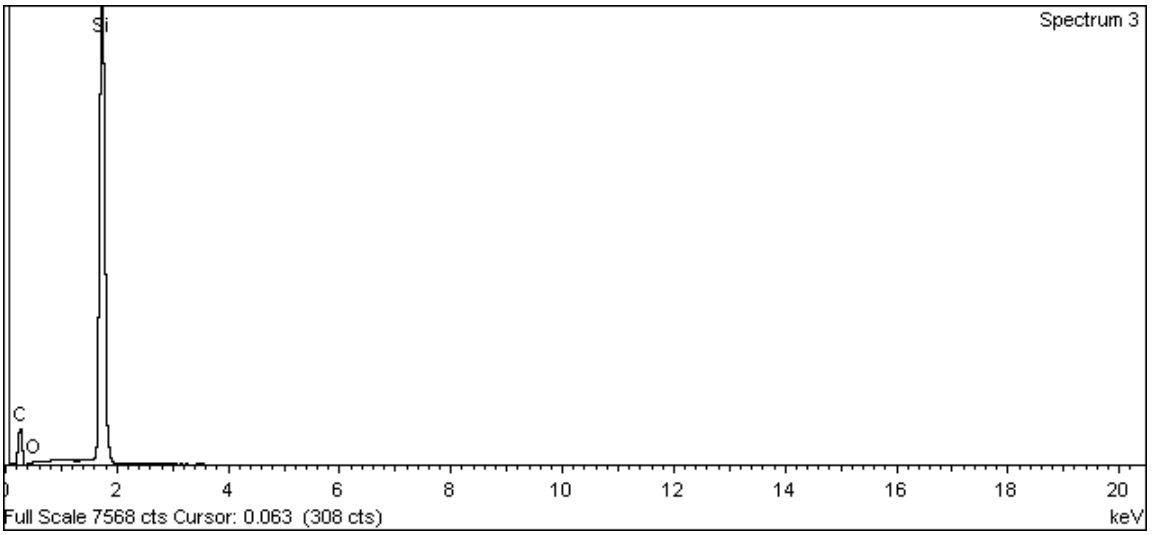

Figure A-49. Surface of iron electrode 1 and EDX analysis at position of Spectrum 3

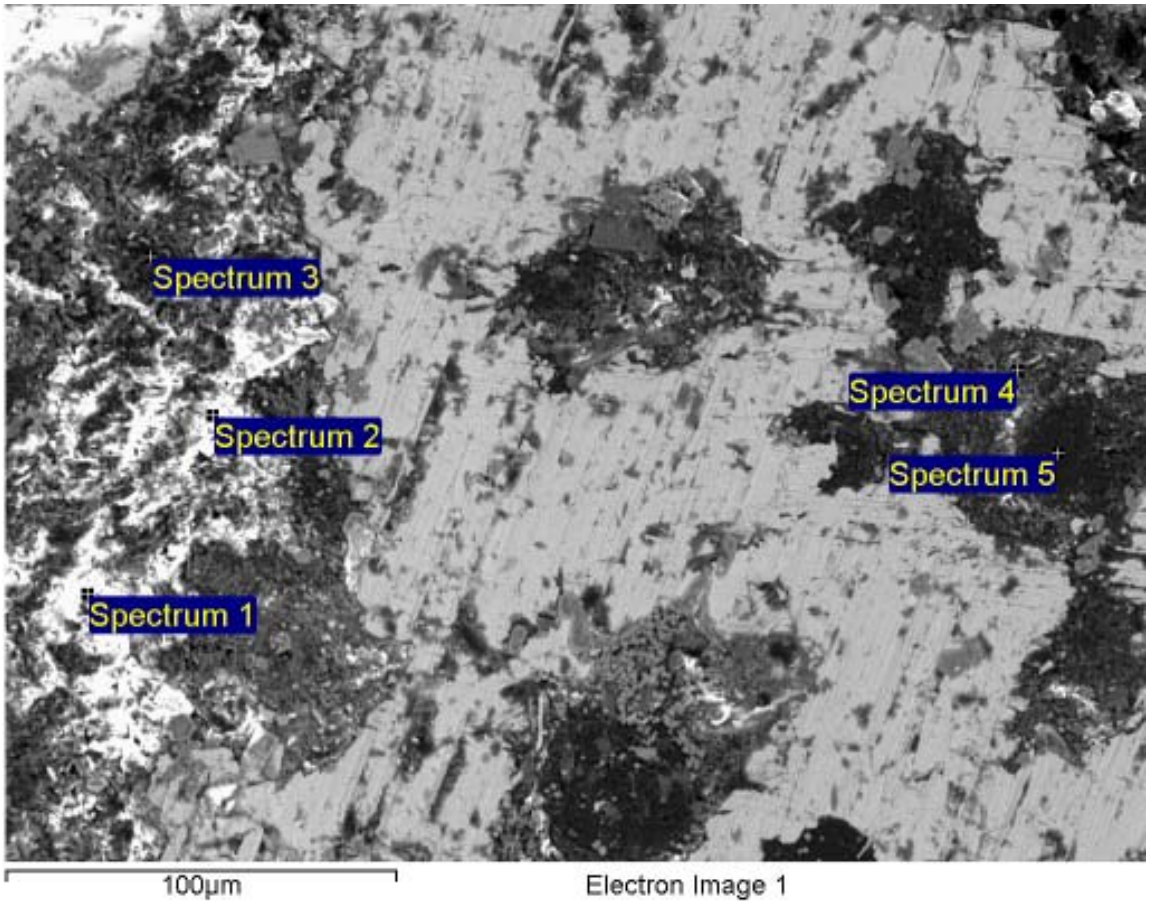

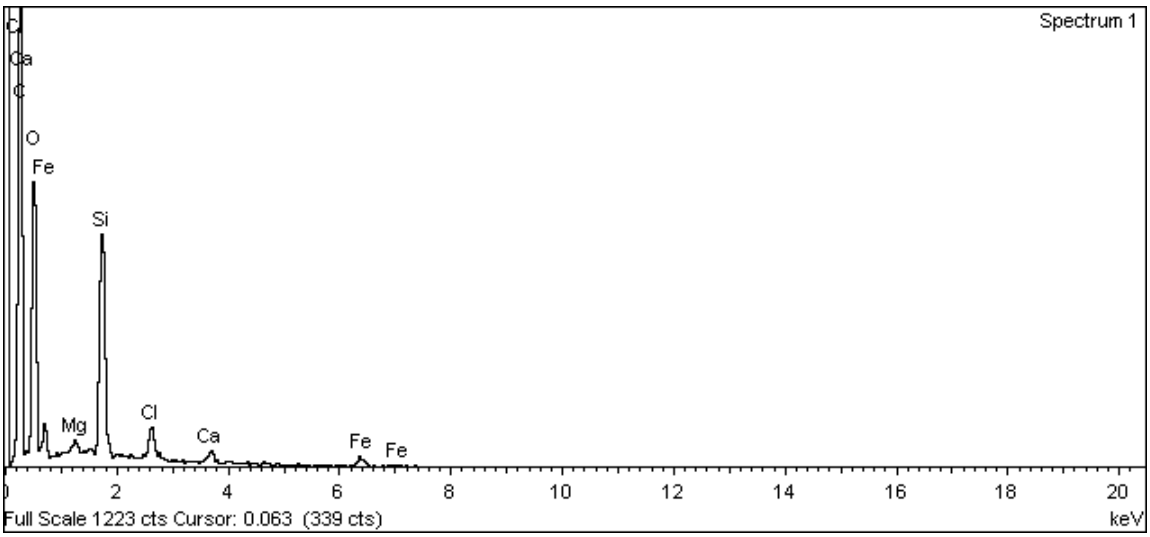

Figure A-50. Surface of iron electrode 1 and EDX analysis at position of Spectrum 1

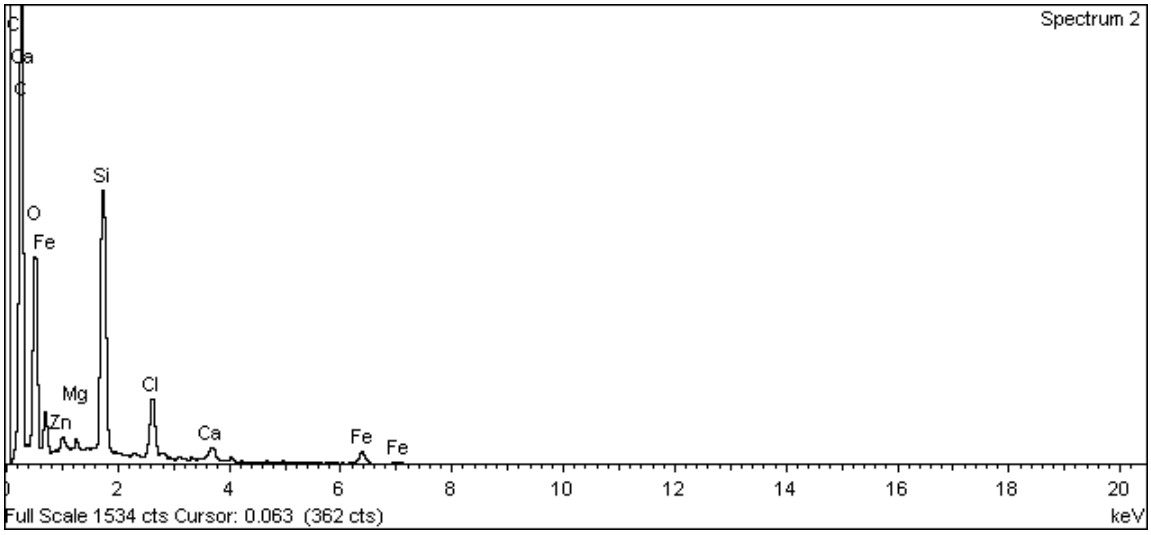

Figure A-51. Surface of iron electrode 1 and EDX analysis at position of Spectrum 2

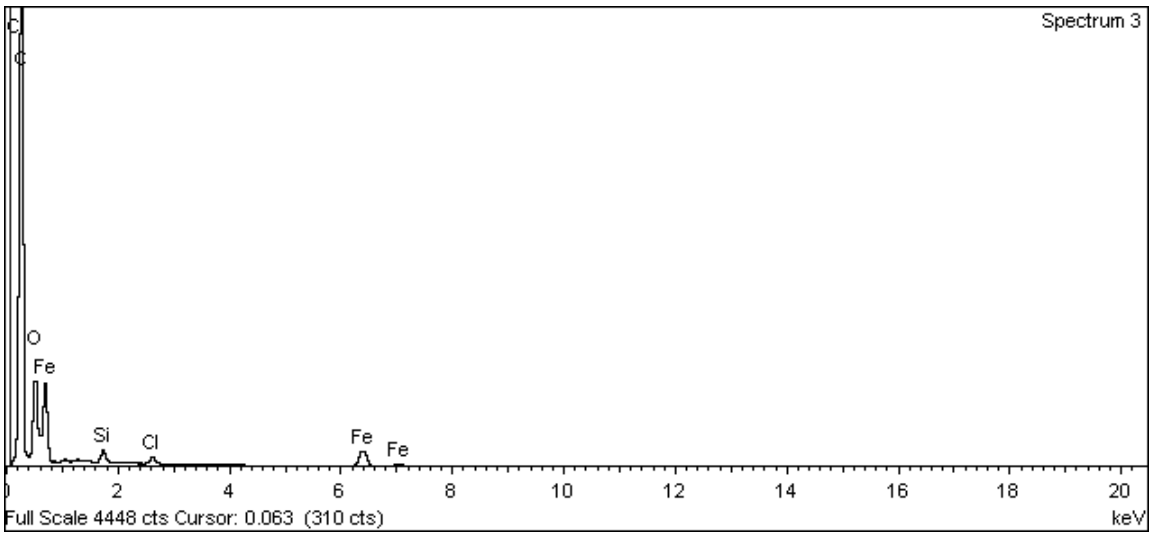

Figure A-52. Surface of iron electrode 1 and EDX analysis at position of Spectrum 3

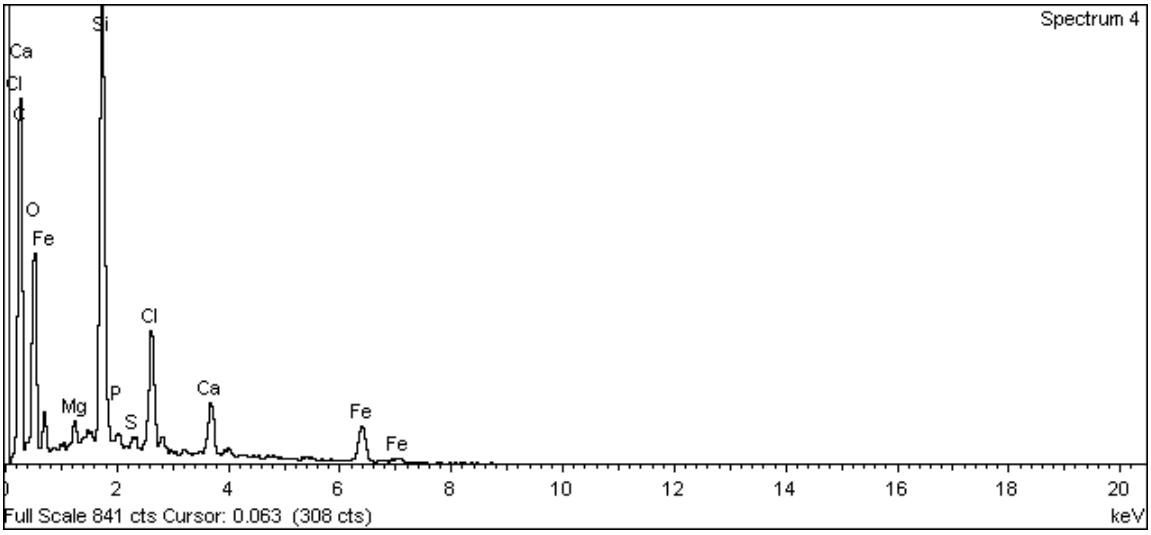

Figure A-53. Surface of iron electrode 1 and EDX analysis at position of Spectrum 4

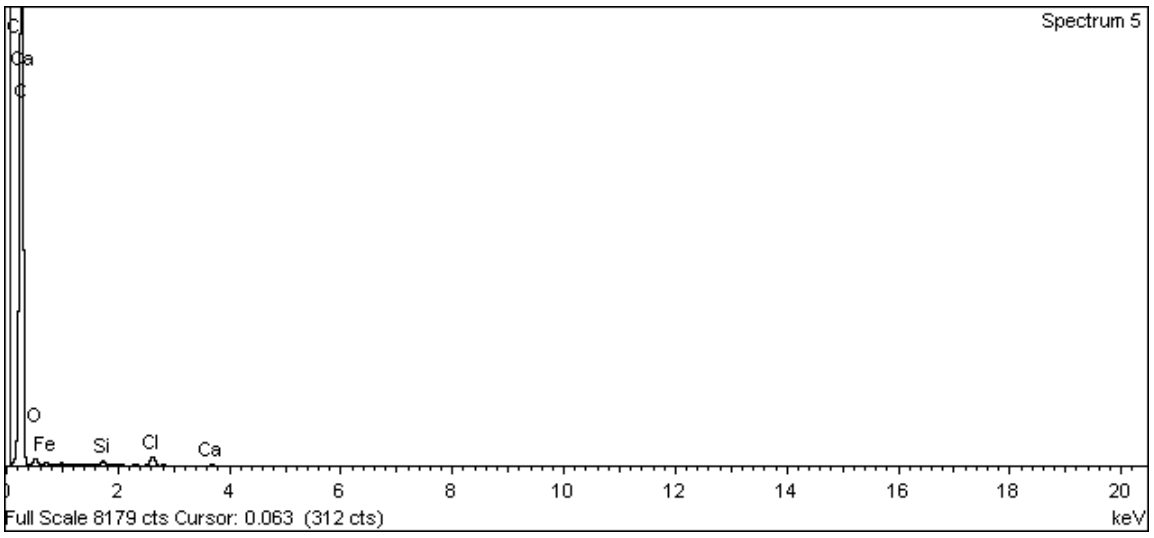

Figure A-54. Surface of iron electrode 1 and EDX analysis at position of Spectrum 5

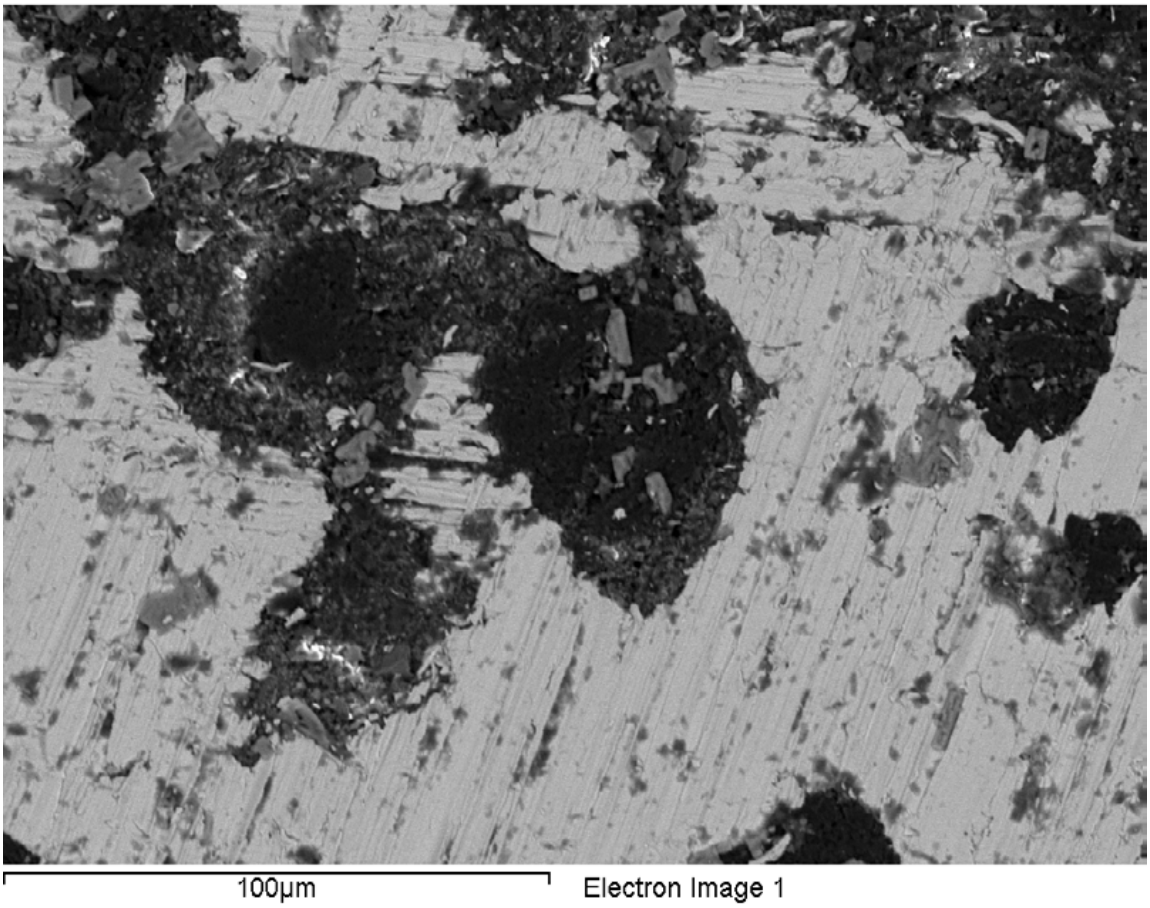

Figure A-55. Surface of iron electrode 1 and EDX analysis – Sum Spectrum

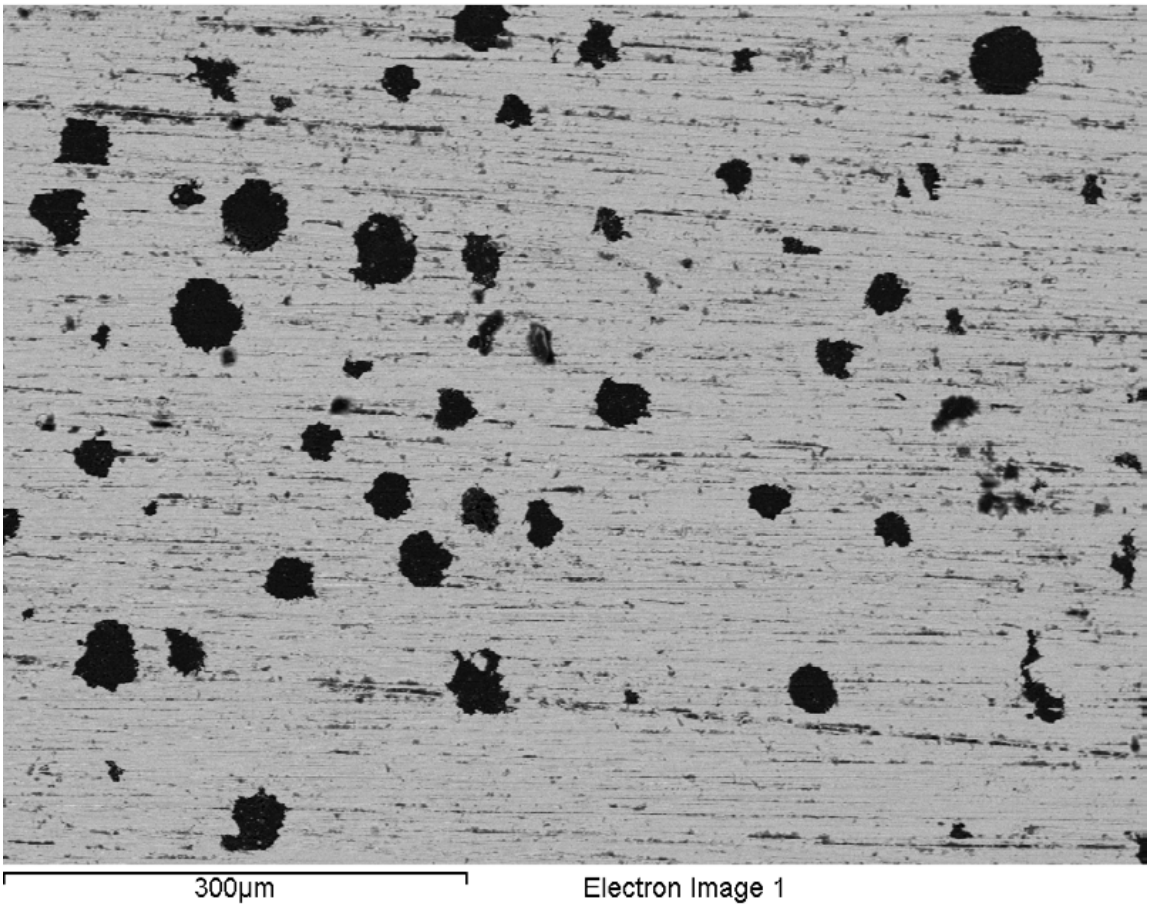

Figure A-56. Surface of iron electrode 1 and EDX analysis – Sum Spectrum

Iron Electrode 2

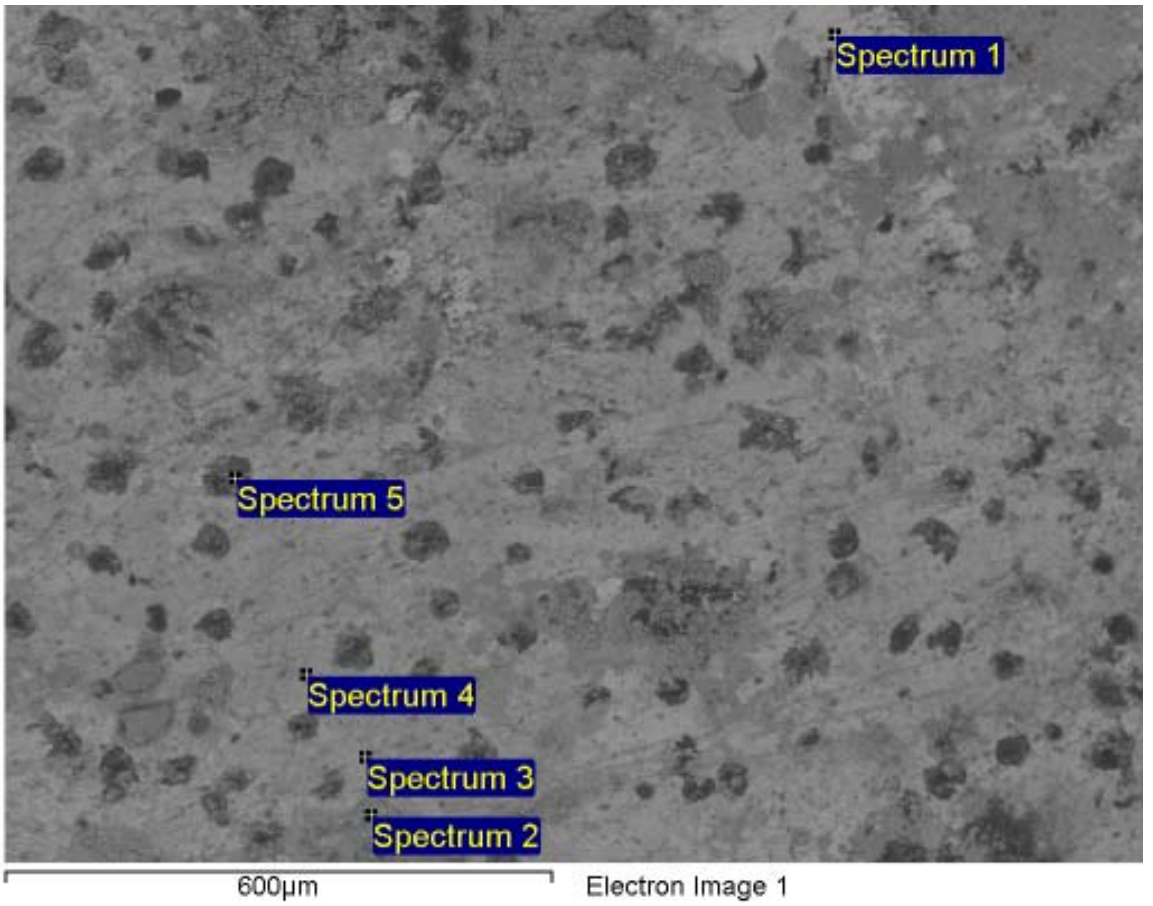

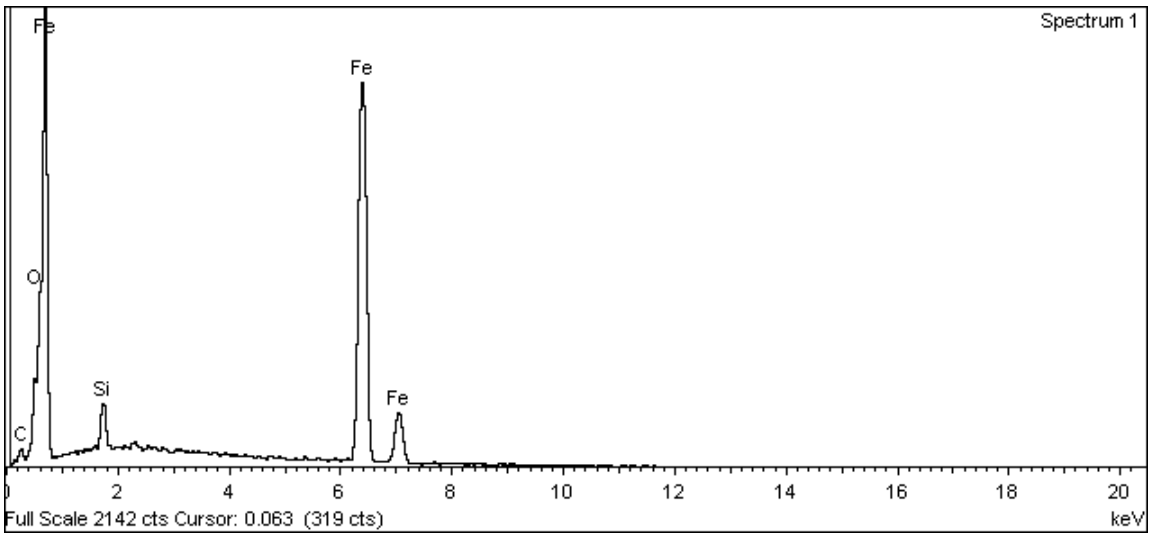

Figure A-57. Surface of iron electrode 2 and EDX analysis at position of Spectrum 1

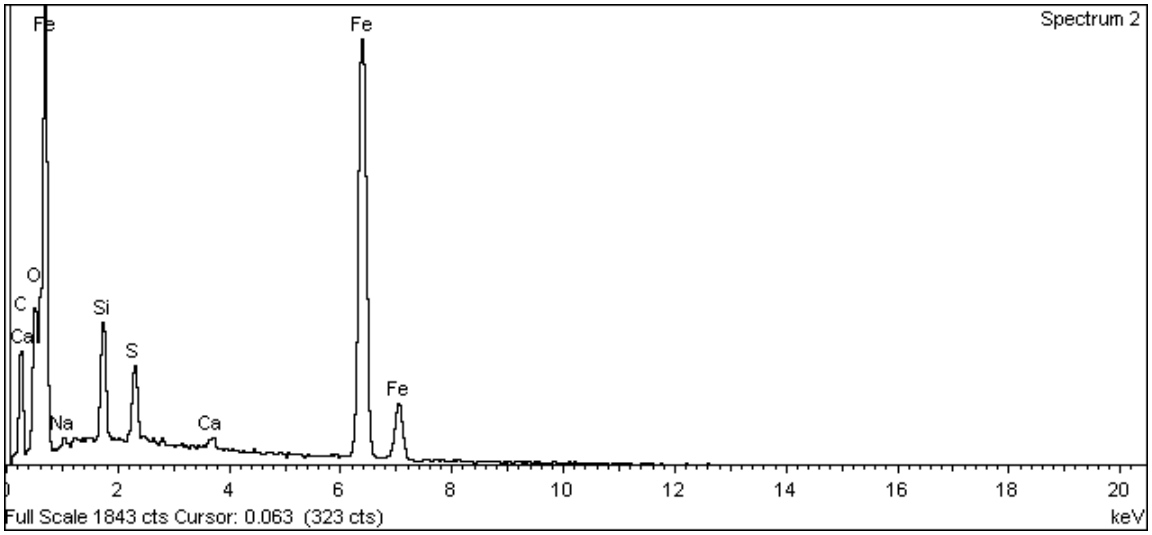

Figure A-58. Surface of iron electrode 2 and EDX analysis at position of Spectrum 2

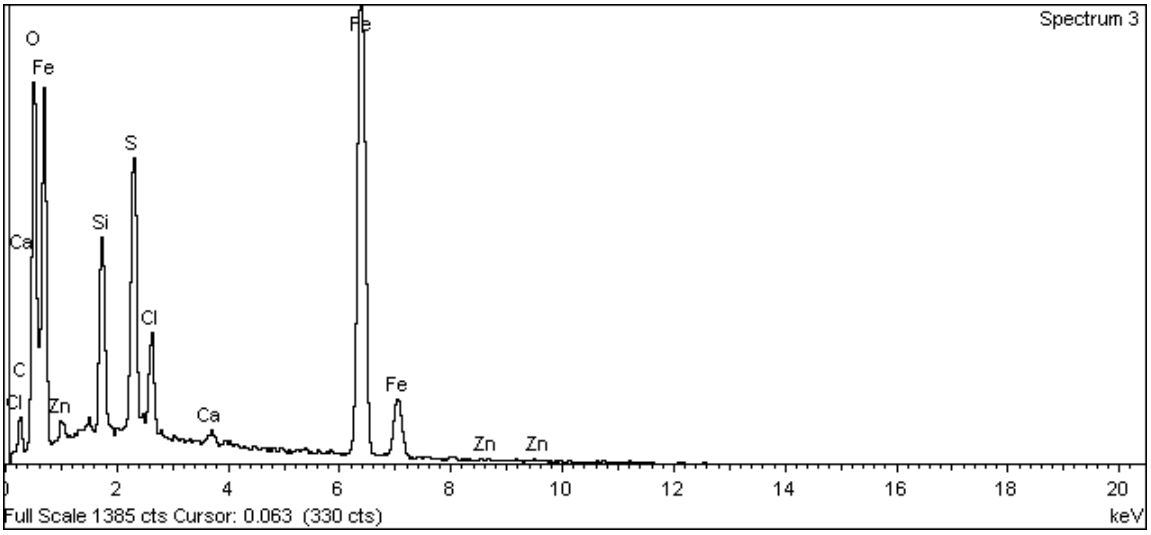

Figure A-59. Surface of iron electrode 2 and EDX analysis at position of Spectrum 3

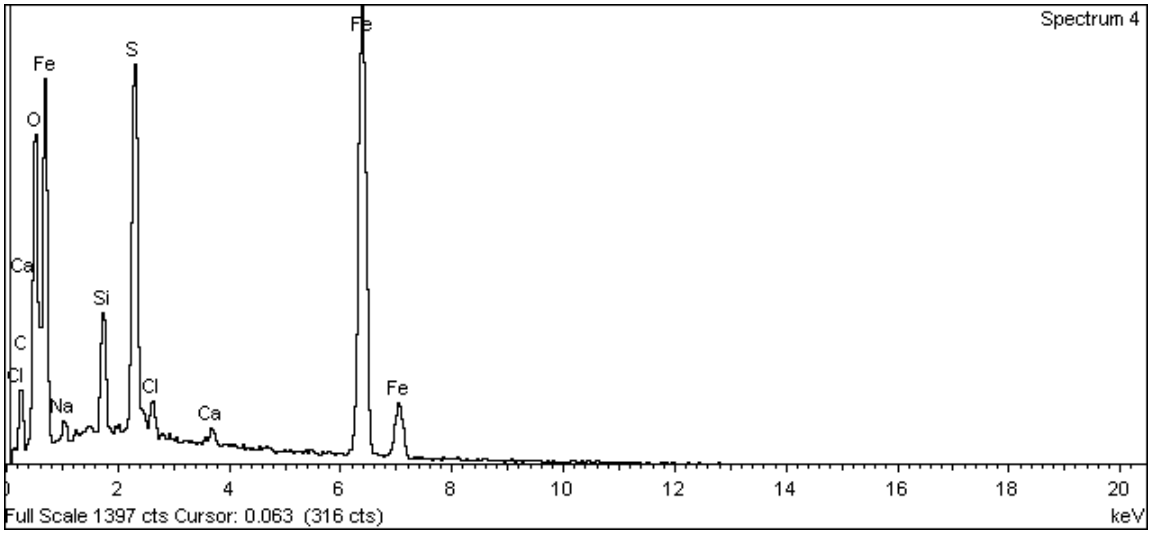

Figure A-60. Surface of iron electrode 2 and EDX analysis at position of Spectrum 4

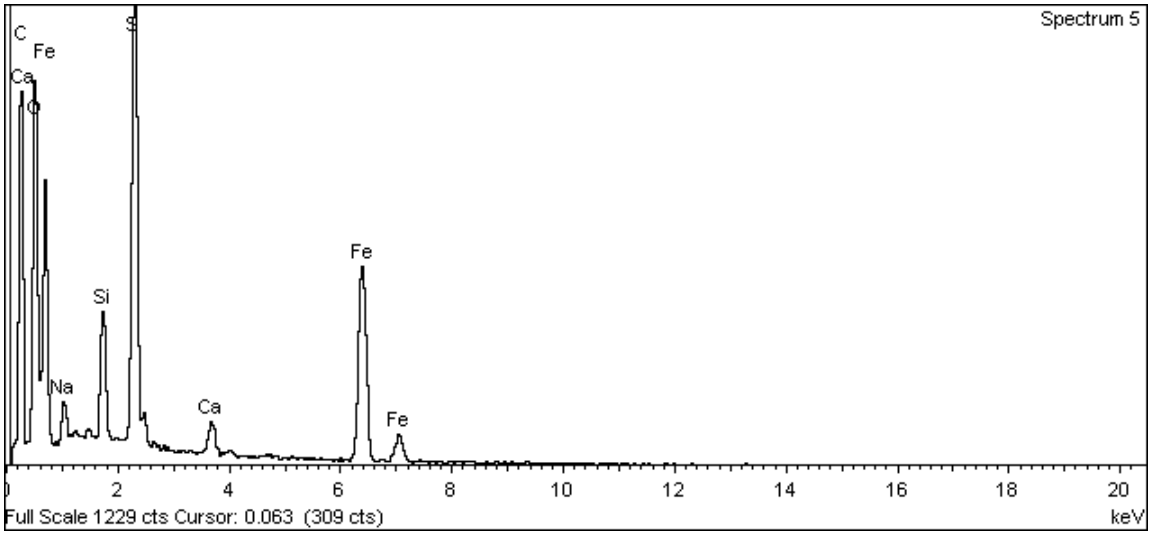

Figure A-61. Surface of iron electrode 2 and EDX analysis at position of Spectrum 5

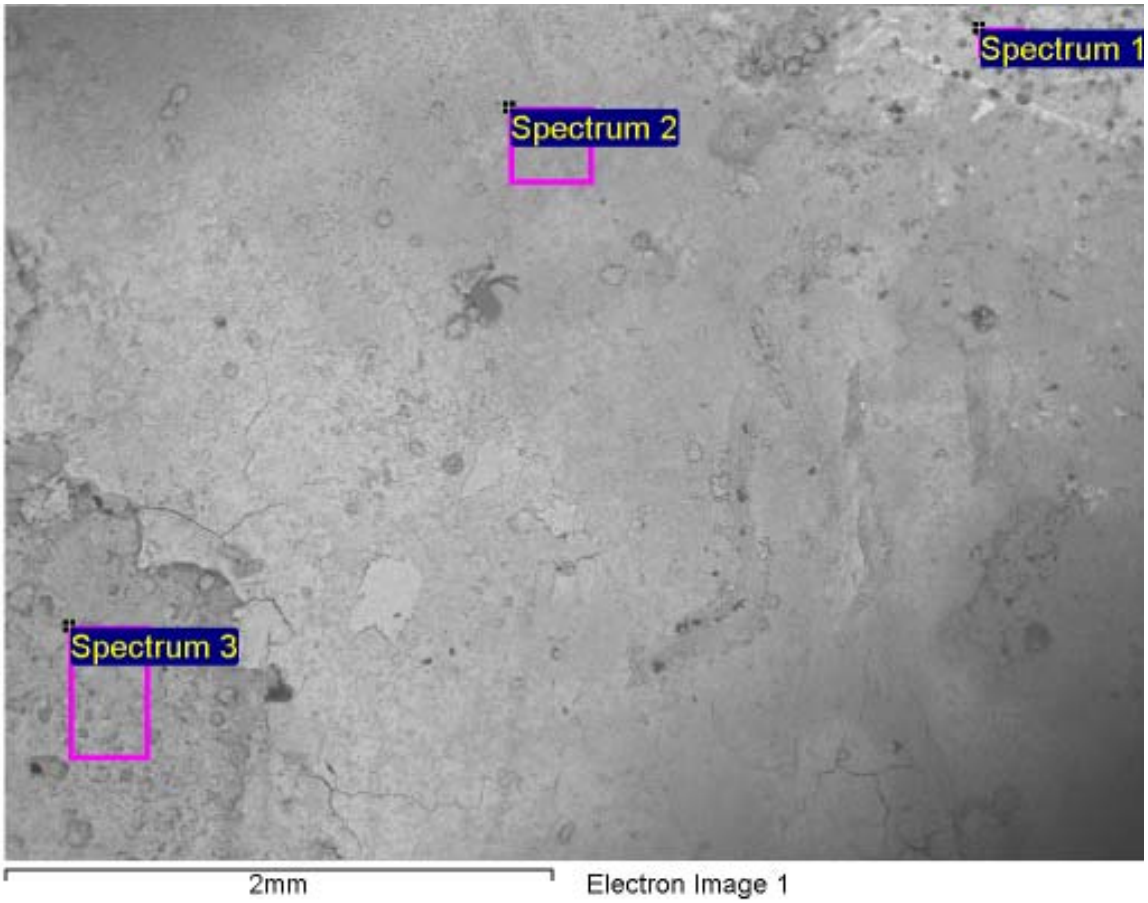

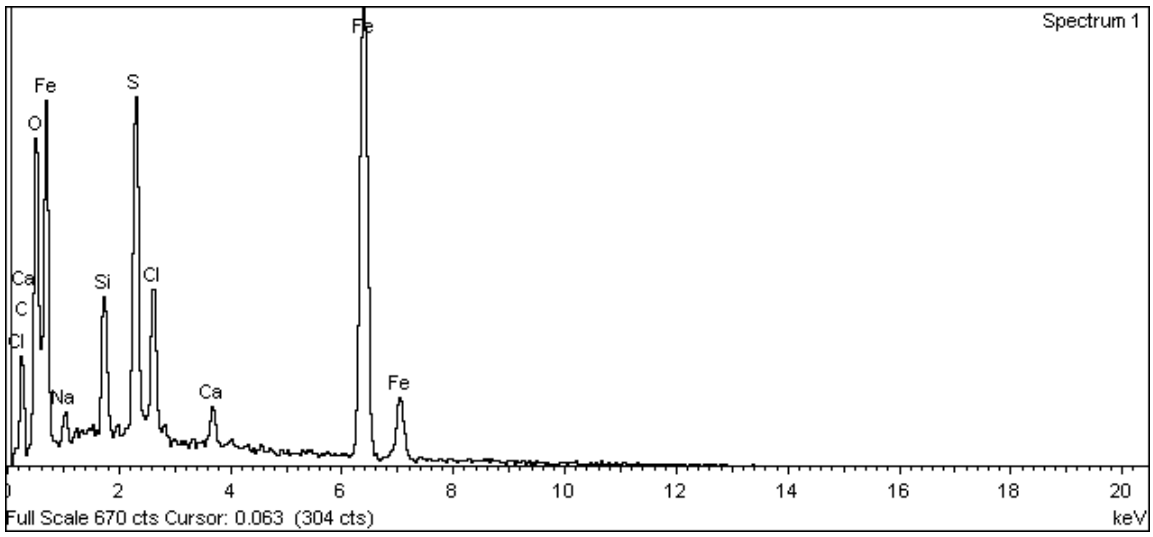

Figure A-62. Surface of iron electrode 2 and EDX analysis at position of Spectrum 1

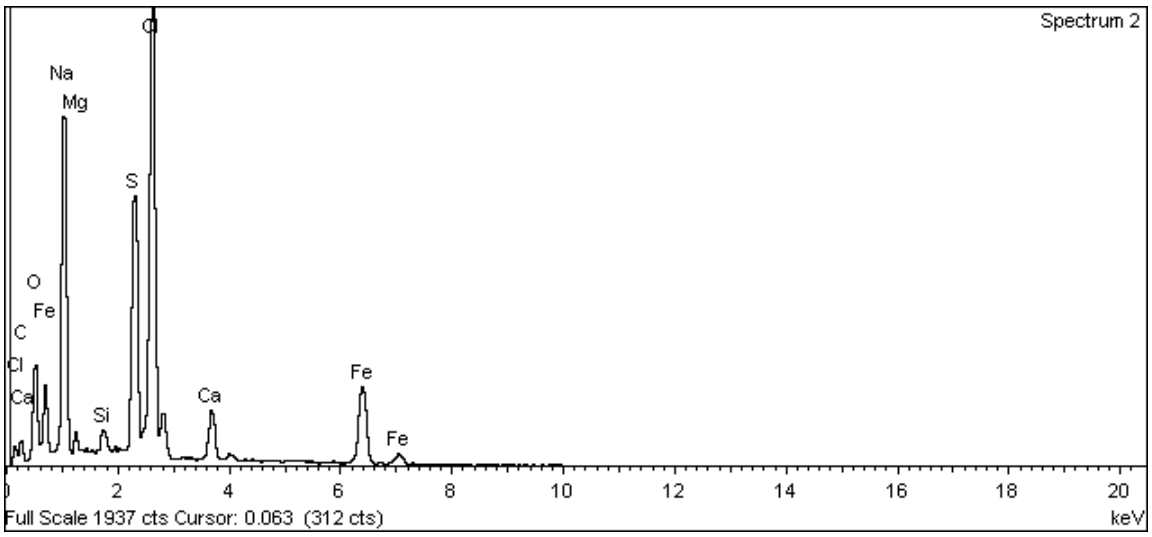

Figure A-63. Surface of iron electrode 2 and EDX analysis at position of Spectrum 2

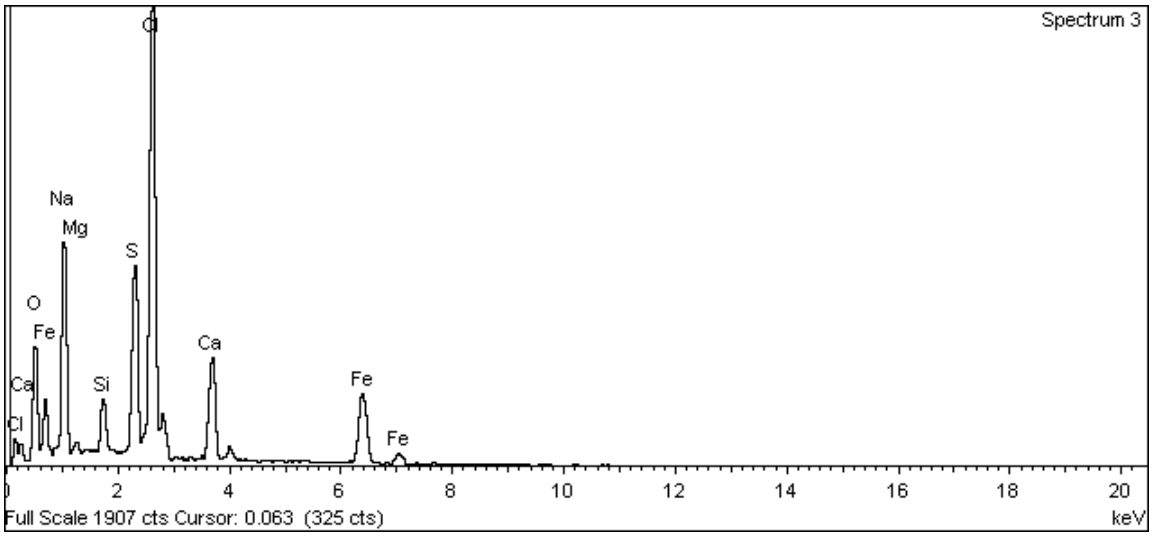

Figure A-64. Surface of iron electrode 2 and EDX analysis at position of Spectrum 3

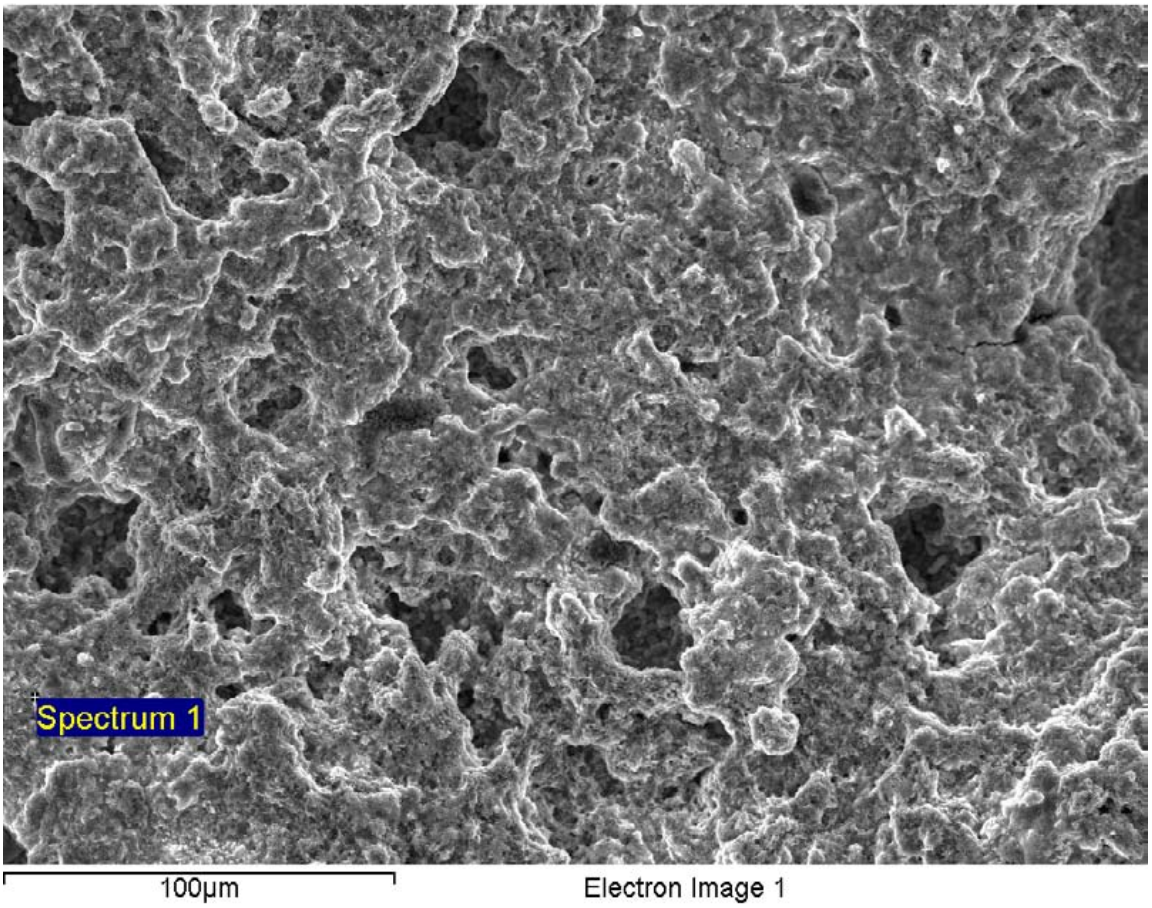

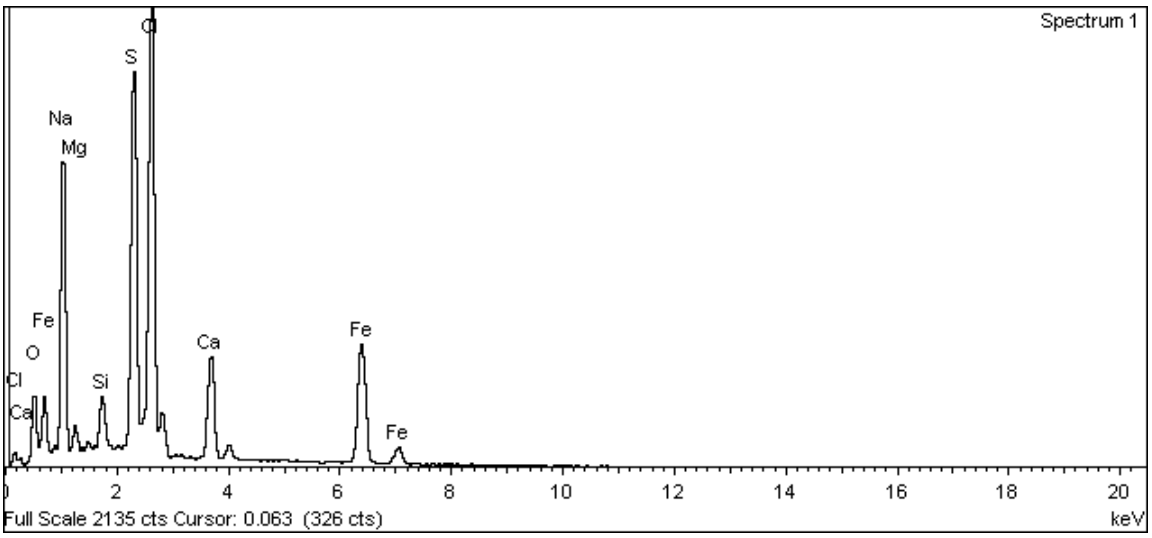

Figure A-65. Surface of iron electrode 2 and EDX analysis at position of Spectrum 1

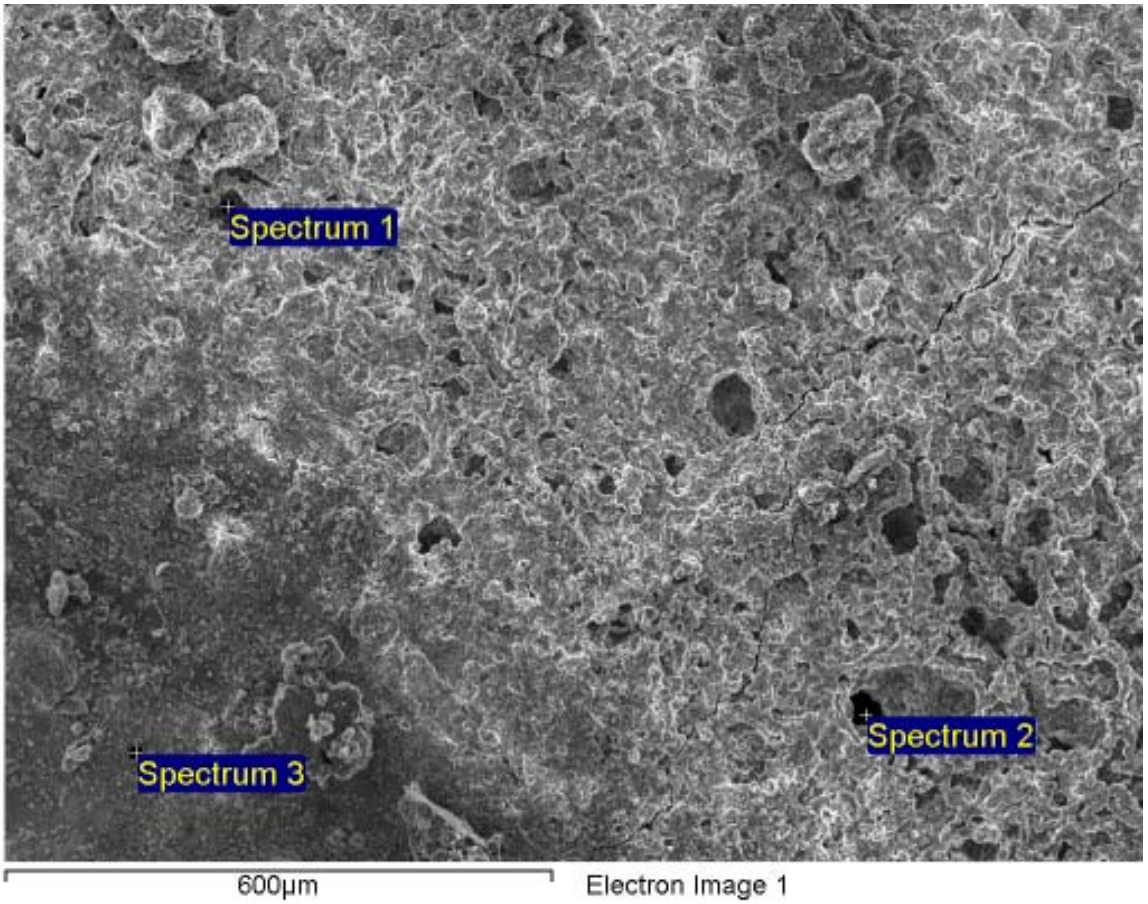

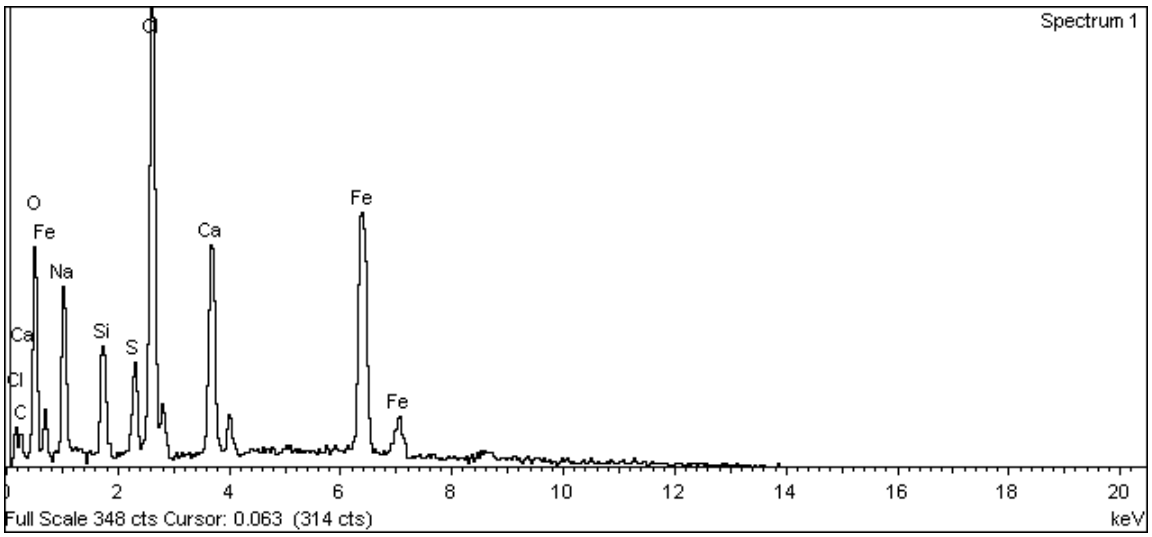

Figure A-66. Surface of iron electrode 2 and EDX analysis at position of Spectrum 1

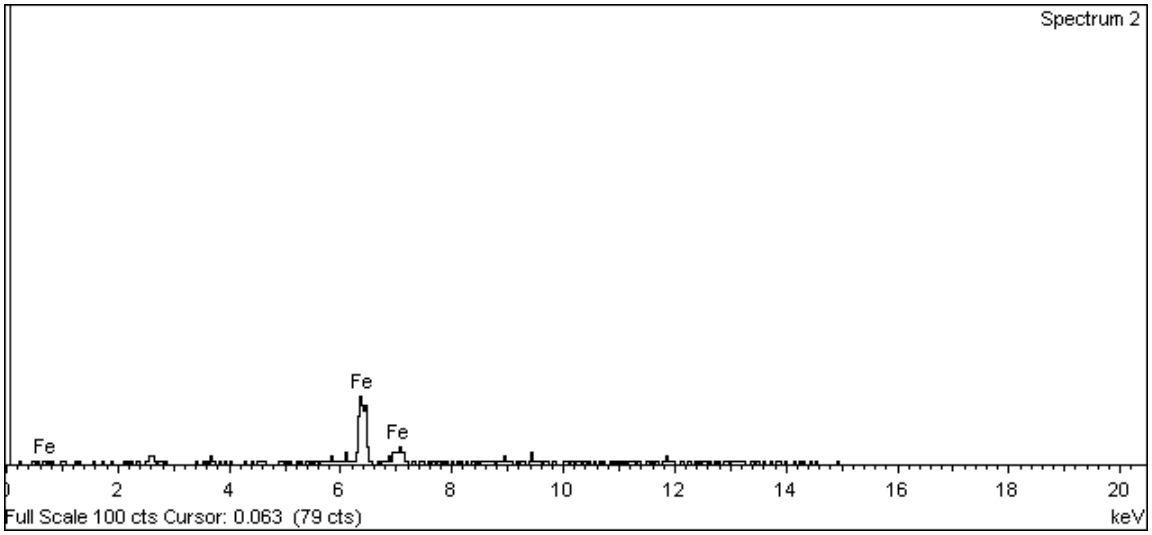

Figure A-67. Surface of iron electrode 2 and EDX analysis at position of Spectrum 2

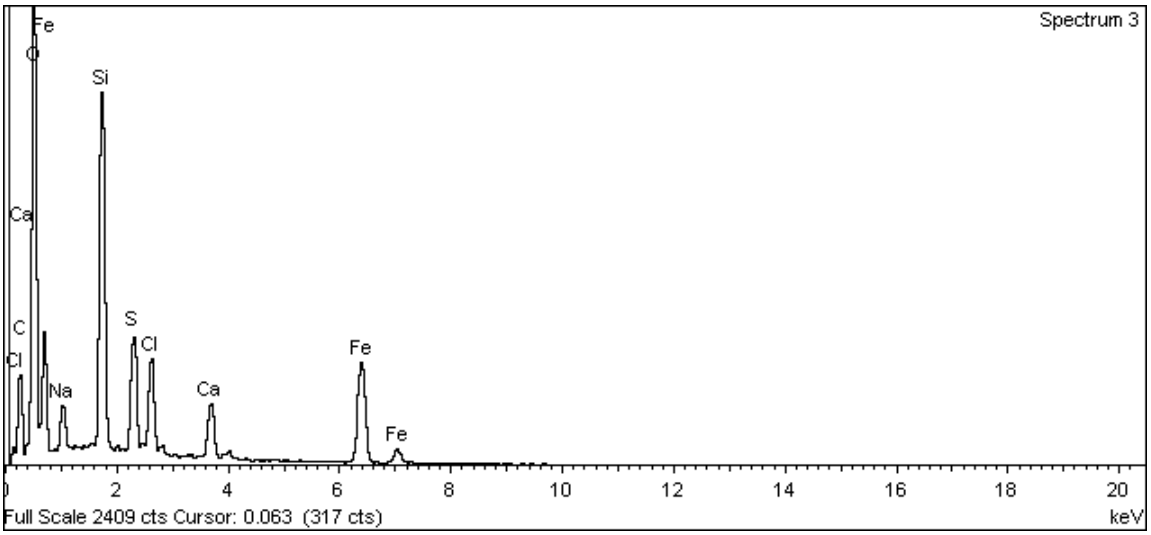

Figure A-68. Surface of iron electrode 2 and EDX analysis at position of Spectrum 3

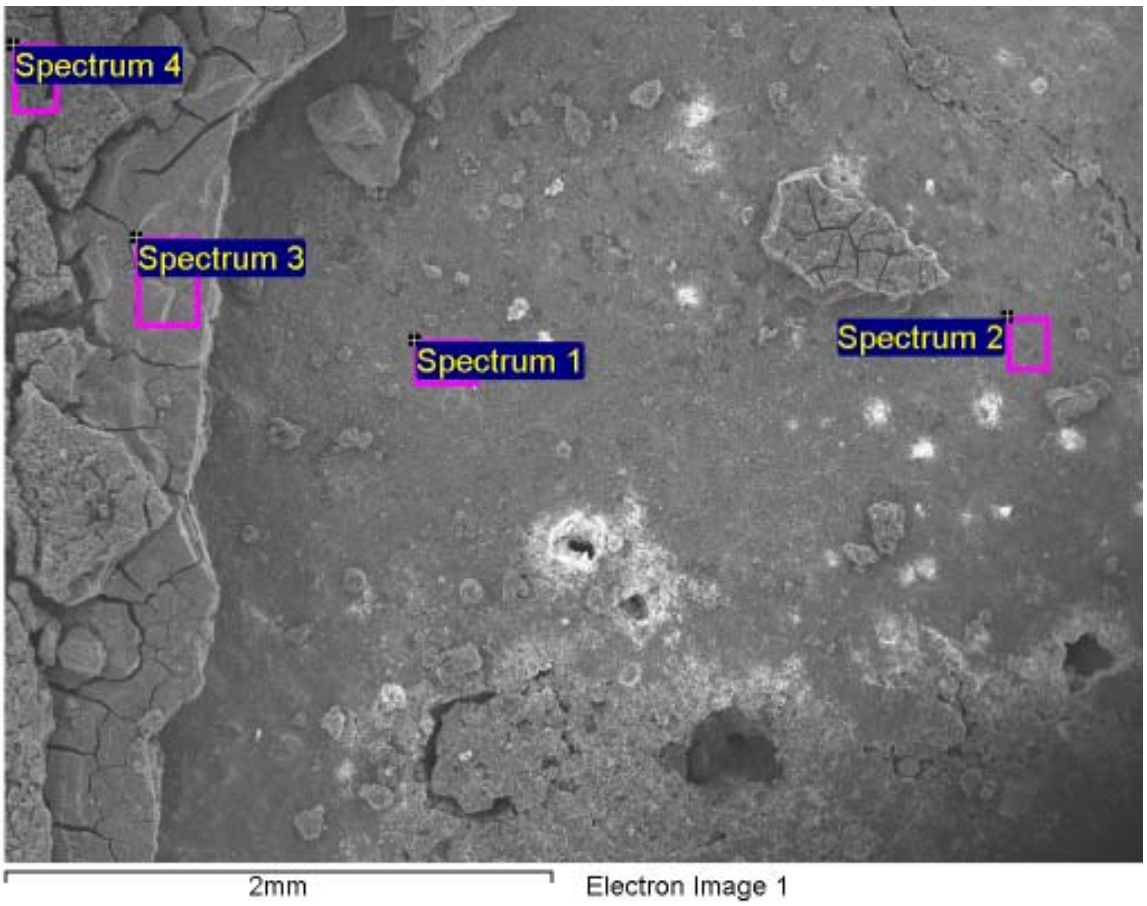

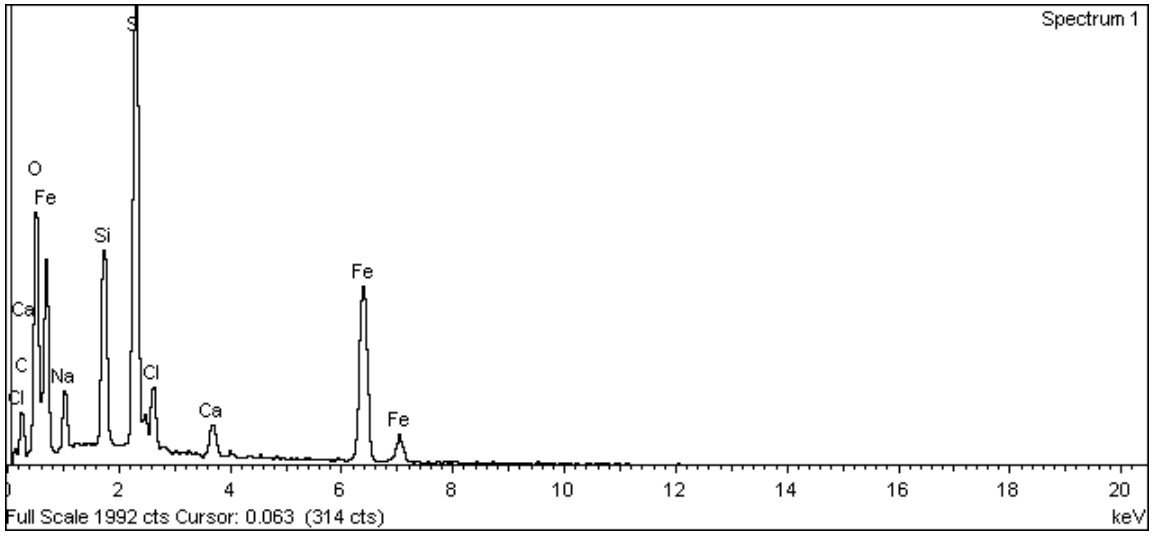

Figure A-69. Surface of iron electrode 2 and EDX analysis at position of Spectrum 1

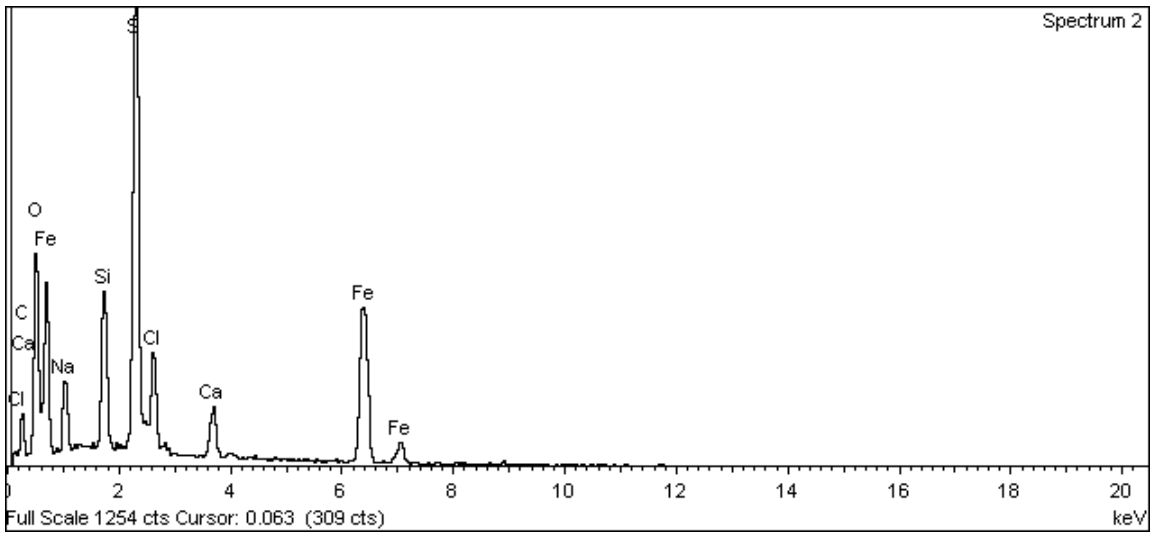

Figure A-70. Surface of iron electrode 2 and EDX analysis at position of Spectrum 2

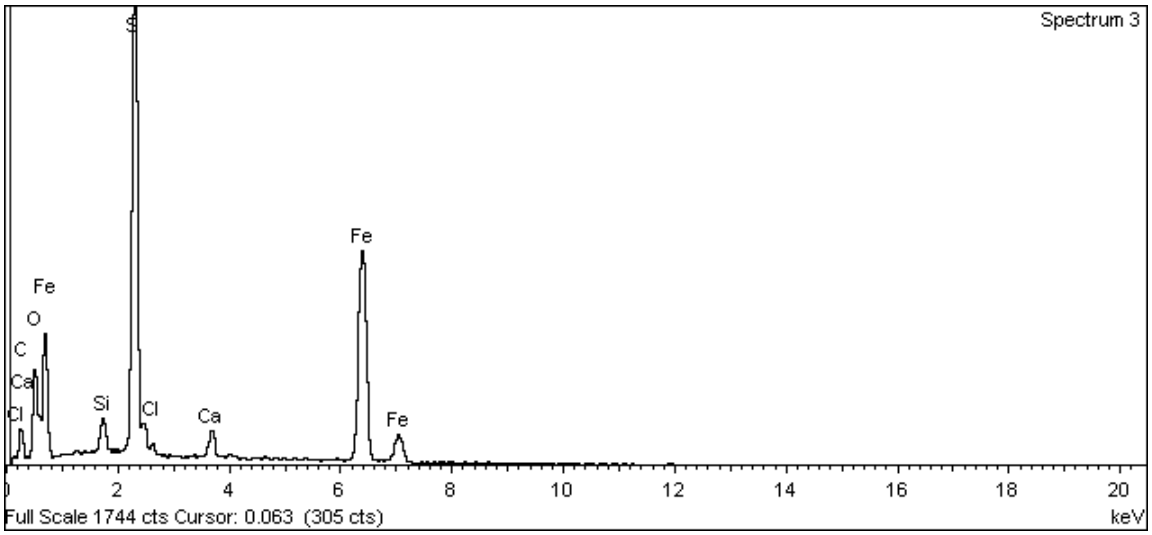

Figure A-71. Surface of iron electrode 2 and EDX analysis at position of Spectrum 3

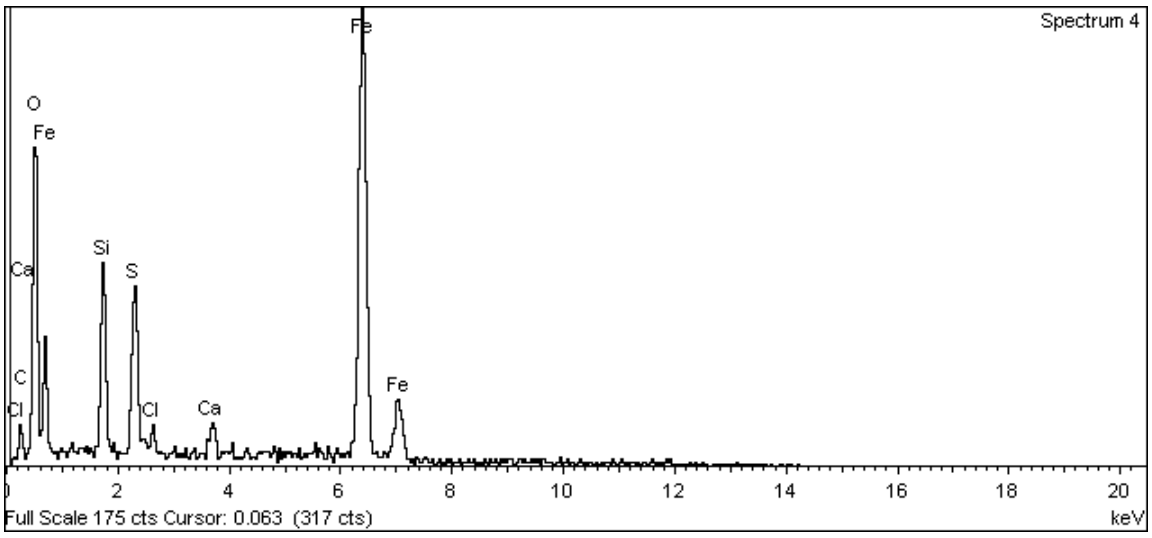

Figure A-72. Surface of iron electrode 2 and EDX analysis at position of Spectrum 4

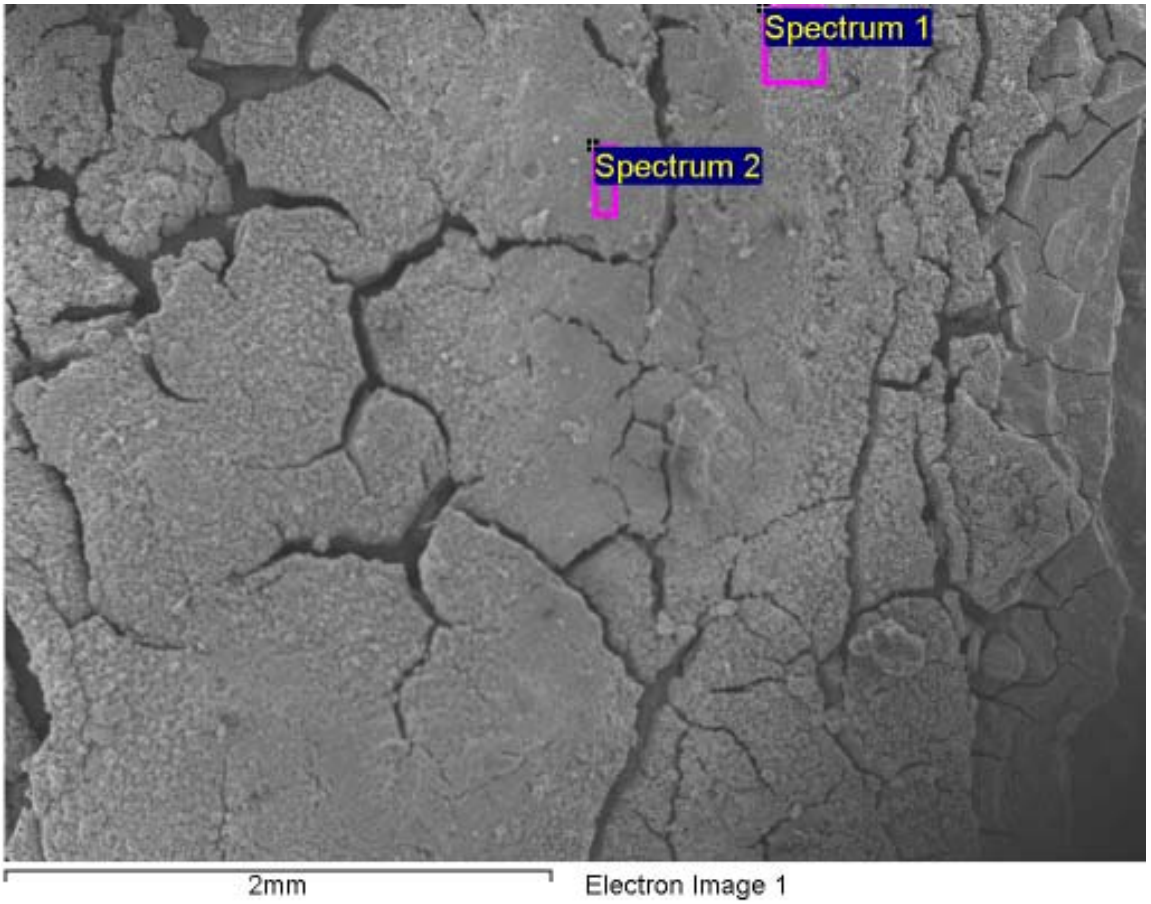

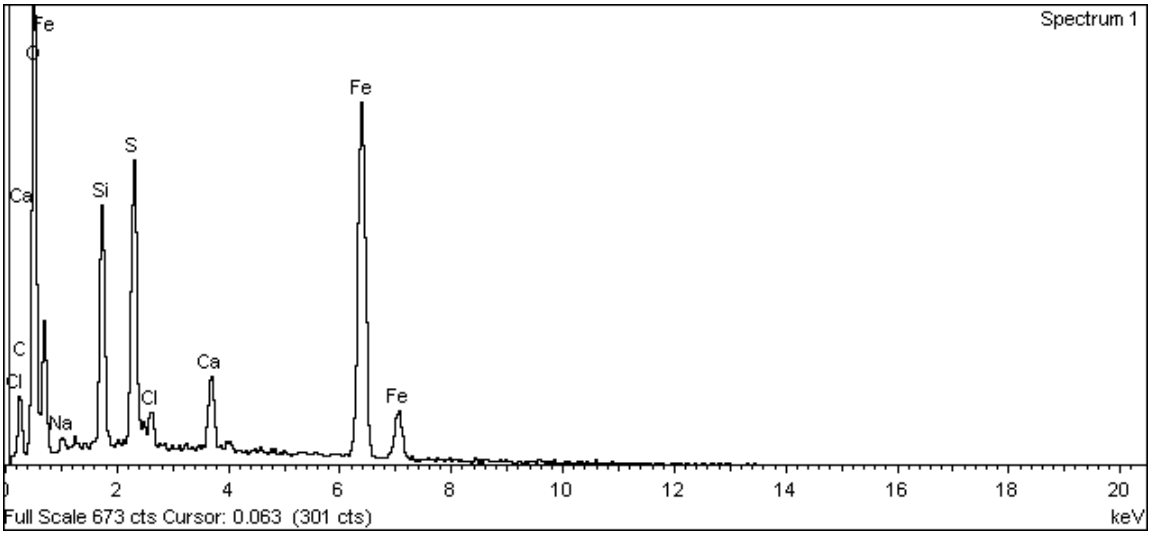

Figure A-73. Surface of iron electrode 2 and EDX analysis at position of Spectrum 1

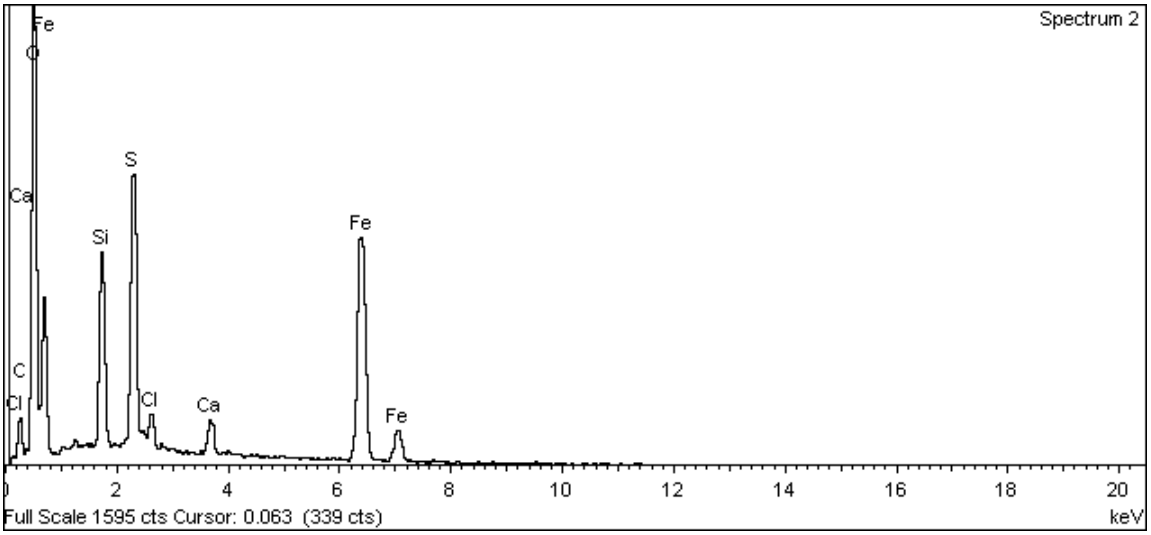

Figure A-74. Surface of iron electrode 2 and EDX analysis at position of Spectrum 2

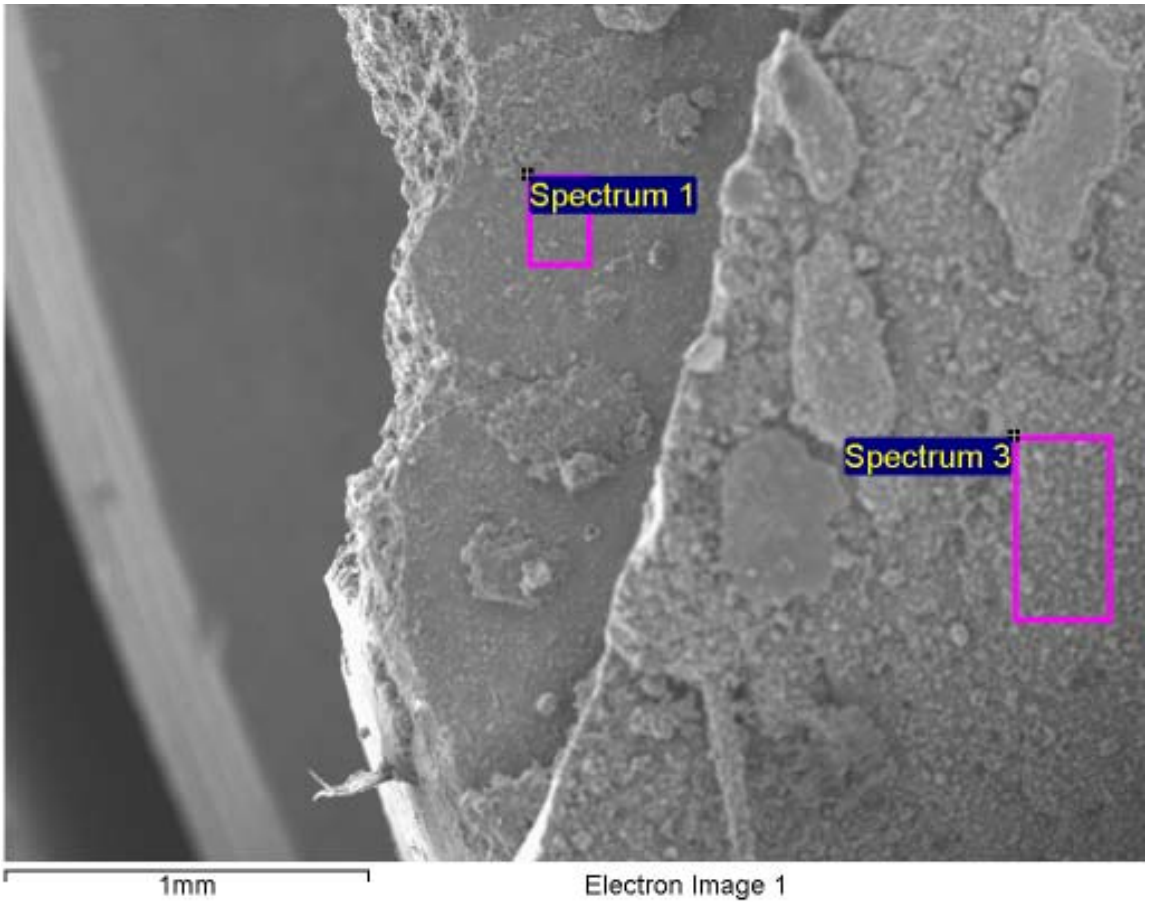

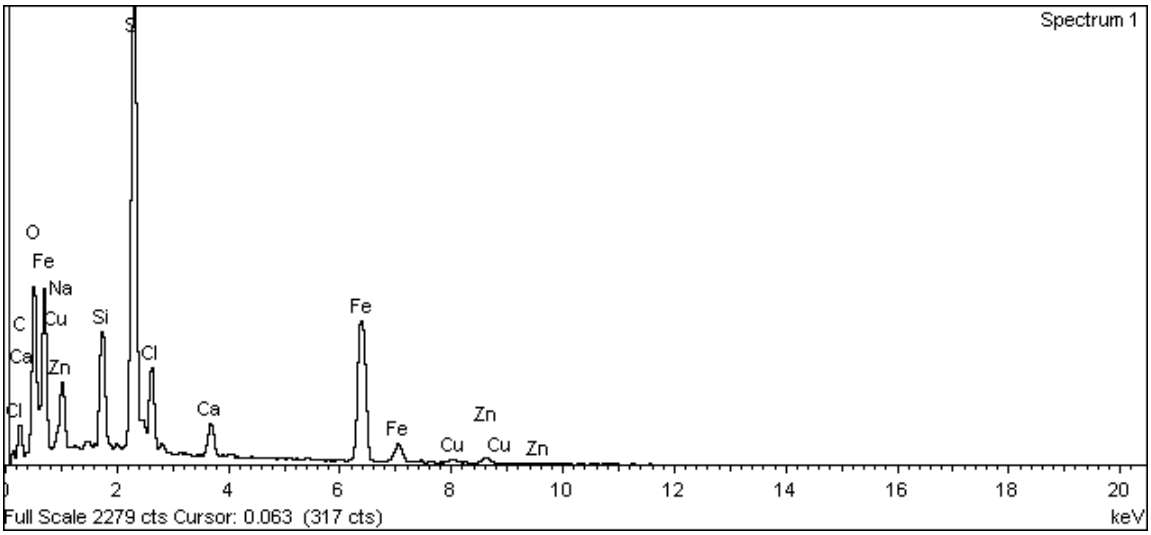

Figure A-75. Surface of iron electrode 2 and EDX analysis at position of Spectrum 1

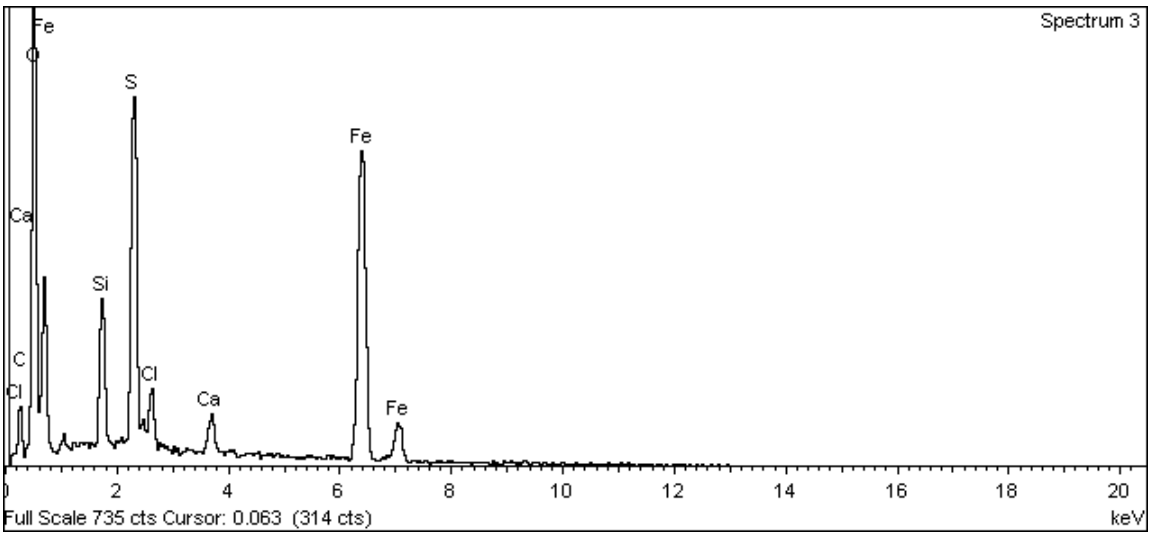

Figure A-76. Surface of iron electrode 2 and EDX analysis at position of Spectrum 3

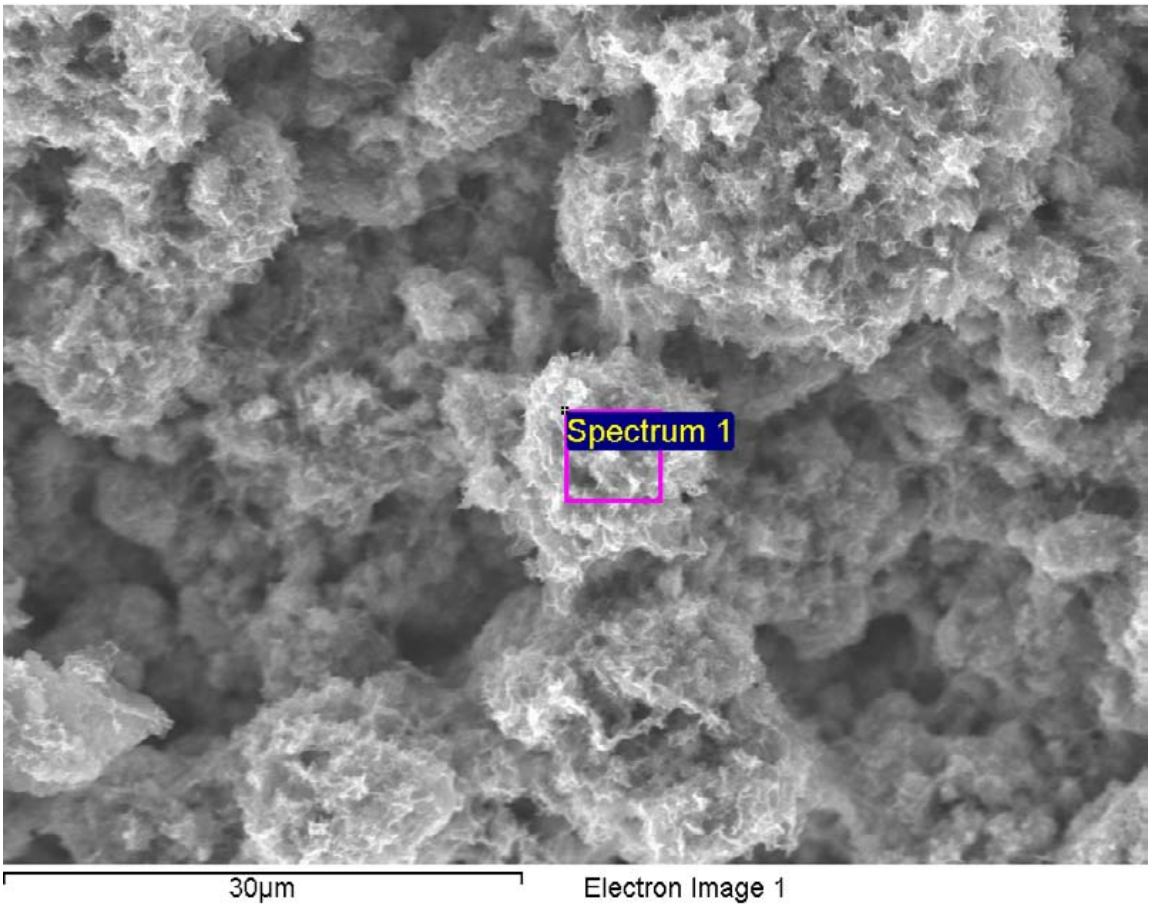

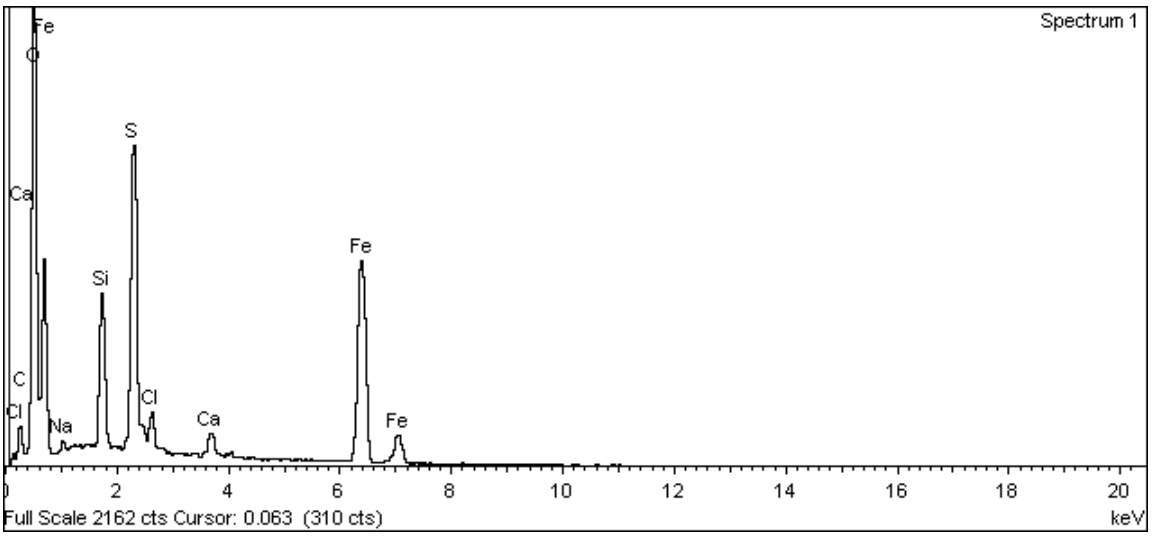

Figure A-77. Surface of iron electrode 2 and EDX analysis at position of Spectrum 1

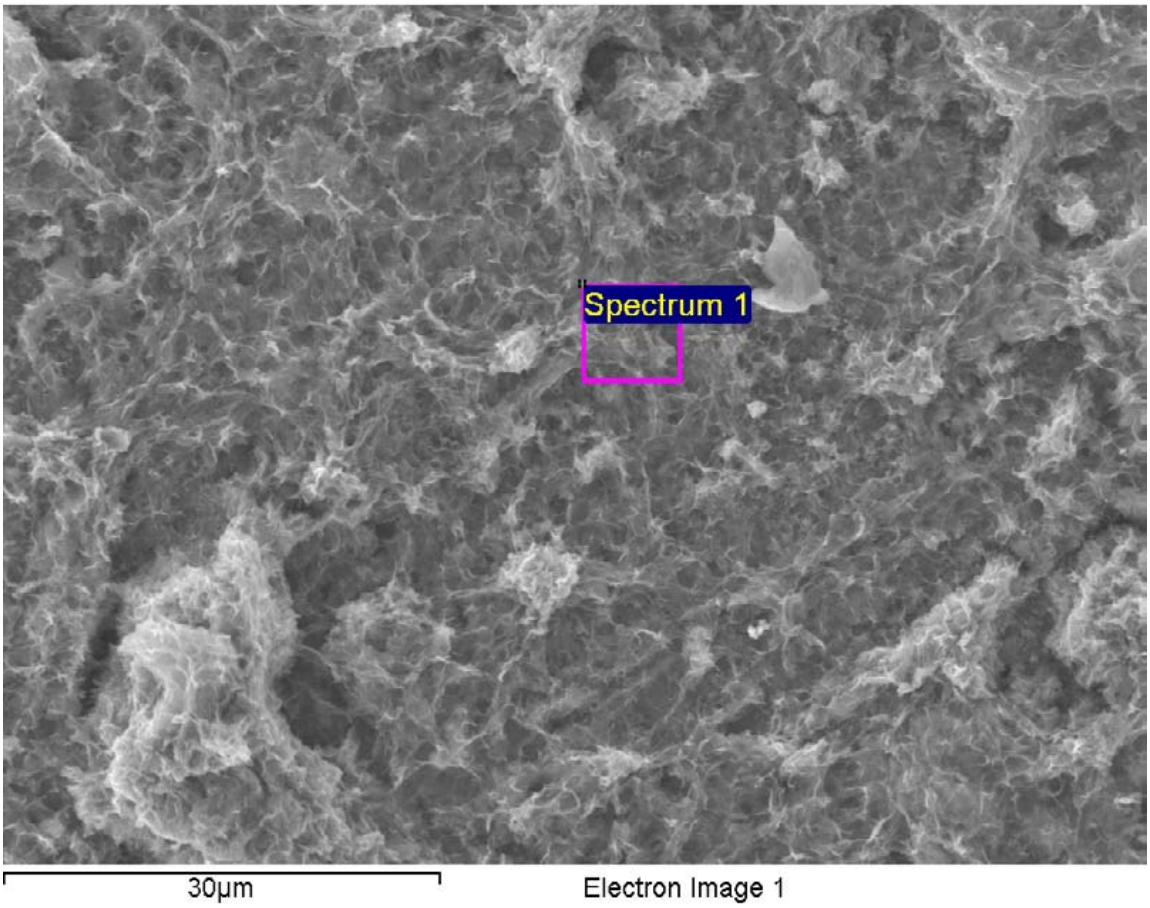

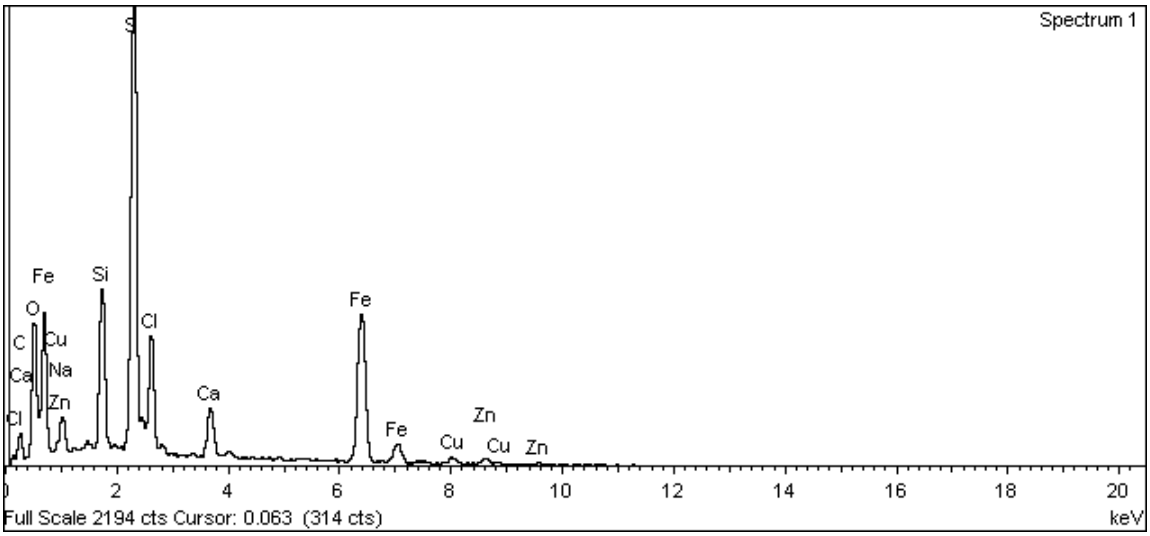

Figure A-78. Surface of iron electrode 2 and EDX analysis at position of Spectrum 1

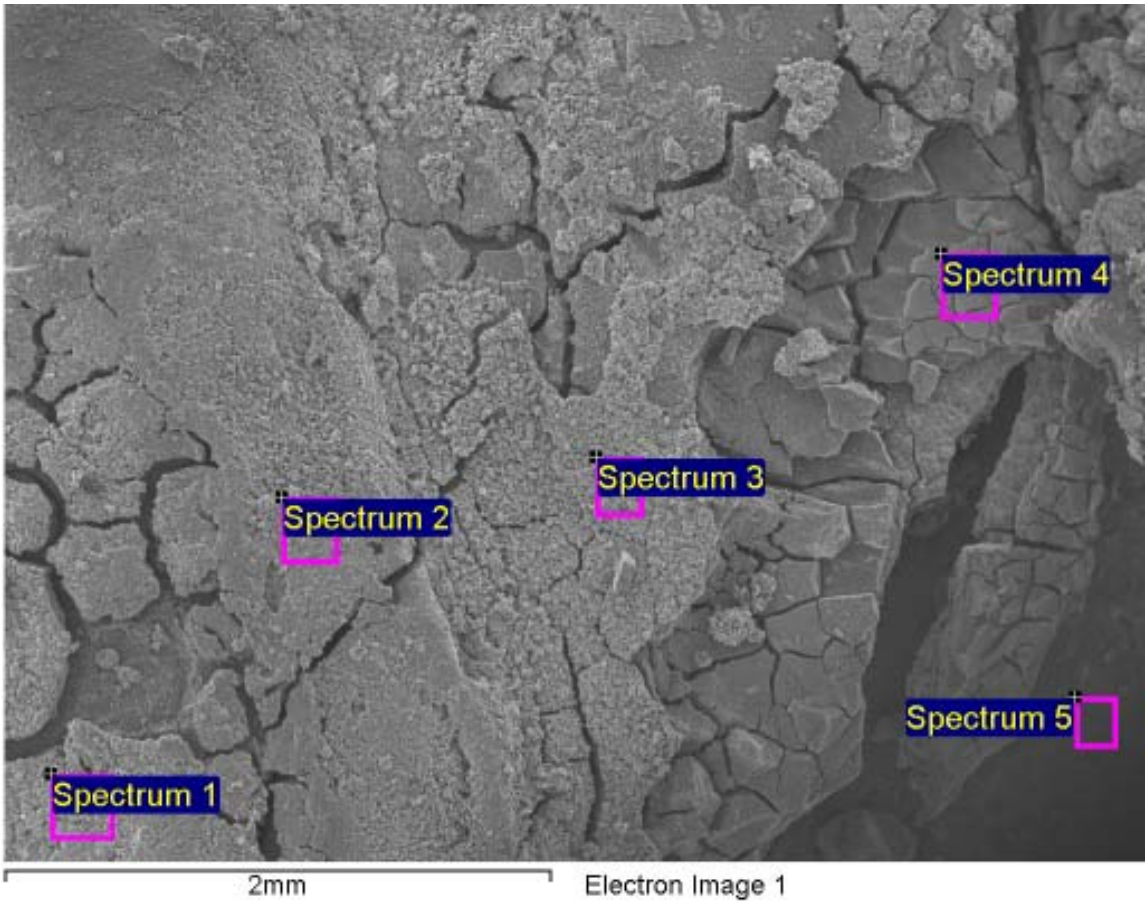

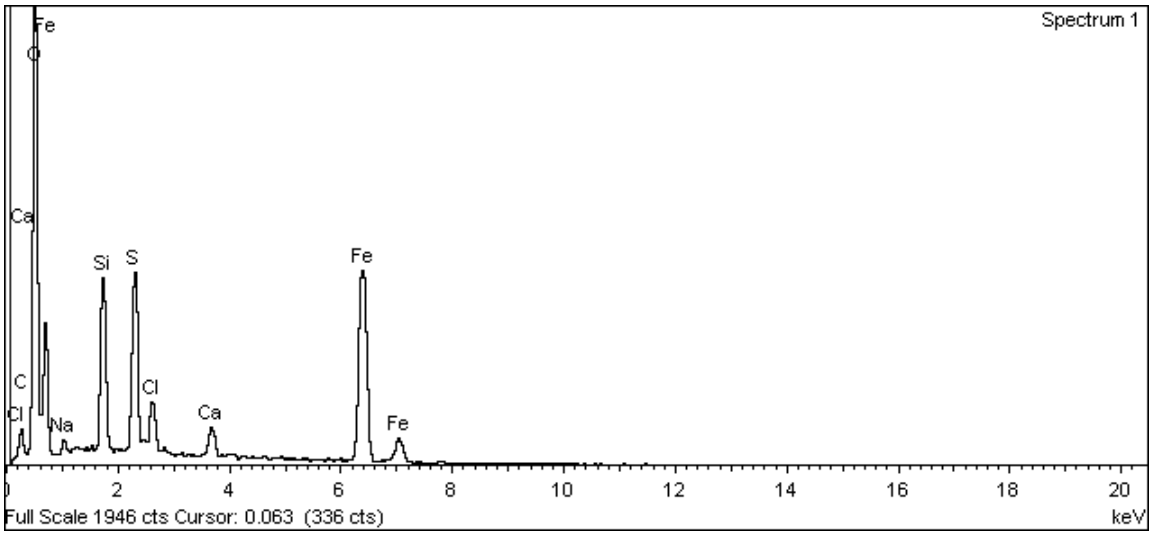

Figure A-79. Surface of iron electrode 2 and EDX analysis at position of Spectrum 1

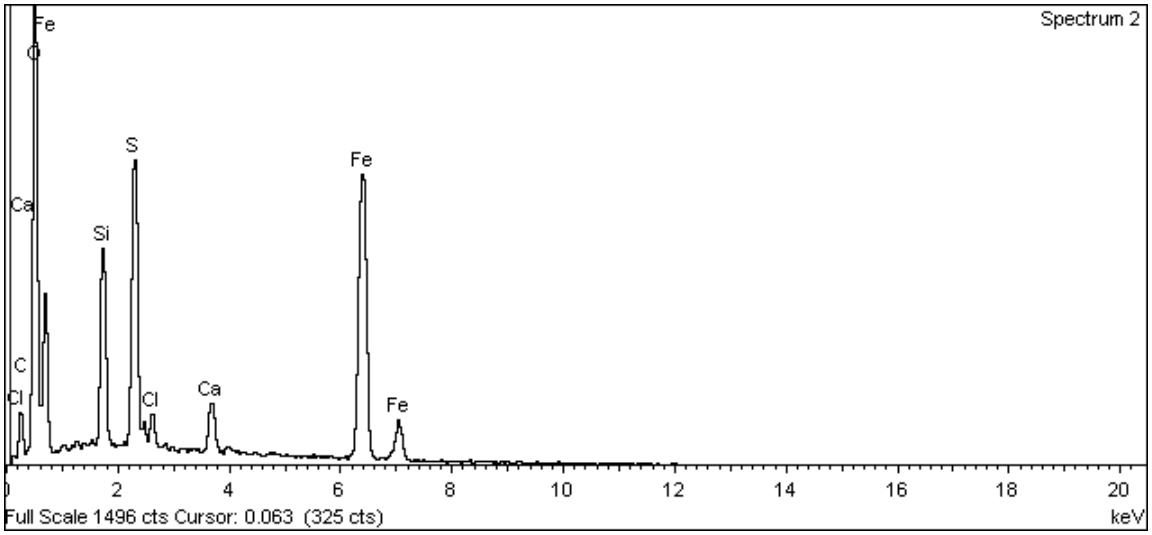

Figure A-80. Surface of iron electrode 2 and EDX analysis at position of Spectrum 2

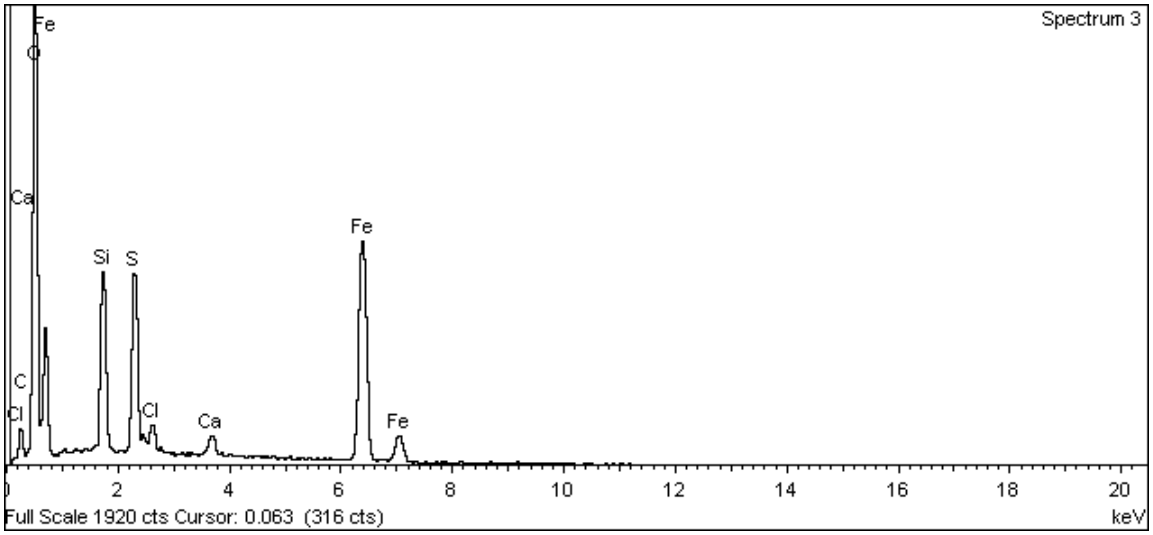

Figure A-81. Surface of iron electrode 2 and EDX analysis at position of Spectrum 3

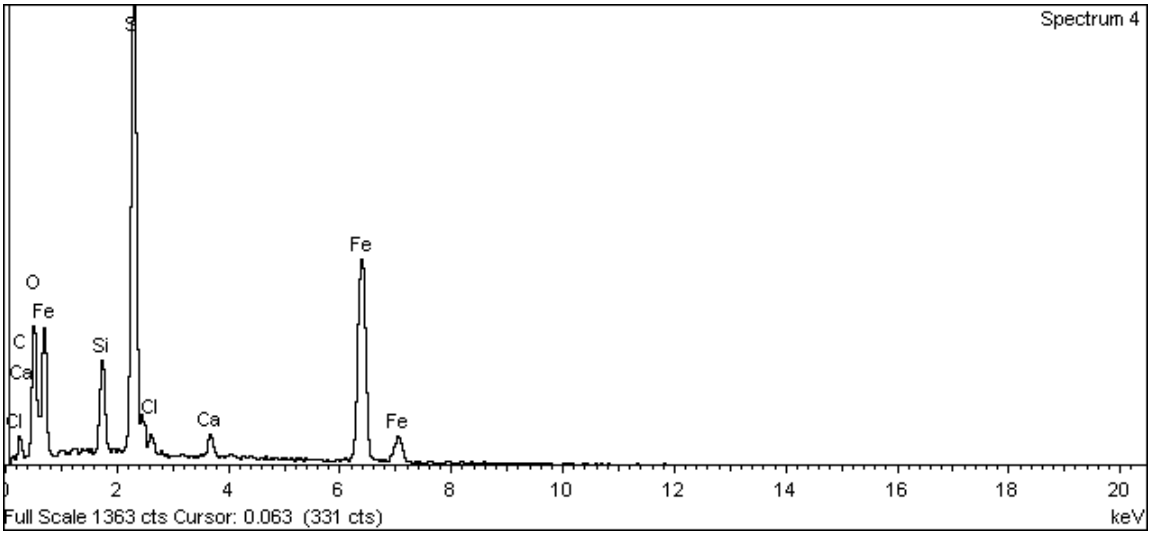

Figure A-82. Surface of iron electrode 2 and EDX analysis at position of Spectrum 4

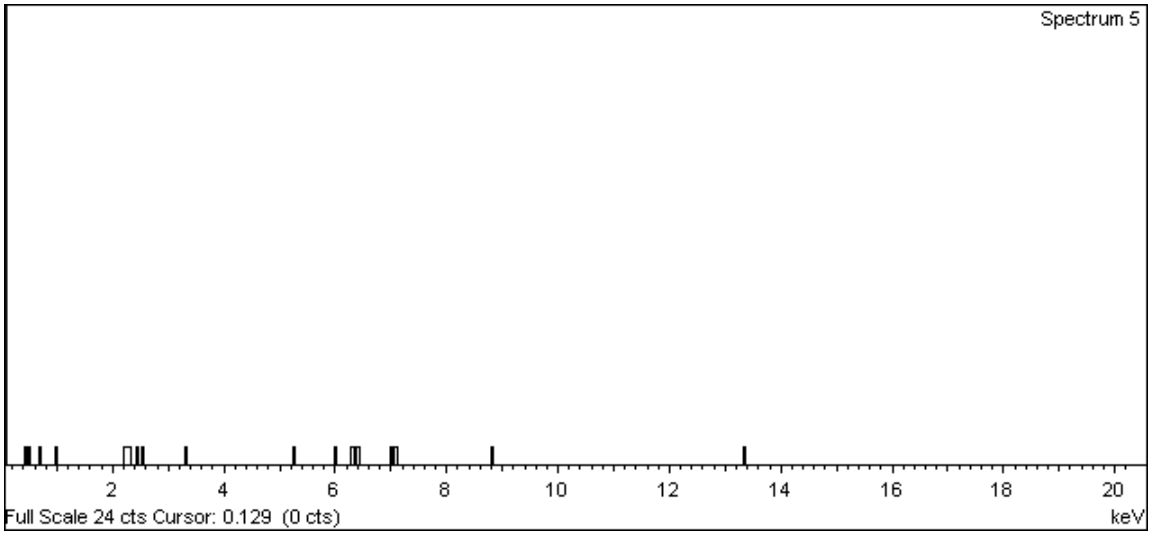

Figure A-83. Surface of iron electrode 2 and EDX analysis at position of Spectrum 5

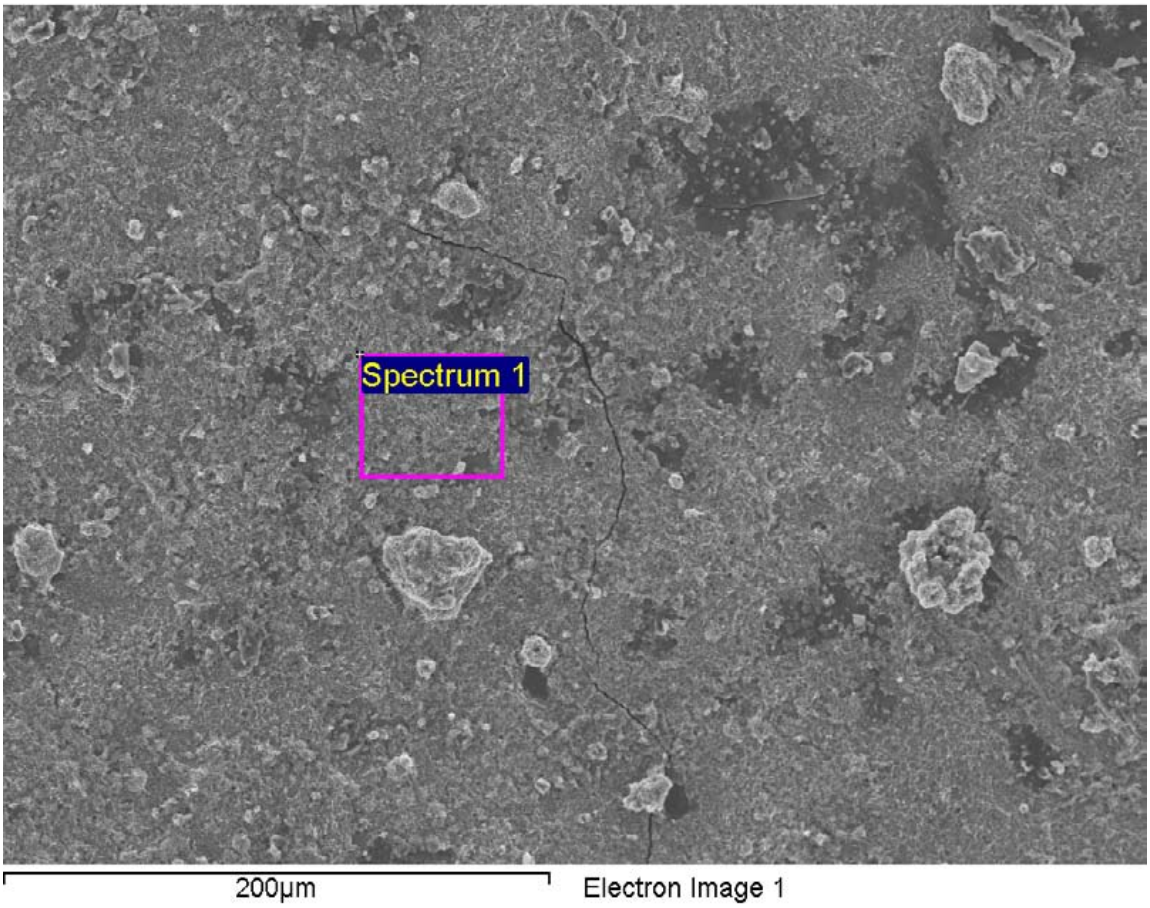

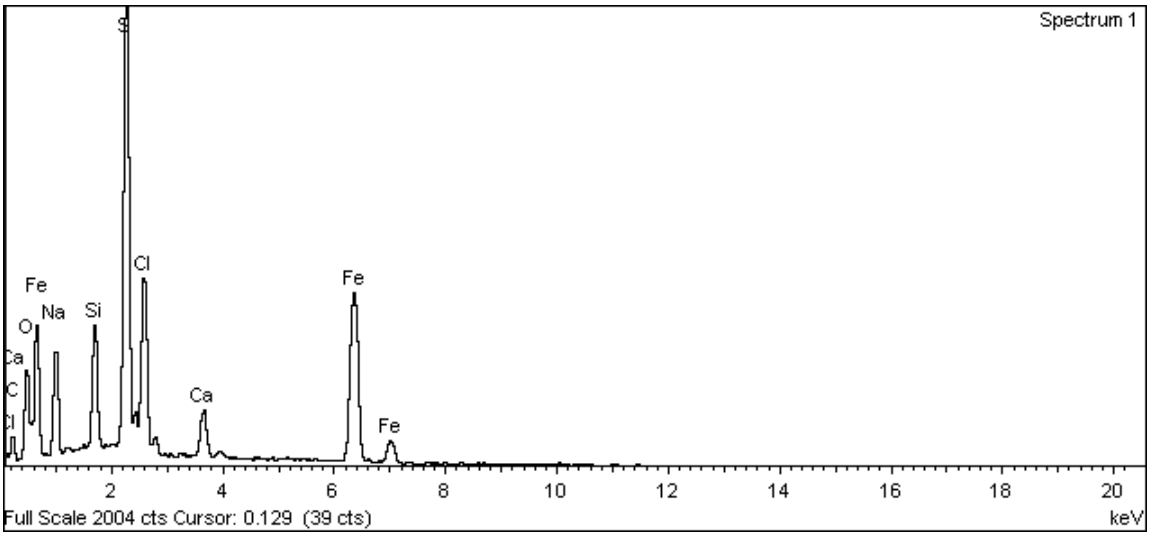

Figure A-84. Surface of iron electrode 2 and EDX analysis at position of Spectrum 1

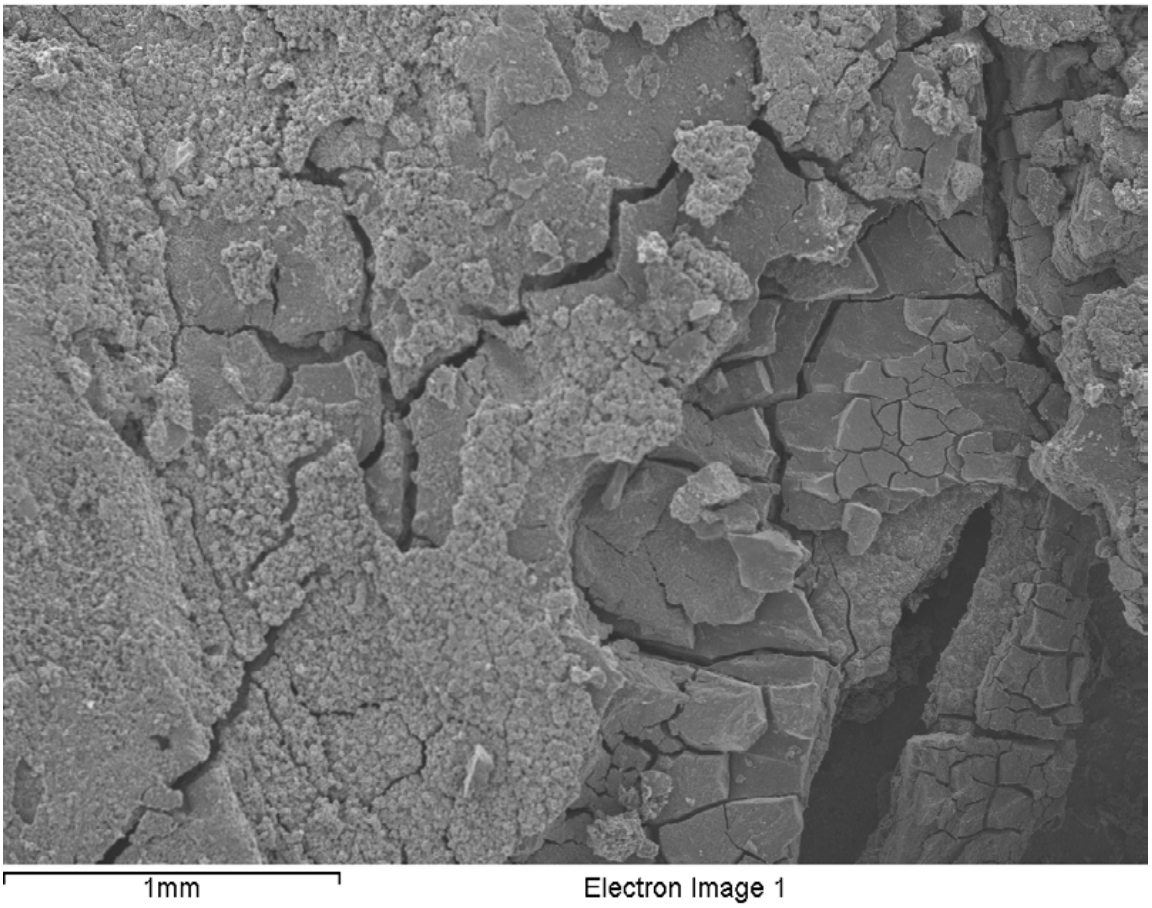

Figure A-85. Surface of iron electrode 2 and EDX analysis – Sum Spectrum

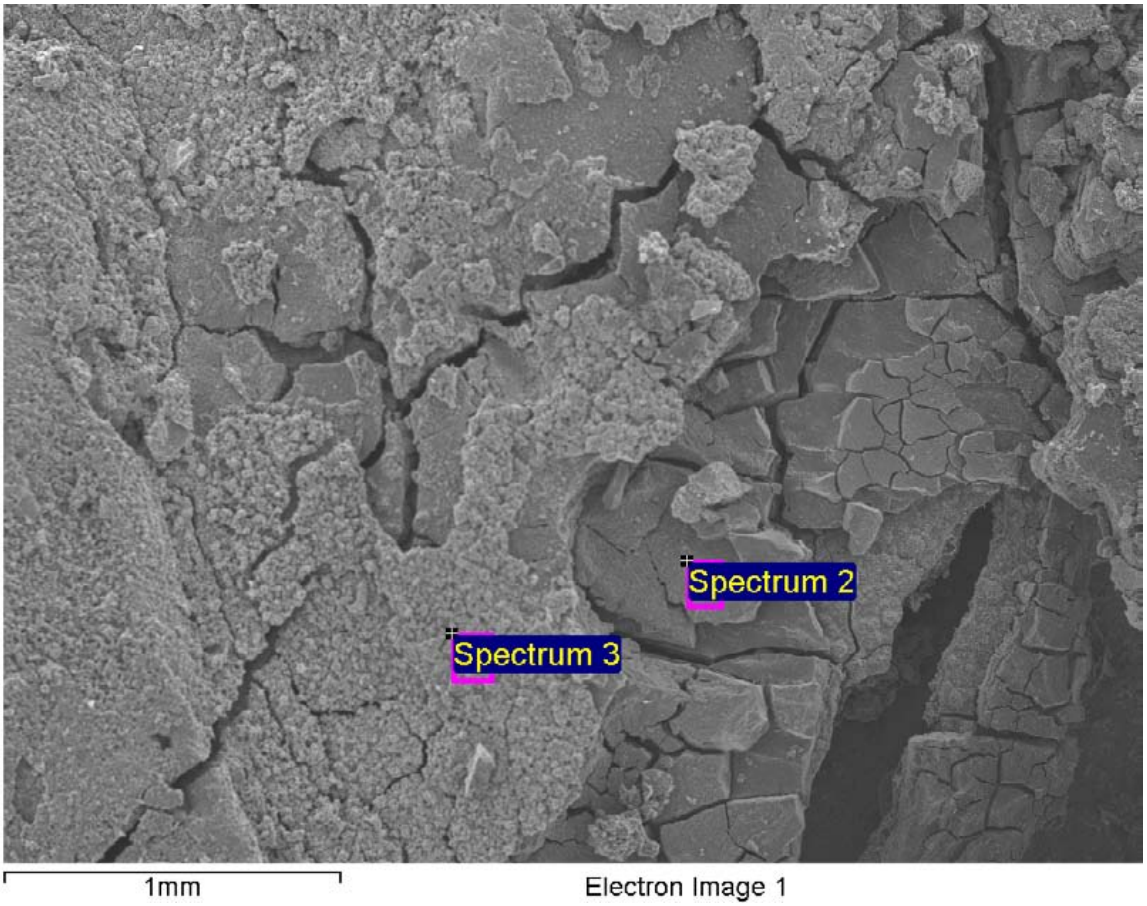

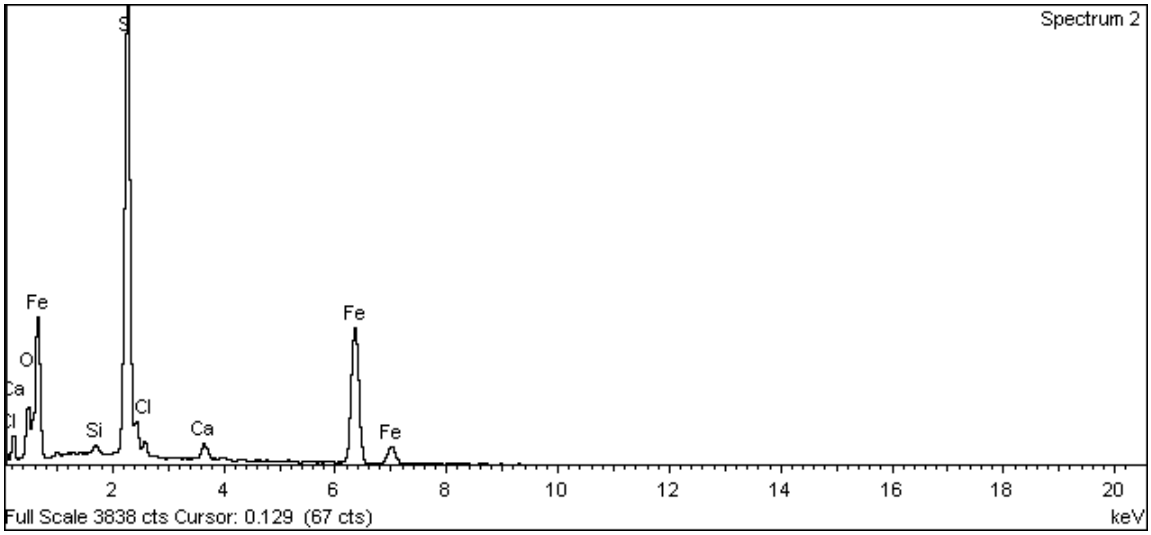

Figure A-86. Surface of iron electrode 2 and EDX analysis at position of Spectrum 2

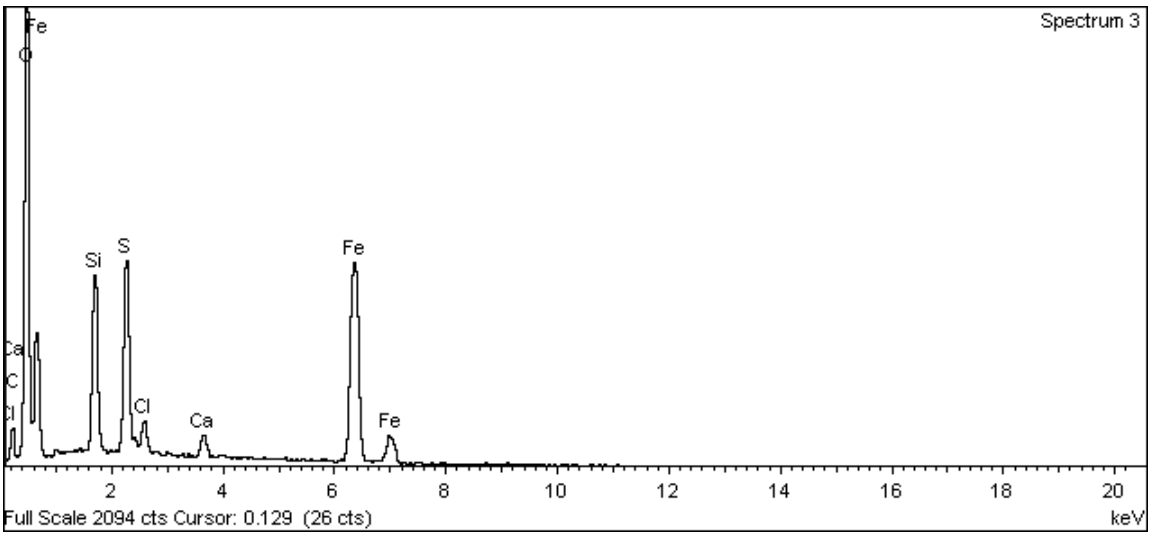

Figure A-87. Surface of iron electrode 2 and EDX analysis at position of Spectrum 3

Iron weight loss specimen

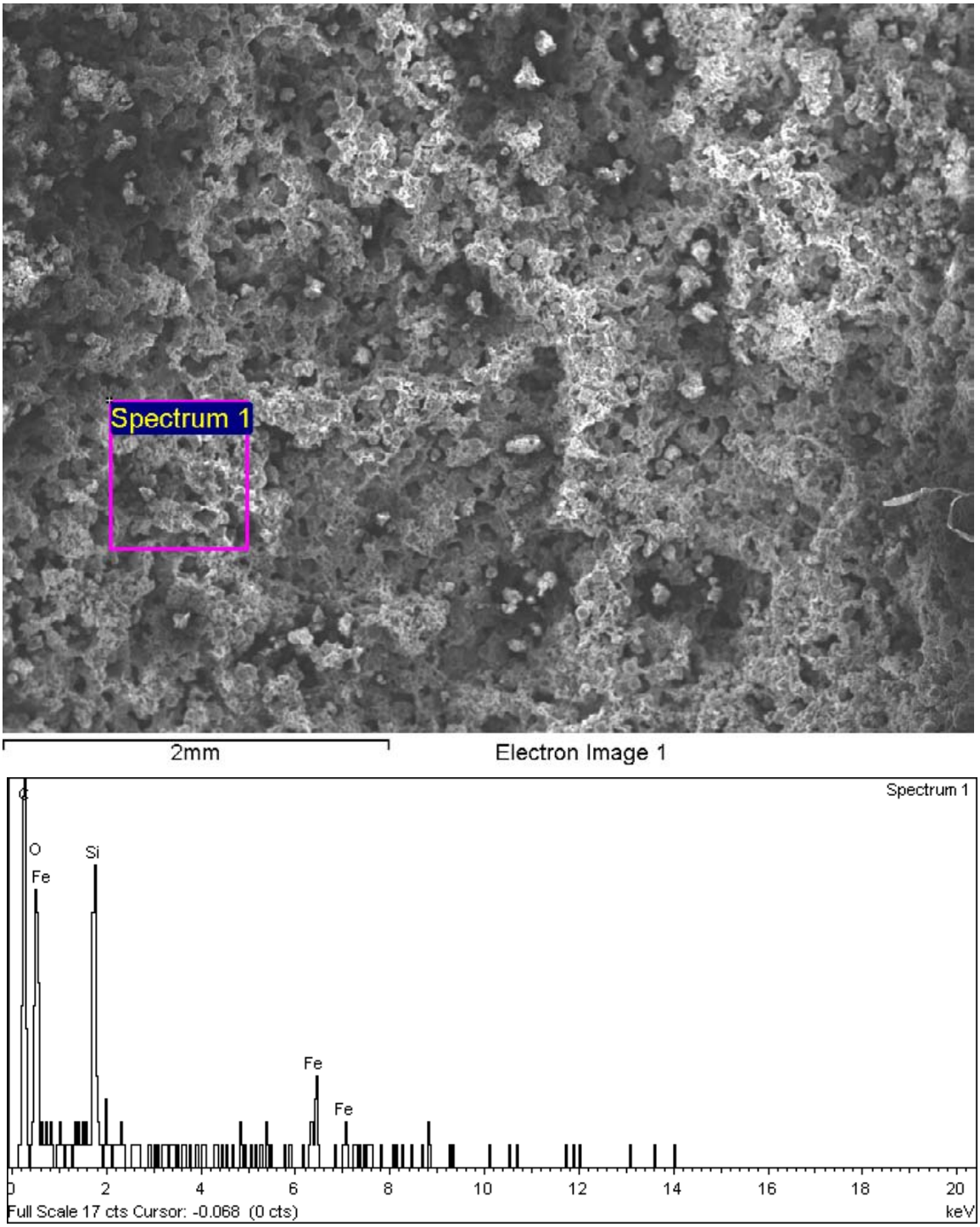

Figure A-88. Surface of iron weight loss specimen and EDX analysis at position of Spectrum 1

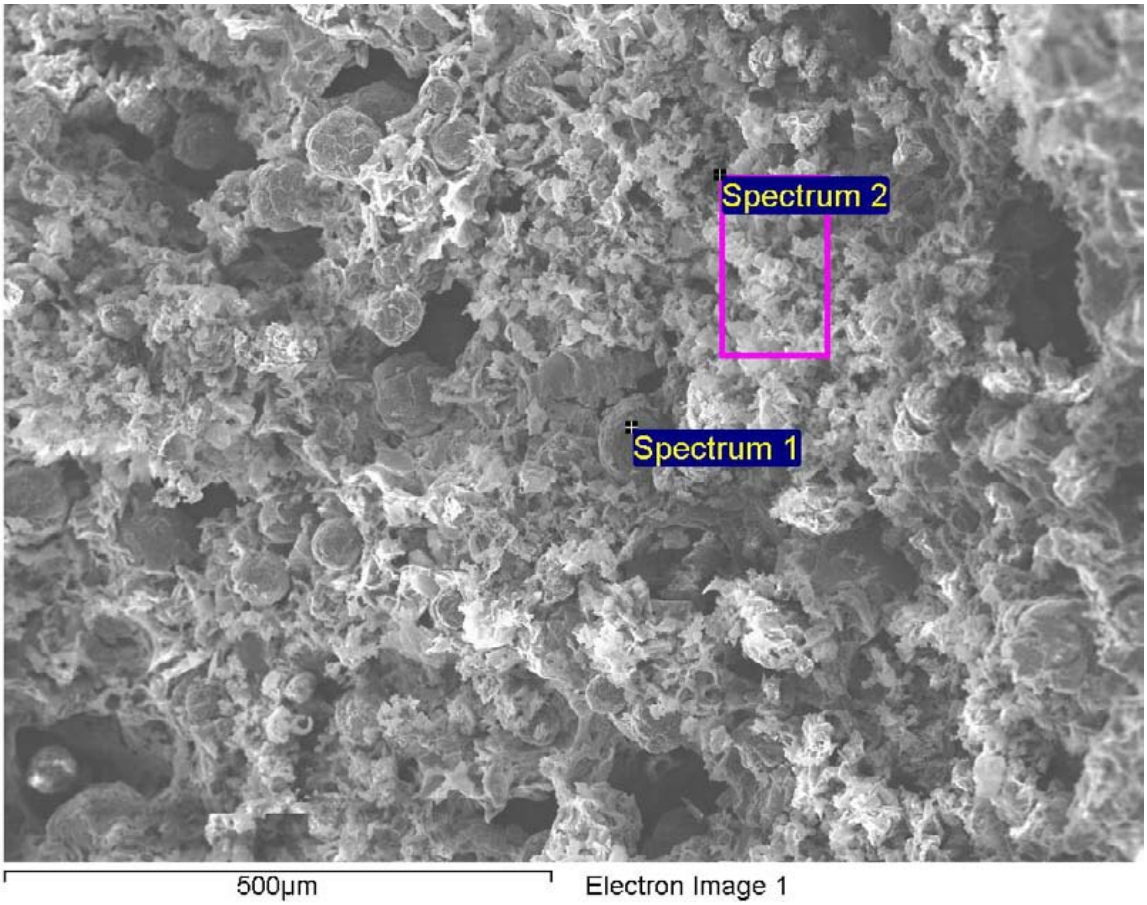

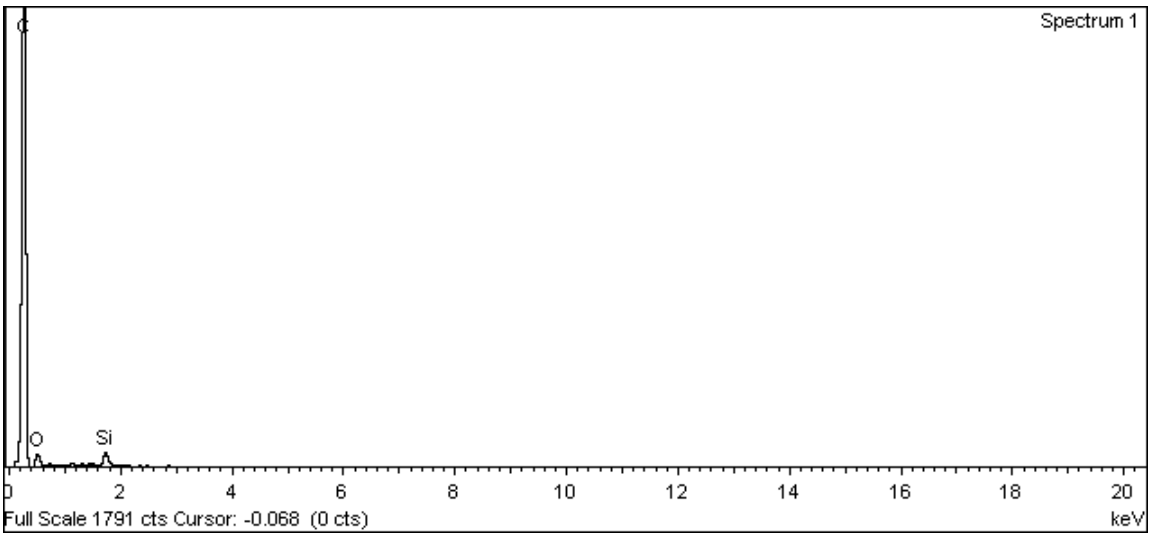

Figure A-89. Surface of iron weight loss specimen and EDX analysis at position of Spectrum 1

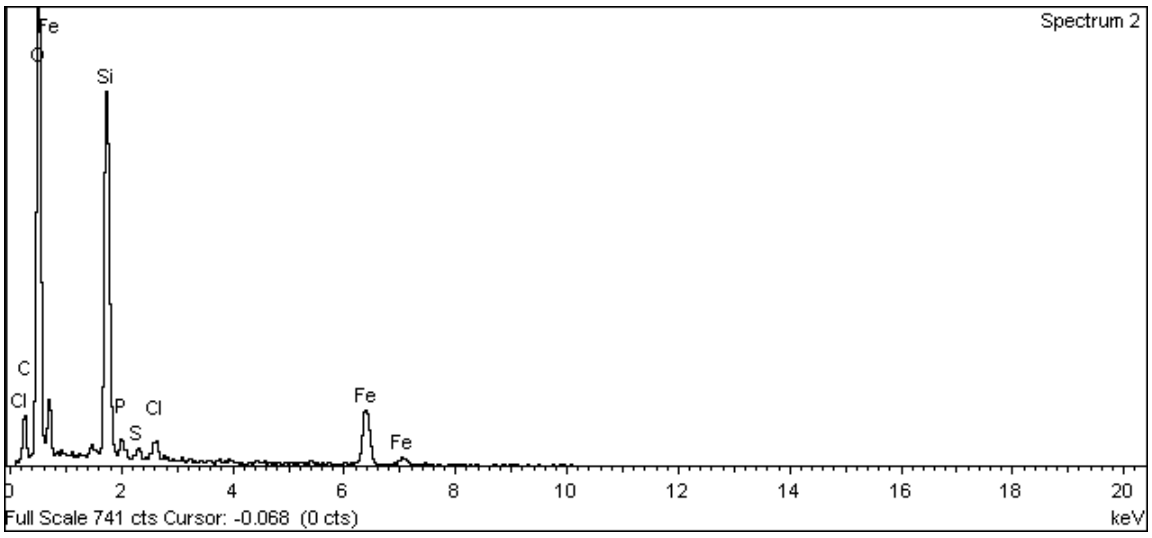

Figure A-90. Surface of iron weight loss specimen and EDX analysis at position of Spectrum 2

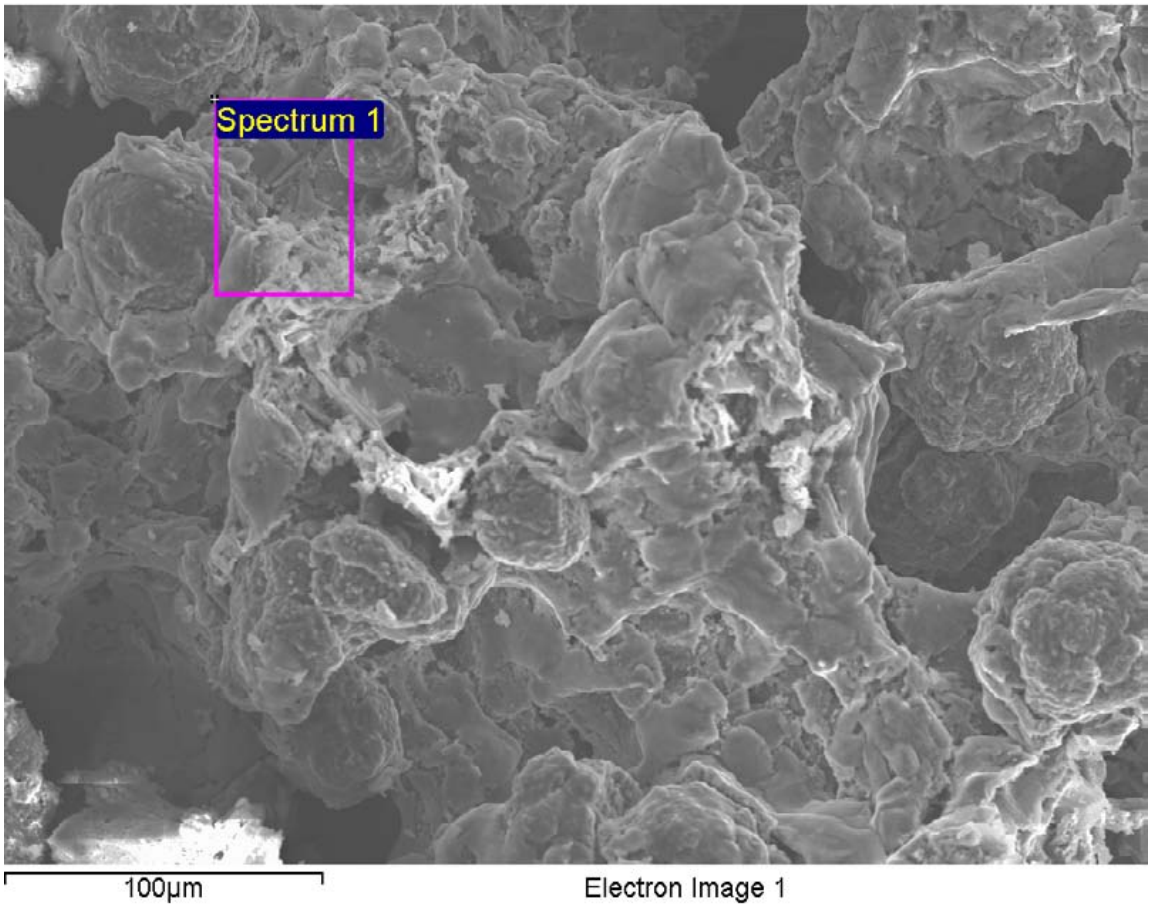

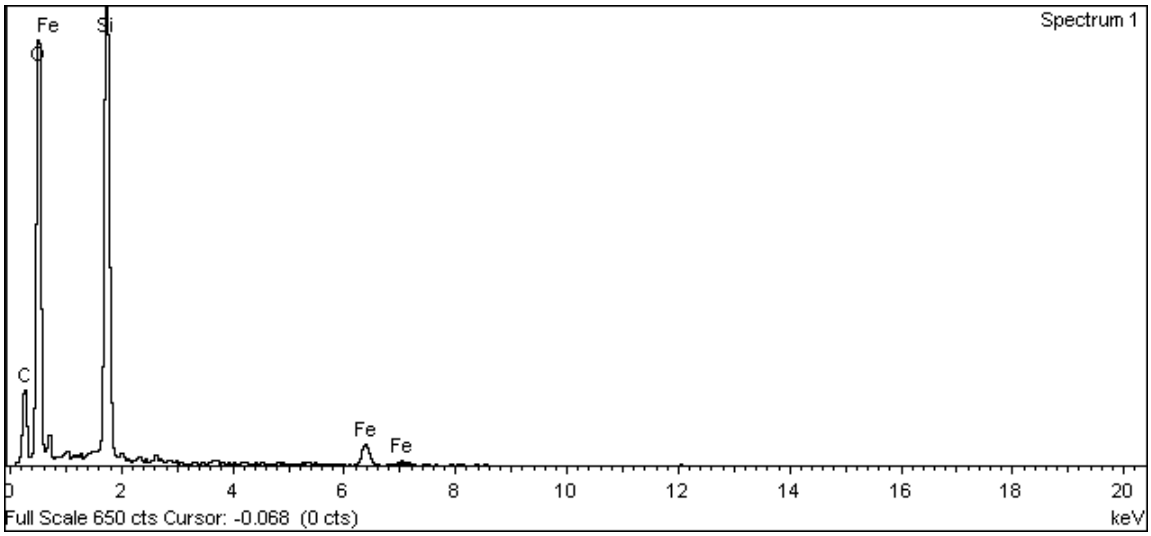

Figure A-91. Surface of iron weight loss specimen and EDX analysis at position of Spectrum 1

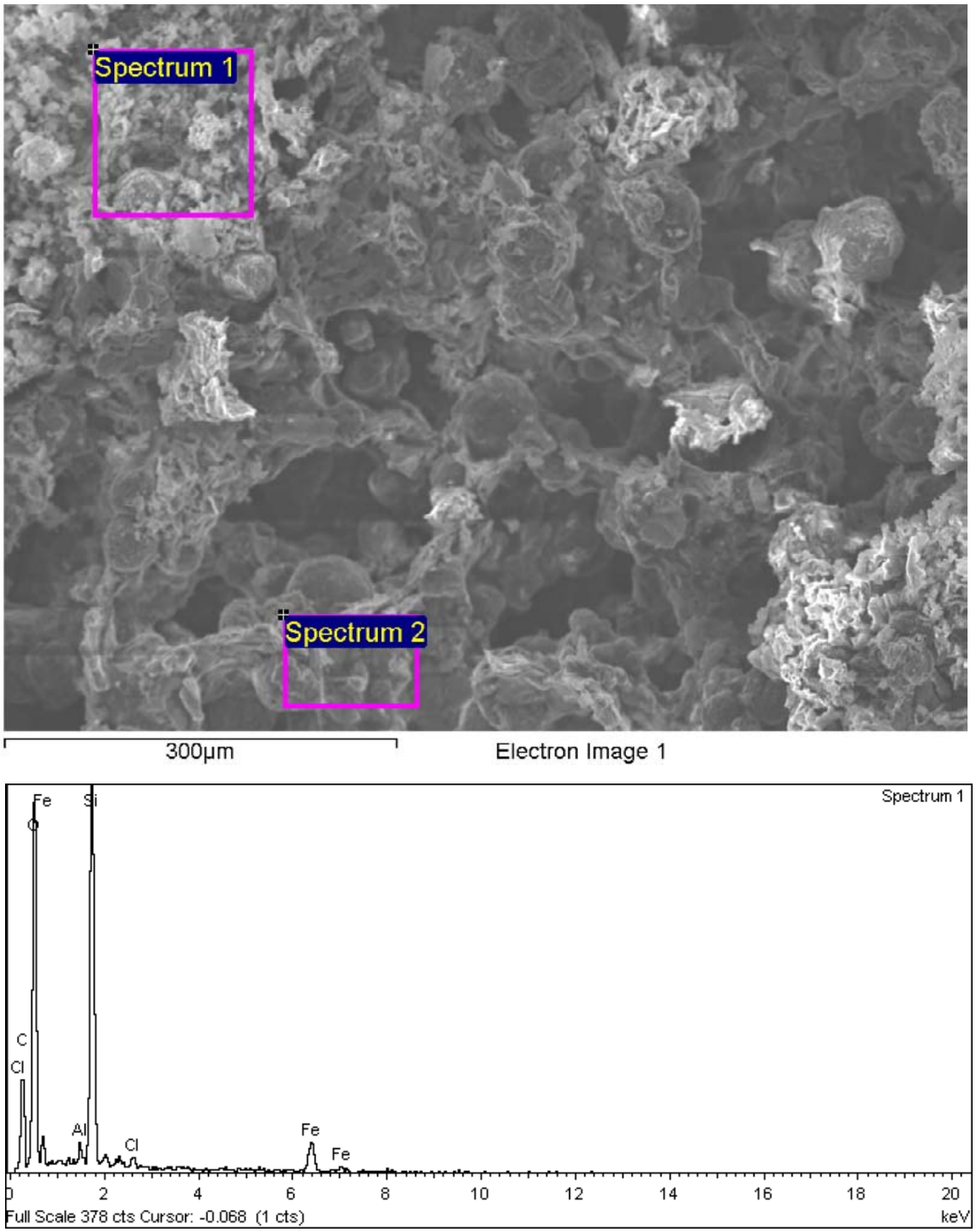

Figure A-92. Surface of iron weight loss specimen and EDX analysis at position of Spectrum 1

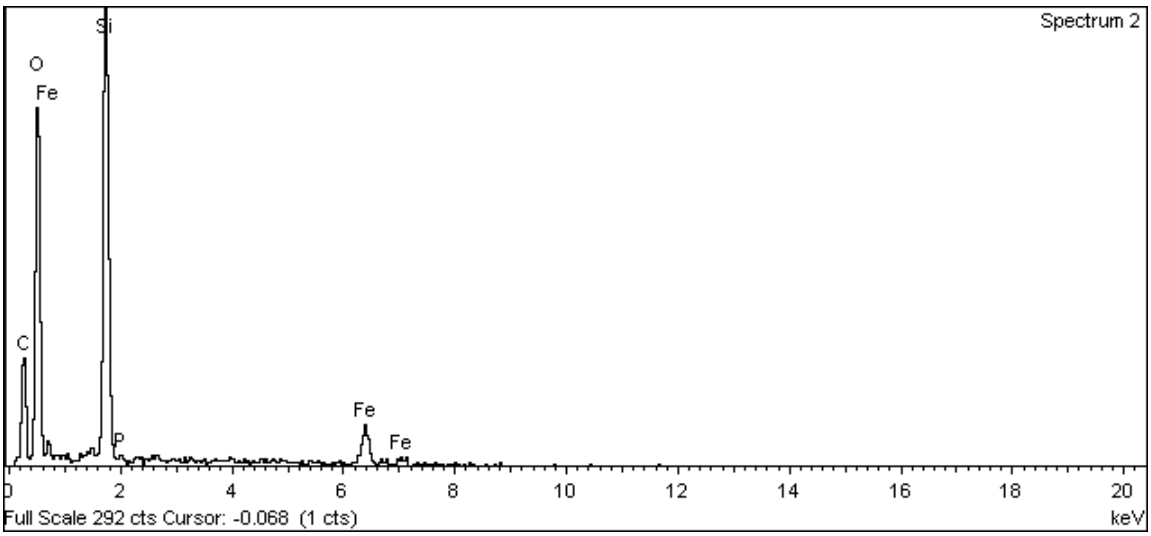

Figure A-93. Surface of iron weight loss specimen and EDX analysis at position of Spectrum 2

Whiskers on iron electrode 2

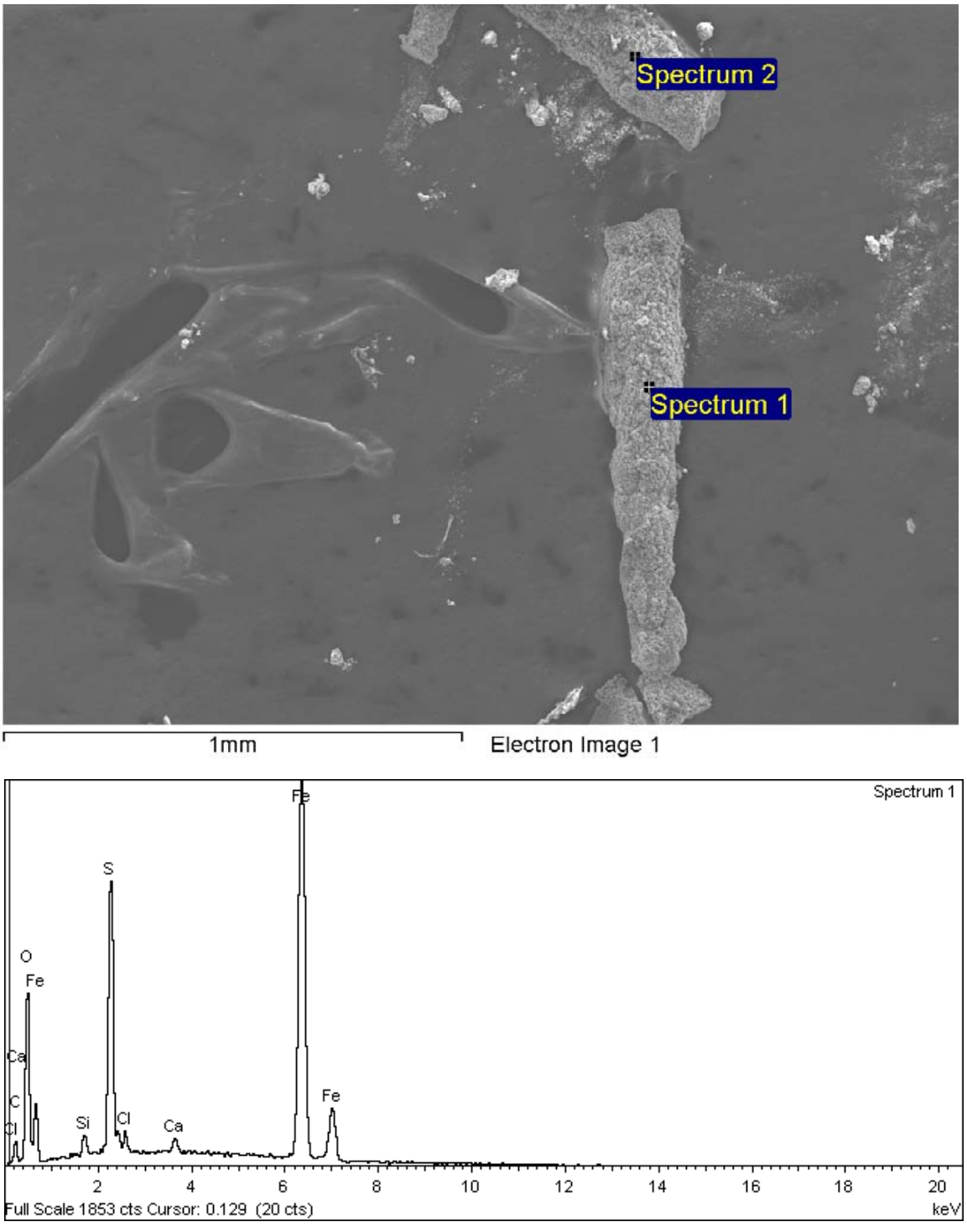

Figure A-94. Surface of whiskers on iron electrode 2 and EDX analysis at position of Spectrum 1

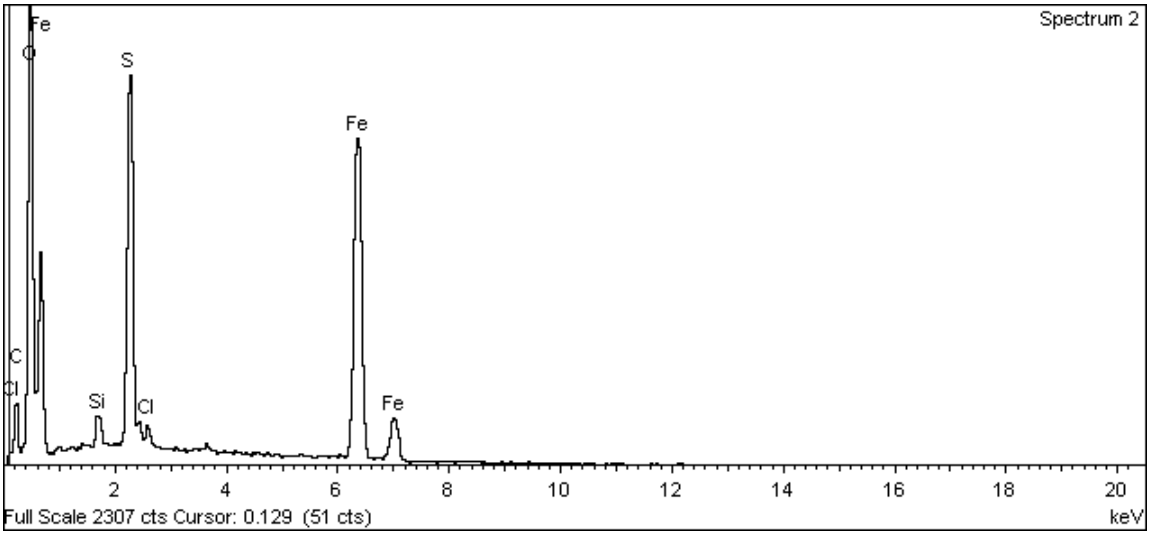

Figure A-95. Surface of whiskers on iron electrode 2 and EDX analysis at position of Spectrum 2

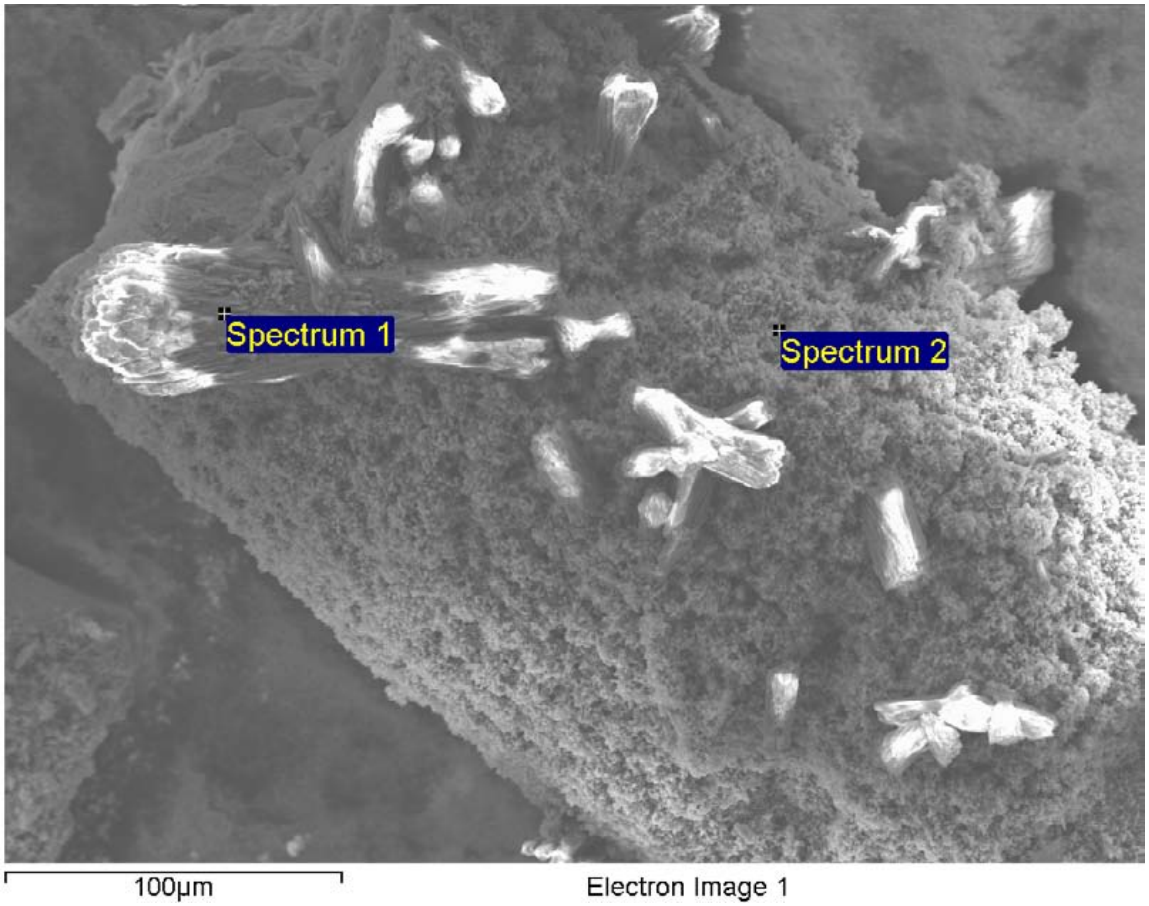

Figure A-96. Surface of whiskers on iron electrode 2 and EDX analysis at position of Spectrum 1

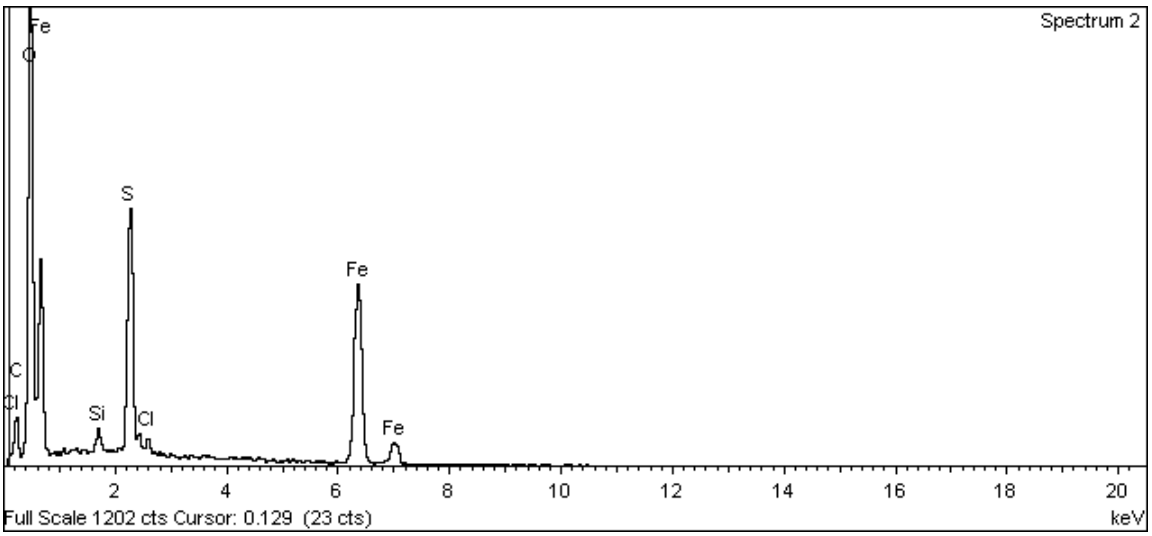

Figure A-97. Surface of whiskers on iron electrode 2 and EDX analysis at position of Spectrum 2

Silver – Silver Chloride electrode

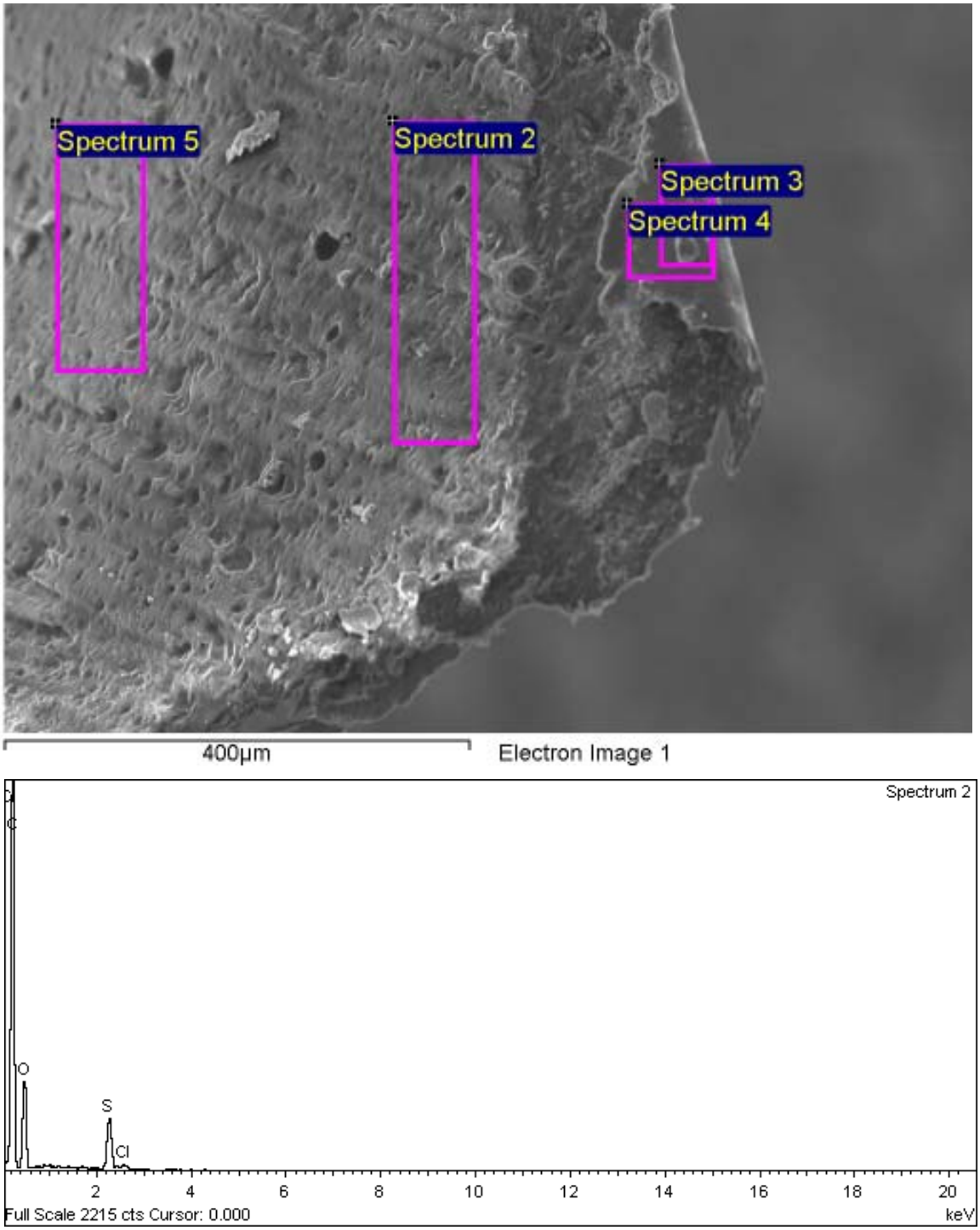

Figure A-98. Surface of silver-silver chloride electrode and EDX analysis at position of Spectrum 2

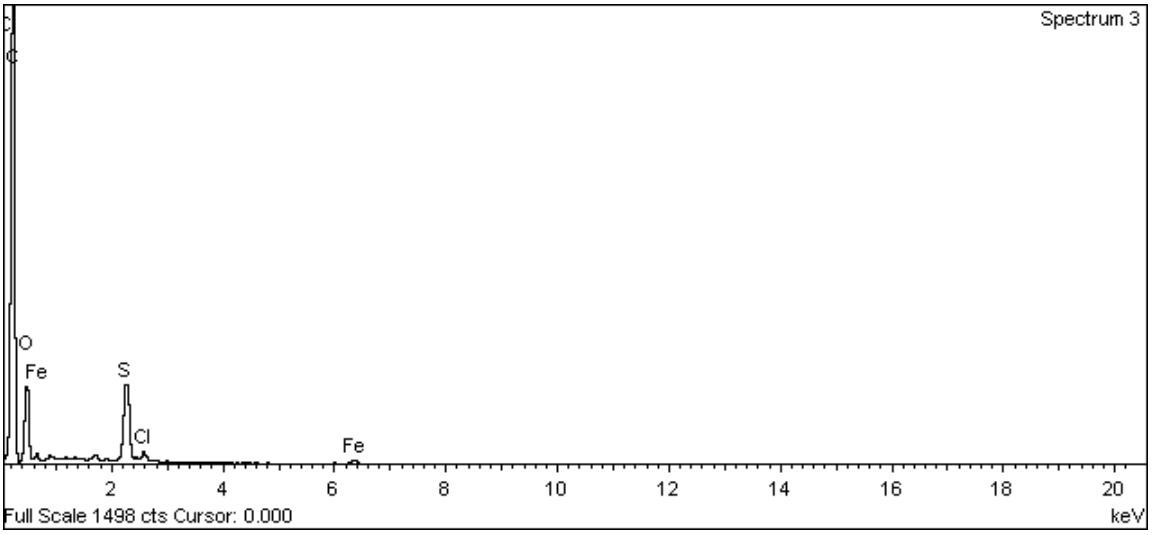

Figure A-99. Surface of silver-silver chloride electrode and EDX analysis at position of Spectrum 3

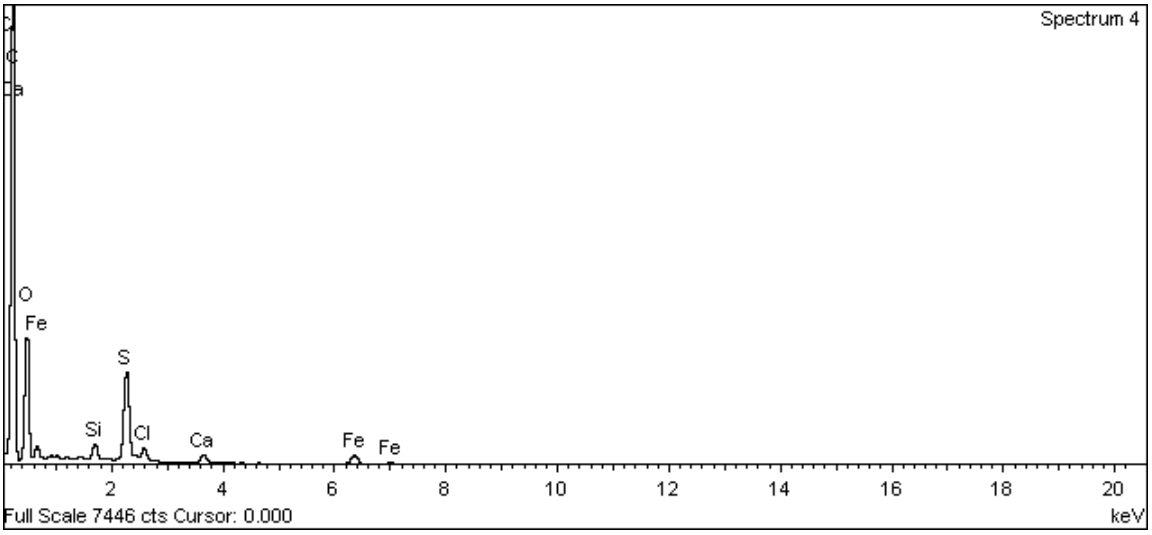

Figure A-100. Surface of silver-silver chloride electrode and EDX analysis at position of Spectrum 4

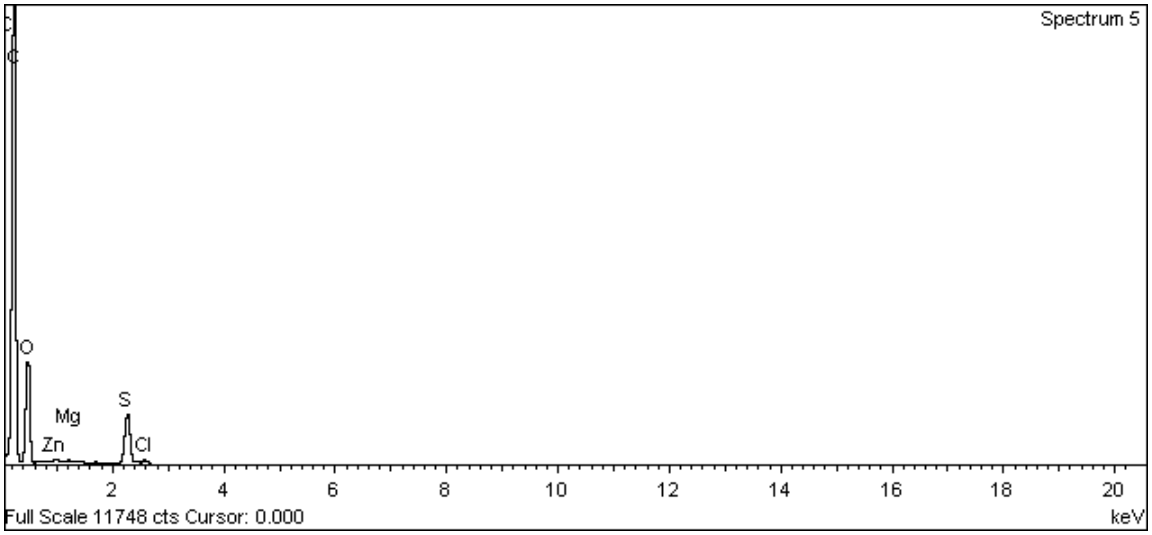

Figure A-101. Surface of silver-silver chloride electrode and EDX analysis at position of Spectrum 5

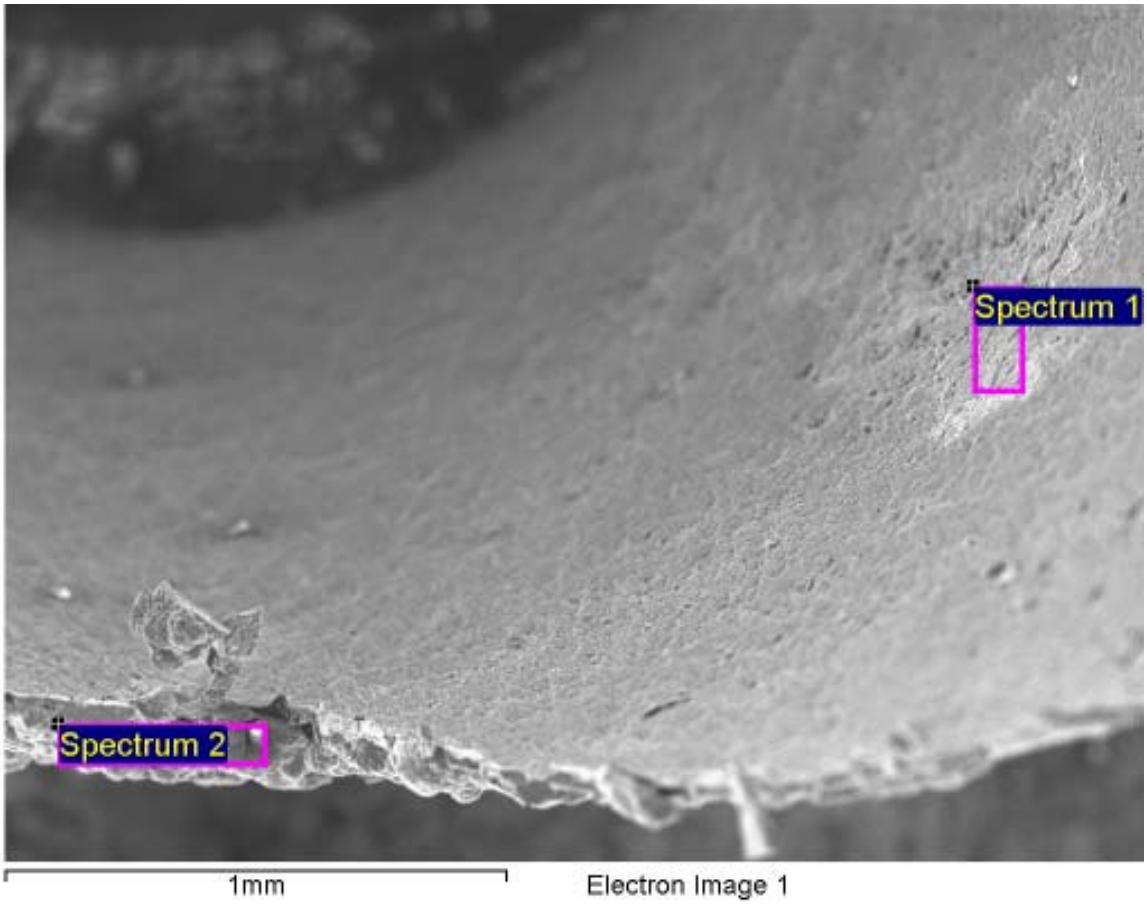

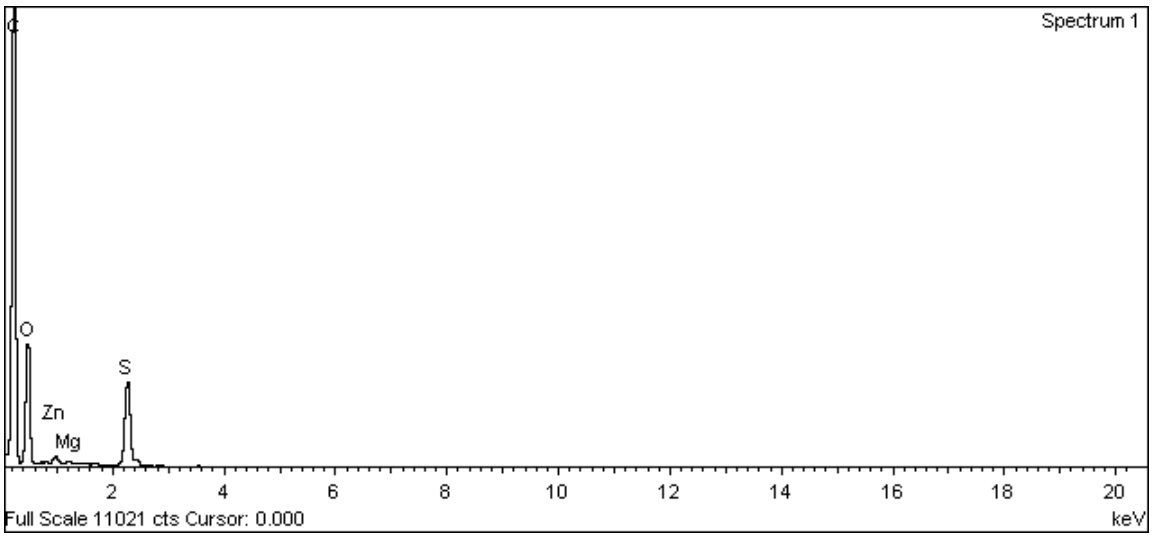

Figure A-102. Surface of silver-silver chloride electrode and EDX analysis at position of Spectrum 1

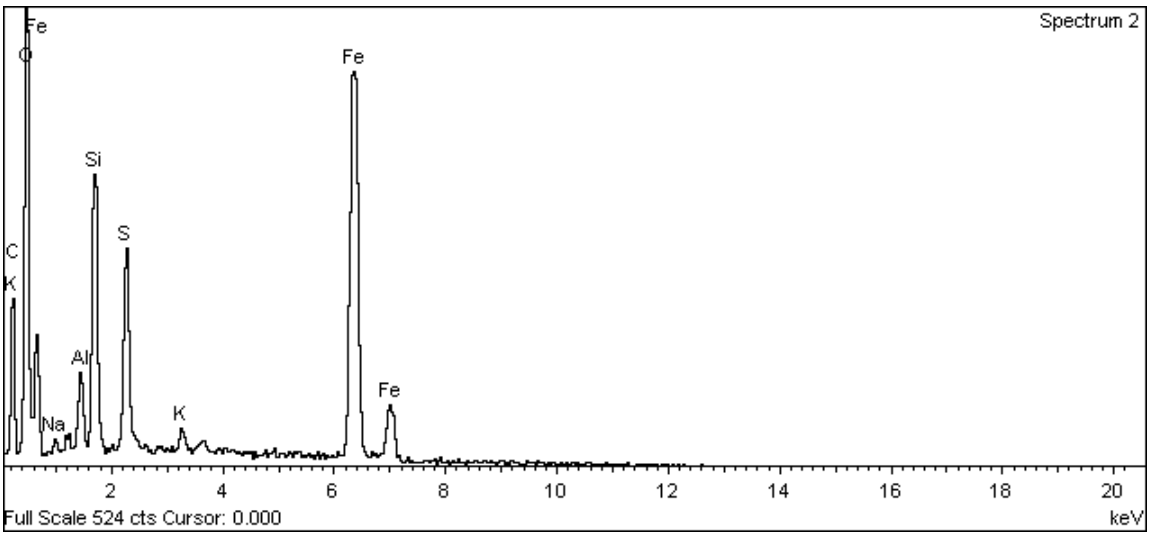

Figure A-103. Surface of silver-silver chloride electrode and EDX analysis at position of Spectrum 2

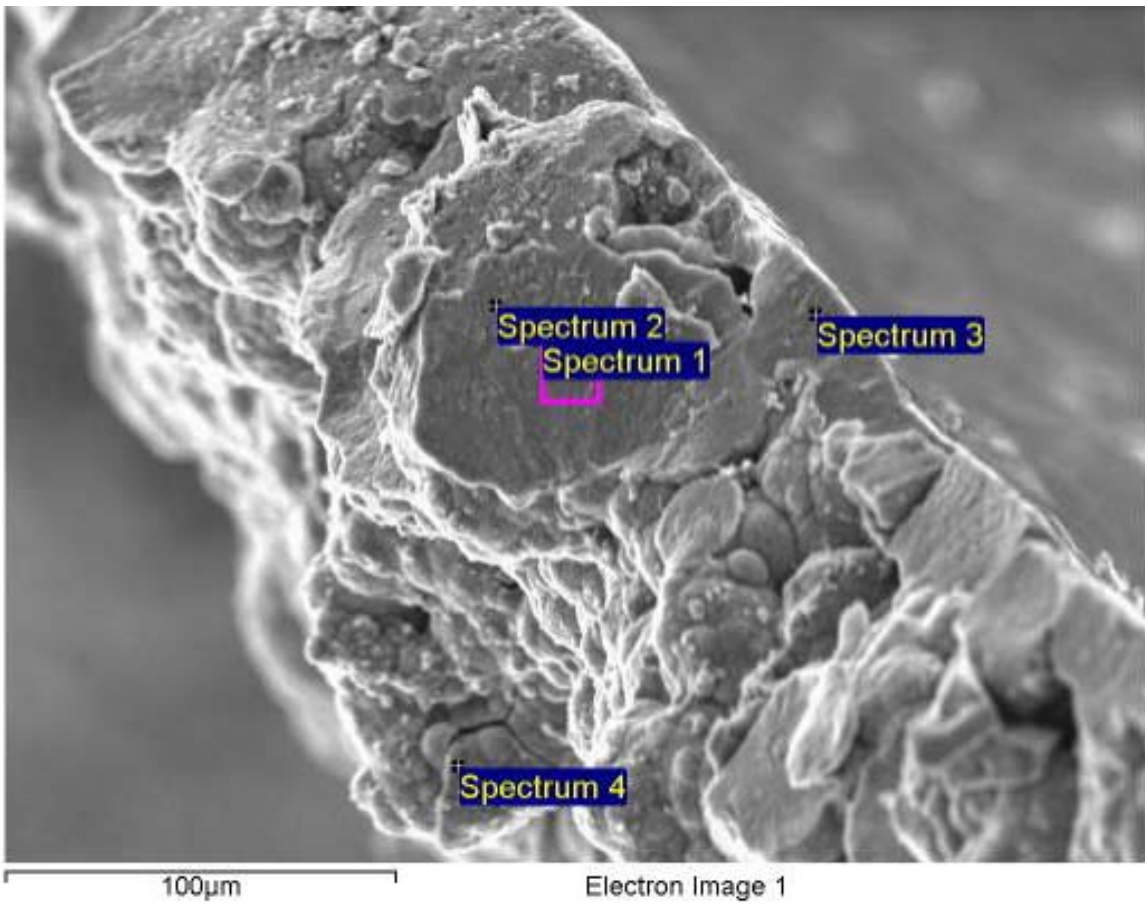

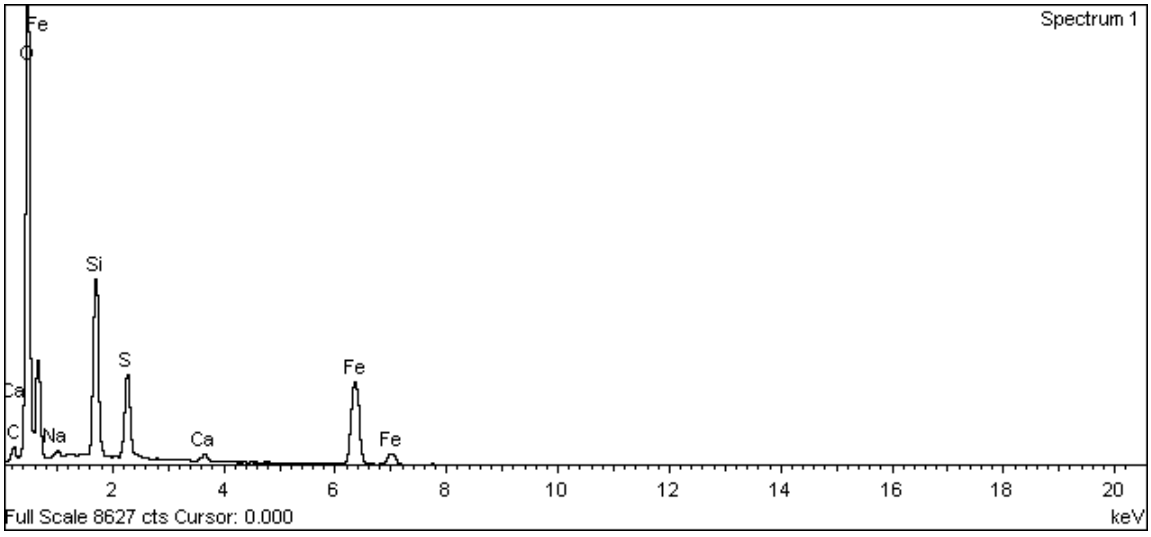

Figure A-104. Surface of silver-silver chloride electrode and EDX analysis at position of Spectrum 1

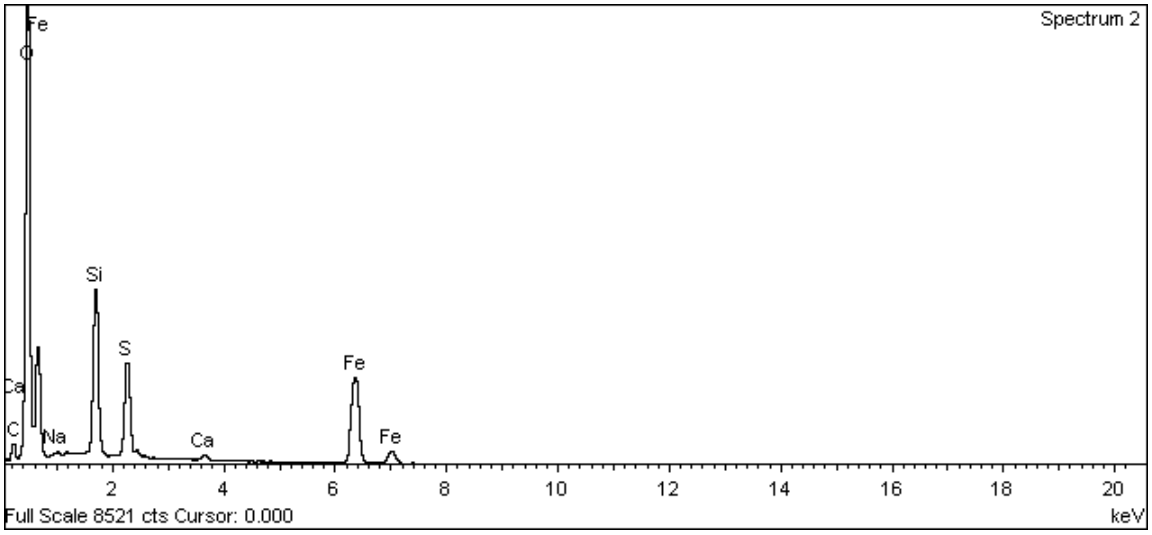

Figure A-105. Surface of silver-silver chloride electrode and EDX analysis at position of Spectrum 2

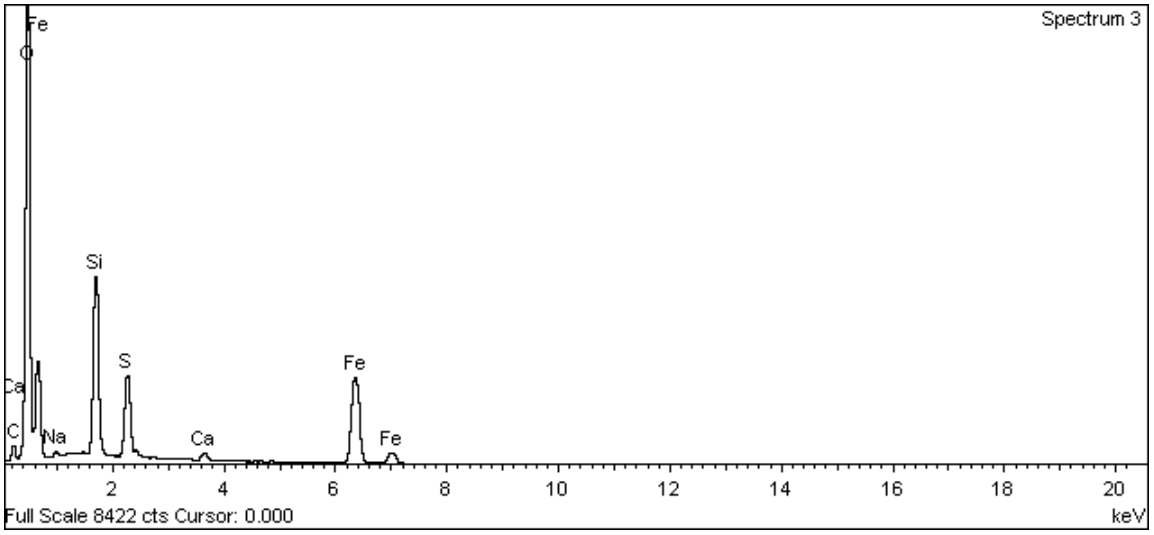

Figure A-106. Surface of silver-silver chloride electrode and EDX analysis at position of Spectrum 3

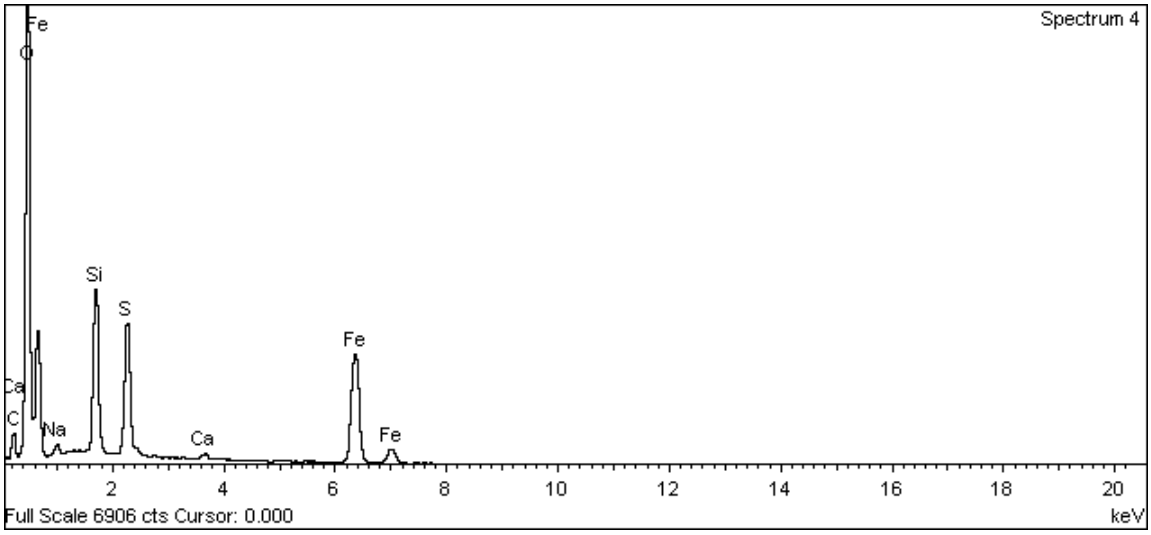

Figure A-107. Surface of silver-silver chloride electrode and EDX analysis at position of Spectrum 4

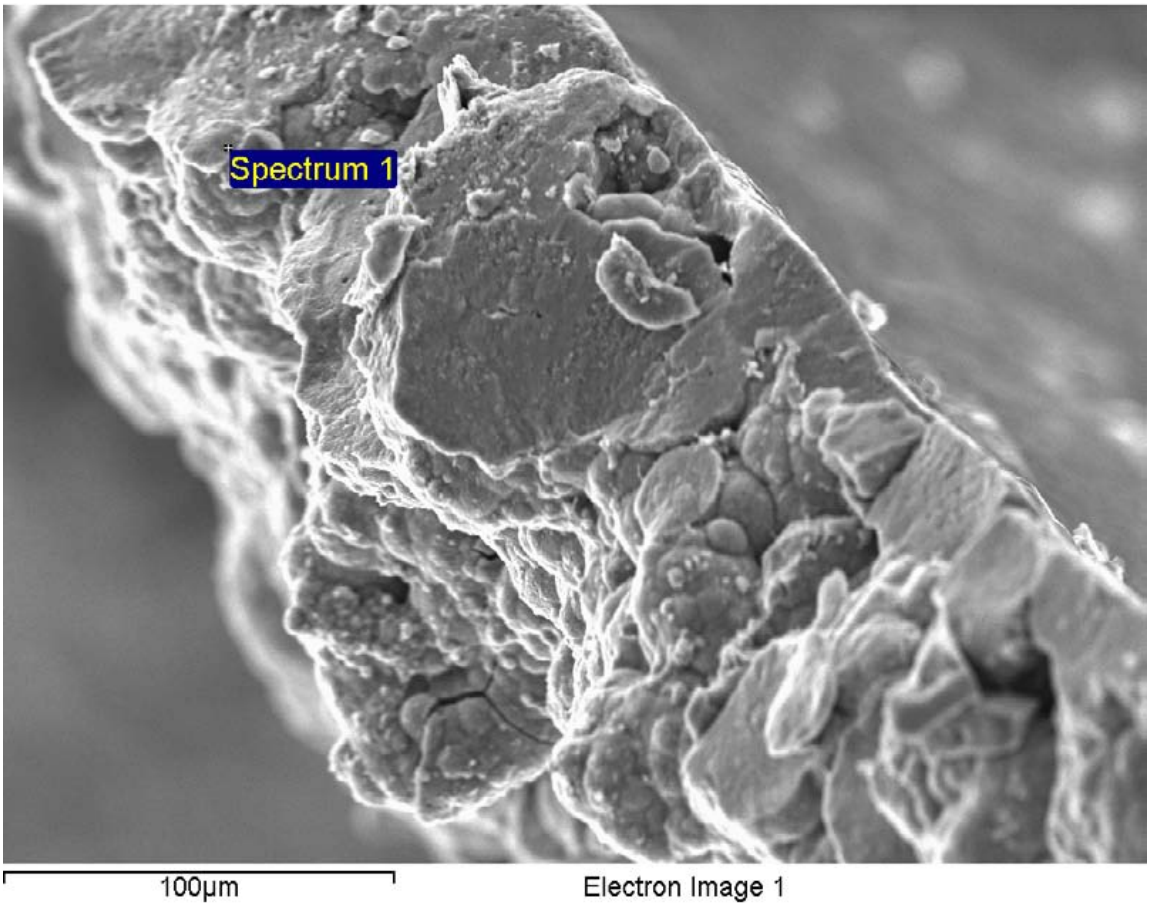

Figure A-108. Surface of silver-silver chloride electrode and EDX analysis at position of Spectrum 1

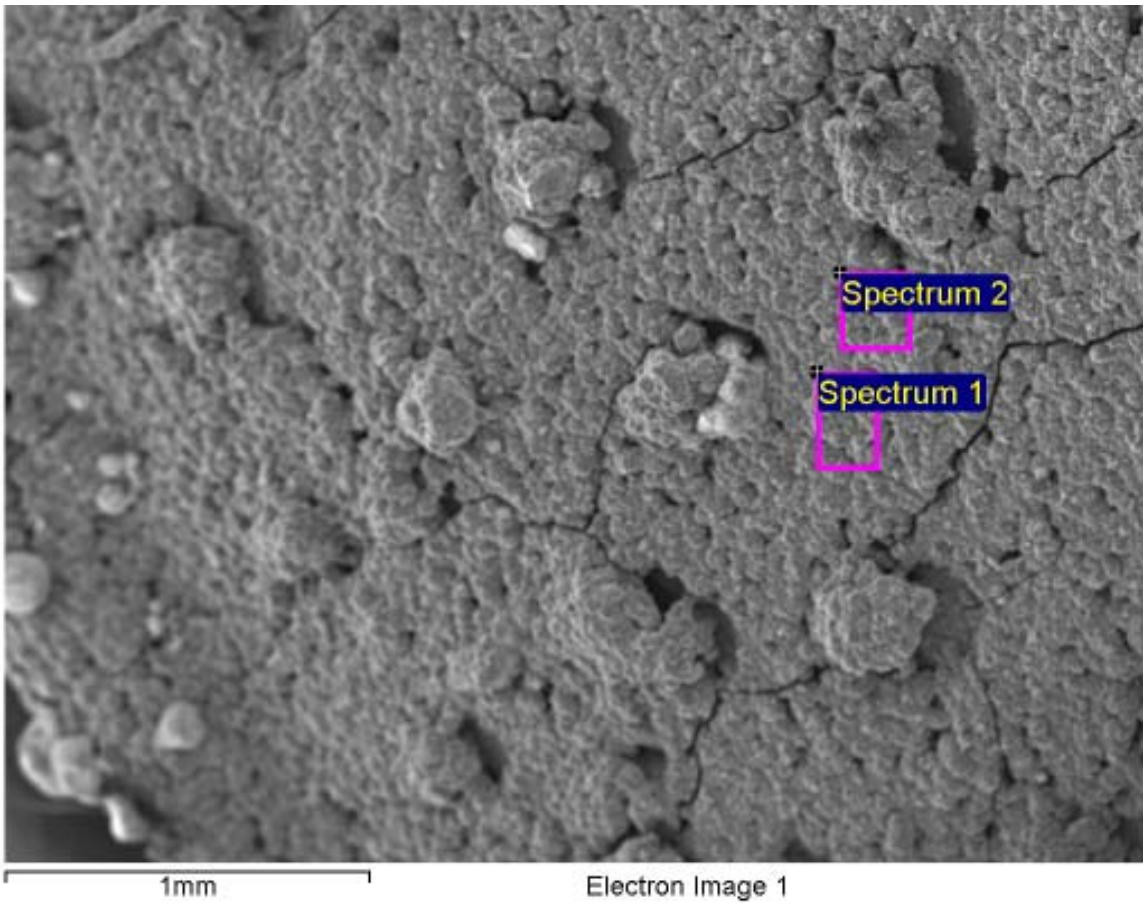

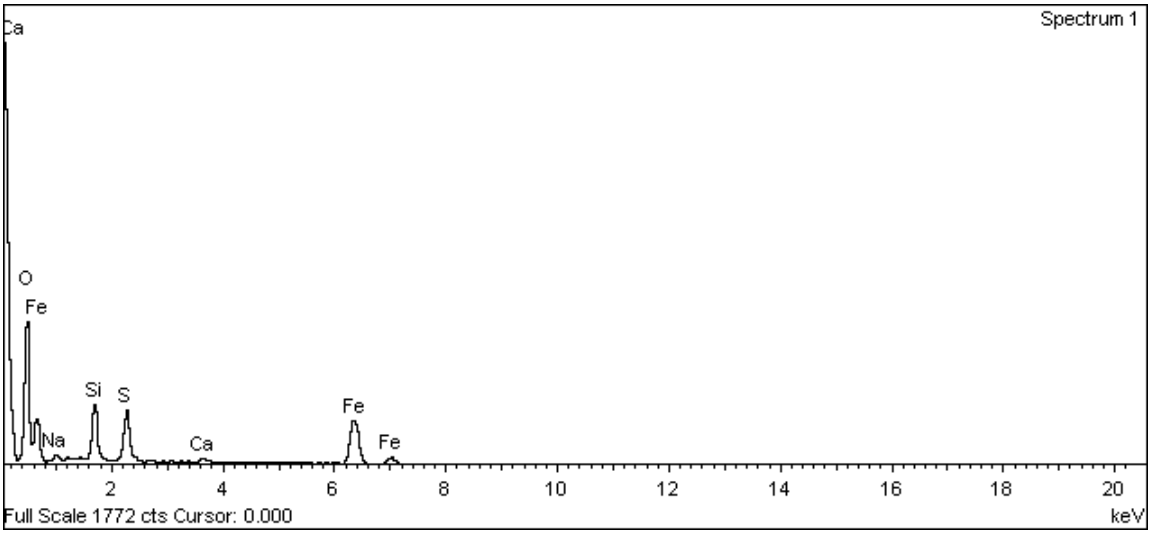

Figure A-109. Surface of silver-silver chloride electrode and EDX analysis at position of Spectrum 1

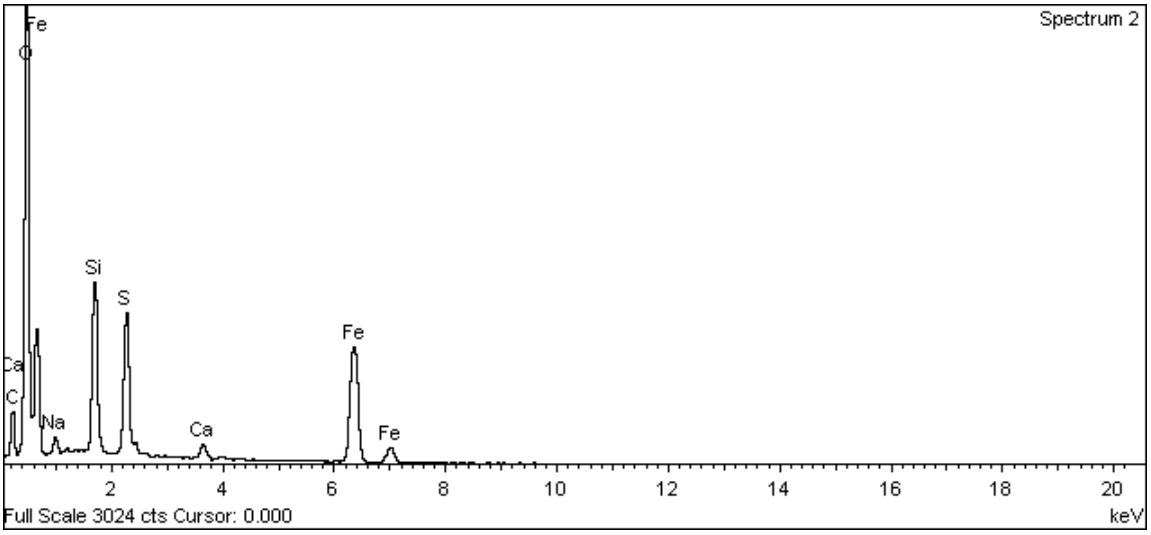

Figure A-110. Surface of silver-silver chloride electrode and EDX analysis at position of Spectrum 2

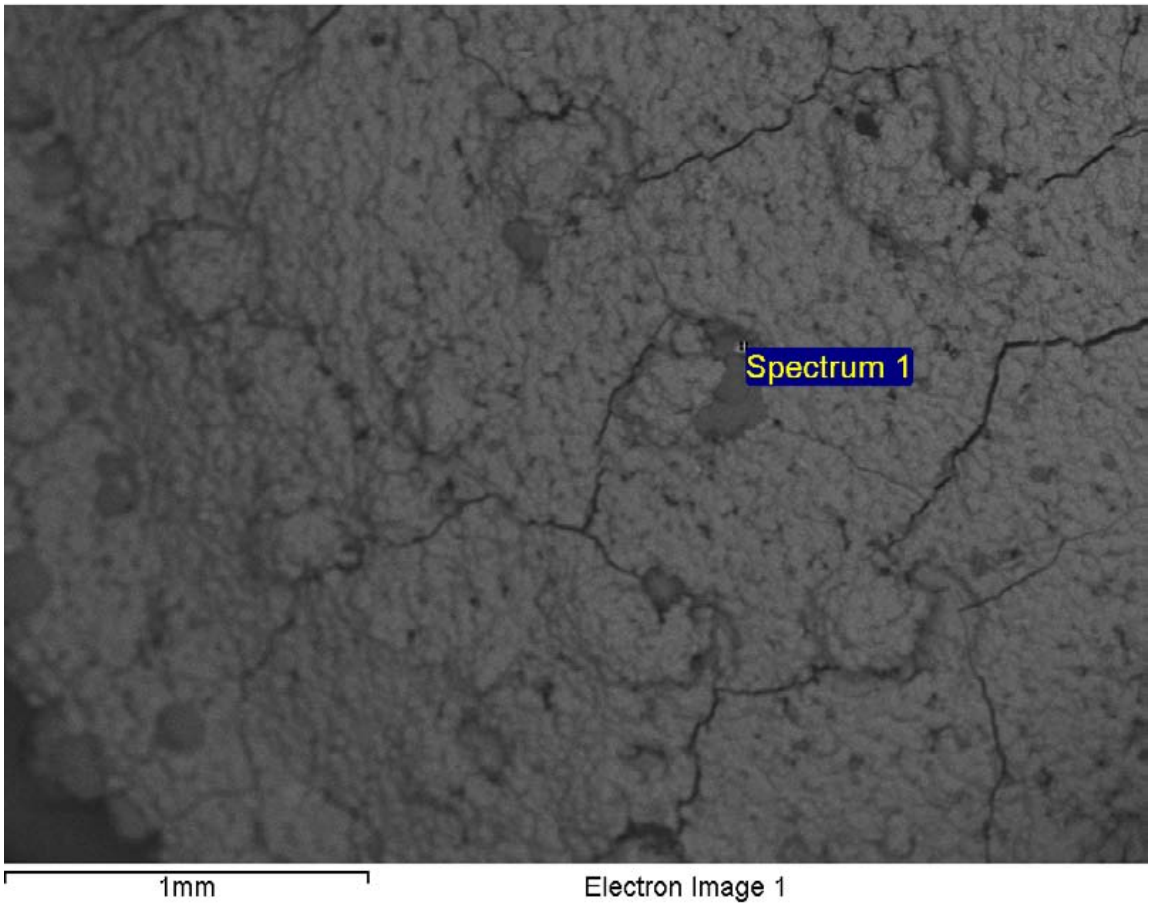

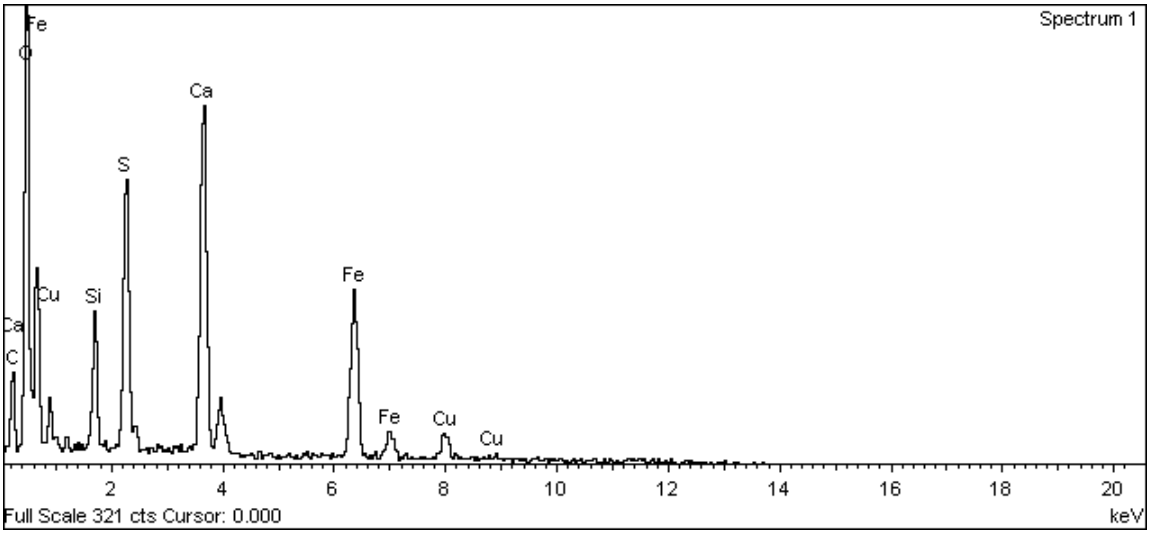

Figure A-111. Surface of silver-silver chloride electrode and EDX analysis at position of Spectrum 1

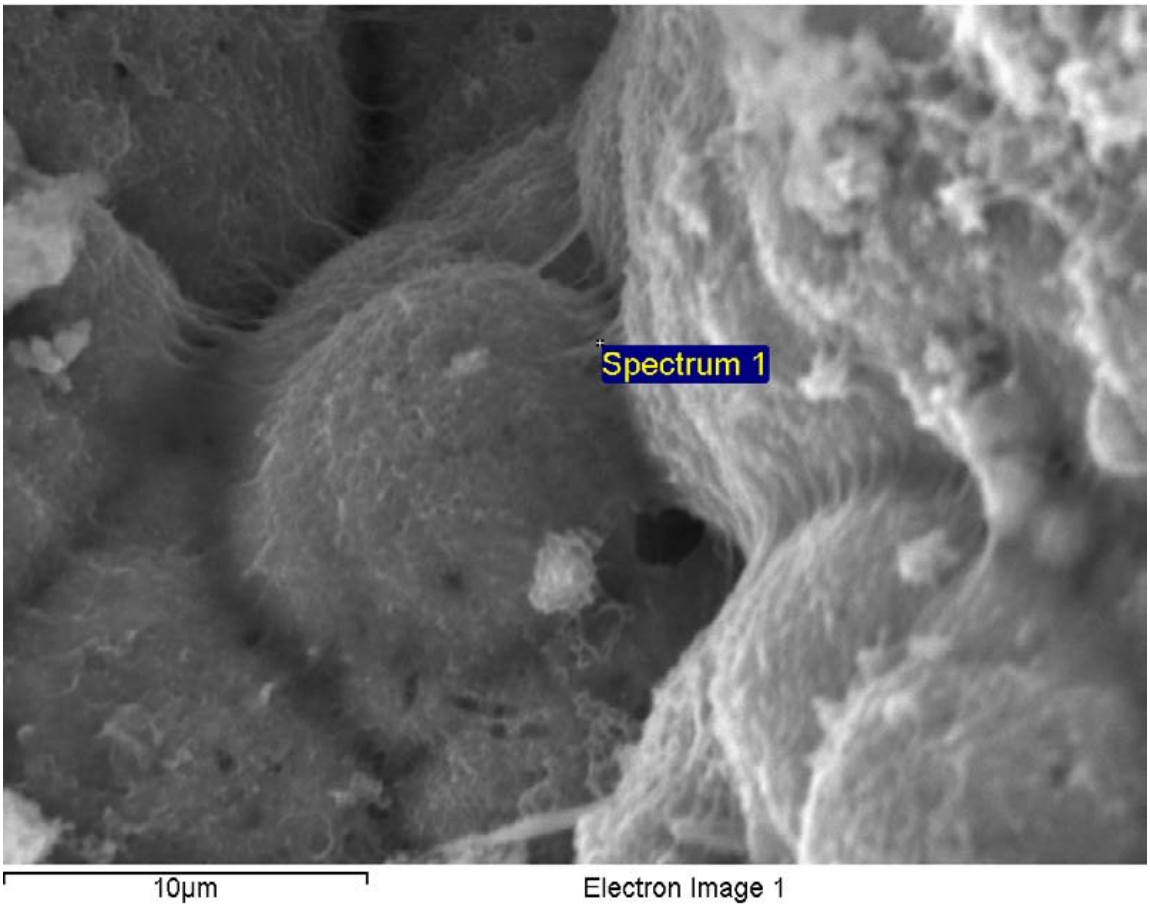

Figure A-112. Surface of silver-silver chloride electrode and EDX analysis at position of Spectrum 1

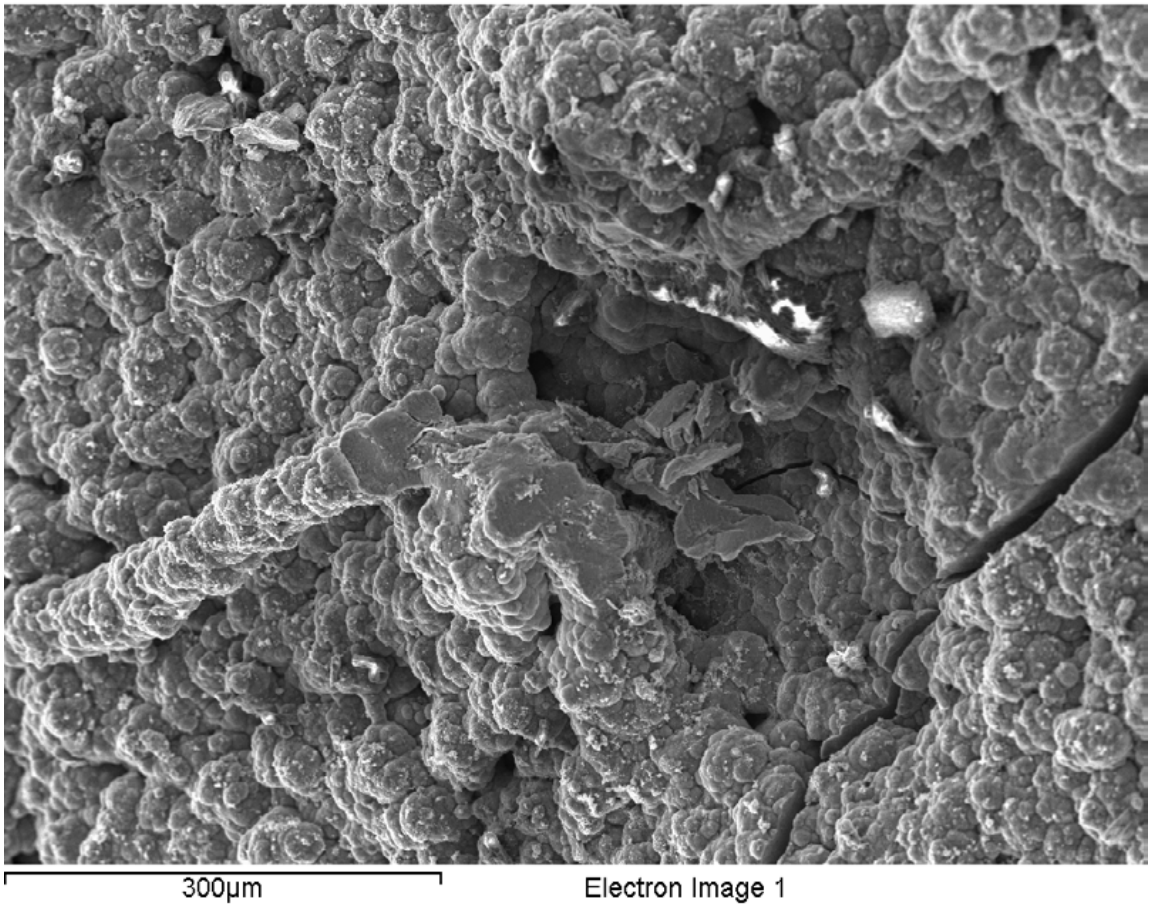

Figure A-113. Surface of silver-silver chloride electrode

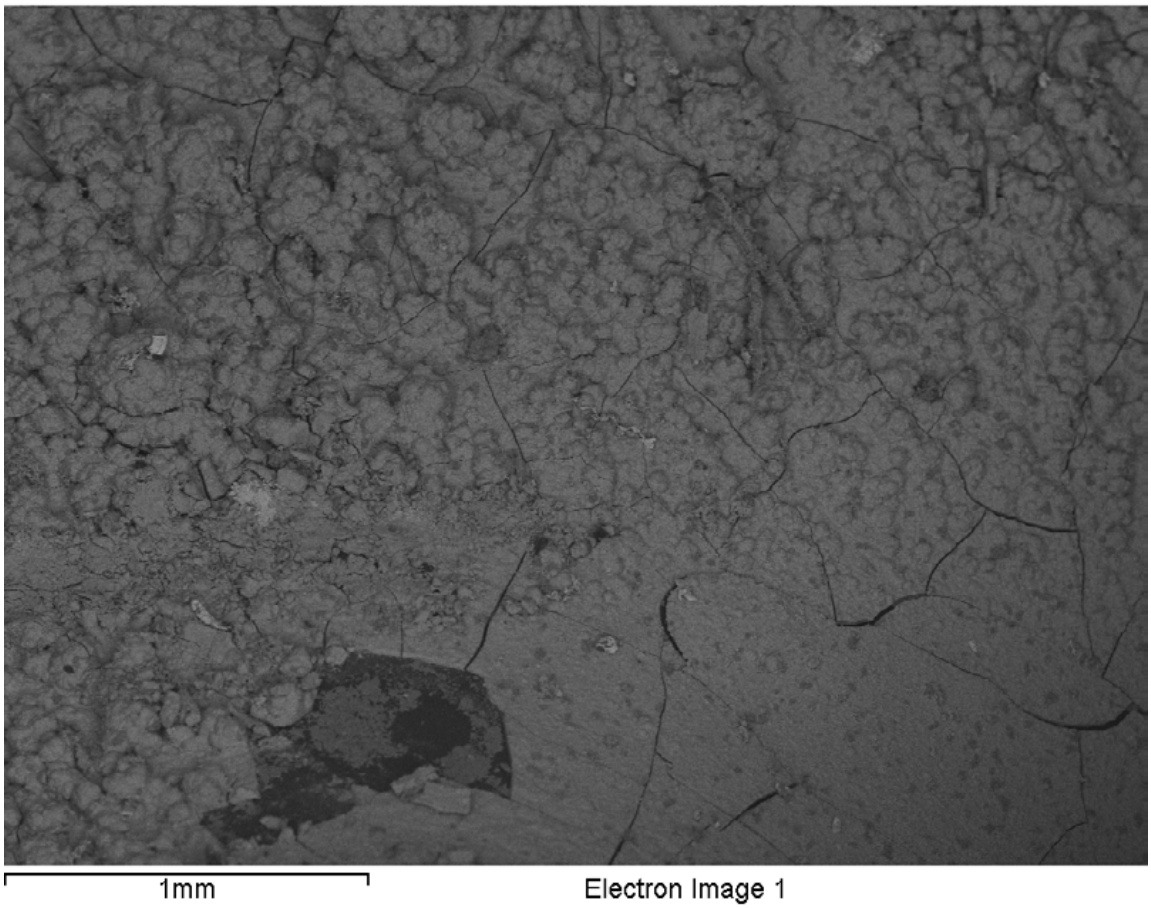

Figure A-114. Surface of silver-silver chloride electrode

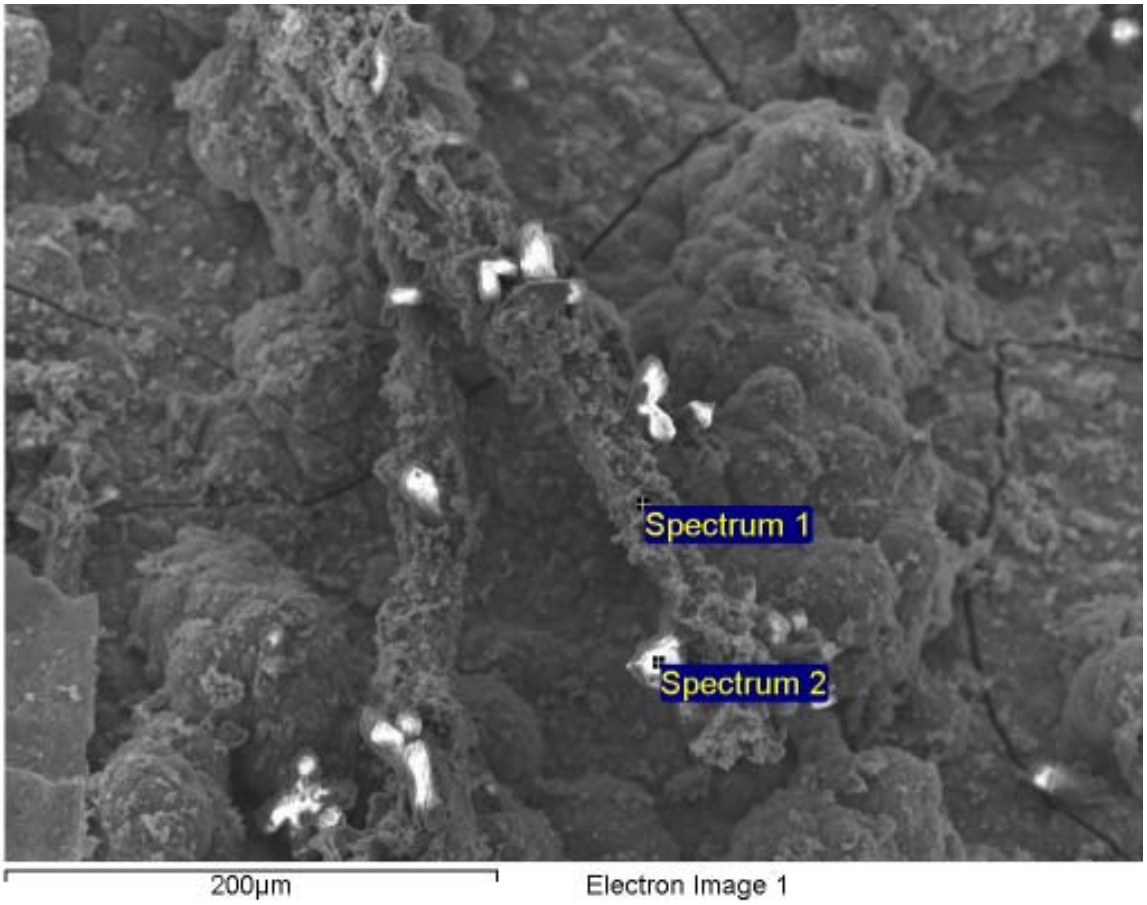

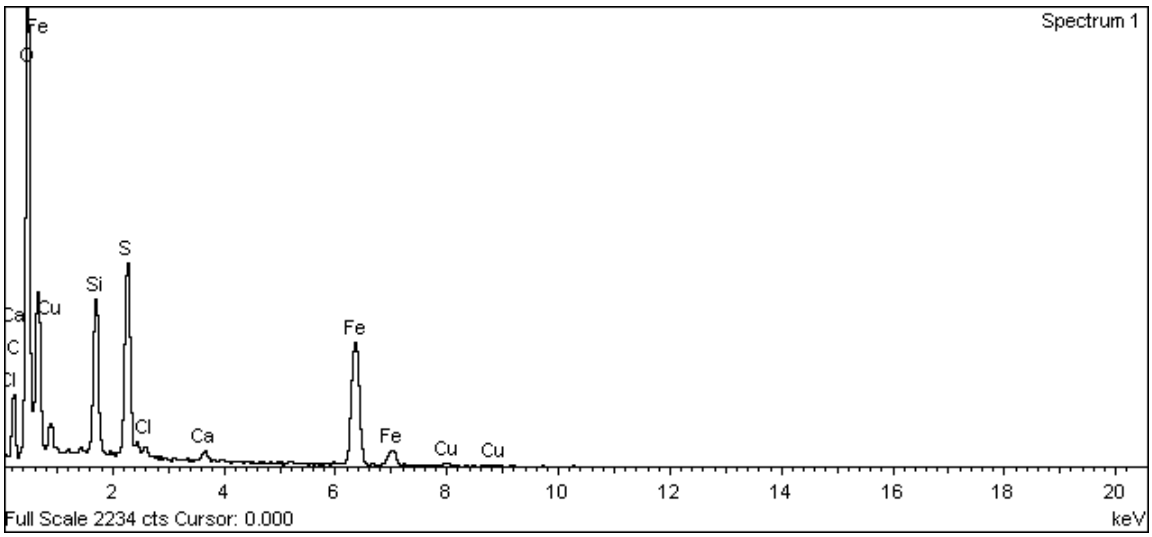

Figure A-115. Surface of silver-silver chloride electrode and EDX analysis at position of Spectrum 1

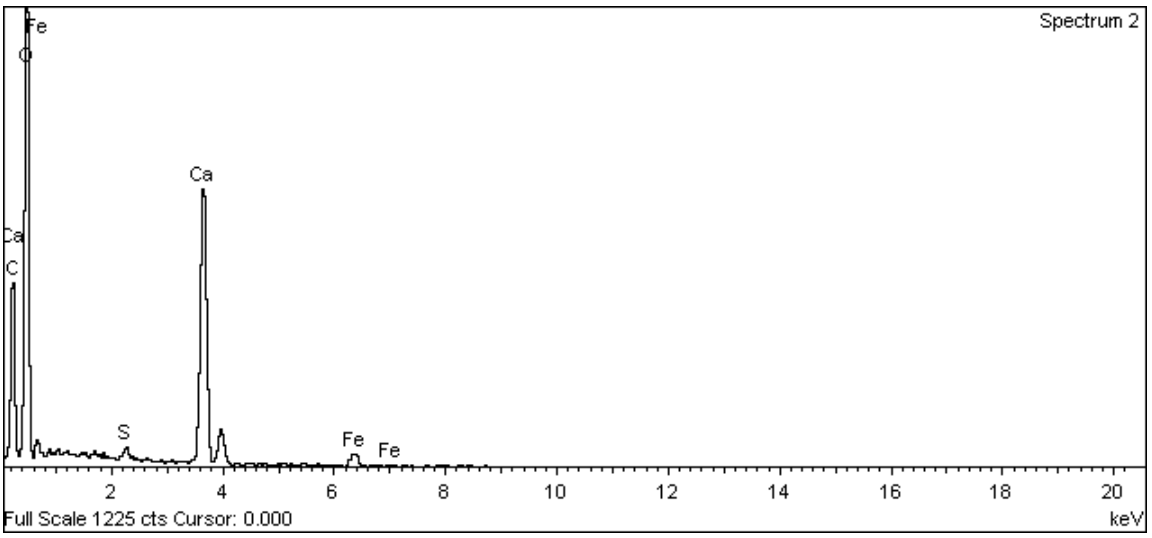

Figure A-116. Surface of silver-silver chloride electrode and EDX analysis at position of Spectrum 2

Black flakes from table

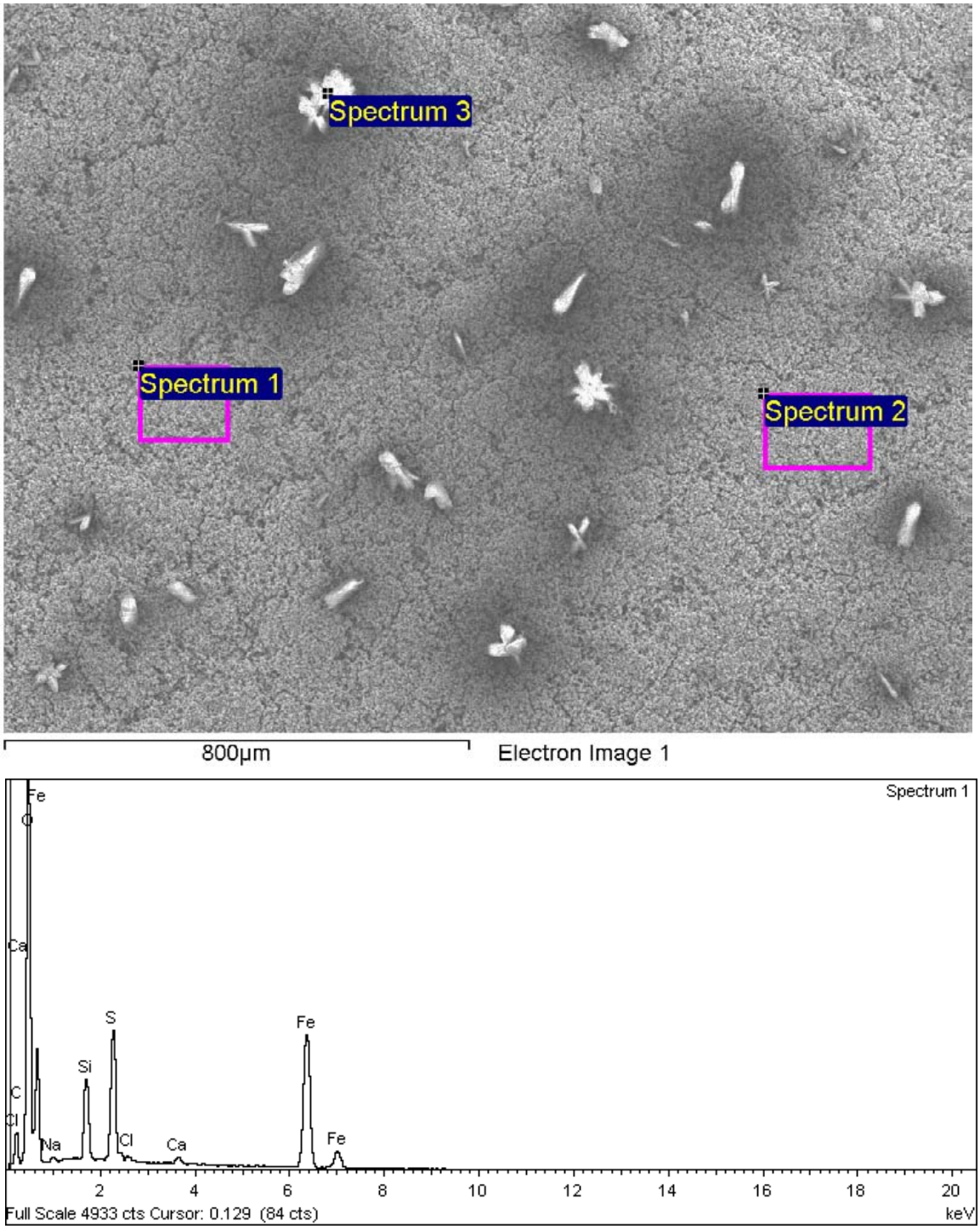

Figure A-117. Surface of black flakes from table and EDX analysis at position of Spectrum 1

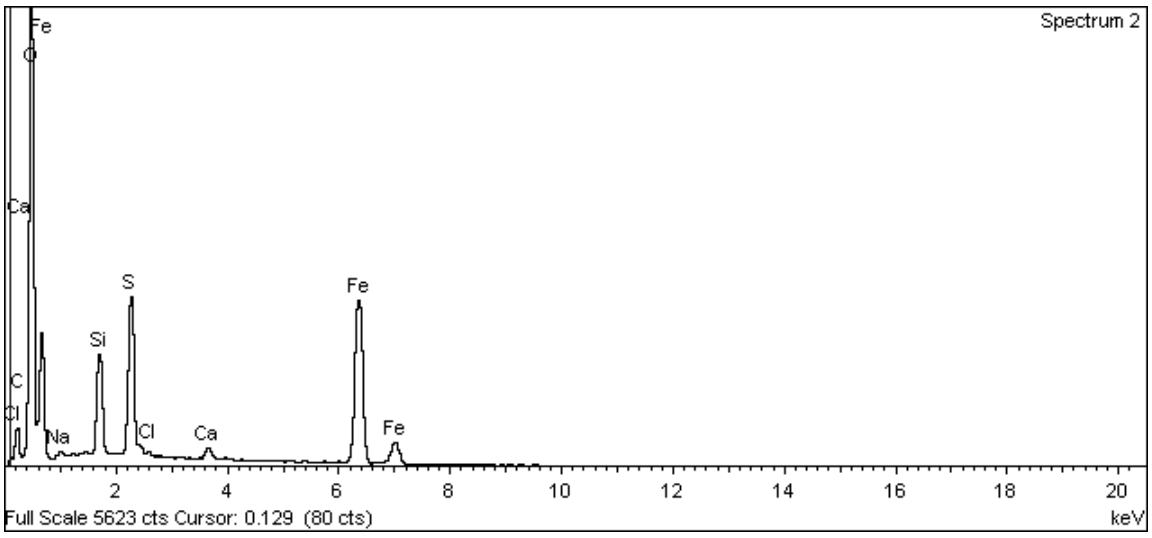

Figure A-118. Surface of black flakes from table and EDX analysis at position of Spectrum 2

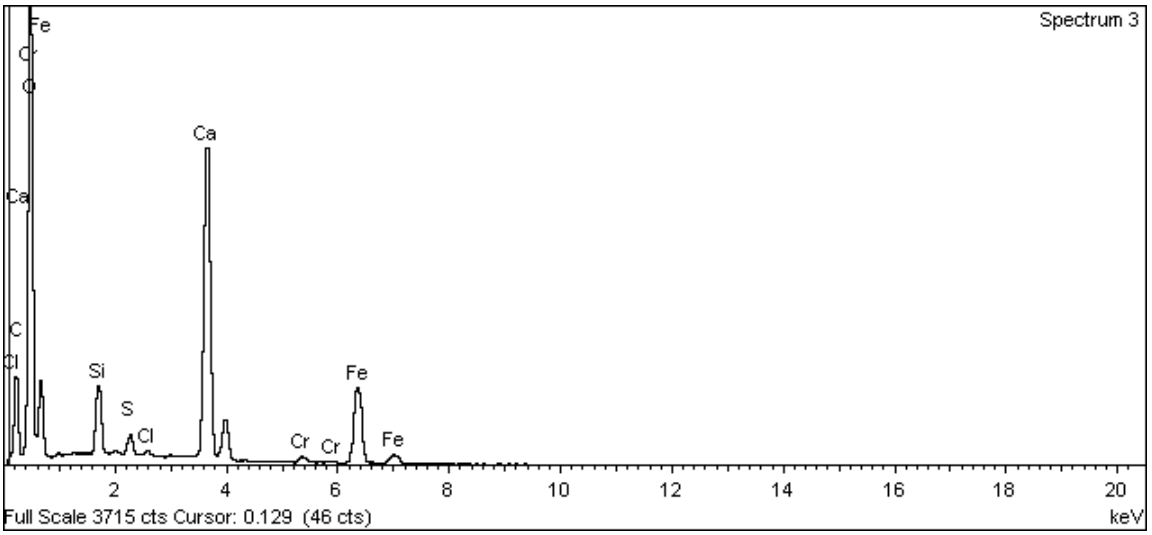

Figure A-119. Surface of black flakes from table and EDX analysis at position of Spectrum 3

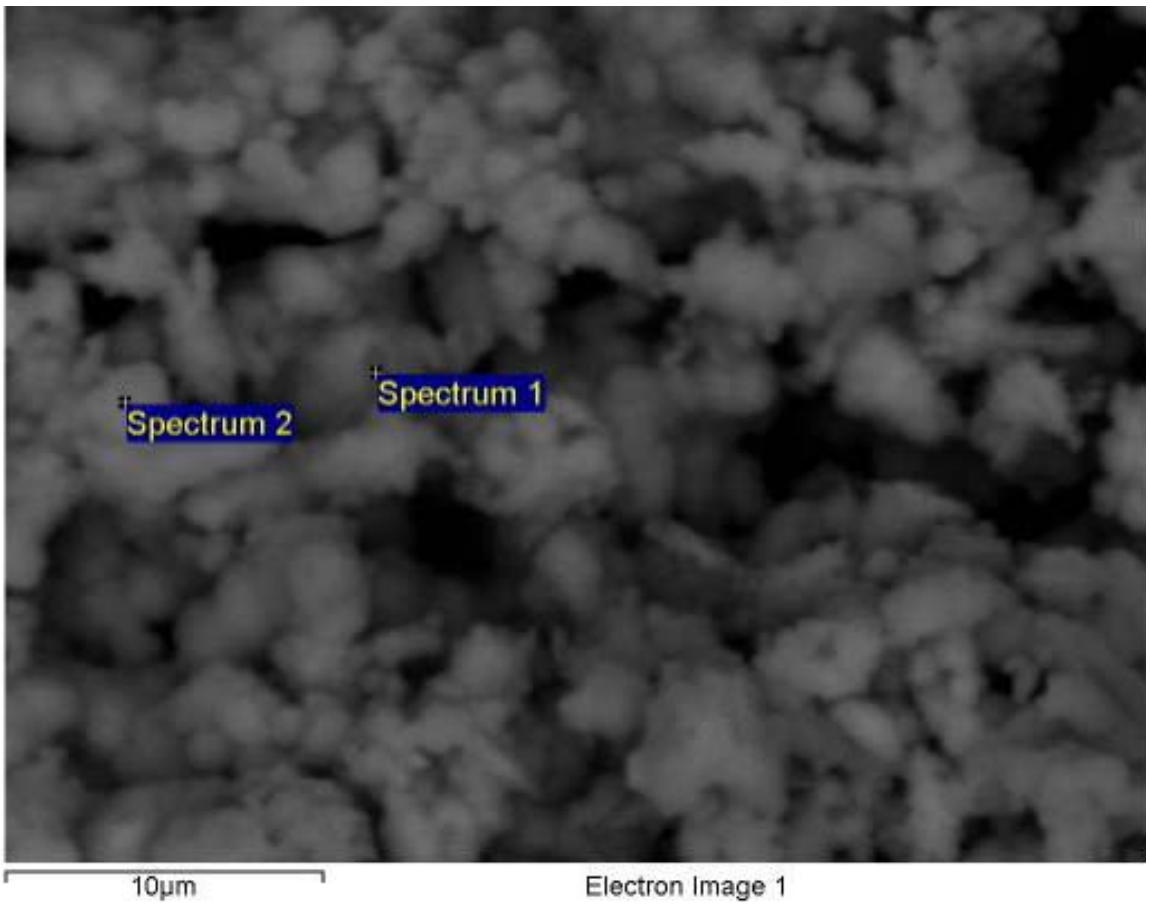

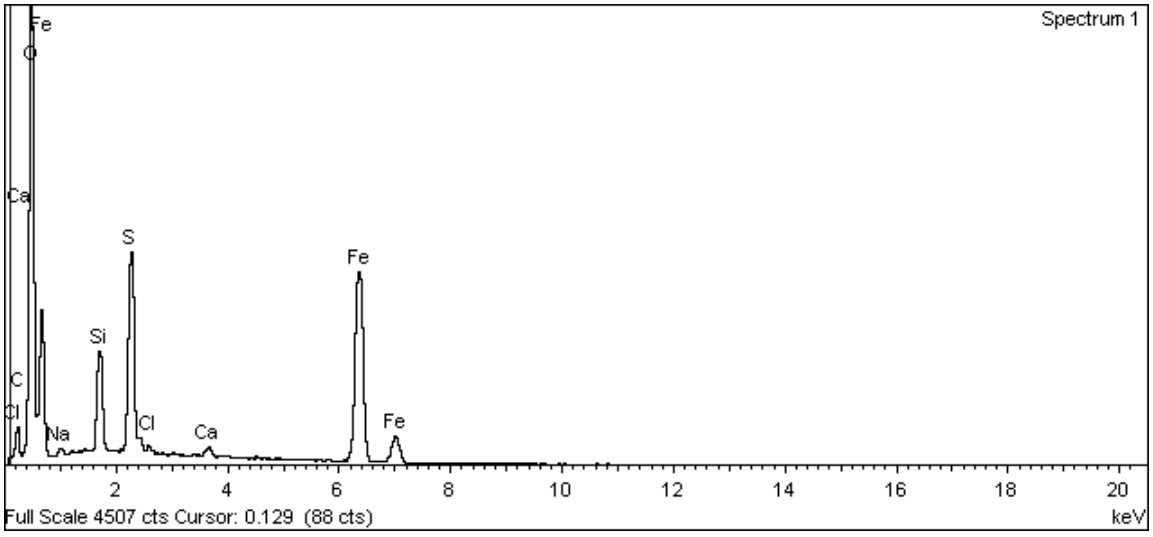

Figure A-120. Surface of black flakes from table and EDX analysis at position of Spectrum 1

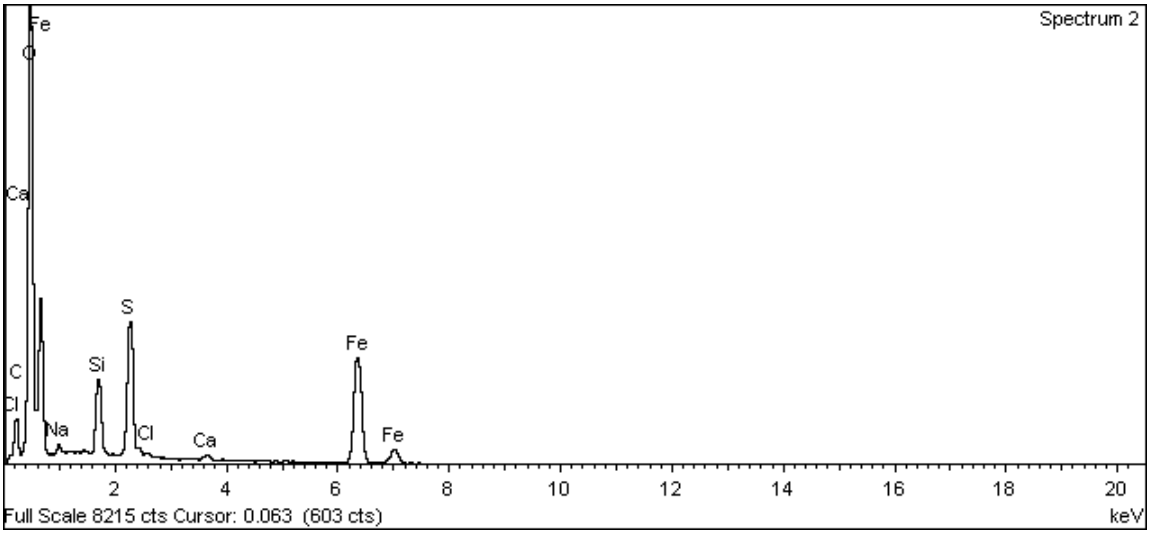

Figure A-121. Surface of black flakes from table and EDX analysis at position of Spectrum 2

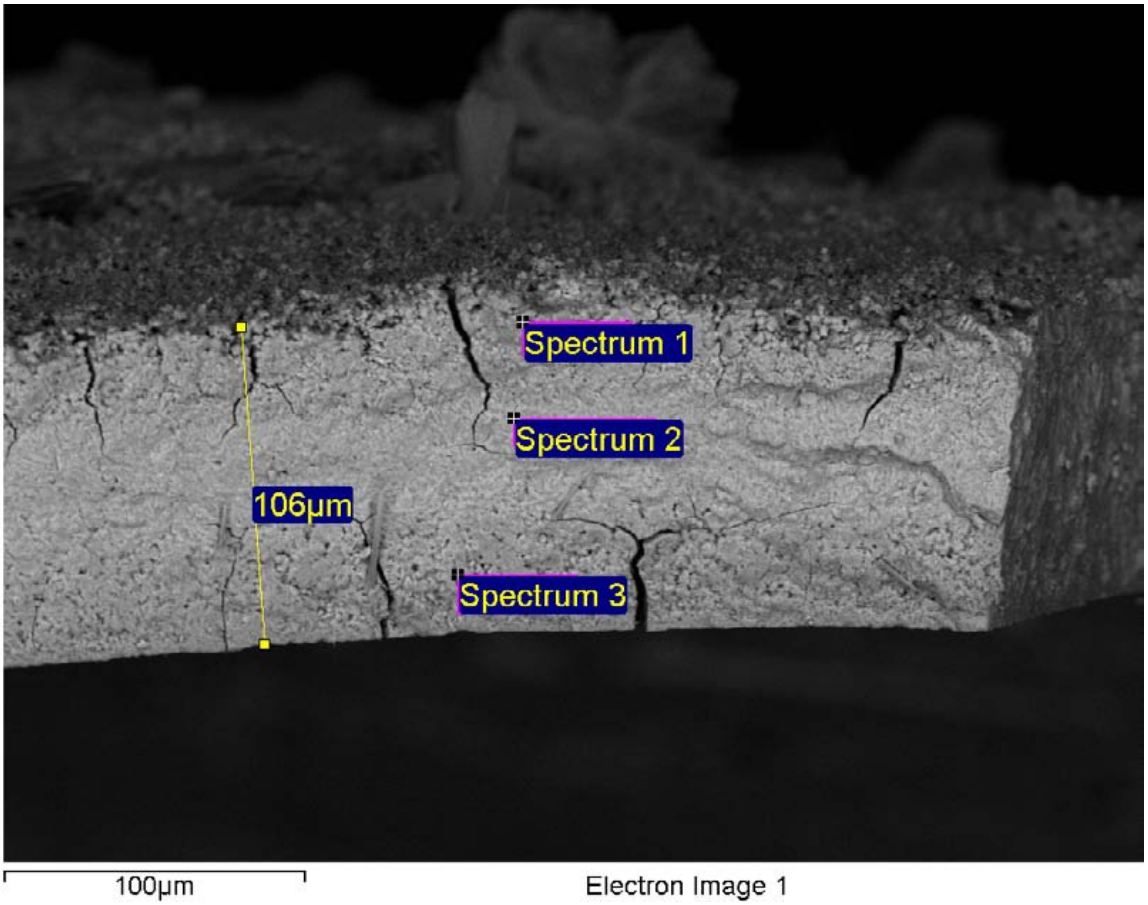

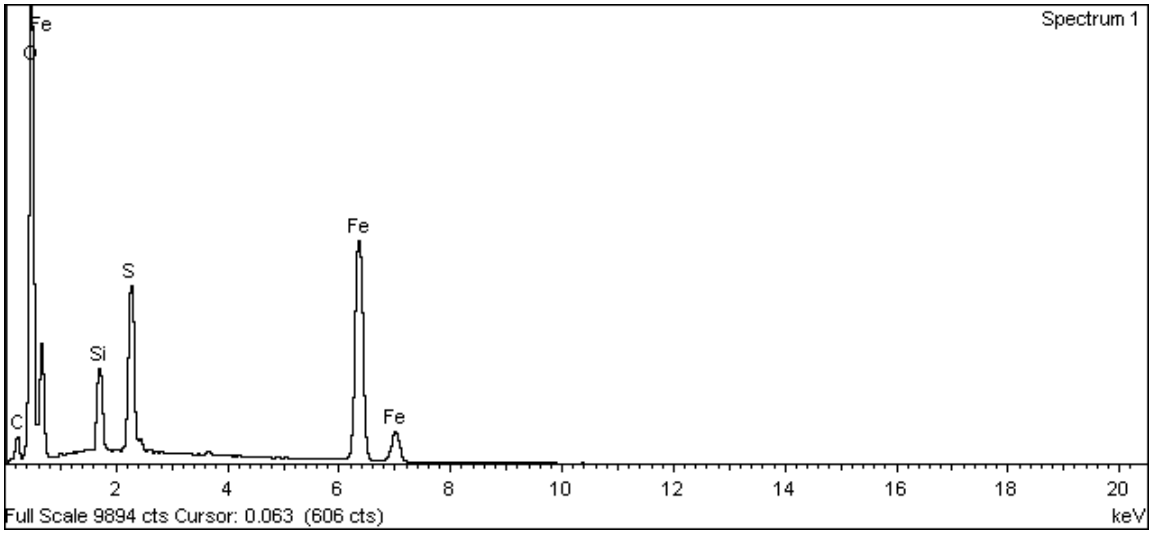

Figure A-122. Surface of black flakes from table and EDX analysis at position of Spectrum 1

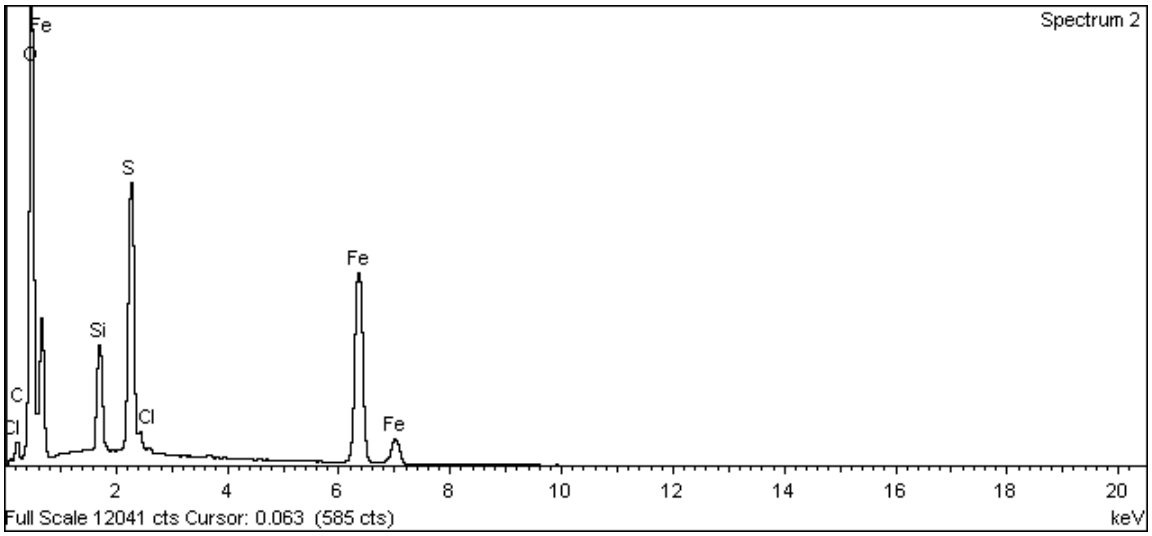

Figure A-123. Surface of black flakes from table and EDX analysis at position of Spectrum 2

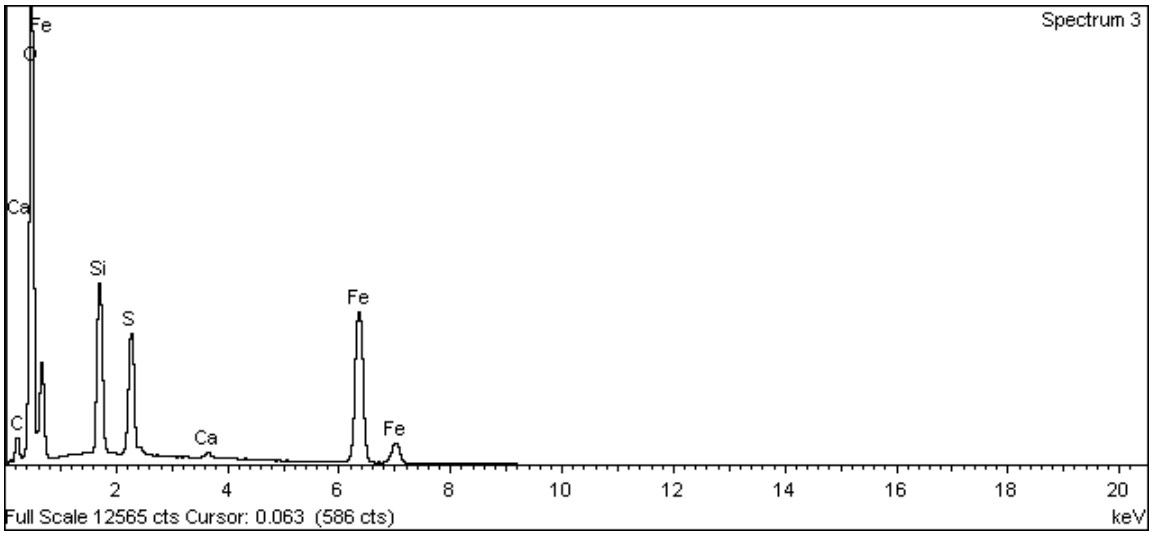

Figure A-124. Surface of black flakes from table and EDX analysis at position of Spectrum 3

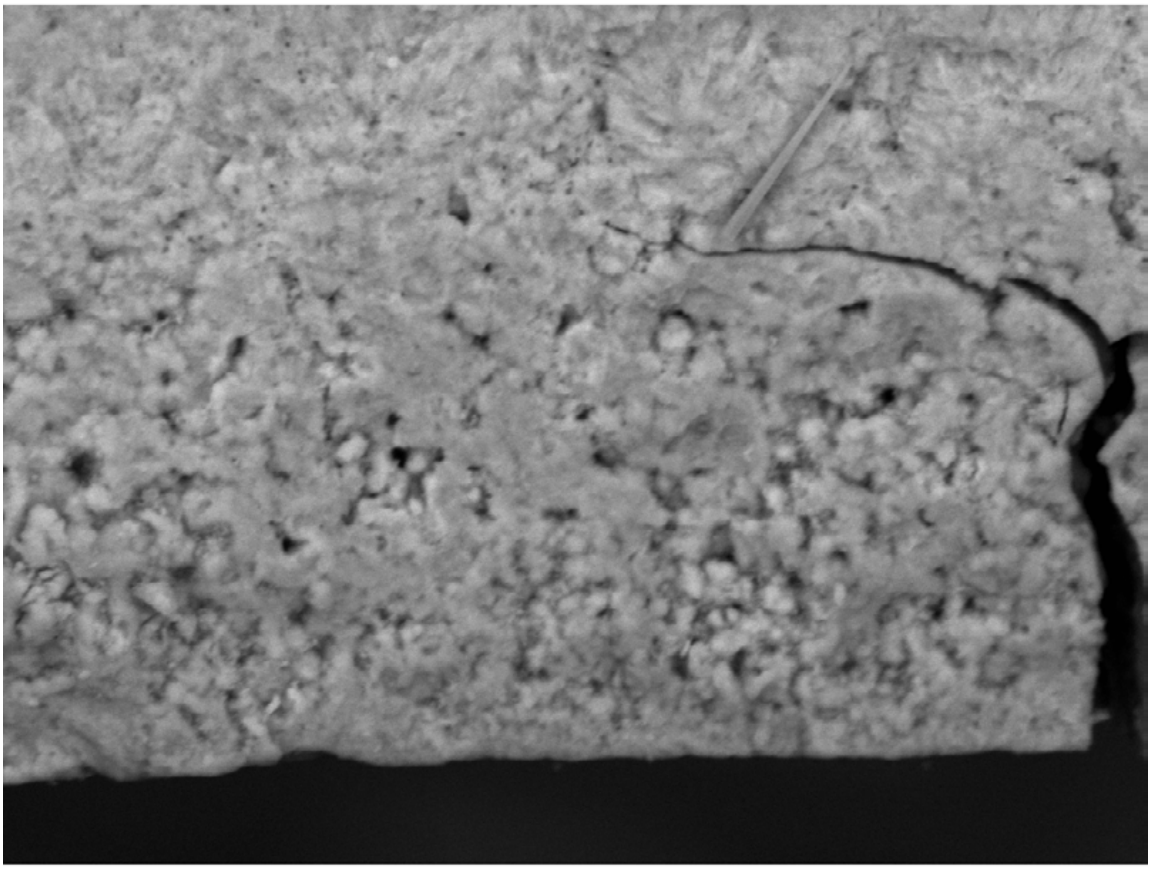

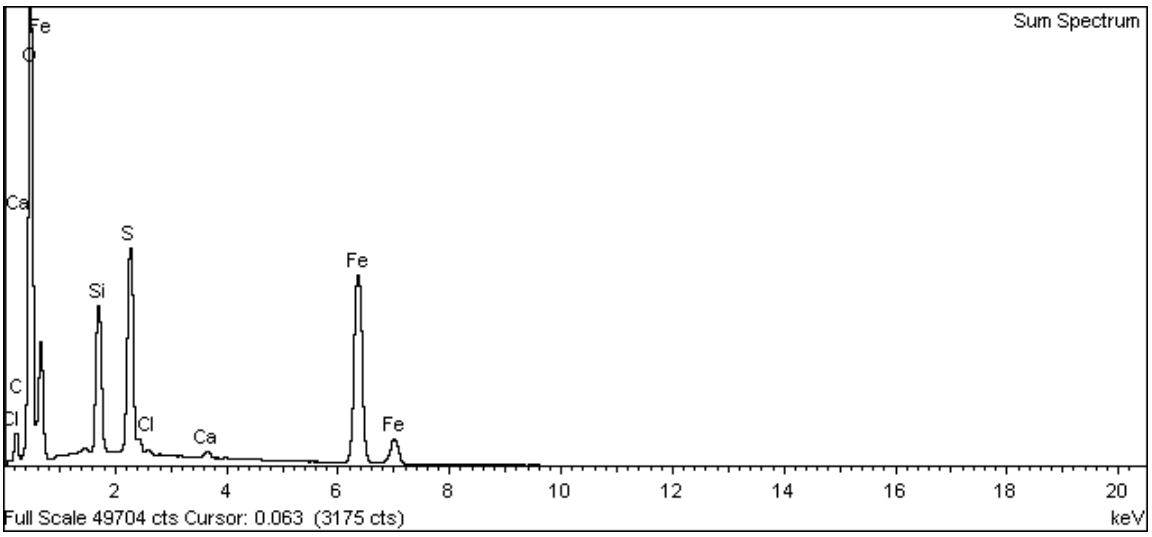

Figure A-125. Surface of black flakes from table and EDX analysis – Sum Spectrum

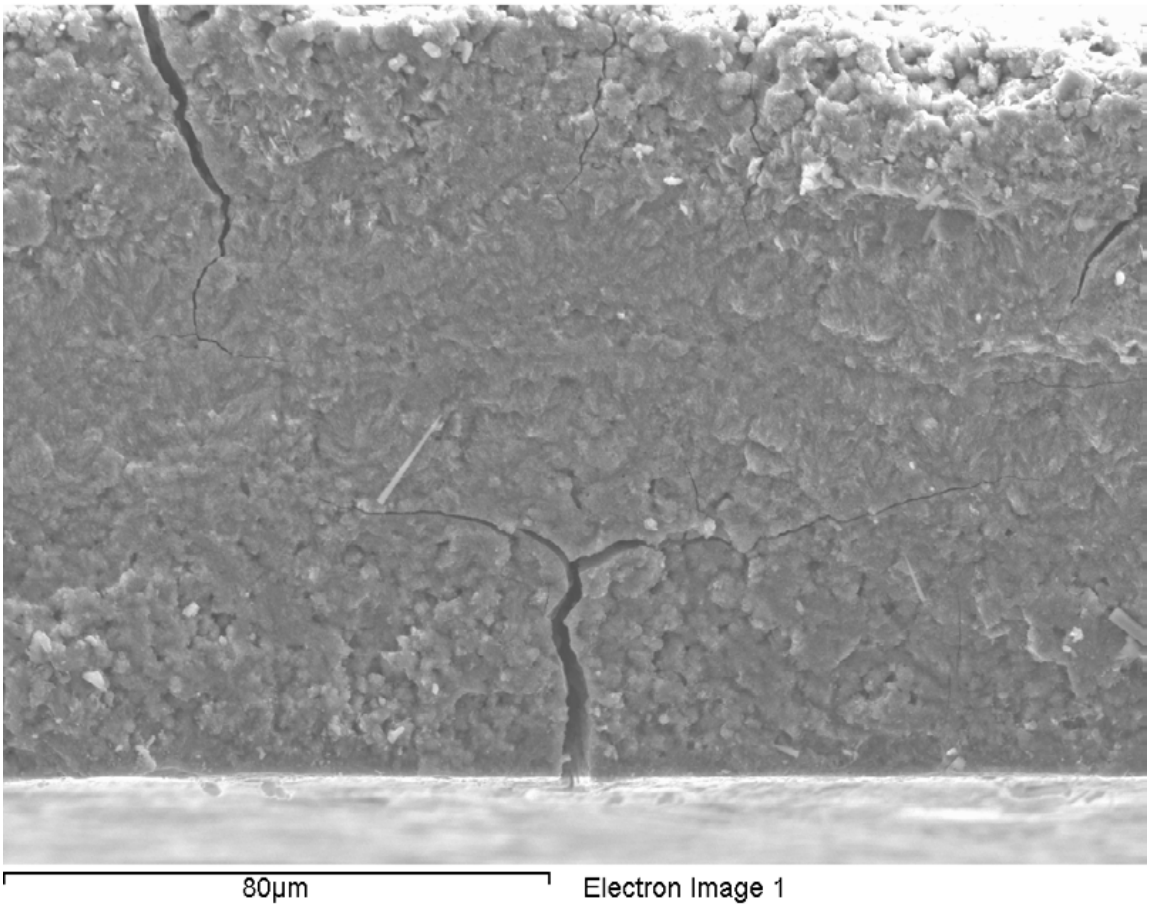

Figure A-126. Surface of black flakes from table and EDX analysis – Sum Spectrum

Black flakes from outer surface of canister

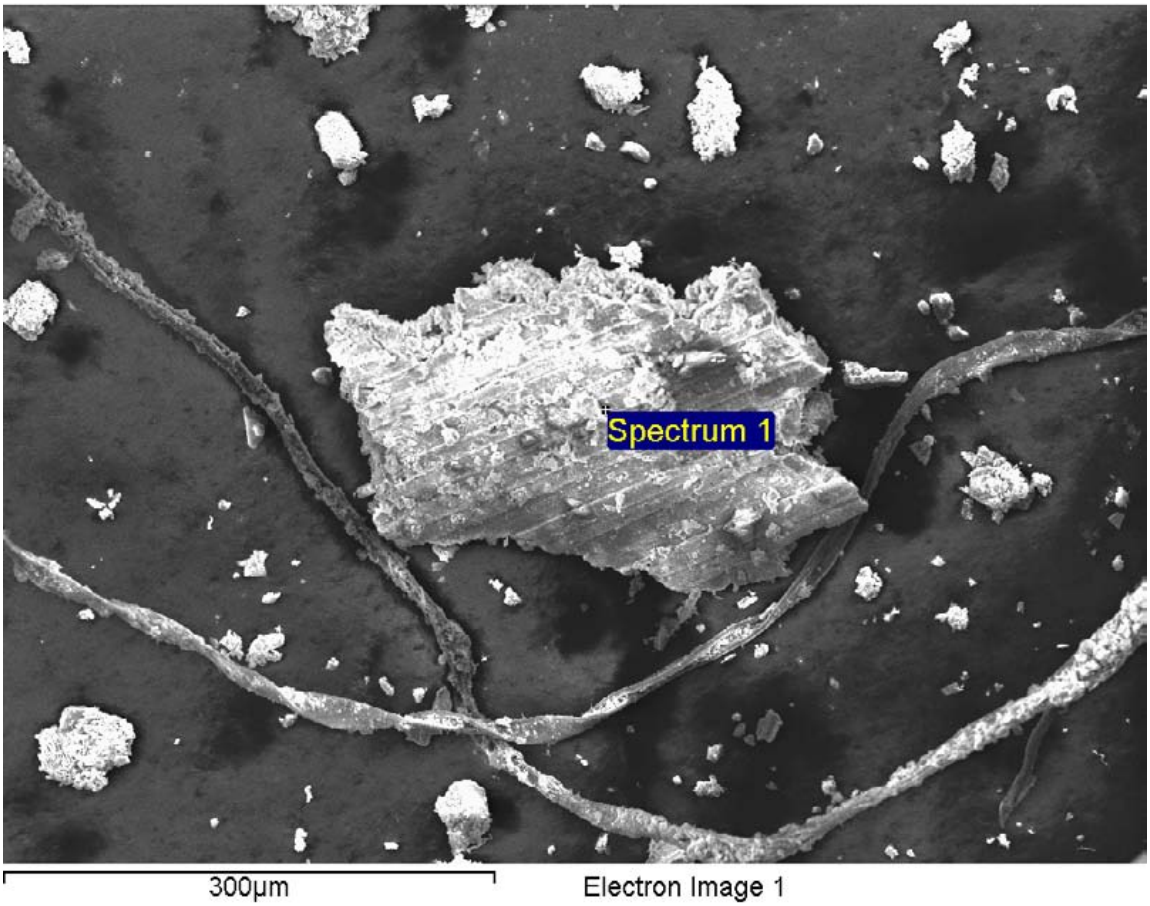

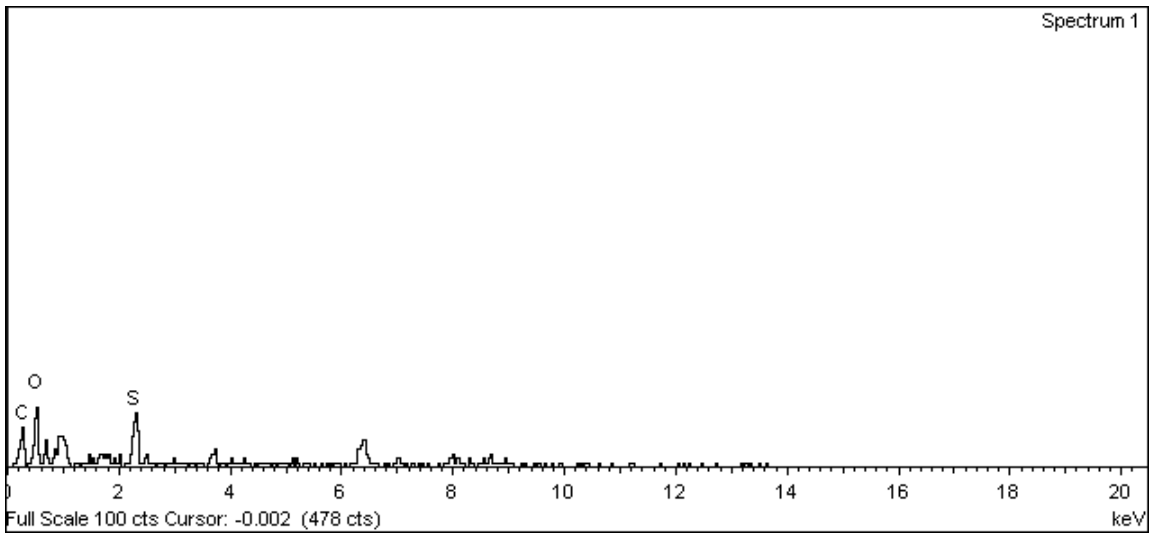

Figure A-127. Surface of black flakes from outer surface of canister and EDX analysis at position of Spectrum 1

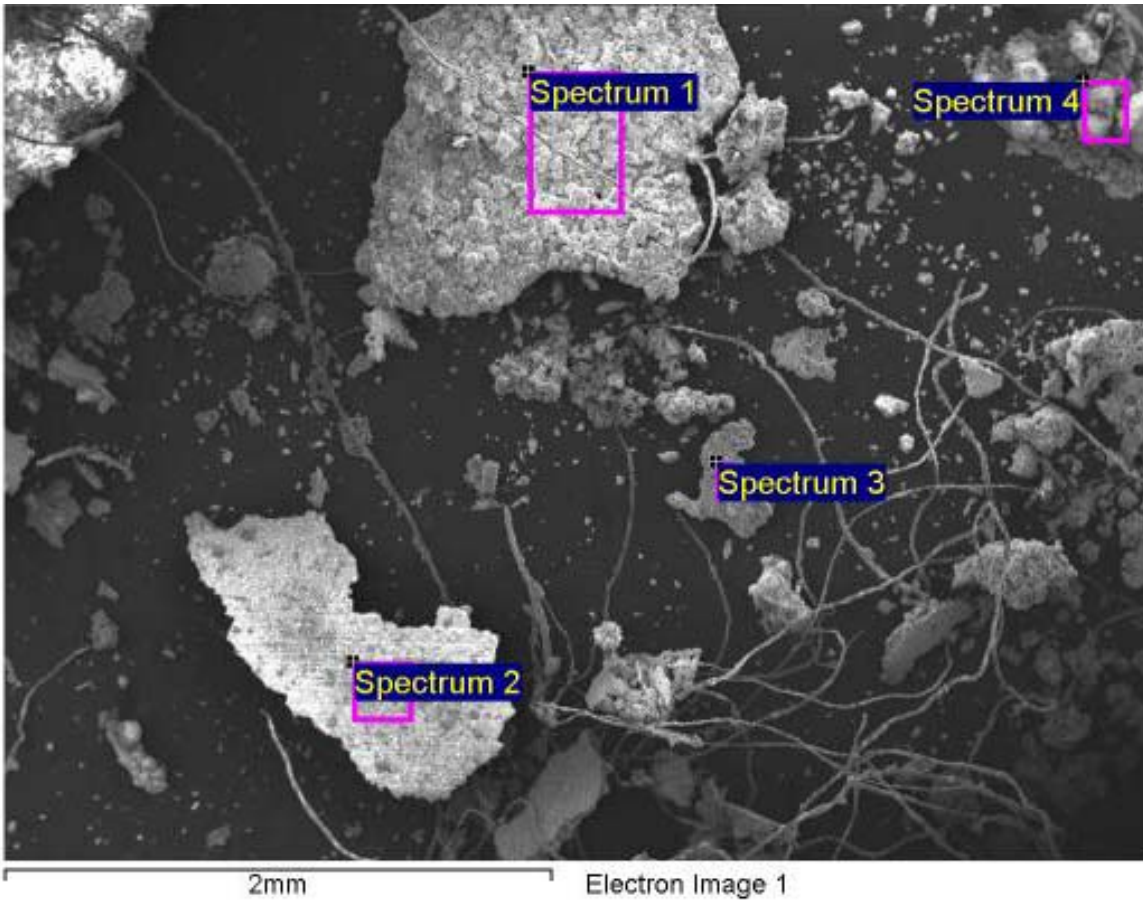

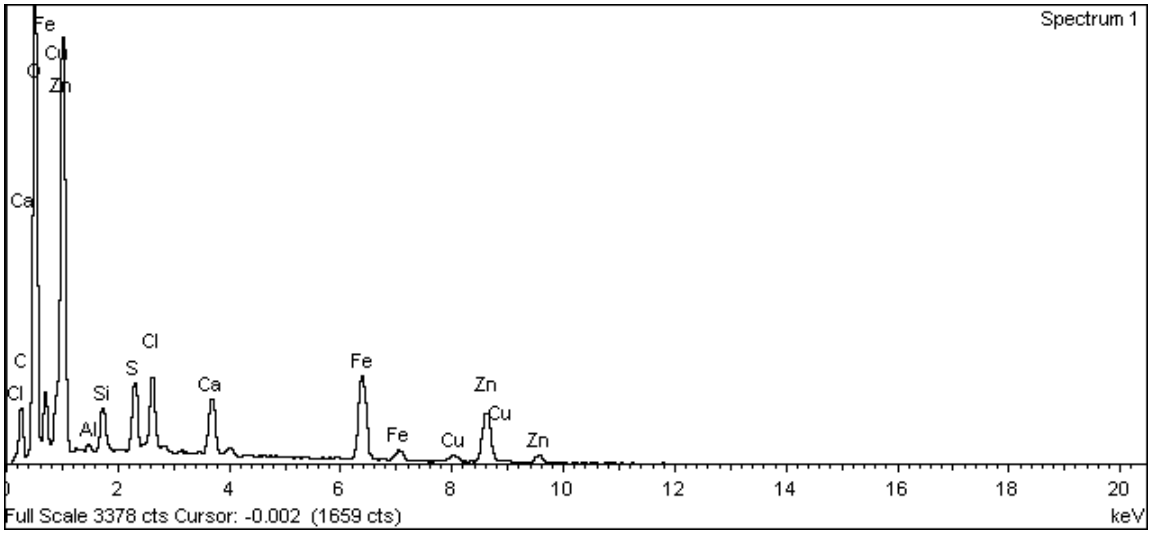

Figure A-128. Surface of black flakes from outer surface of canister and EDX analysis at position of Spectrum 1

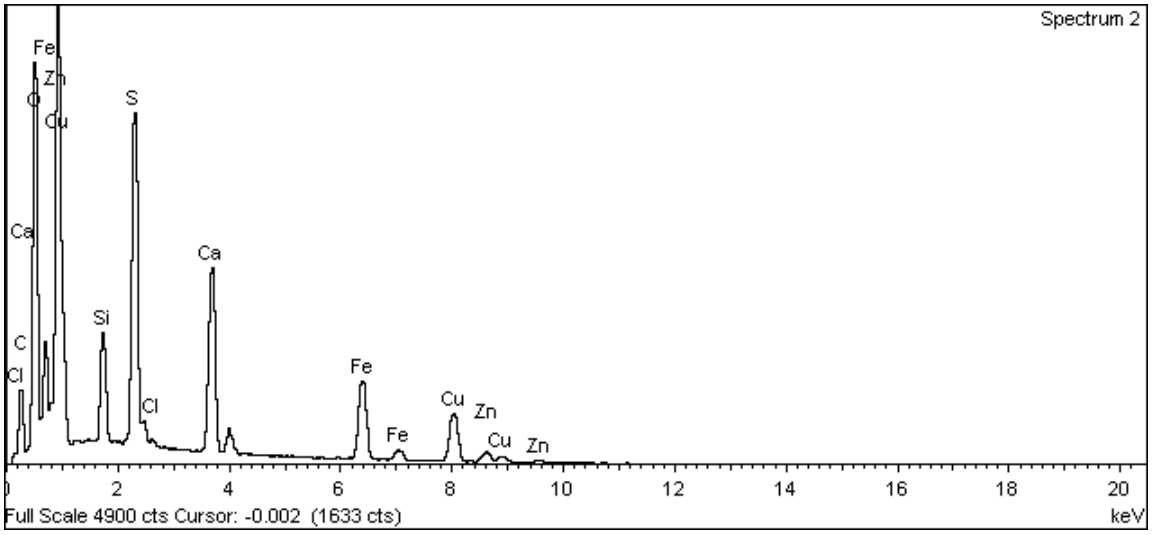

Figure A-129. Surface of black flakes from outer surface of canister and EDX analysis at position of Spectrum 2

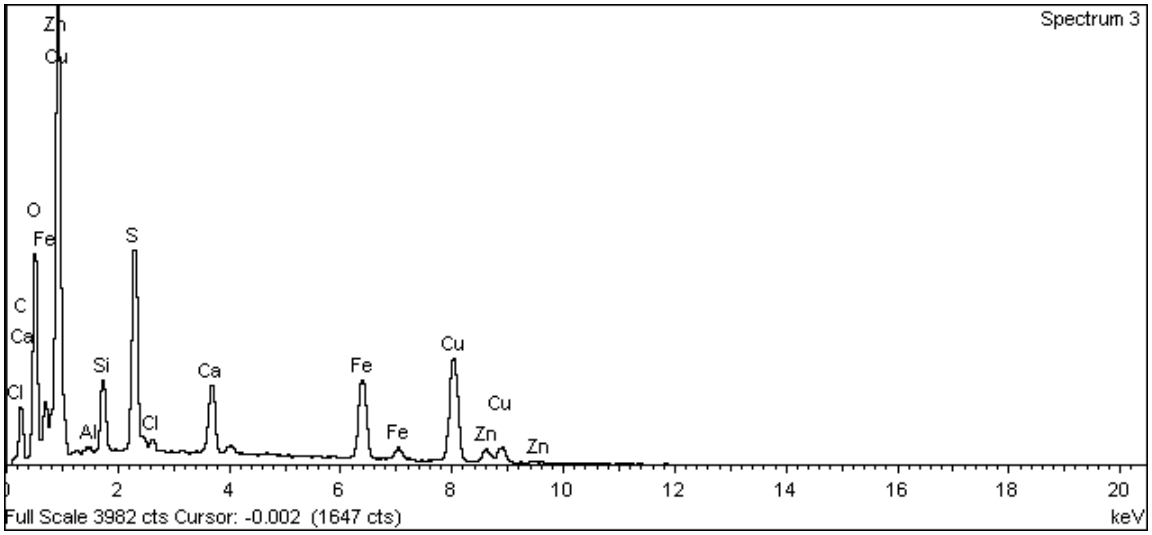

Figure A-130. Surface of black flakes from outer surface of canister and EDX analysis at position of Spectrum 3

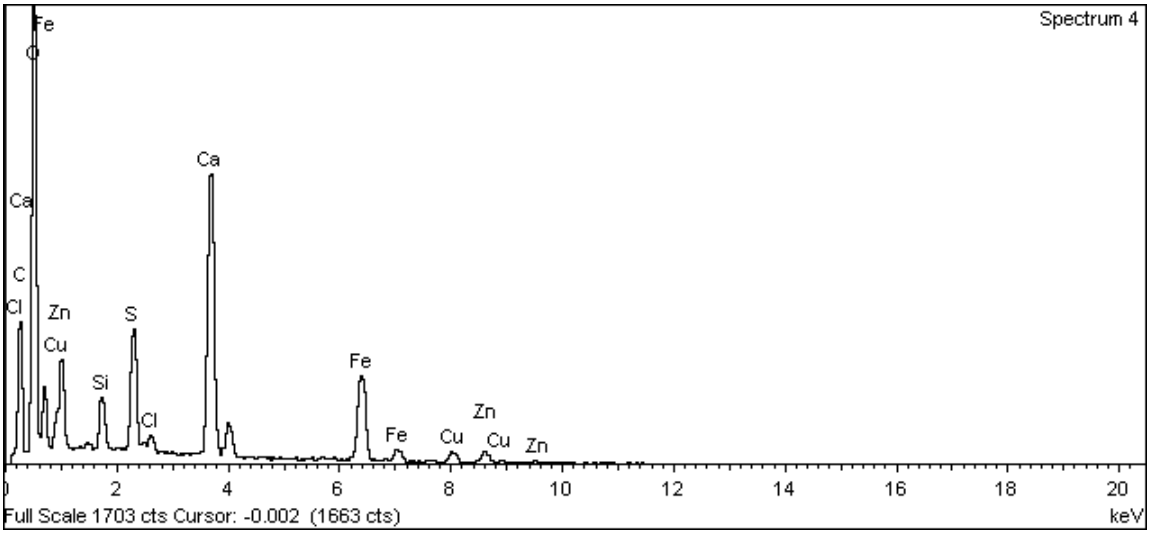

Figure A-131. Surface of black flakes from outer surface of canister and EDX analysis at position of Spectrum 4

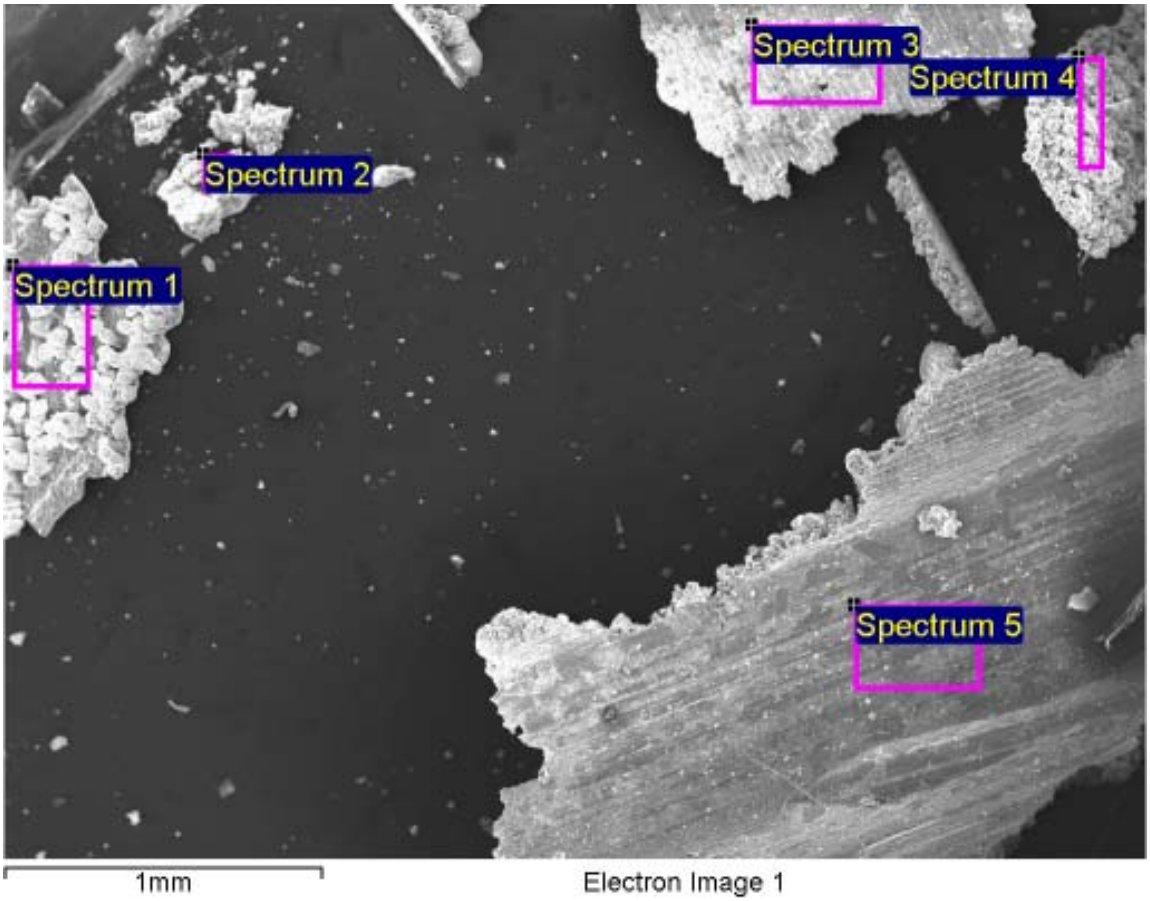

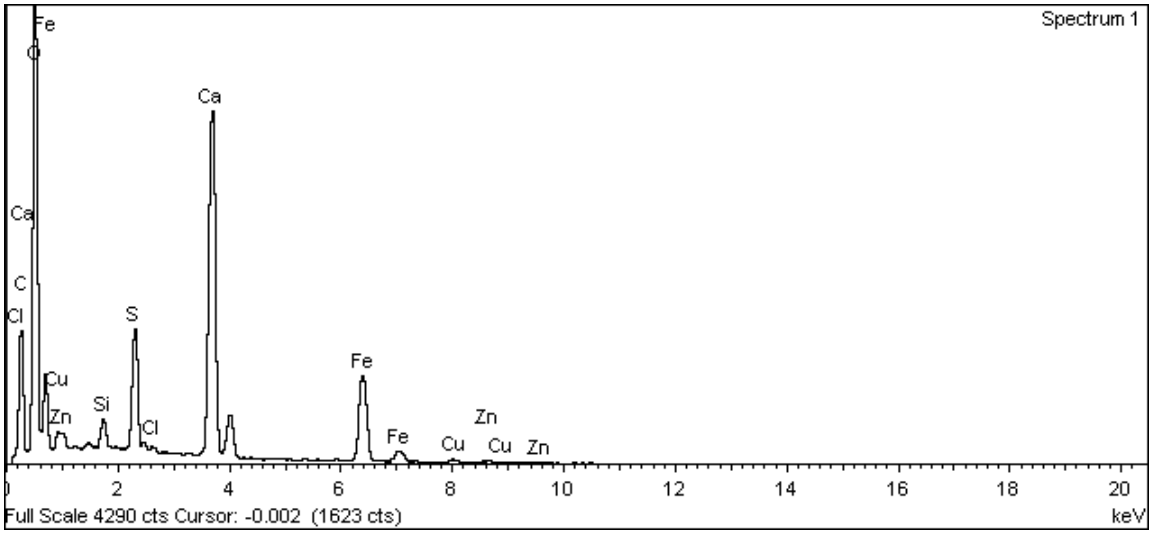

Figure A-132. Surface of black flakes from outer surface of canister and EDX analysis at position of Spectrum 1

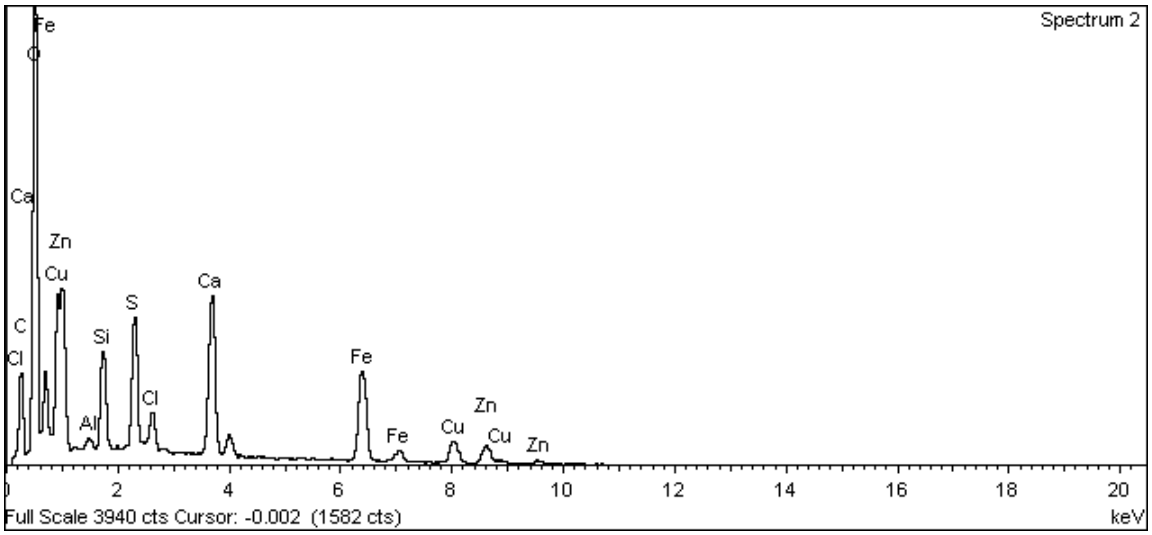

Figure A-133. Surface of black flakes from outer surface of canister and EDX analysis at position of Spectrum 2

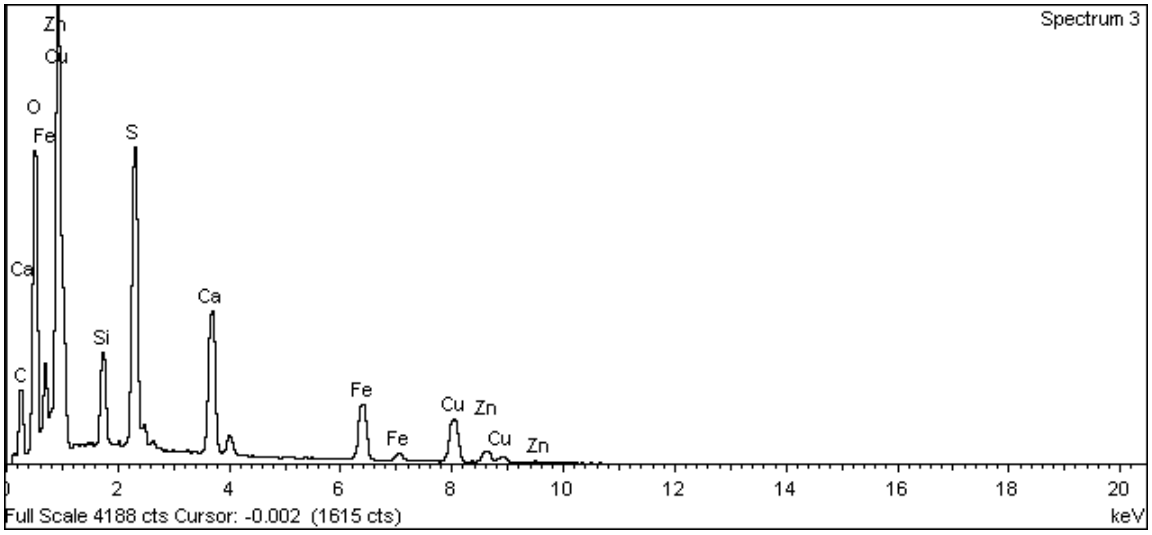

Figure A-134. Surface of black flakes from outer surface of canister and EDX analysis at position of Spectrum 3

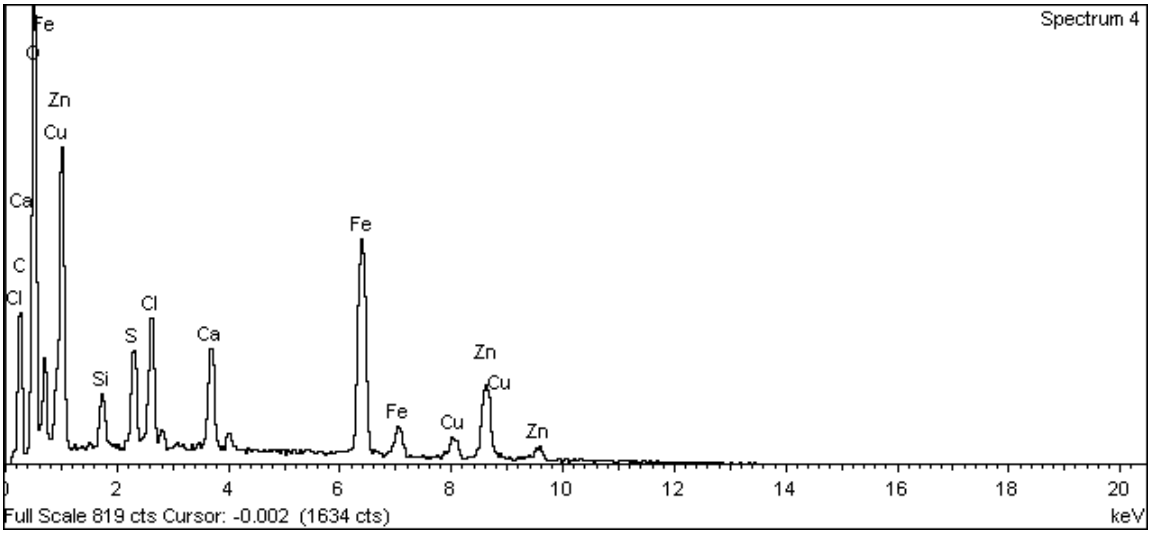

Figure A-135. Surface of black flakes from outer surface of canister and EDX analysis at position of Spectrum 4

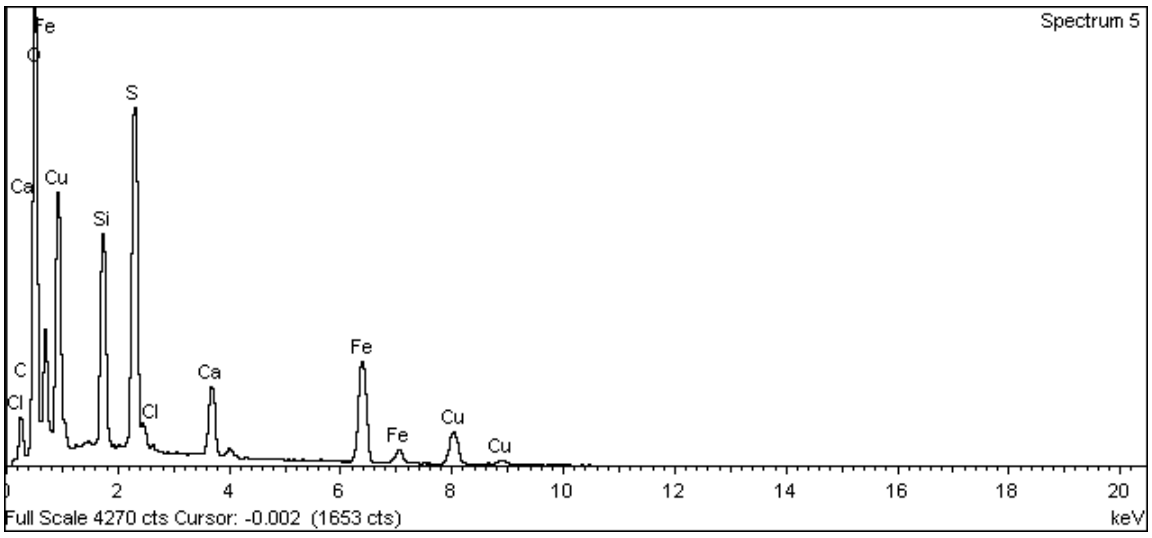

Figure A-136. Surface of black flakes from outer surface of canister and EDX analysis at position of Spectrum 5

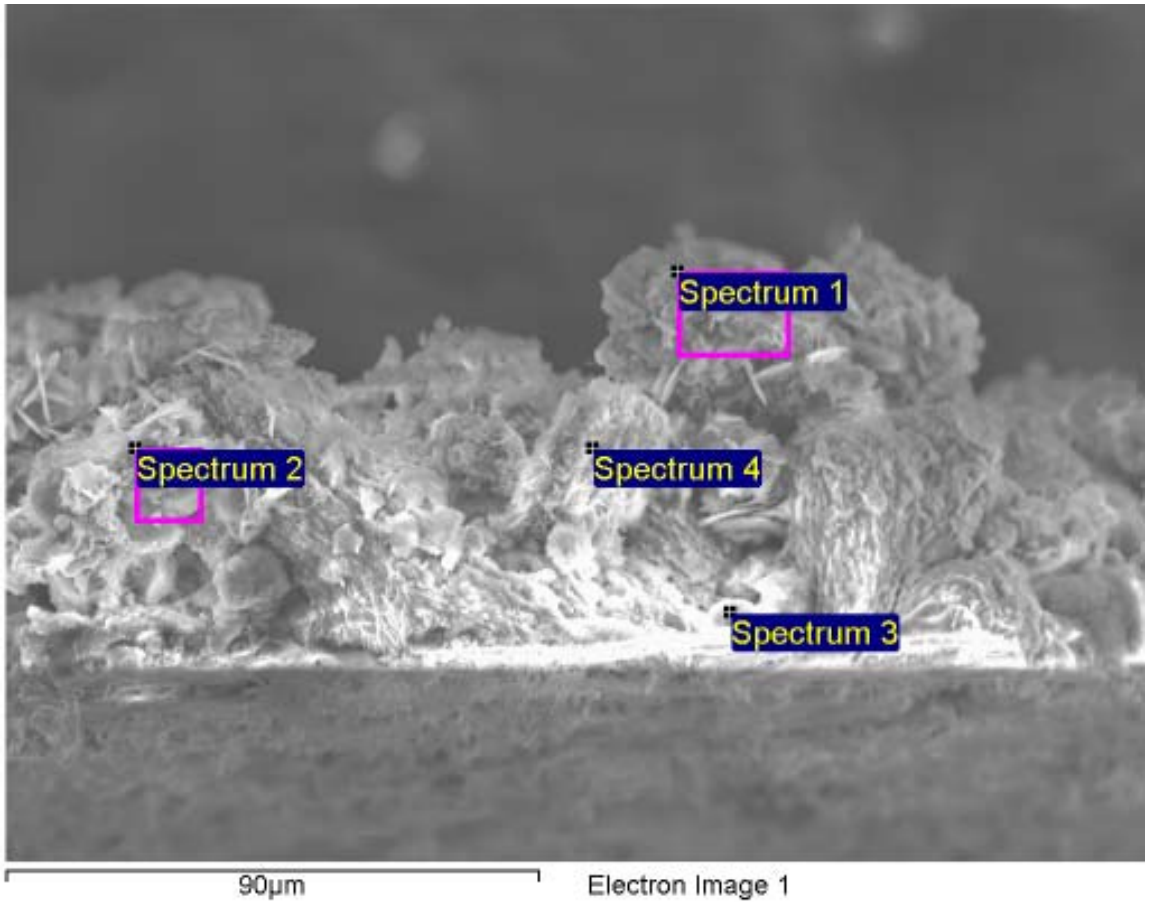

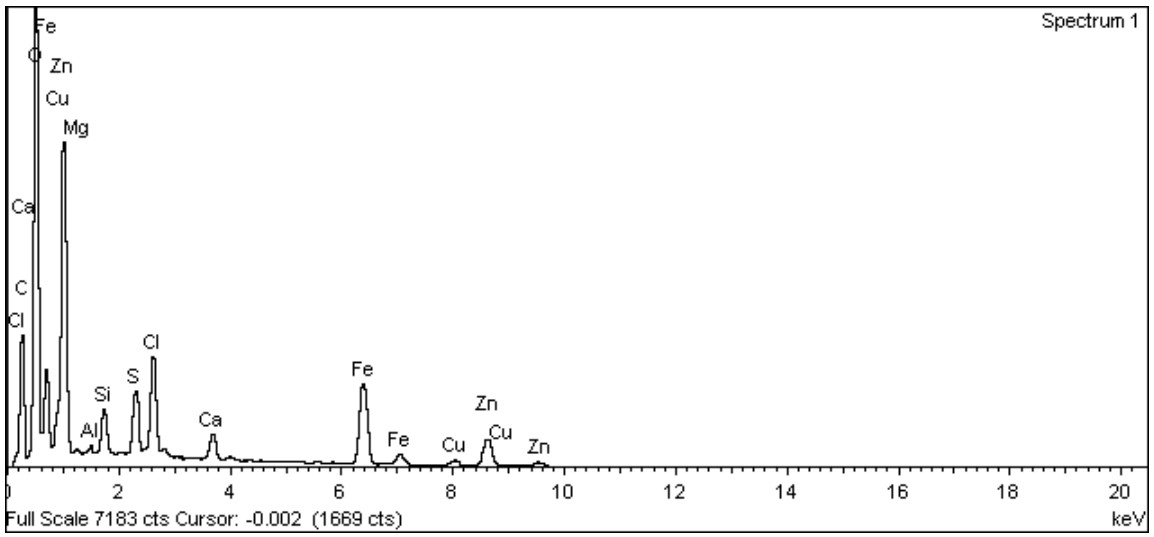

Figure A-137. Surface of black flakes from outer surface of canister and EDX analysis at position of Spectrum 1

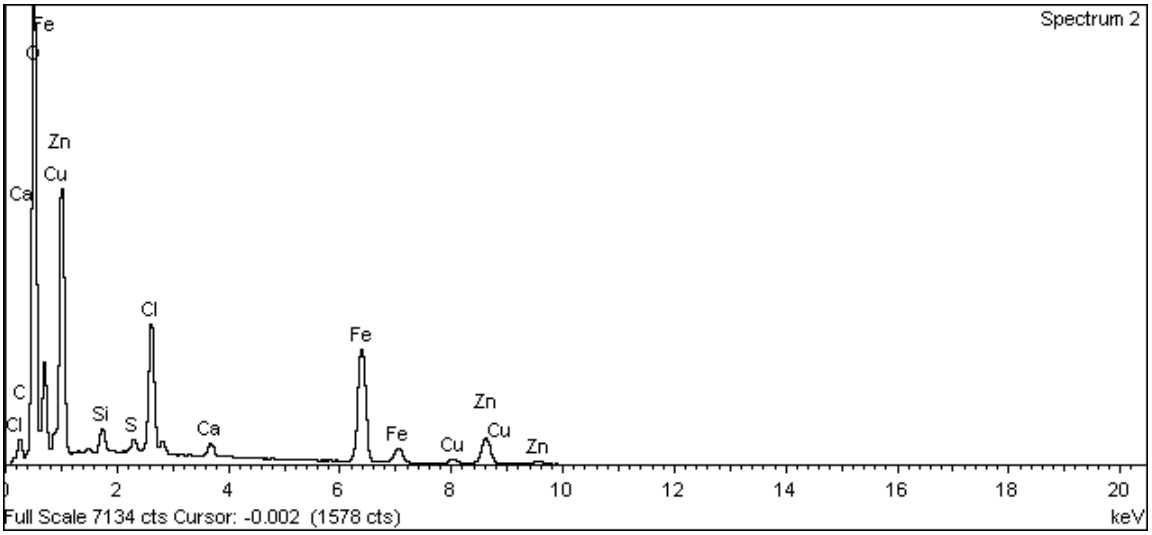

Figure A-138. Surface of black flakes from outer surface of canister and EDX analysis at position of Spectrum 2

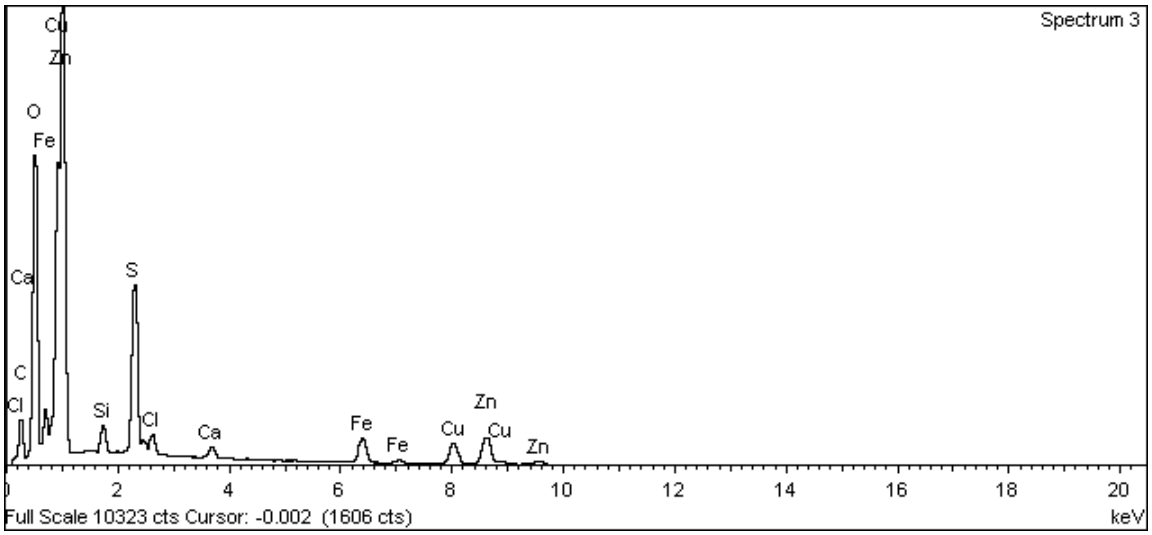

Figure A-139. Surface of black flakes from outer surface of canister and EDX analysis at position of Spectrum 3

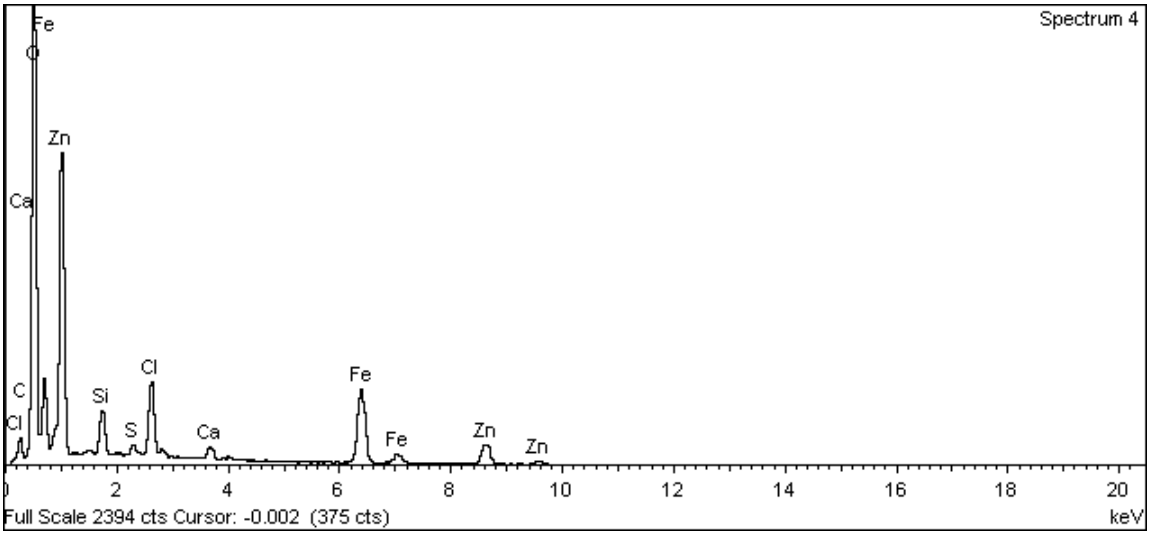

Figure A-140. Surface of black flakes from outer surface of canister and EDX analysis at position of Spectrum 4

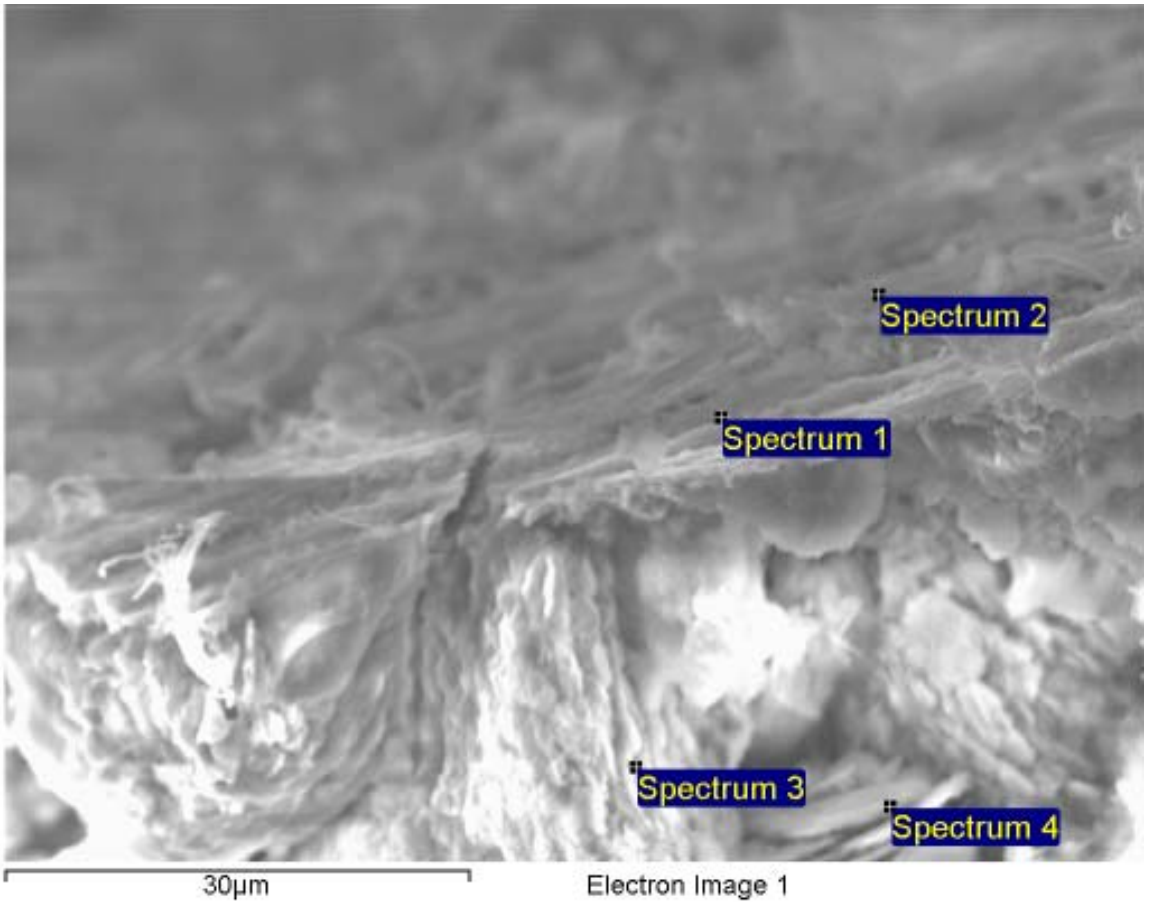

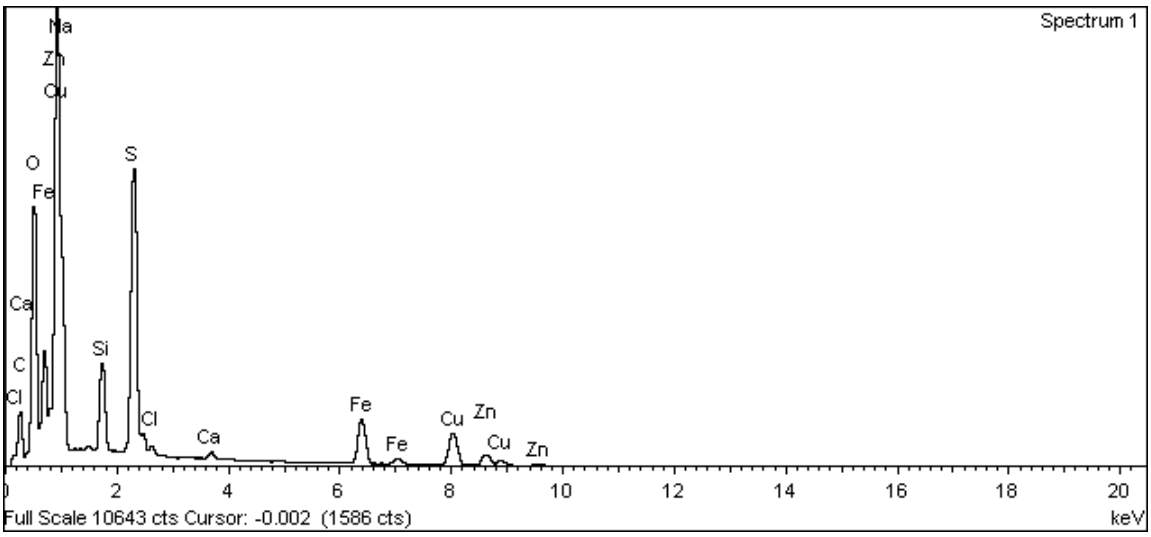

Figure A-141. Surface of black flakes from outer surface of canister and EDX analysis at position of Spectrum 1

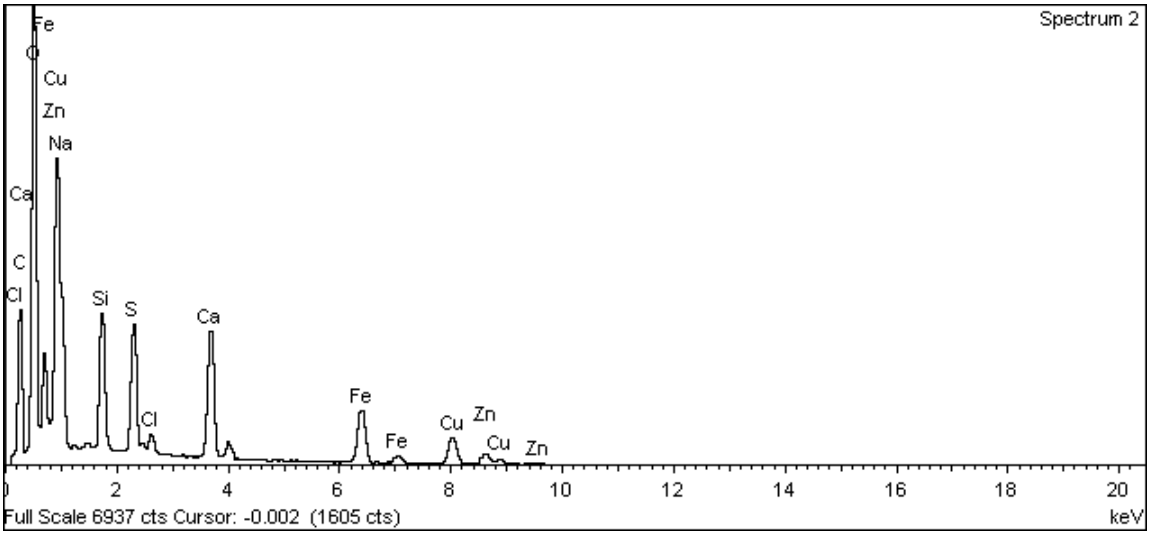

Figure A-142. Surface of black flakes from outer surface of canister and EDX analysis at position of Spectrum 2

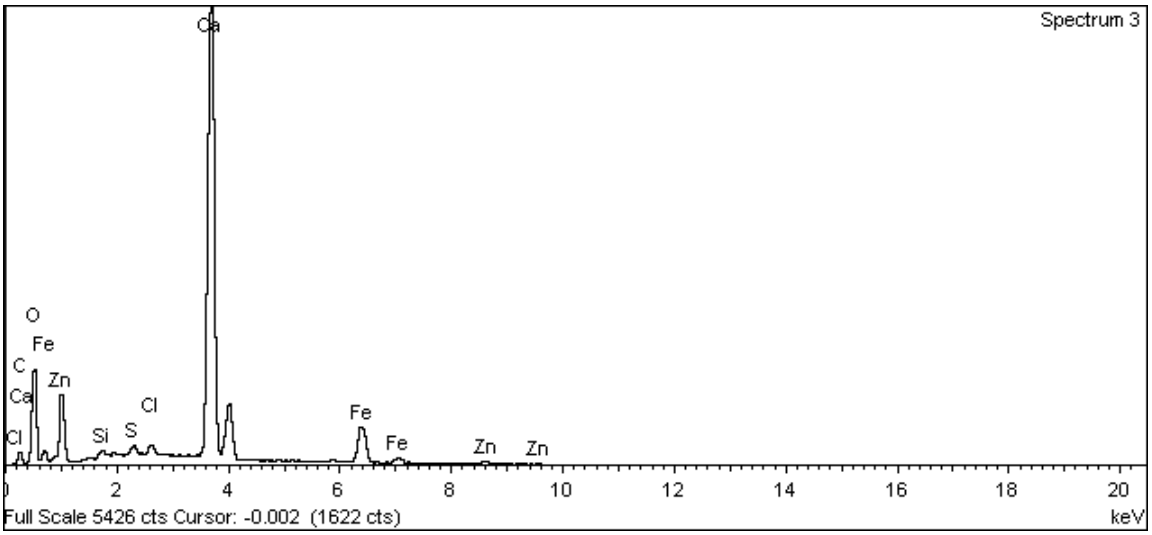

Figure A-143. Surface of black flakes from outer surface of canister and EDX analysis at position of Spectrum 3

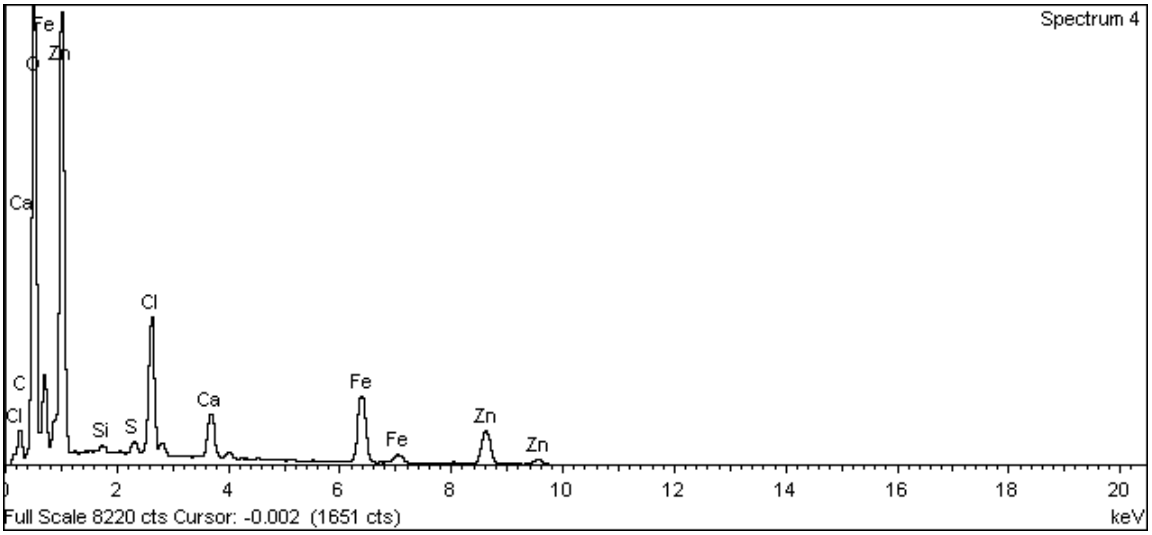

Figure A-144. Surface of black flakes from outer surface of canister and EDX analysis at position of Spectrum 4

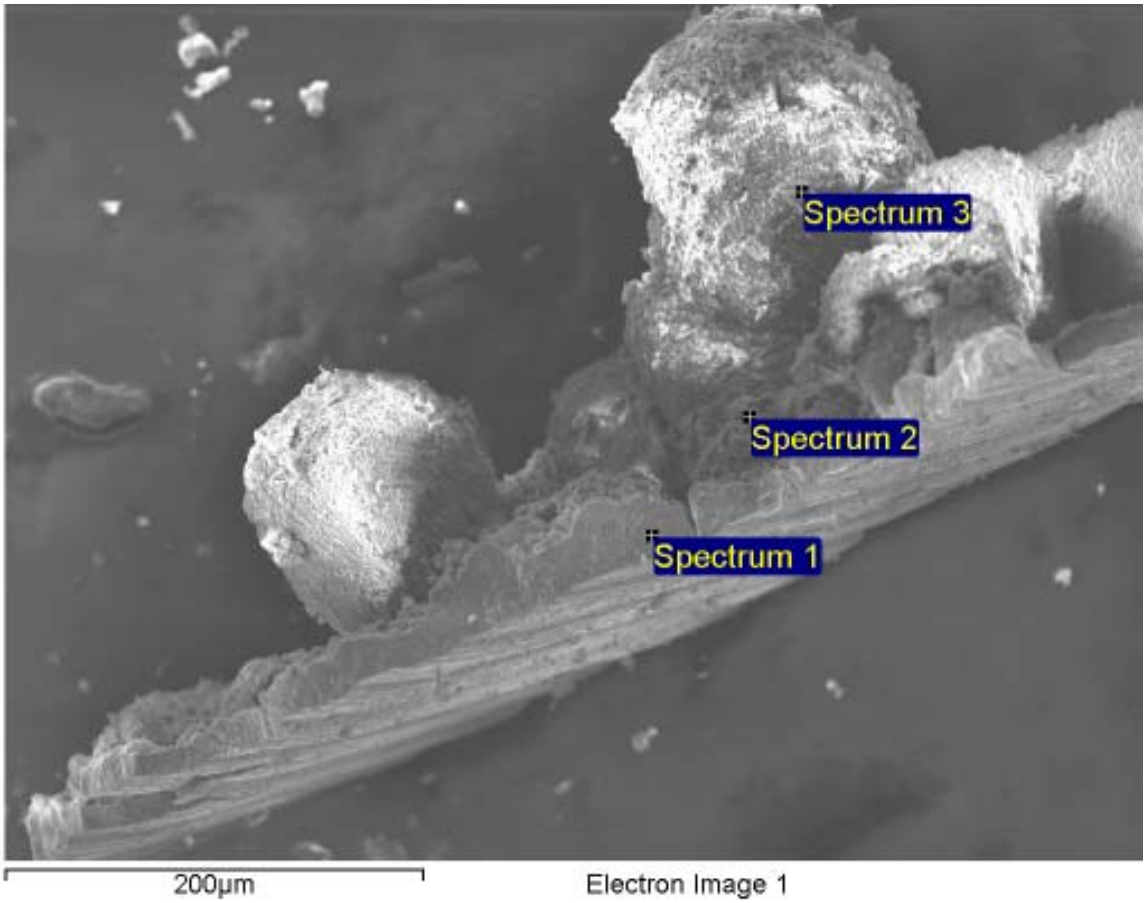

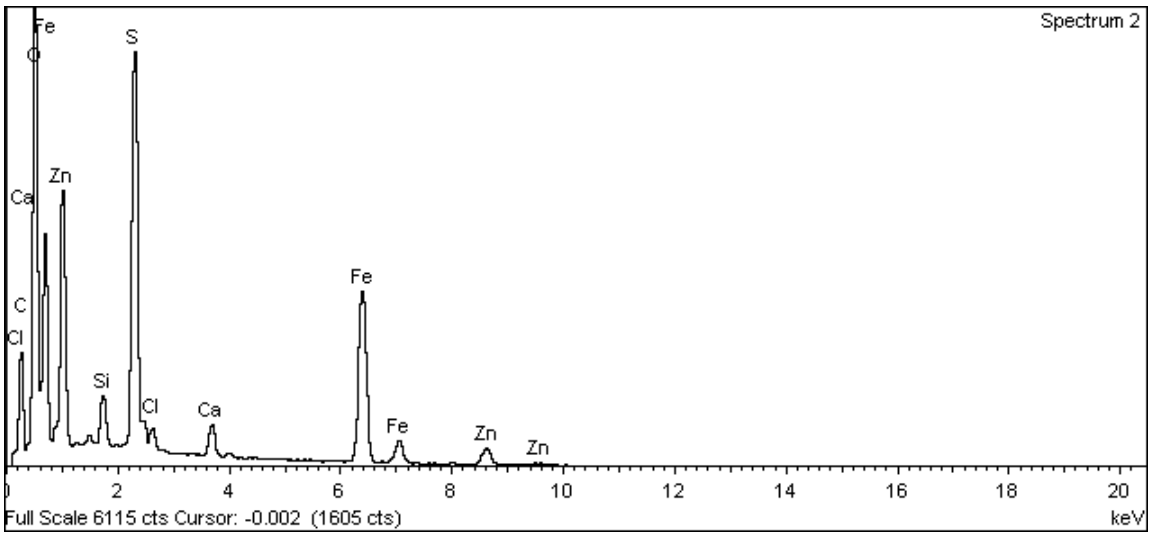

Figure A-145. Surface of black flakes from outer surface of canister and EDX analysis at position of Spectrum 2 (Spectrum 1 is not shown here)

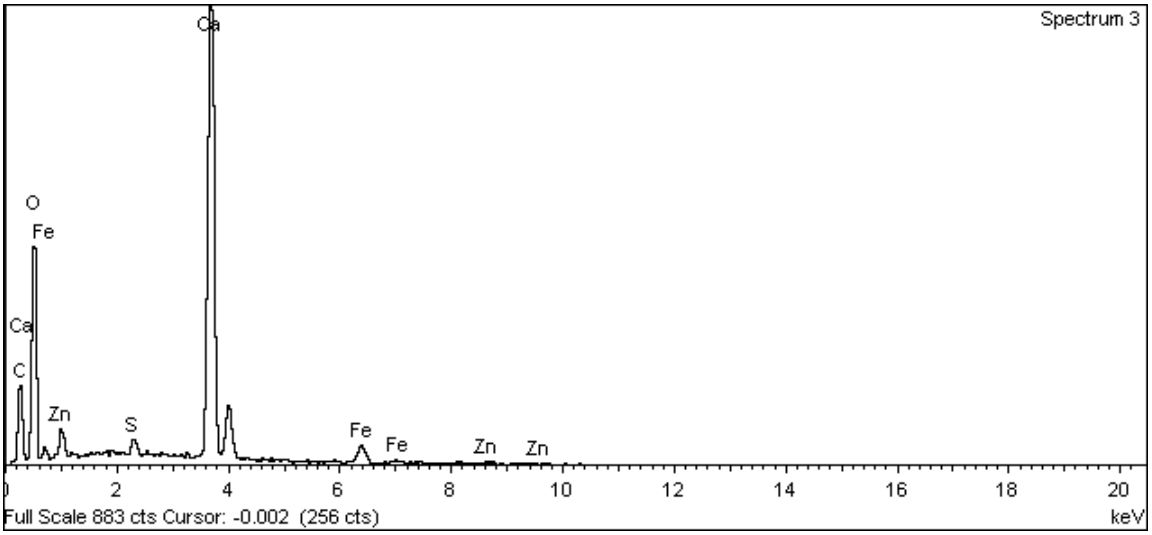

Figure A-146. Surface of black flakes from outer surface of canister and EDX analysis at position of Spectrum 3

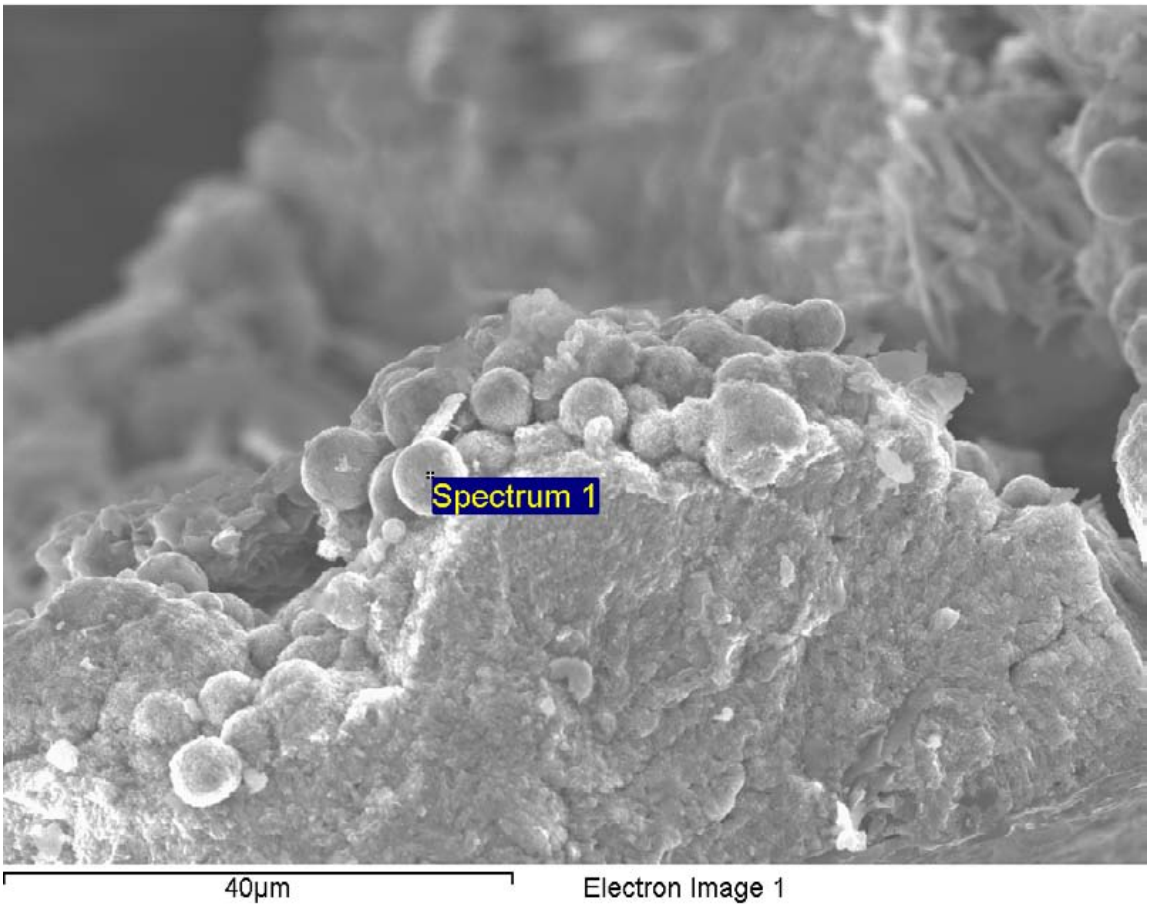

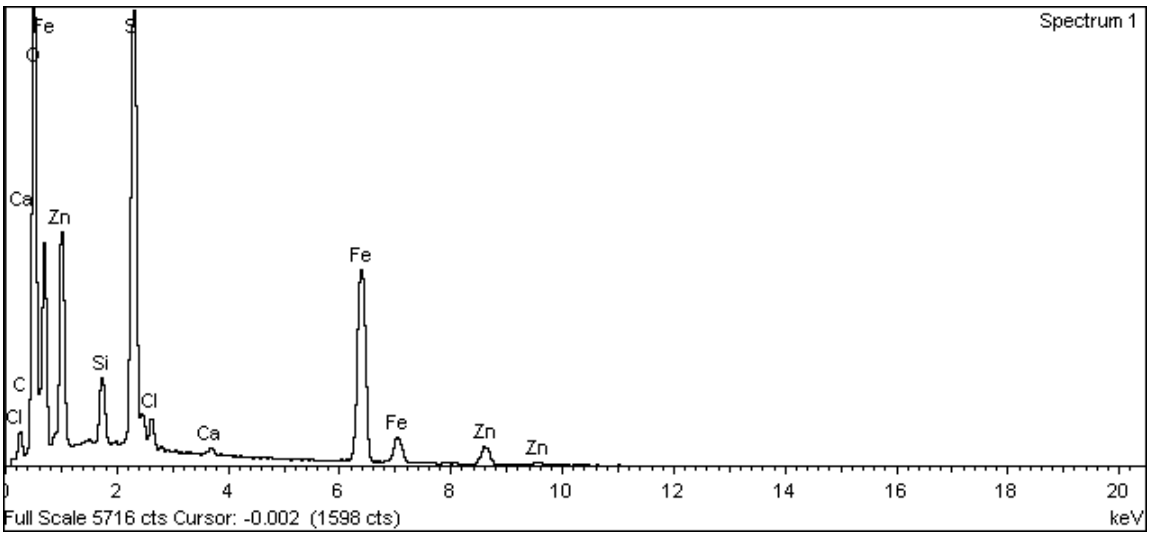

Figure A-147. Surface of black flakes from outer surface of canister and EDX analysis at position of Spectrum 1

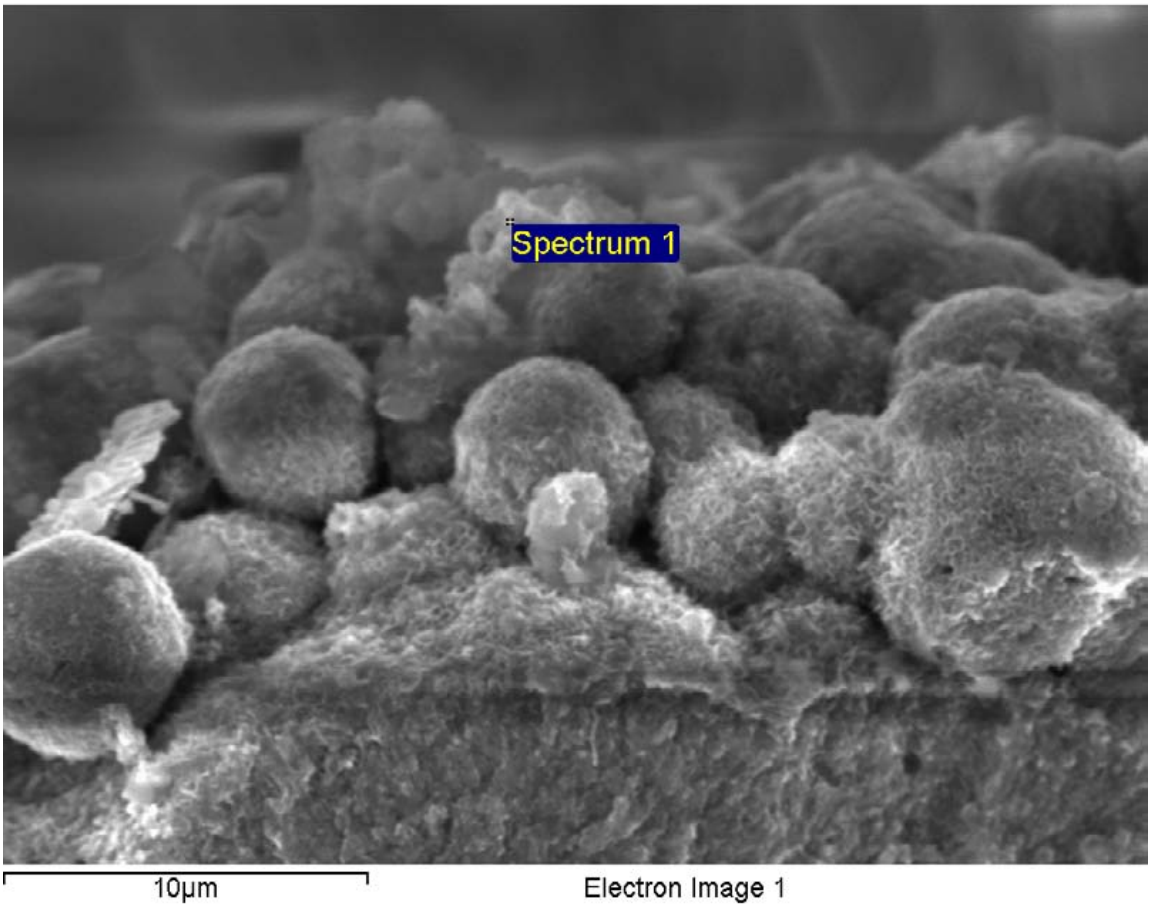

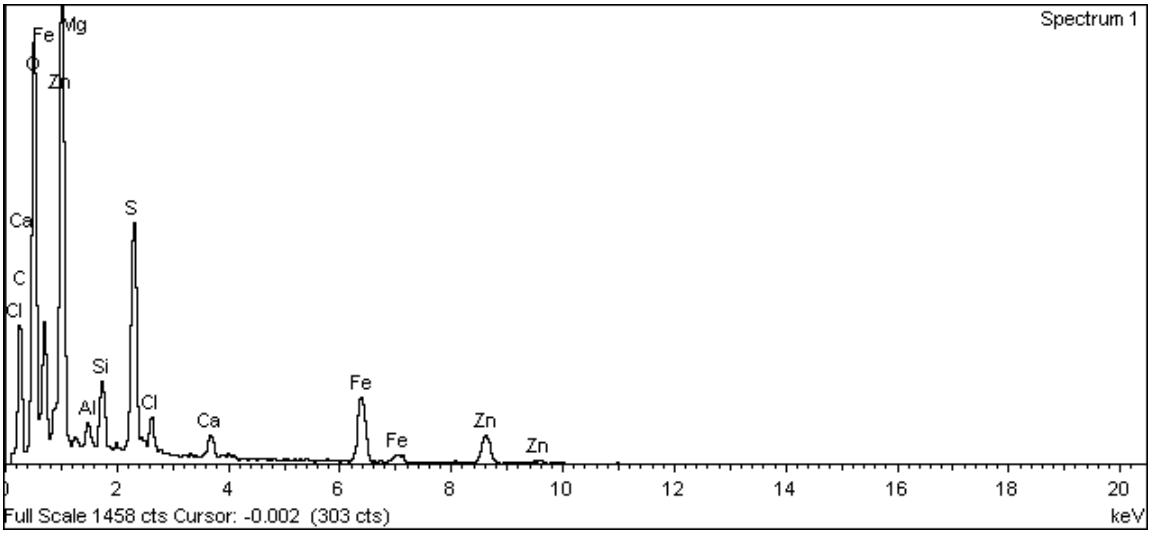

Figure A-148. Surface of black flakes from outer surface of canister and EDX analysis at position of Spectrum 1

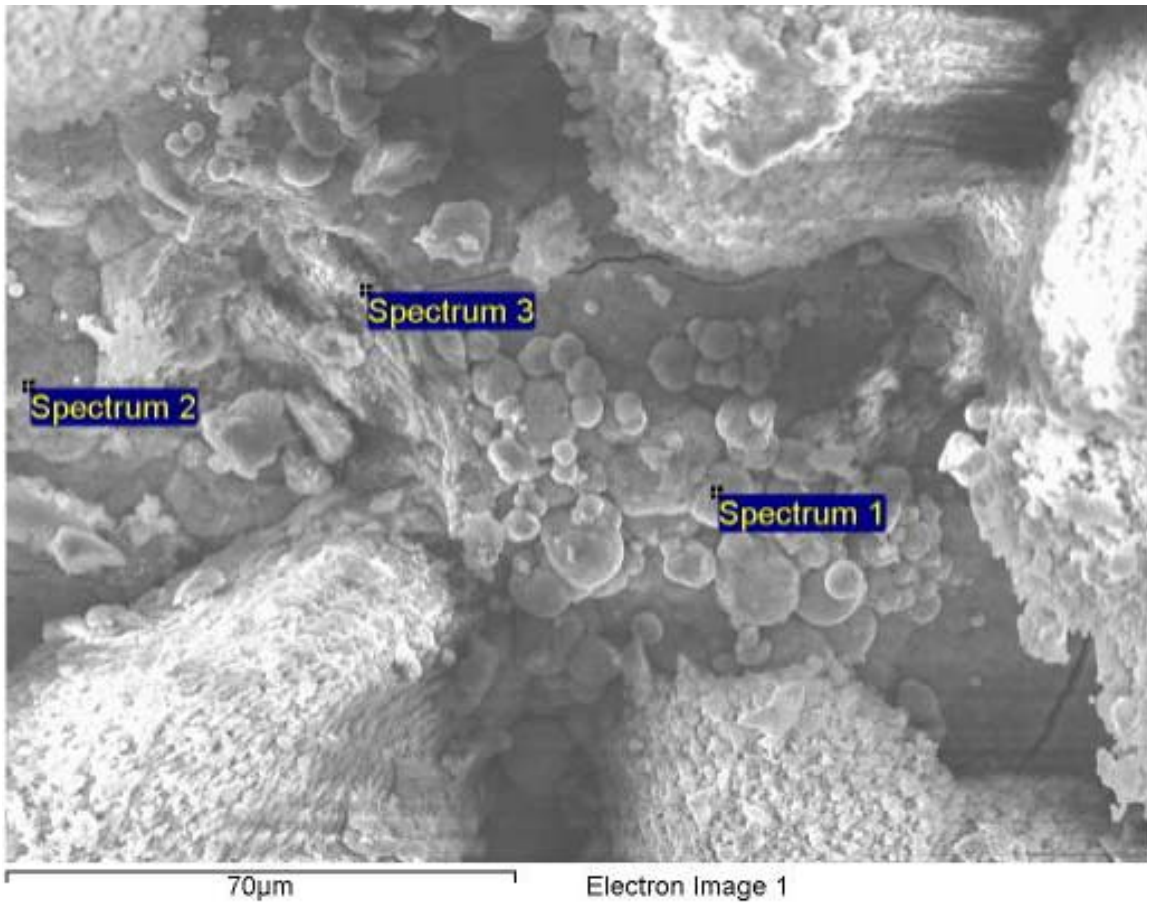

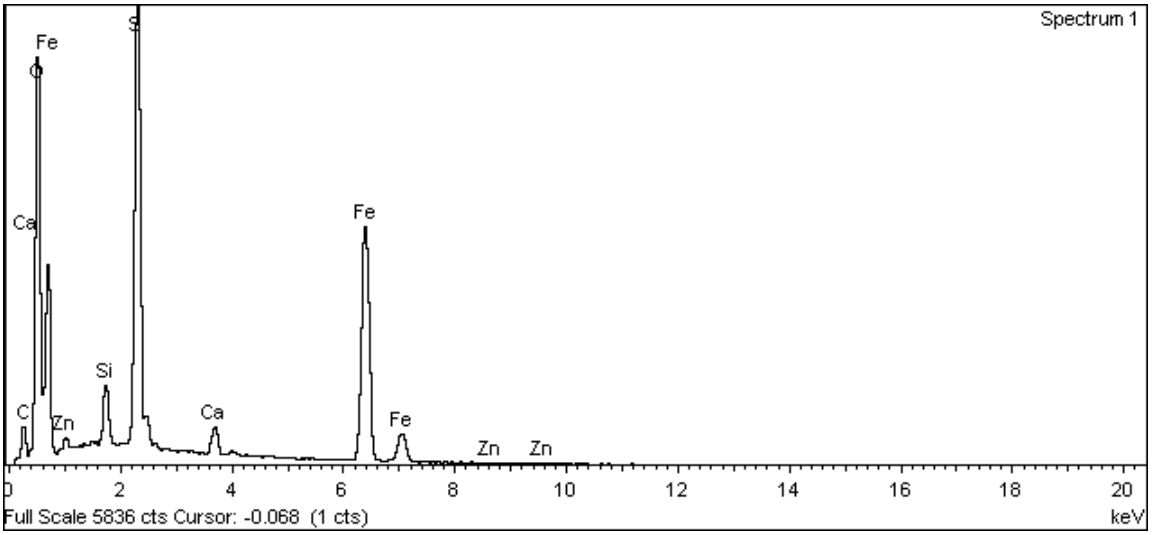

Figure A-149. Surface of black flakes from outer surface of canister and EDX analysis at position of Spectrum 1

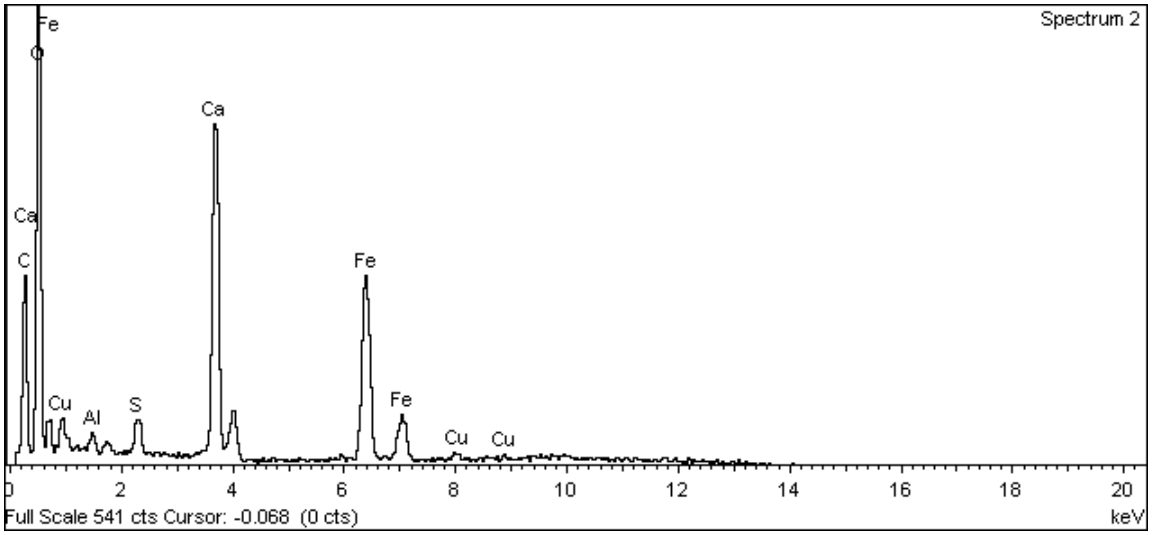

Figure A-150. Surface of black flakes from outer surface of canister and EDX analysis at position of Spectrum 2

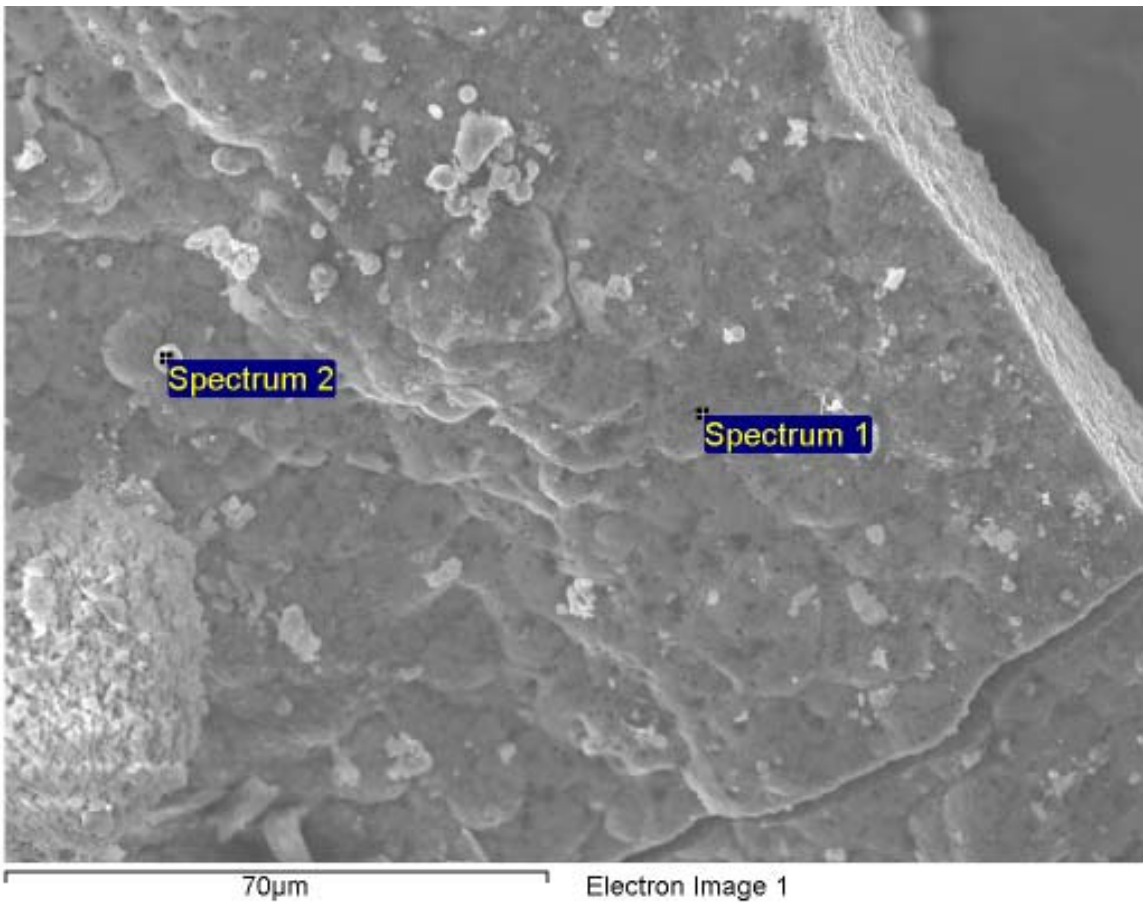

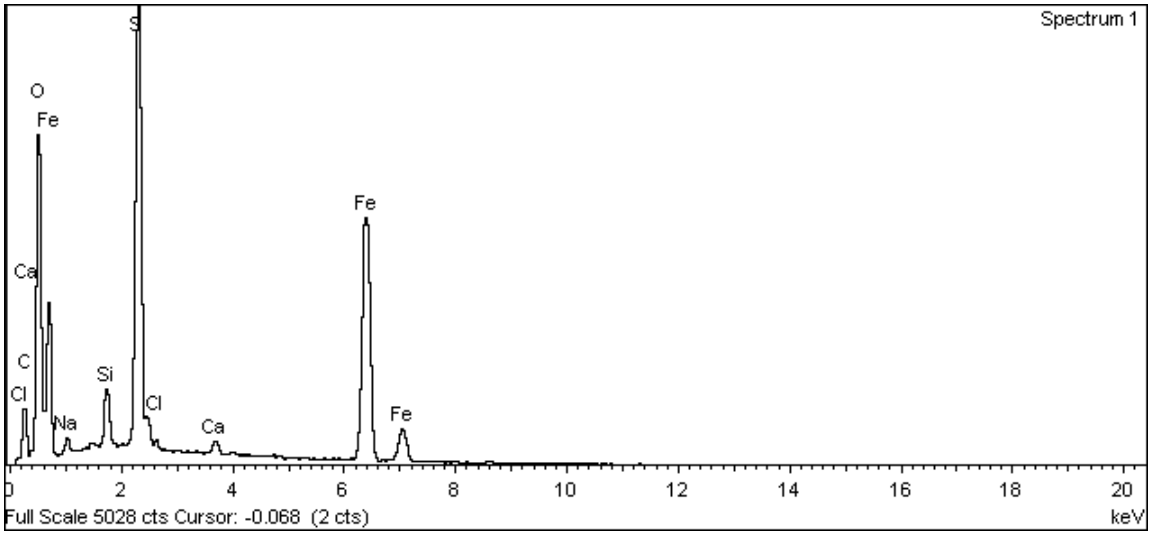

Figure A-151. Surface of black flakes from outer surface of canister and EDX analysis at position of Spectrum 1

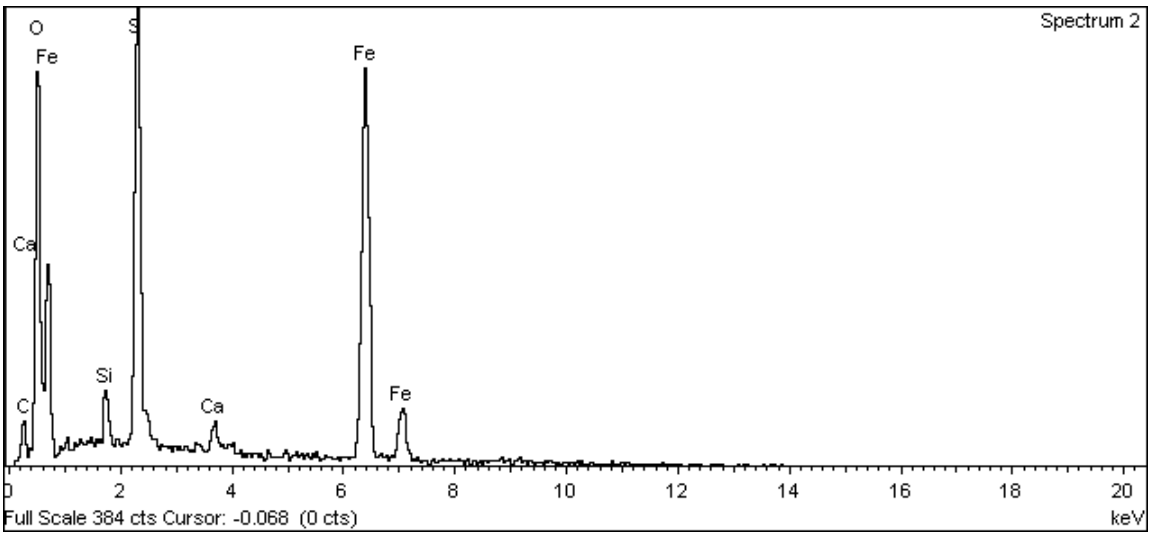

Figure A-152. Surface of black flakes from outer surface of canister and EDX analysis at position of Spectrum 2

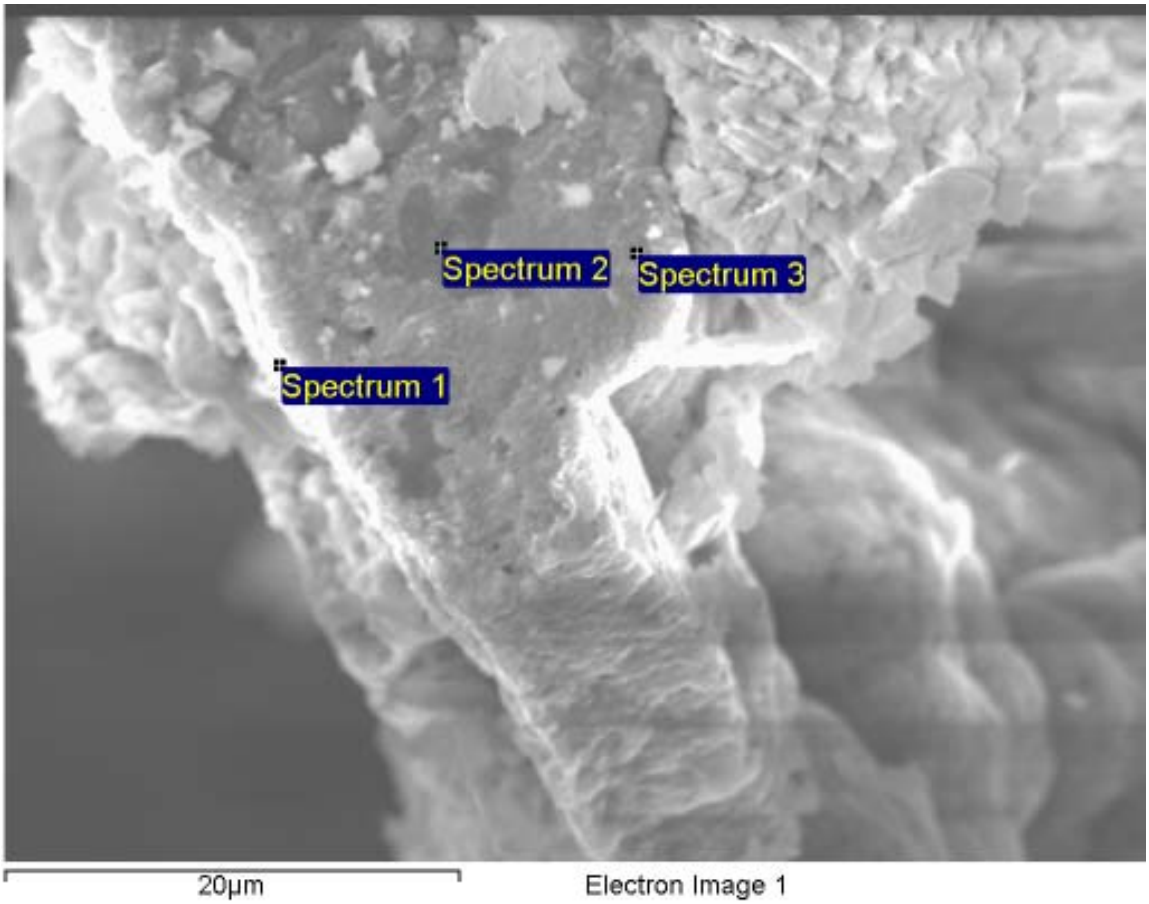

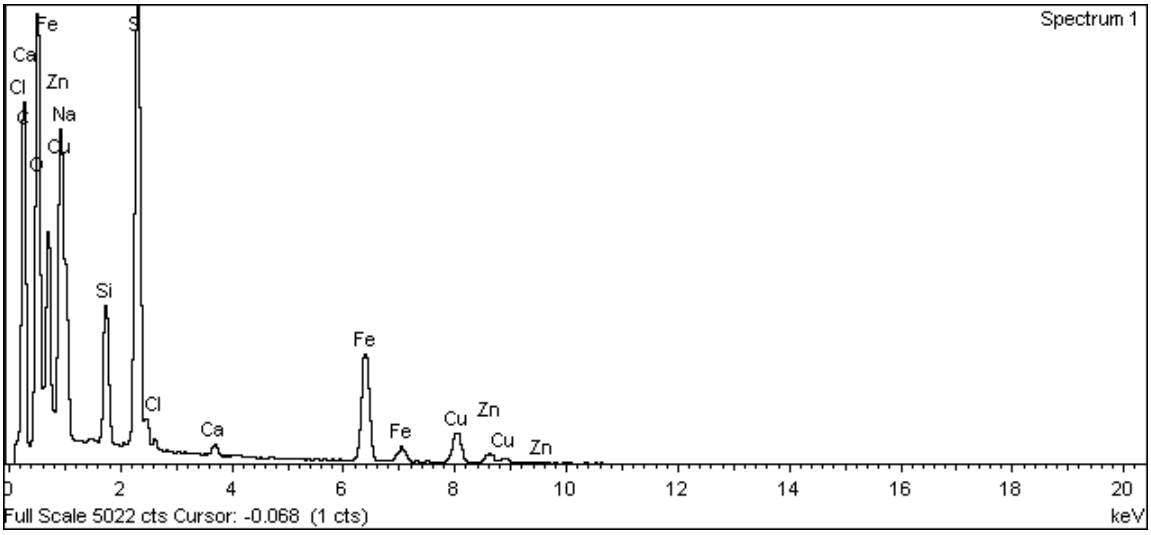

Figure A-153. Surface of black flakes from outer surface of canister and EDX analysis at position of Spectrum 1

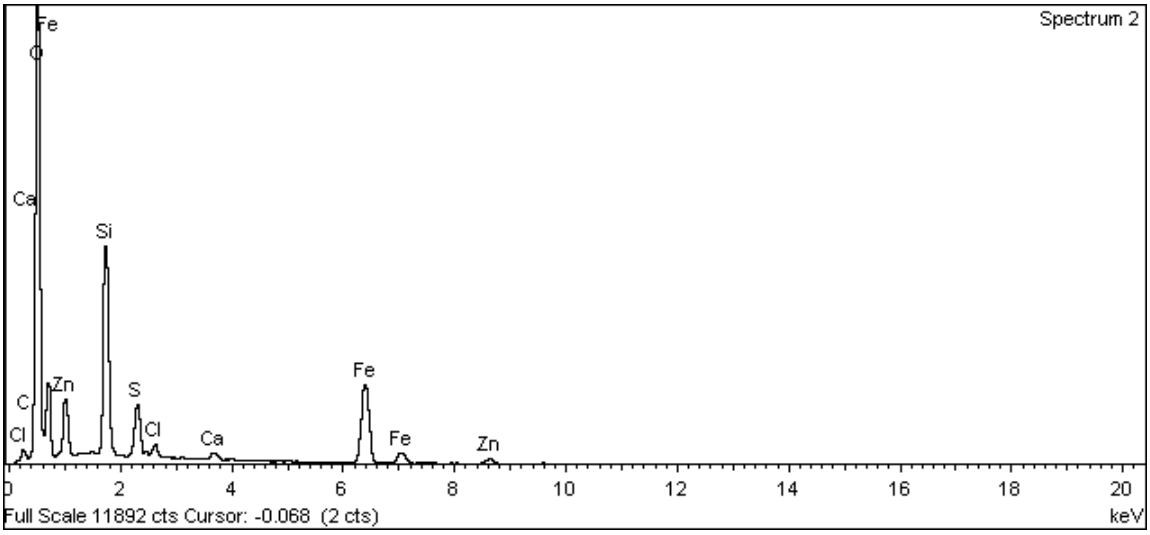

Figure A-154. Surface of black flakes from outer surface of canister and EDX analysis at position of Spectrum 2 (Spectrum 3 is not shown here)

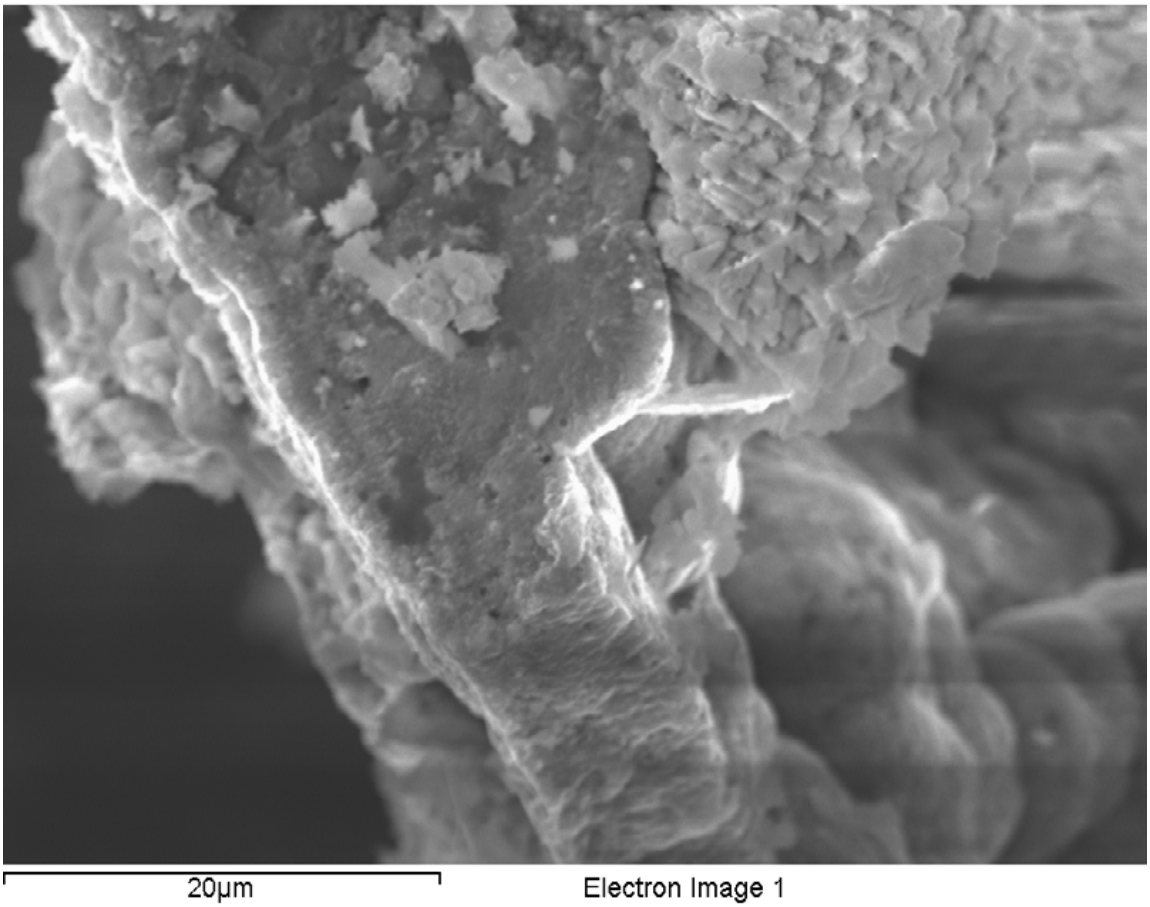

Figure A-155. Surface of black flakes from outer surface of canister and EDX analysis – Sum Spectrum

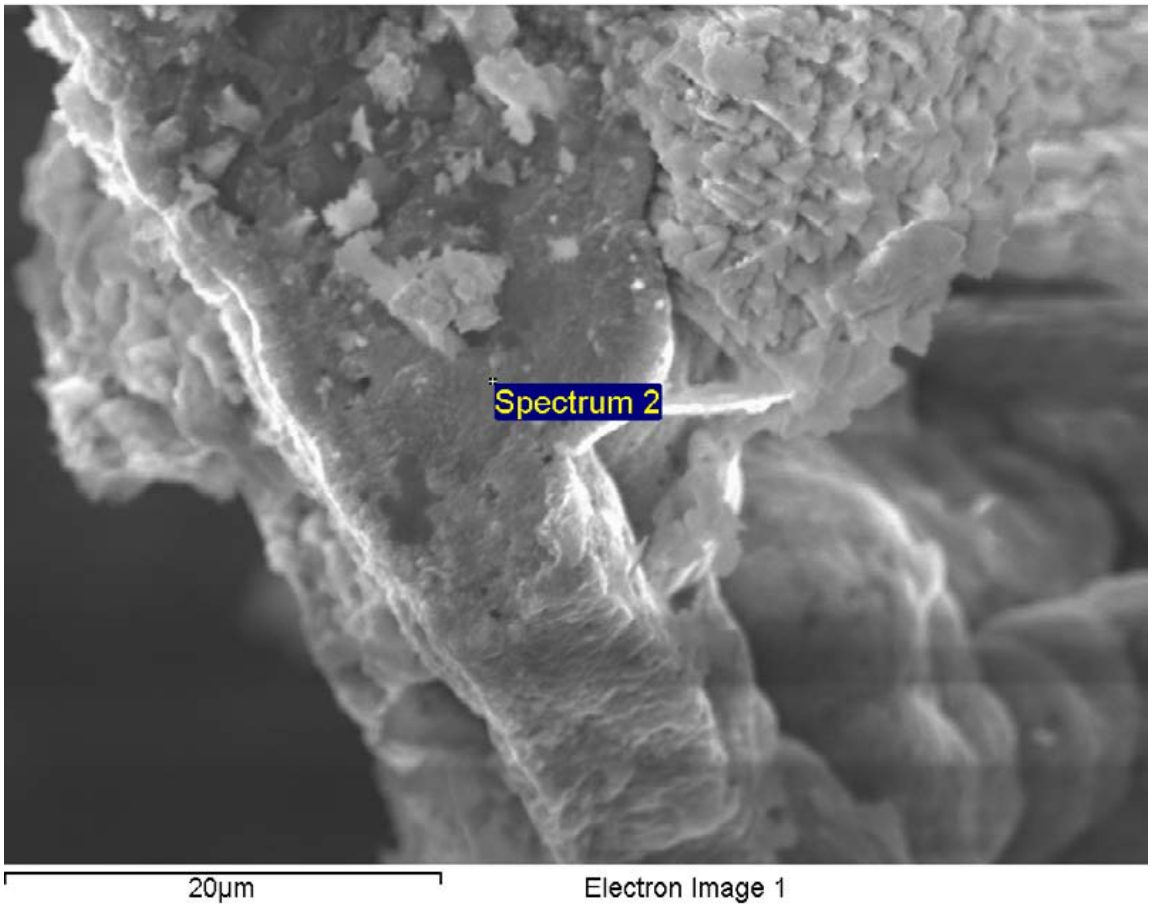

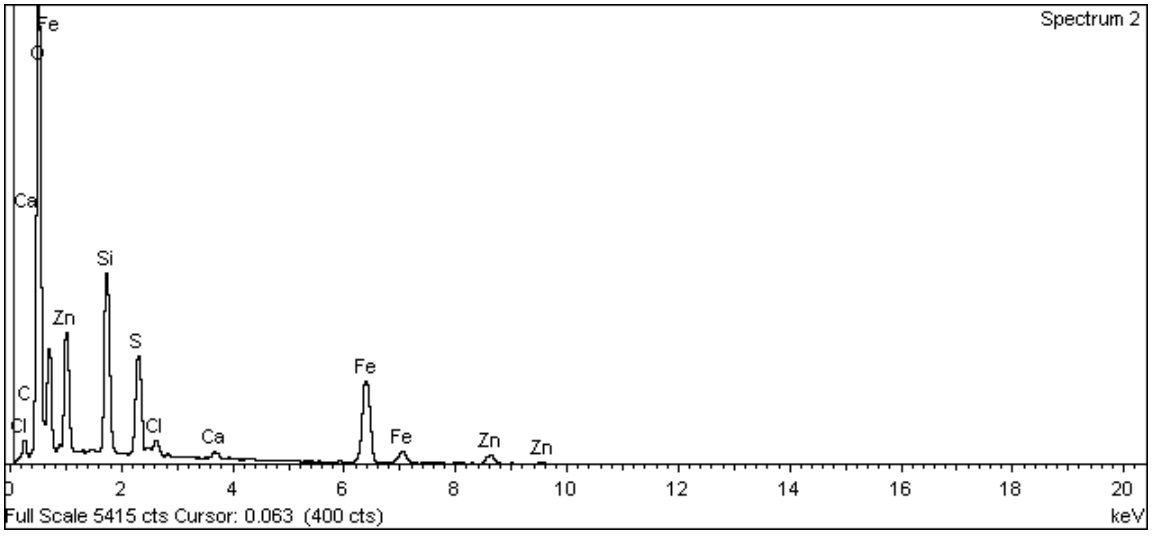

Figure A-156. Surface of black flakes from outer surface of canister and EDX analysis at position of Spectrum 2

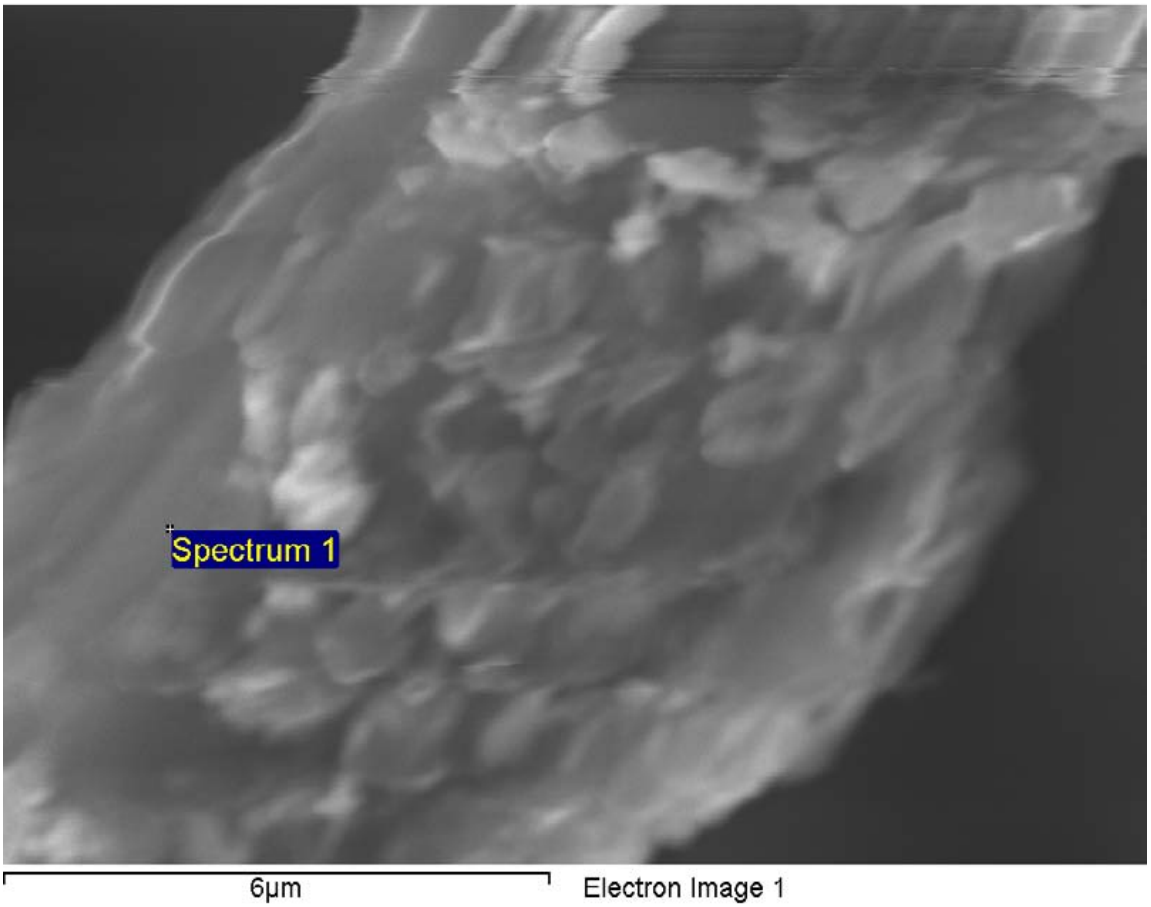

Figure A-157. Surface of black flakes from outer surface of canister and EDX analysis at position of Spectrum 1

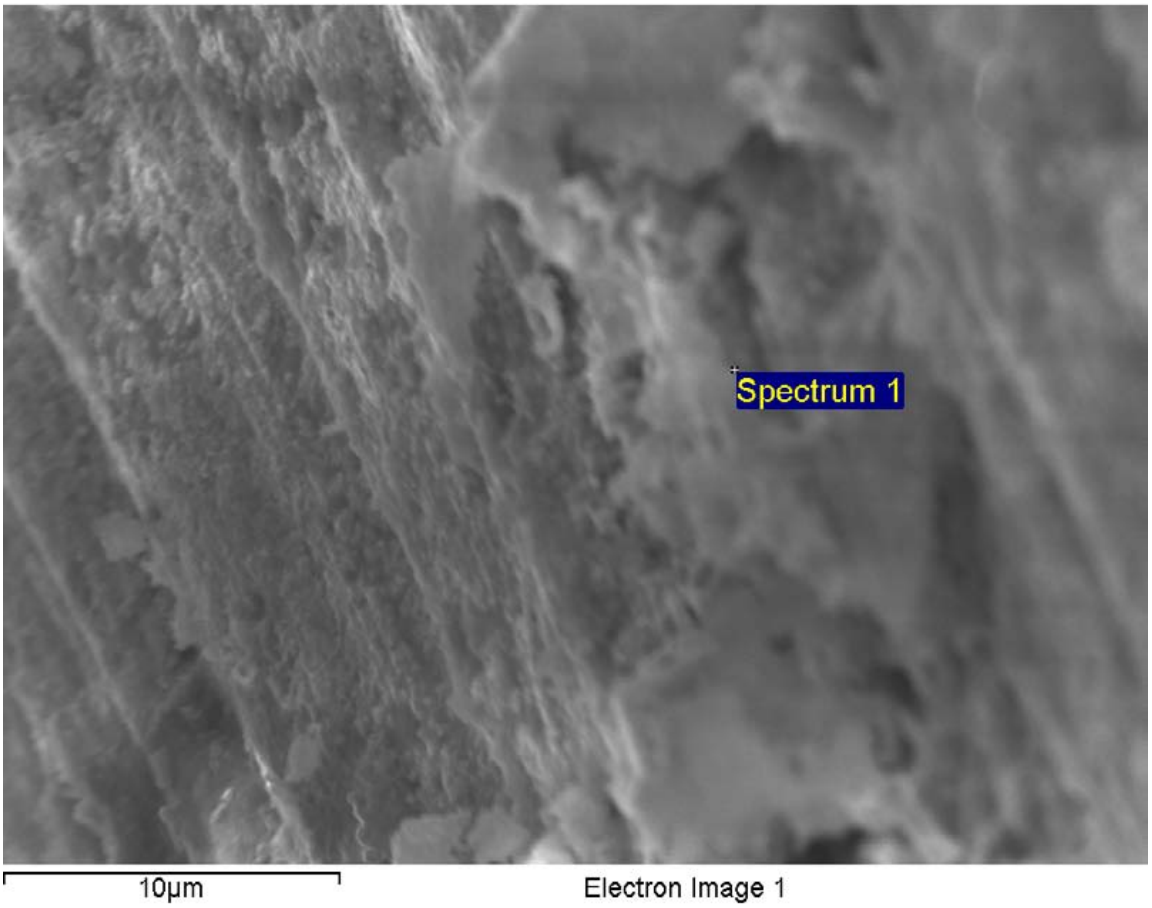

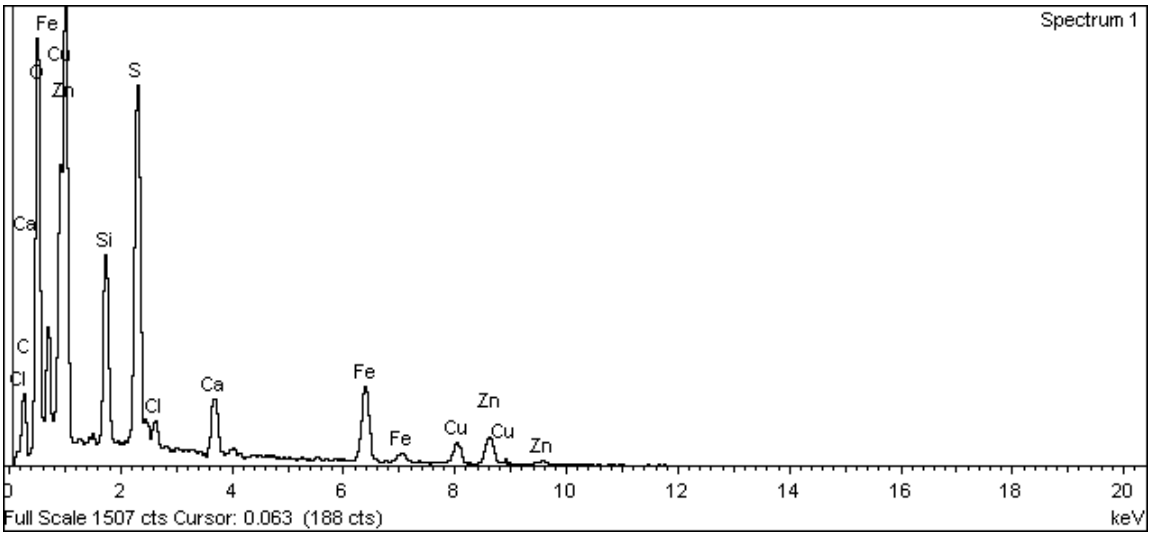

Figure A-158. Surface of black flakes from outer surface of canister and EDX analysis at position of Spectrum 1

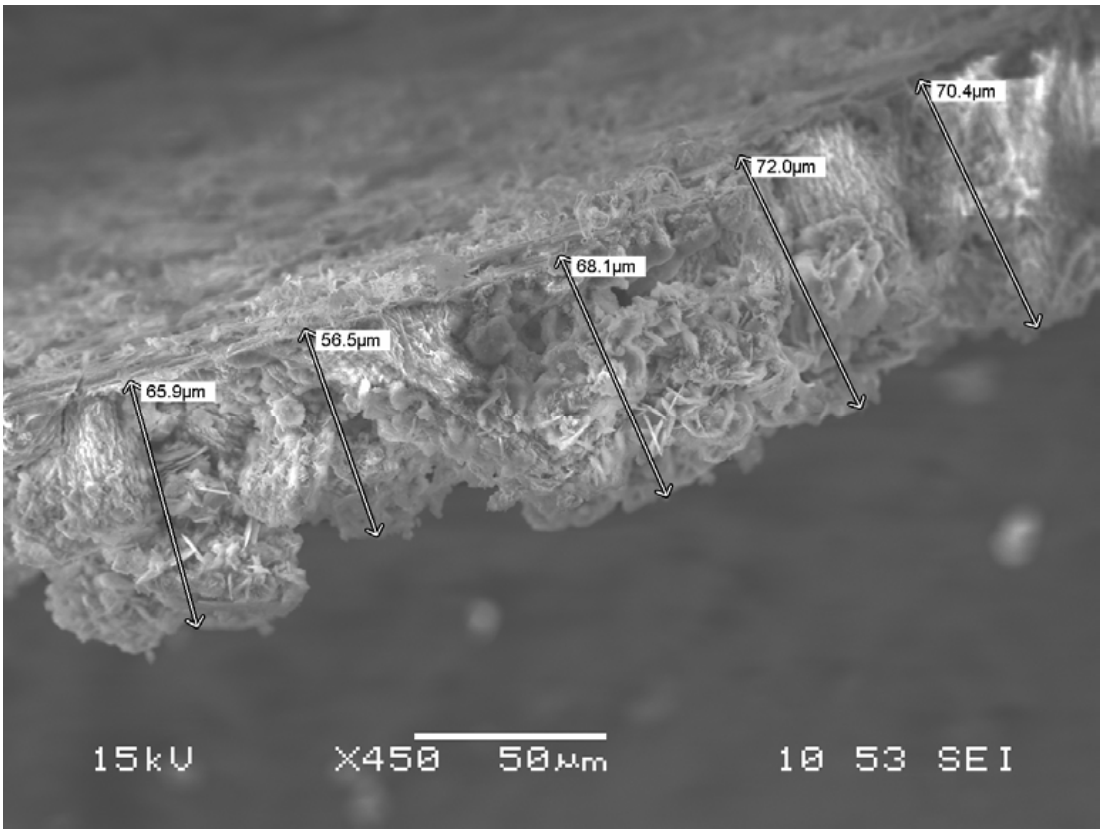

Figure A-159. Surface of black flakes from outer surface of canister

Copper canister inner surface around the top hole

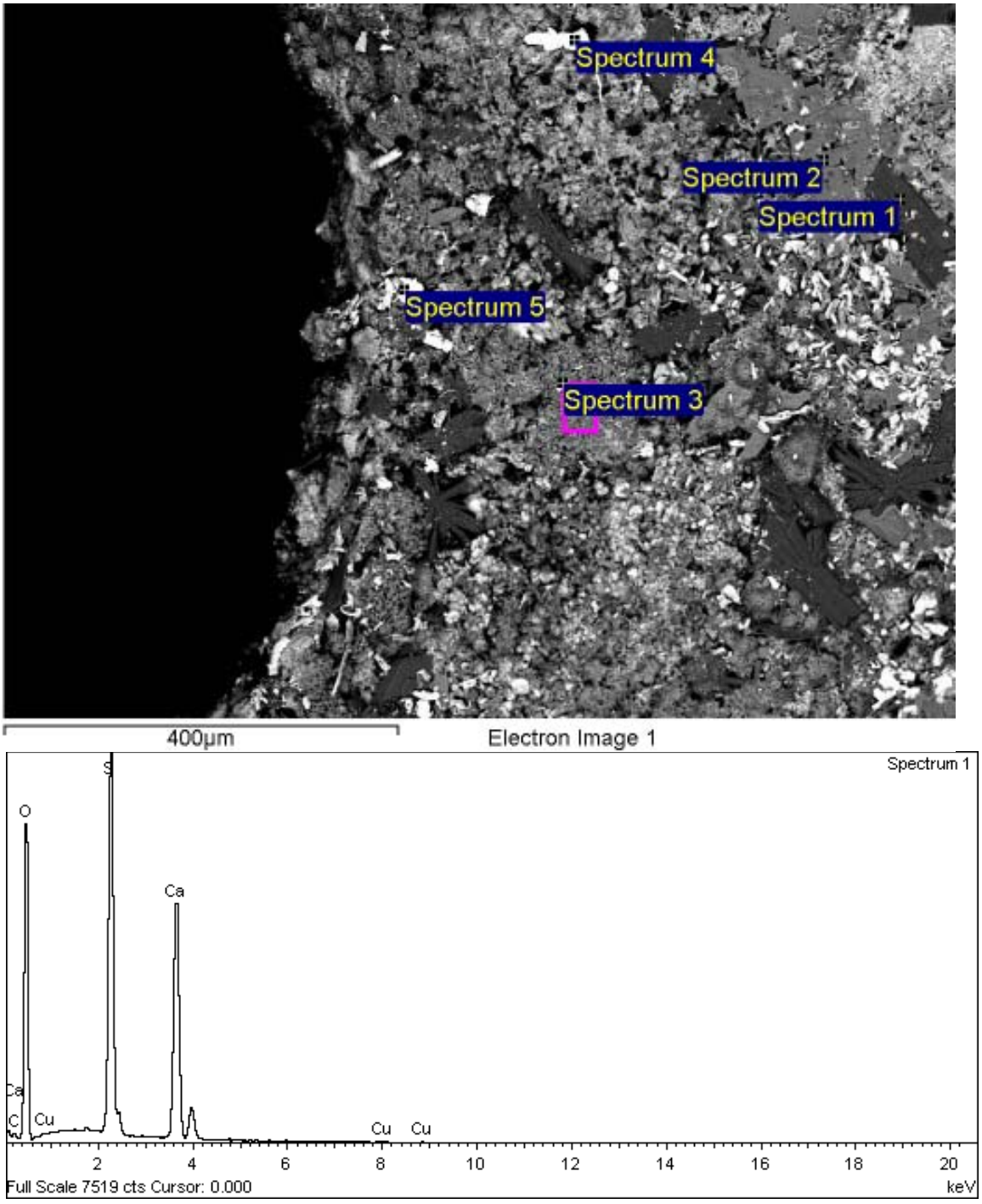

Figure A-160. Inner surface of copper canister around the top hole and EDX analysis at position of Spectrum 1

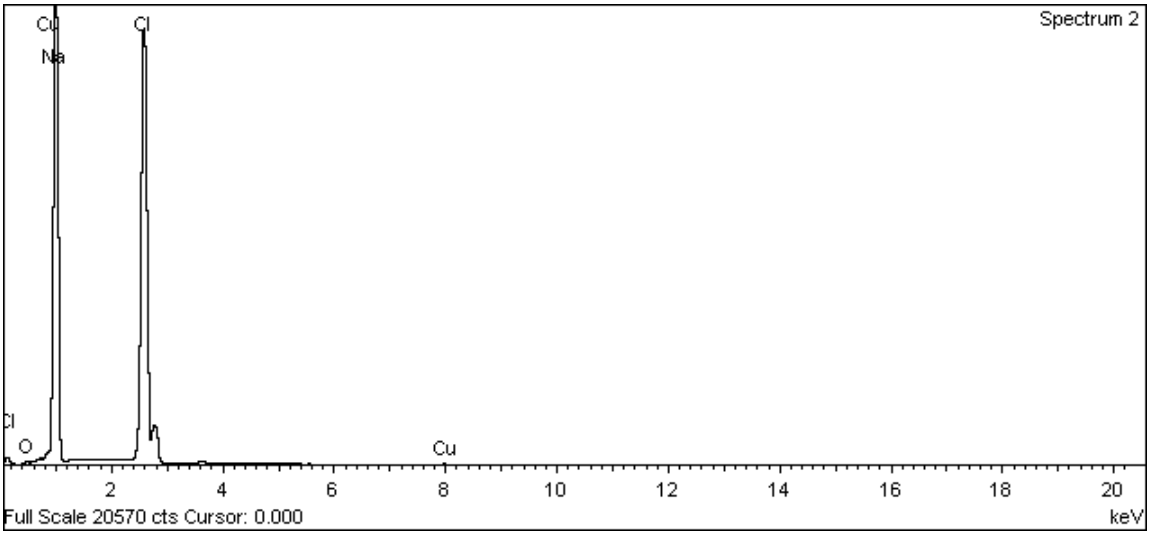

Figure A-161. Inner surface of copper canister around the top hole and EDX analysis at position of Spectrum 2

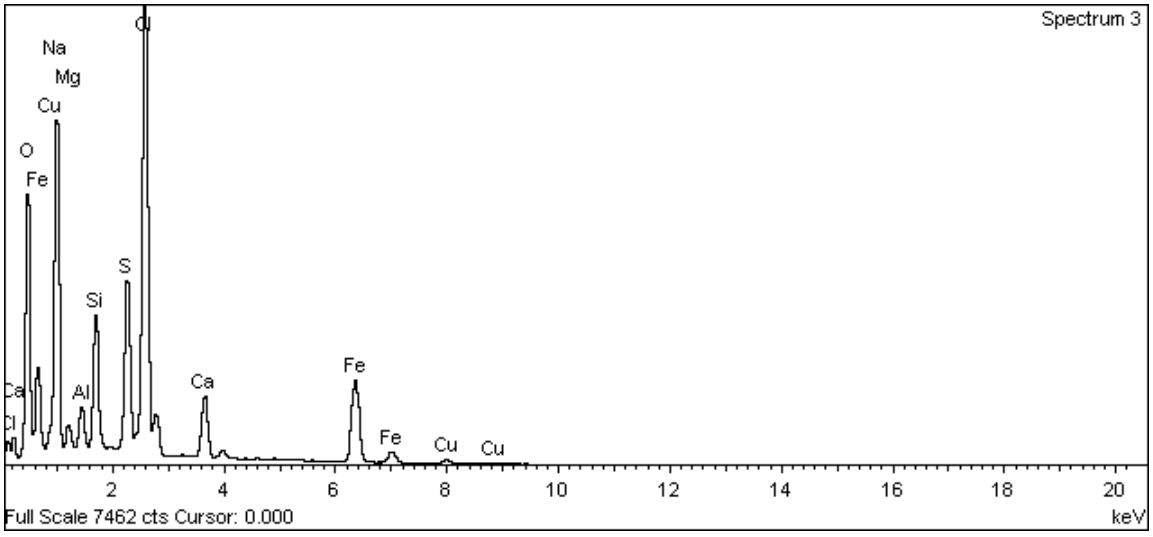

Figure A-162. Inner surface of copper canister around the top hole and EDX analysis at position of Spectrum 3

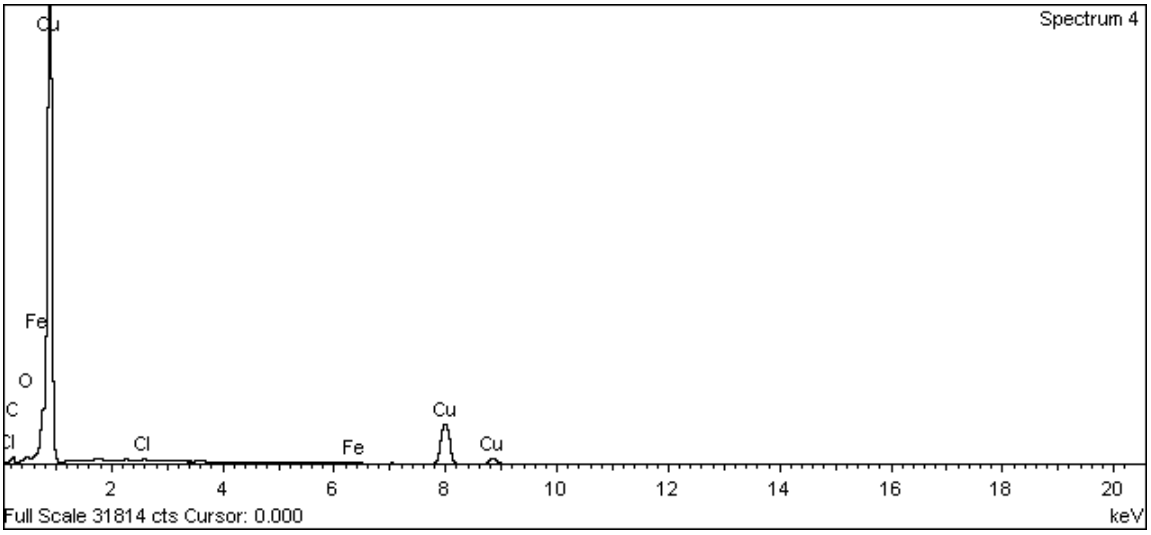

Figure A-163. Inner surface of copper canister around the top hole and EDX analysis at position of Spectrum 4

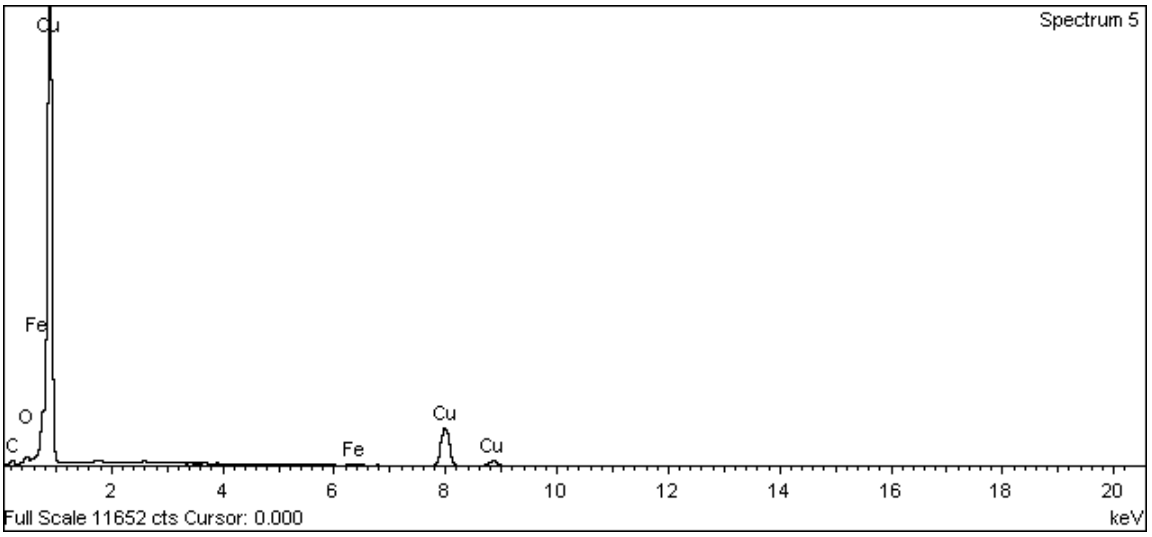

Figure A-164. Inner surface of copper canister around the top hole and EDX analysis at position of Spectrum 5

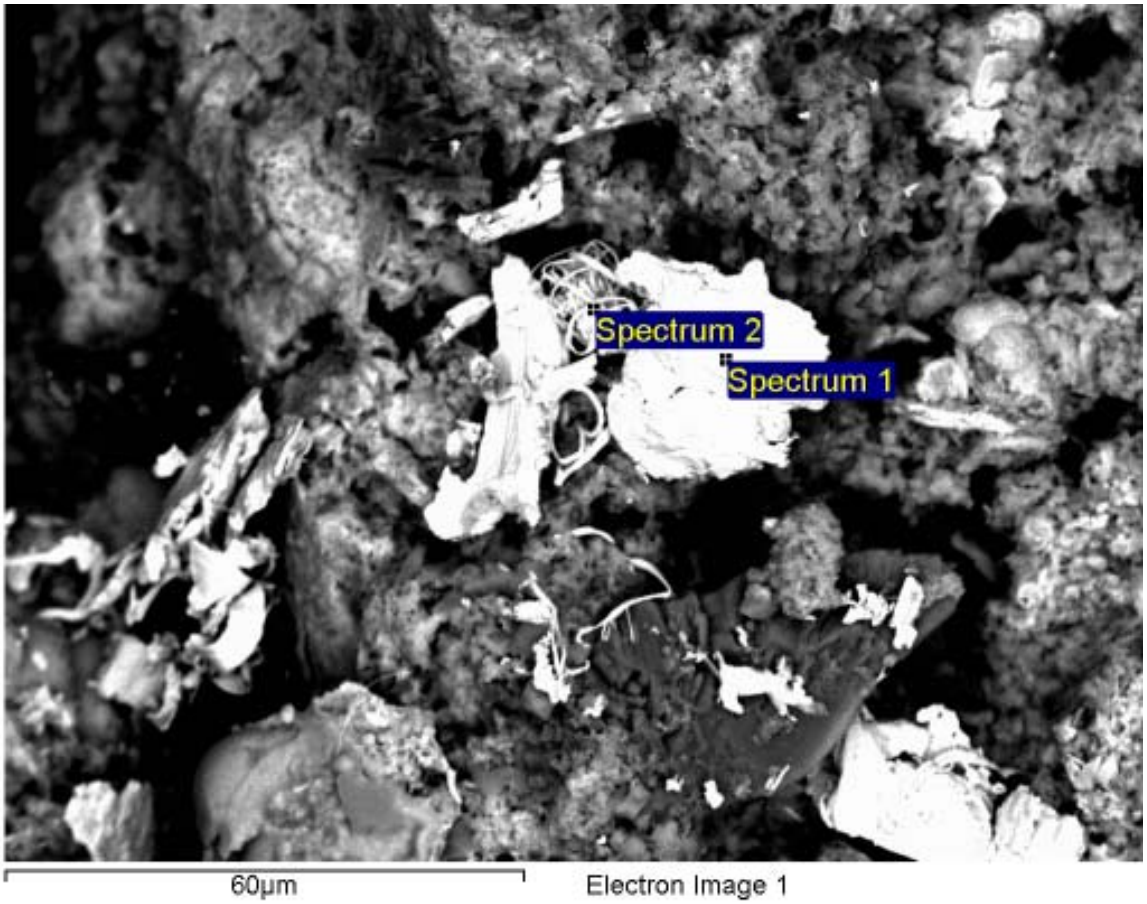

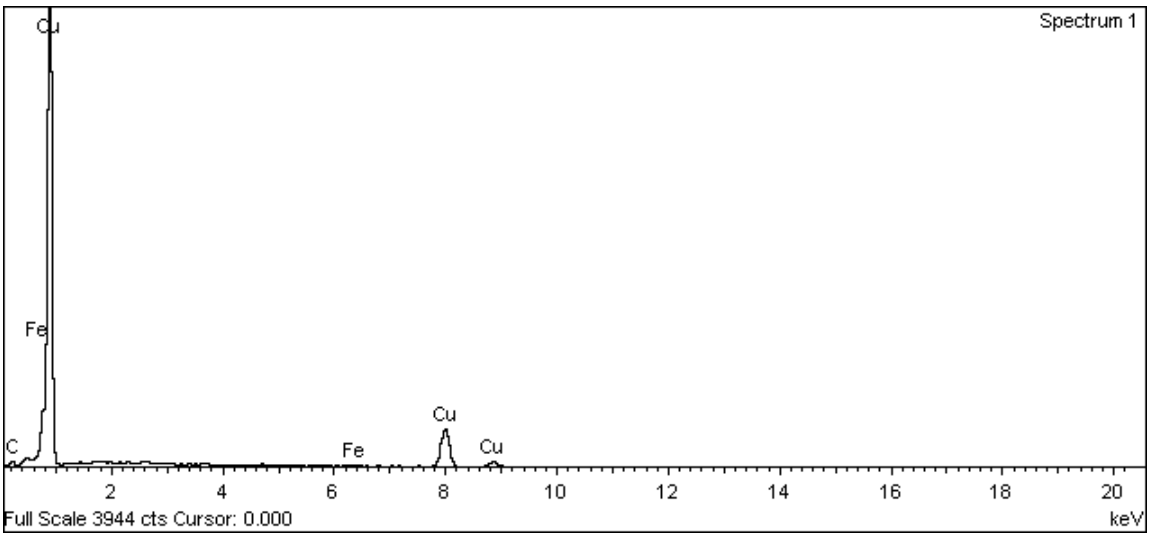

Figure A-165. Inner surface of copper canister around the top hole and EDX analysis at position of Spectrum 1

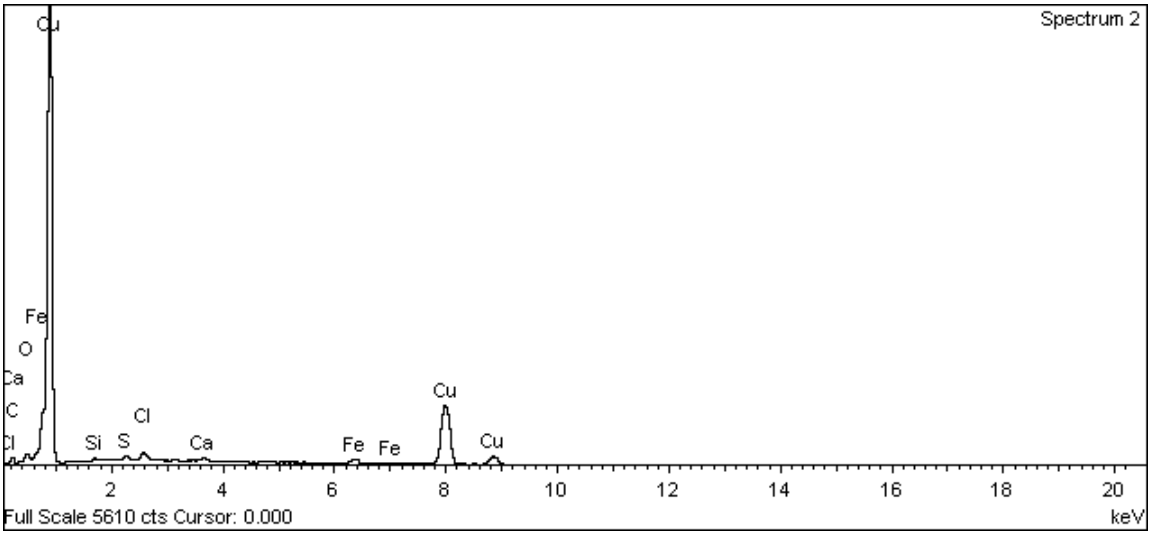

Figure A-166. Inner surface of copper canister around the top hole and EDX analysis at position of Spectrum 2

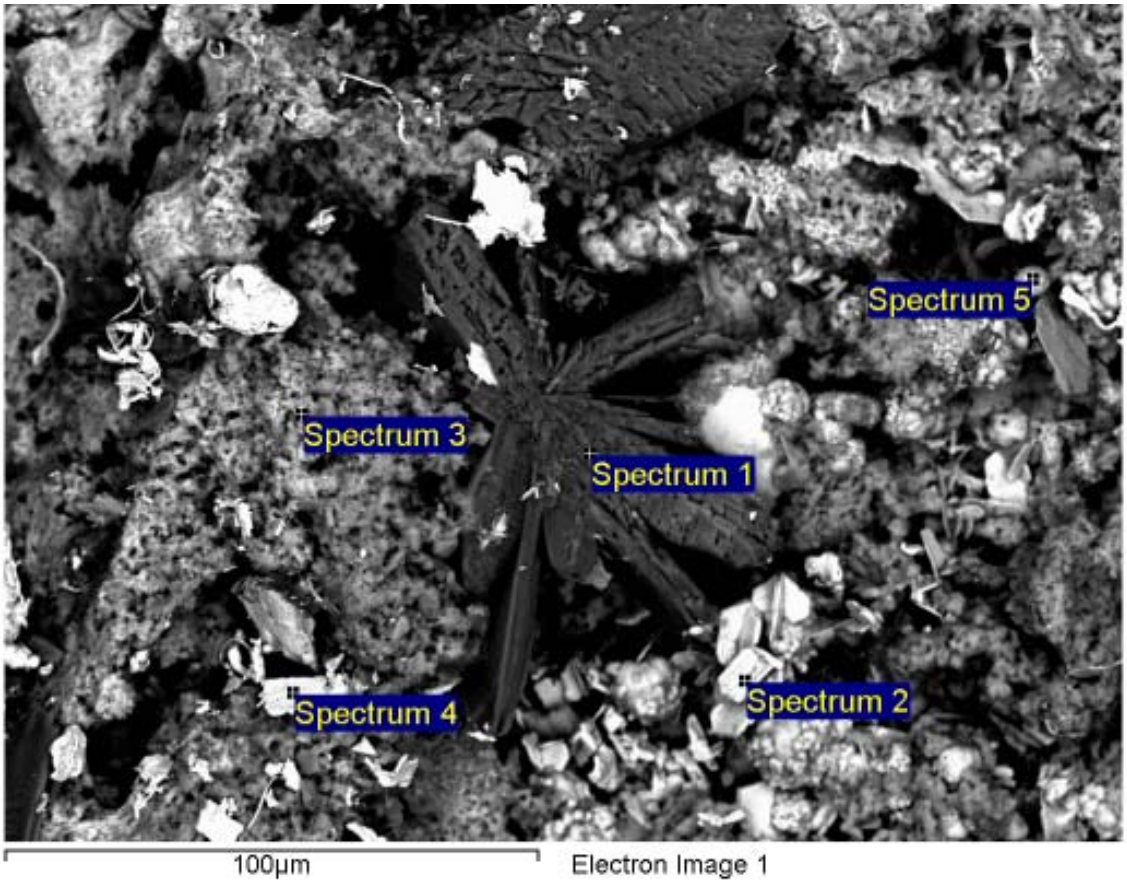

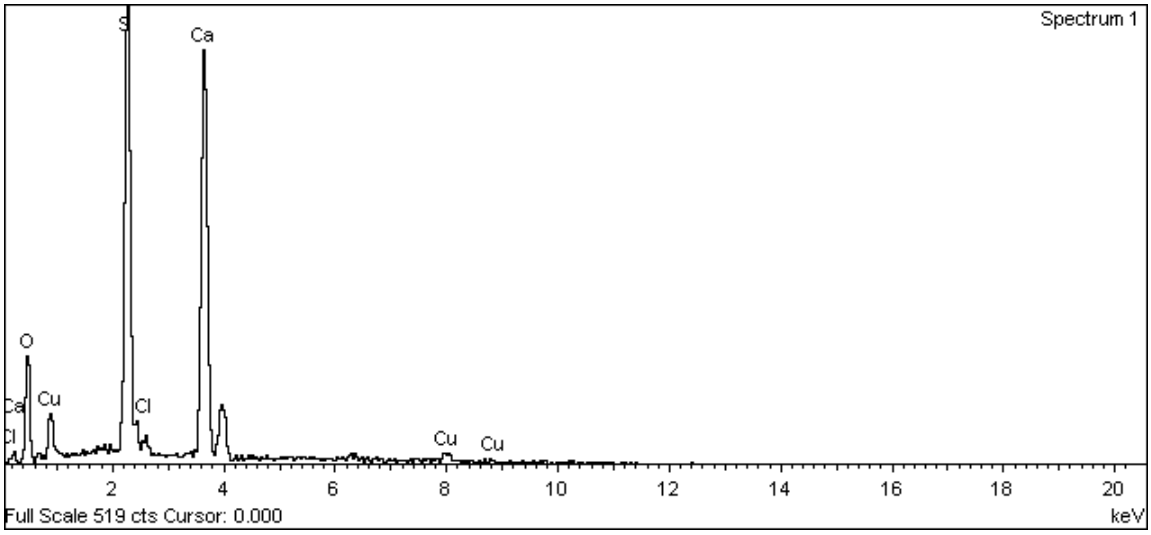

Figure A-167. Inner surface of copper canister around the top hole and EDX analysis at position of Spectrum 1

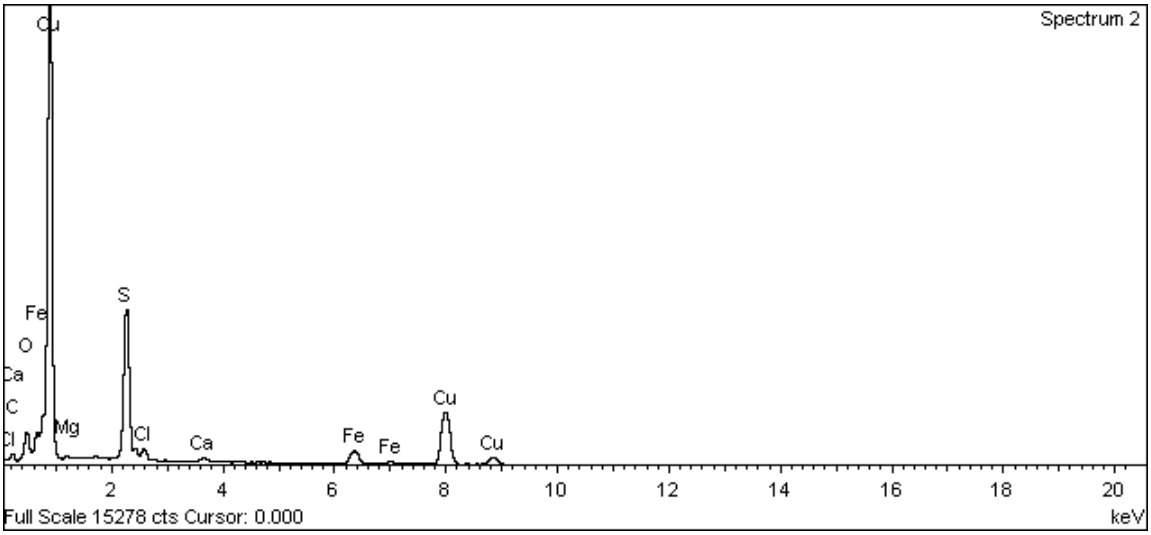

Figure A-168. Inner surface of copper canister around the top hole and EDX analysis at position of Spectrum 2

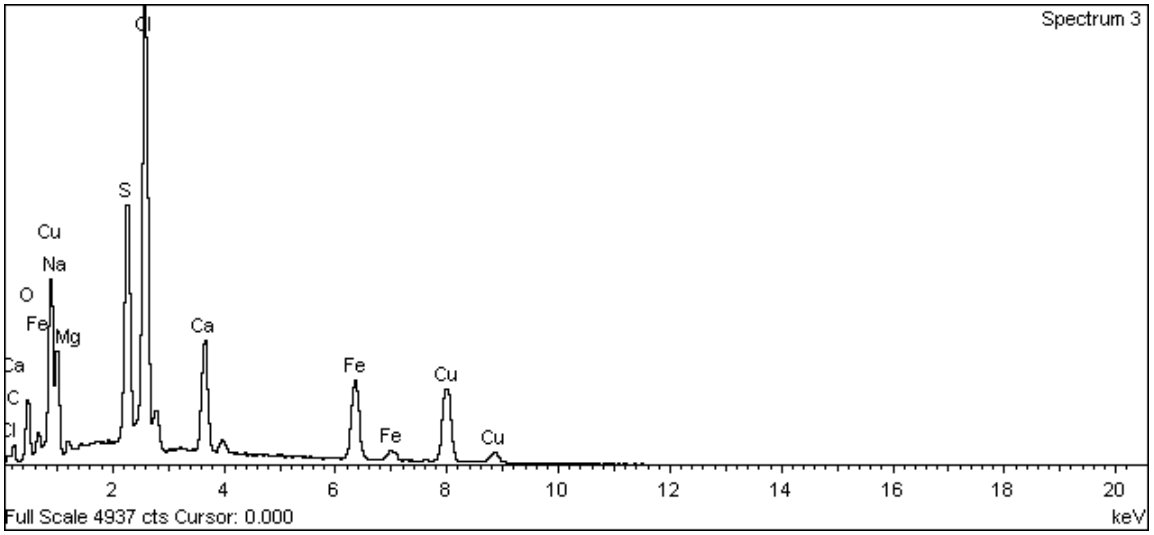

Figure A-169. Inner surface of copper canister around the top hole and EDX analysis at position of Spectrum 3

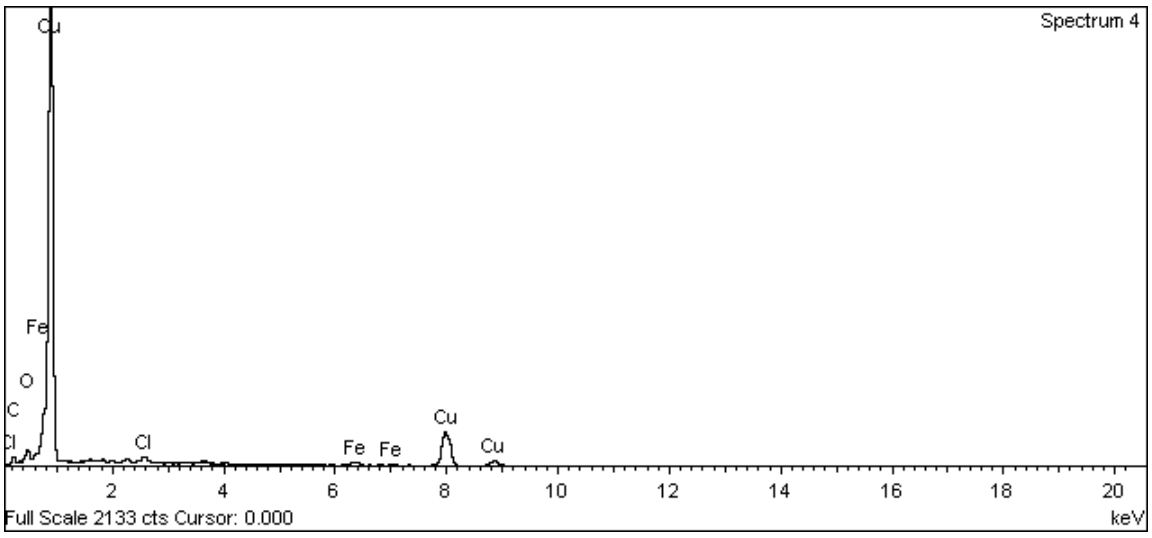

Figure A-170. Inner surface of copper canister around the top hole and EDX analysis at position of Spectrum 4

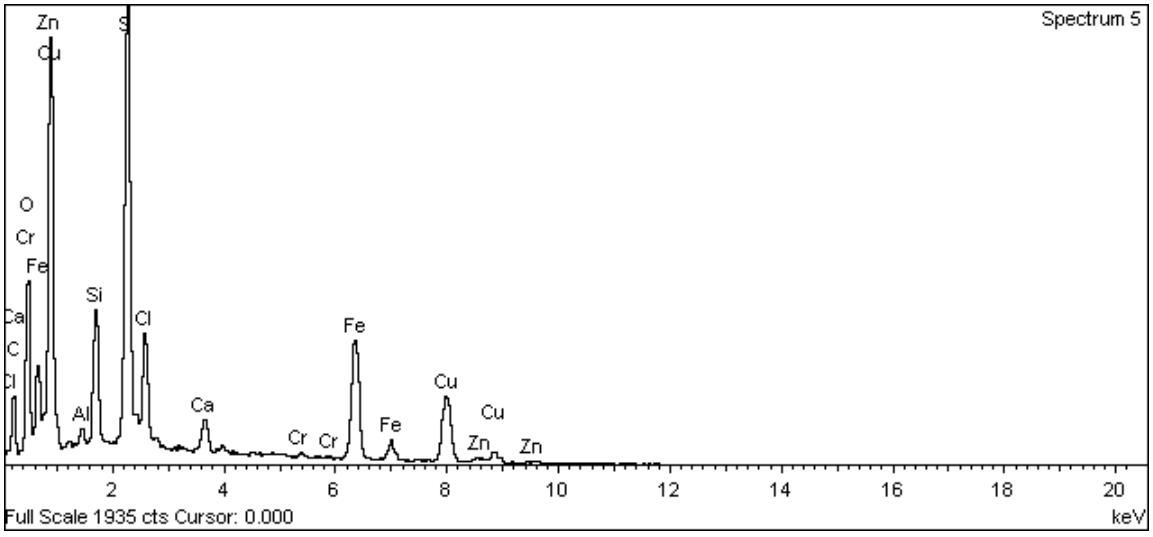

Figure A-171. Inner surface of copper canister around the top hole and EDX analysis at position of Spectrum 5

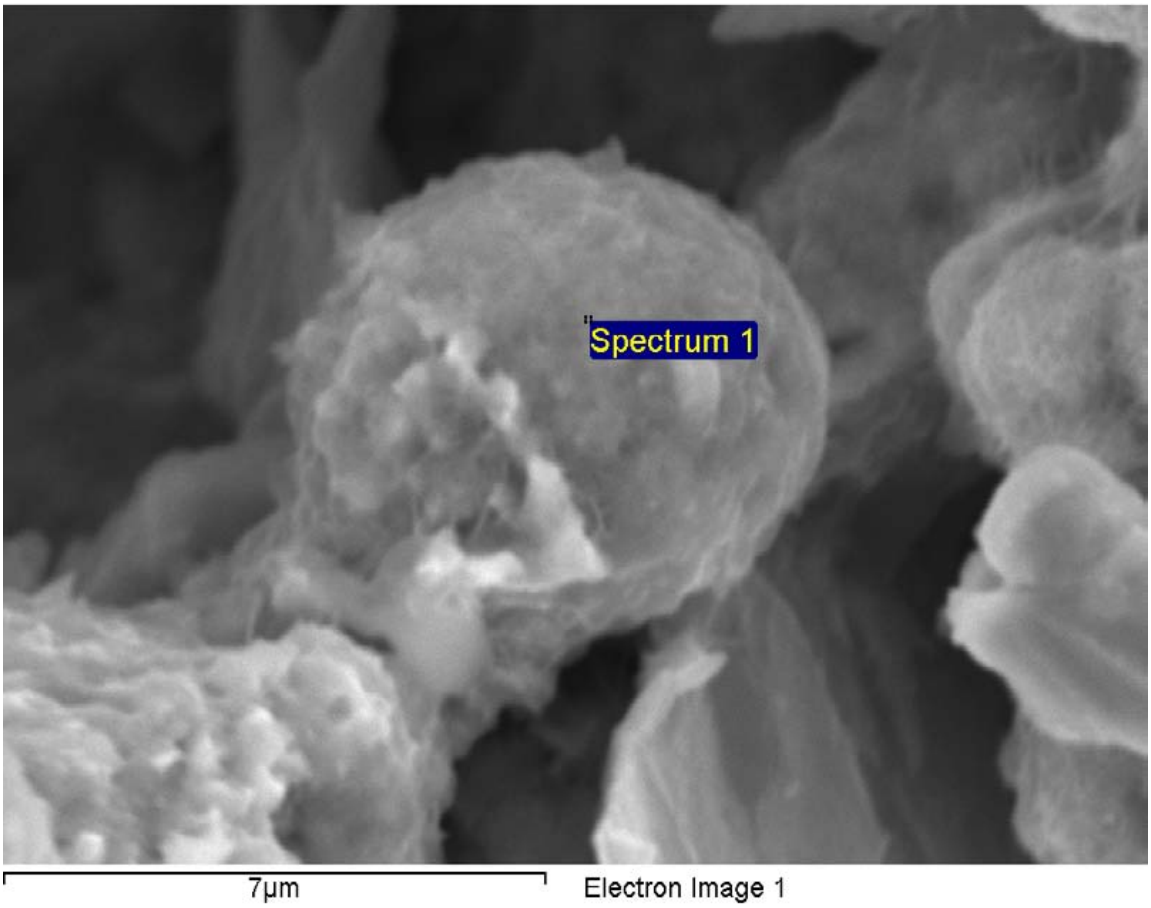

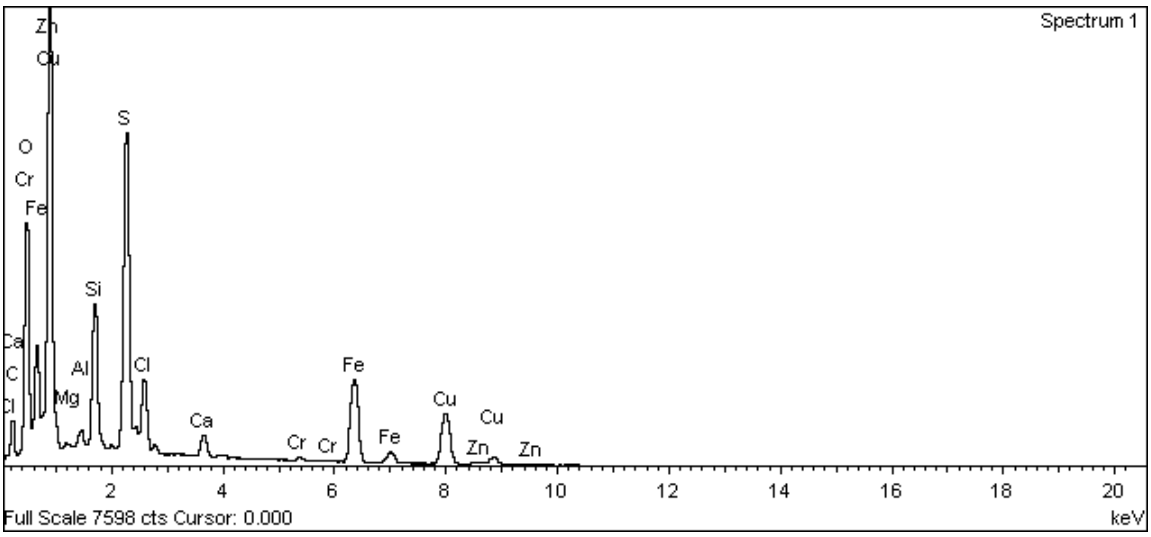

Figure A-172. Inner surface of copper canister around the top hole and EDX analysis at position of Spectrum 1

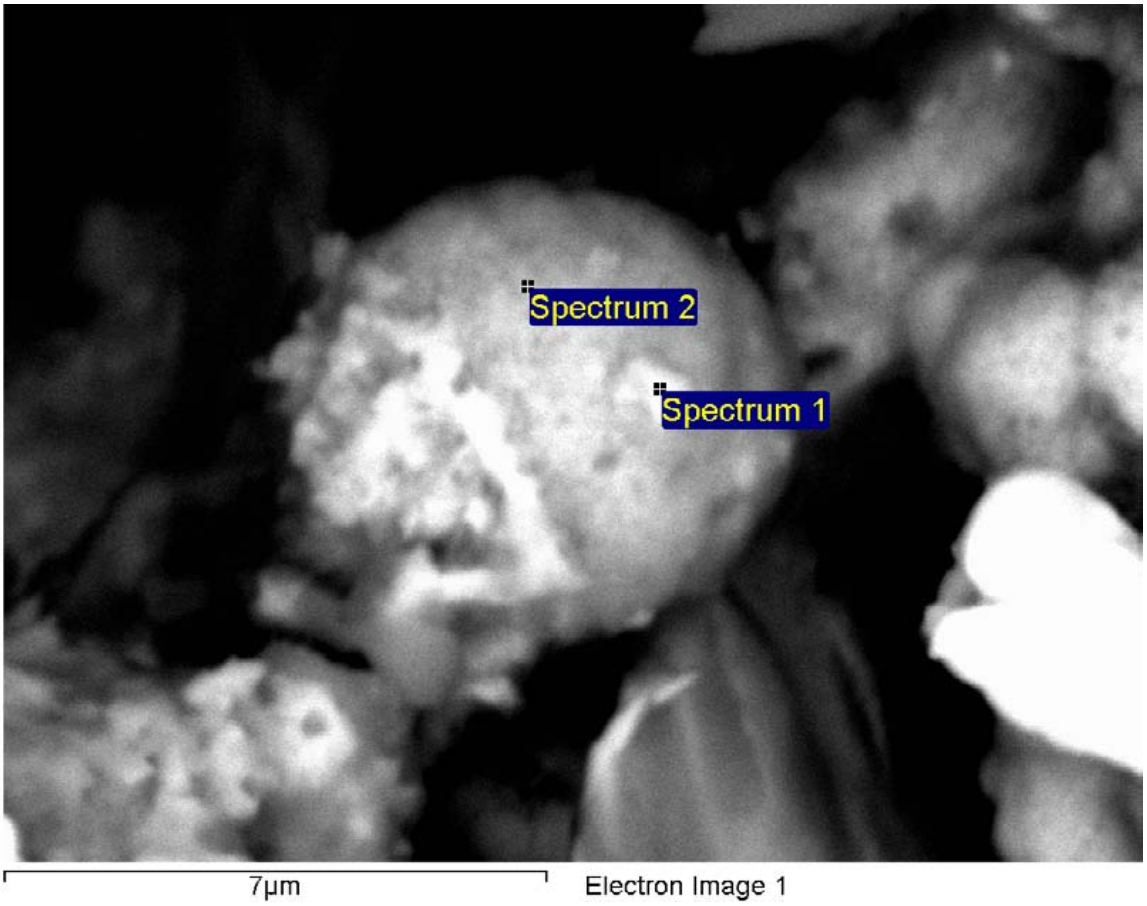

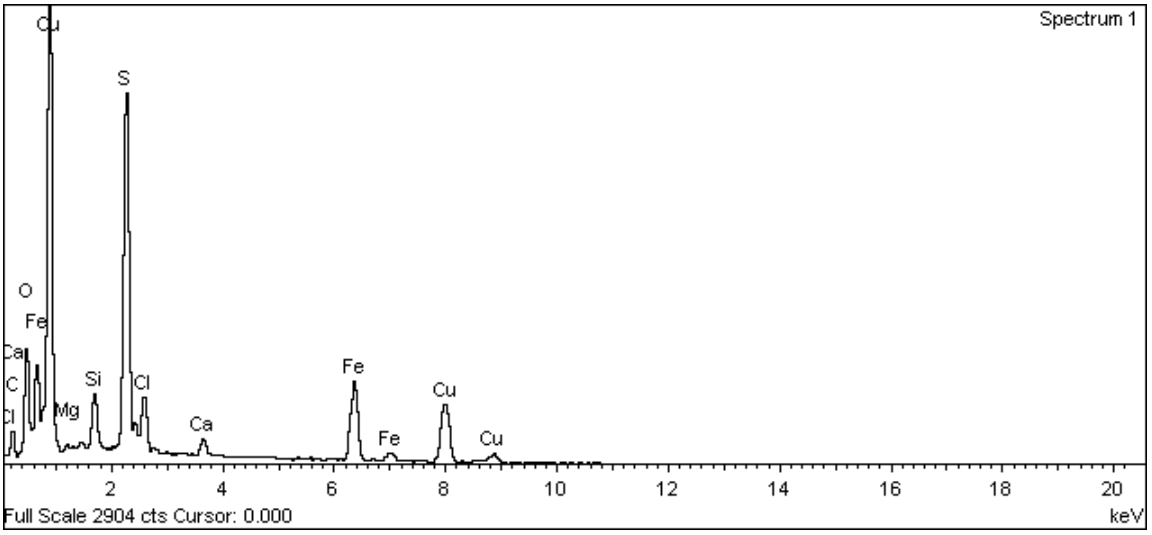

Figure A-173. Inner surface of copper canister around the top hole and EDX analysis at position of Spectrum 1

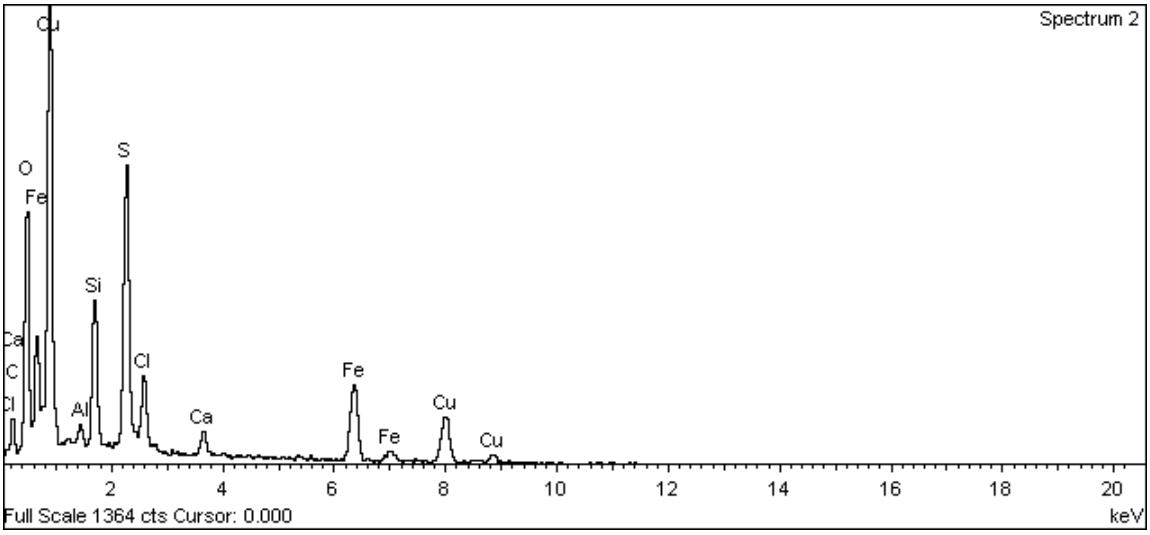

Figure A-174. Inner surface of copper canister around the top hole and EDX analysis at position of Spectrum 2

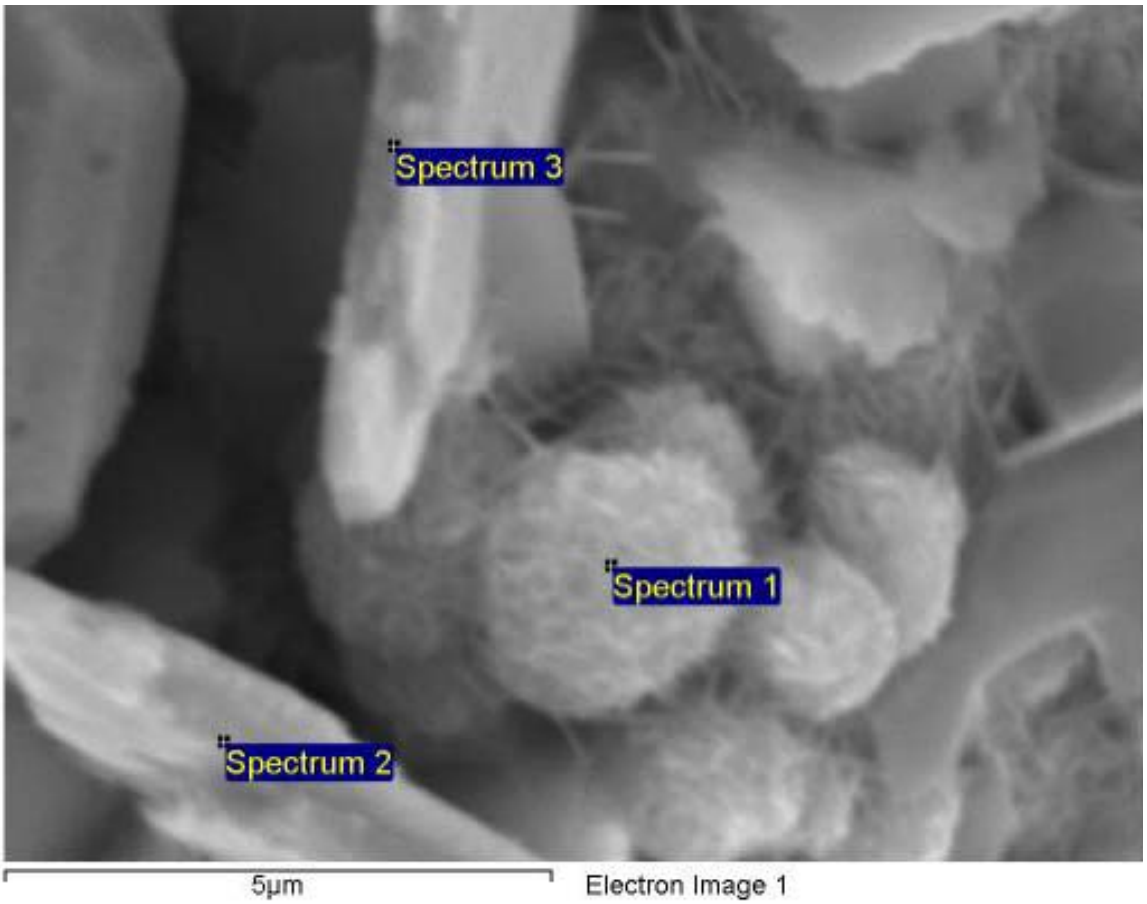

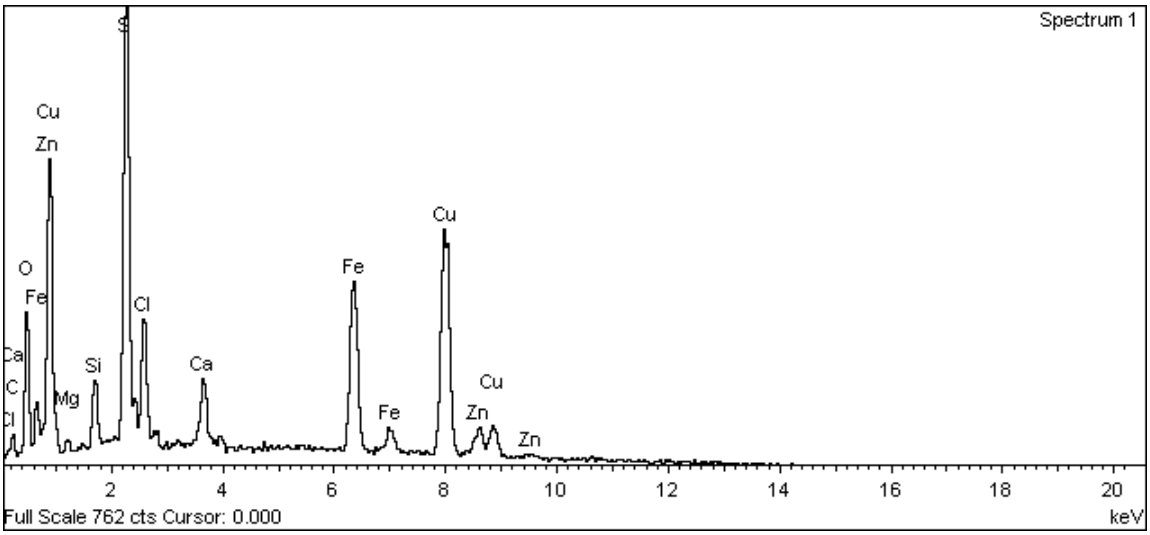

Figure A-175. Inner surface of copper canister around the top hole and EDX analysis at position of Spectrum 1

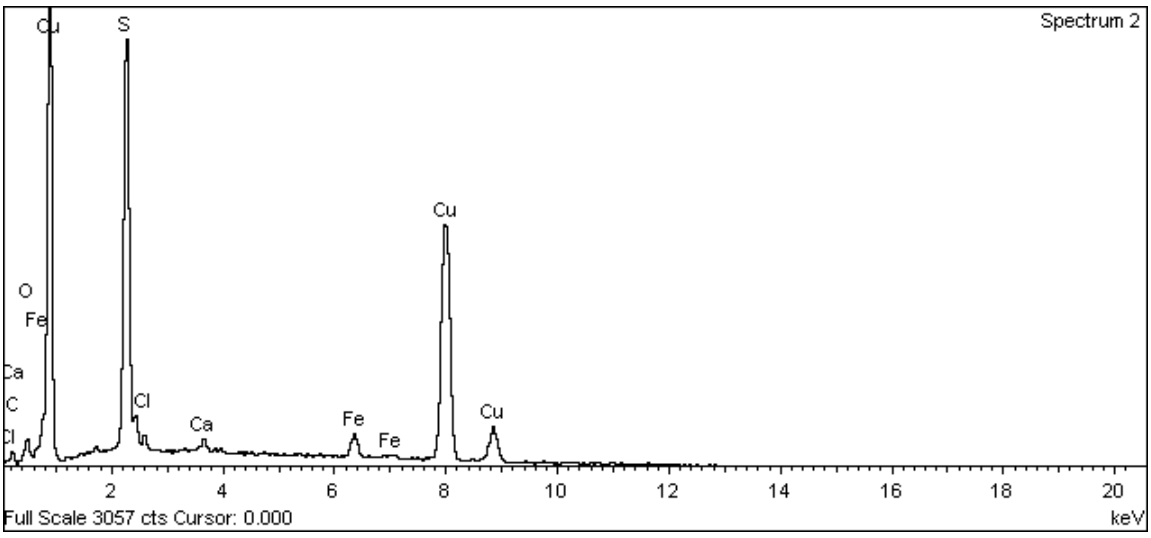

Figure A-176. Inner surface of copper canister around the top hole and EDX analysis at position of Spectrum 2

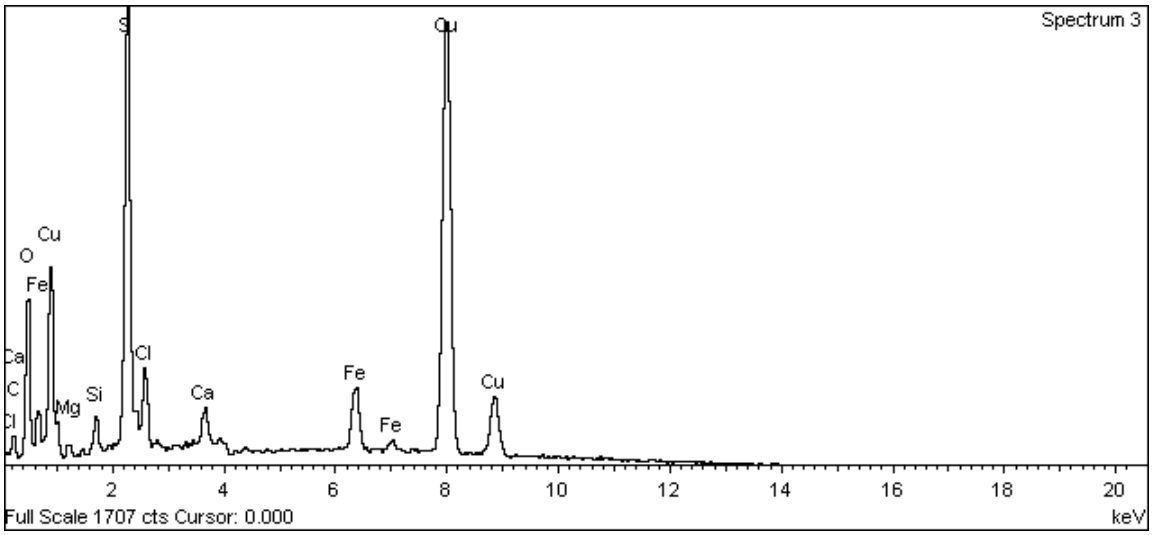

Figure A-177. Inner surface of copper canister around the top hole and EDX analysis at position of Spectrum 3

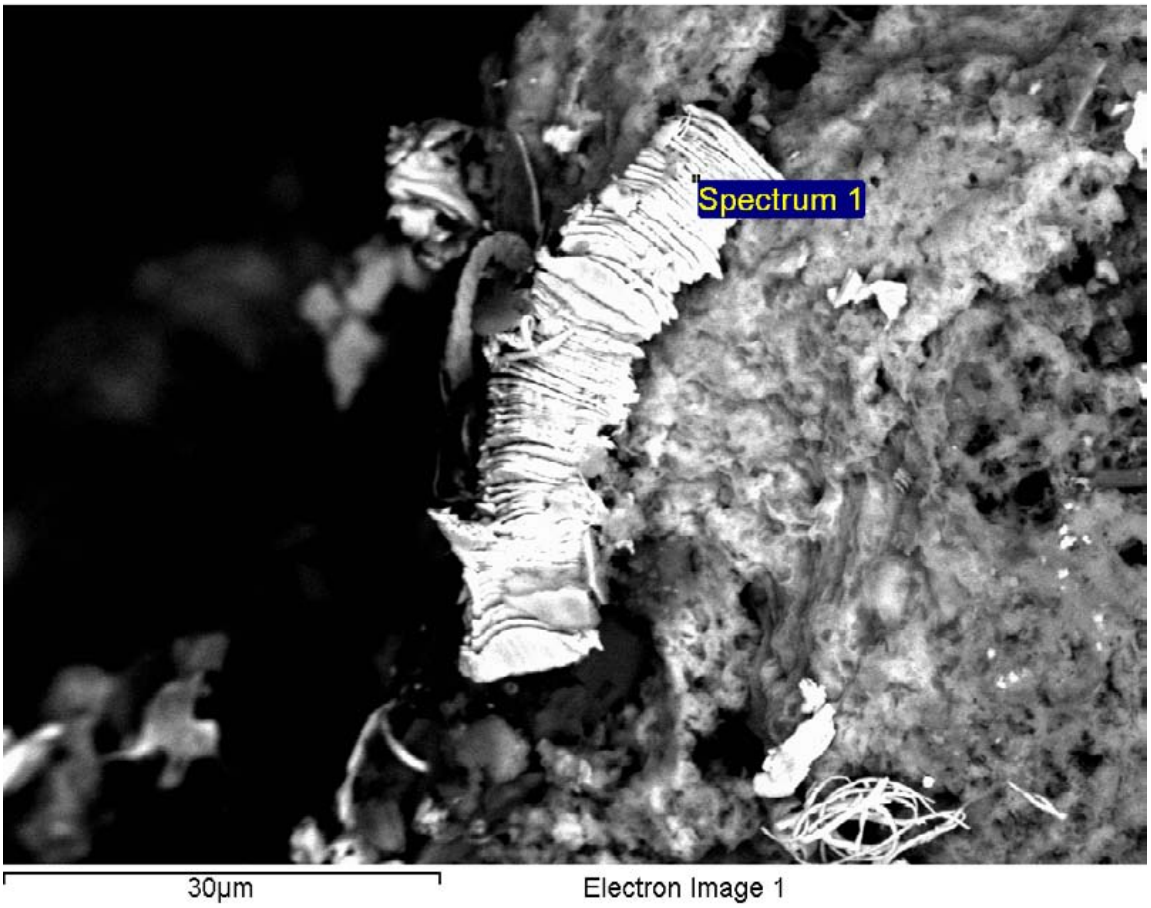

Figure A-178. Inner surface of copper canister around the top hole and EDX analysis at position of Spectrum 1

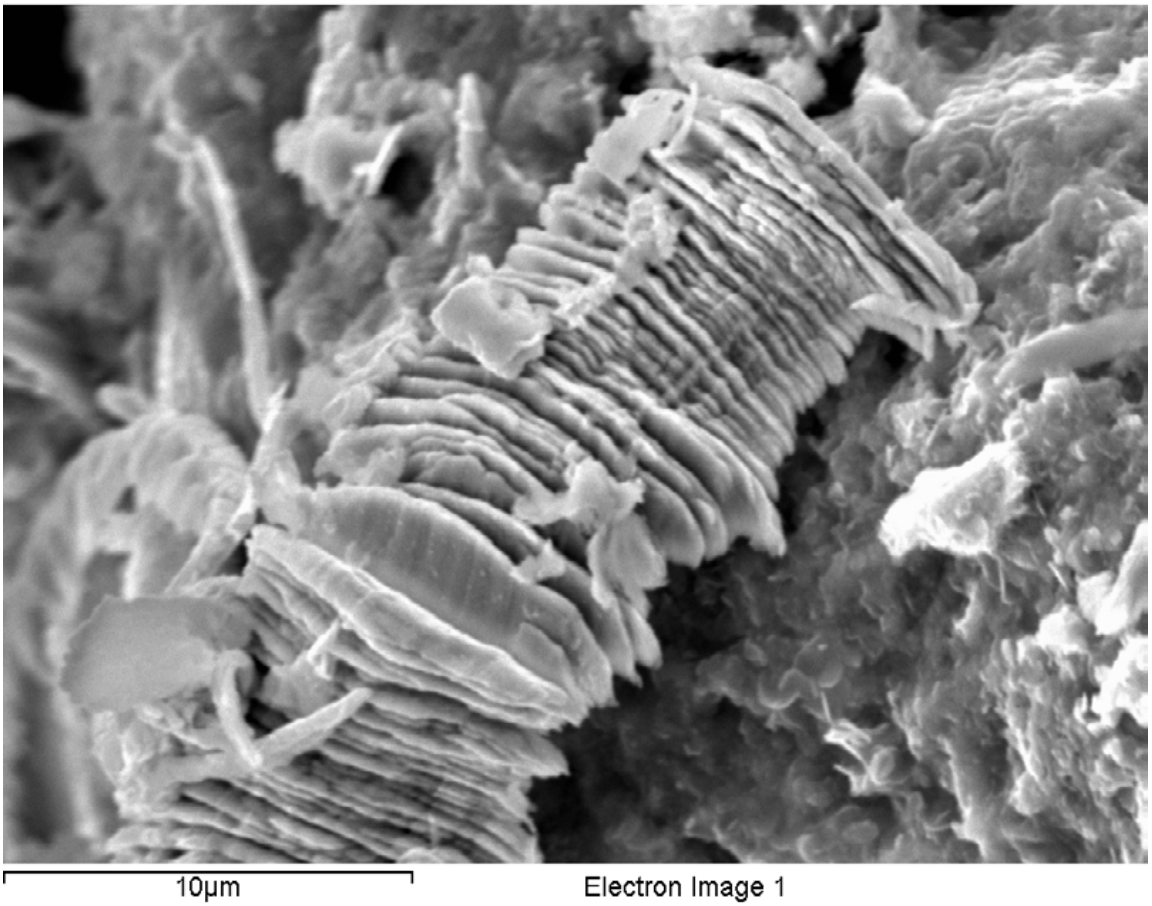

Figure A-179. Inner surface of copper canister around the top hole

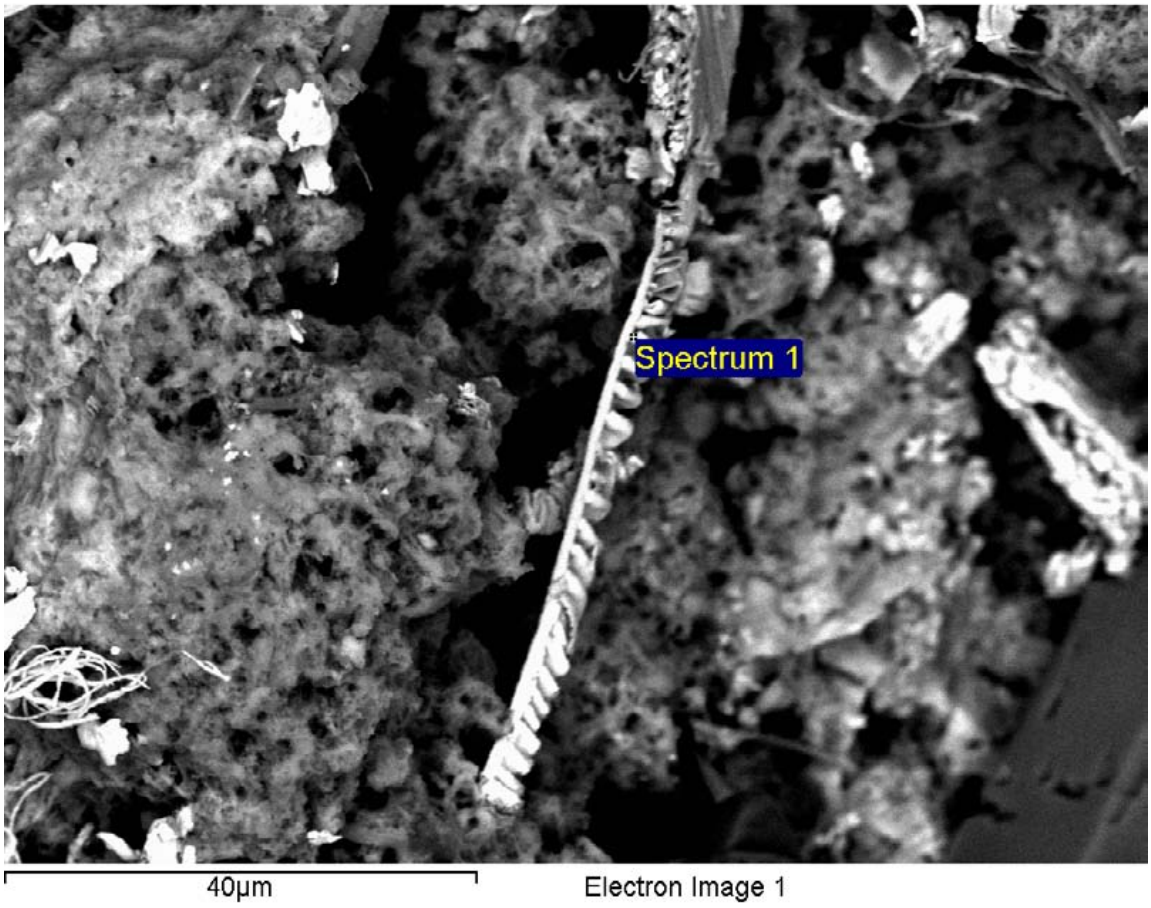

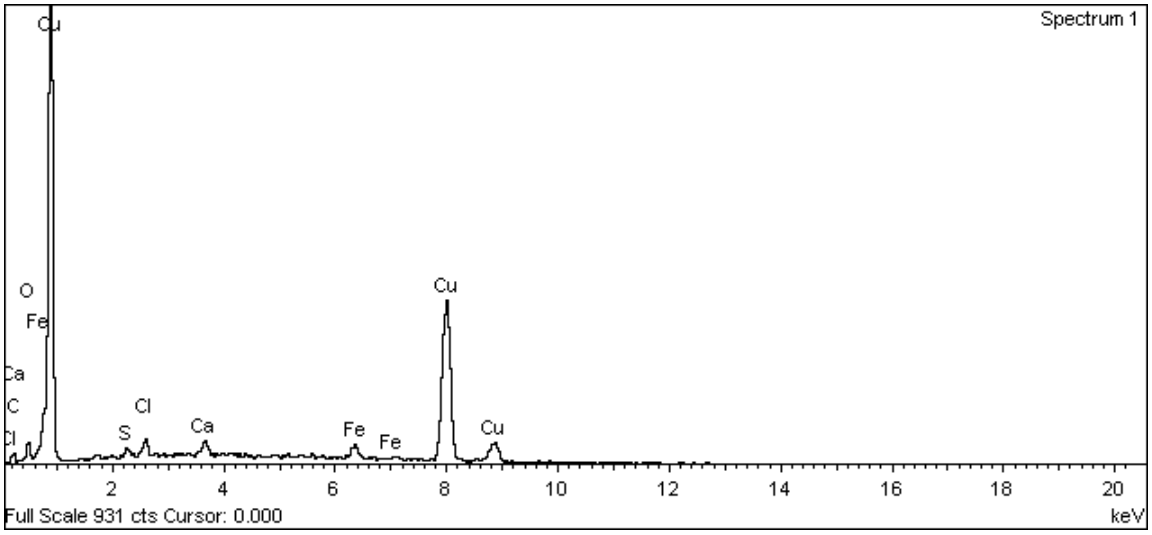

Figure A-180. Inner surface of copper canister around the top hole and EDX analysis at position of Spectrum 1

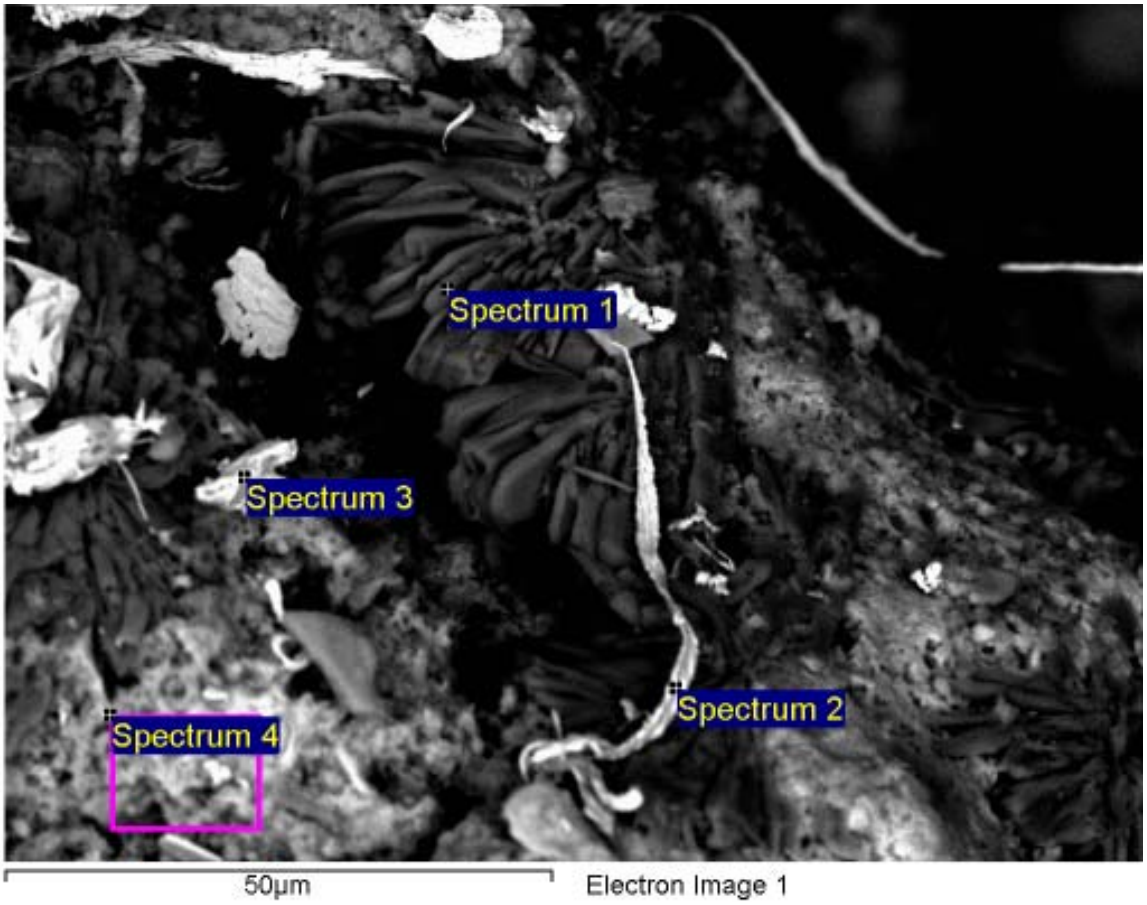

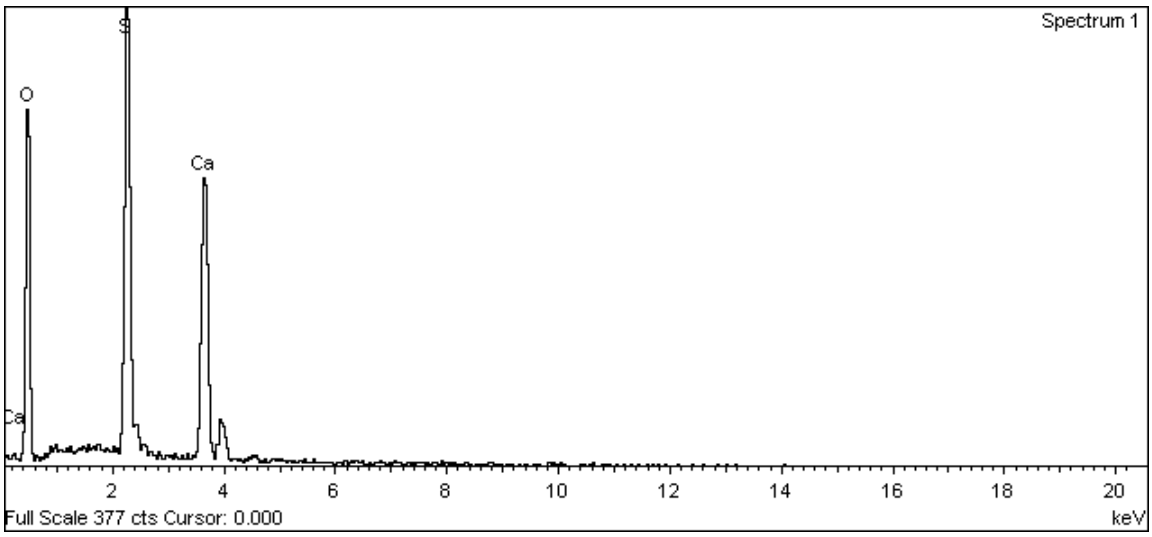

Figure A-181. Inner surface of copper canister around the top hole and EDX analysis at position of Spectrum 1

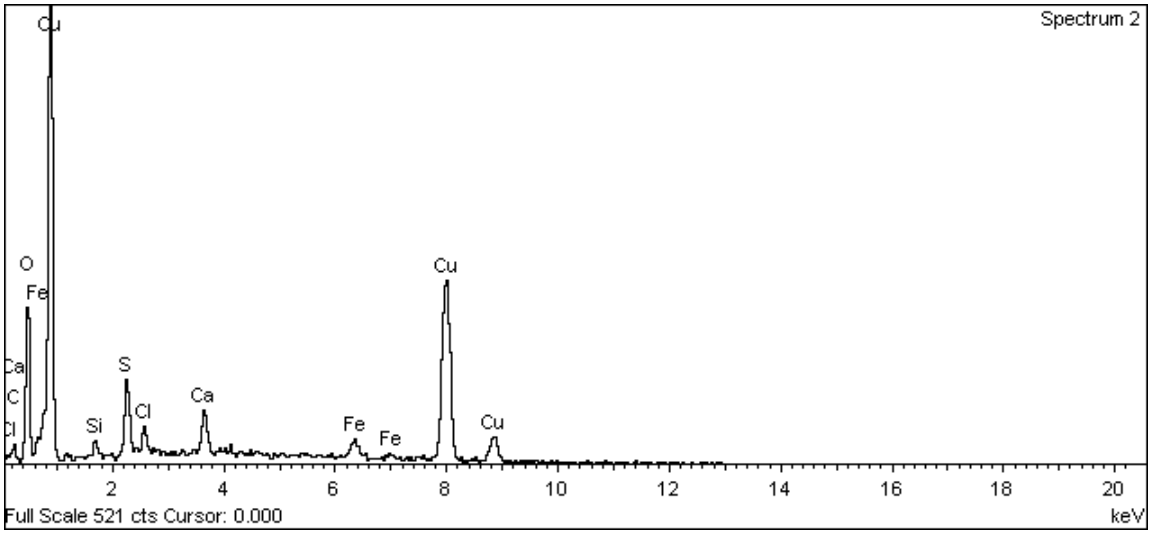

Figure A-182. Inner surface of copper canister around the top hole and EDX analysis at position of Spectrum 2

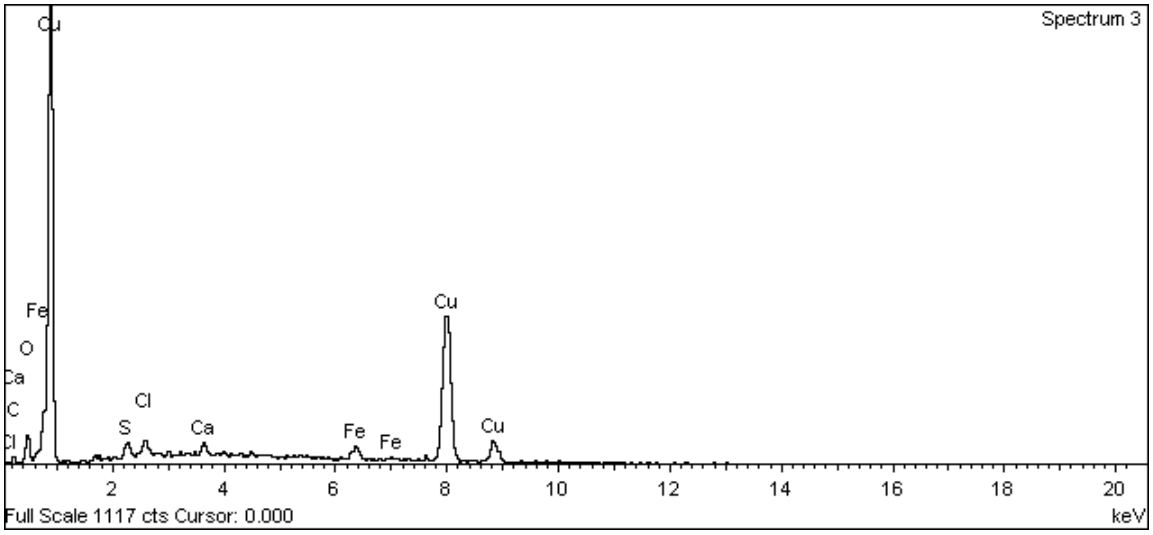

Figure A-183. Inner surface of copper canister around the top hole and EDX analysis at position of Spectrum 3

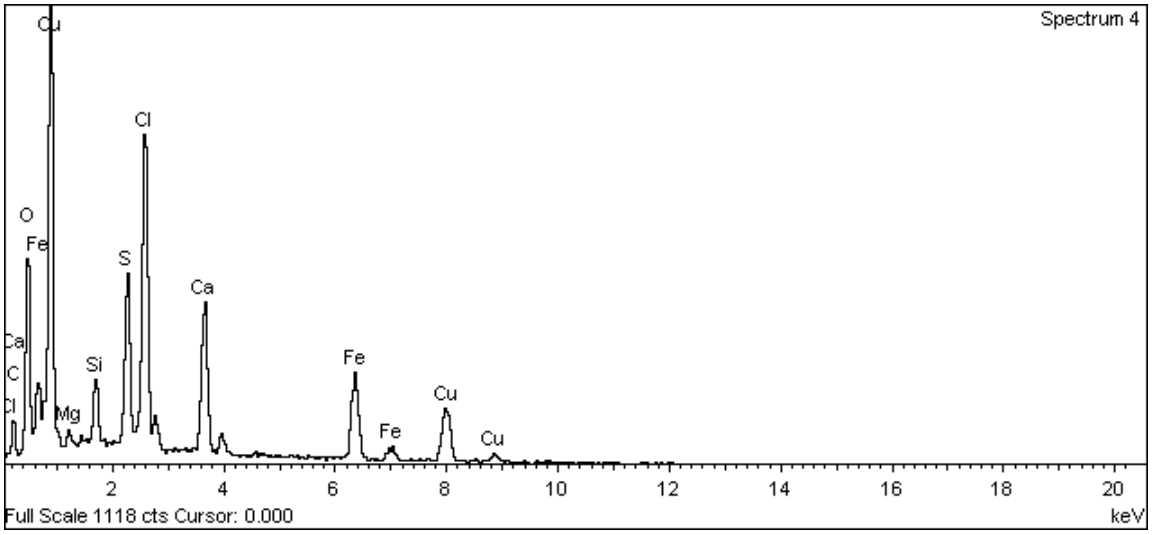

Figure A-184. Inner surface of copper canister around the top hole and EDX analysis at position of Spectrum 4

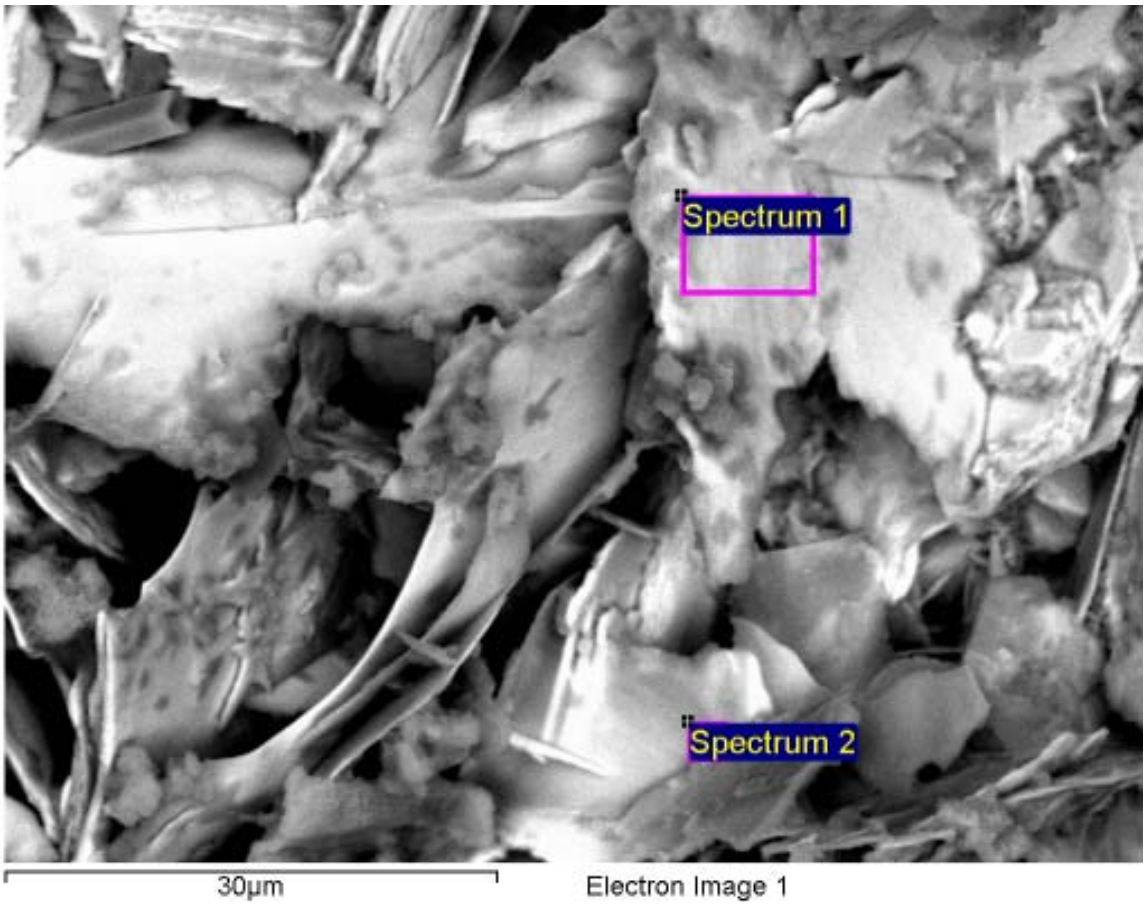

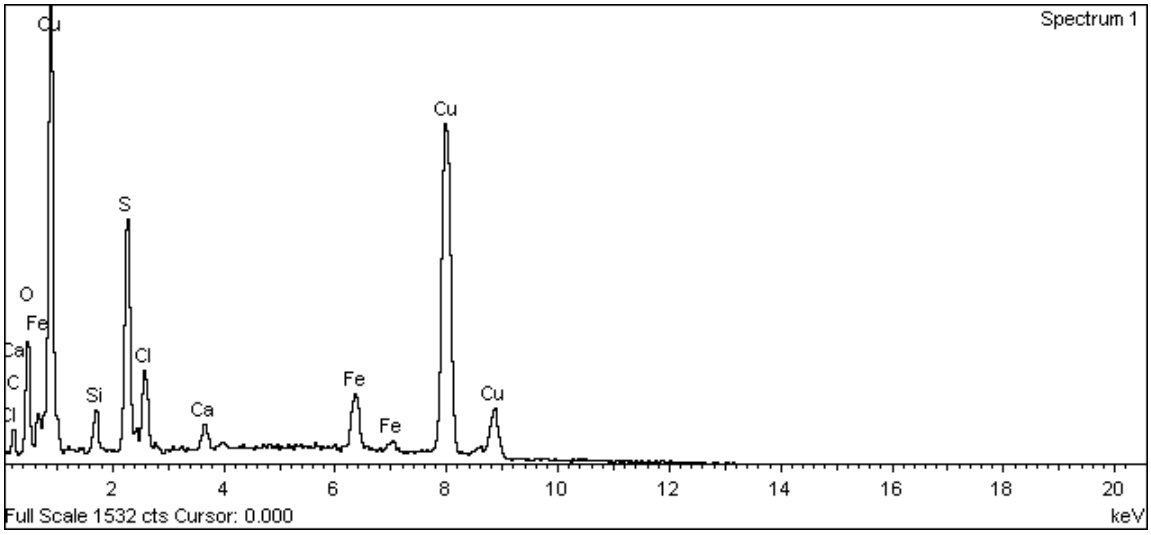

Figure A-185. Inner surface of copper canister around the top hole and EDX analysis at position of Spectrum 1

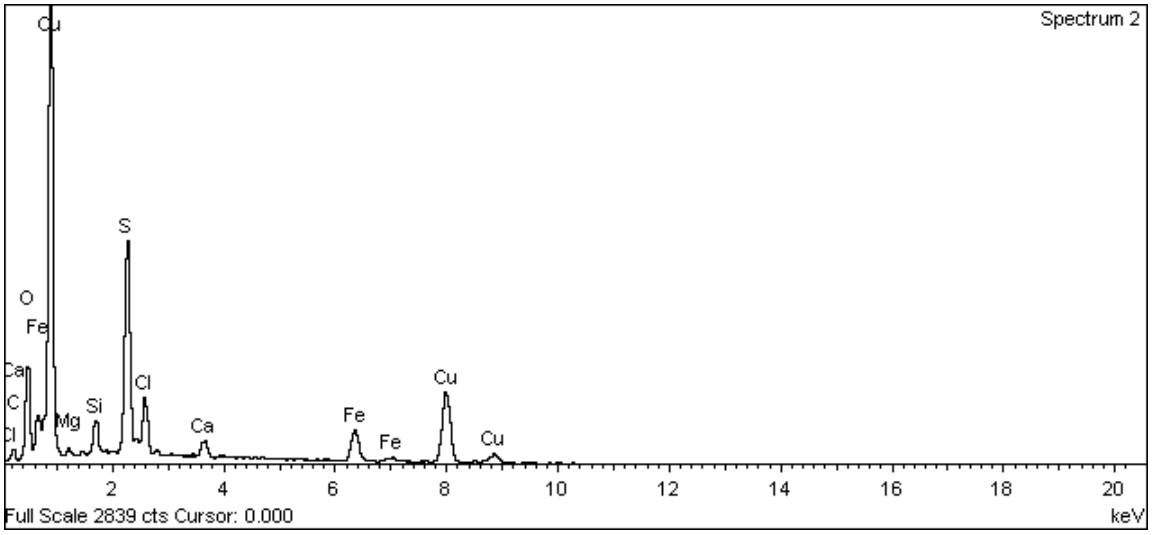

Figure A-186. Inner surface of copper canister around the top hole and EDX analysis at position of Spectrum 2

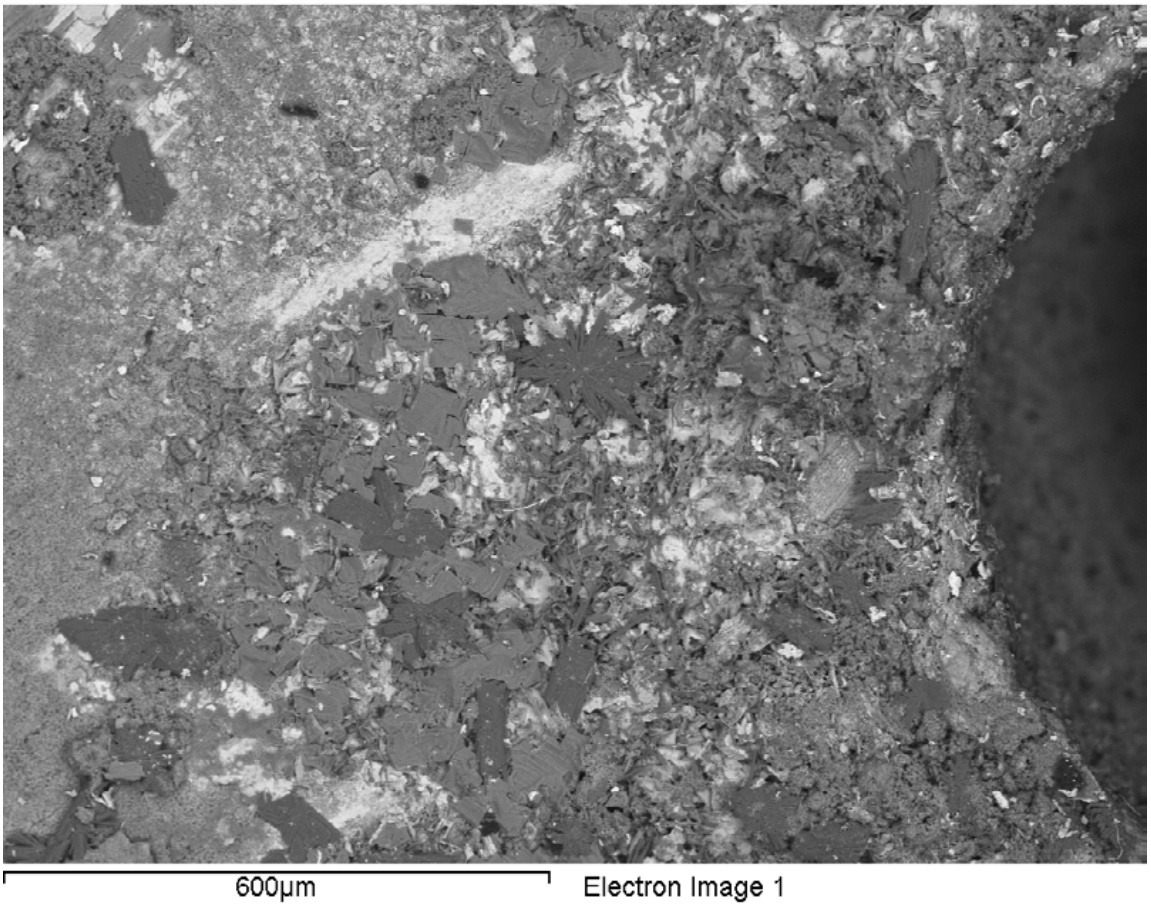

Figure A-187. Inner surface of copper canister around the top hole and EDX analysis – sum spectrum for whole area of image

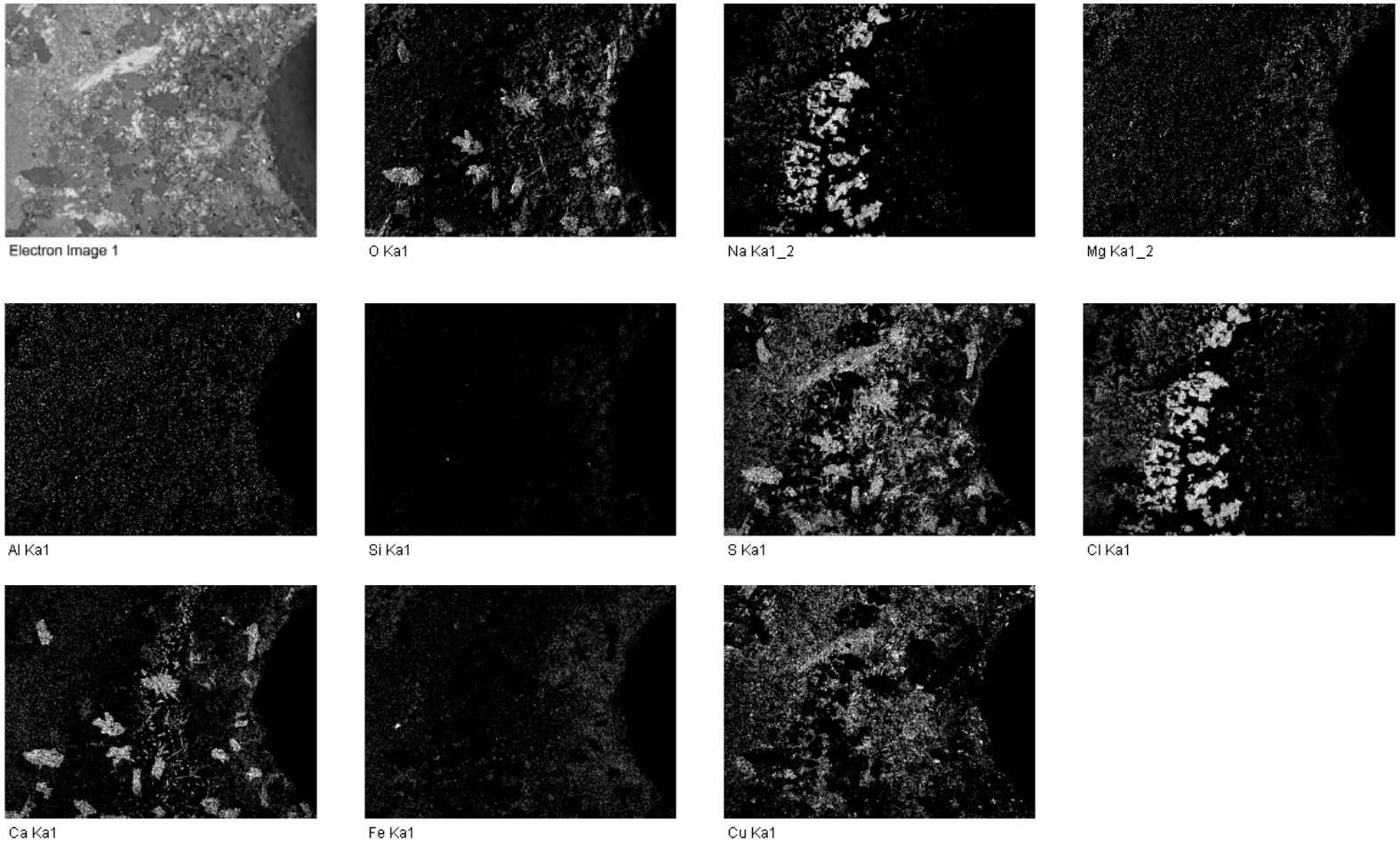

Figure A-188. Elemental maps for Inner surface of copper canister around the top hole

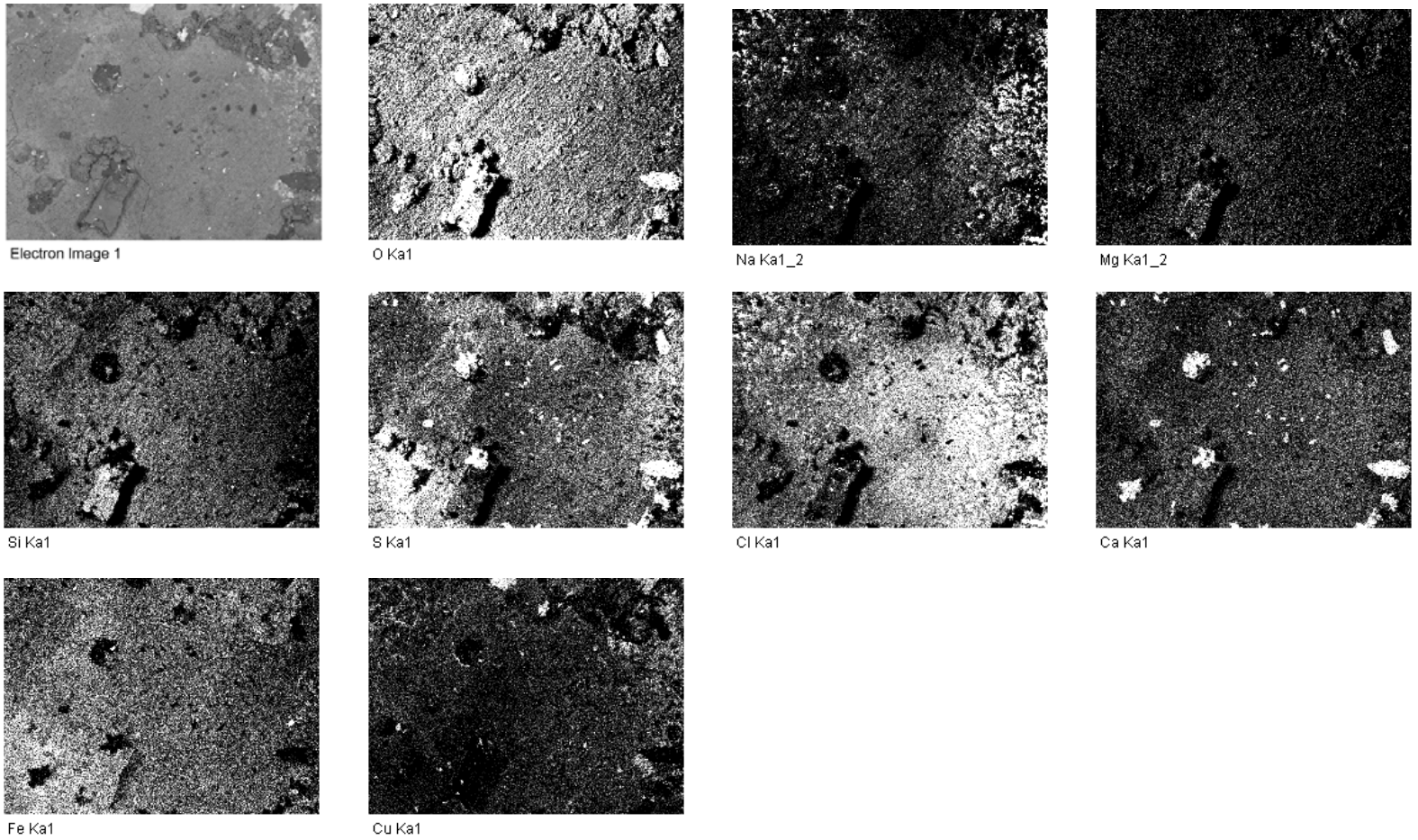

Figure A-189. Elemental maps for Inner surface of copper canister around the top hole

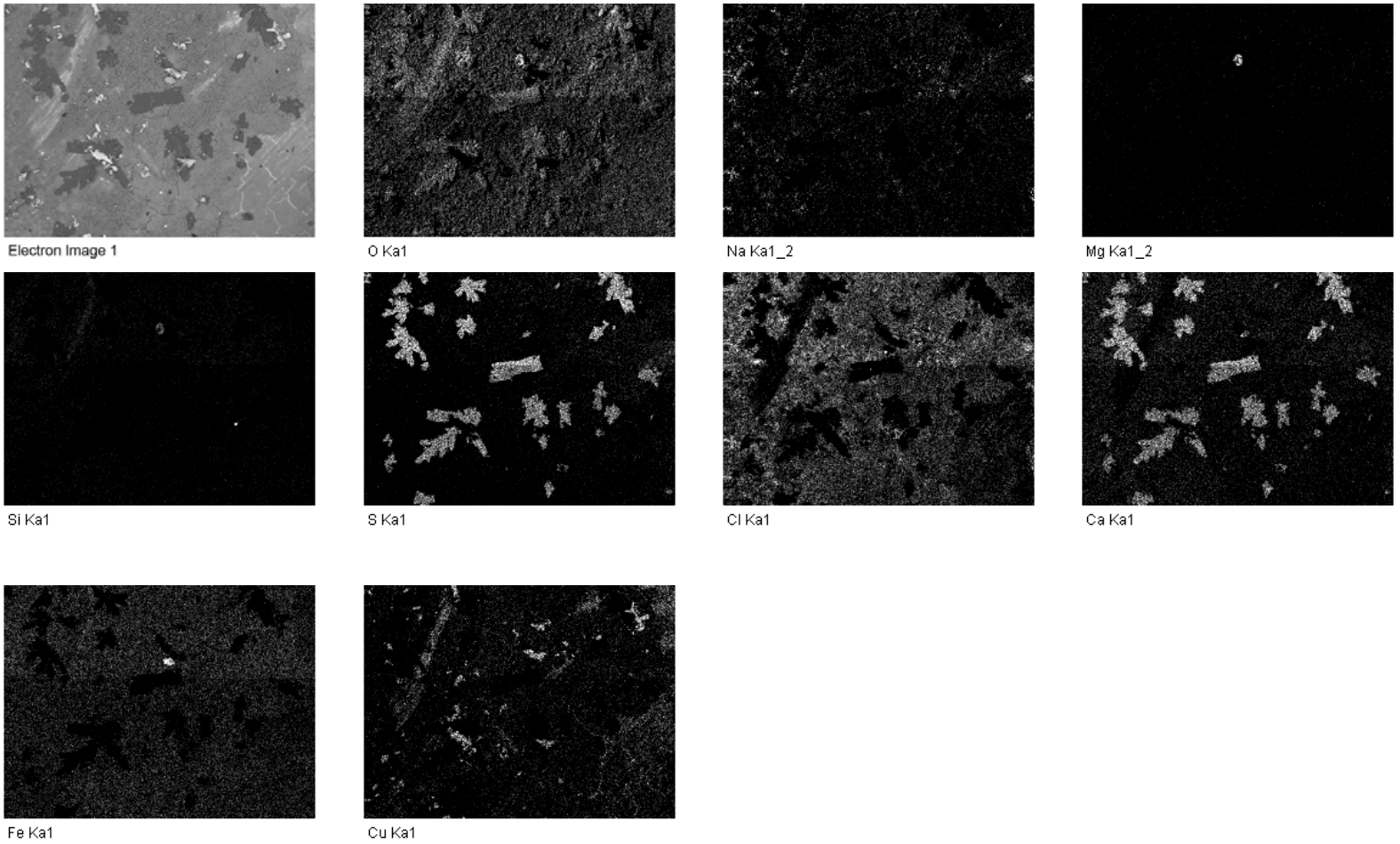

Figure A-190. Elemental maps for inner surface of copper canister around the top hole

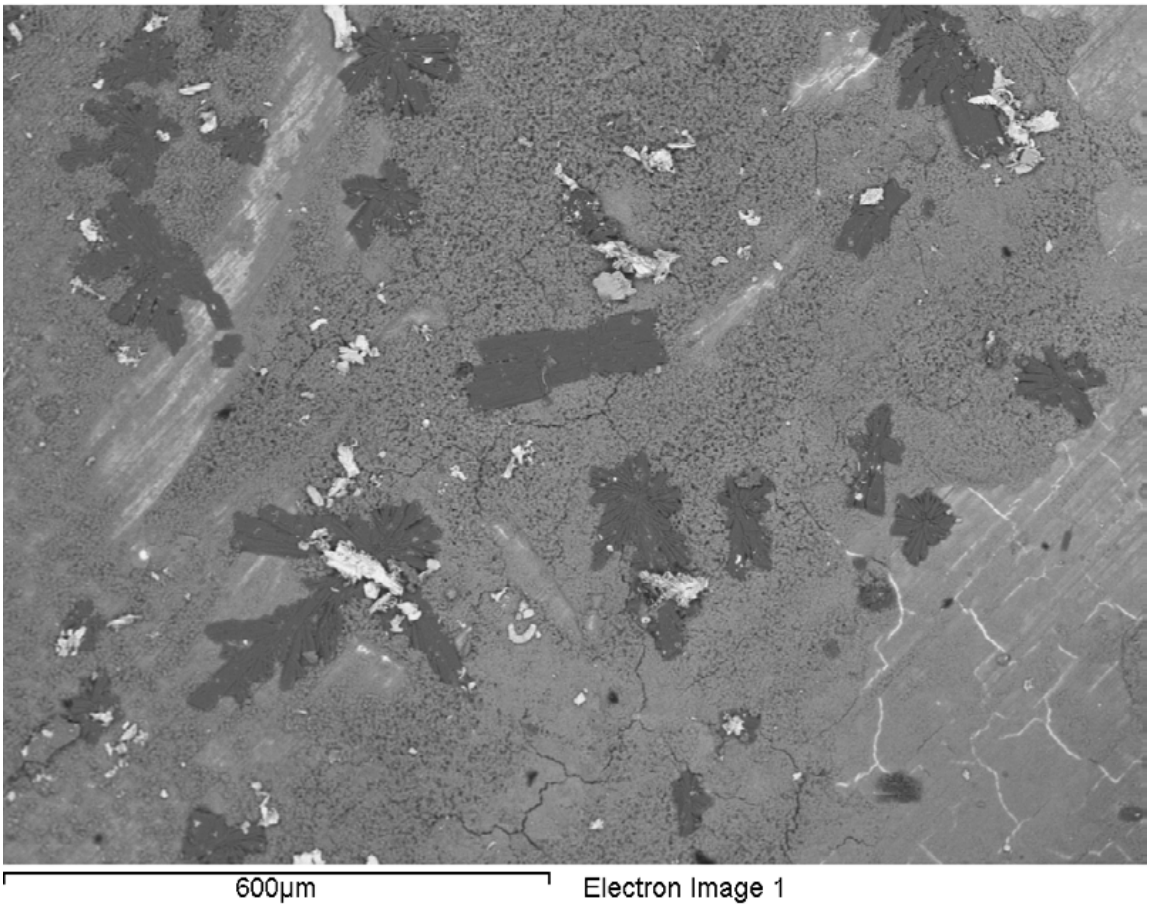

Figure A-191. Inner surface of copper canister around the top hole and EDX analysis – Sum Spectrum

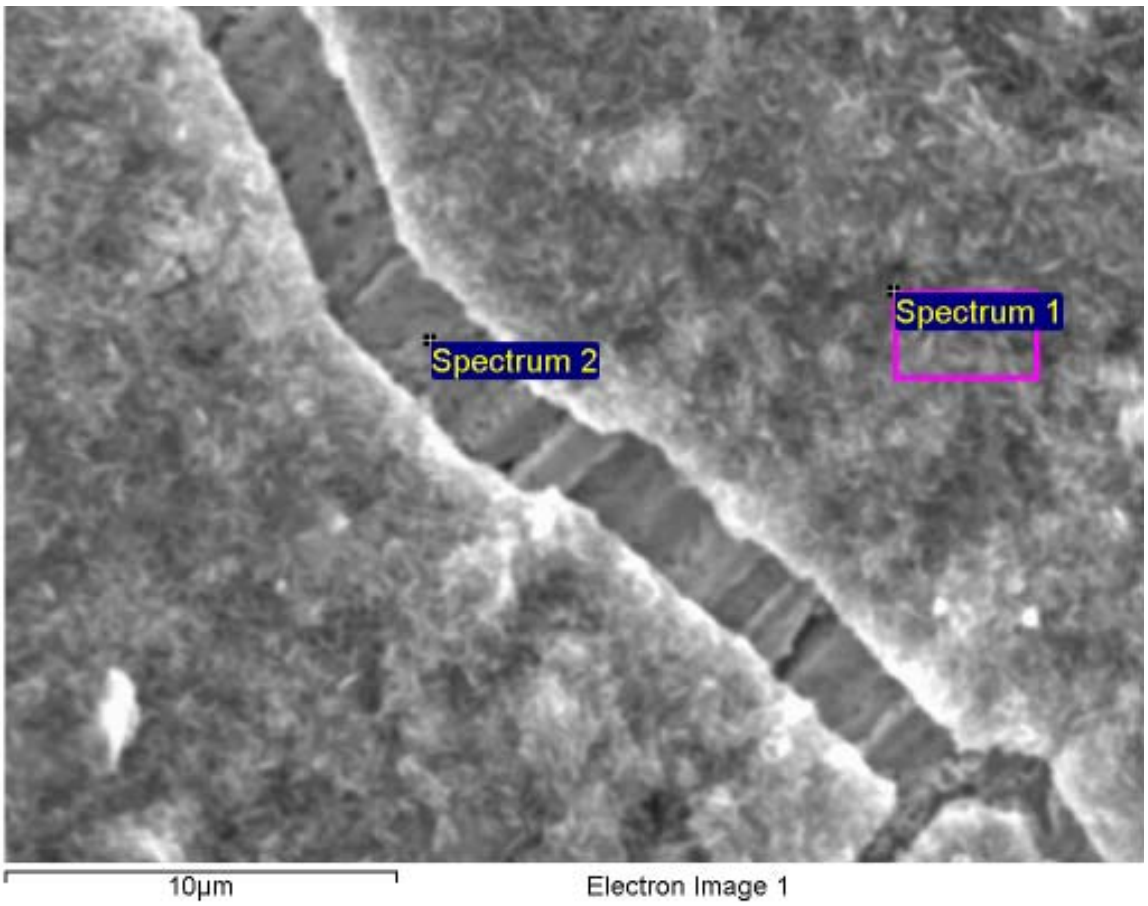

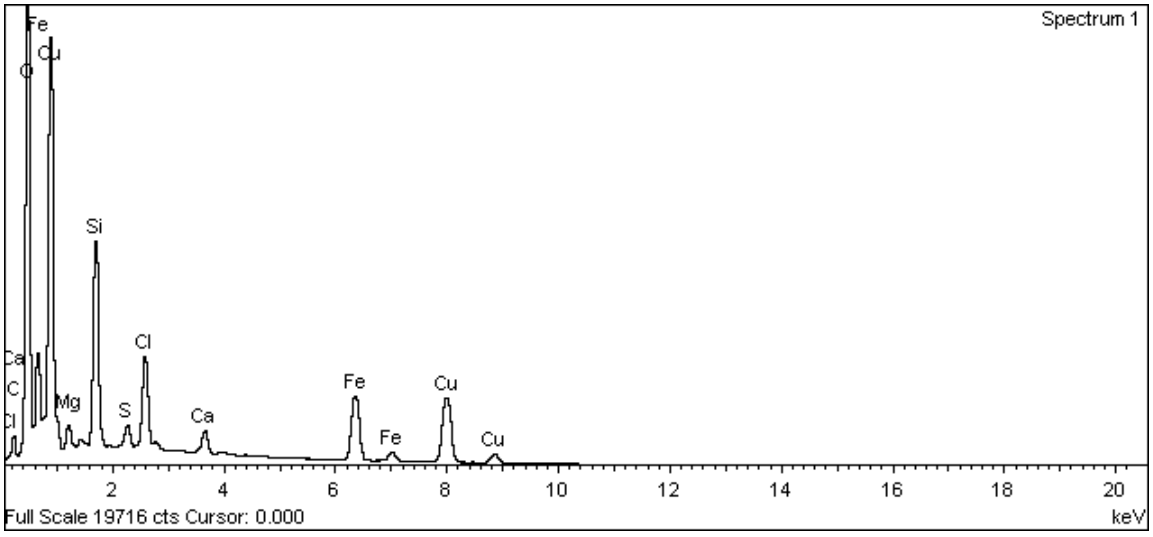

Figure A-192. Inner surface of copper canister around the top hole and EDX analysis at position of Spectrum 1

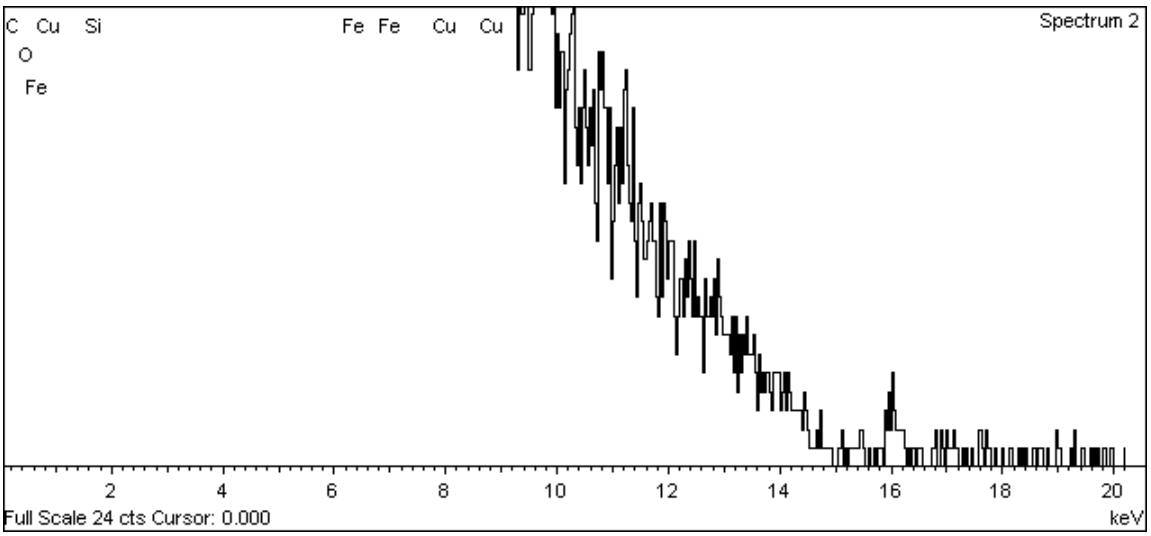

Figure A-193. Inner surface of copper canister around the top hole and EDX analysis at position of Spectrum 2

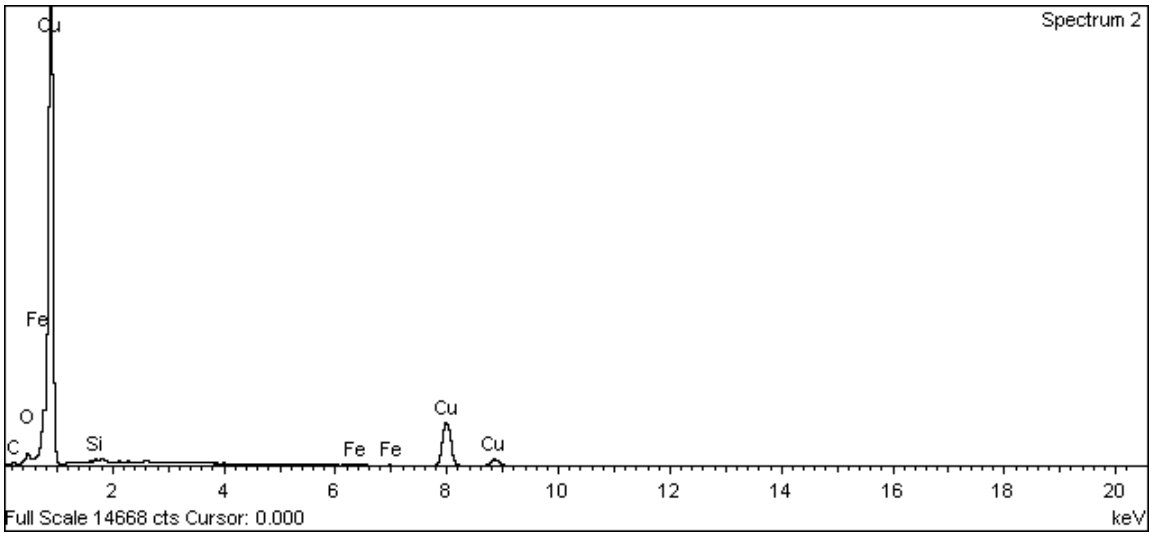

Figure A-194. Inner surface of copper canister around the top hole and EDX analysis at position of Spectrum 2

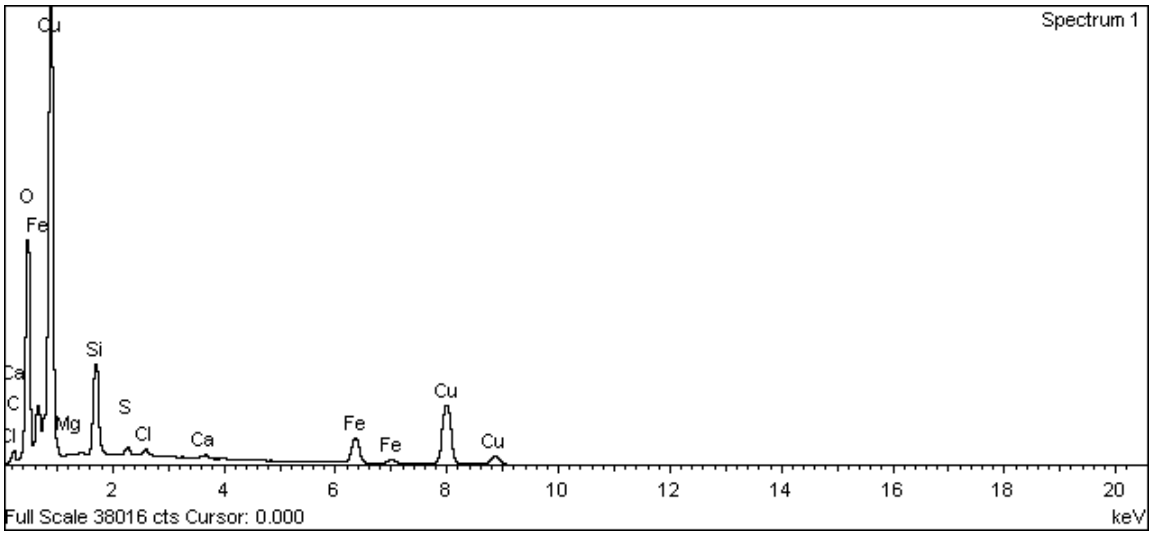

Figure A-195. Inner surface of copper canister around the top hole and EDX analysis at position of Spectrum 1

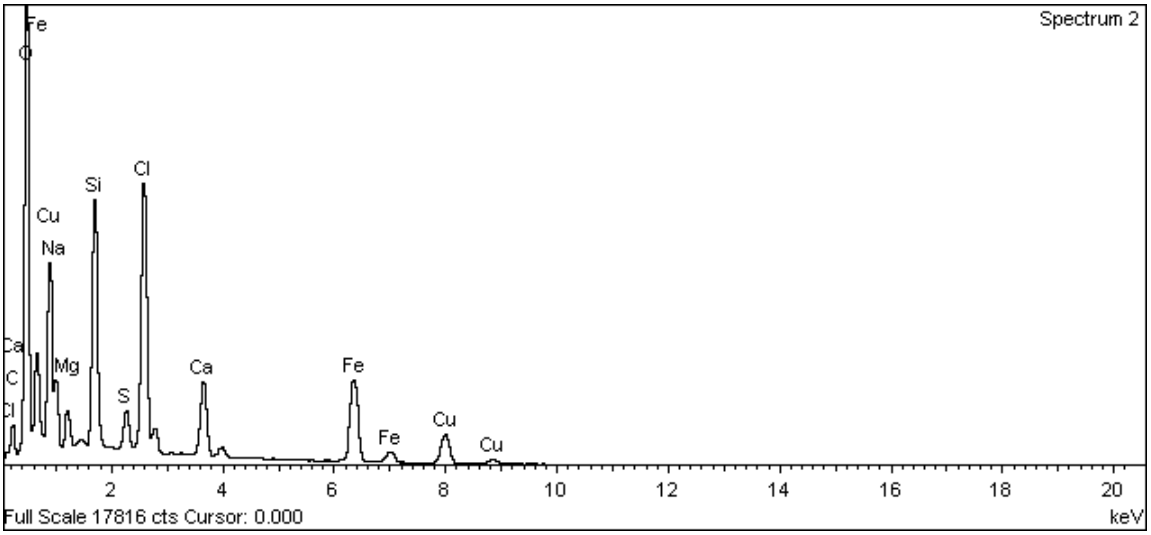

Figure A-196. Inner surface of copper canister around the top hole and EDX analysis at position of Spectrum 2

Copper can inner surface of lid near top hole

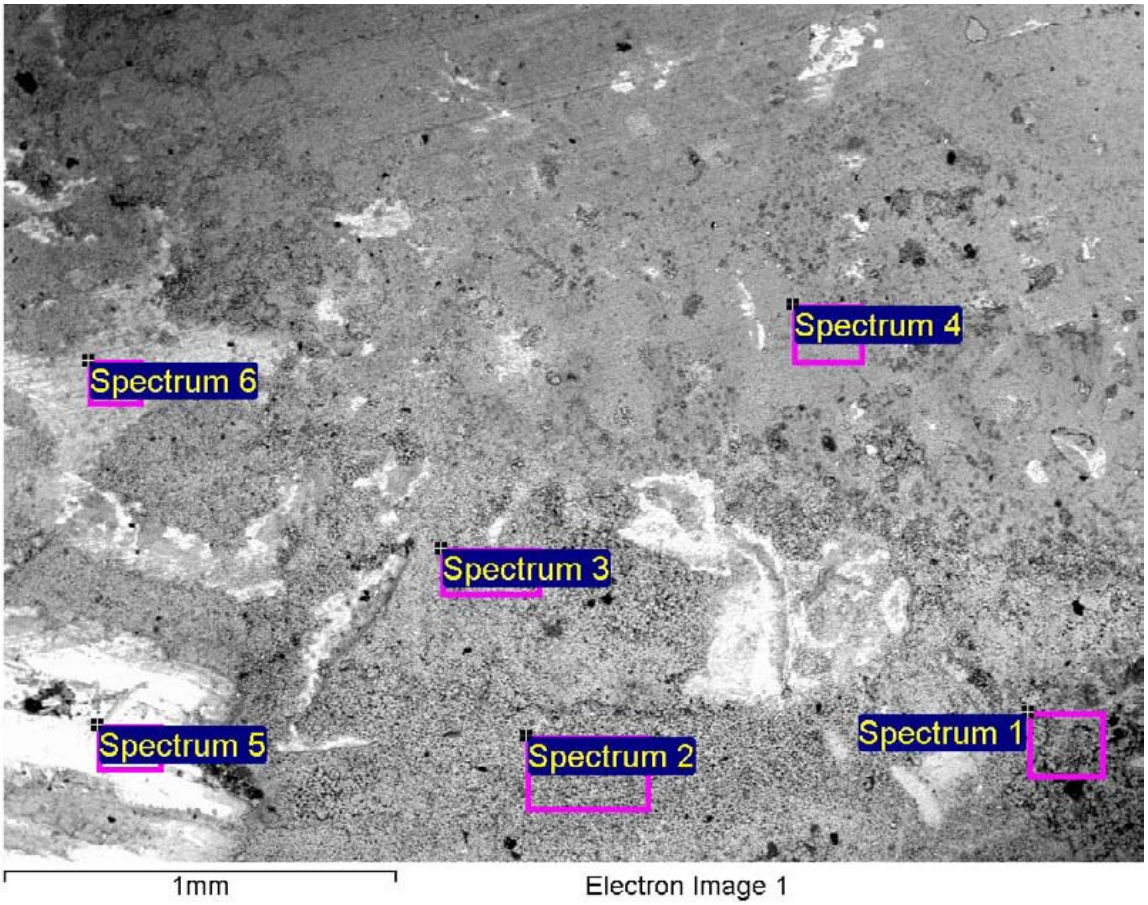

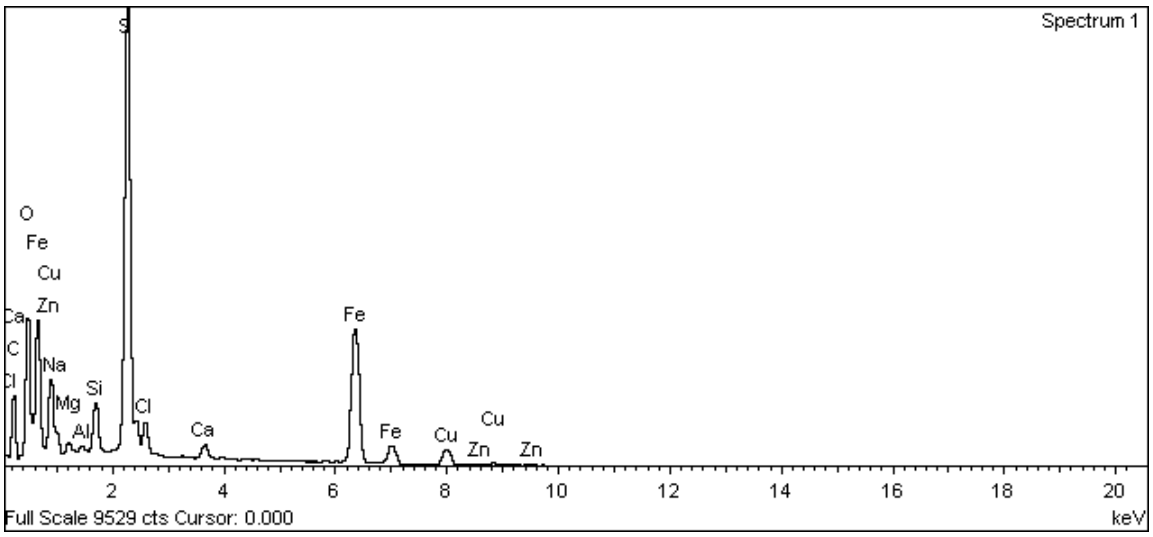

Figure A-197. Inner surface of copper canister lid near top hole and EDX analysis at position of Spectrum 1

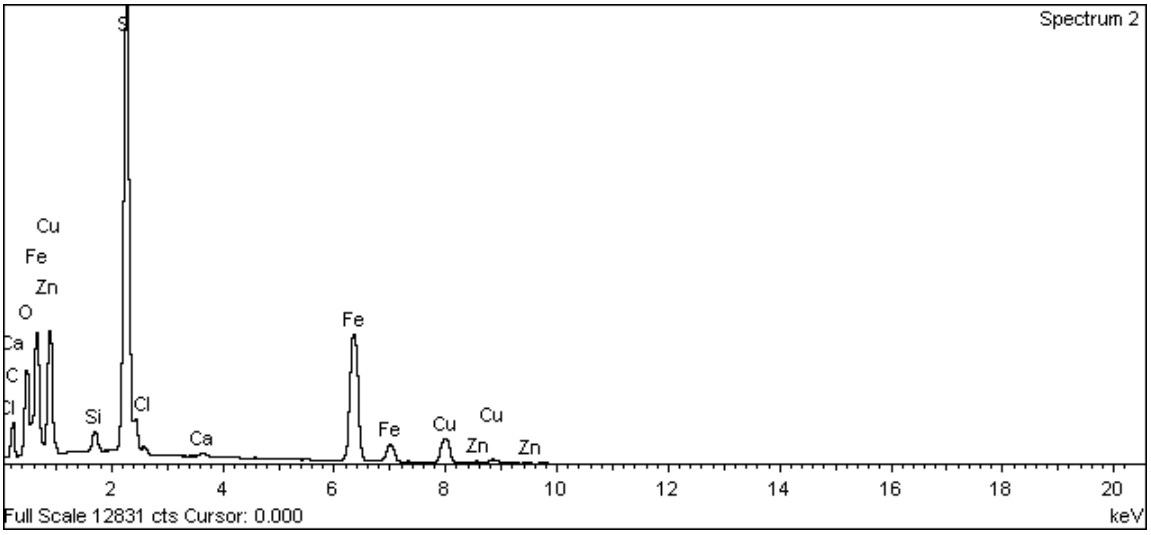

Figure A-198. Inner surface of copper canister lid near top hole and EDX analysis at position of Spectrum 2

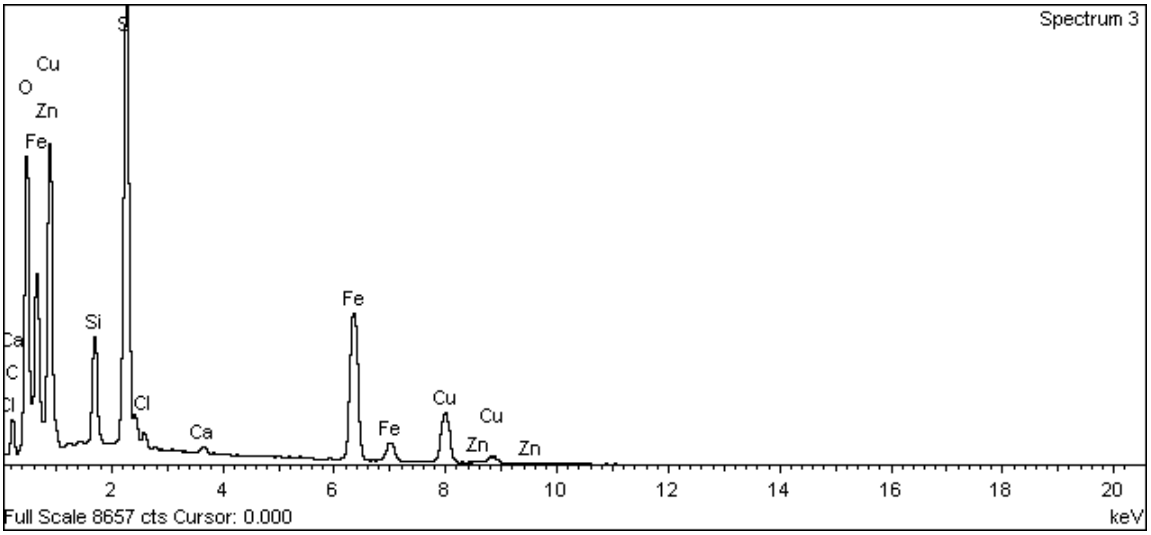

Figure A-199. Inner surface of copper canister lid near top hole and EDX analysis at position of Spectrum 3

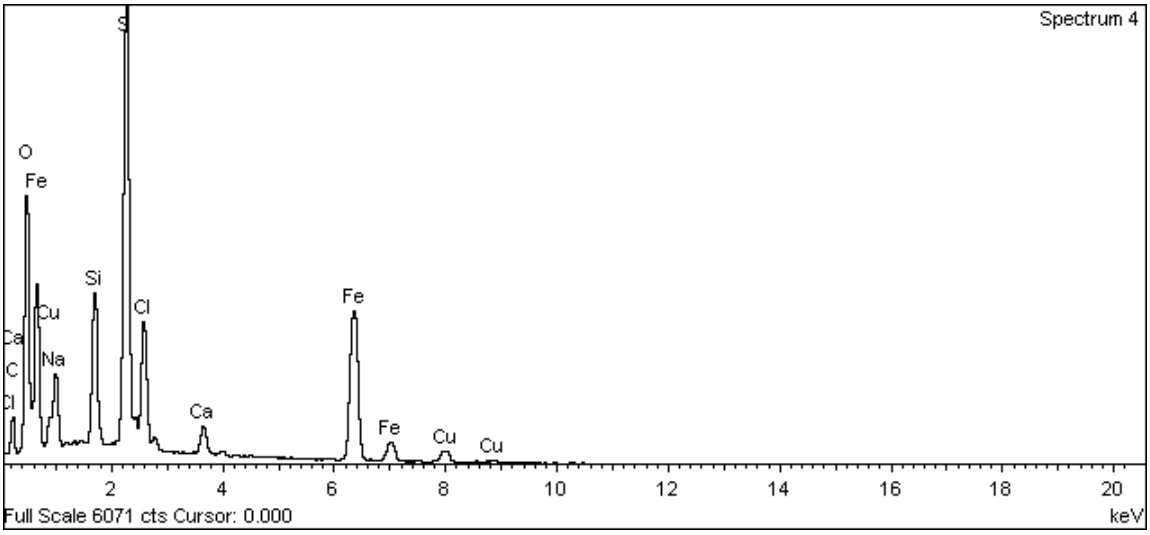

Figure A-200. Inner surface of copper canister lid near top hole and EDX analysis at position of Spectrum 4

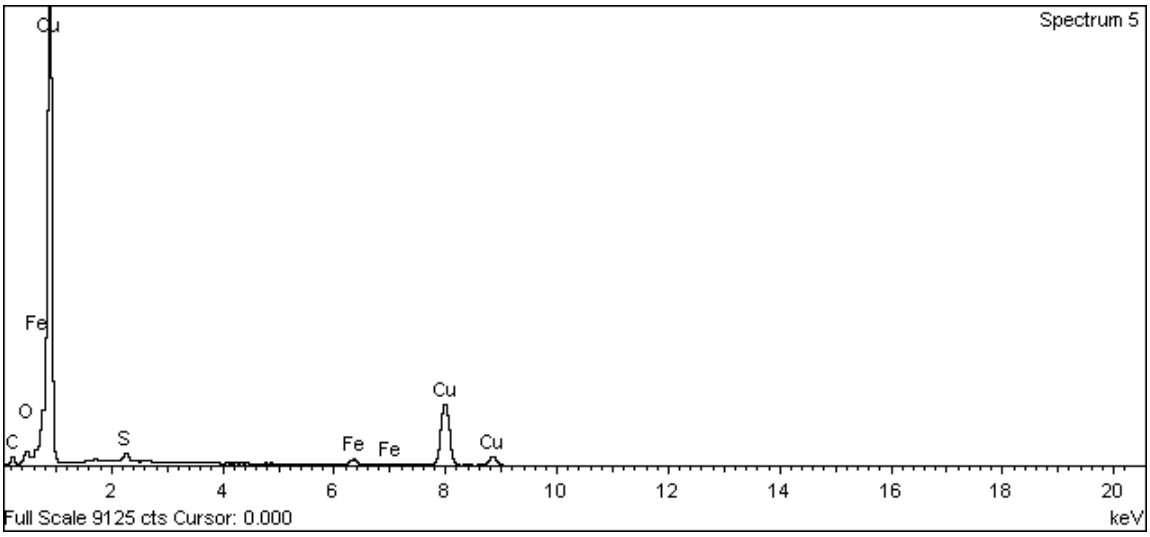

Figure A-201. Inner surface of copper canister lid near top hole and EDX analysis at position of Spectrum 5

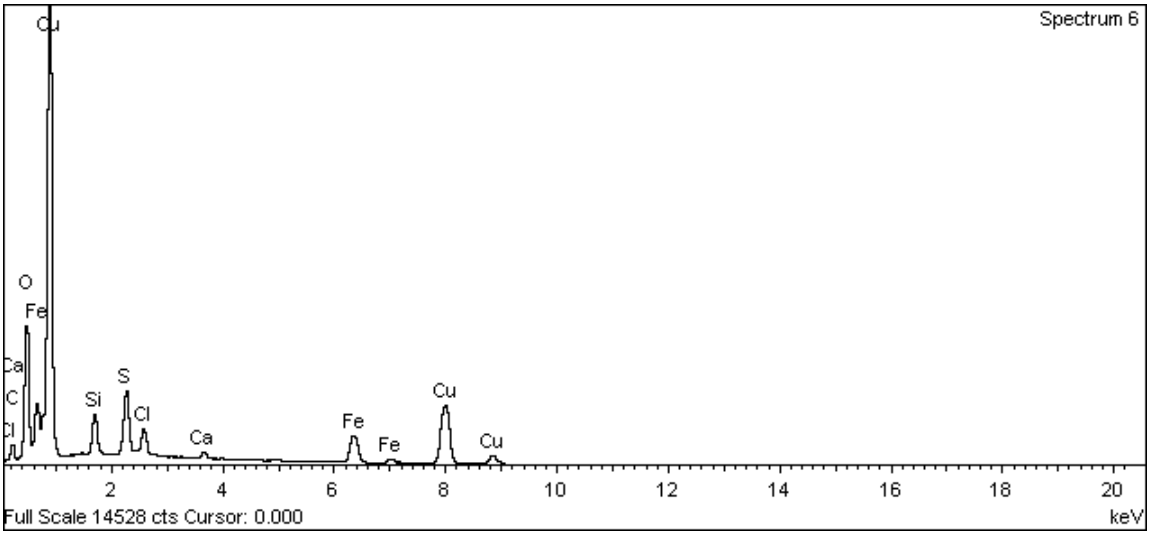

Figure A-202. Inner surface of copper canister lid near top hole and EDX analysis at position of Spectrum 6

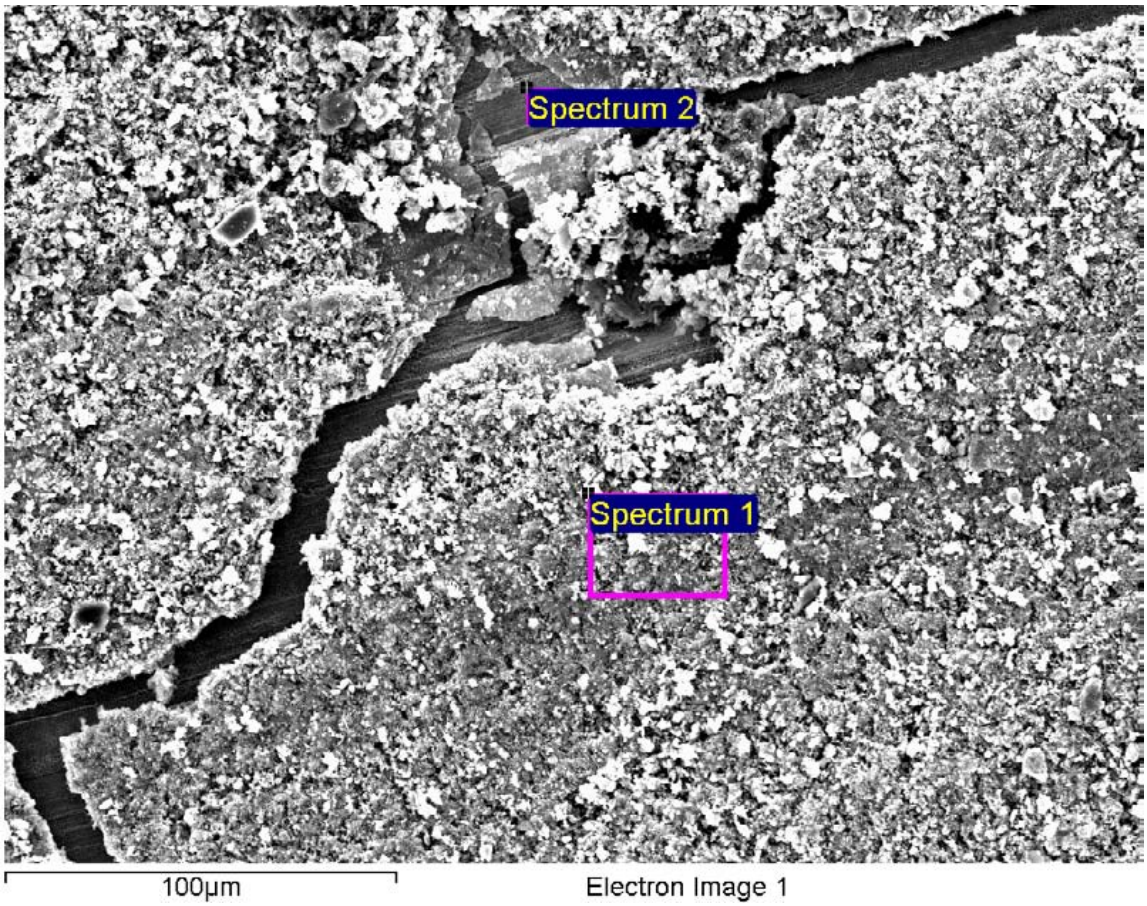

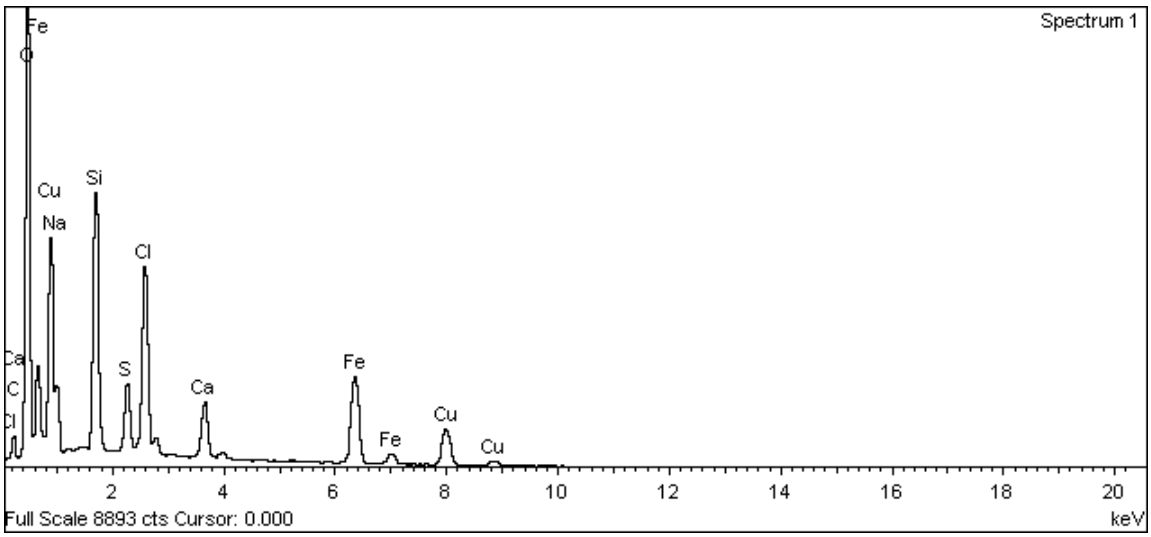

Figure A-203. Inner surface of copper canister lid near top hole and EDX analysis at position of Spectrum 1

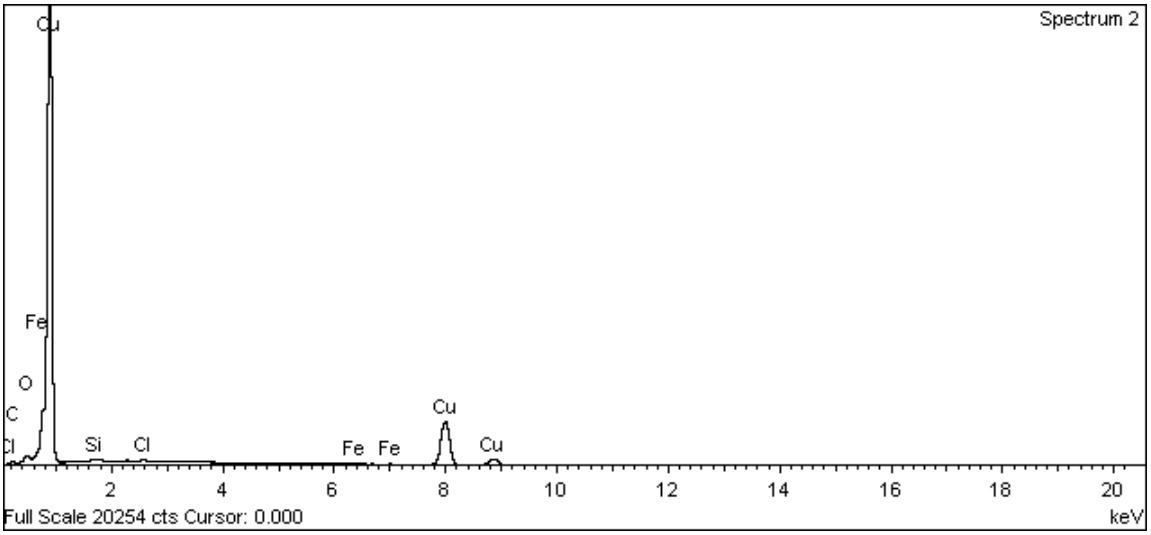

Figure A-204. Inner surface of copper canister lid near top hole and EDX analysis at position of Spectrum 2

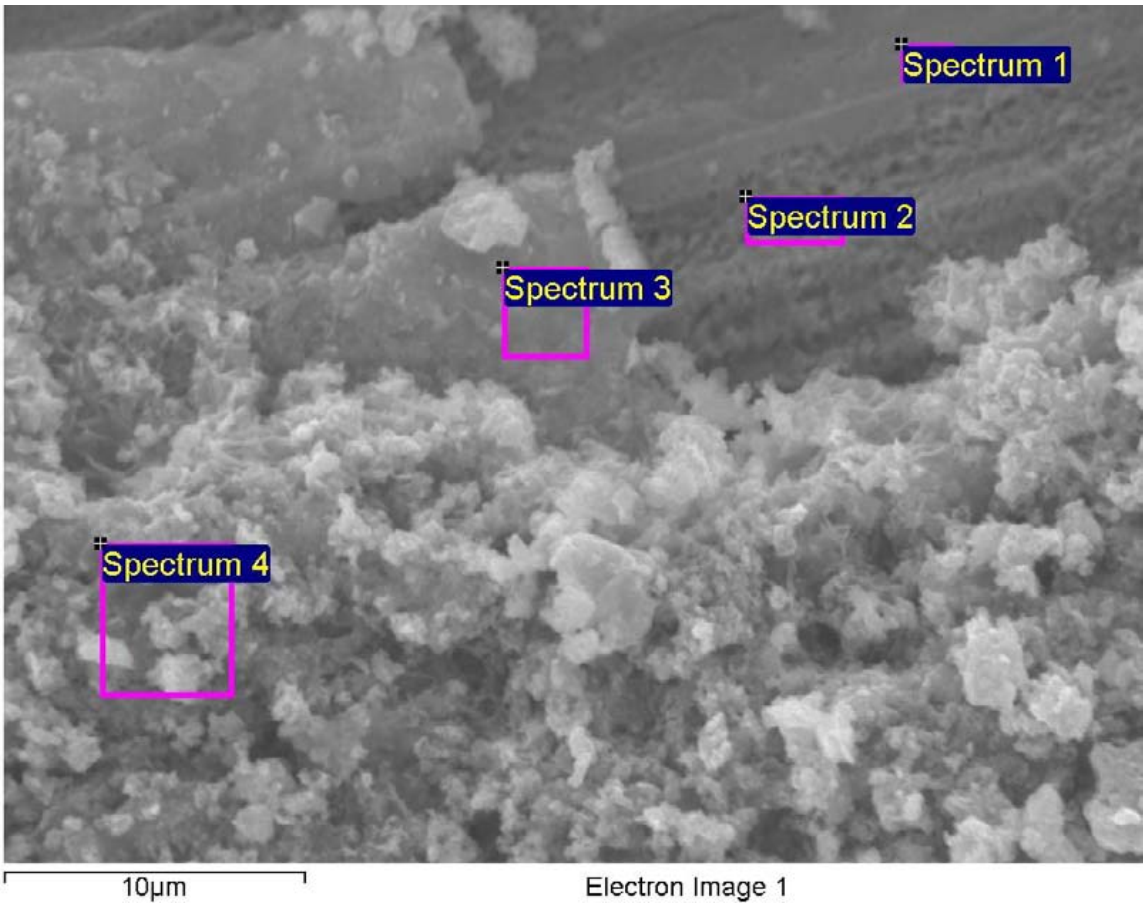

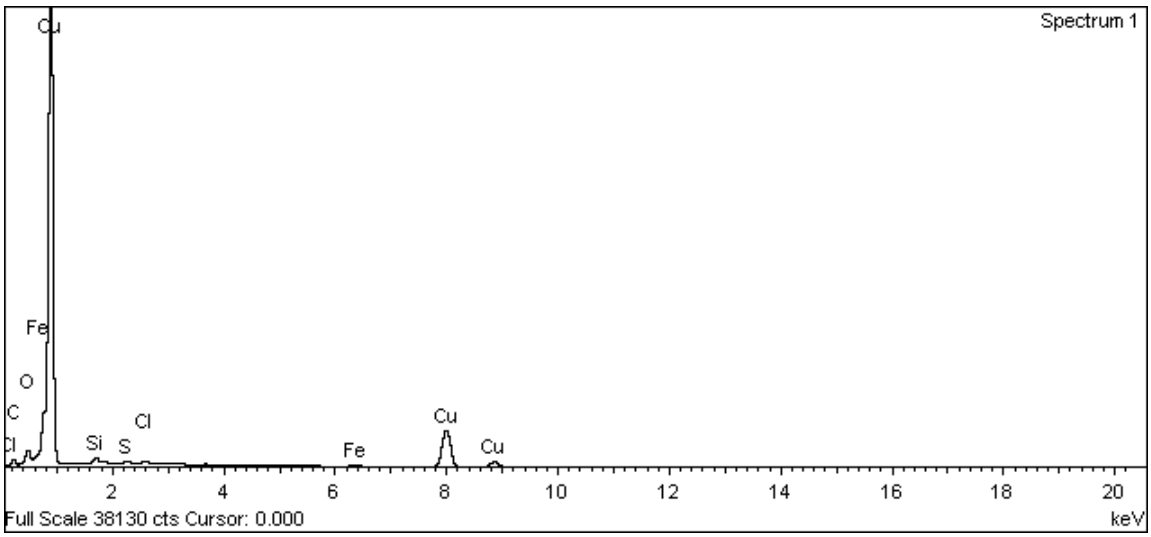

Figure A-205. Inner surface of copper canister lid near top hole and EDX analysis at position of Spectrum 1

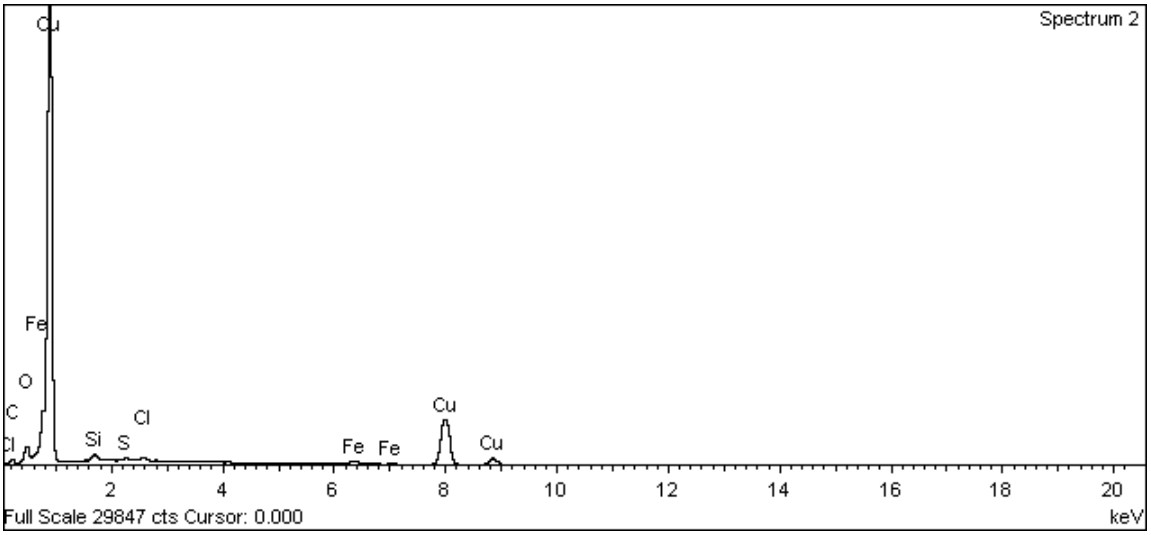

Figure A-206. Inner surface of copper canister lid near top hole and EDX analysis at position of Spectrum 2

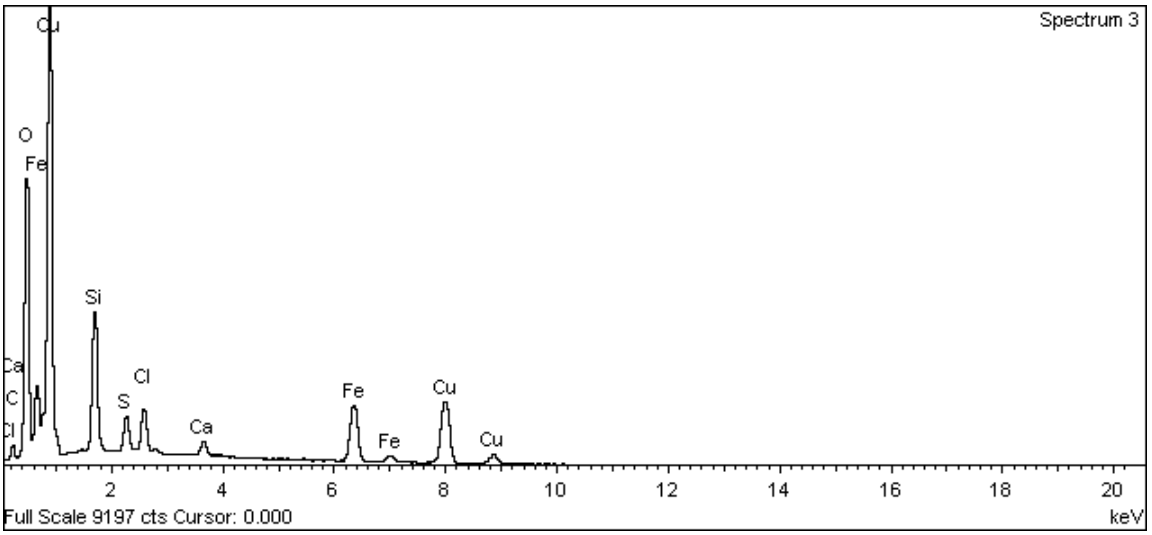

Figure A-207. Inner surface of copper canister lid near top hole and EDX analysis at position of Spectrum 3

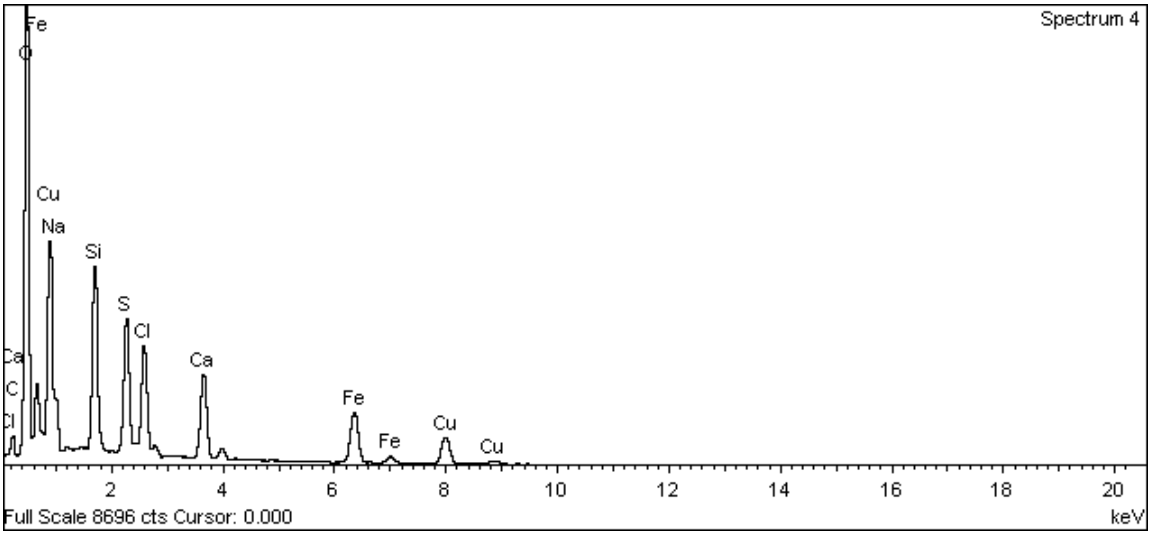

Figure A-208. Inner surface of copper canister lid near top hole and EDX analysis at position of Spectrum 4

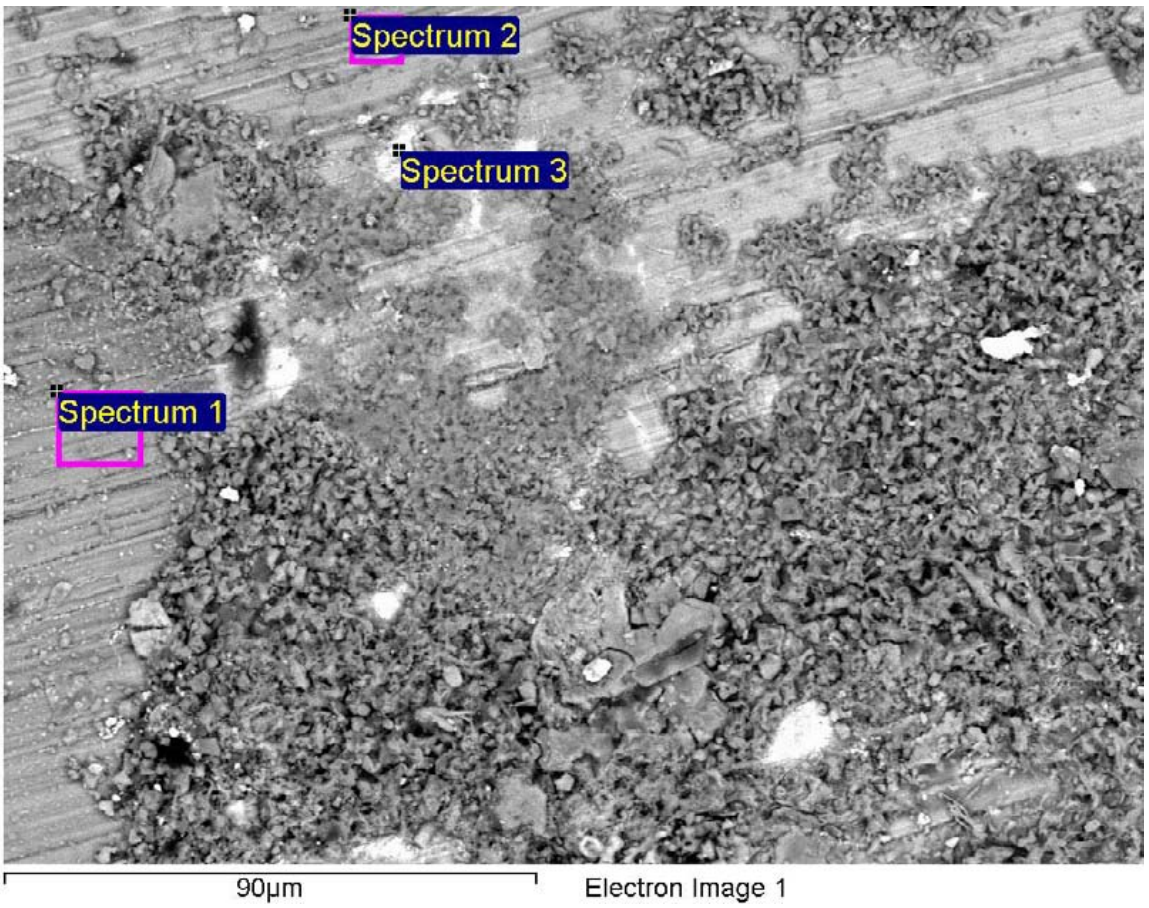

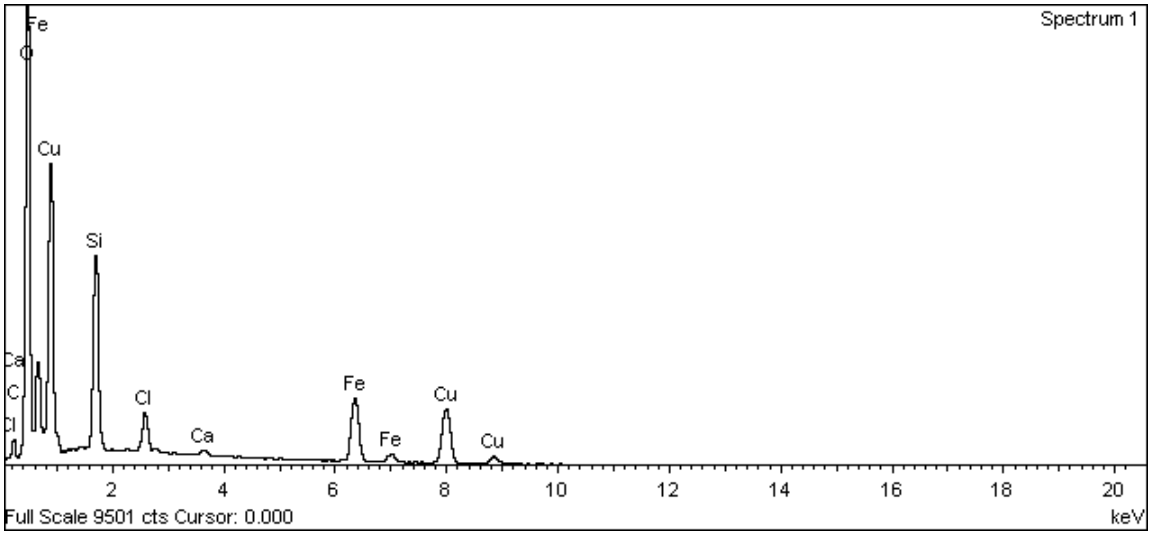

Figure A-209. Inner surface of copper canister lid near top hole and EDX analysis at position of Spectrum 1

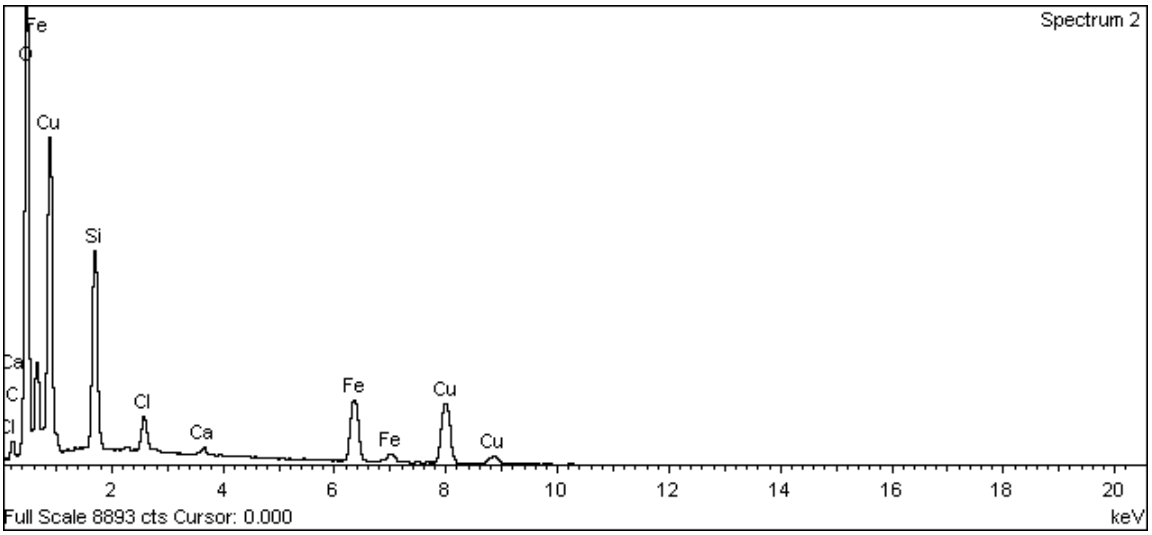

Figure A-210. Inner surface of copper canister lid near top hole and EDX analysis at position of Spectrum 2

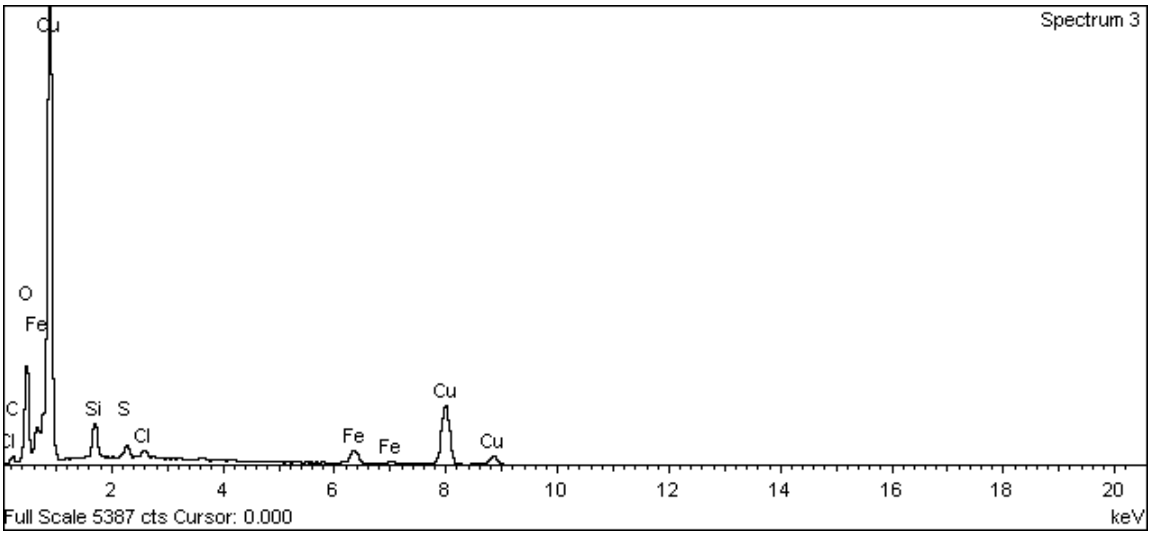

Figure A-211. Inner surface of copper canister lid near top hole and EDX analysis at position of Spectrum 3

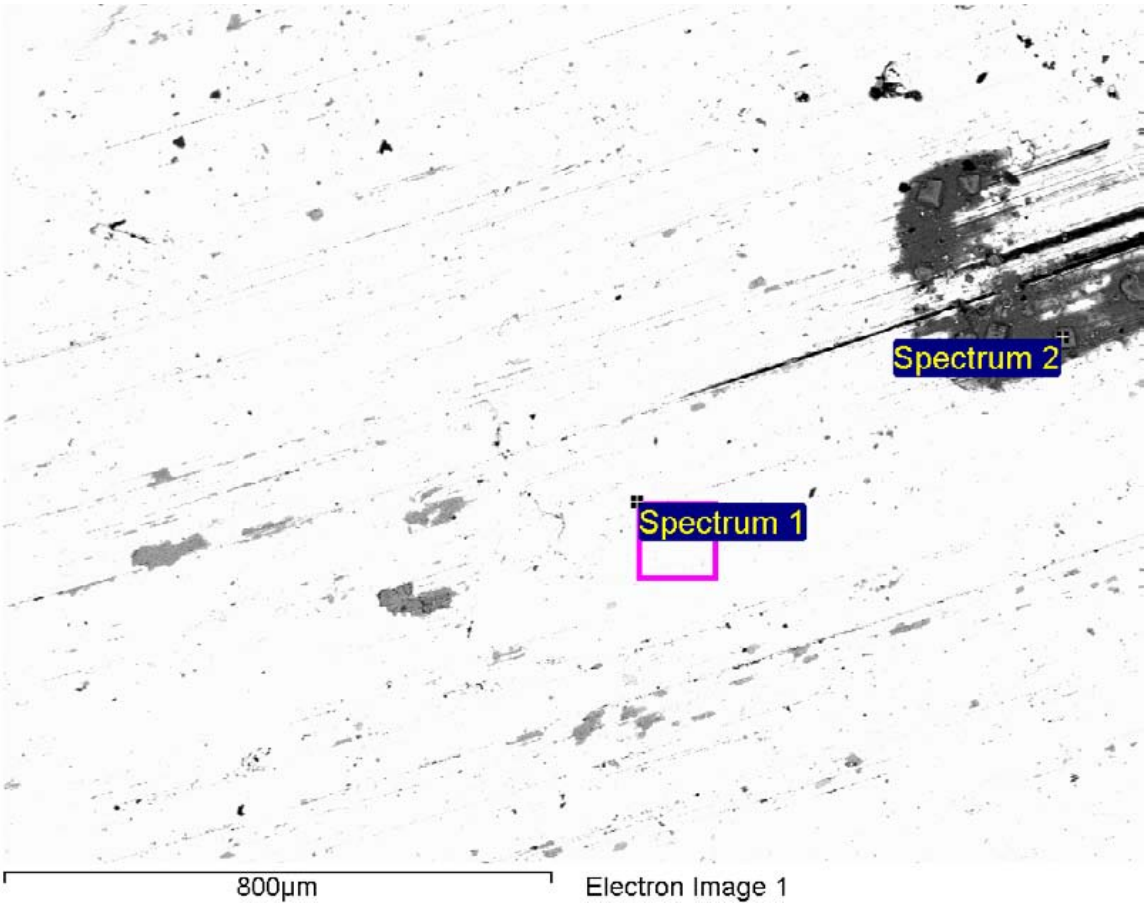

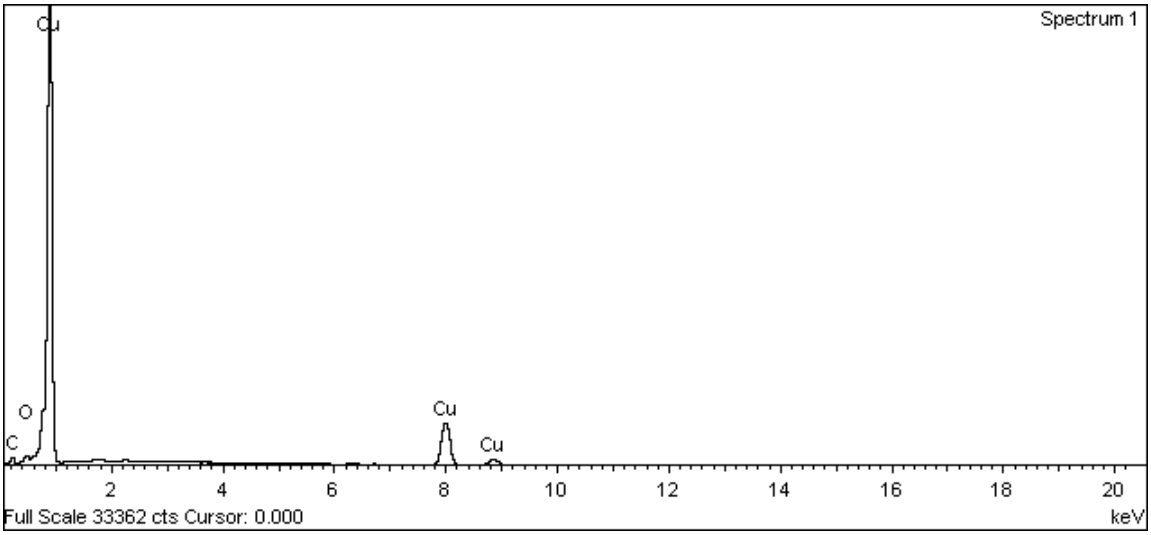

Figure A-212. Inner surface of copper canister lid near top hole and EDX analysis at position of Spectrum 1

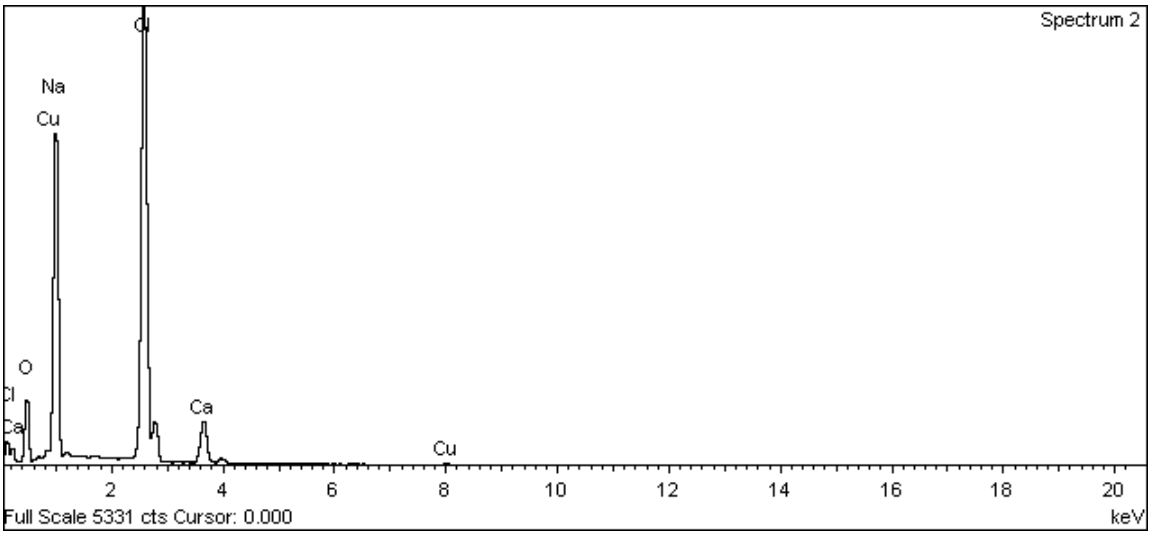

Figure A-213. Inner surface of copper canister lid near top hole and EDX analysis at position of Spectrum 2

Copper can outer surface around top hole

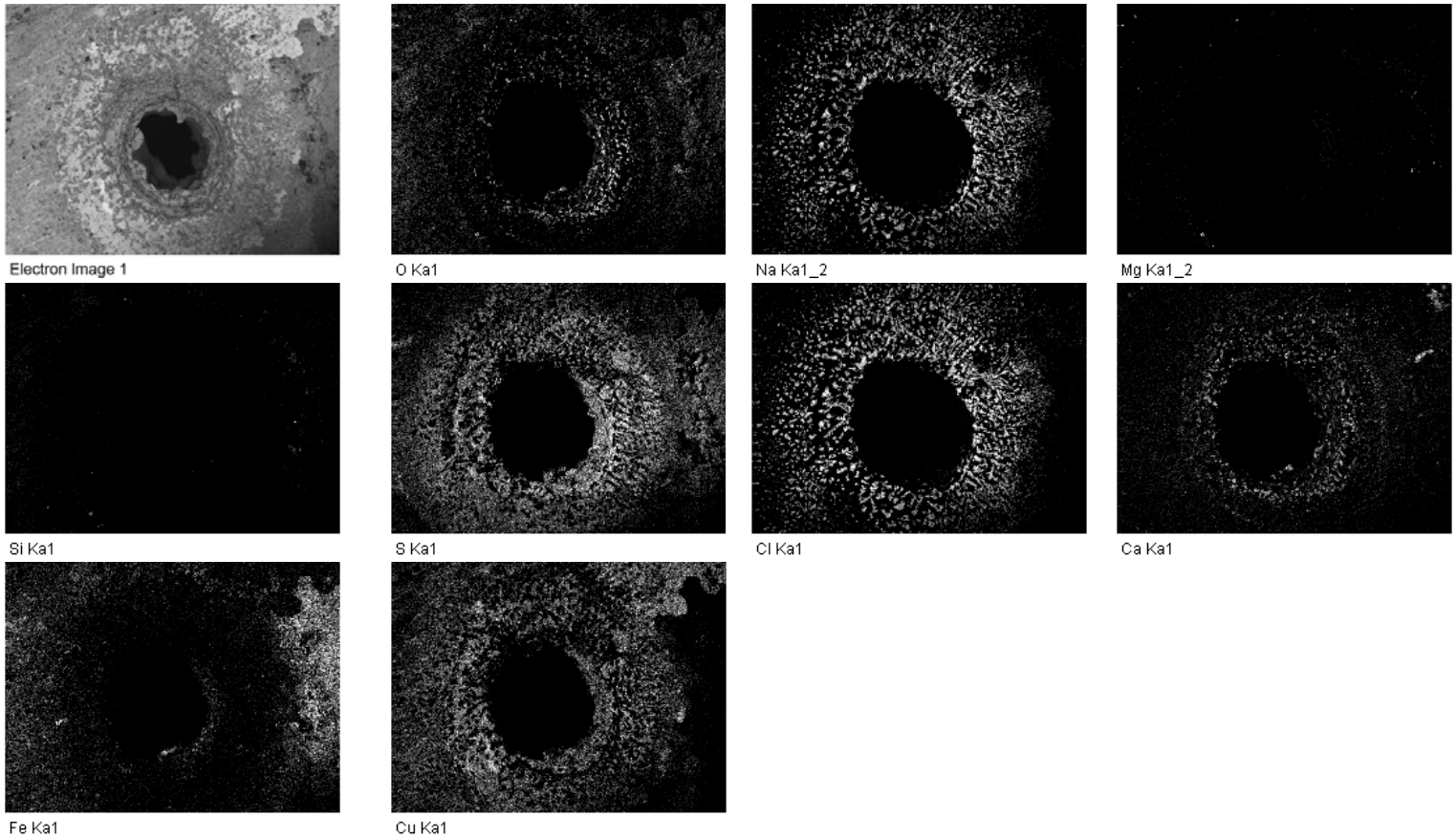

Figure A-214. Elemental maps for outer surface of copper canister around the top hole

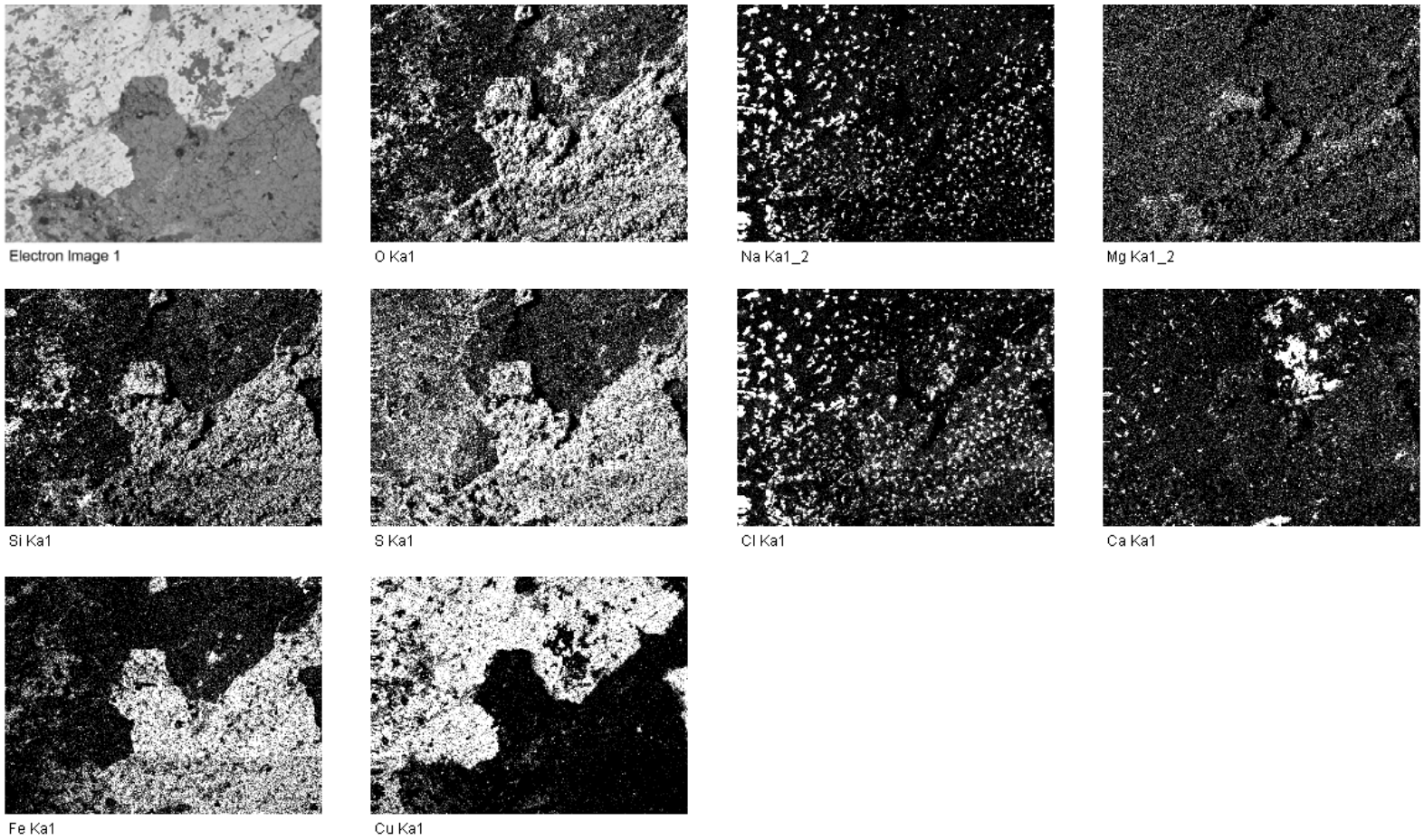

Figure A-215. Elemental maps for outer surface of copper canister around the top hole

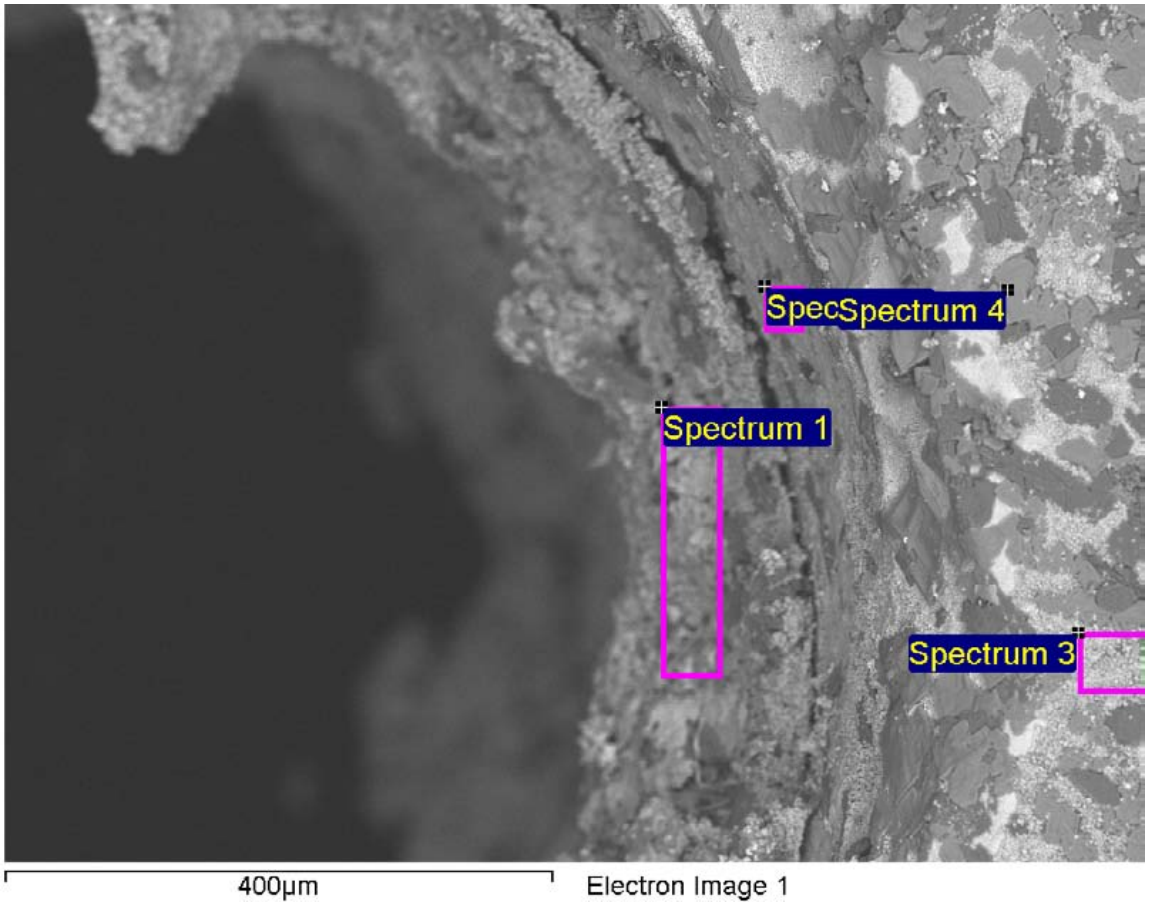

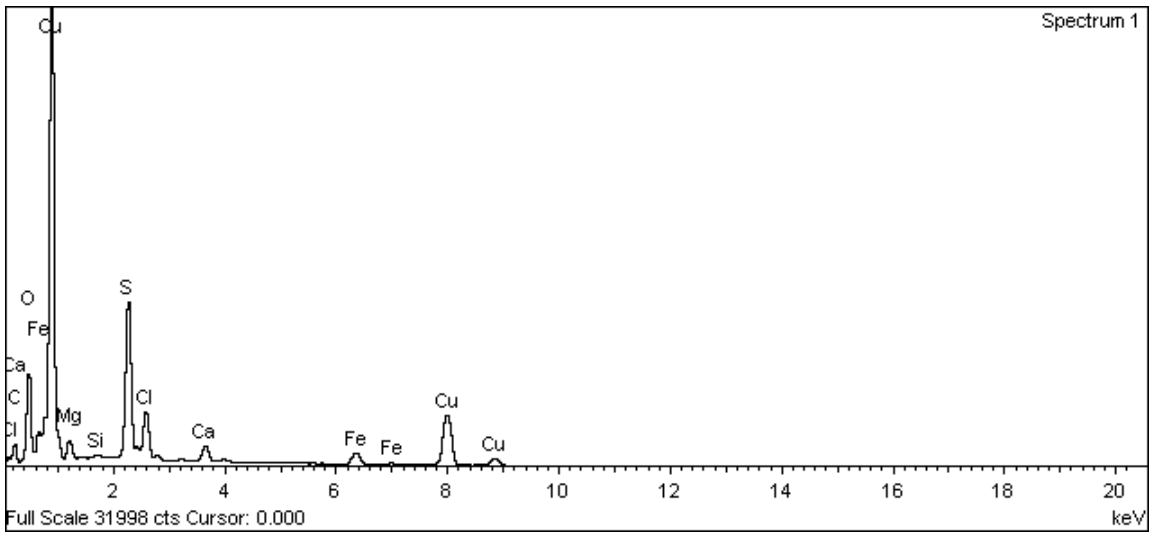

Figure A-216. Outer surface of copper canister near top hole and EDX analysis at position of Spectrum 1

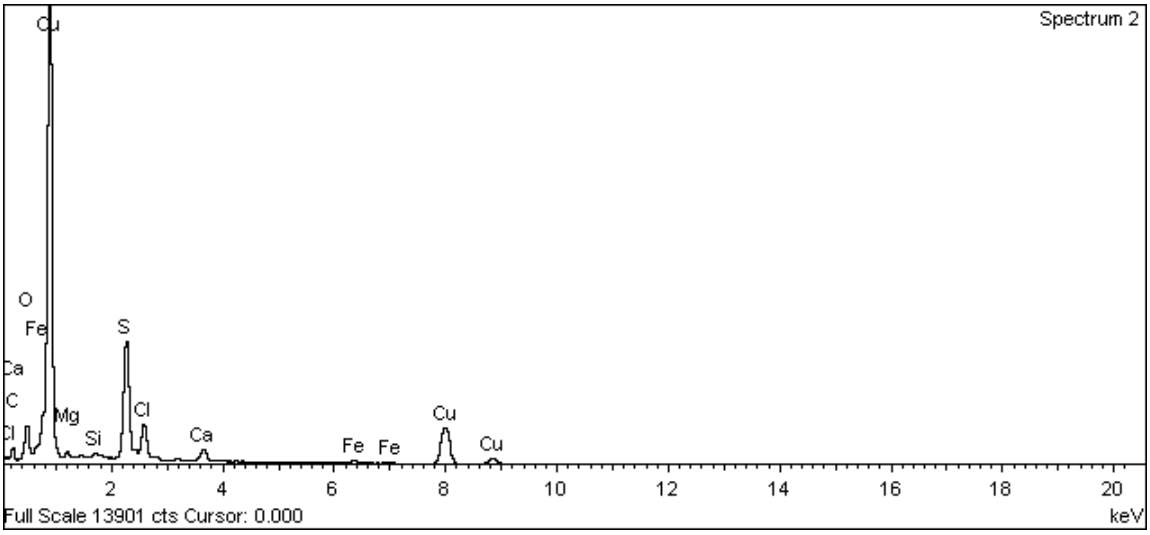

Figure A-217. Outer surface of copper canister near top hole and EDX analysis at position of Spectrum 2 (the Spectrum 2 analysis area is the pink square to the left of the Spectrum 4 label in the SEM image)

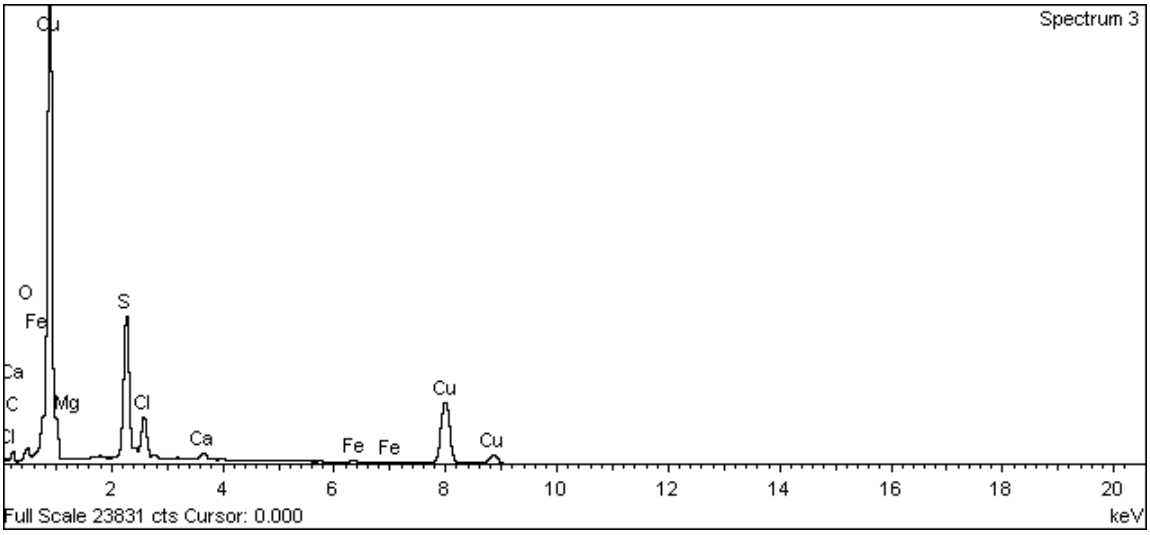

Figure A-218. Outer surface of copper canister near top hole and EDX analysis at position of Spectrum 3

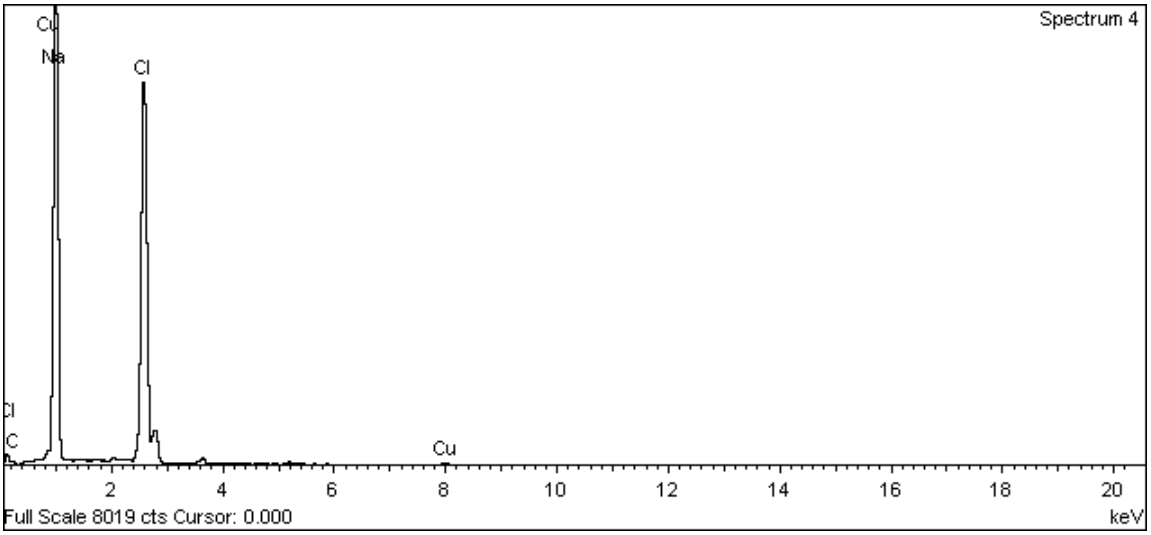

Figure A-219. Outer surface of copper canister near top hole and EDX analysis at position of Spectrum 4

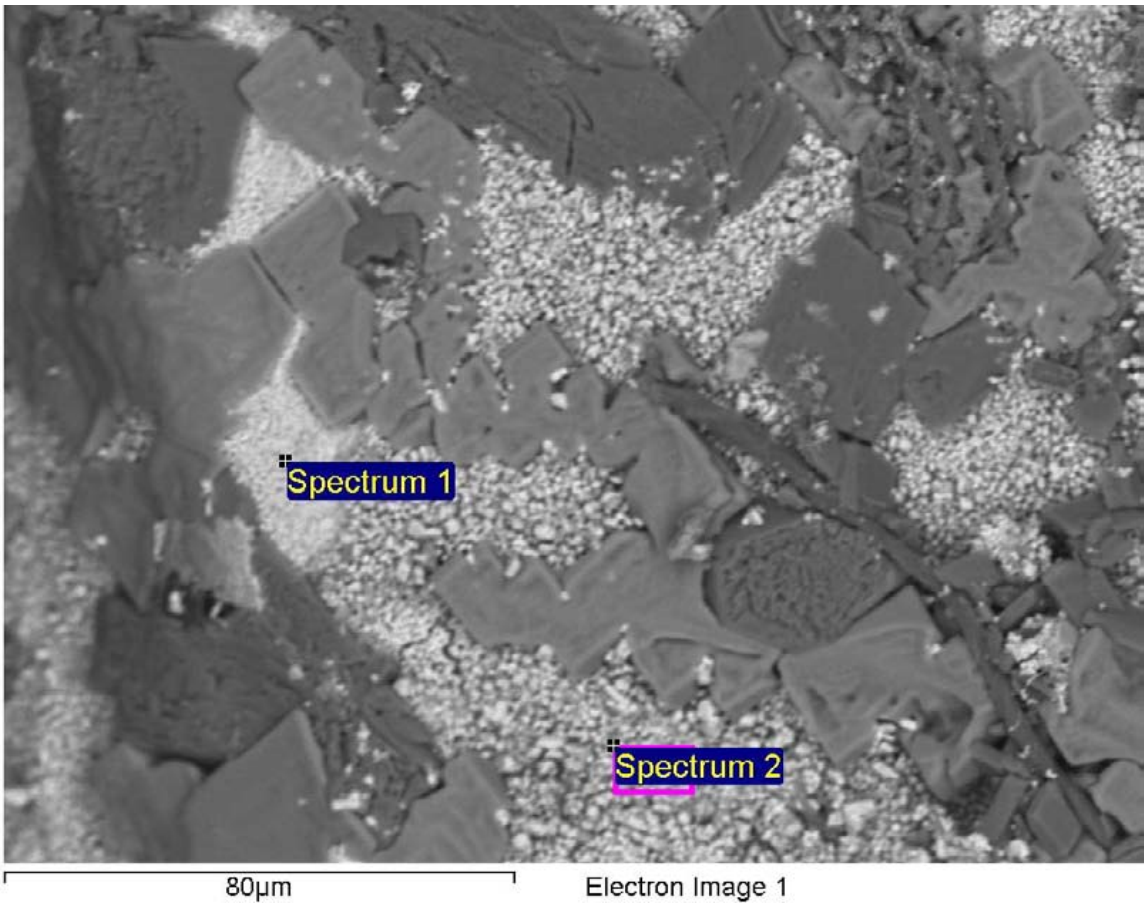

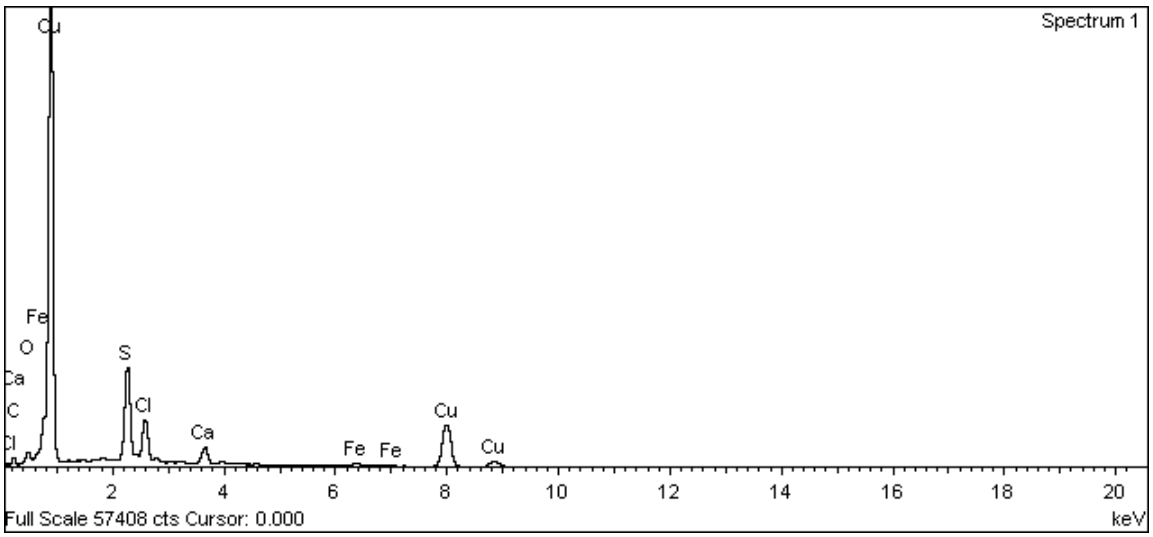

Figure A-220. Outer surface of copper canister near top hole and EDX analysis at position of Spectrum 1

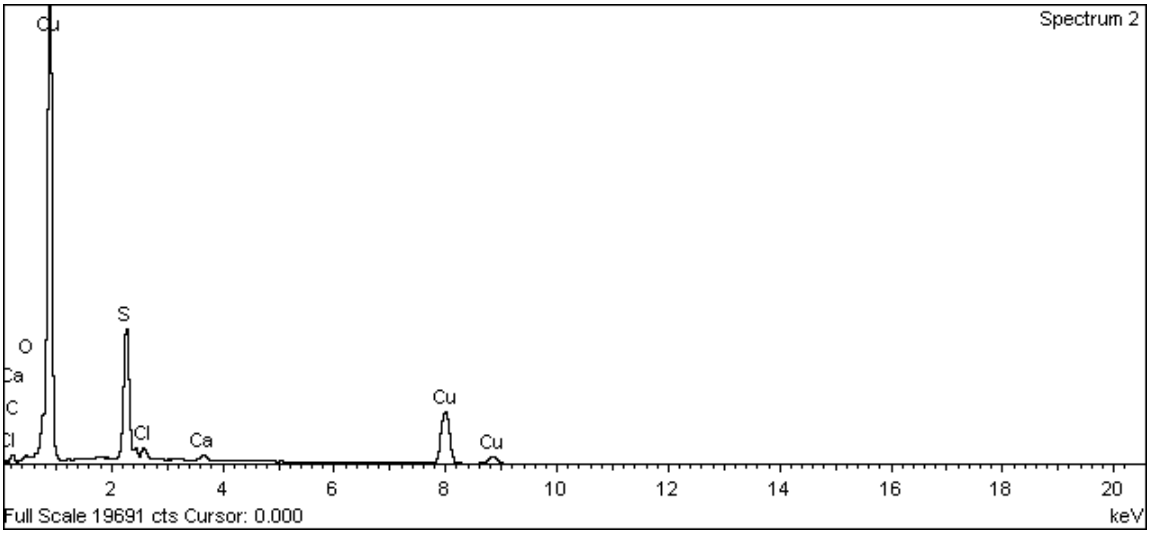

Figure A-221. Outer surface of copper canister near top hole and EDX analysis at position of Spectrum 2

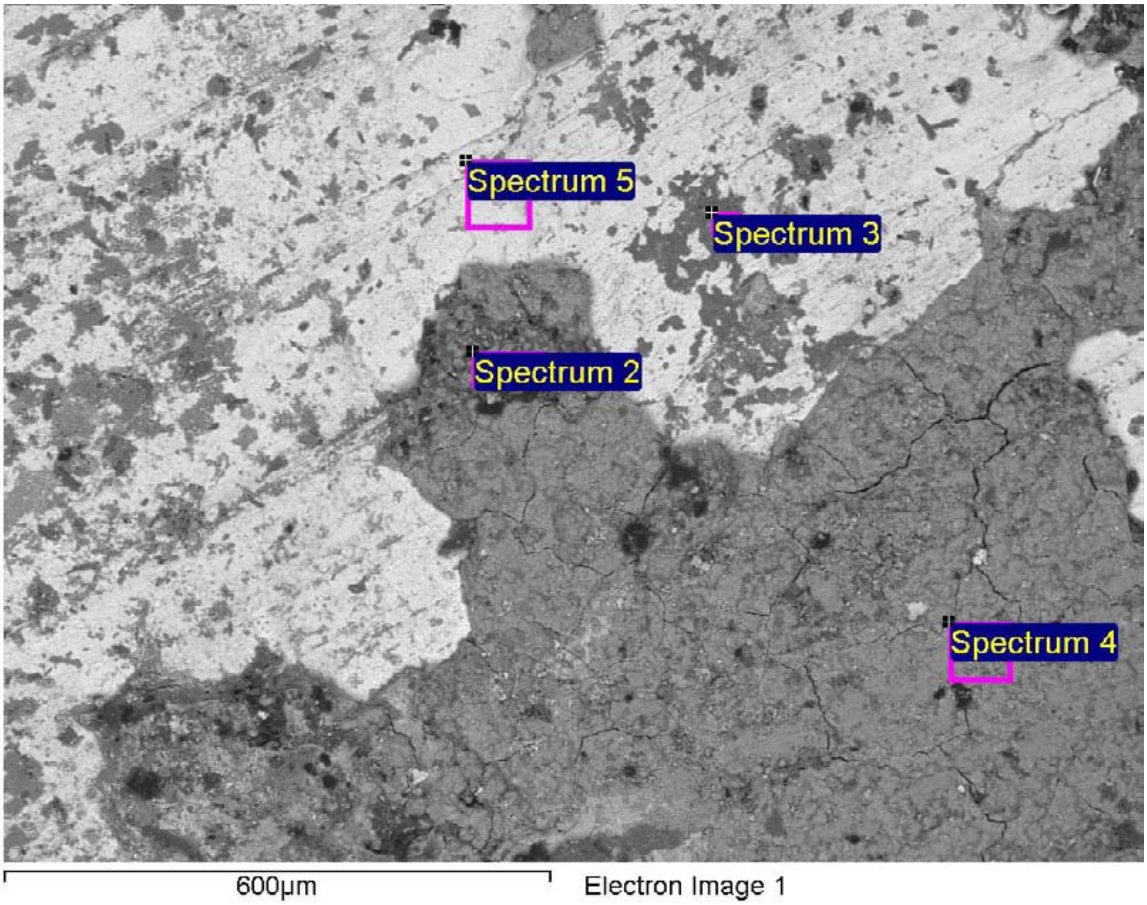

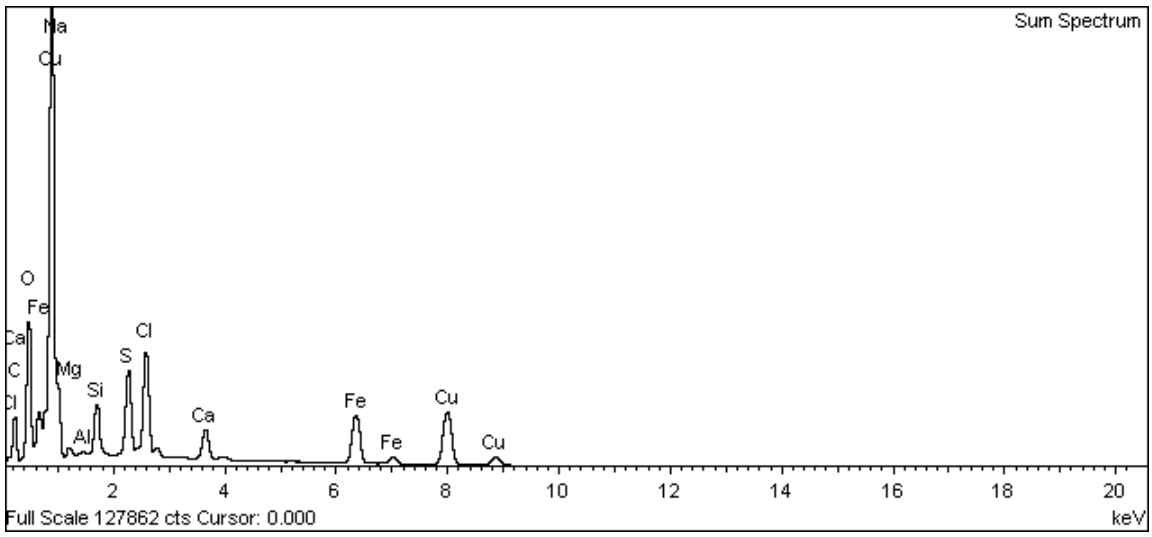

Figure A-222. Outer surface of copper canister near top hole and EDX analysis – Sum Spectrum

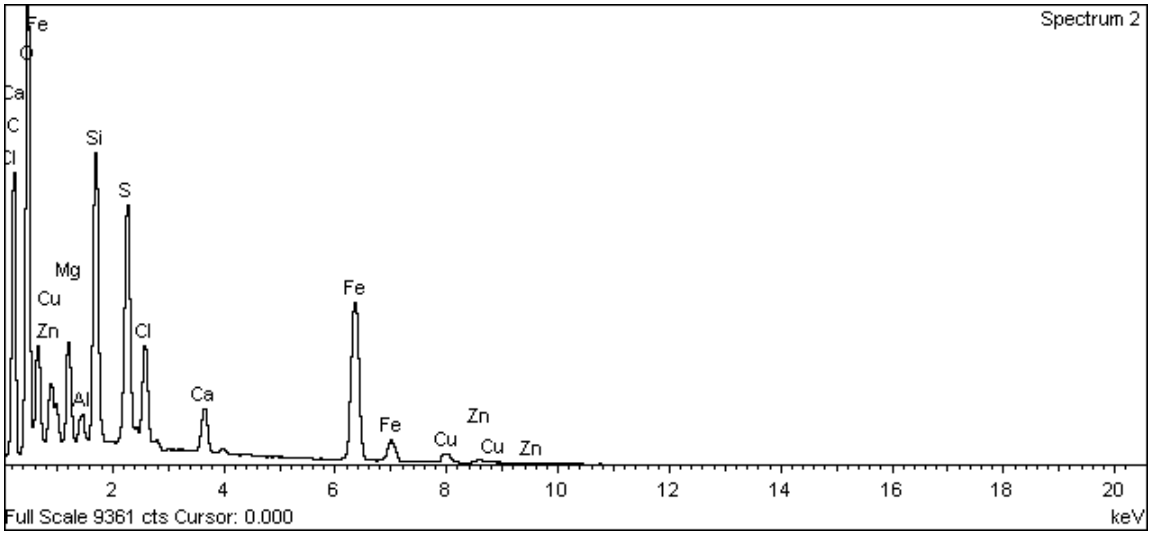

Figure A-223. Outer surface of copper canister near top hole and EDX analysis at position of Spectrum 2

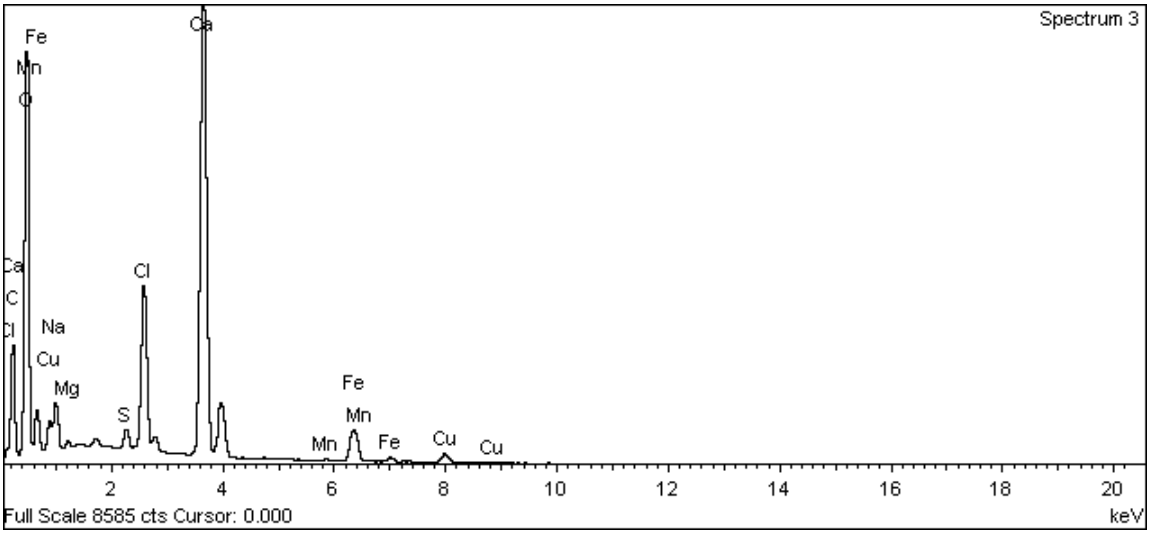

Figure A-224. Outer surface of copper canister near top hole and EDX analysis at position of Spectrum 3

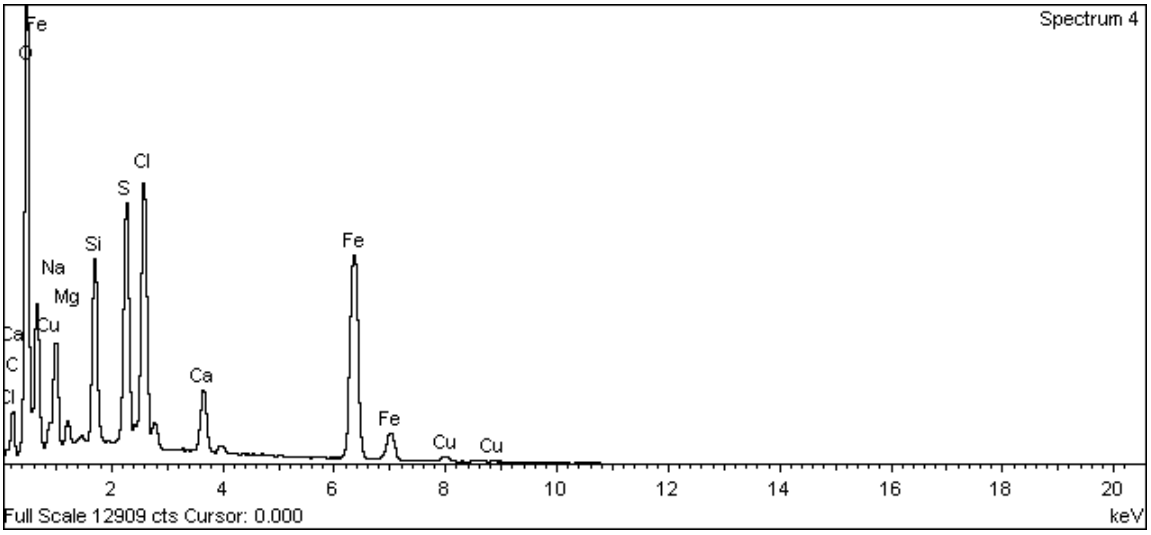

Figure A-225. Outer surface of copper canister near top hole and EDX analysis at position of Spectrum 4

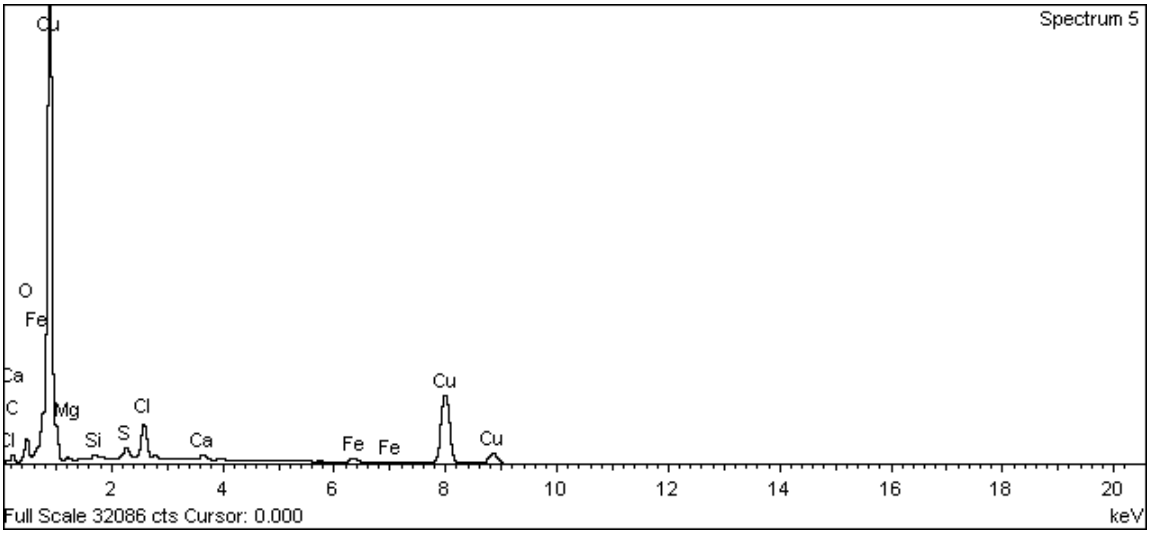

Figure A-226. Outer surface of copper canister near top hole and EDX analysis at position of Spectrum 5

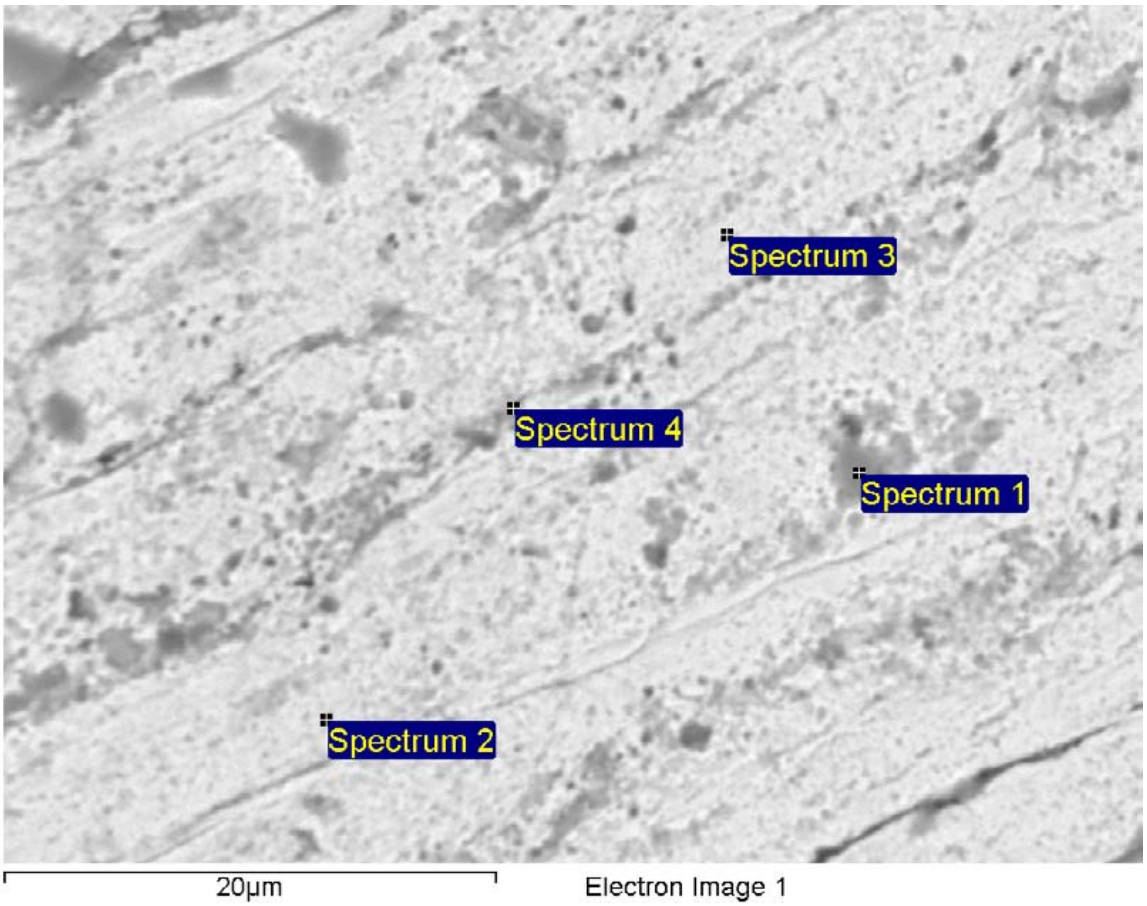

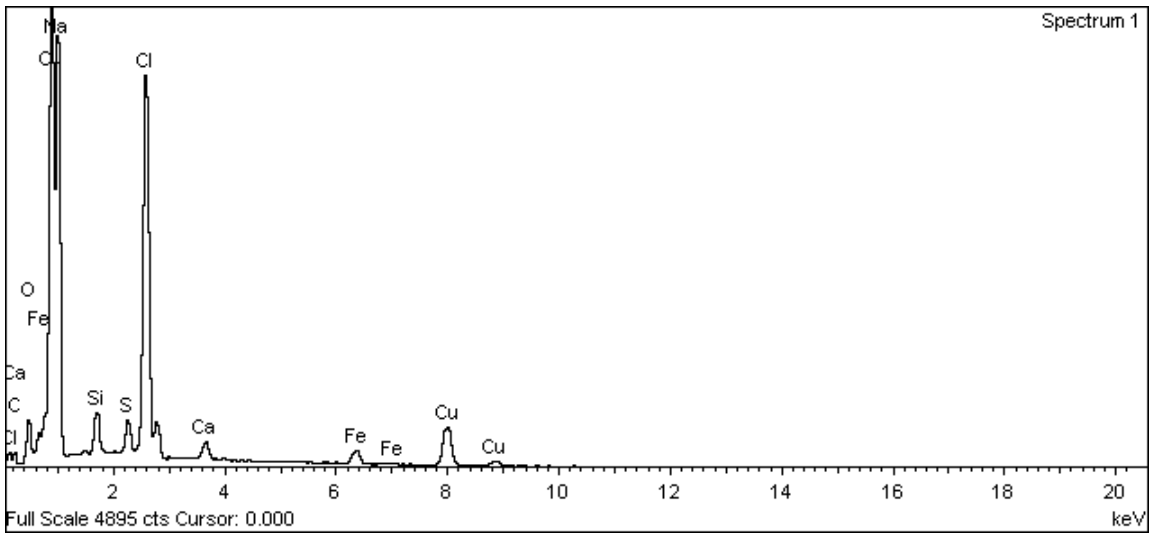

Figure A-227. Outer surface of copper canister near top hole and EDX analysis at position of Spectrum 1

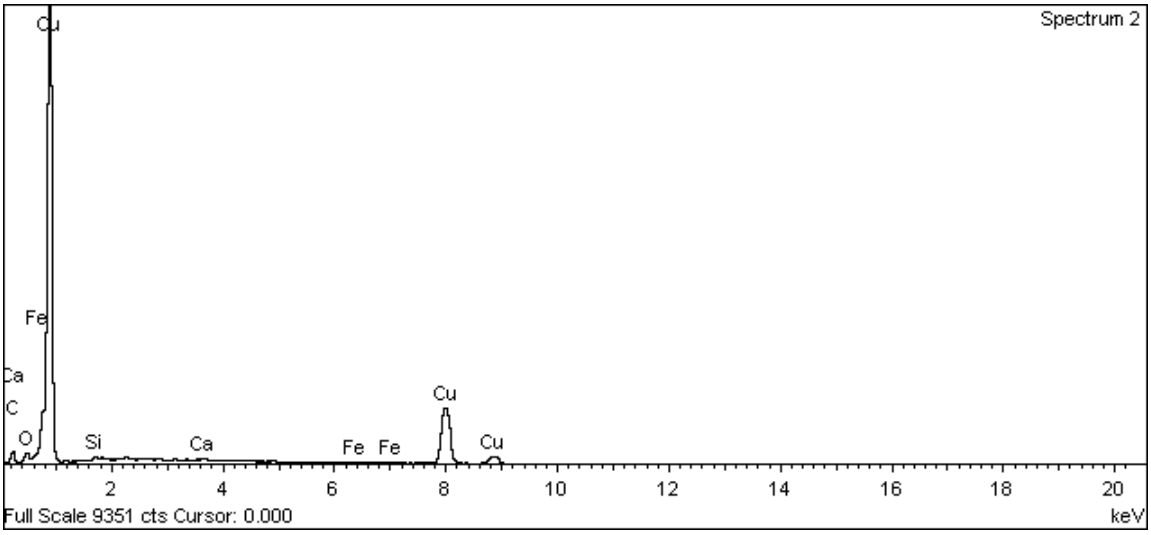

Figure A-228. Outer surface of copper canister near top hole and EDX analysis at position of Spectrum 2

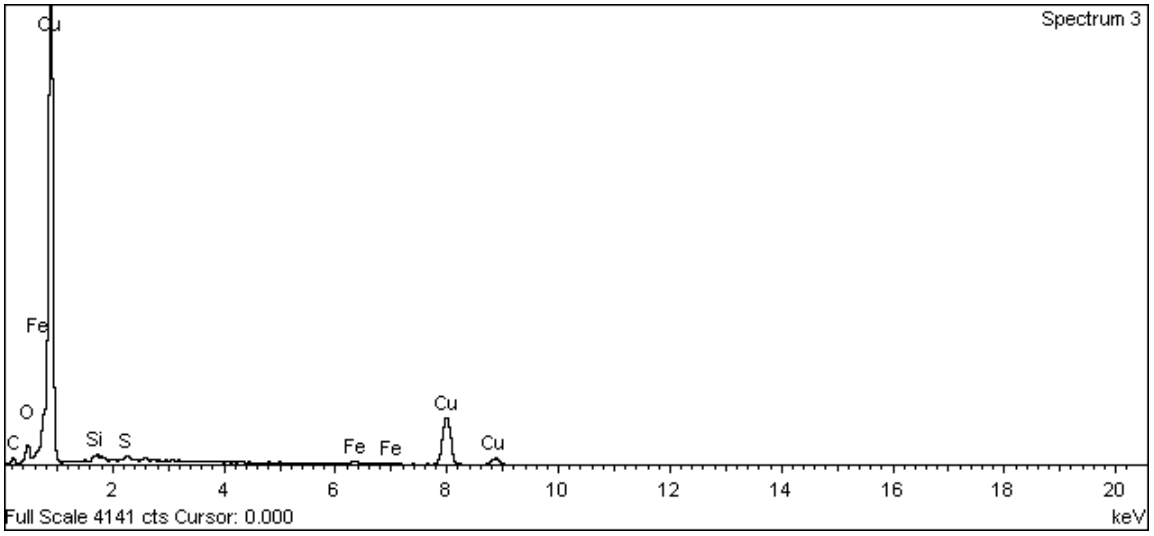

Figure A-229. Outer surface of copper canister near top hole and EDX analysis at position of Spectrum 3

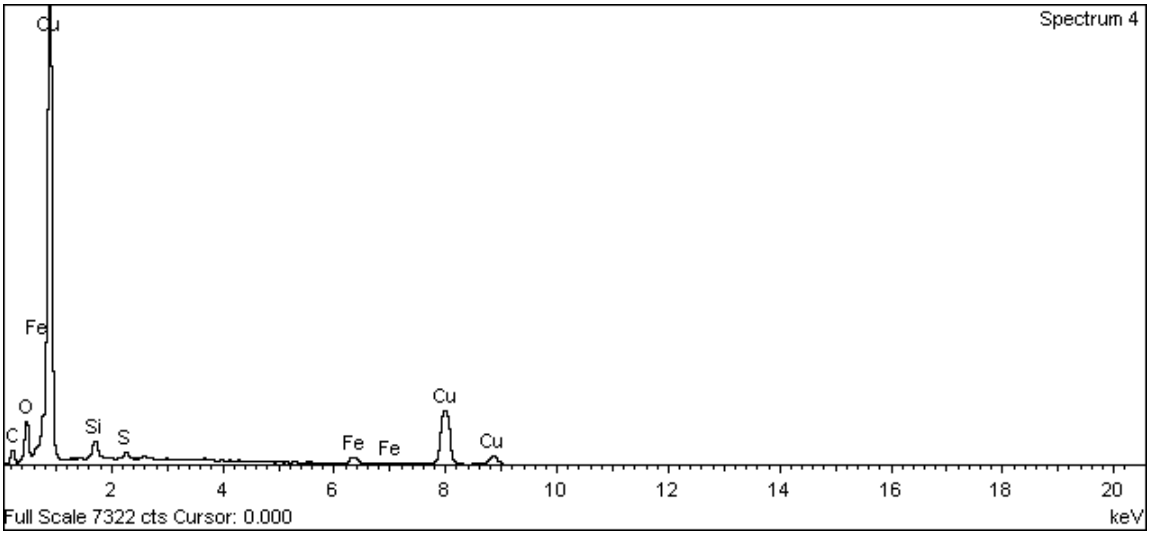

Figure A-230. Outer surface of copper canister near top hole and EDX analysis at position of Spectrum 4

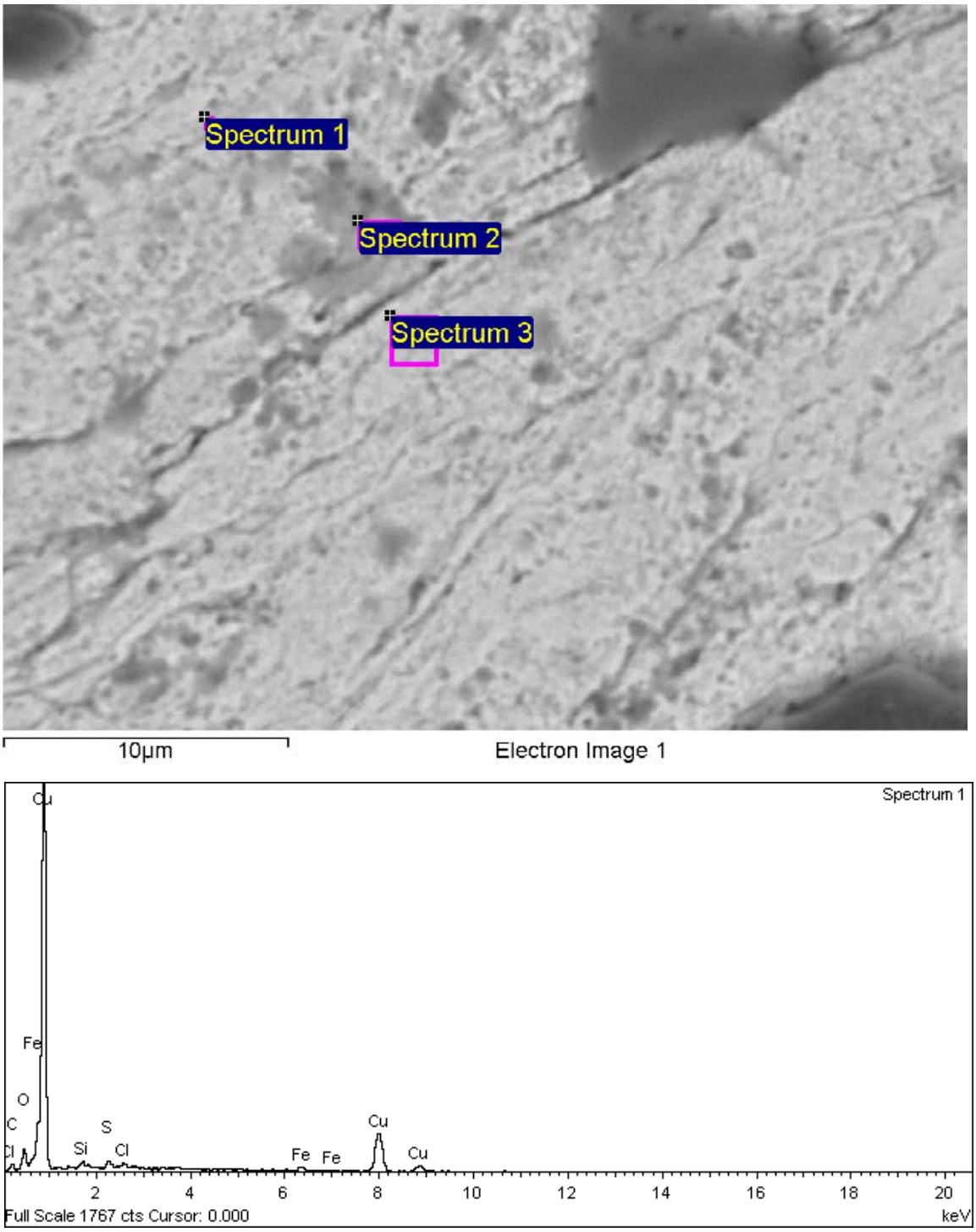

Figure A-231. Outer surface of copper canister near top hole and EDX analysis at position of Spectrum 1

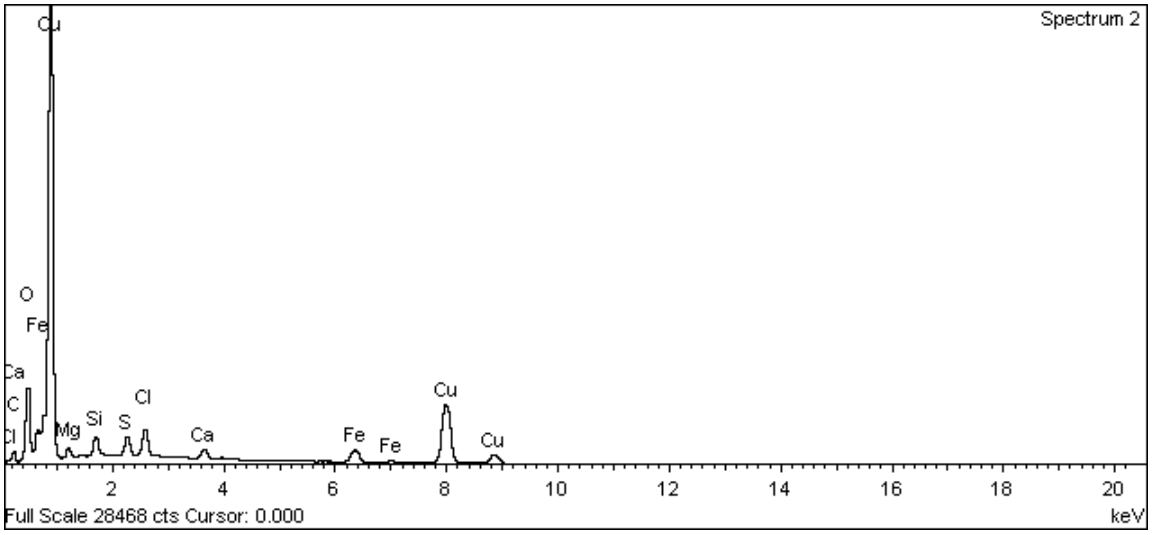

Figure A-232. Outer surface of copper canister near top hole and EDX analysis at position of Spectrum 2

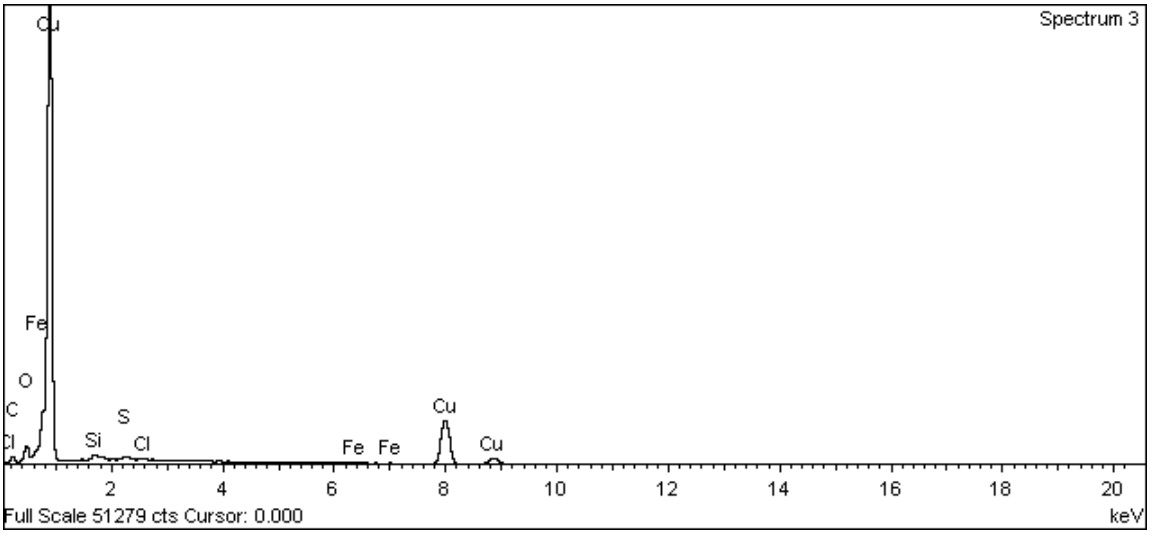

Figure A-233. Outer surface of copper canister near top hole and EDX analysis at position of Spectrum 3

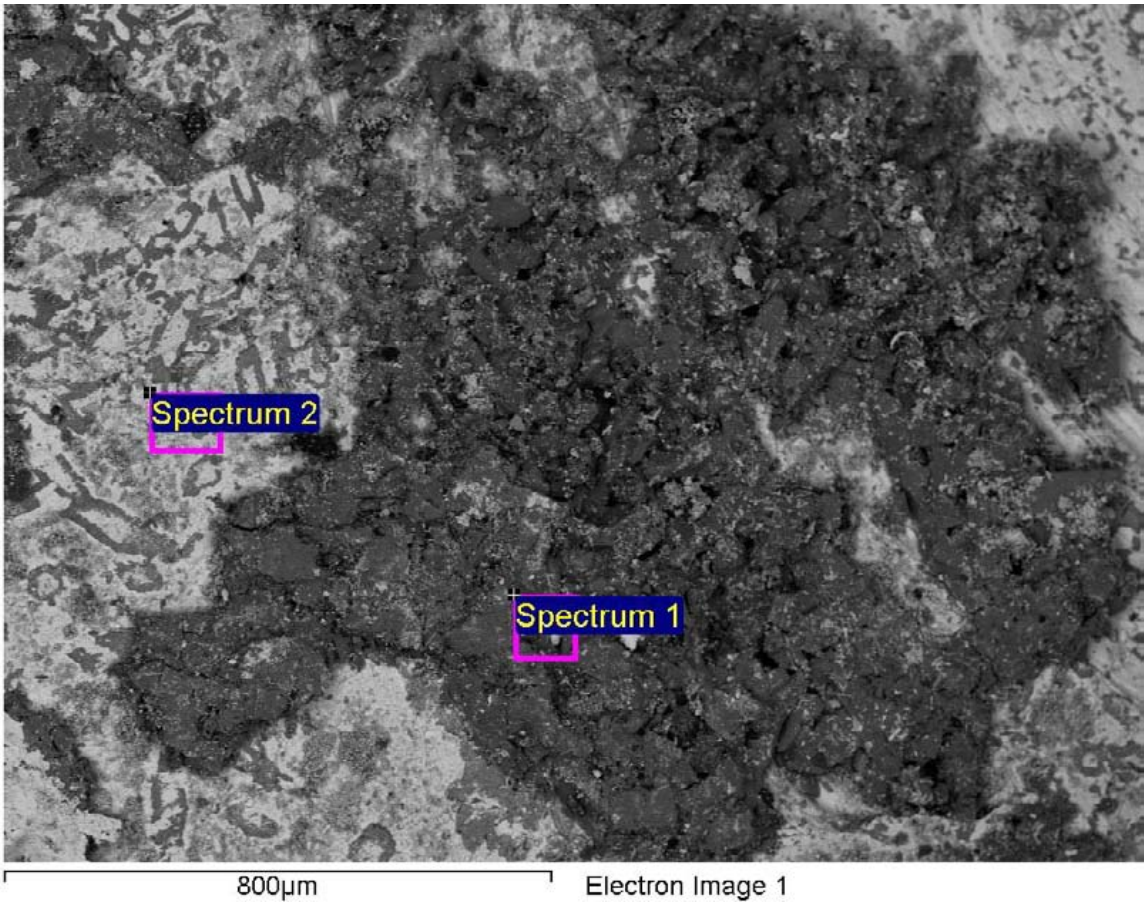

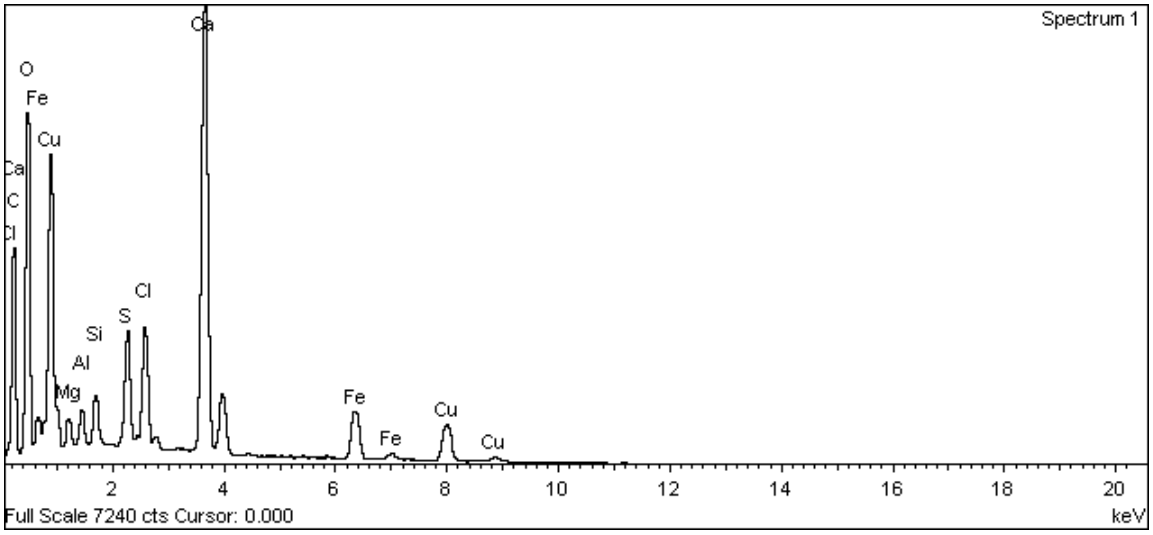

Figure A-234. Outer surface of copper canister near top hole and EDX analysis at position of Spectrum 1

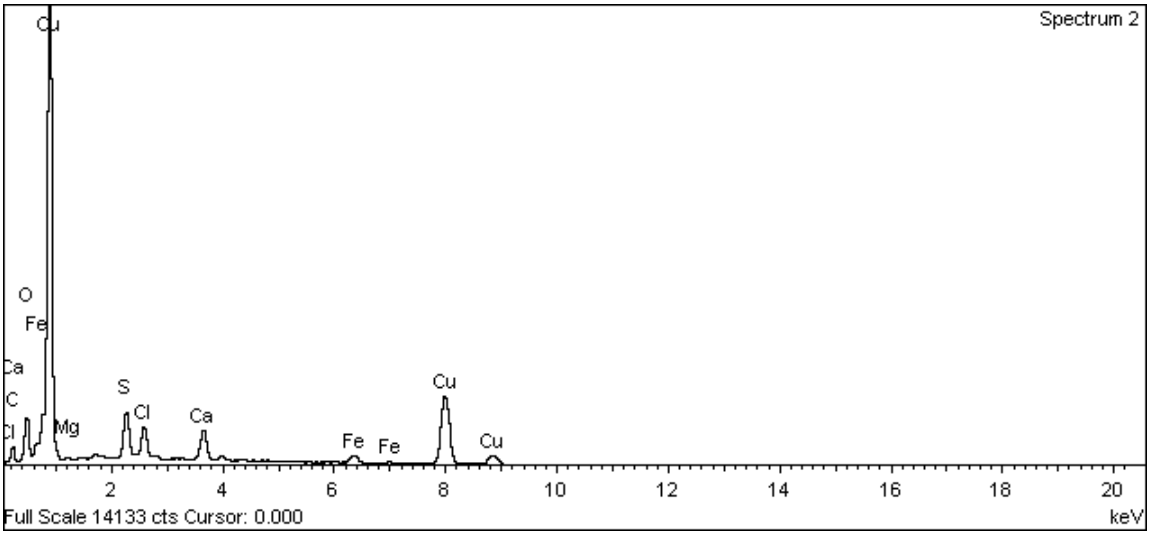

Figure A-235. Outer surface of copper canister near top hole and EDX analysis at position of Spectrum 2

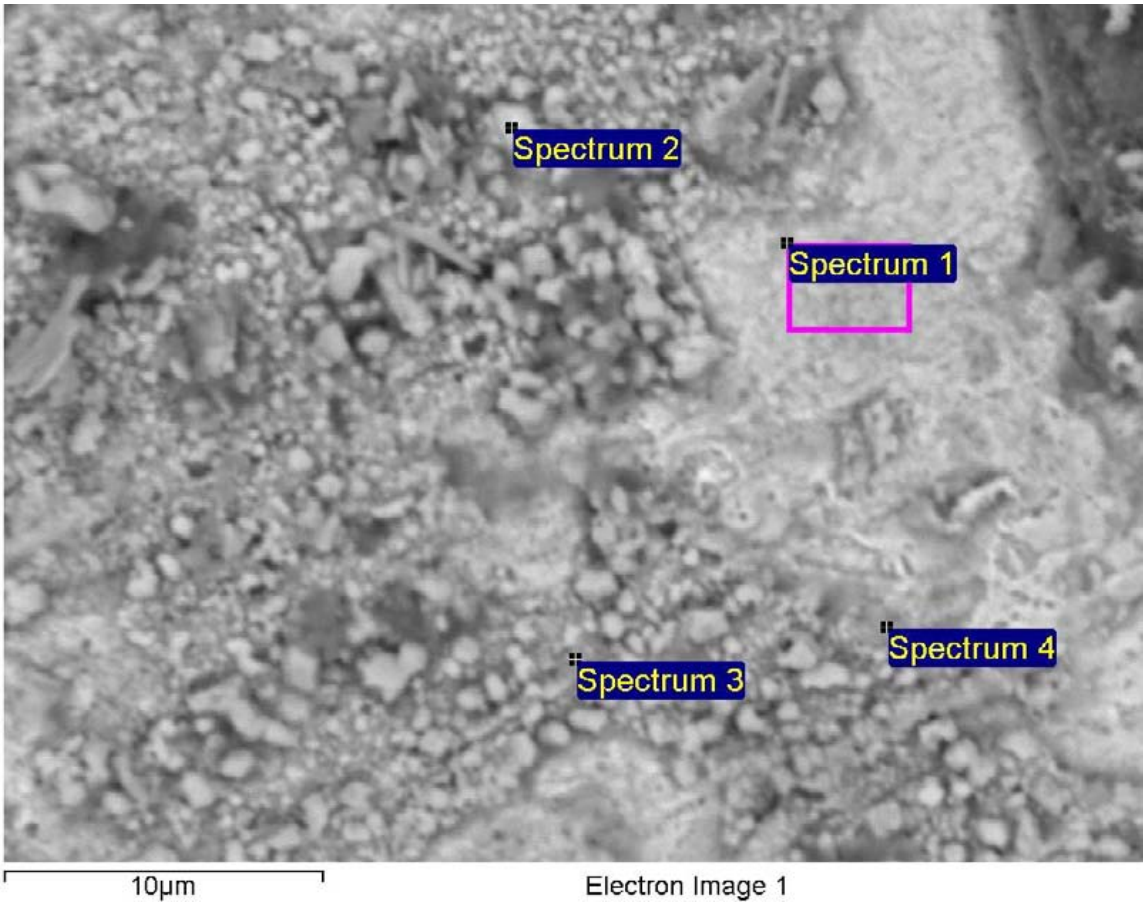

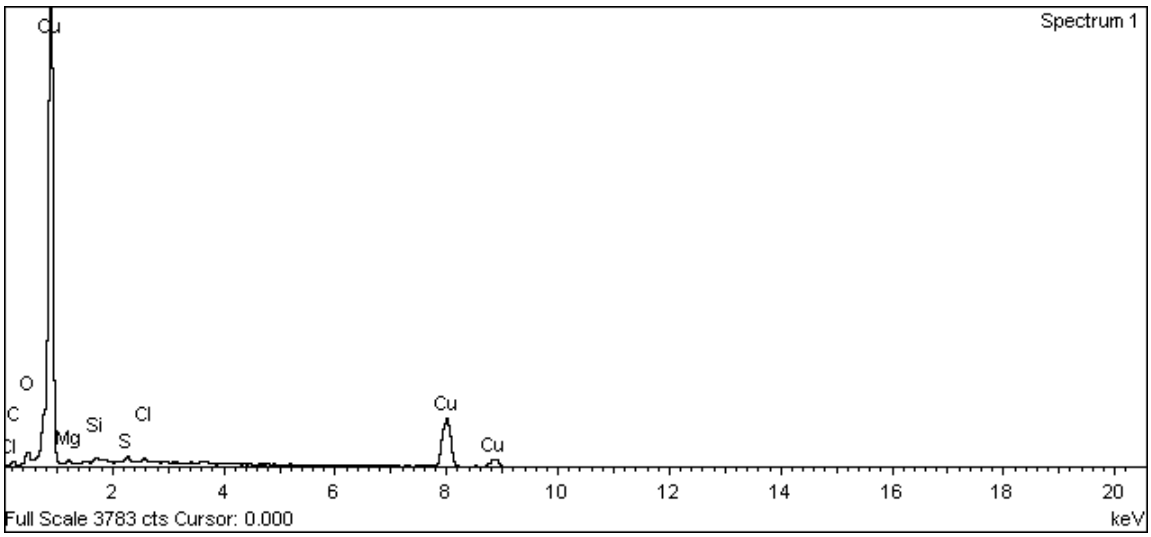

Figure A-236. Outer surface of copper canister near top hole and EDX analysis at position of Spectrum 1

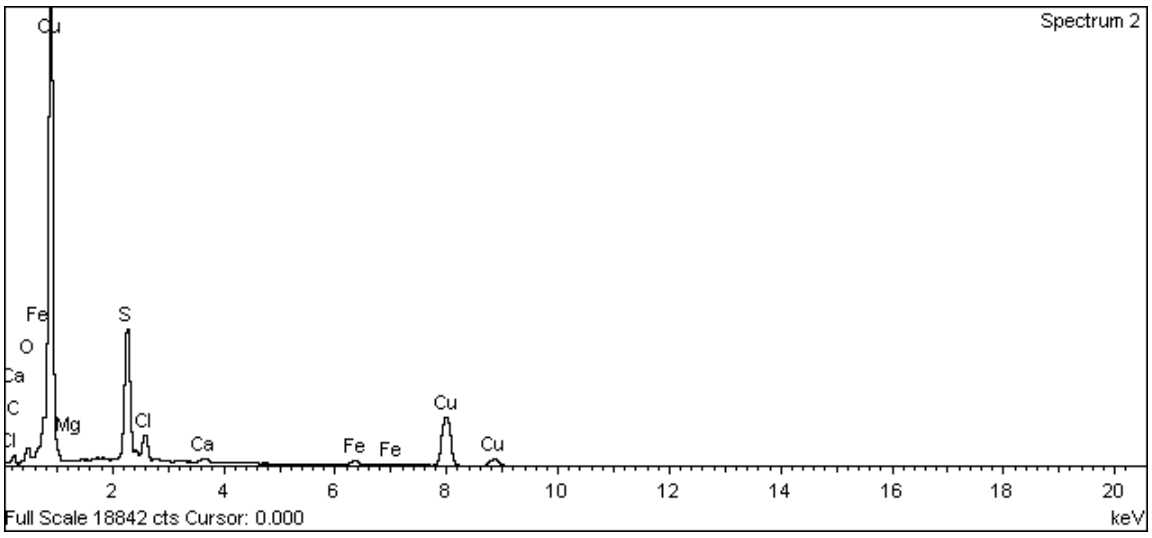

Figure A-237. Outer surface of copper canister near top hole and EDX analysis at position of Spectrum 2

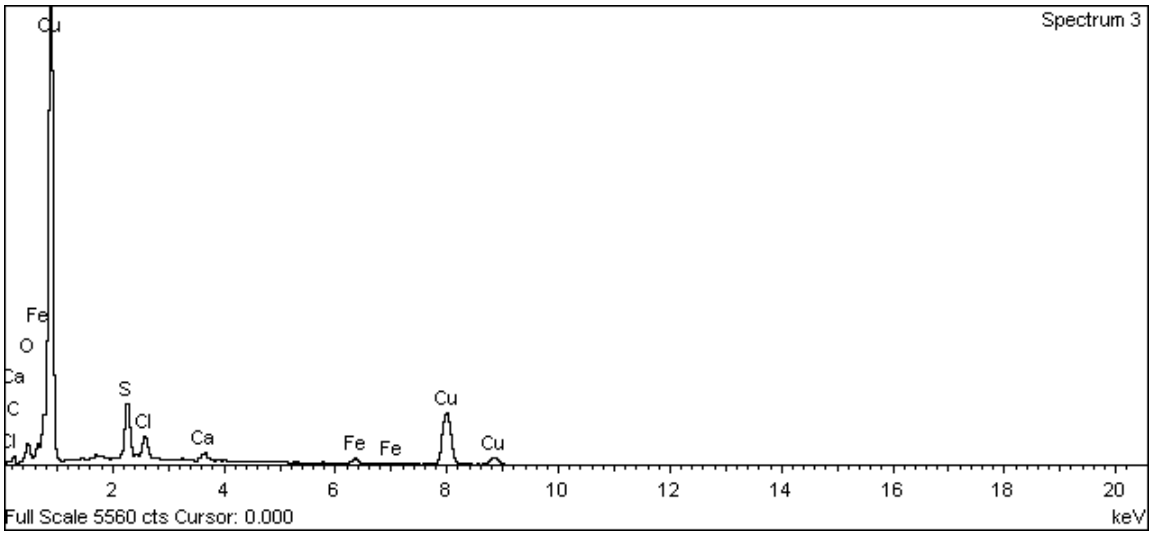

Figure A-238. Outer surface of copper canister near top hole and EDX analysis at position of Spectrum 3

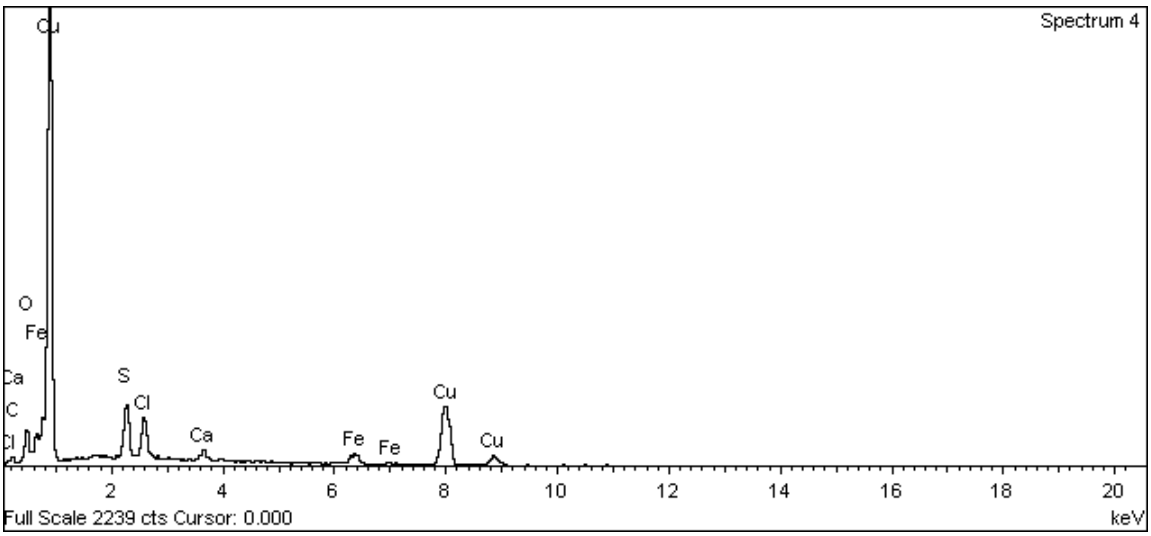

Figure A-239. Outer surface of copper canister near top hole and EDX analysis at position of Spectrum 4

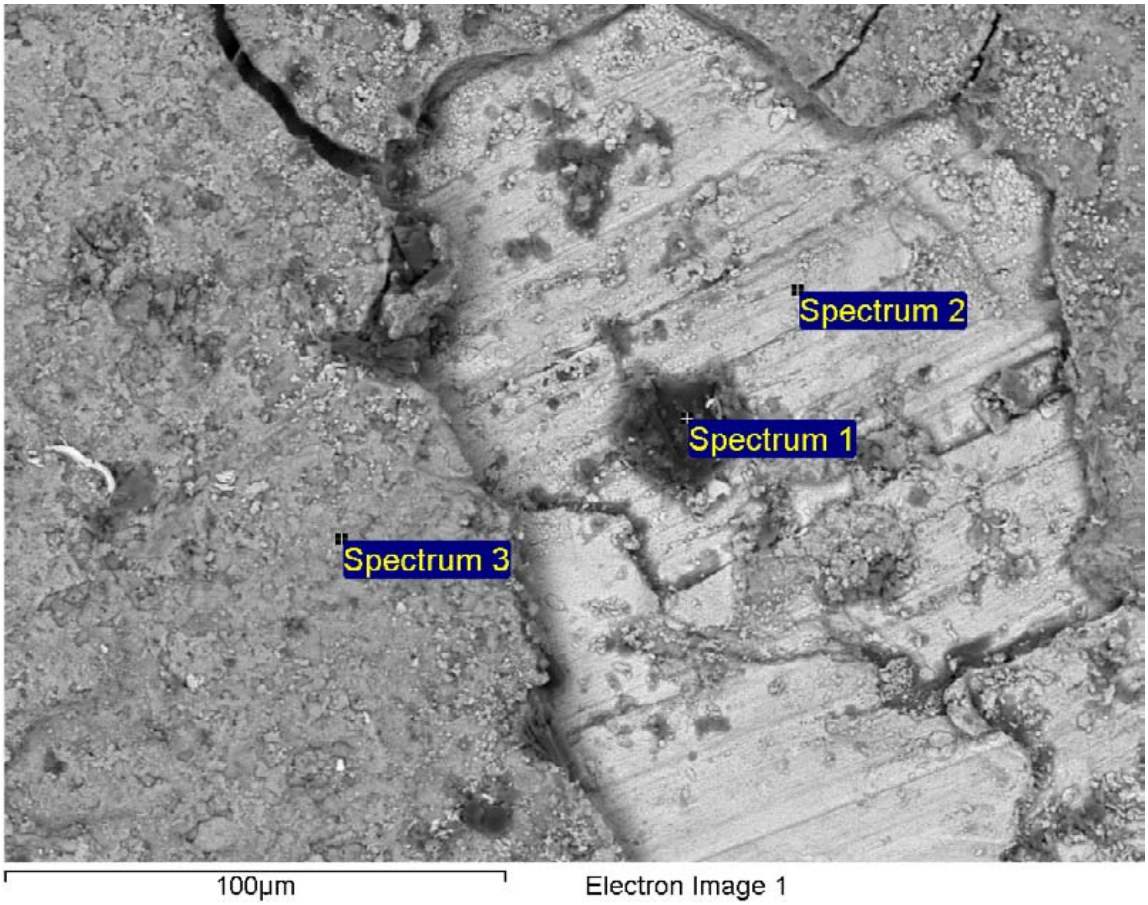

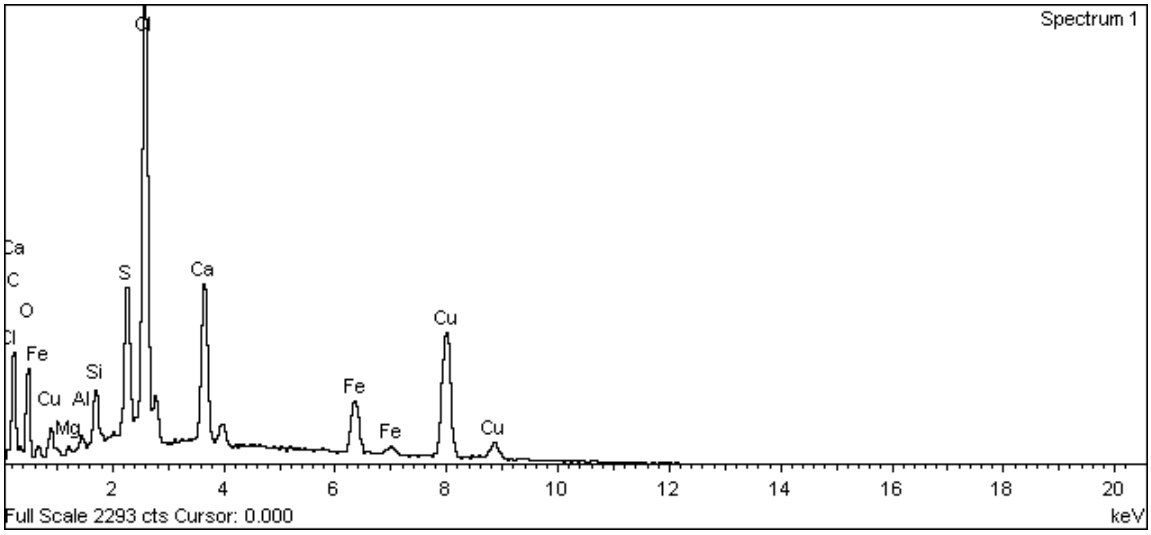

Figure A-240. Outer surface of copper canister near top hole and EDX analysis at position of Spectrum 1

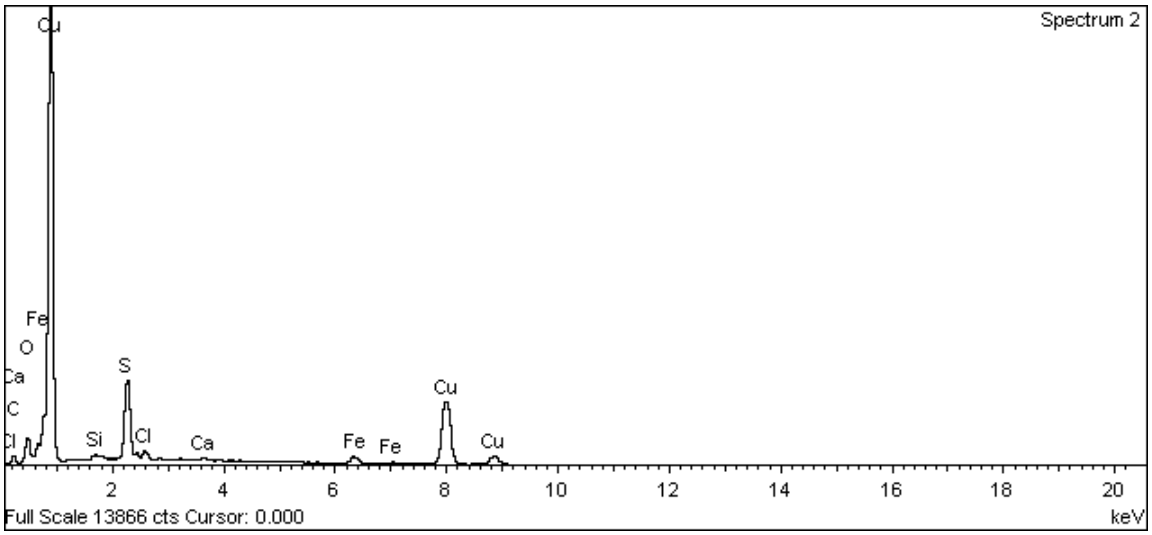

Figure A-241. Outer surface of copper canister near top hole and EDX analysis at position of Spectrum 2

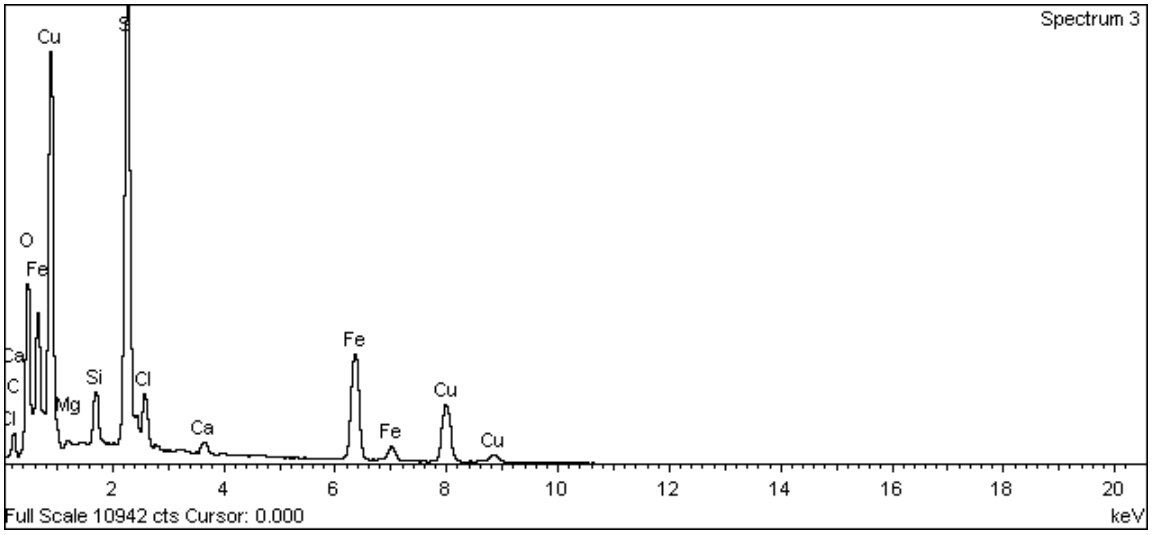

Figure A-242. Outer surface of copper canister near top hole and EDX analysis at position of Spectrum 3

Copper can inner surface around bottom hole

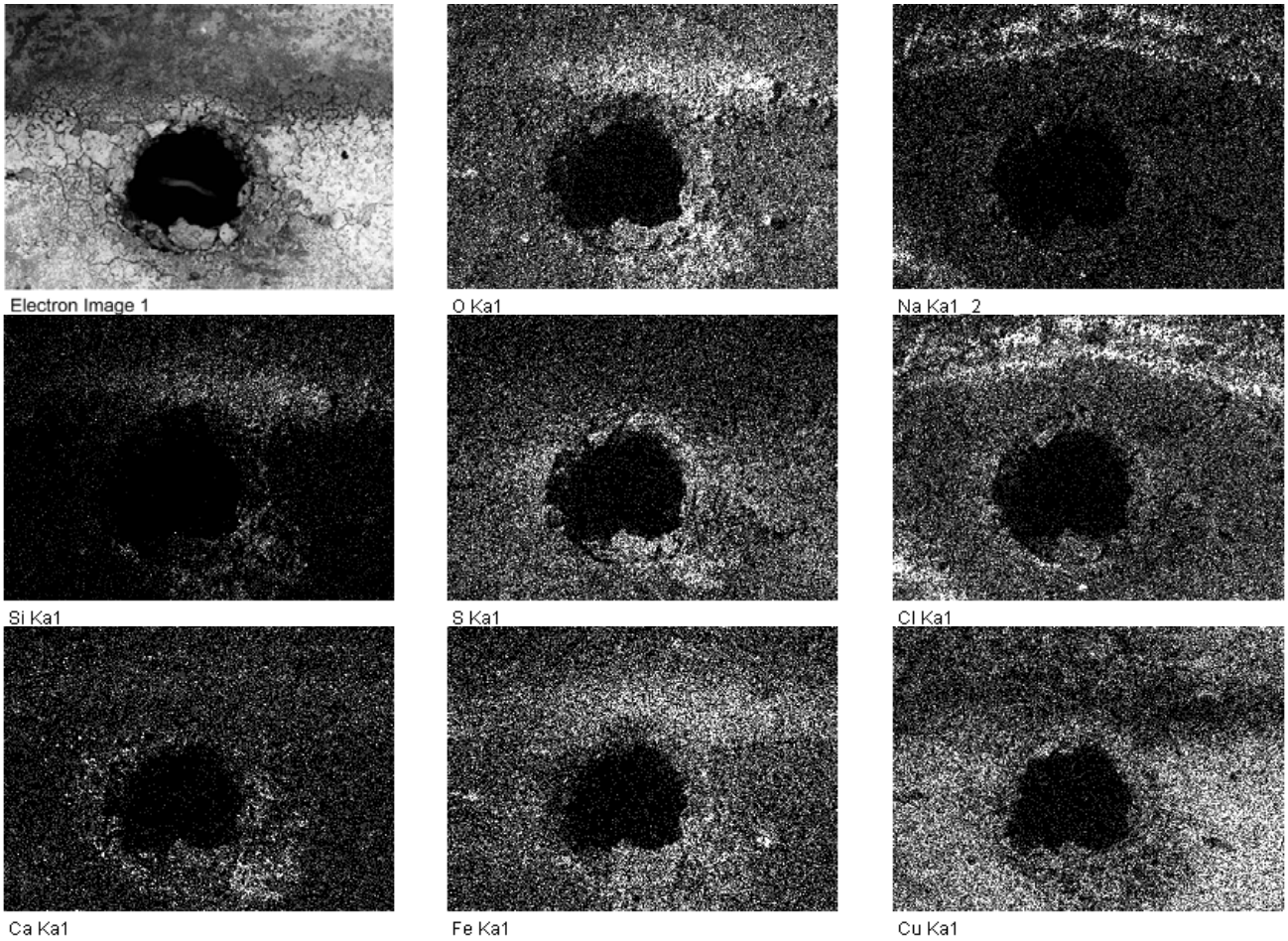

Figure A-243. Elemental maps for Inner surface of copper canister around the bottom hole

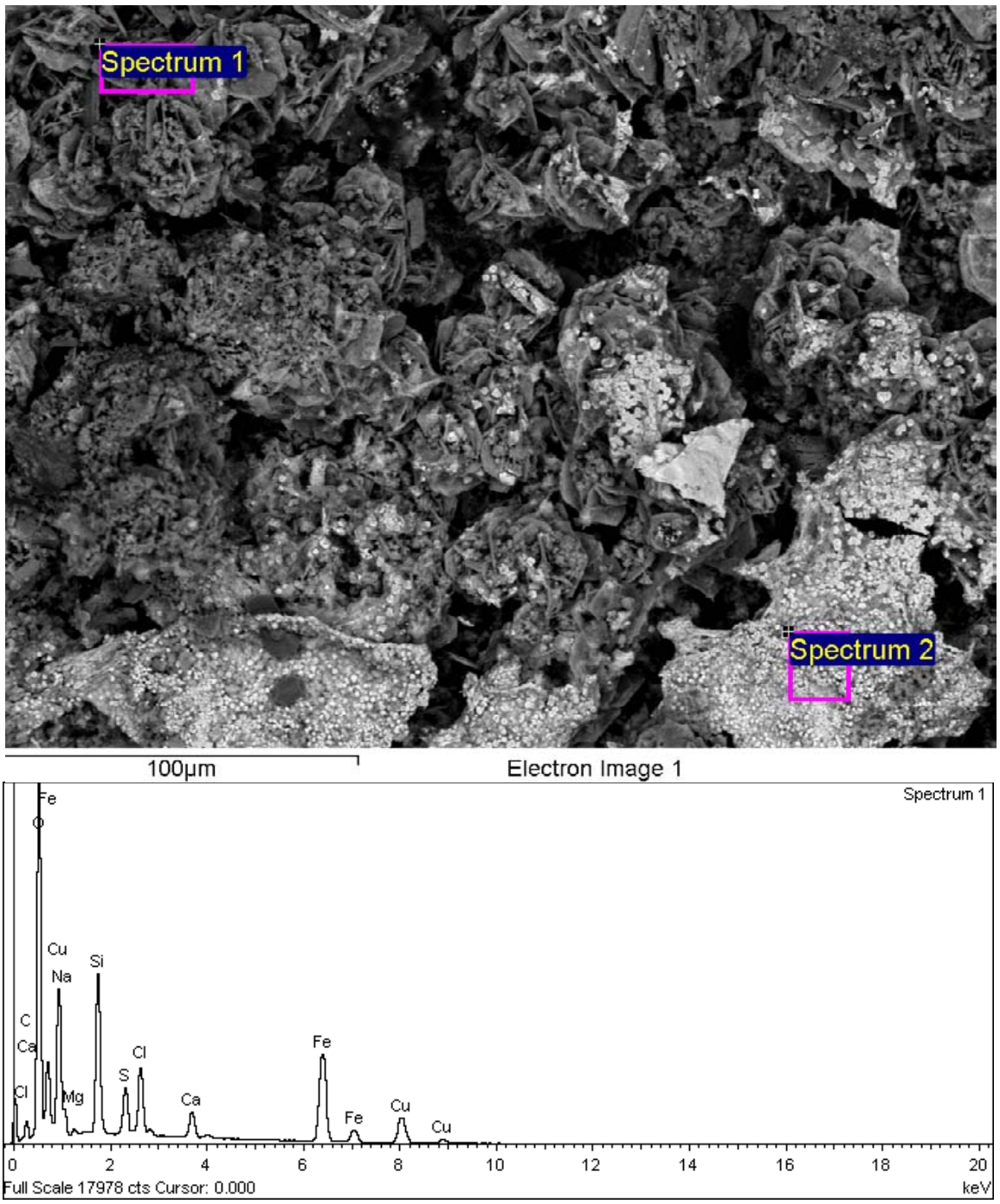

Figure A-244. Inner surface of copper canister around bottom hole and EDX analysis at position of Spectrum 1

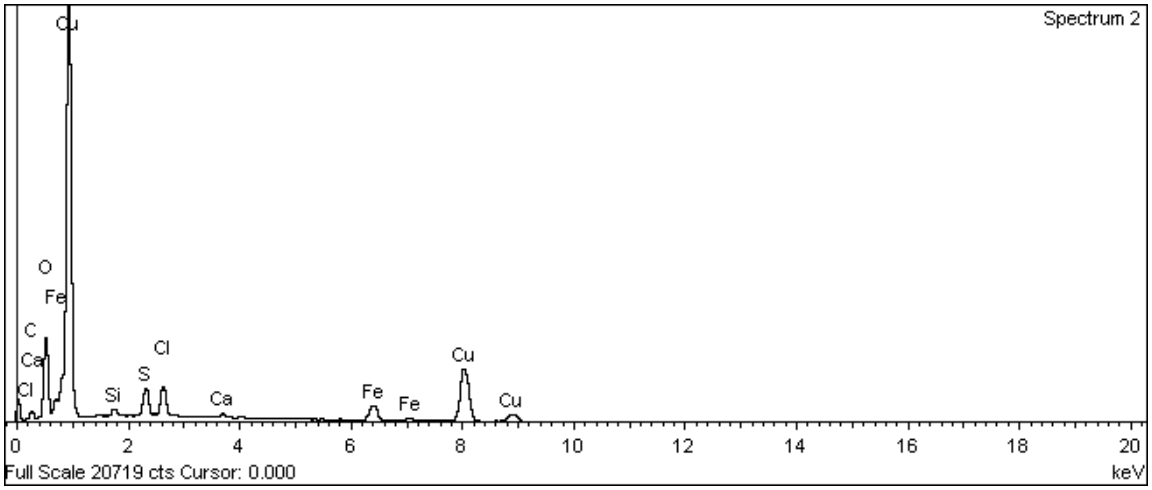

Figure A-245. Inner surface of copper canister around bottom hole and EDX analysis at position of Spectrum 2

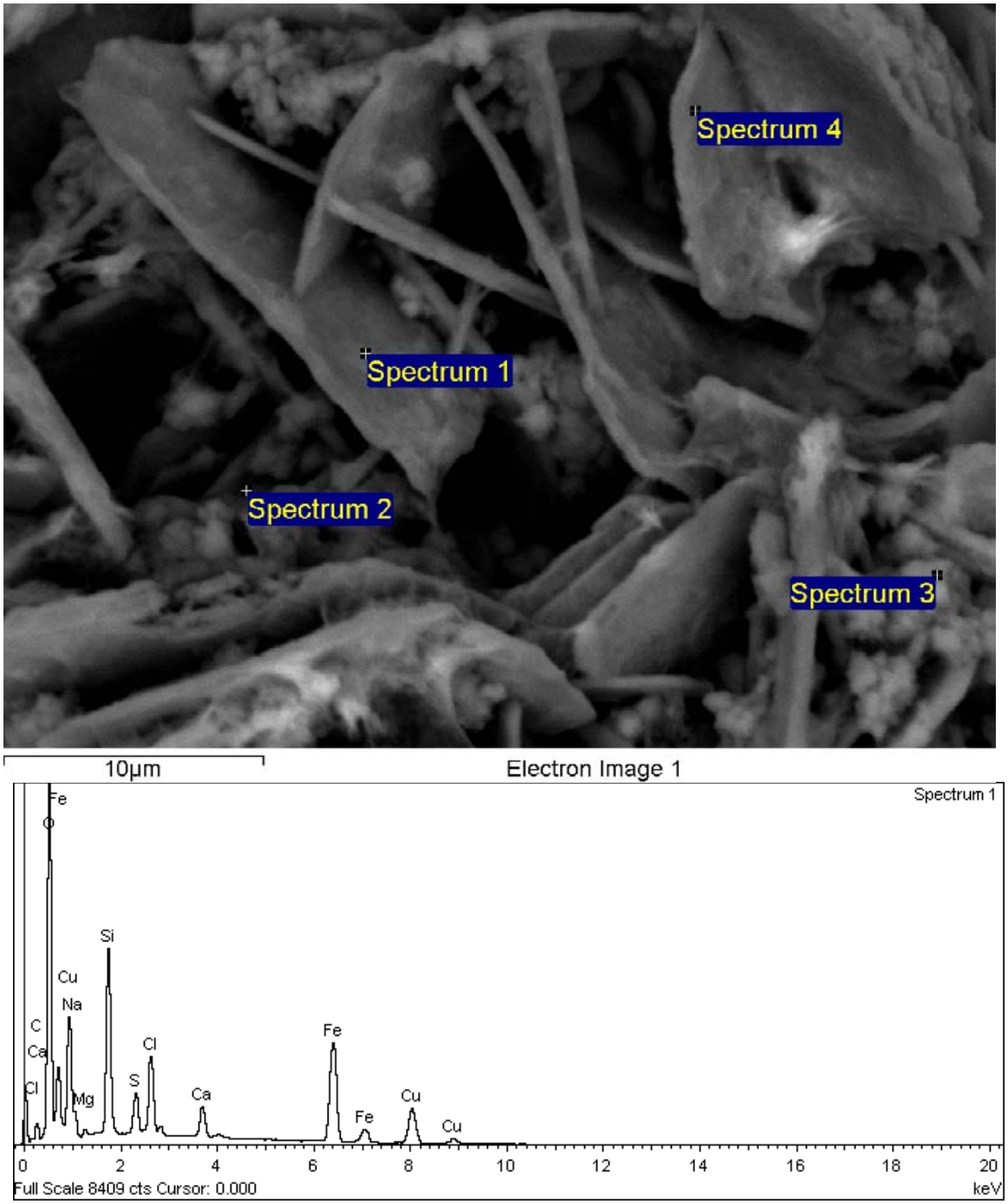

Figure A-246. Inner surface of copper canister around bottom hole and EDX analysis at position of Spectrum 1

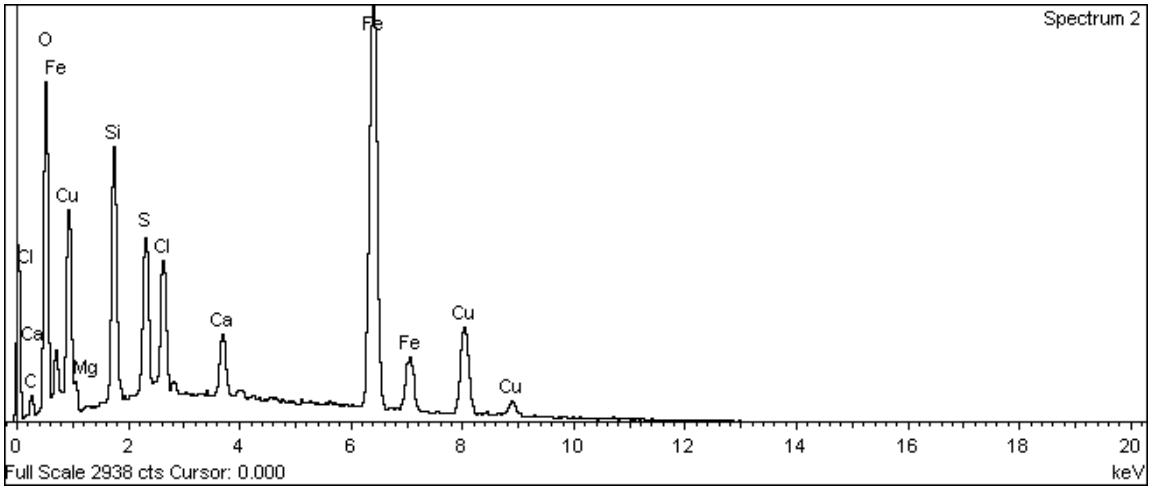

Figure A-247 Inner surface of copper canister around bottom hole and EDX analysis at position of Spectrum 2

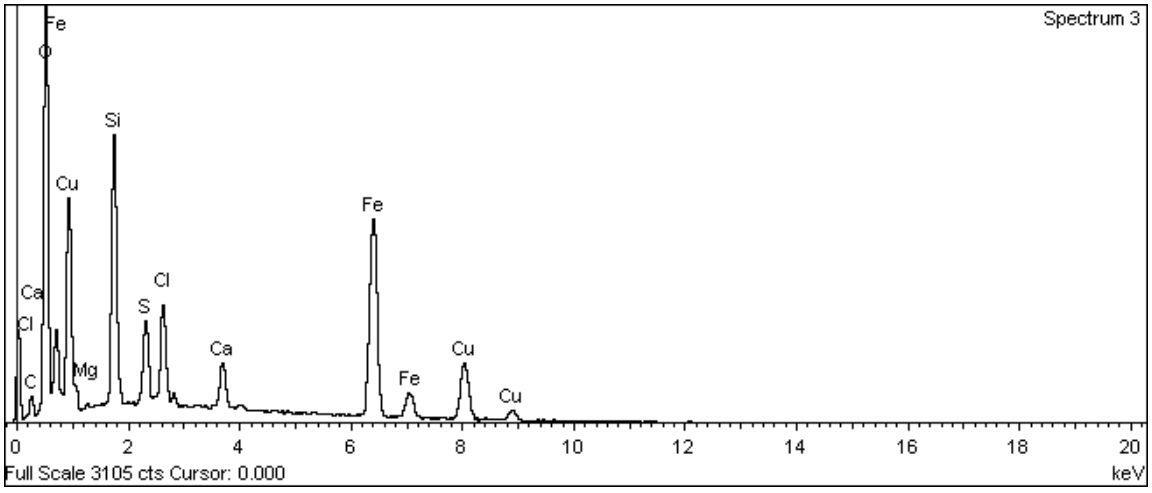

Figure A-248. Inner surface of copper canister around bottom hole and EDX analysis at position of Spectrum 3

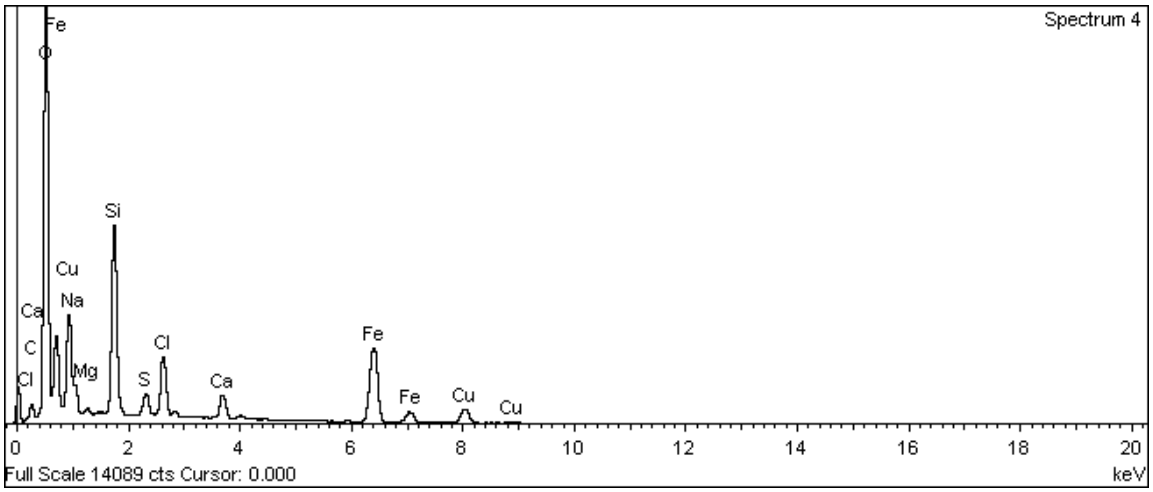

Figure A-249. Inner surface of copper canister around bottom hole and EDX analysis at position of Spectrum 4

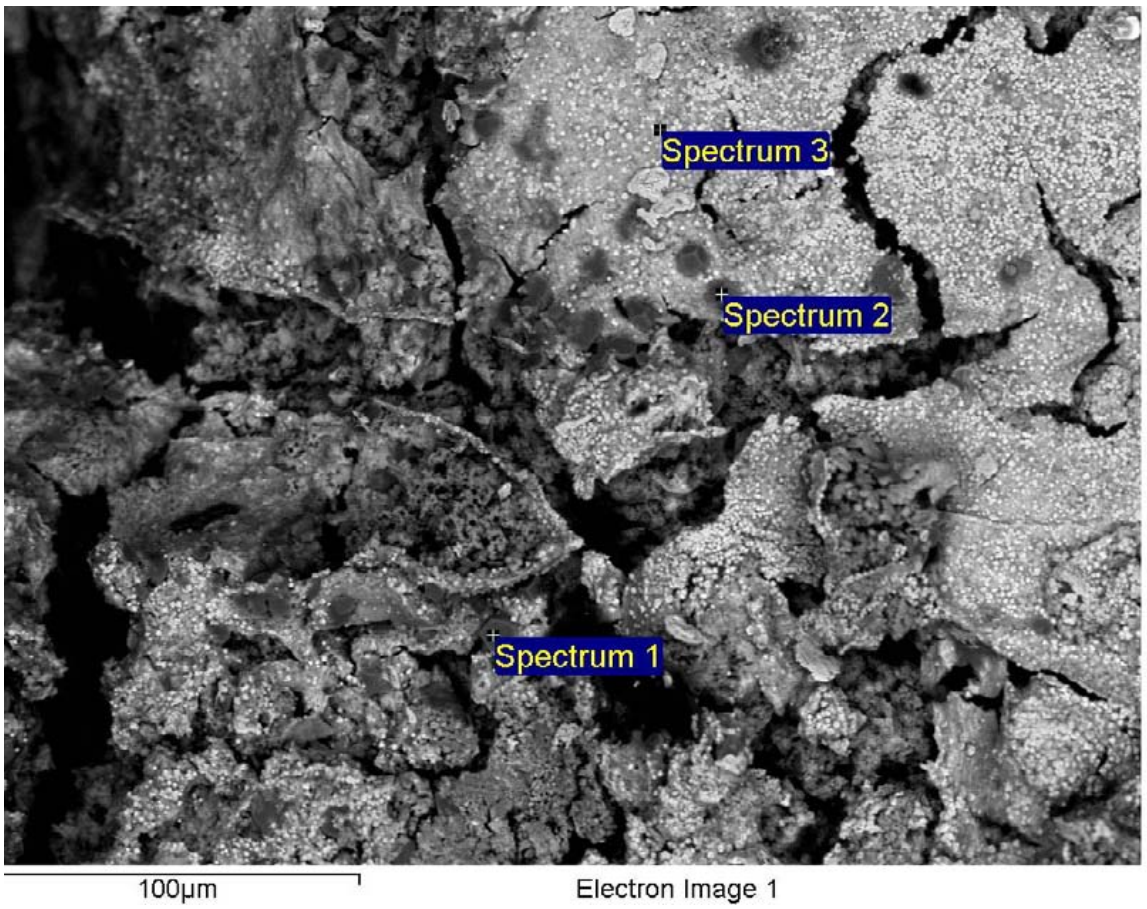

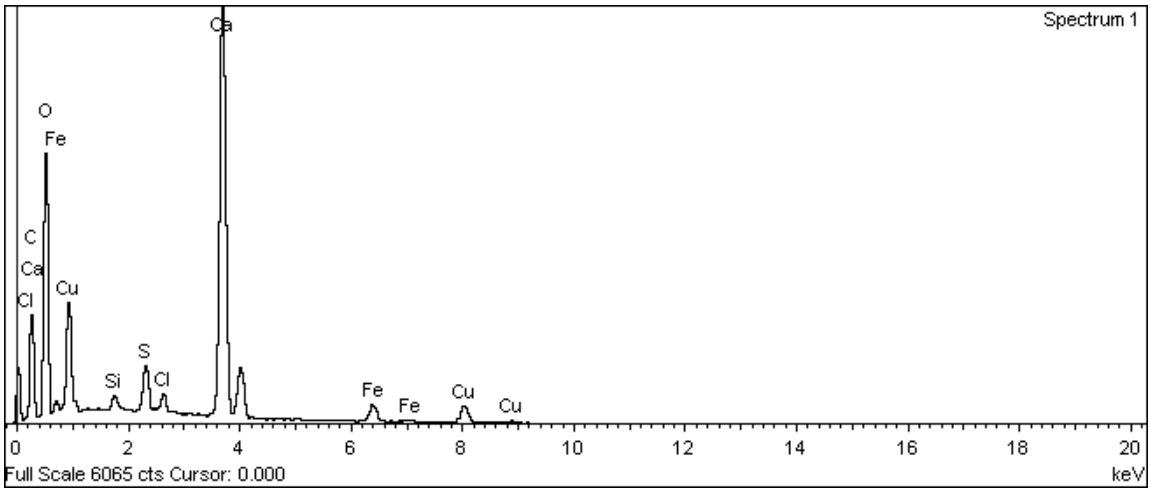

Figure A-250. Inner surface of copper canister around bottom hole and EDX analysis at position of Spectrum 1

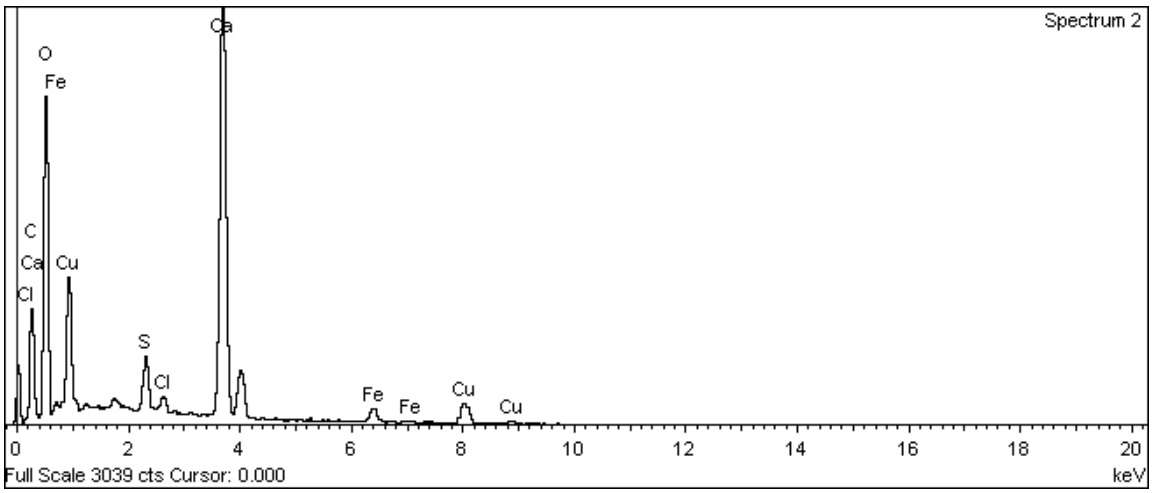

Figure A-251. Inner surface of copper canister around bottom hole and EDX analysis at position of Spectrum 2

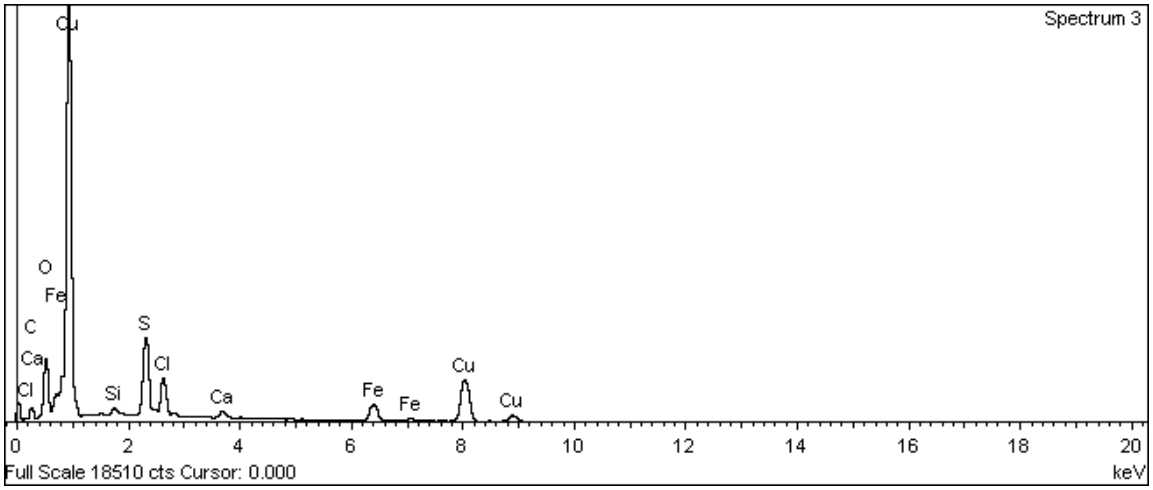

Figure A-252. Inner surface of copper canister around bottom hole and EDX analysis at position of Spectrum 3

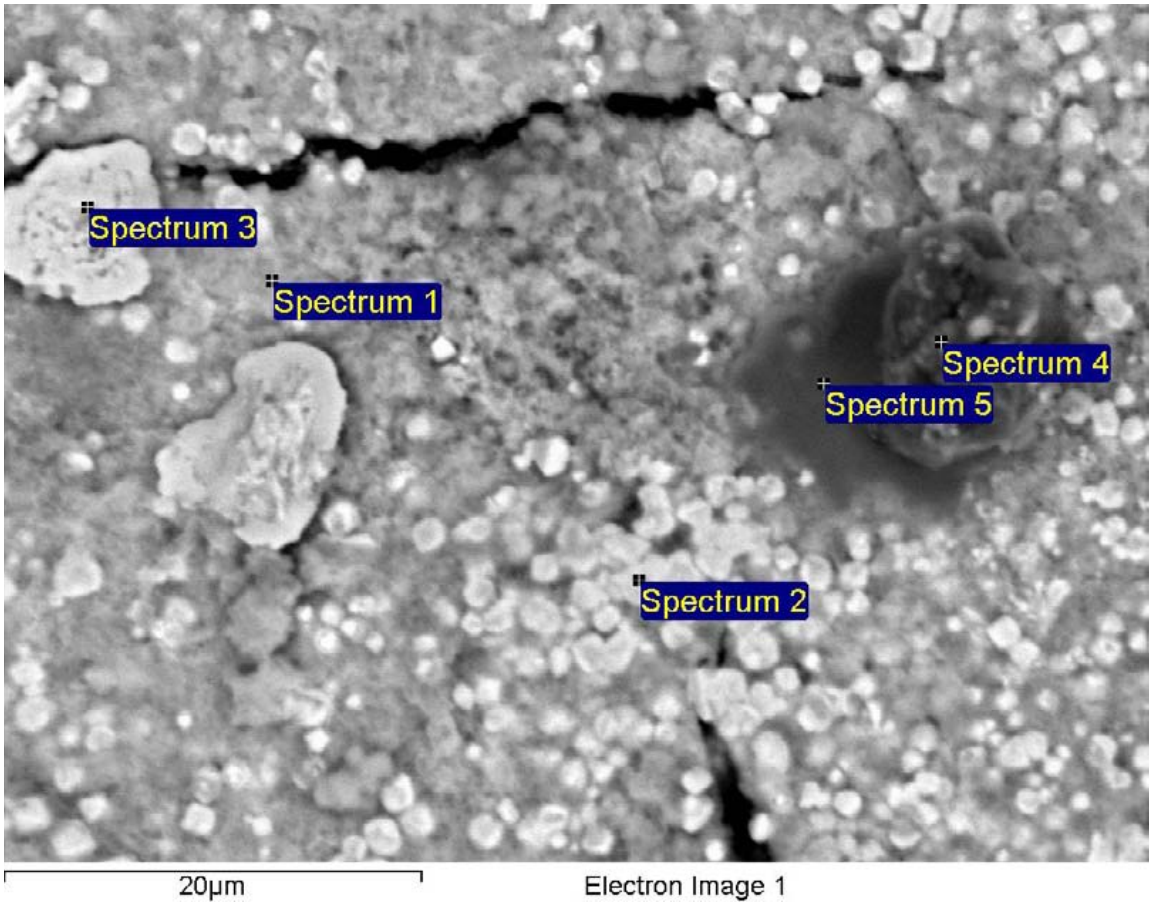

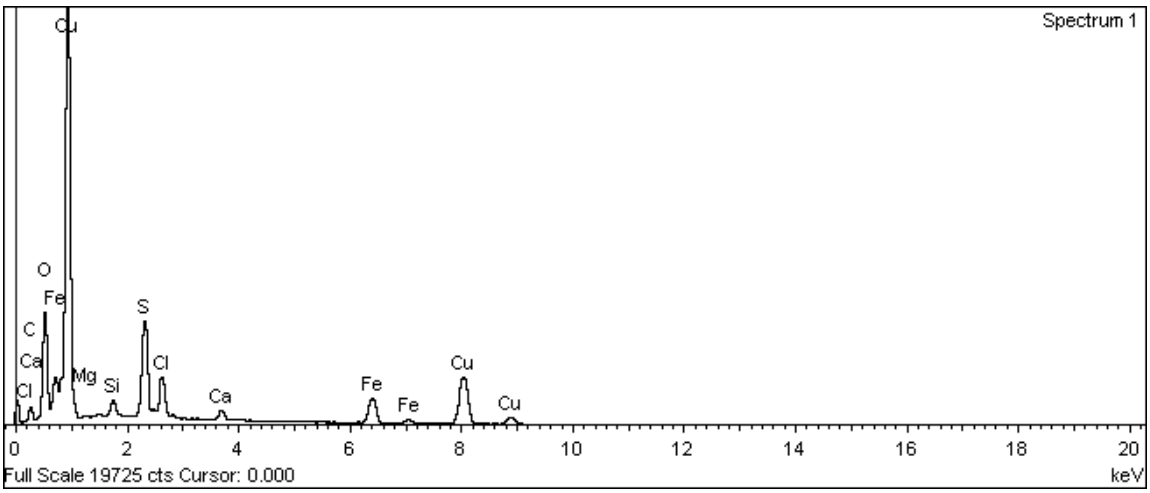

Figure A-253. Inner surface of copper canister around bottom hole and EDX analysis at position of Spectrum 1

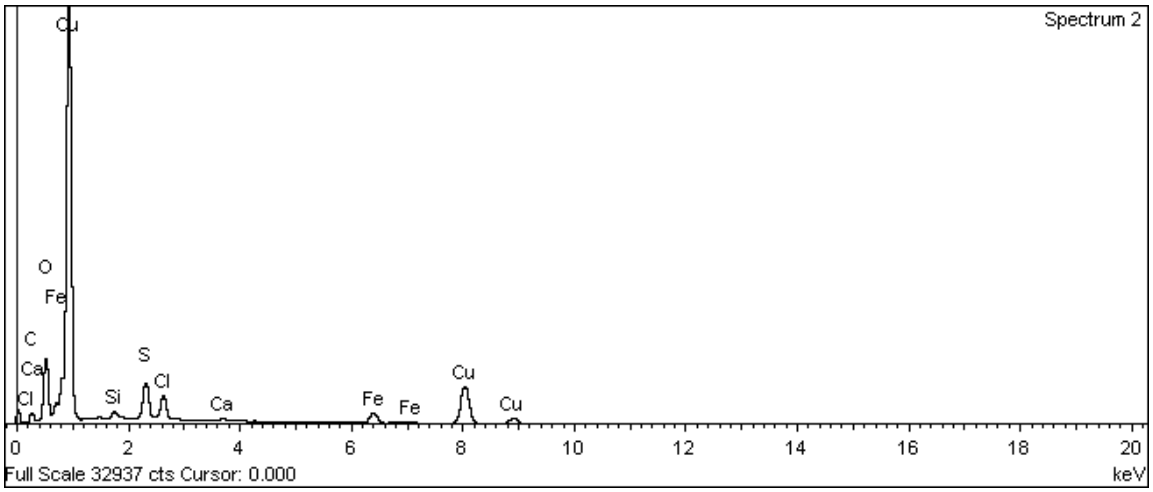

Figure A-254. Inner surface of copper canister around bottom hole and EDX analysis at position of Spectrum 2

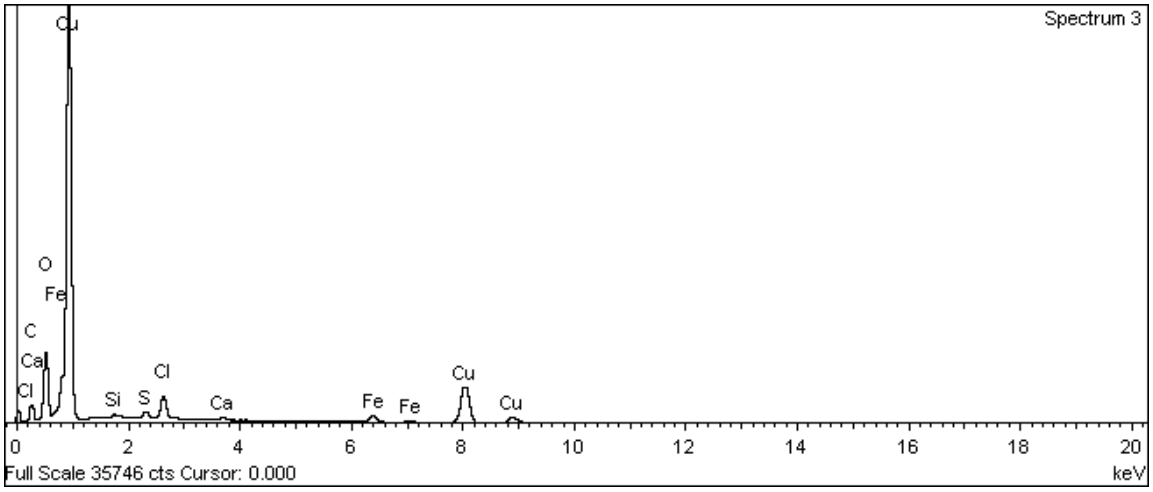

Figure A-255. Inner surface of copper canister around bottom hole and EDX analysis at position of Spectrum 3

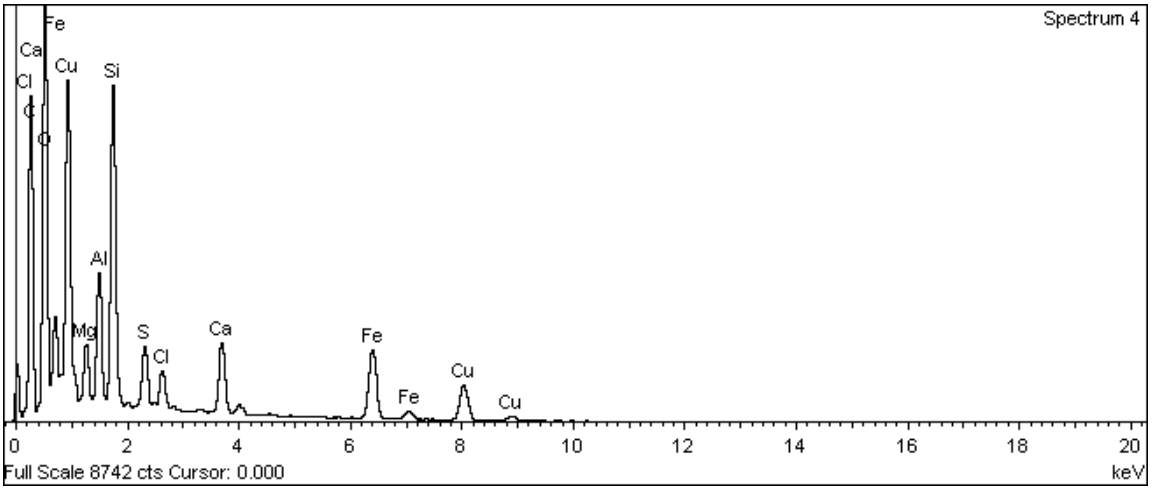

Figure A-256. Inner surface of copper canister around bottom hole and EDX analysis at position of Spectrum 4

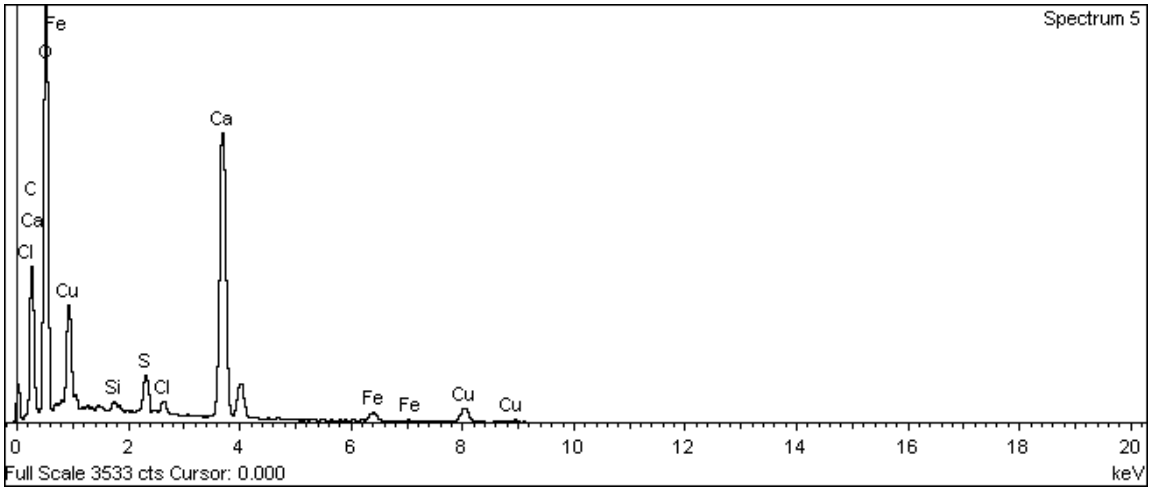

Figure A-257. Inner surface of copper canister around bottom hole and EDX analysis at position of Spectrum 5

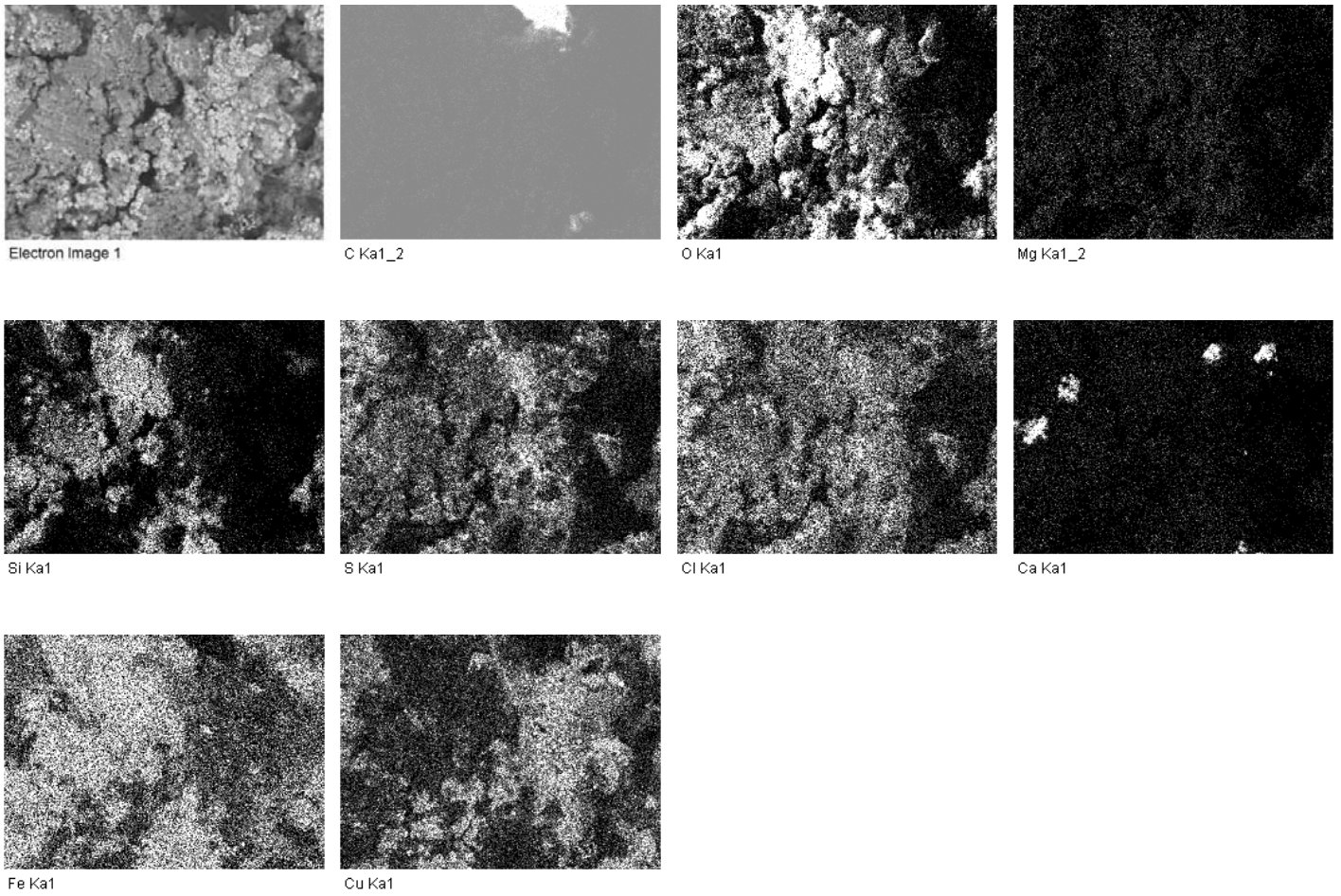

Figure A-258. Elemental maps for Inner surface of copper canister around the top hole

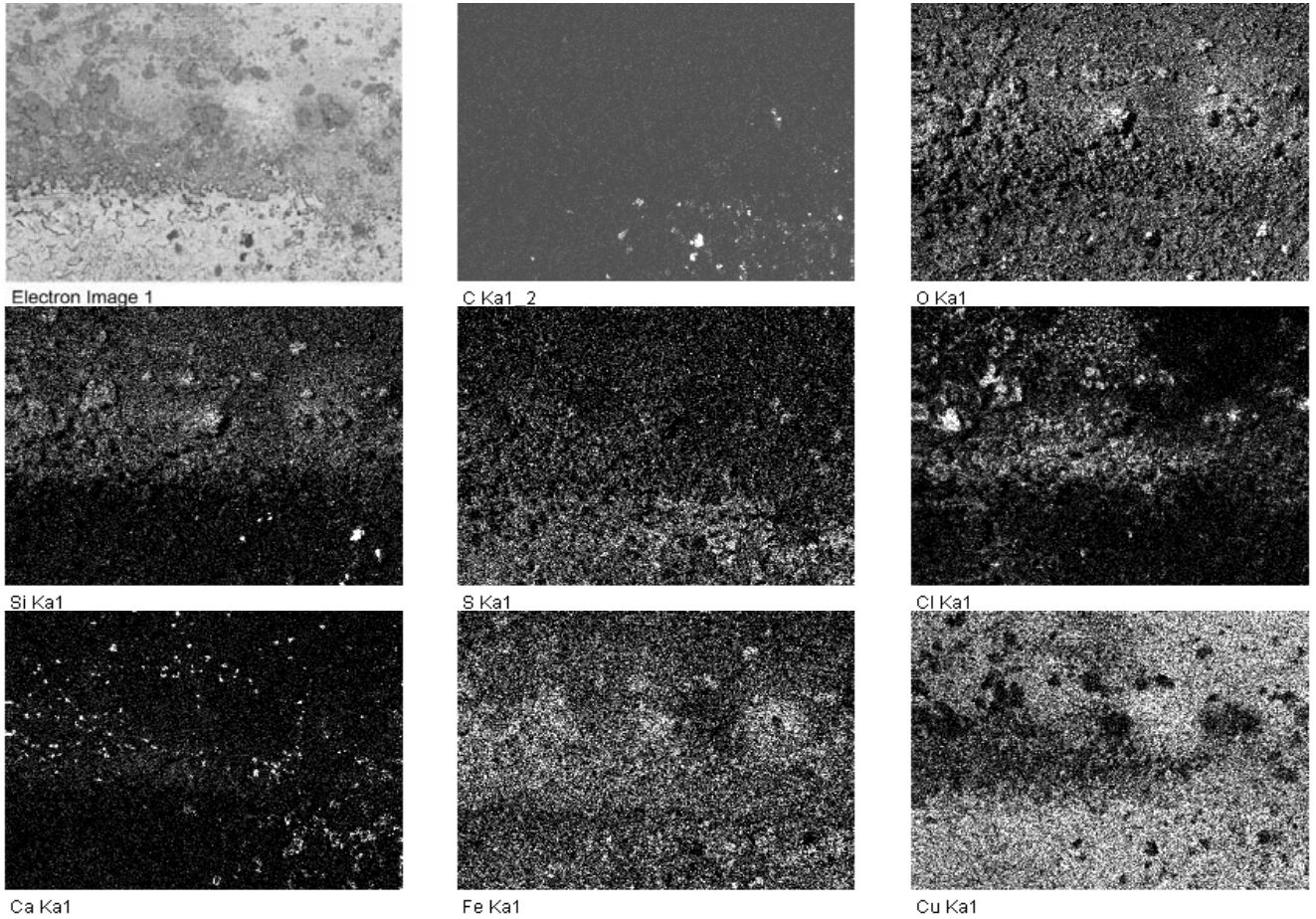

Figure A-259. Elemental maps for Inner surface of copper canister around the top hole

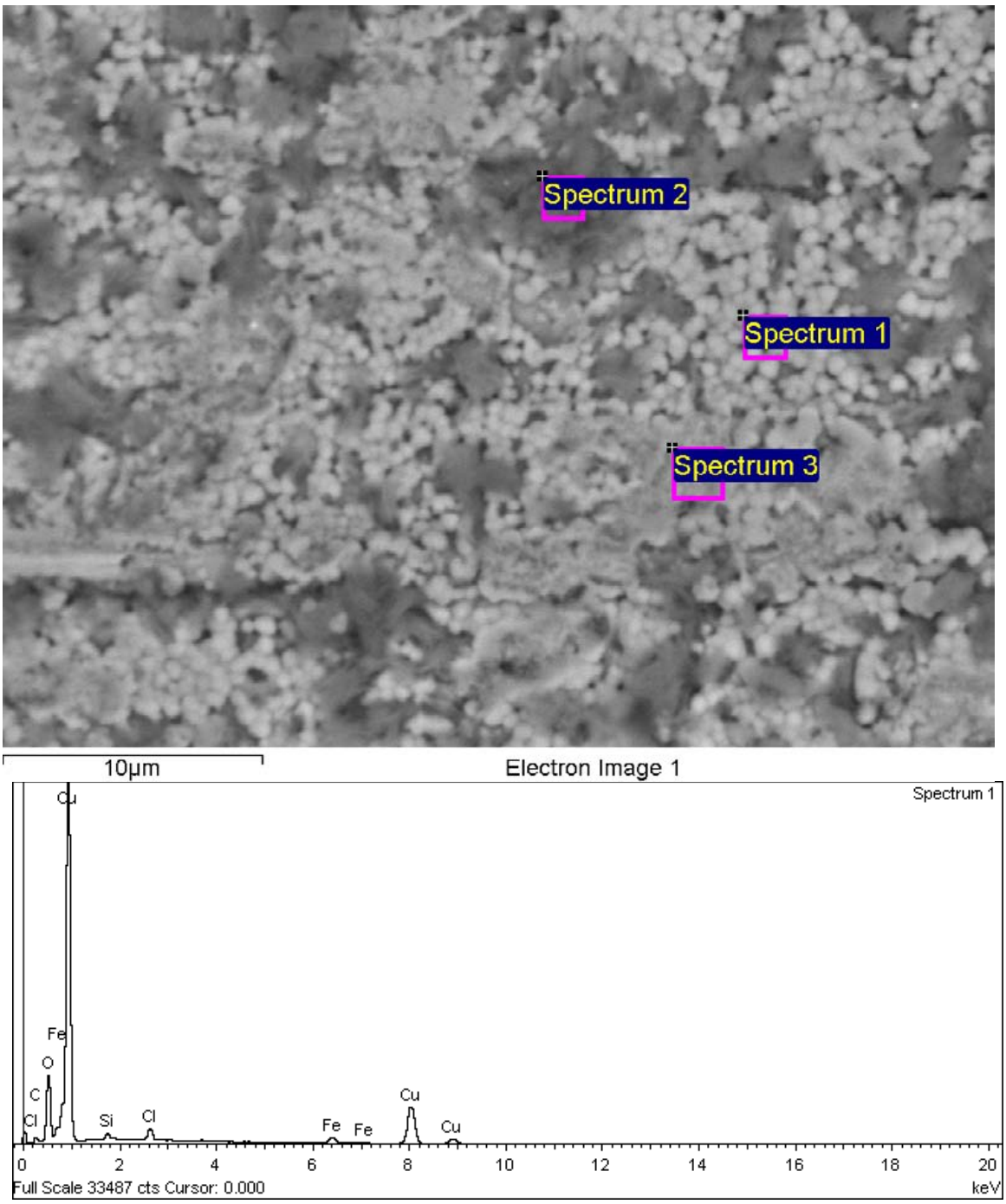

Figure A-260. Inner surface of copper canister around bottom hole and EDX analysis at position of Spectrum 1

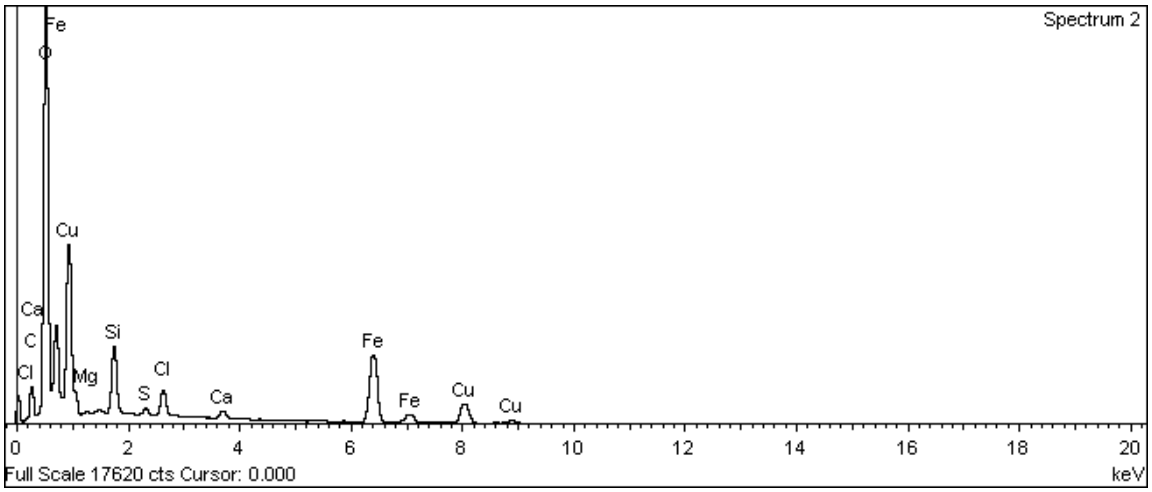

Figure A-261. Inner surface of copper canister around bottom hole and EDX analysis at position of Spectrum 2

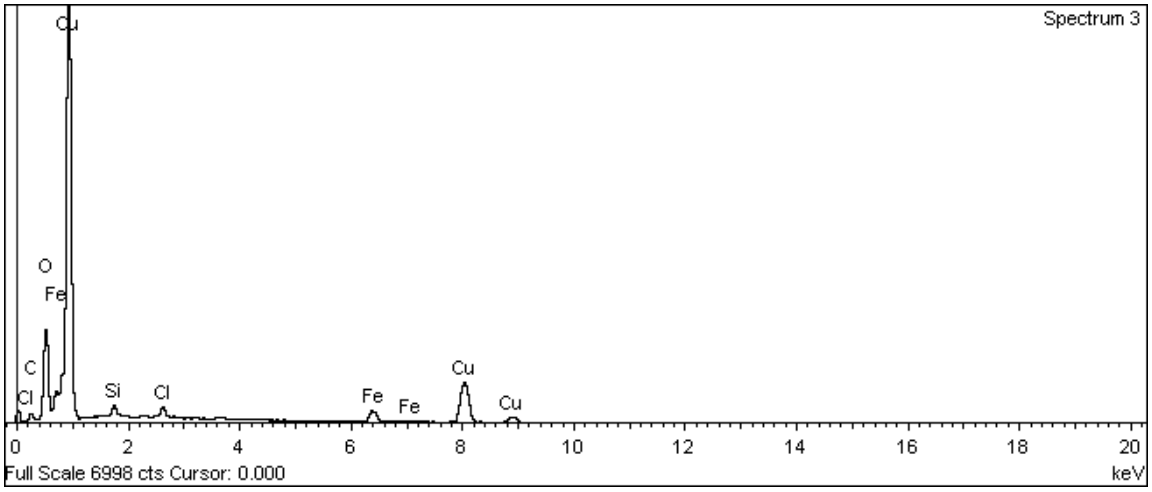

Figure A-262. Inner surface of copper canister around bottom hole and EDX analysis at position of Spectrum 3

Copper can outer surface around bottom hole

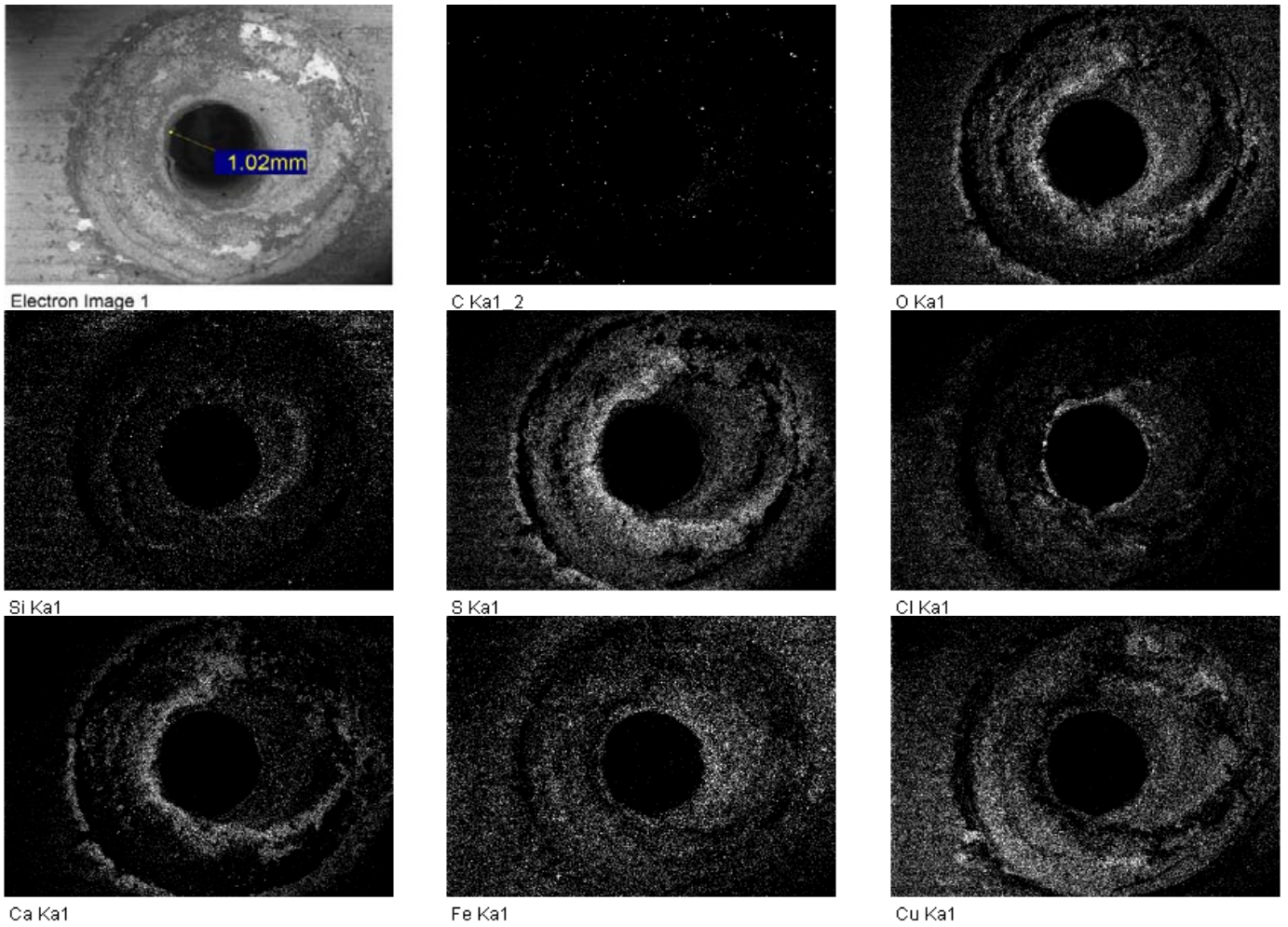

Figure A-263. Elemental maps for outer surface of copper canister around the bottom hole

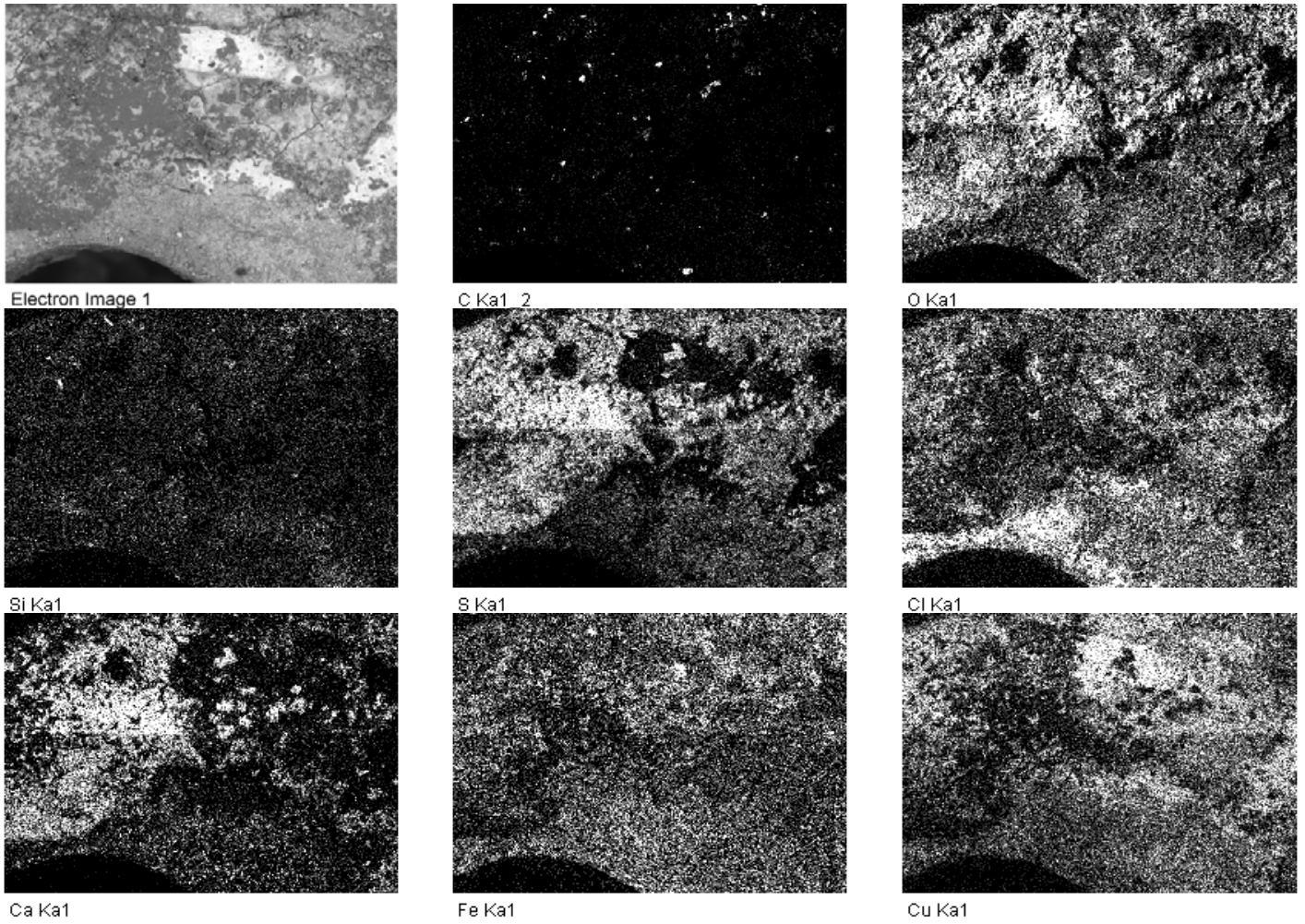

Figure A-264. Elemental maps for outer surface of copper canister around the bottom hole

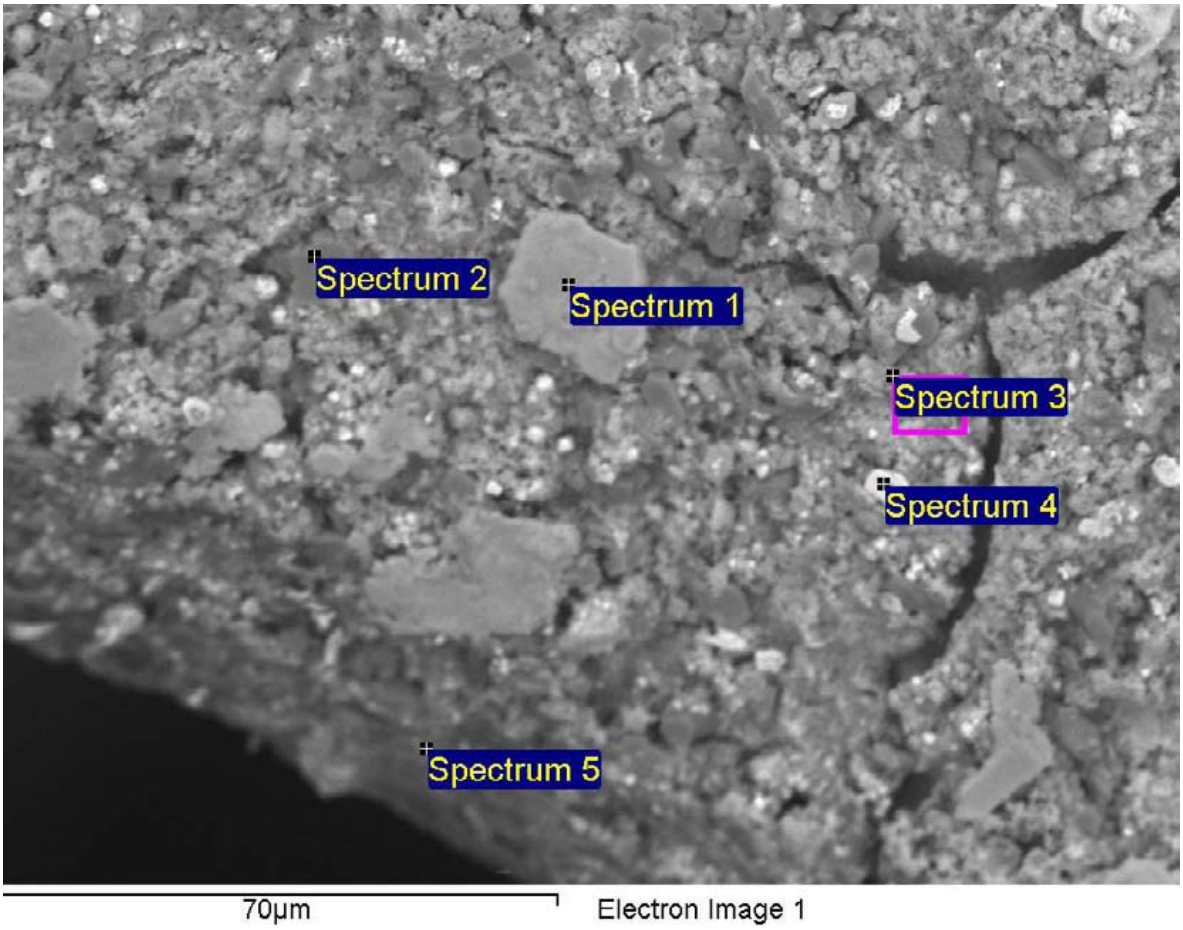

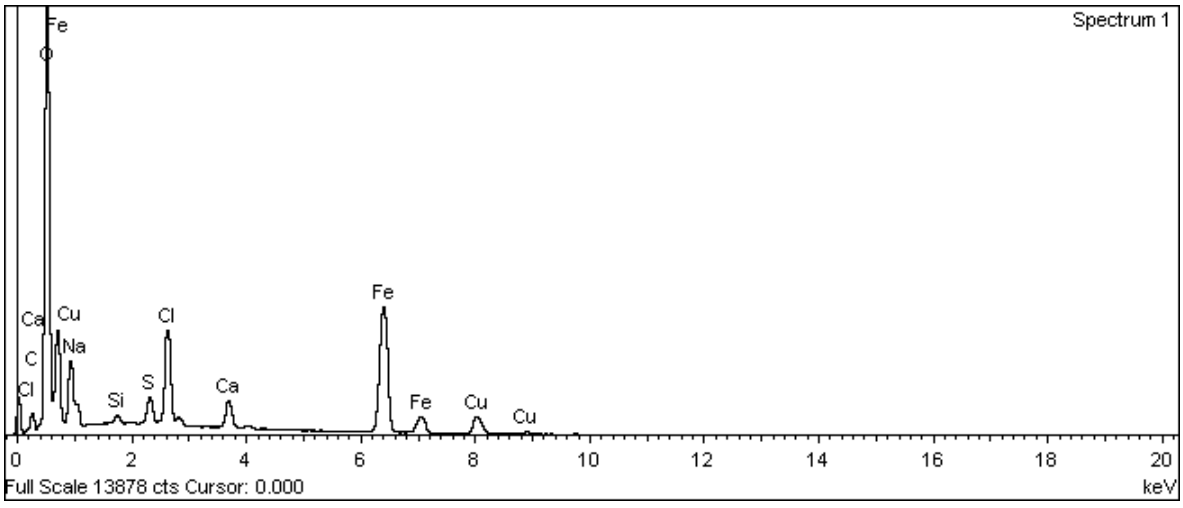

Figure A-265. Outer surface of copper canister around bottom hole and EDX analysis at position of Spectrum 1

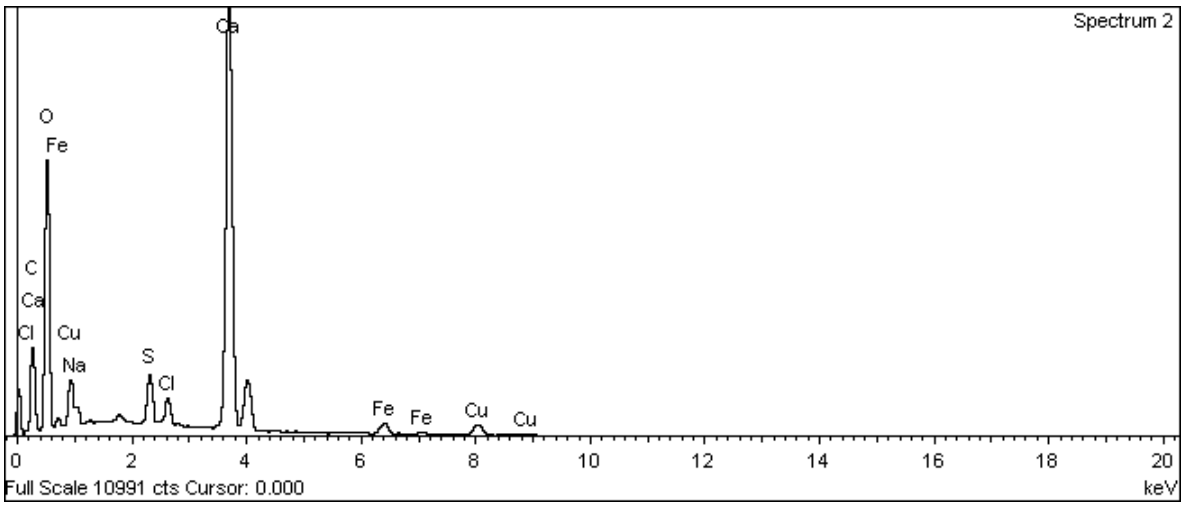

Figure A-266. Outer surface of copper canister around bottom hole and EDX analysis at position of Spectrum 2

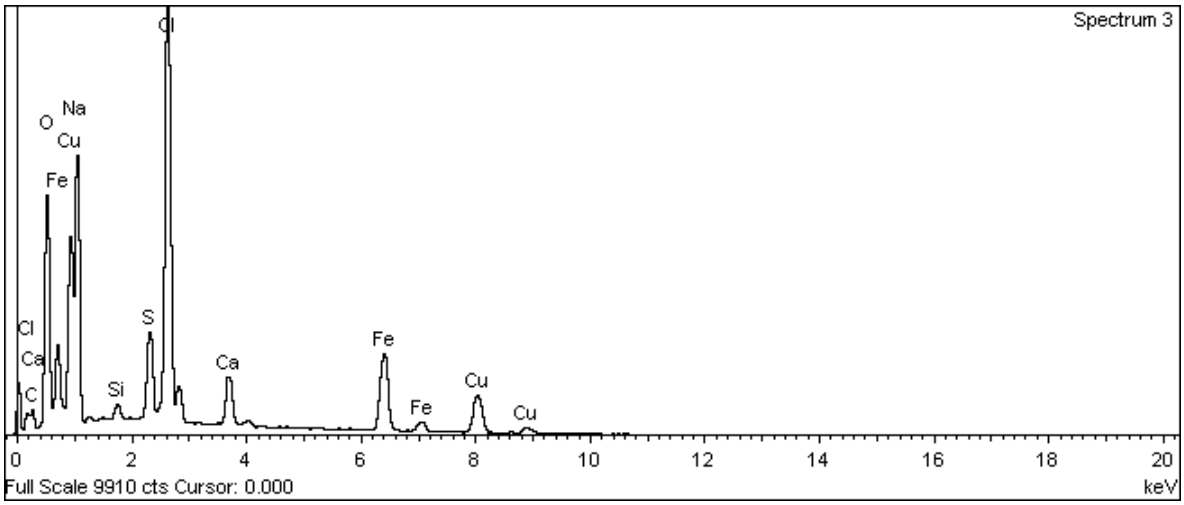

Figure A-267. Outer surface of copper canister around bottom hole and EDX analysis at position of Spectrum 3

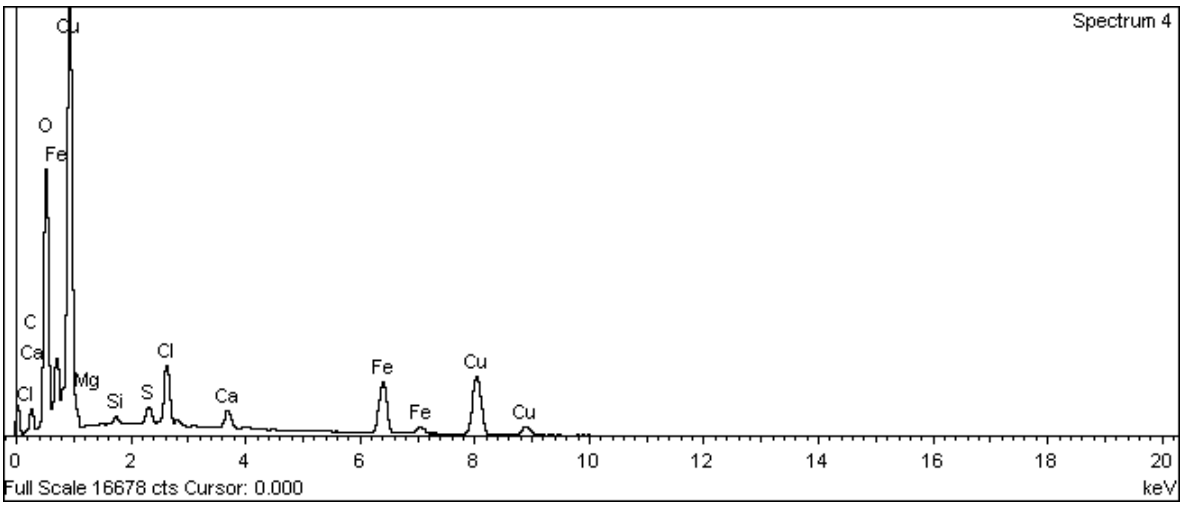

Figure A-268. Outer surface of copper canister around bottom hole and EDX analysis at position of Spectrum 5

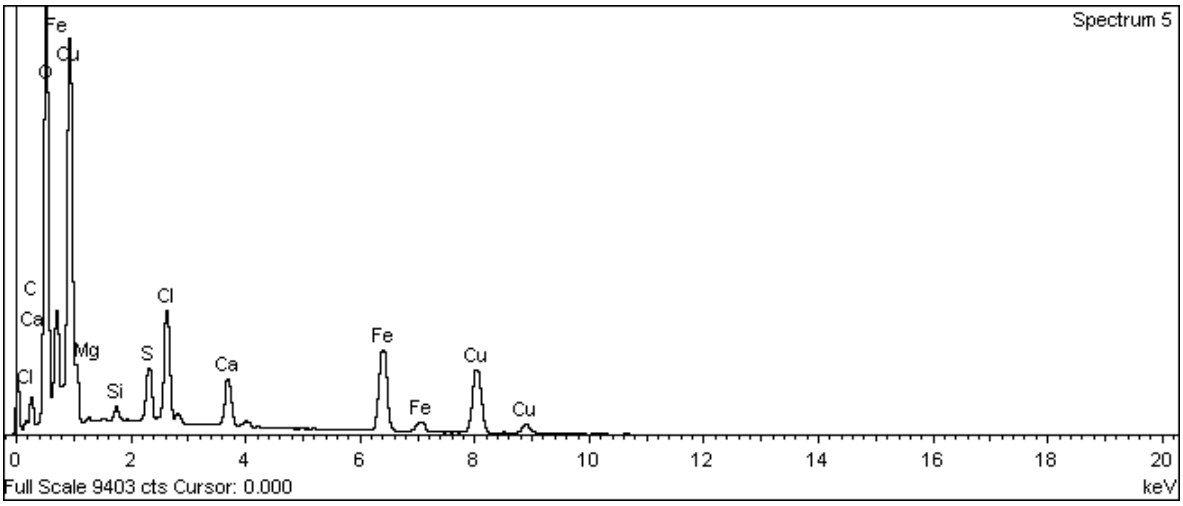

Figure A-269. Outer surface of copper canister around bottom hole and EDX analysis at position of Spectrum 5

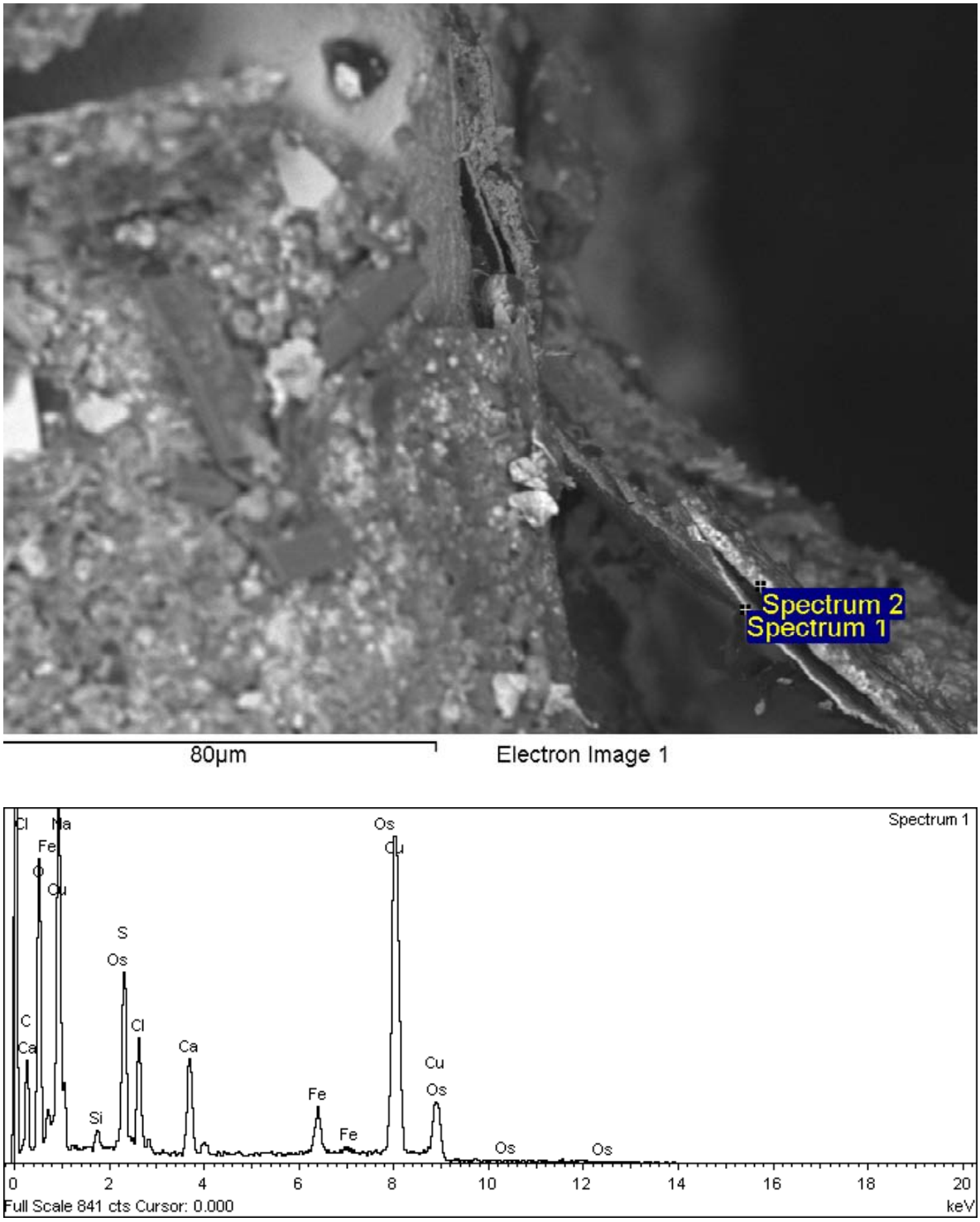

Figure A-270. Outer surface of copper canister around bottom hole and EDX analysis at position of Spectrum 1

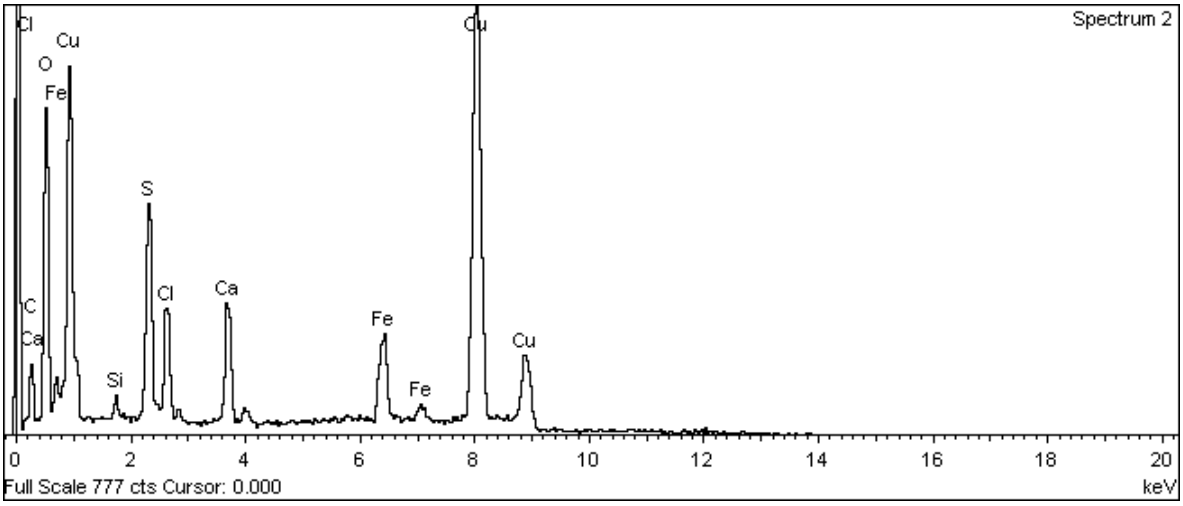

Figure A-271. Outer surface of copper canister around bottom hole and EDX analysis at position of Spectrum 2

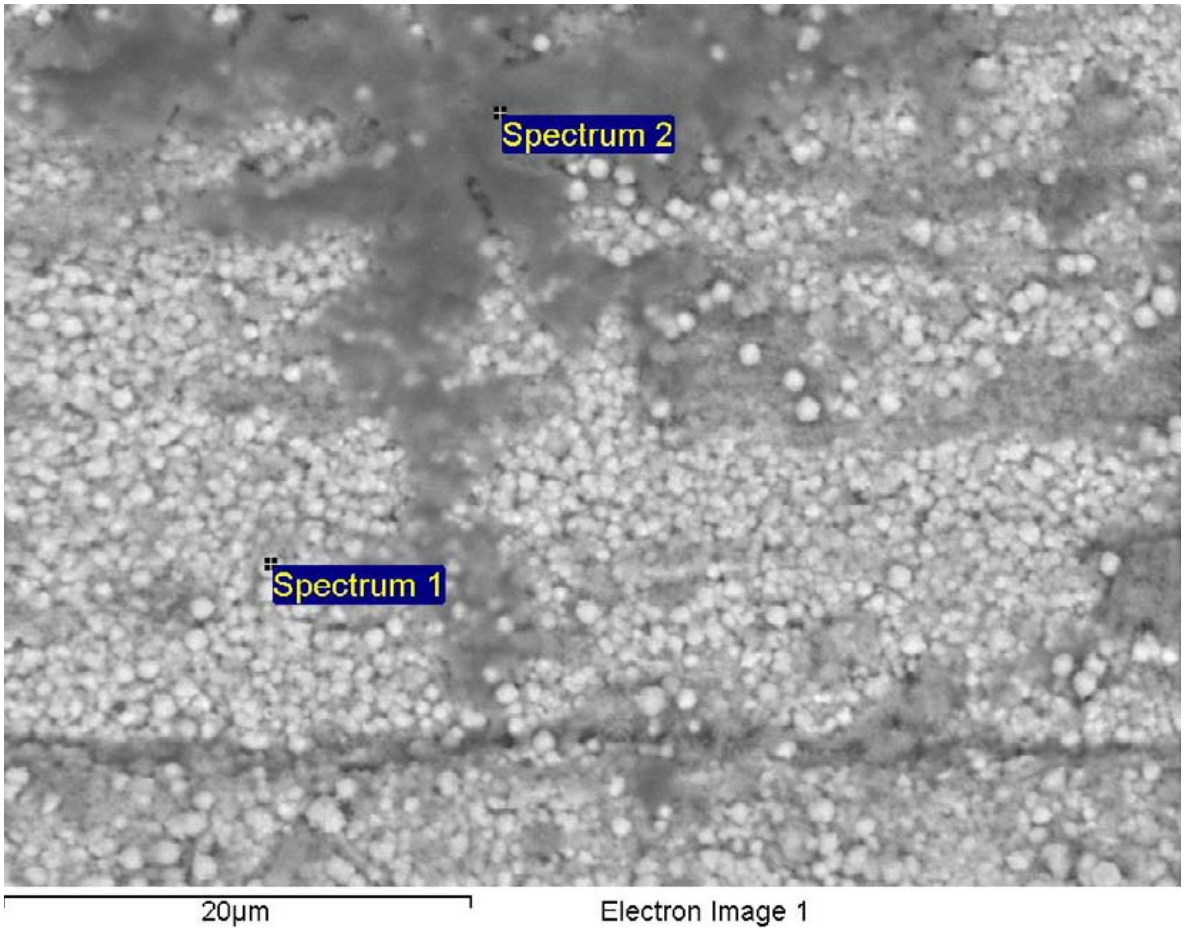

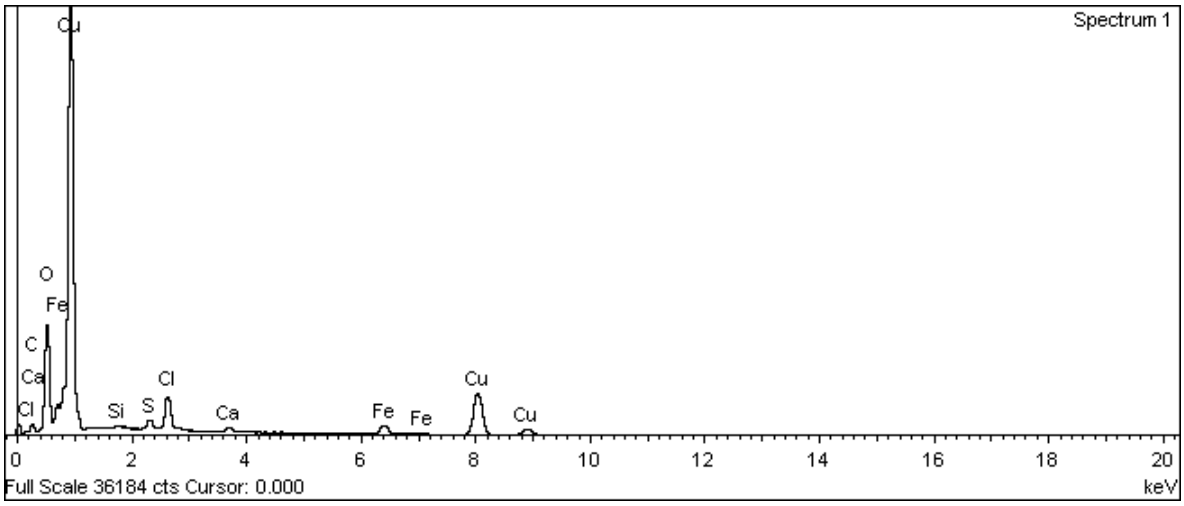

Figure A-272. Outer surface of copper canister around bottom hole and EDX analysis at position of Spectrum 1

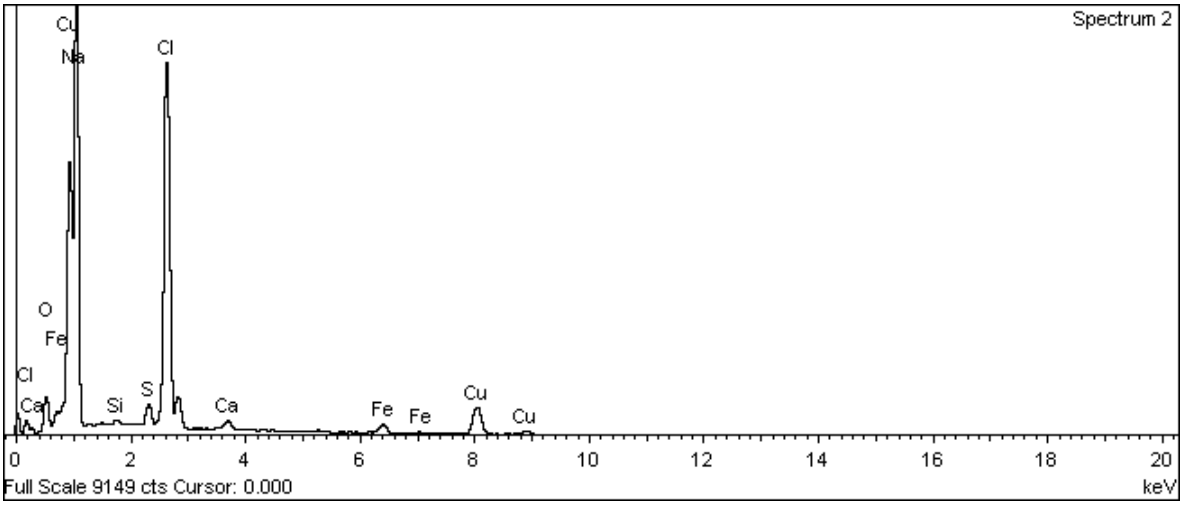

Figure A-273. Outer surface of copper canister around bottom hole and EDX analysis at position of Spectrum 2

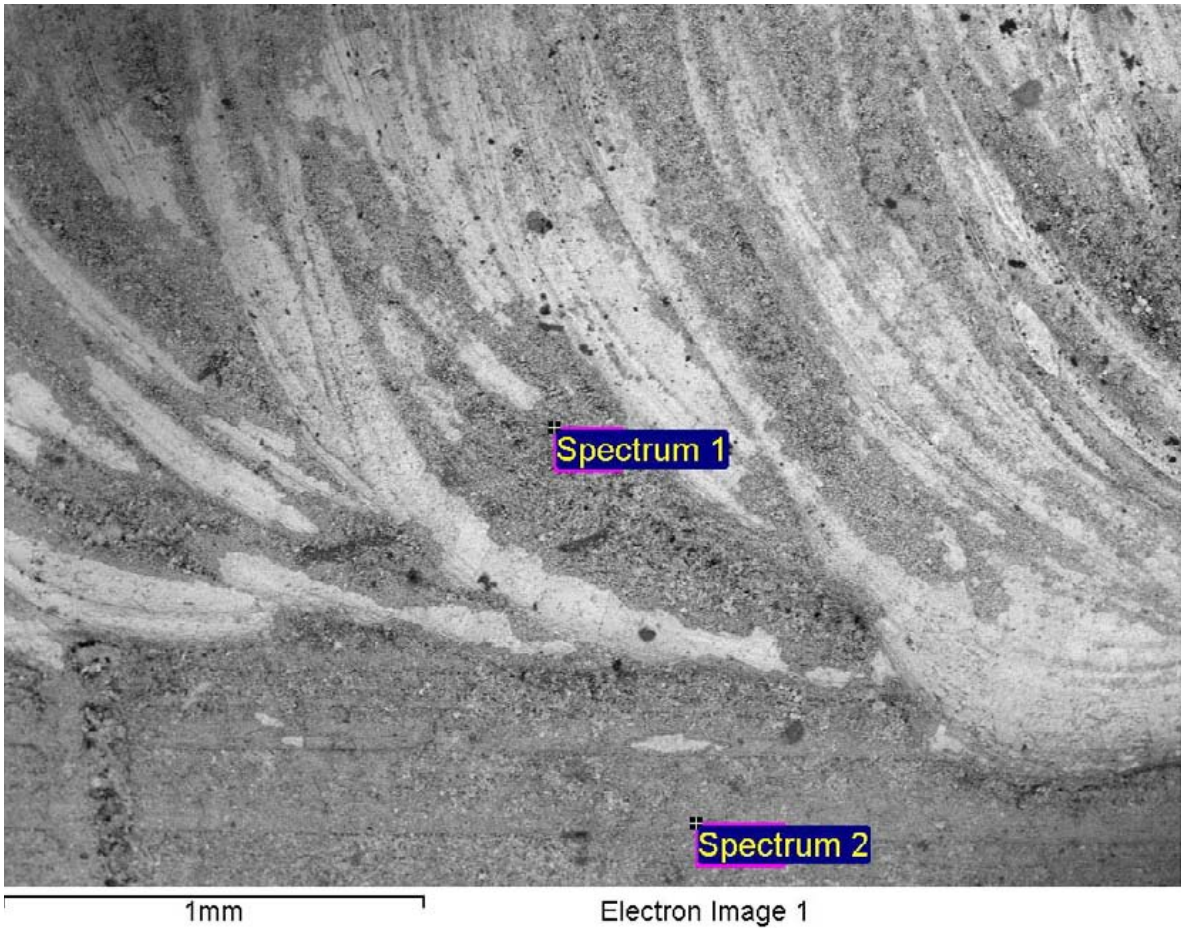

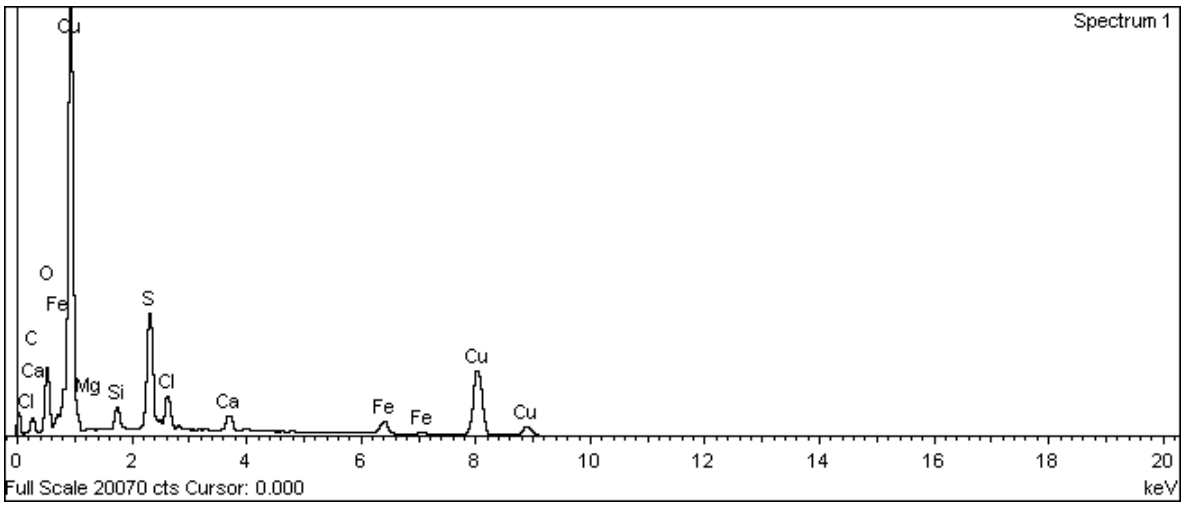

Figure A-274. Outer surface of copper canister around bottom hole and EDX analysis at position of Spectrum 1

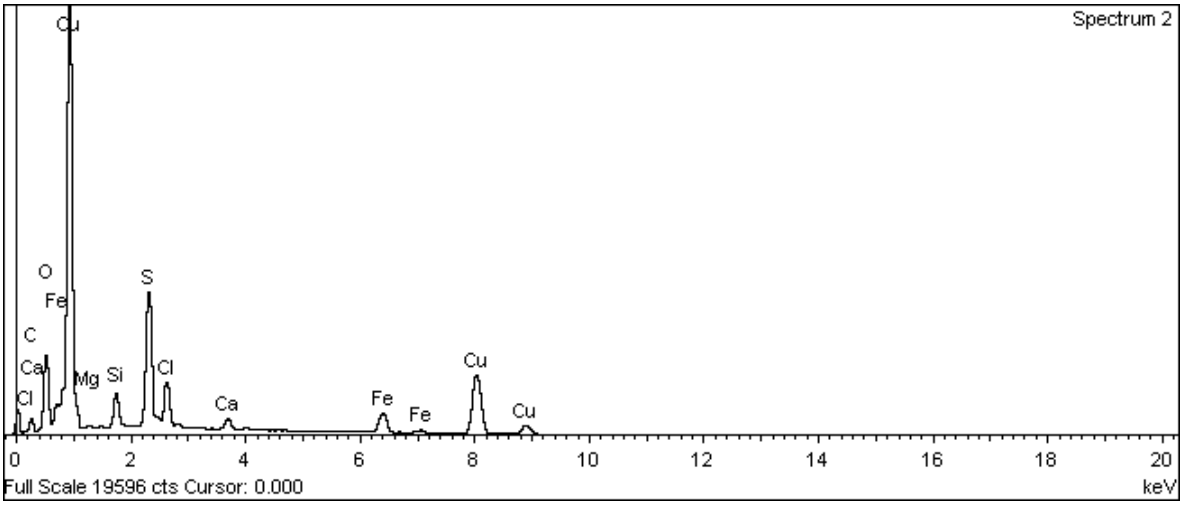

Figure A-275. Outer surface of copper canister around bottom hole and EDX analysis at position of Spectrum 2

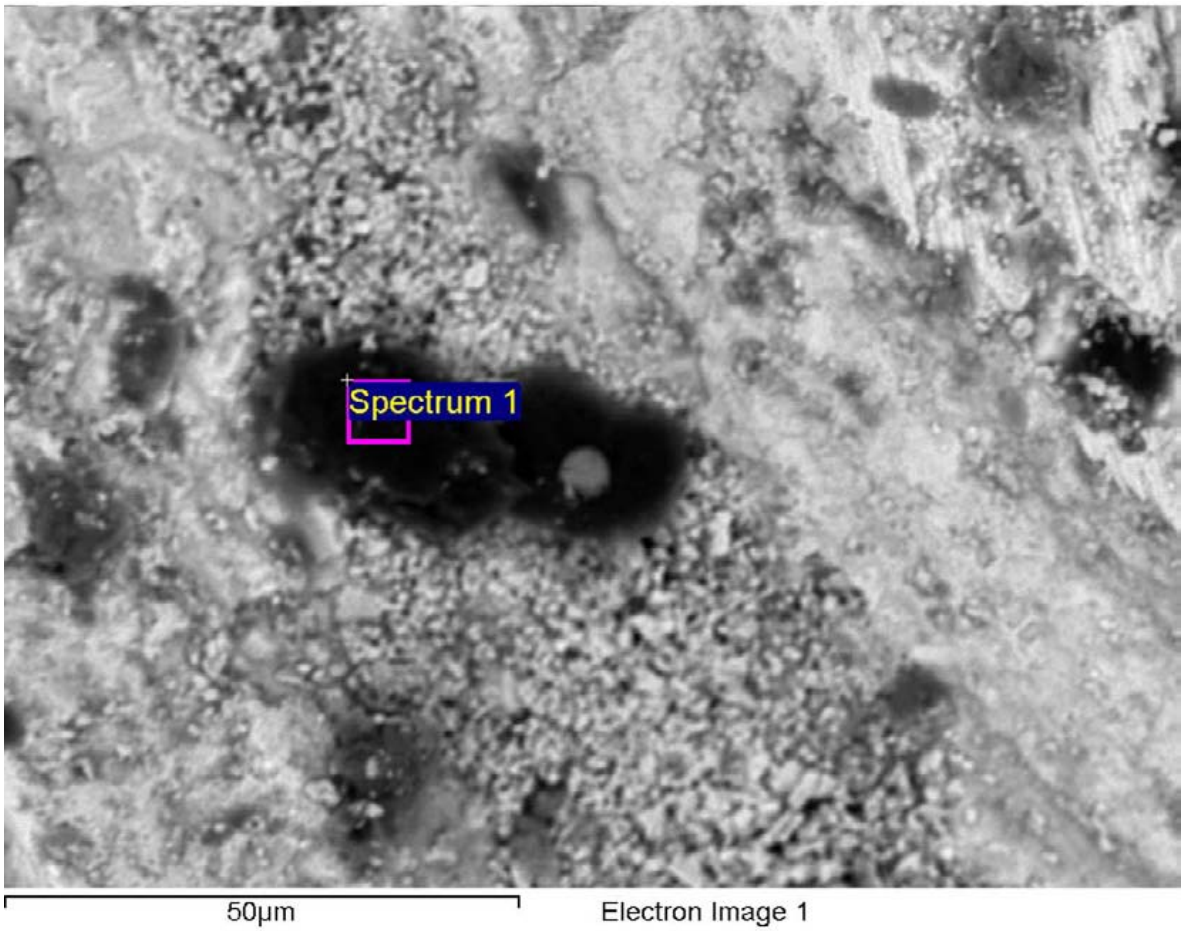

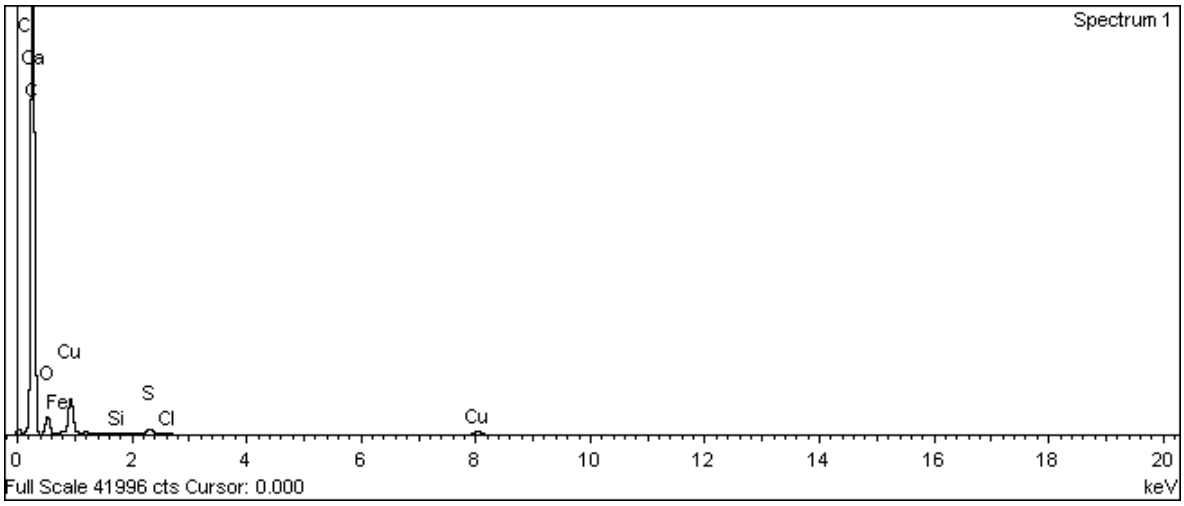

Figure A-276. Outer surface of copper canister around bottom hole and EDX analysis at position of Spectrum 1

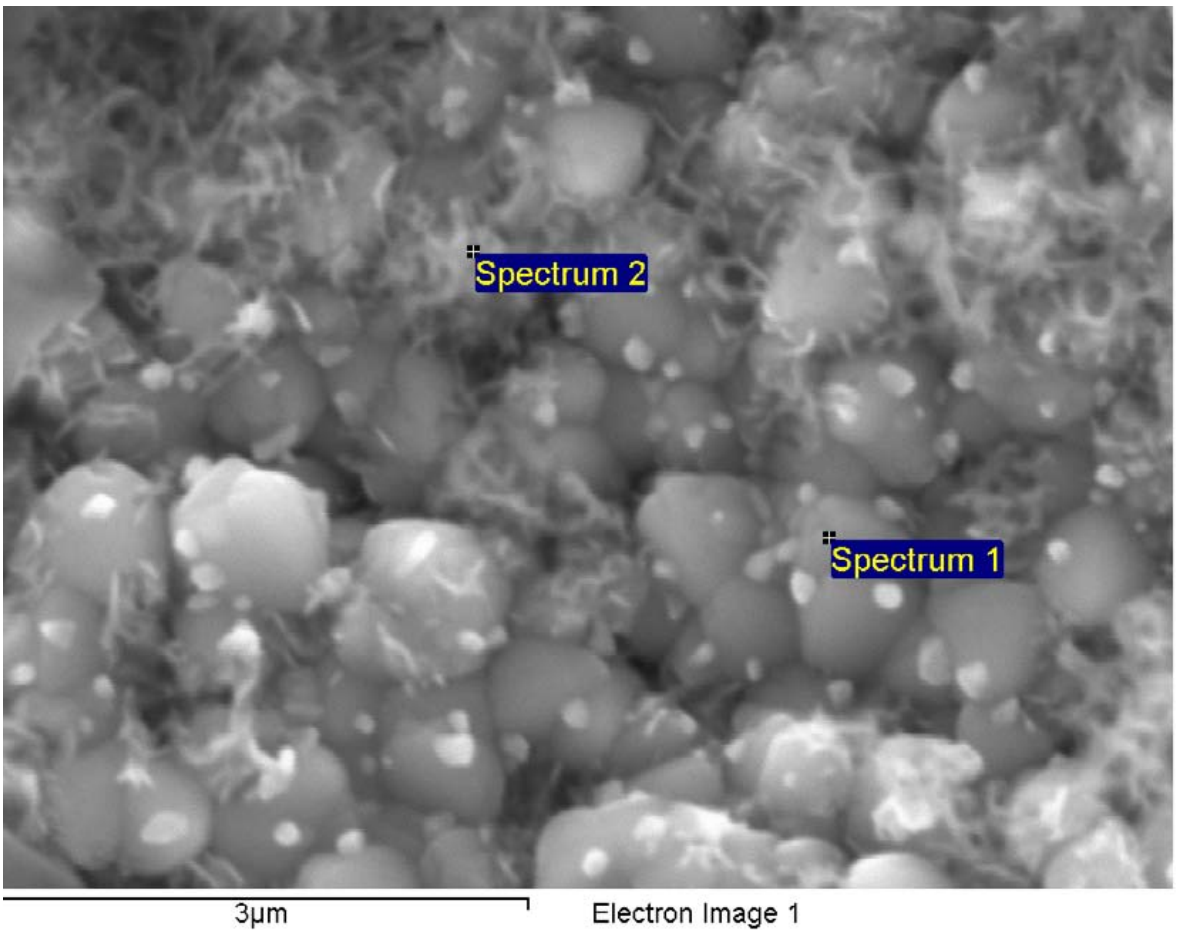

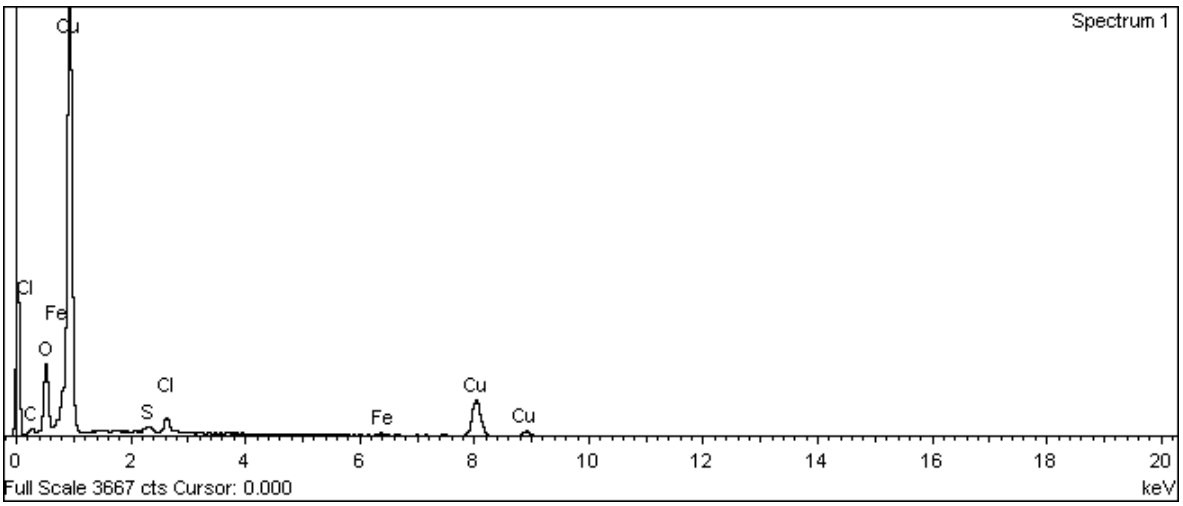

Figure A-277. Outer surface of copper canister around bottom hole and EDX analysis at position of Spectrum 1

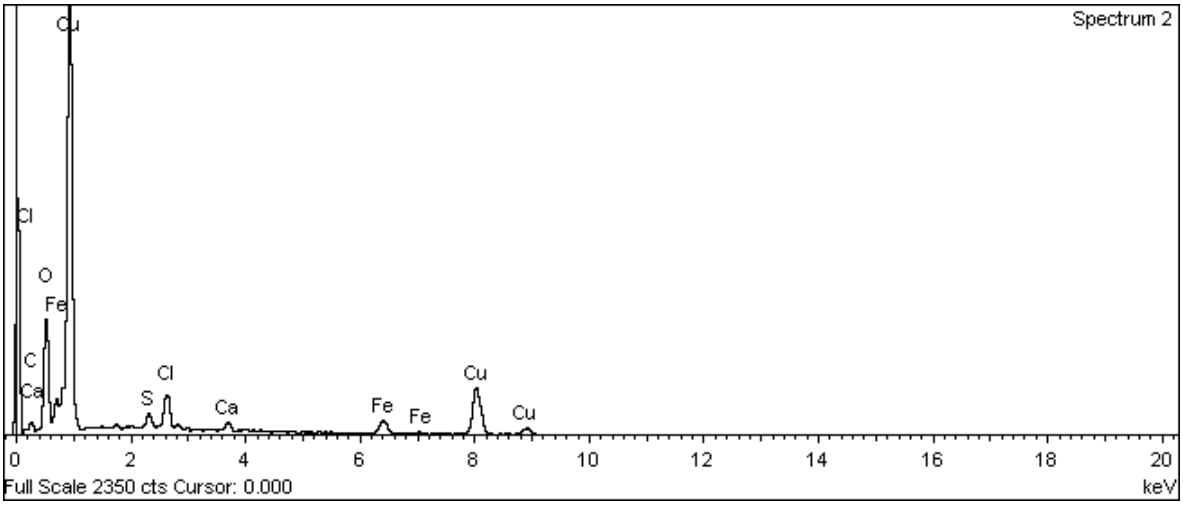

Figure A-278. Outer surface of copper canister around bottom hole and EDX analysis at position of Spectrum 2

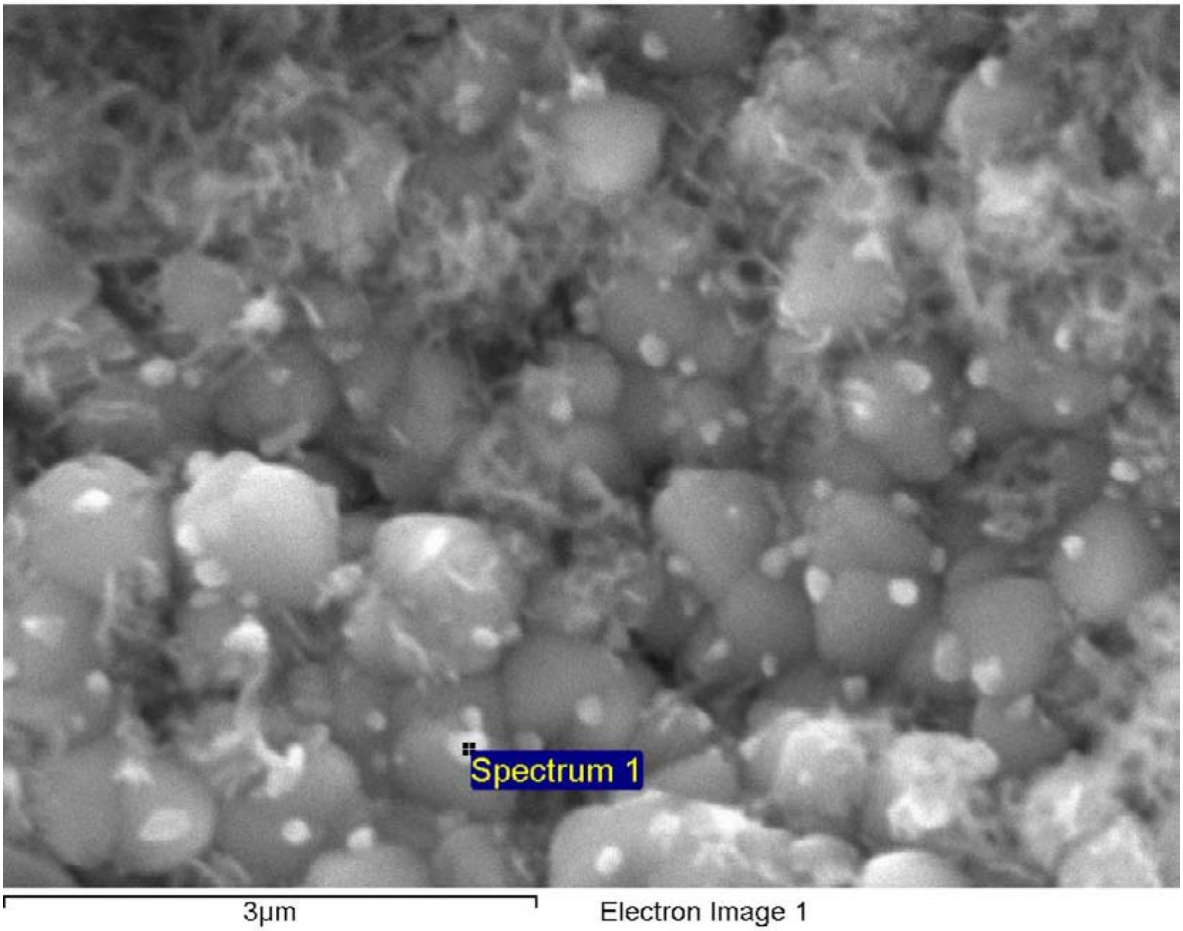

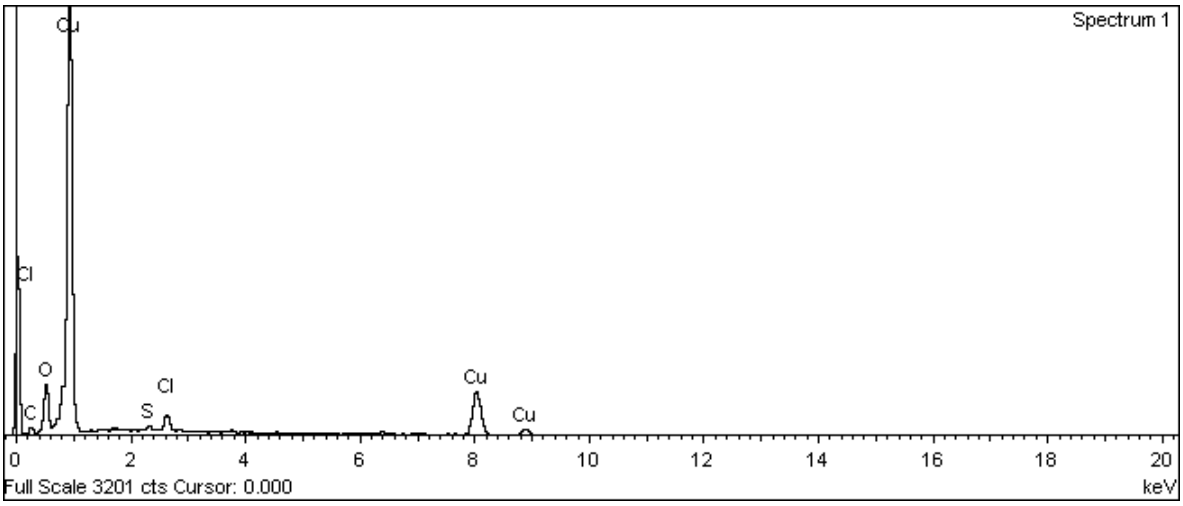

Figure A-279. Outer surface of copper canister around bottom hole and EDX analysis at position of Spectrum 1

Copper can inner surface

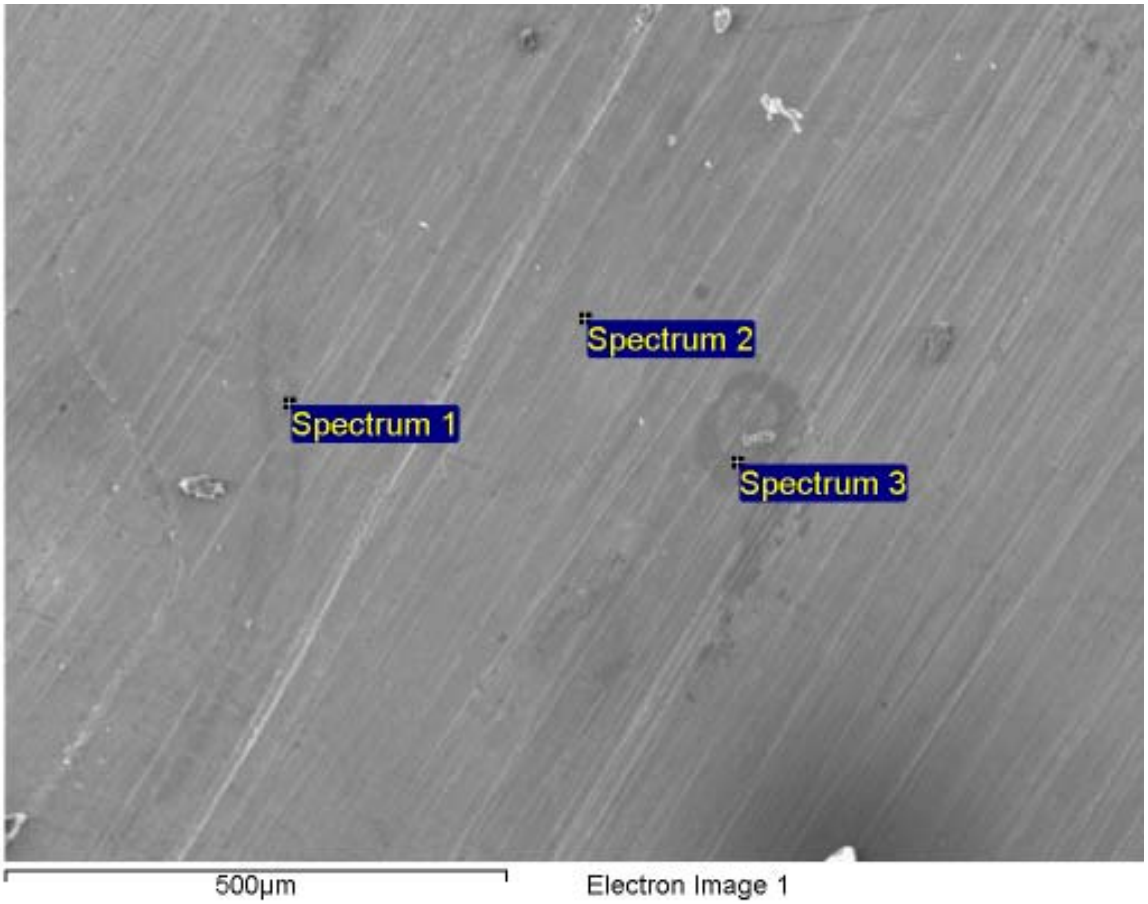

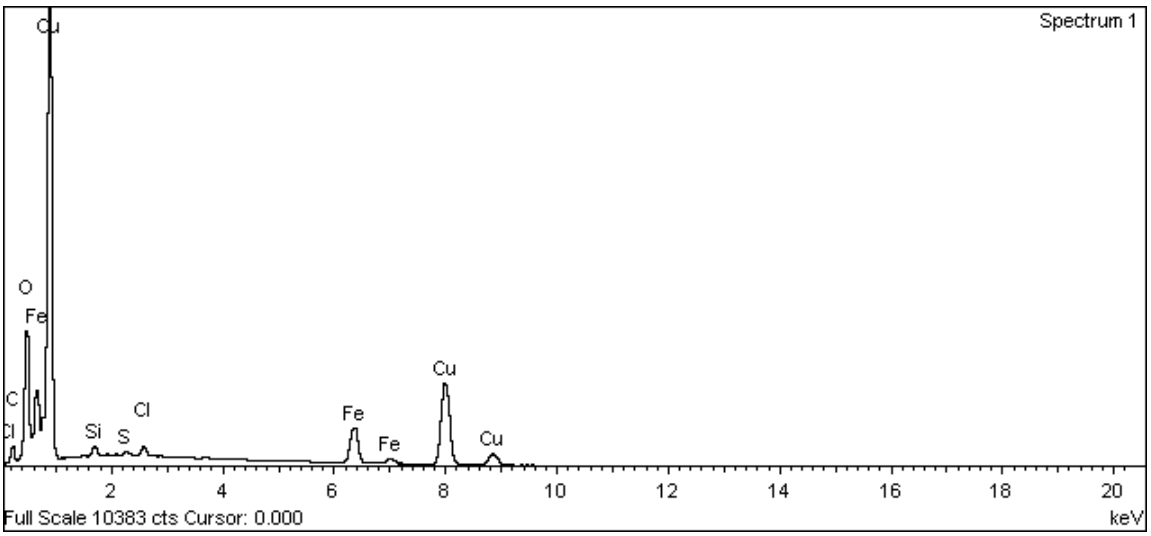

Figure A-280. Inner surface of copper canister and EDX analysis at position of Spectrum 1

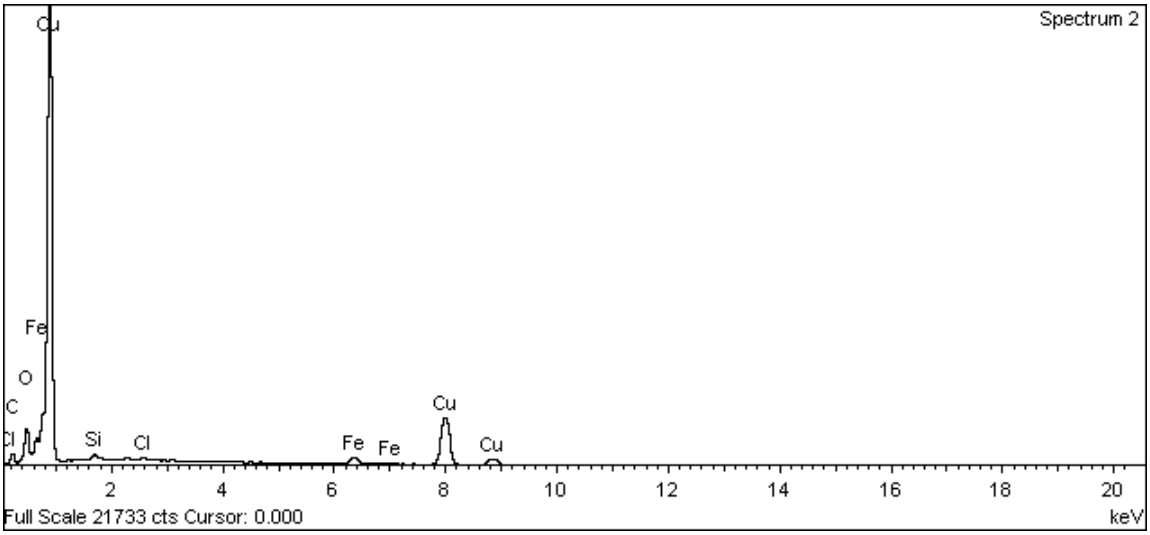

Figure A-281. Inner surface of copper canister and EDX analysis at position of Spectrum 2

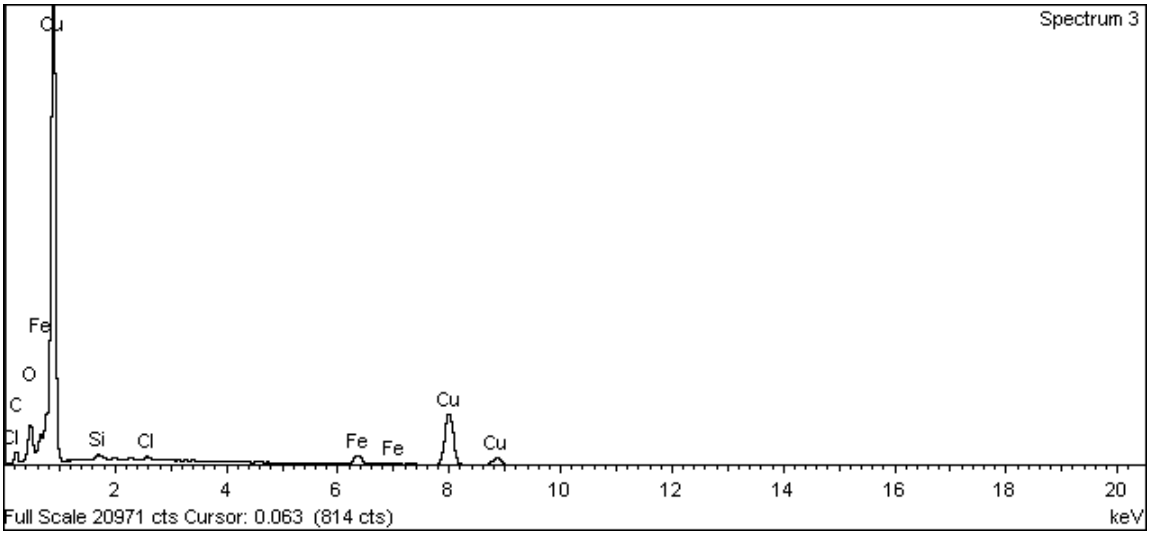

Figure A-282. Inner surface of copper canister and EDX analysis at position of Spectrum 3

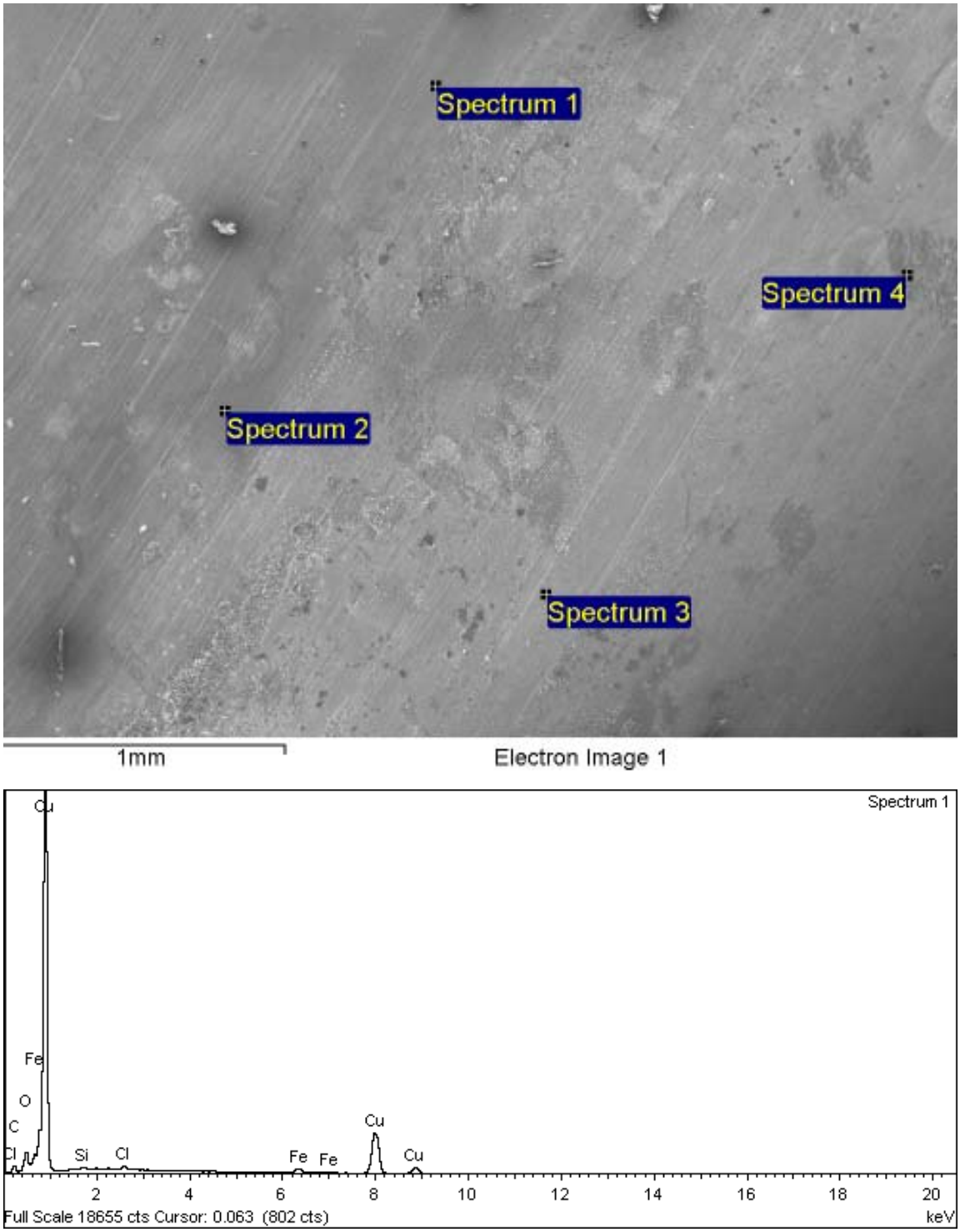

Figure A-283. Inner surface of copper canister and EDX analysis at position of Spectrum 1

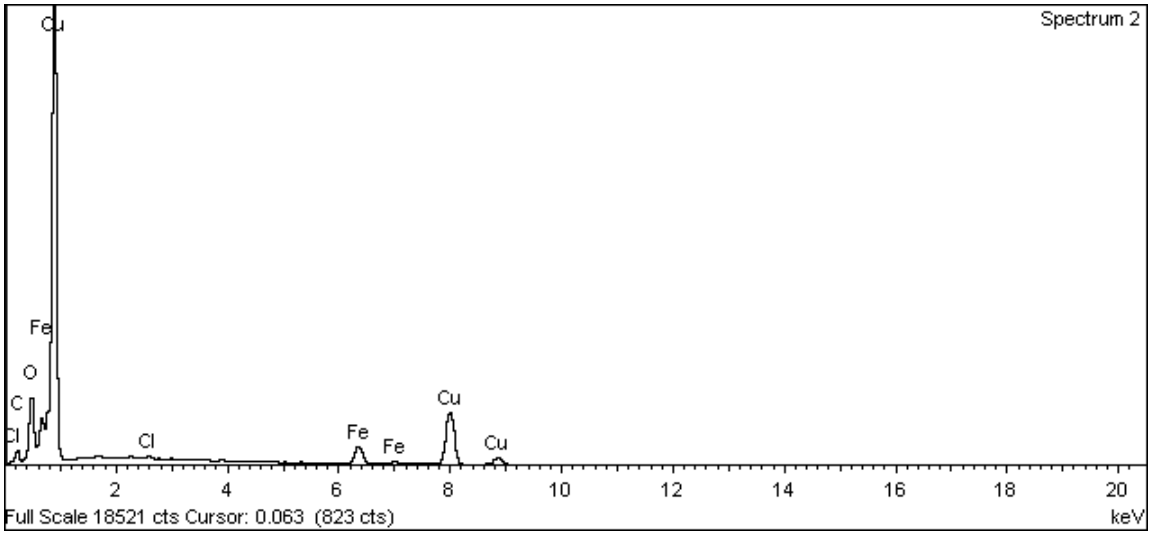

Figure A-284. Inner surface of copper canister and EDX analysis at position of Spectrum 2

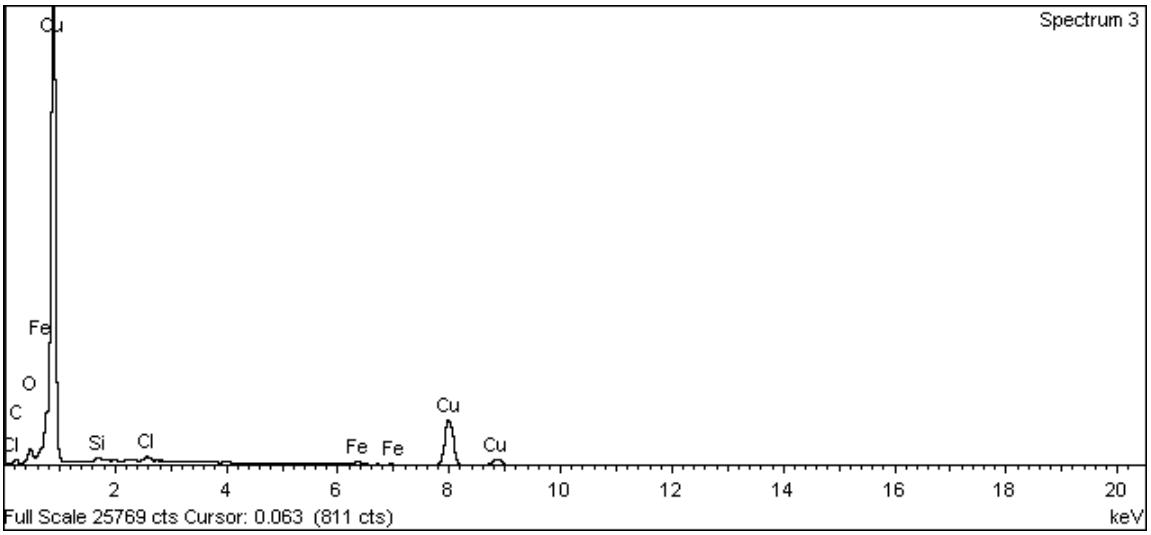

Figure A-285. Inner surface of copper canister and EDX analysis at position of Spectrum 3 (Spectrum 4 is not shown here)

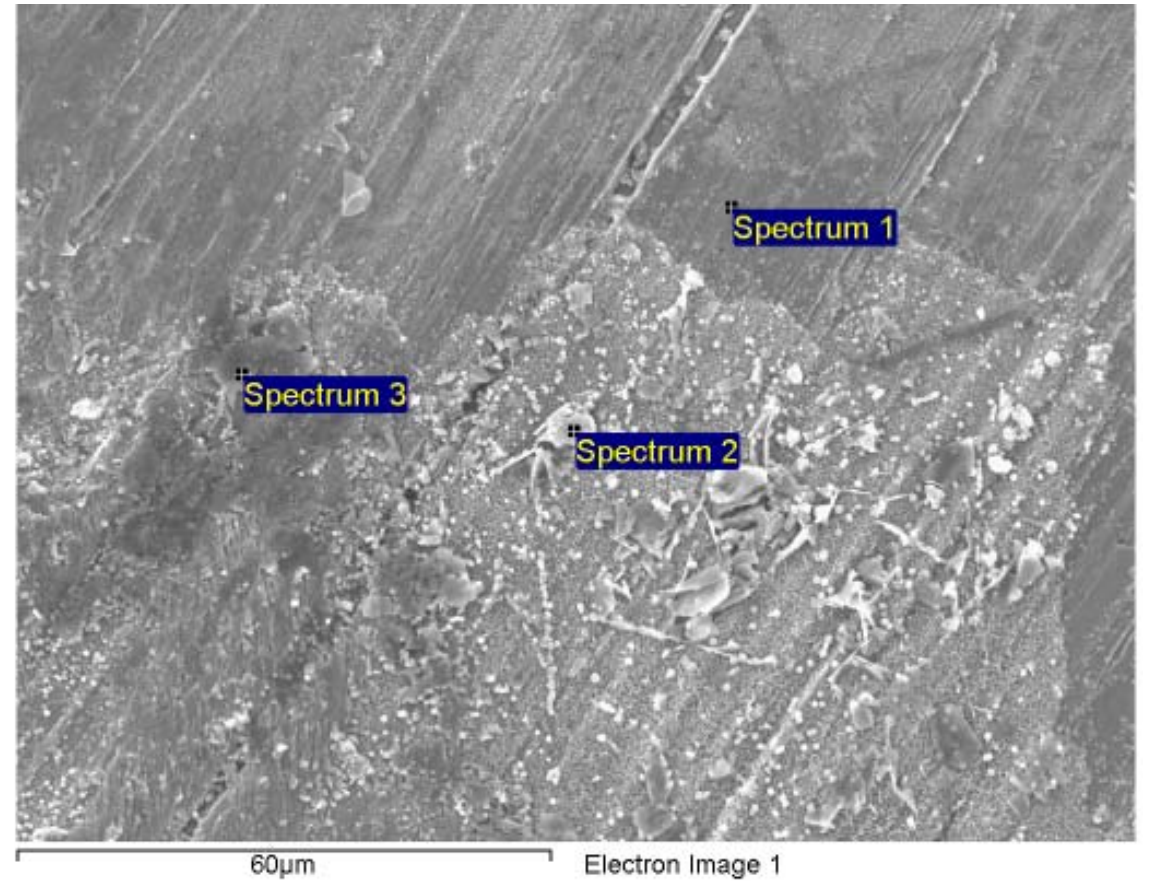

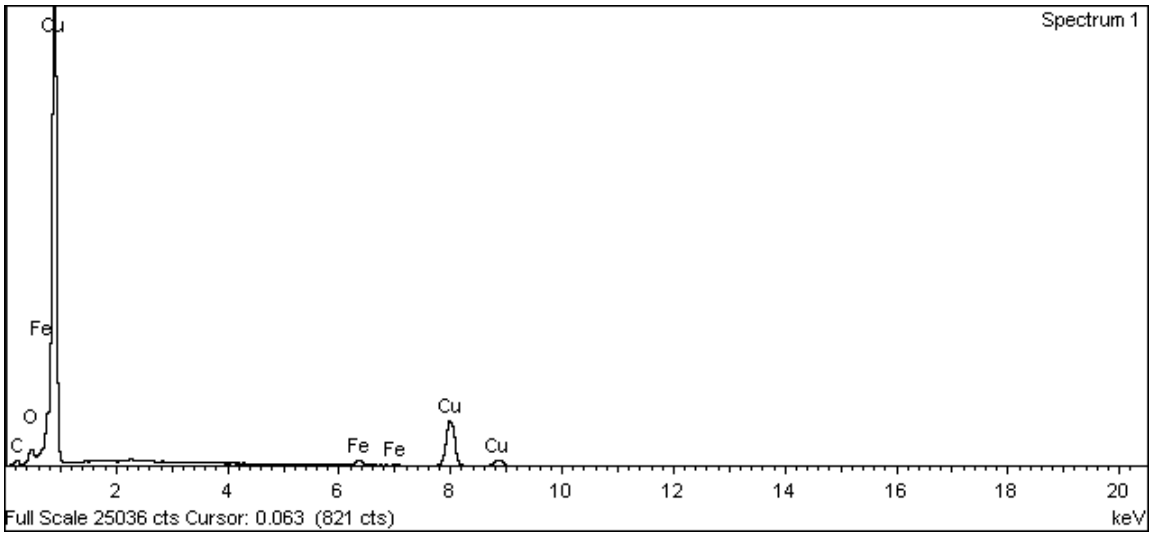

Figure A-286. Inner surface of copper canister and EDX analysis at position of Spectrum 1

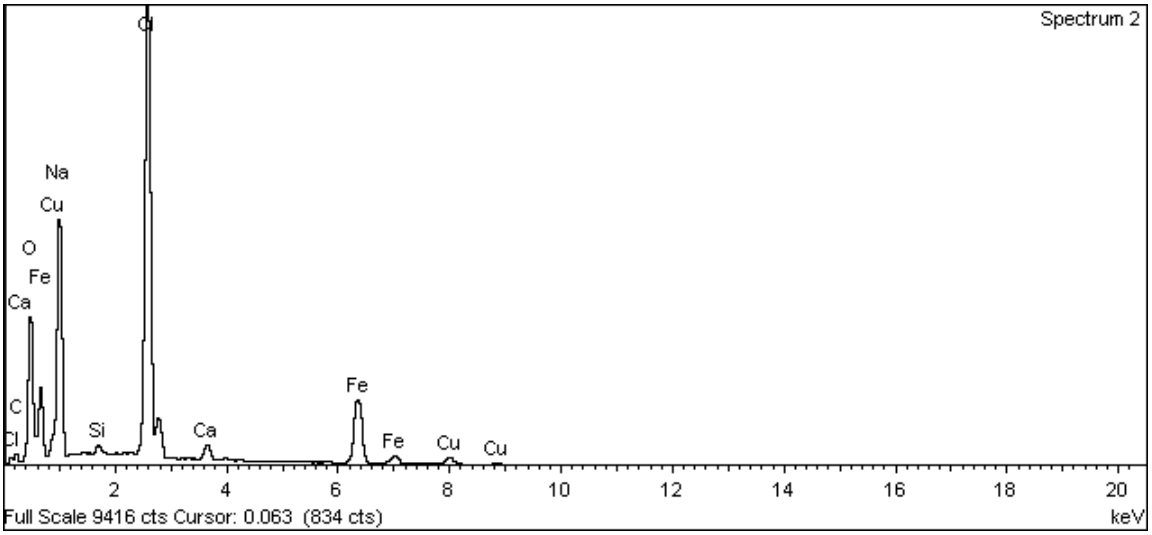

Figure A-287. Inner surface of copper canister and EDX analysis at position of Spectrum 2

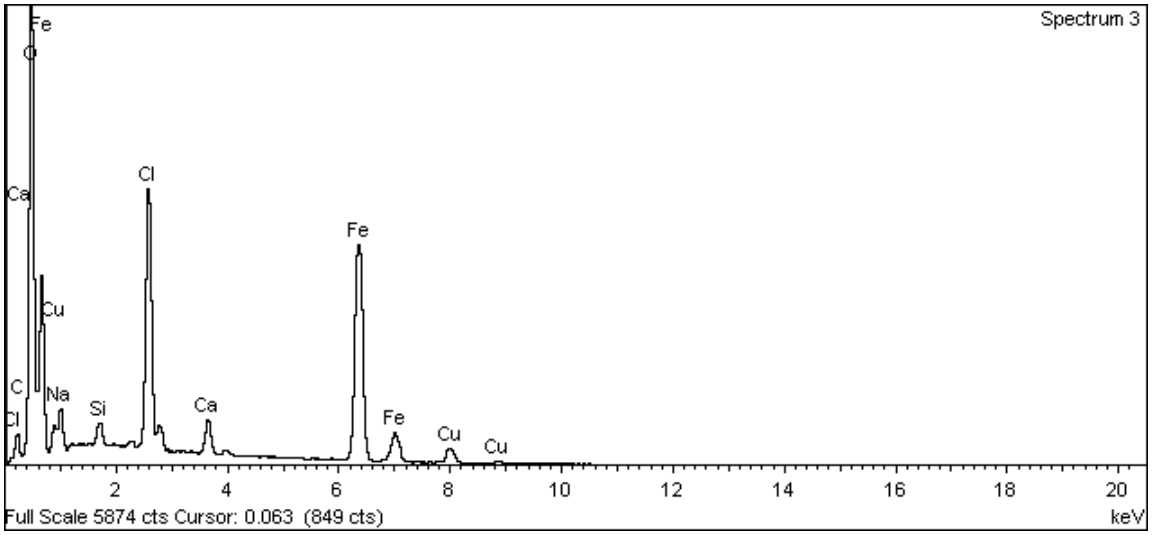

Figure A-288. Inner surface of copper canister and EDX analysis at position of Spectrum 3

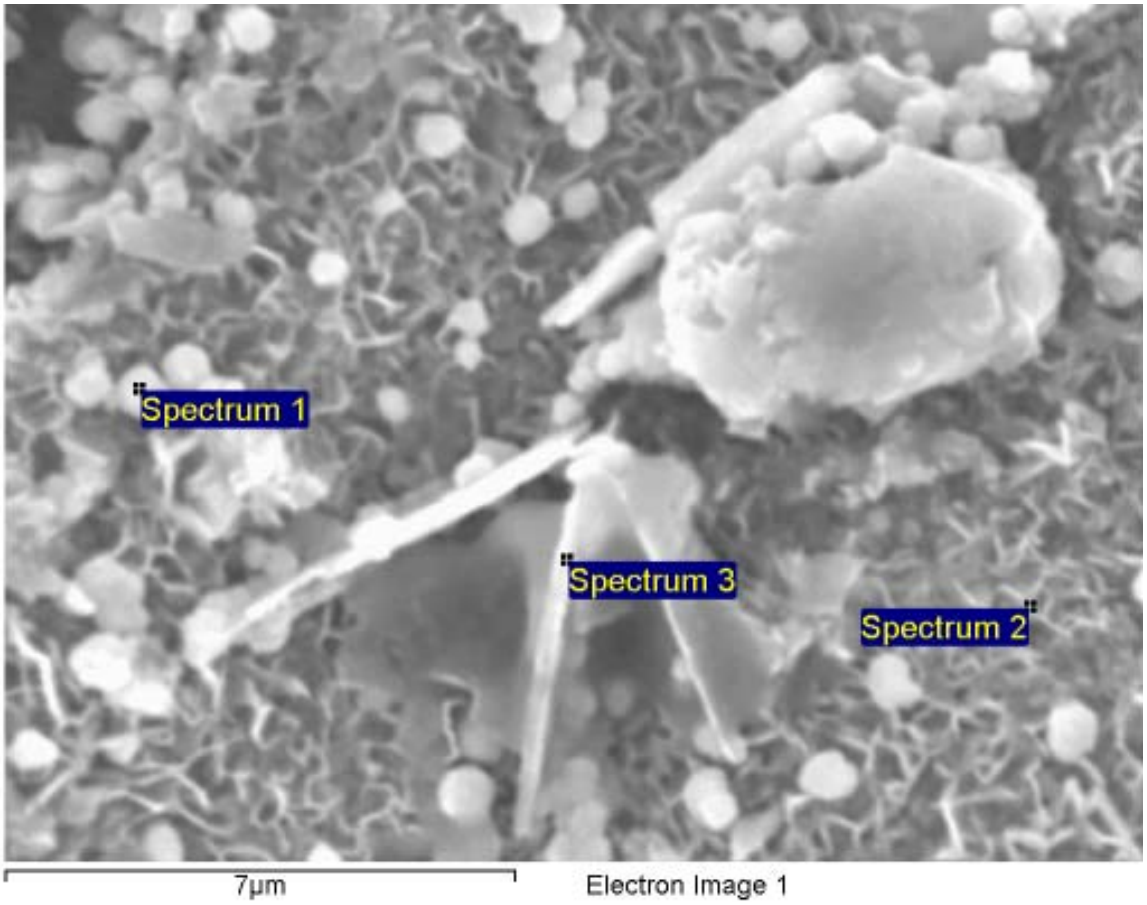

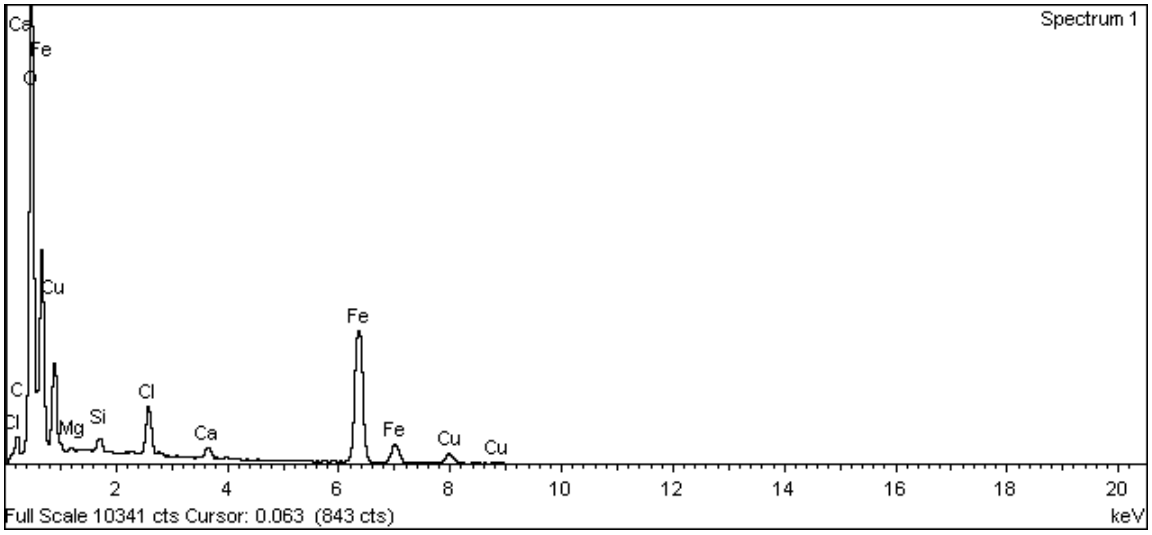

Figure A-289. Inner surface of copper canister and EDX analysis at position of Spectrum 1

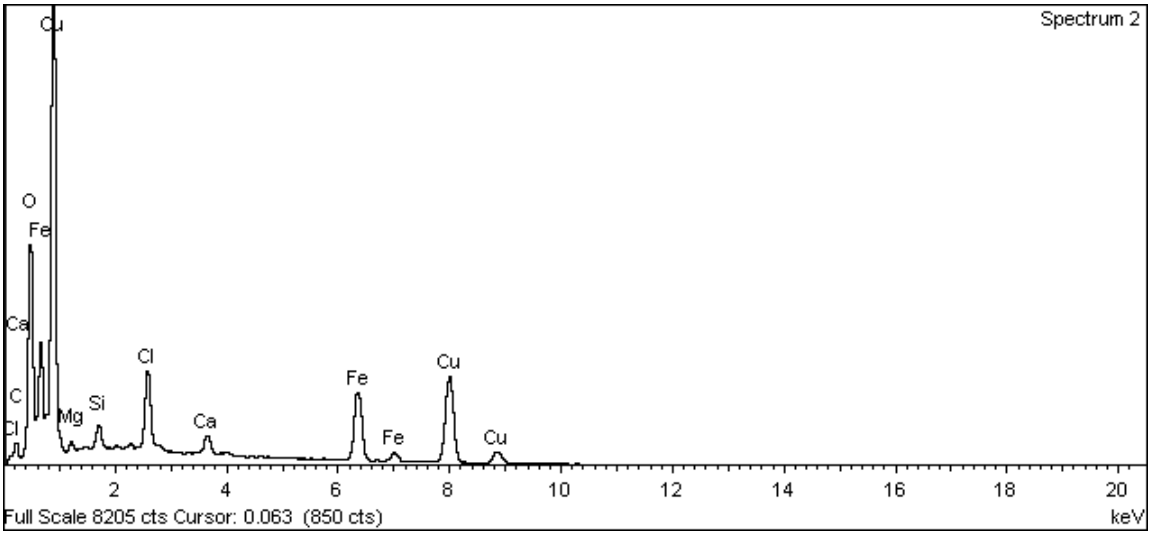

Figure A-290. Inner surface of copper canister and EDX analysis at position of Spectrum 2

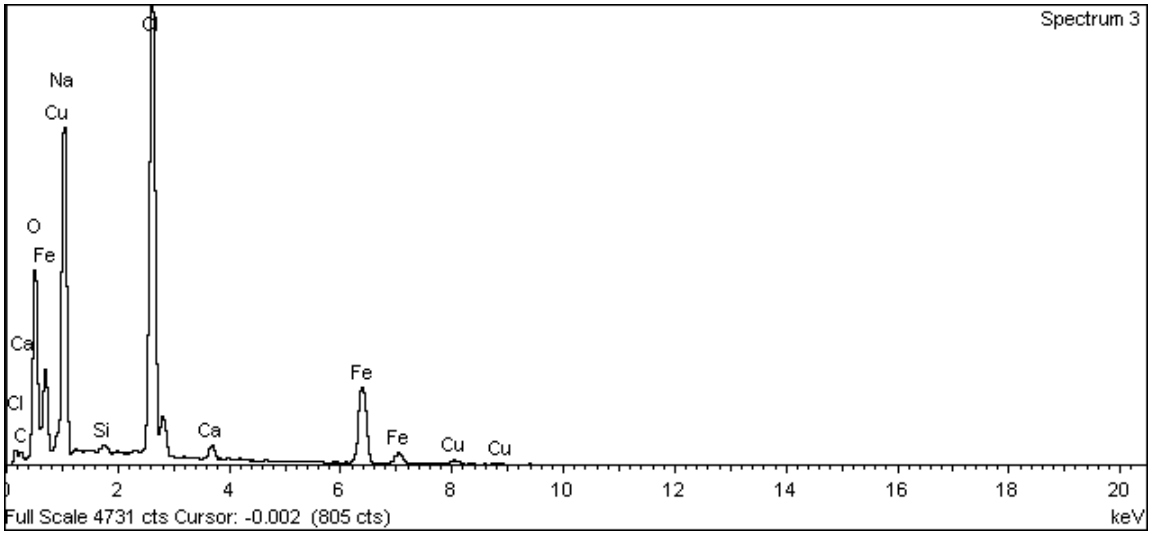

Figure A-291. Inner surface of copper canister and EDX analysis at position of Spectrum 3

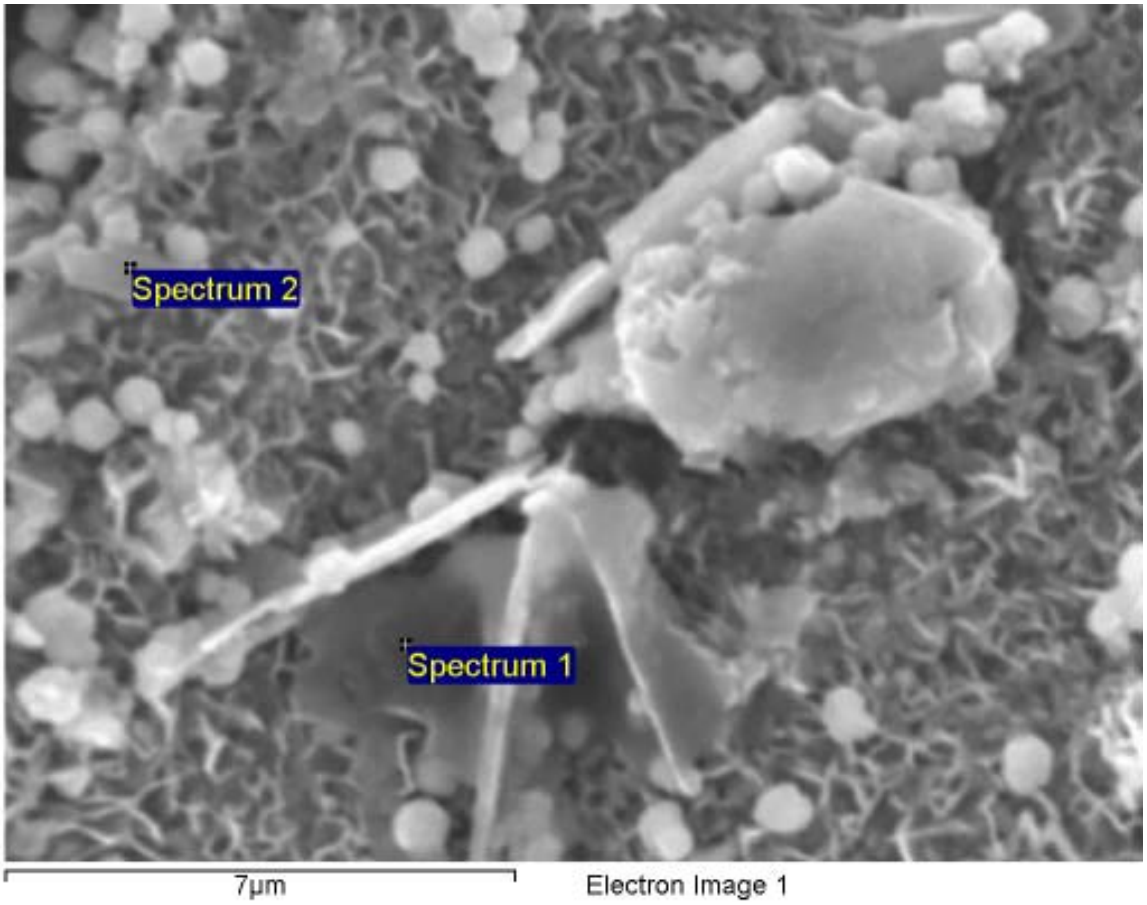

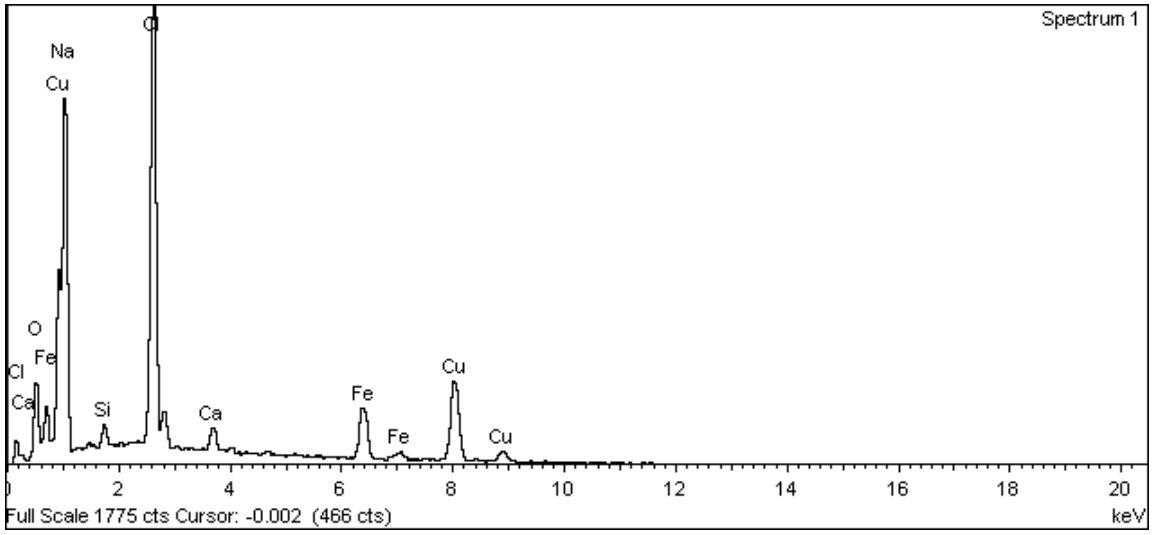

Figure A-292. Inner surface of copper canister and EDX analysis at position of Spectrum 1

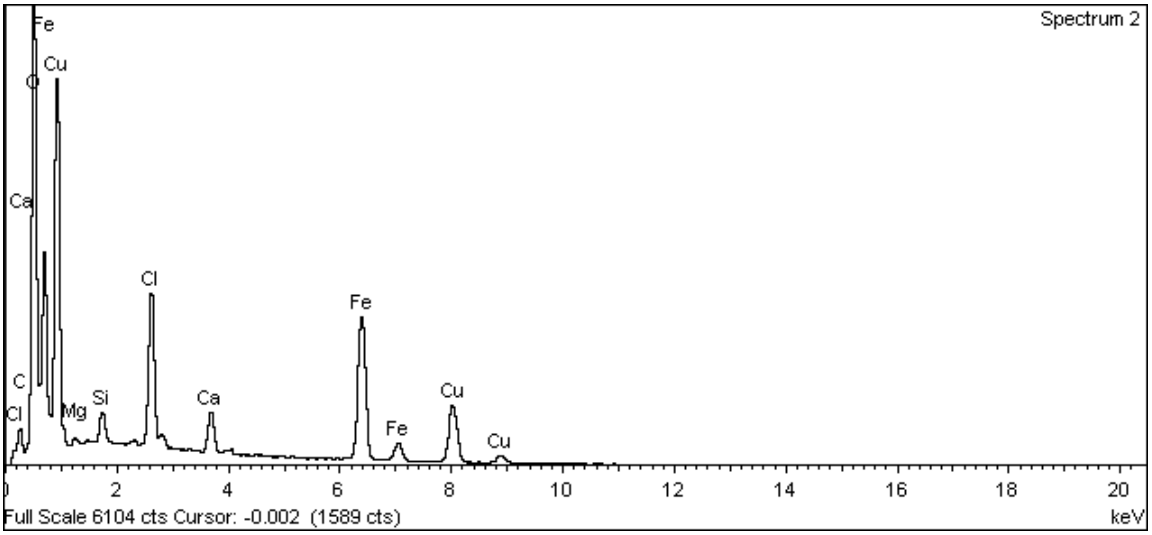

Figure A-293. Inner surface of copper canister and EDX analysis at position of Spectrum 2

Copper can outer surface

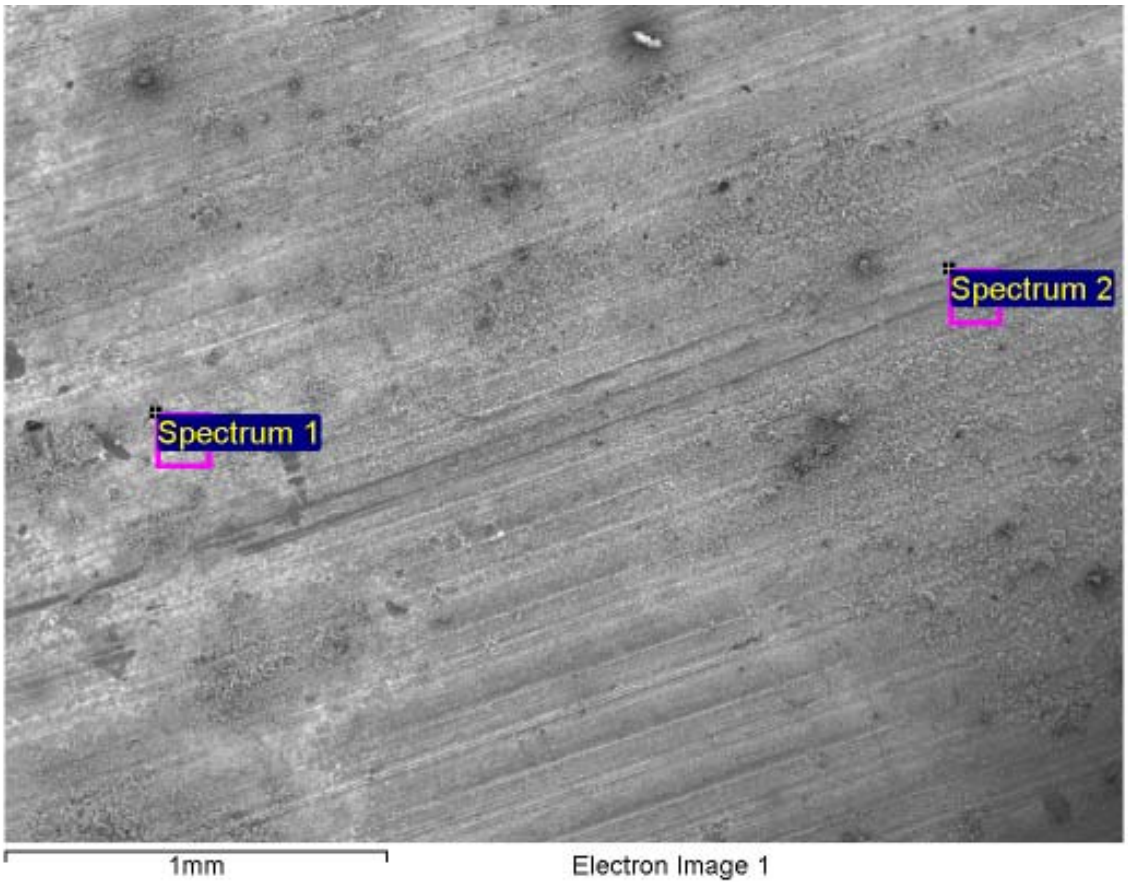

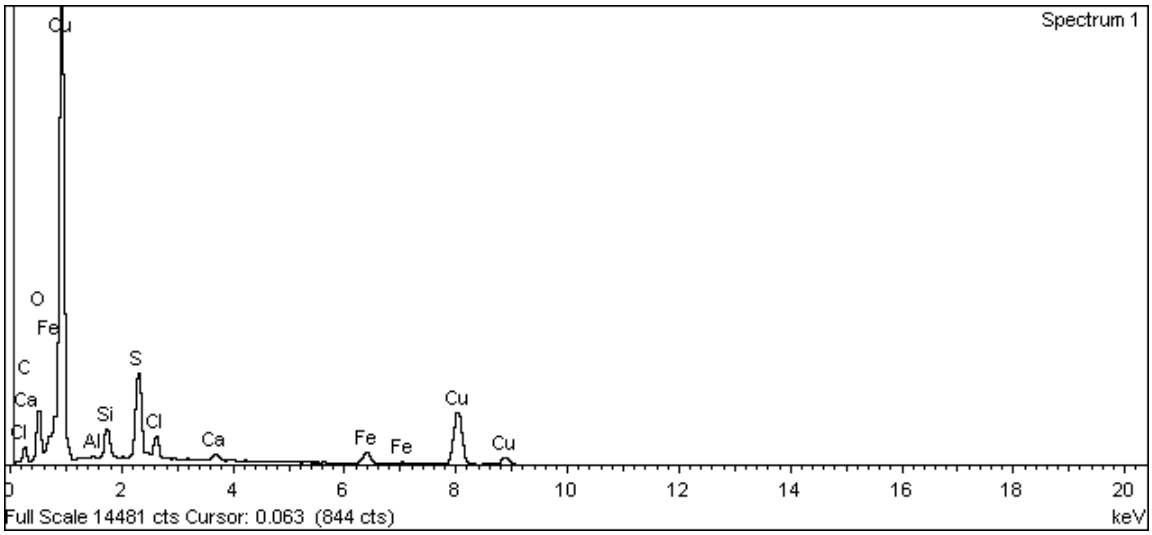

Figure A-294. Outer surface of copper canister and EDX analysis at position of Spectrum 1

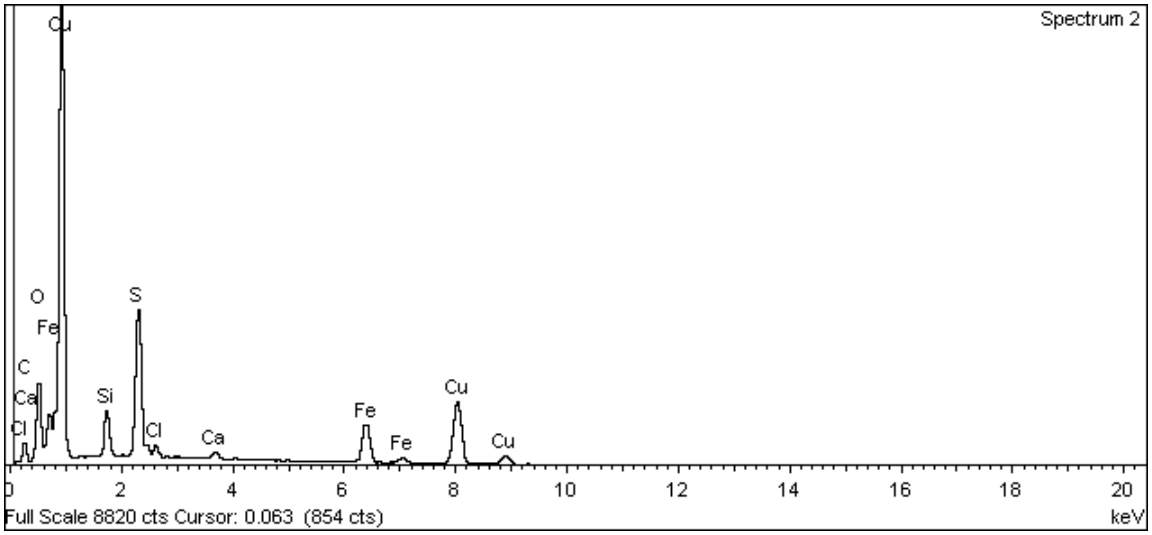

Figure A-295. Outer surface of copper canister and EDX analysis at position of Spectrum 2

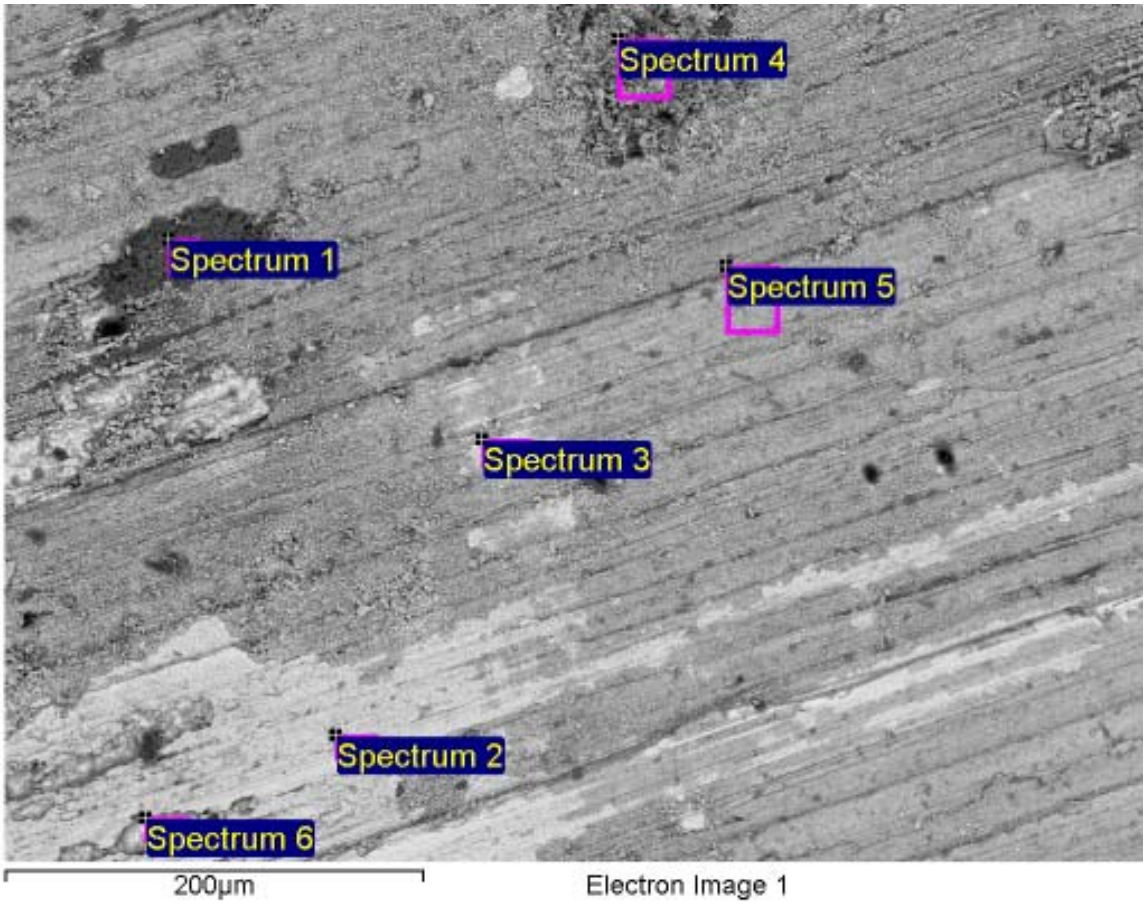

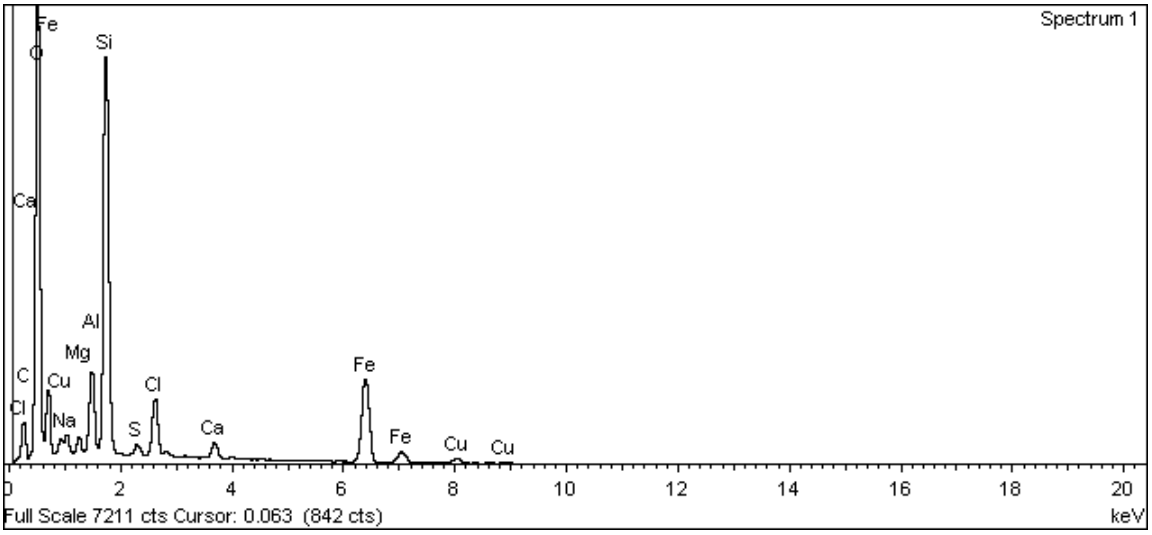

Figure A-296. Outer surface of copper canister and EDX analysis at position of Spectrum 1

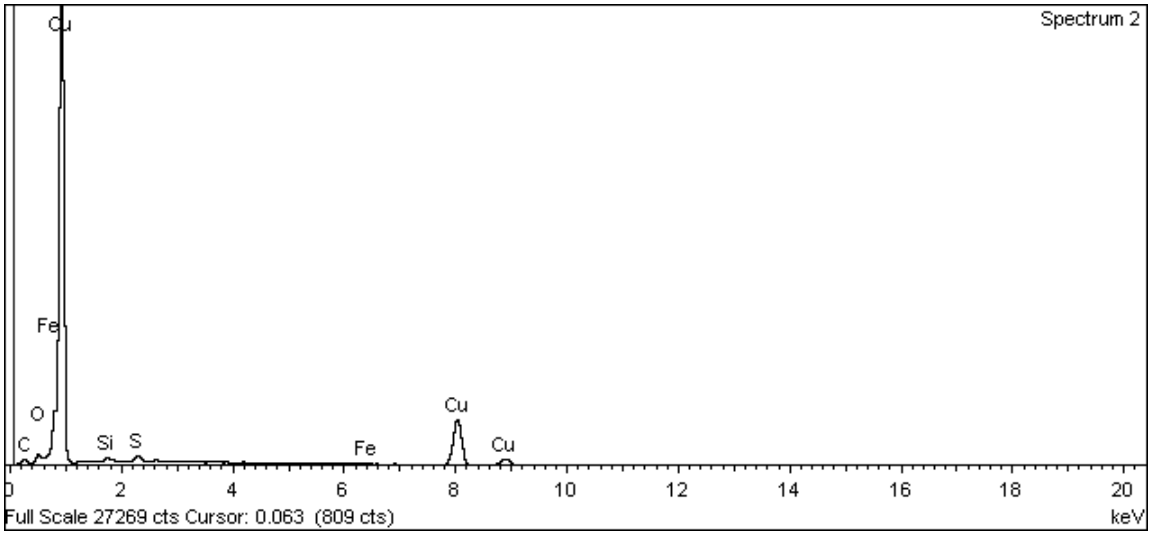

Figure A-297. Outer surface of copper canister and EDX analysis at position of Spectrum 2

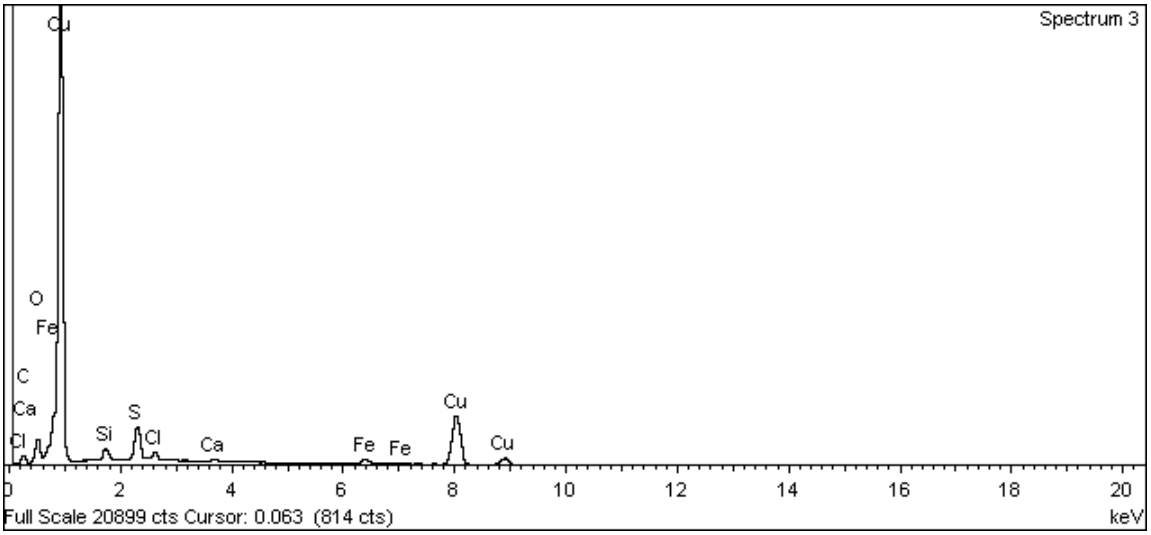

Figure A-298. Outer surface of copper canister and EDX analysis at position of Spectrum 3

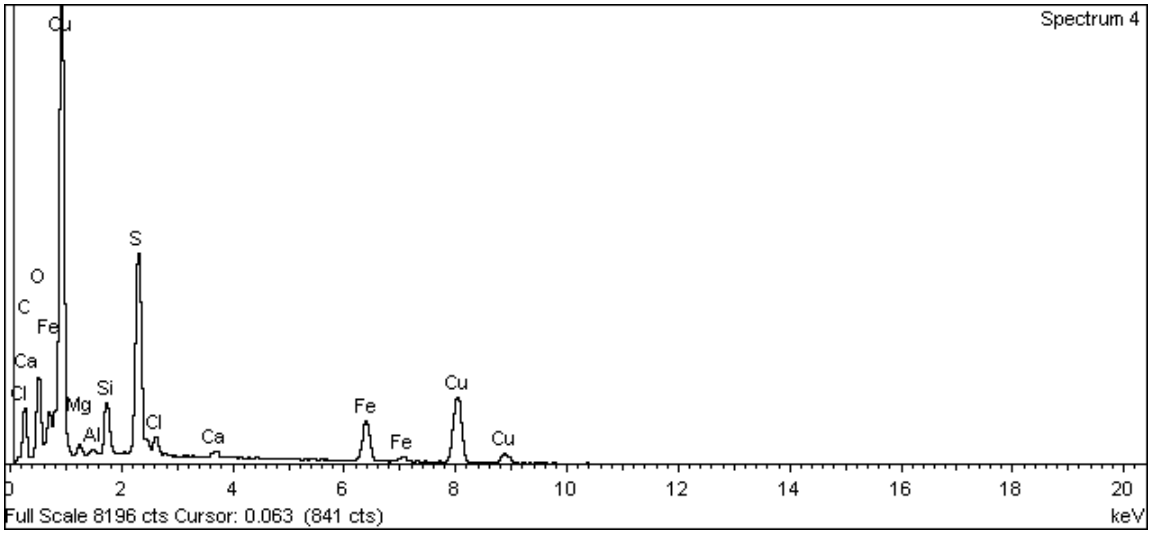

Figure A-299. Outer surface of copper canister and EDX analysis at position of Spectrum 4

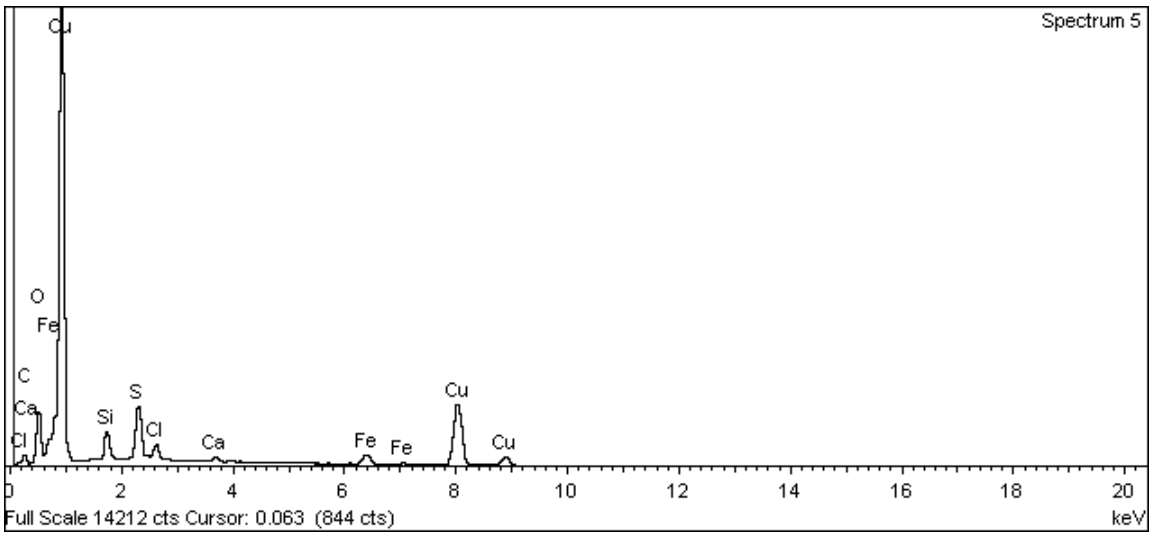

Figure A-300. Outer surface of copper canister and EDX analysis at position of Spectrum 5

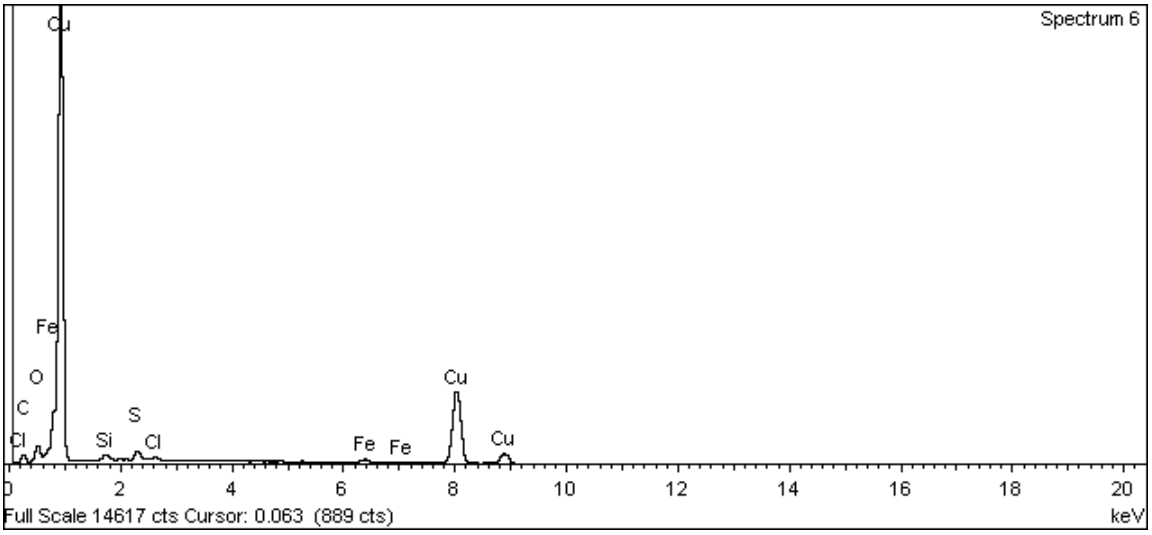

Figure A-301. Outer surface of copper canister and EDX analysis at position of Spectrum 6

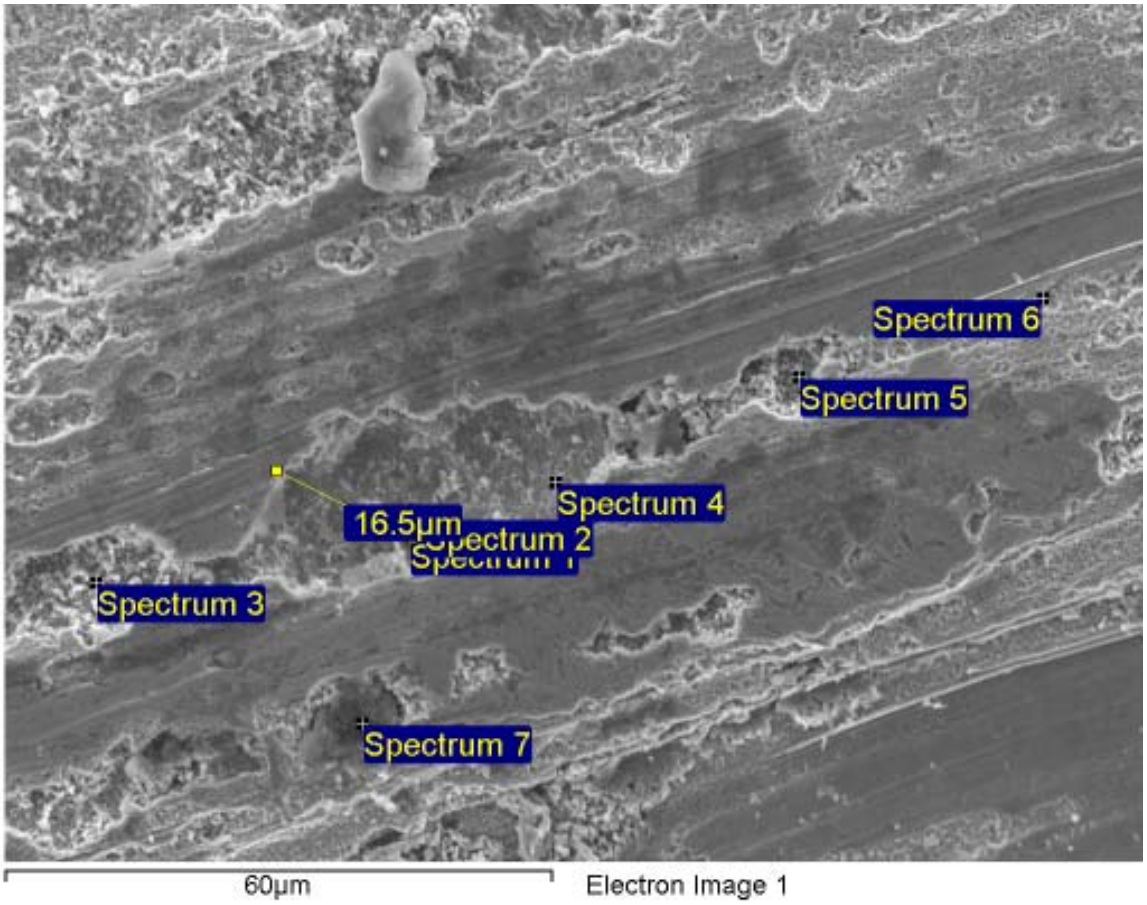

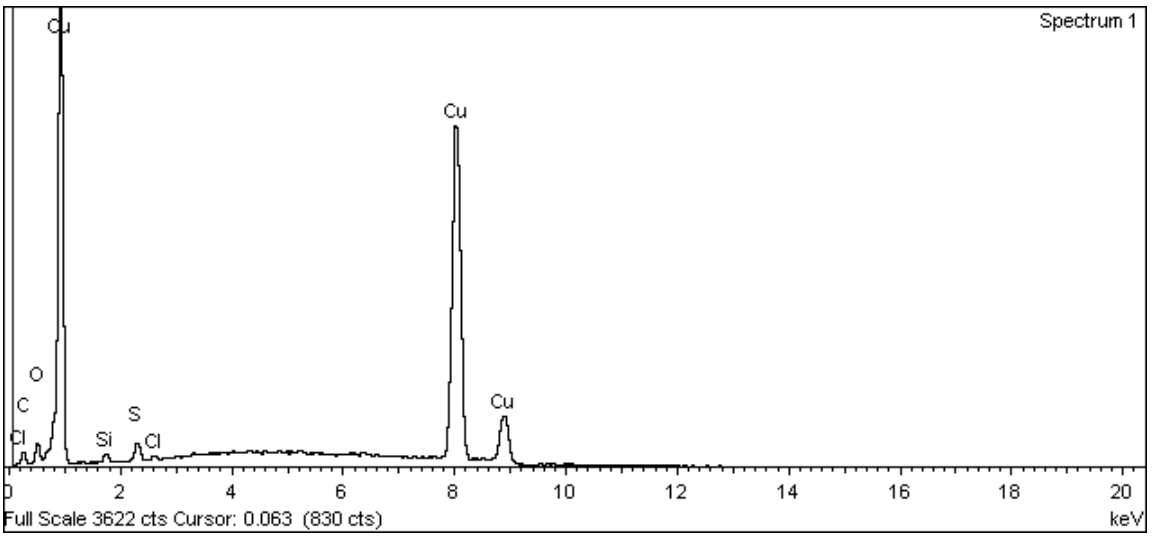

Figure A-302. Outer surface of copper canister and EDX analysis at position of Spectrum 1 (the 16.5 µm marker indicates the width of the crater)

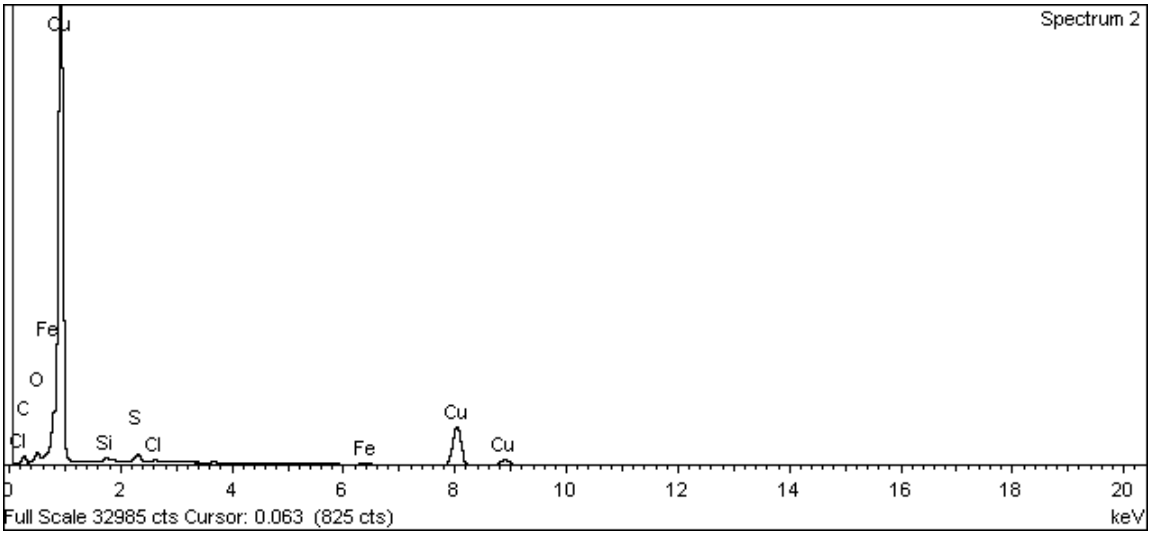

Figure A-303. Outer surface of copper canister and EDX analysis at position of Spectrum 2

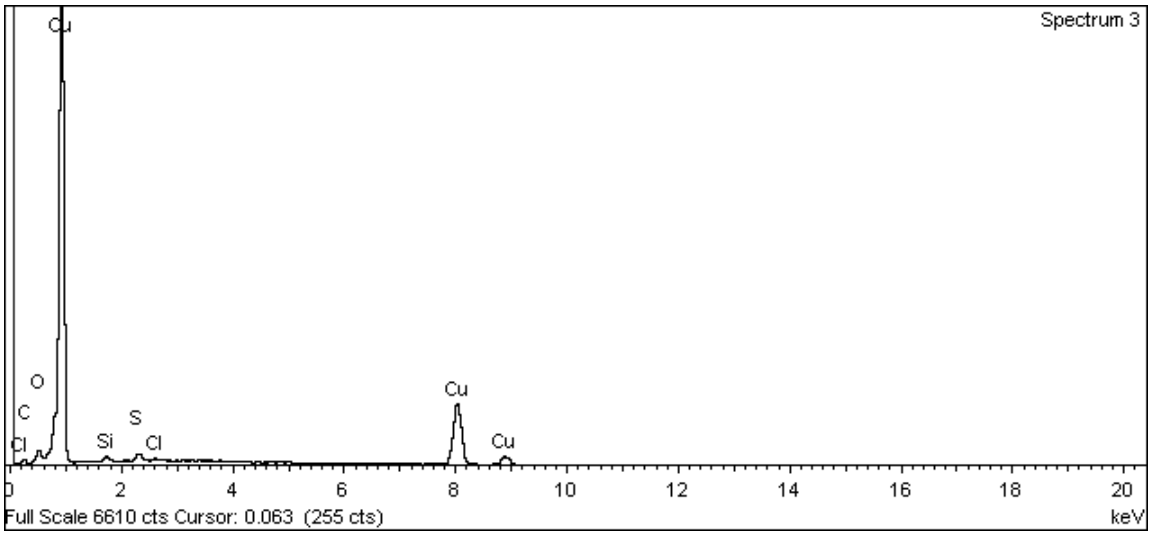

Figure A-304. Outer surface of copper canister and EDX analysis at position of Spectrum 3

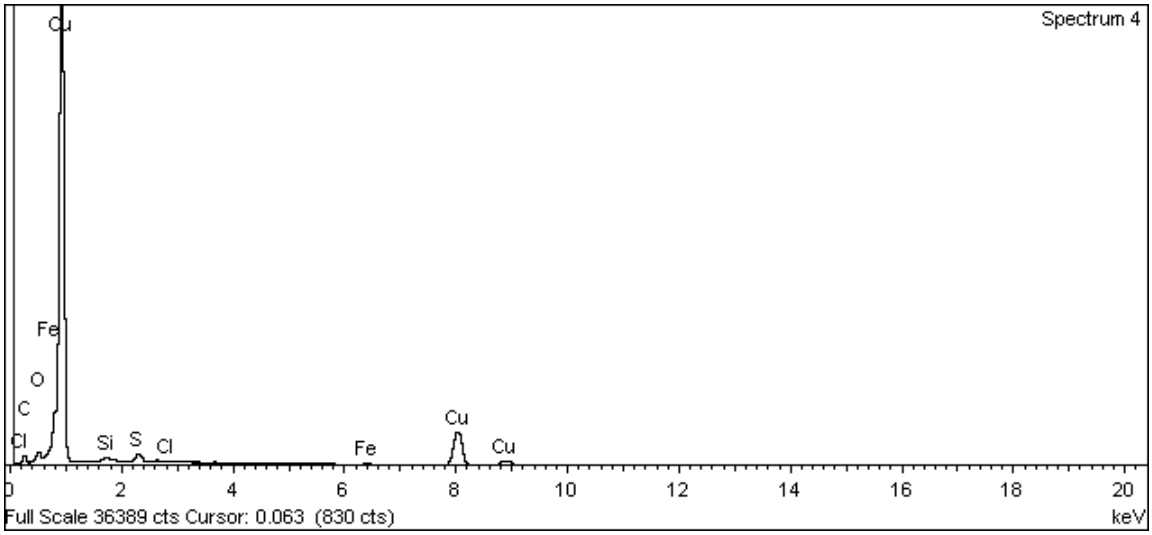

Figure A-305. Outer surface of copper canister and EDX analysis at position of Spectrum 4

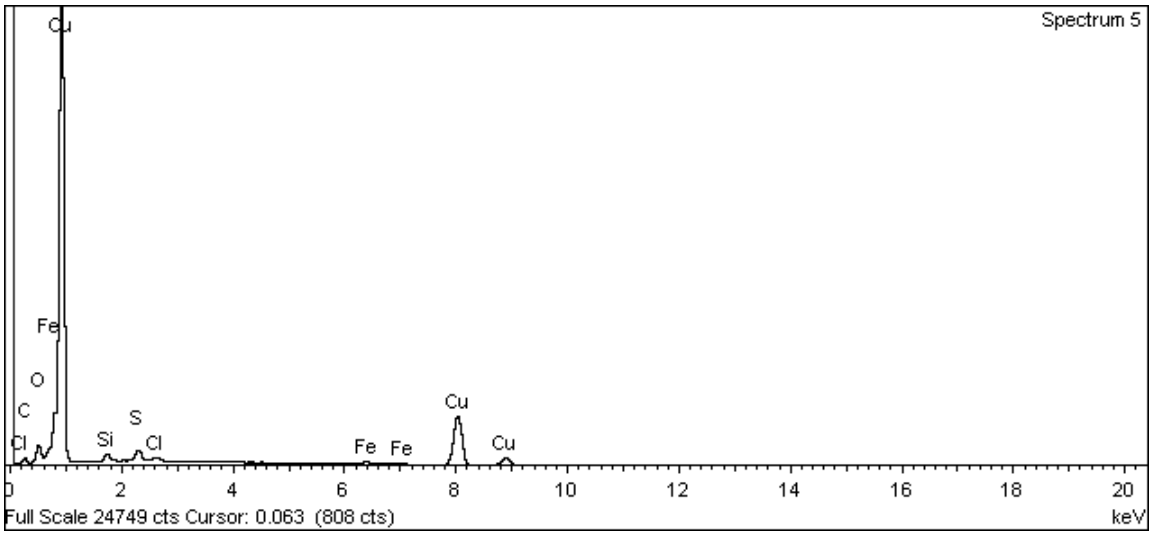

Figure A-306. Outer surface of copper canister and EDX analysis at position of Spectrum 5

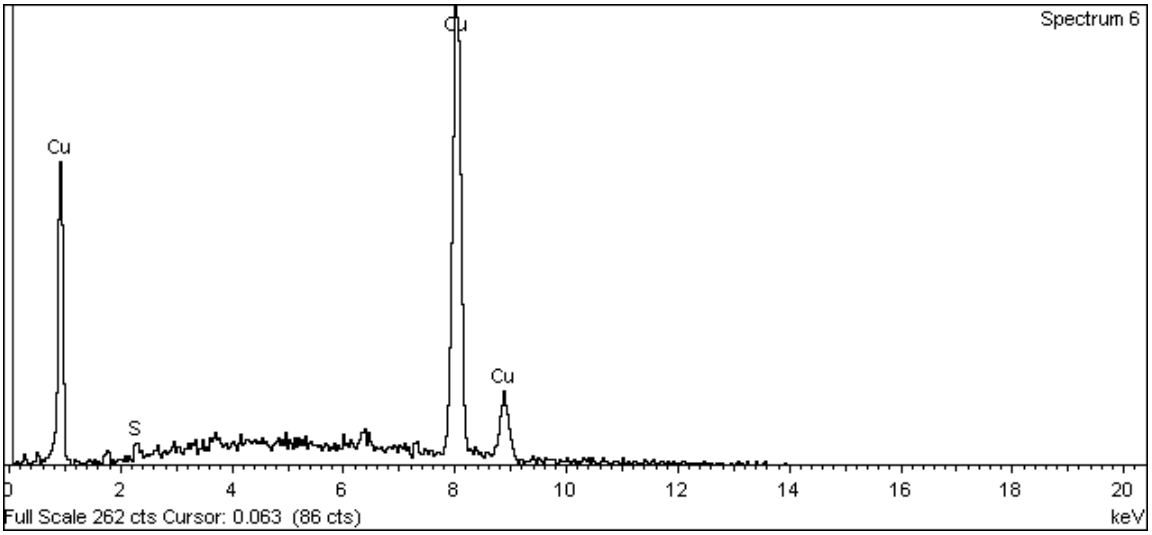

Figure A-307. Outer surface of copper canister and EDX analysis at position of Spectrum 6

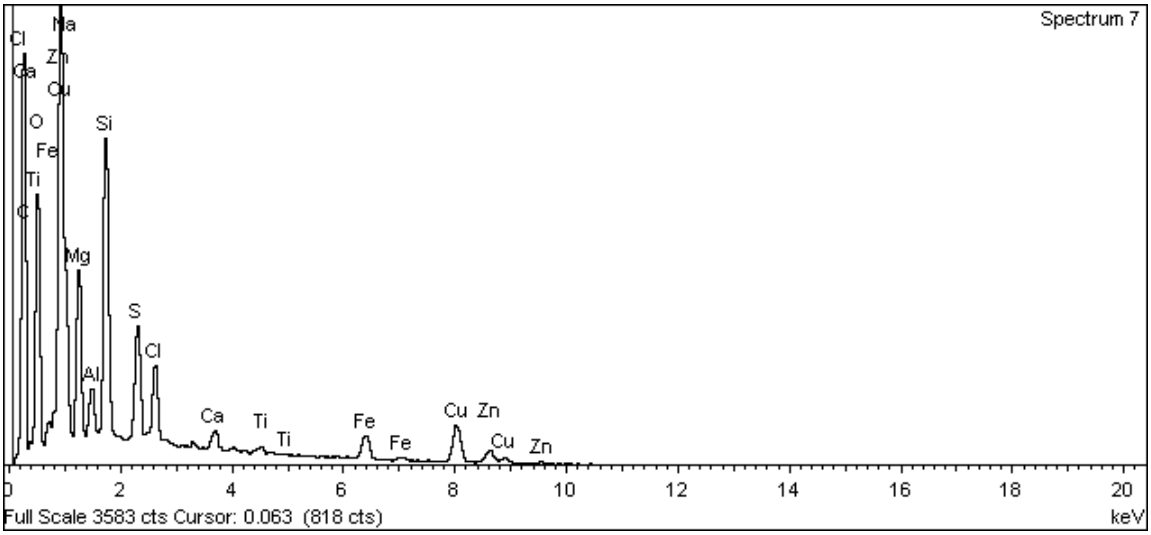

Figure A-308. Outer surface of copper canister and EDX analysis at position of Spectrum 7

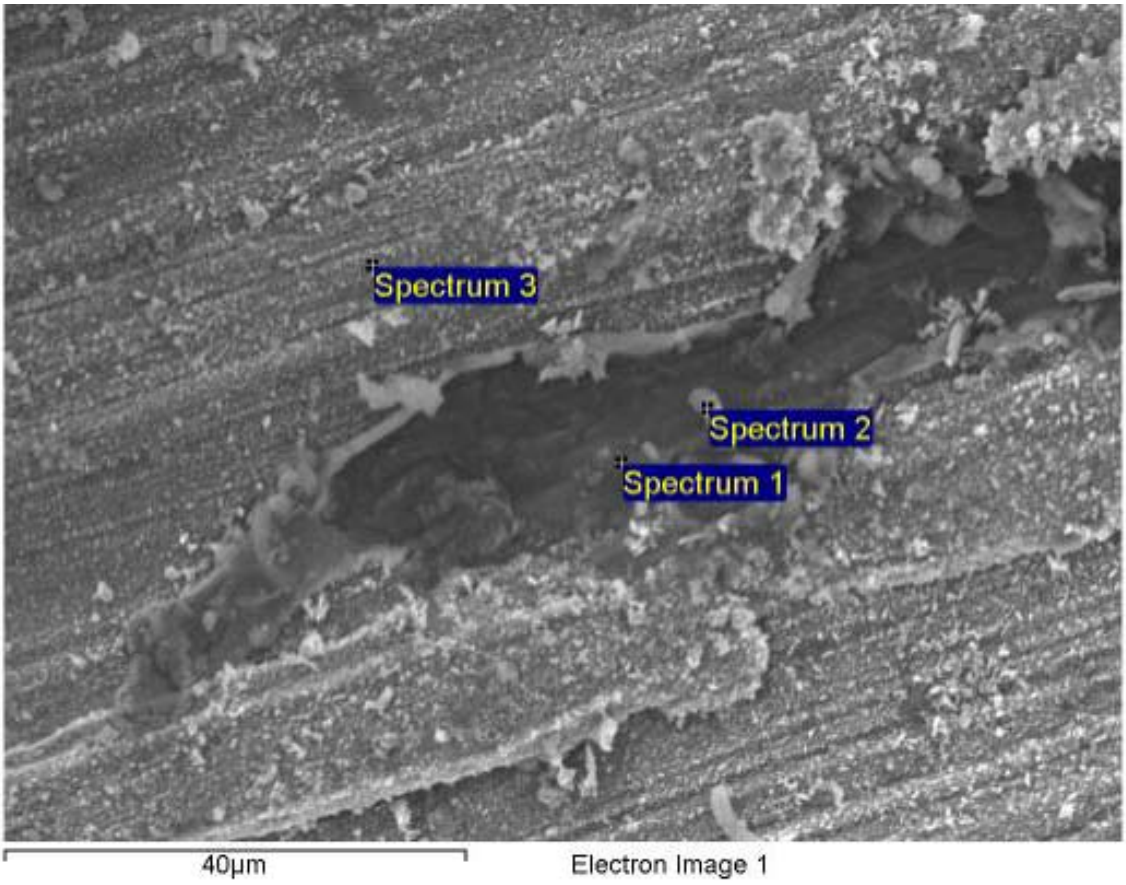

Figure A-309. Outer surface of copper canister and EDX analysis at position of Spectrum 1

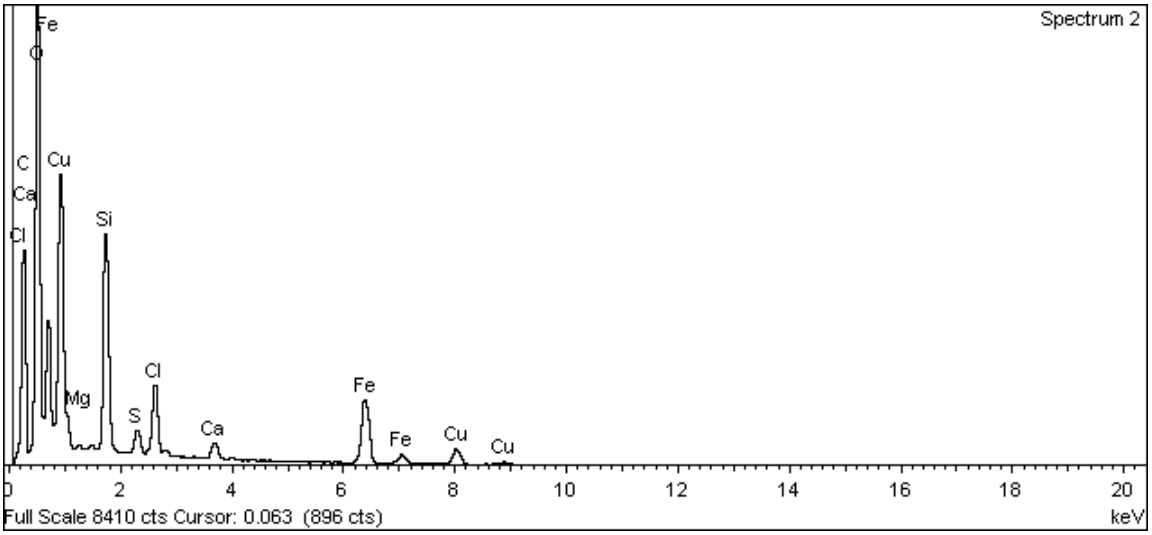

Figure A-310. Outer surface of copper canister and EDX analysis at position of Spectrum 2

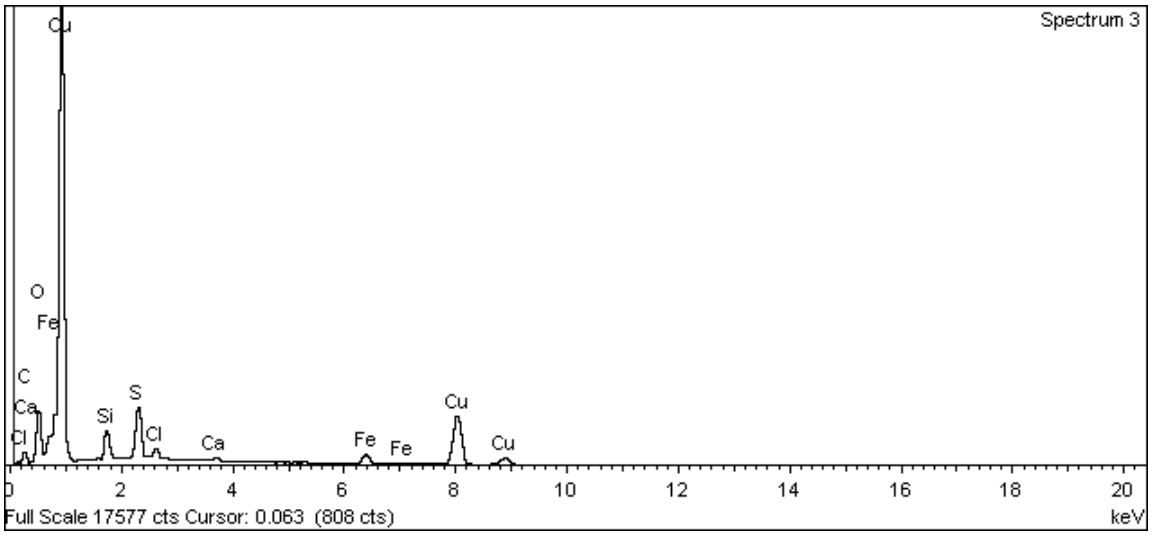

Figure A-311. Outer surface of copper canister and EDX analysis at position of Spectrum 3

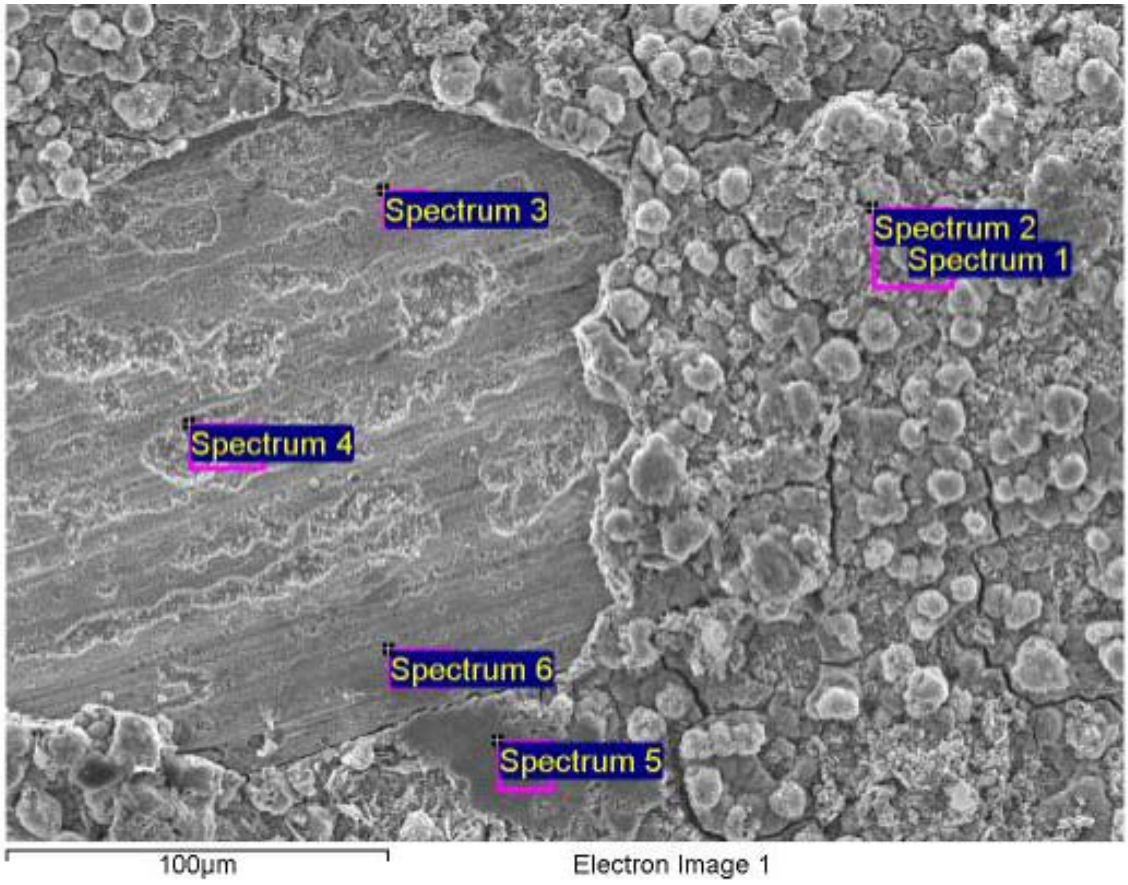

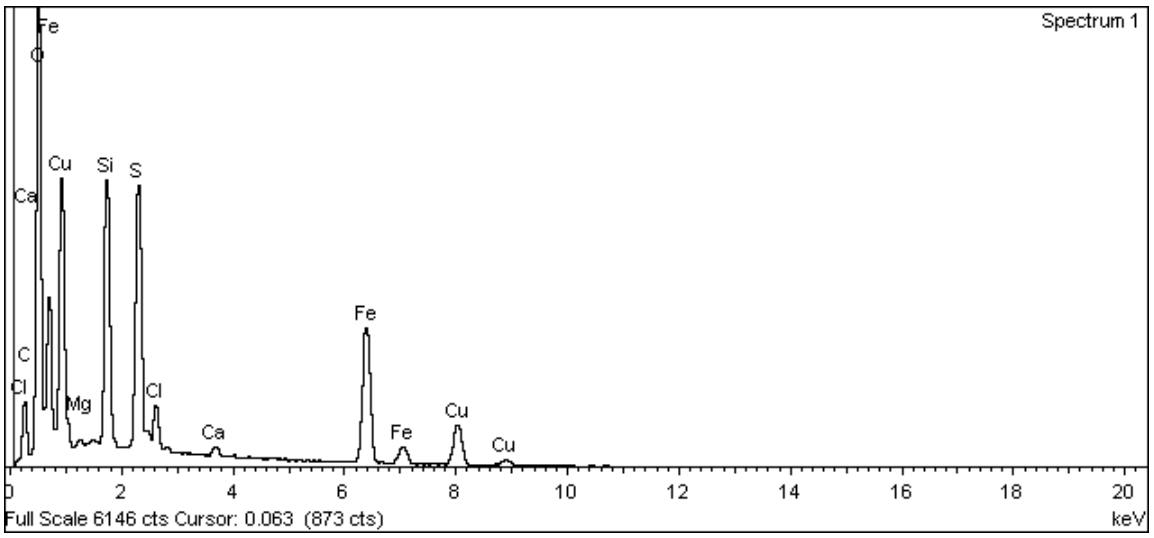

Figure A-312. Outer surface of copper canister and EDX analysis at position of Spectrum 1

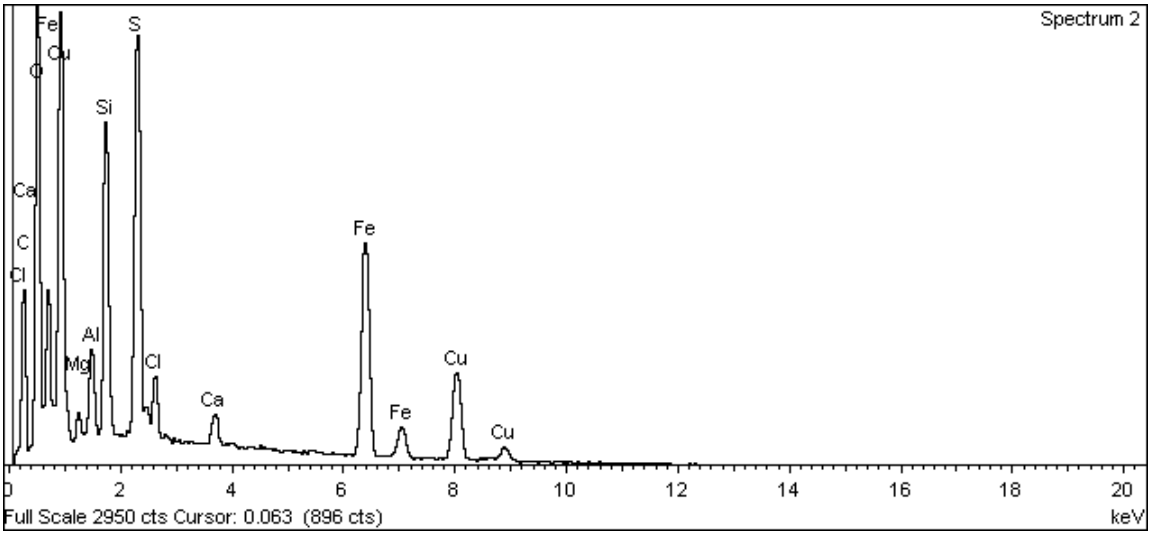

Figure A-313. Outer surface of copper canister and EDX analysis at position of Spectrum 2

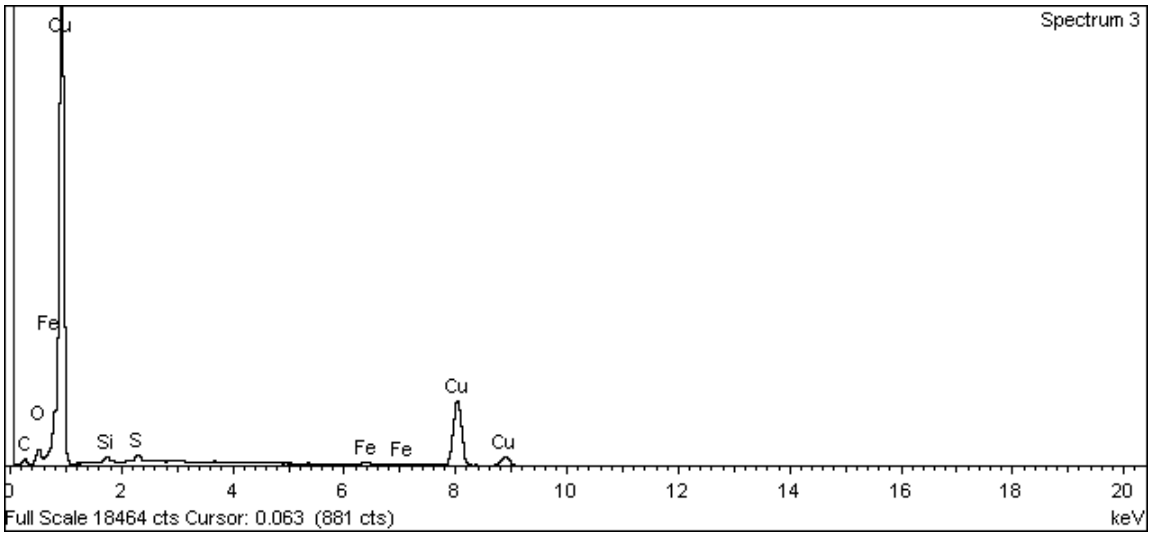

Figure A-314. Outer surface of copper canister and EDX analysis at position of Spectrum 3

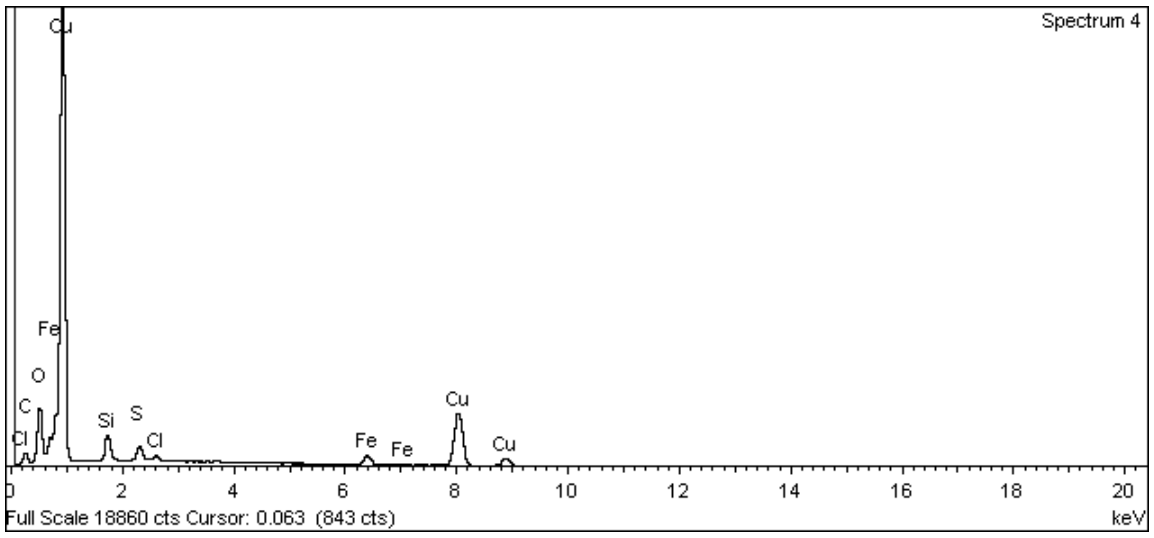

Figure A-315. Outer surface of copper canister and EDX analysis at position of Spectrum 4

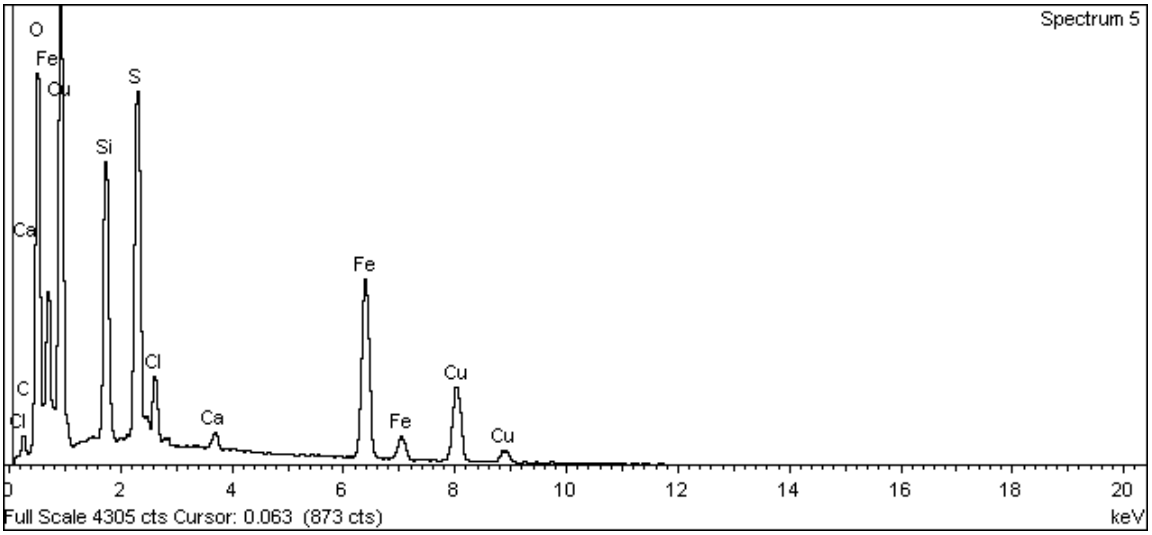

Figure A-316. Outer surface of copper canister and EDX analysis at position of Spectrum 5

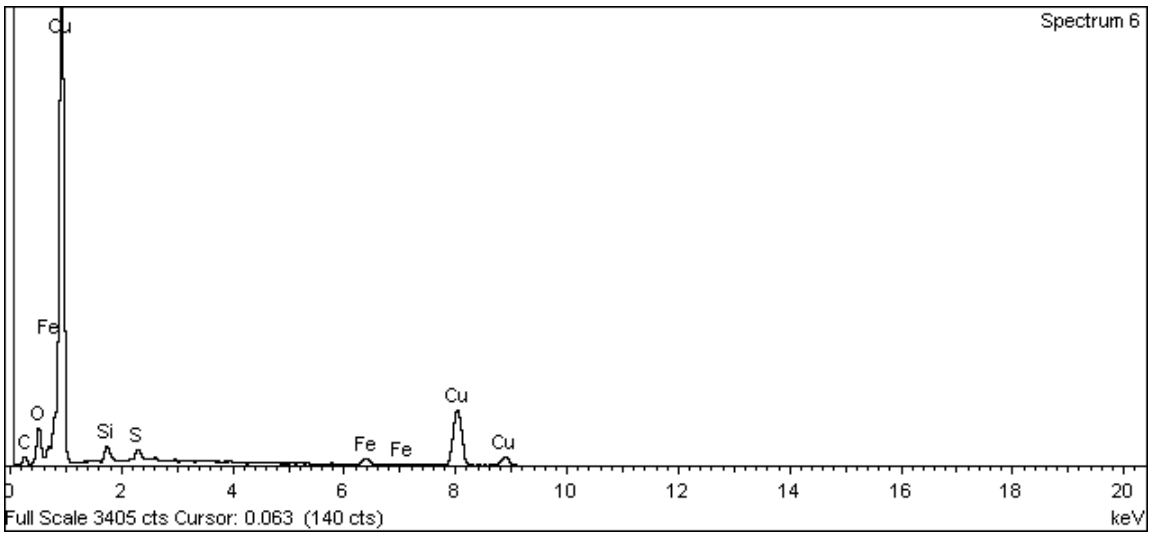

Figure A-317. Outer surface of copper canister and EDX analysis at position of Spectrum 6

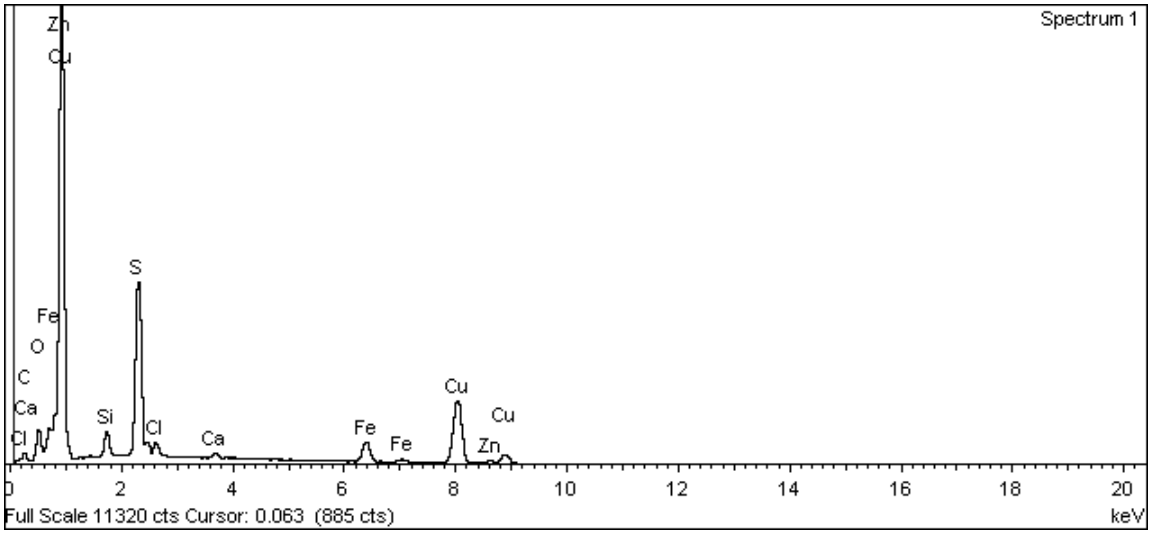

Figure A-318. Outer surface of copper canister and EDX analysis at position of Spectrum 1

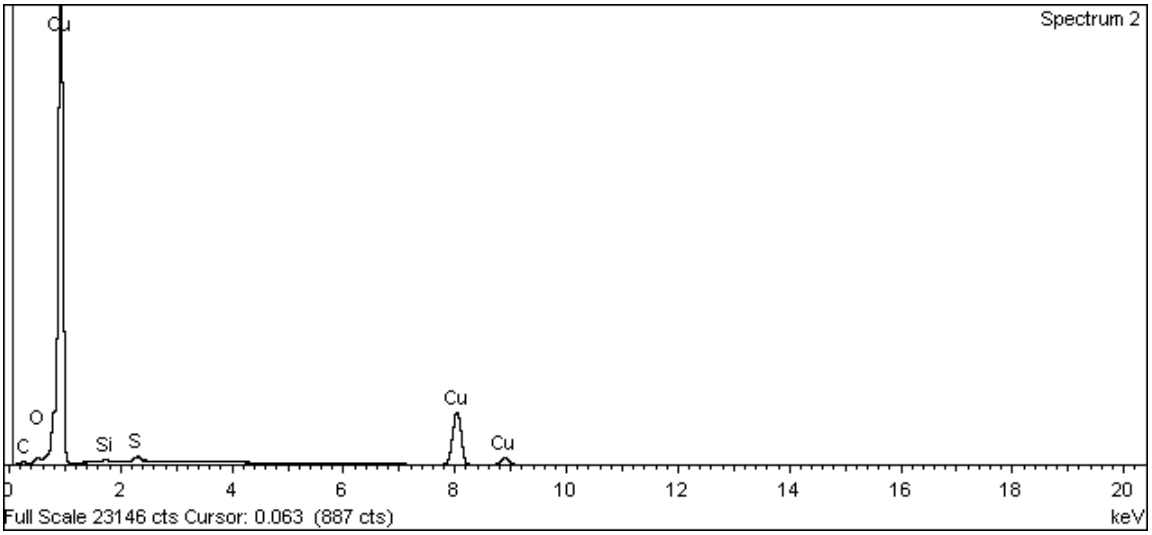

Figure A-319. Outer surface of copper canister and EDX analysis at position of Spectrum 2

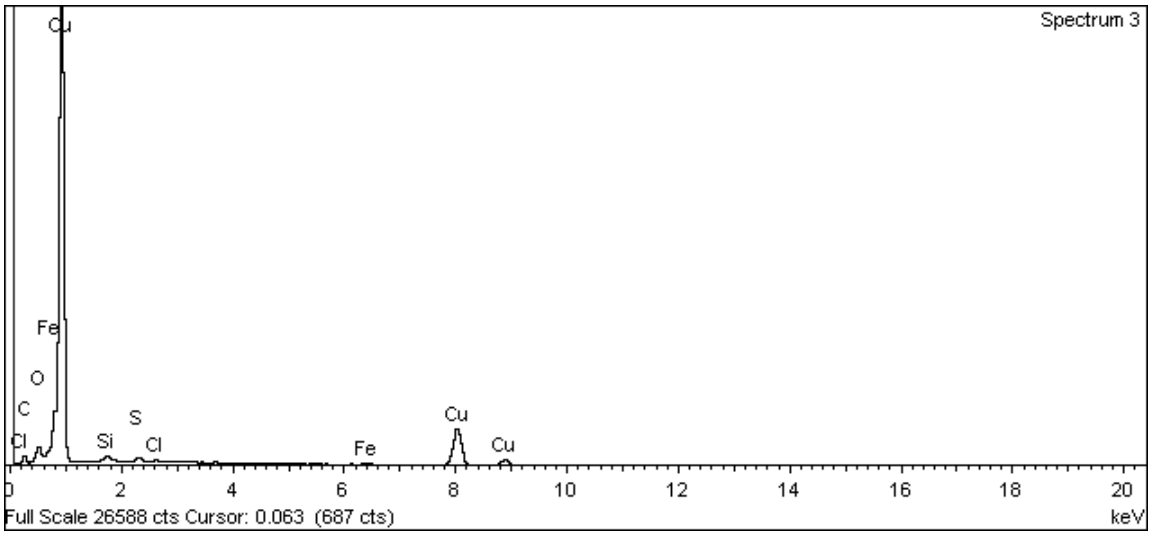

Figure A-320. Outer surface of copper canister and EDX analysis at position of Spectrum 3

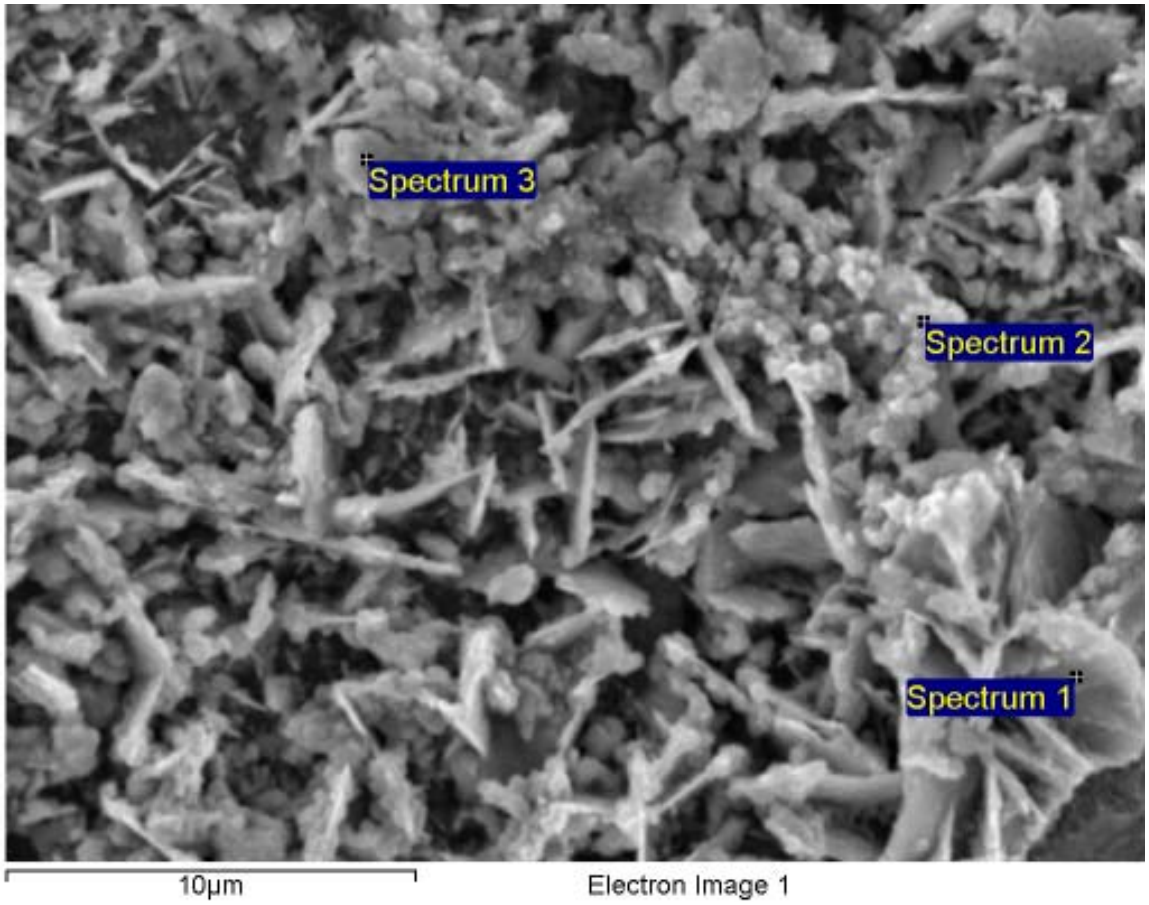

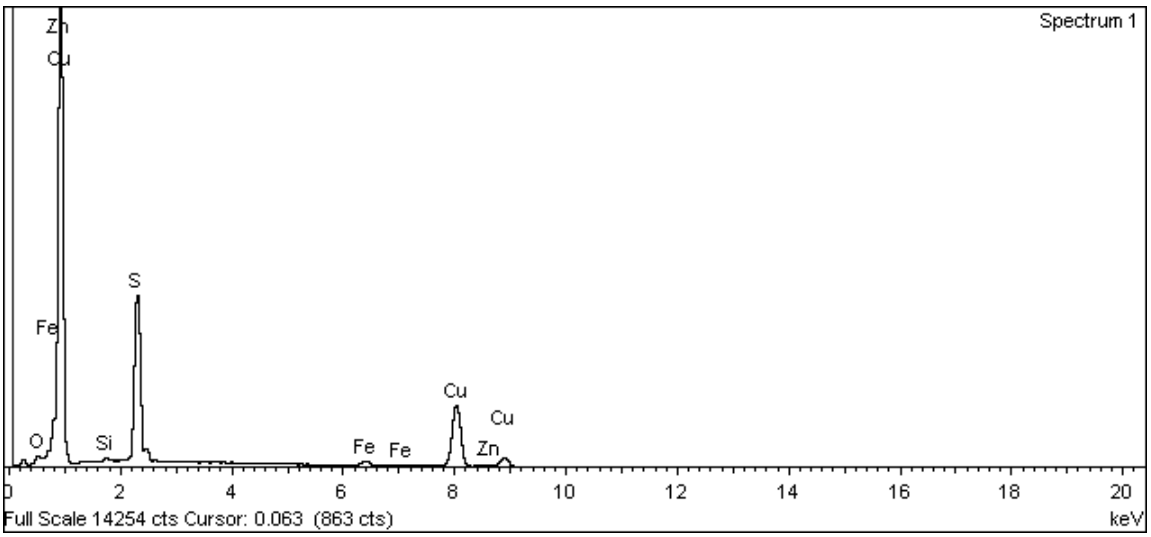

Figure A-321. Outer surface of copper canister and EDX analysis at position of Spectrum 1

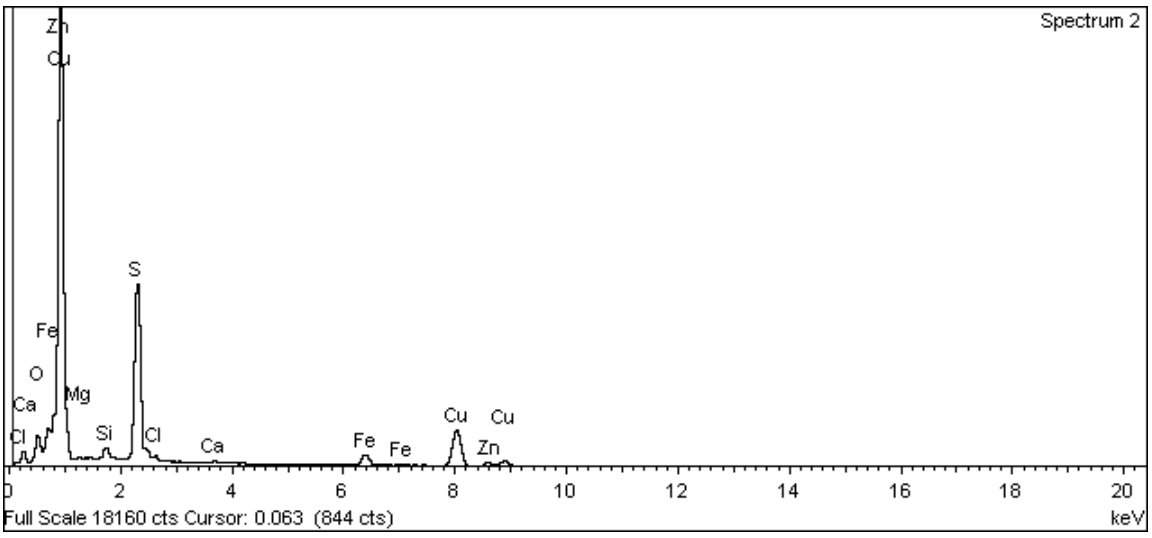

Figure A-322. Outer surface of copper canister and EDX analysis at position of Spectrum 2

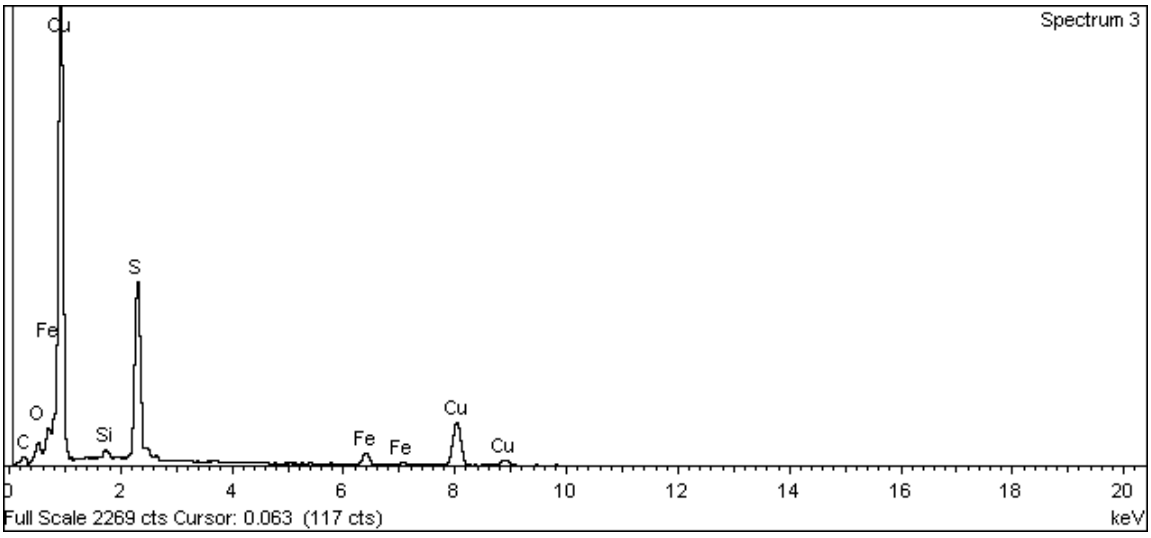

Figure A-323. Outer surface of copper canister and EDX analysis at position of Spectrum 3

Surface of Cast Iron insert

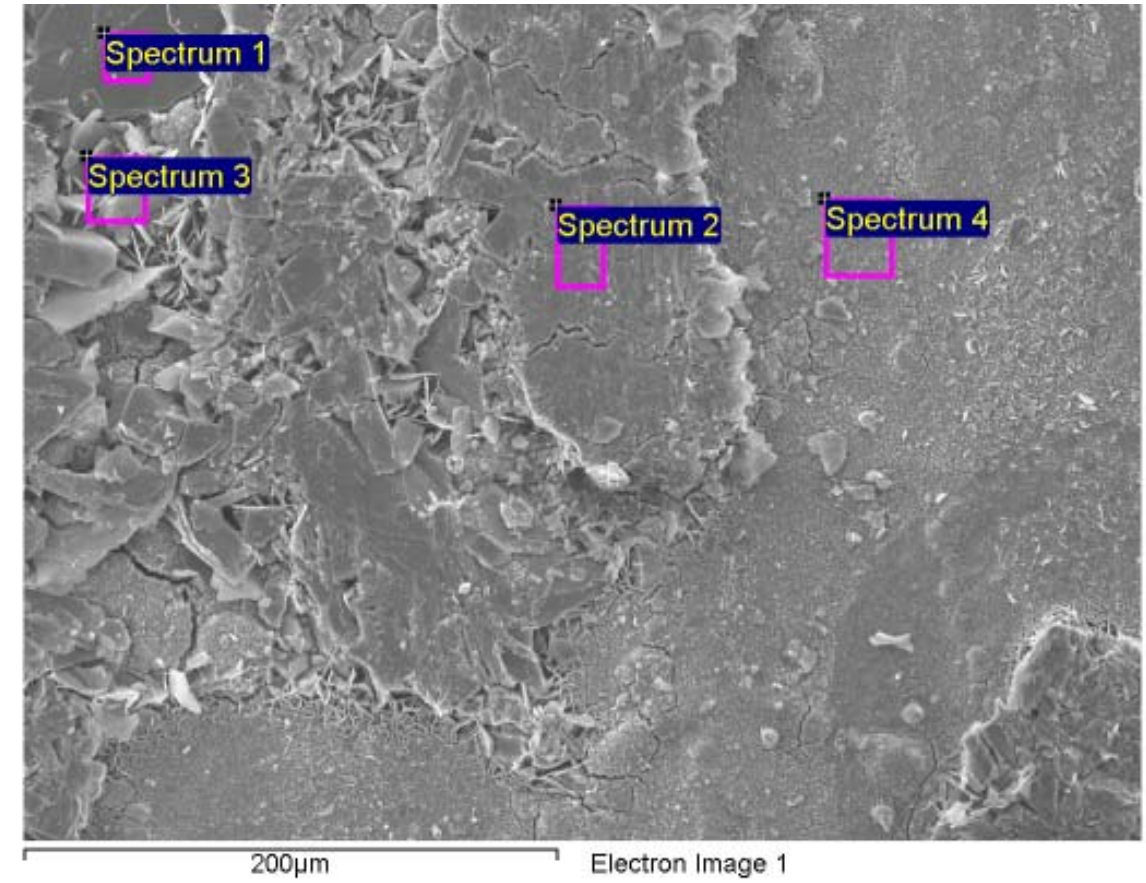

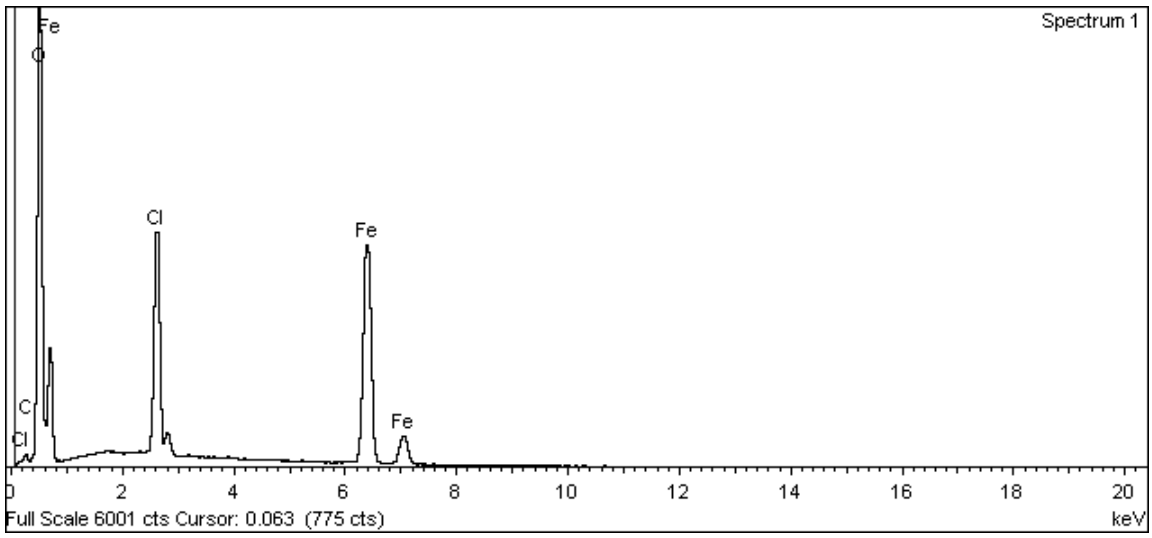

Figure A-324. Surface of cast iron insert and EDX analysis at position of Spectrum 1

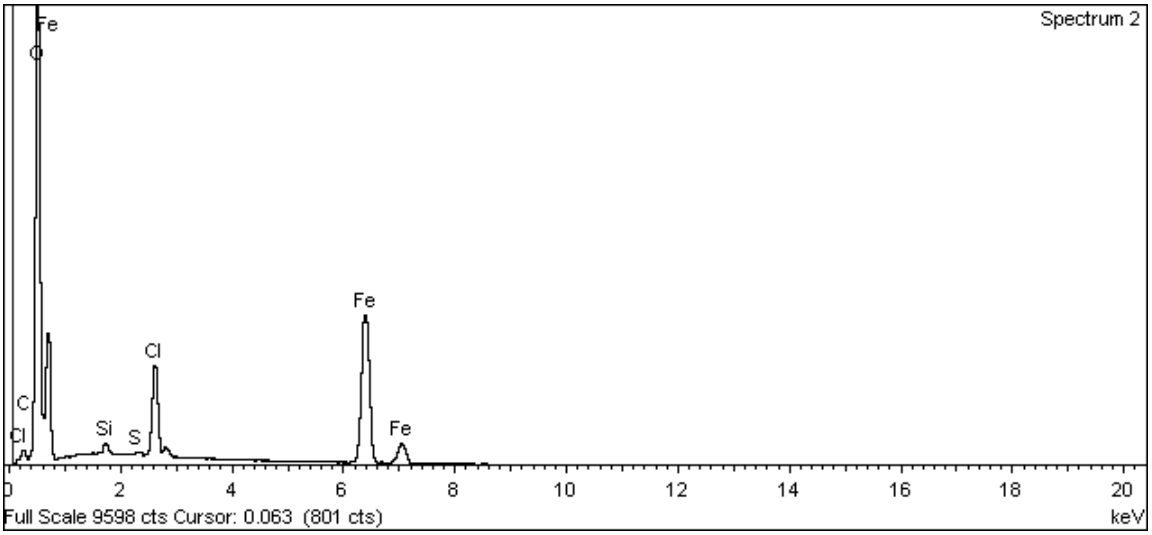

Figure A-325. Surface of cast iron insert and EDX analysis at position of Spectrum 2

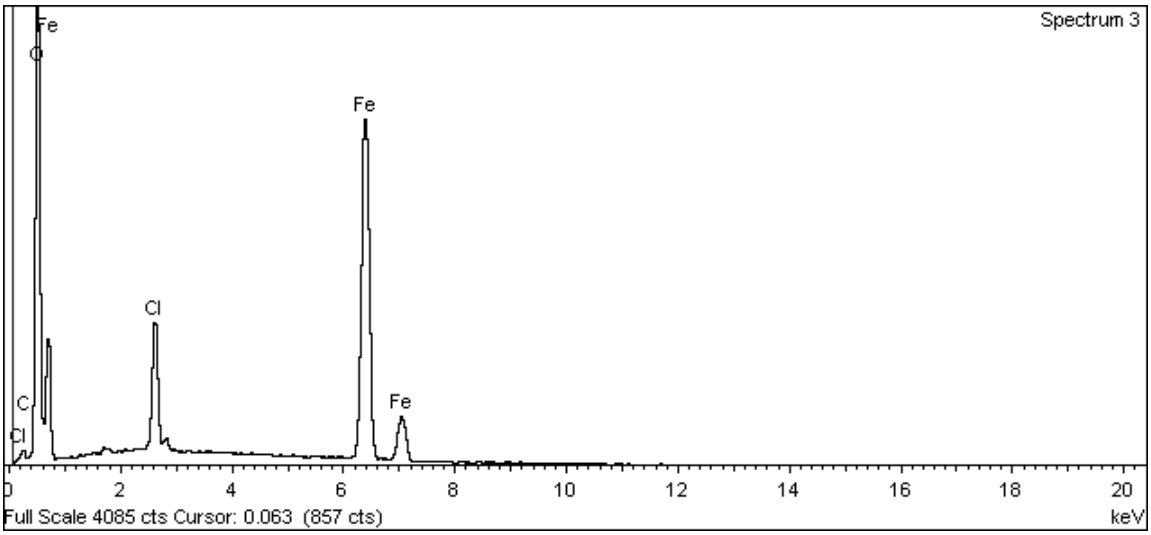

Figure A-326. Surface of cast iron insert and EDX analysis at position of Spectrum 3

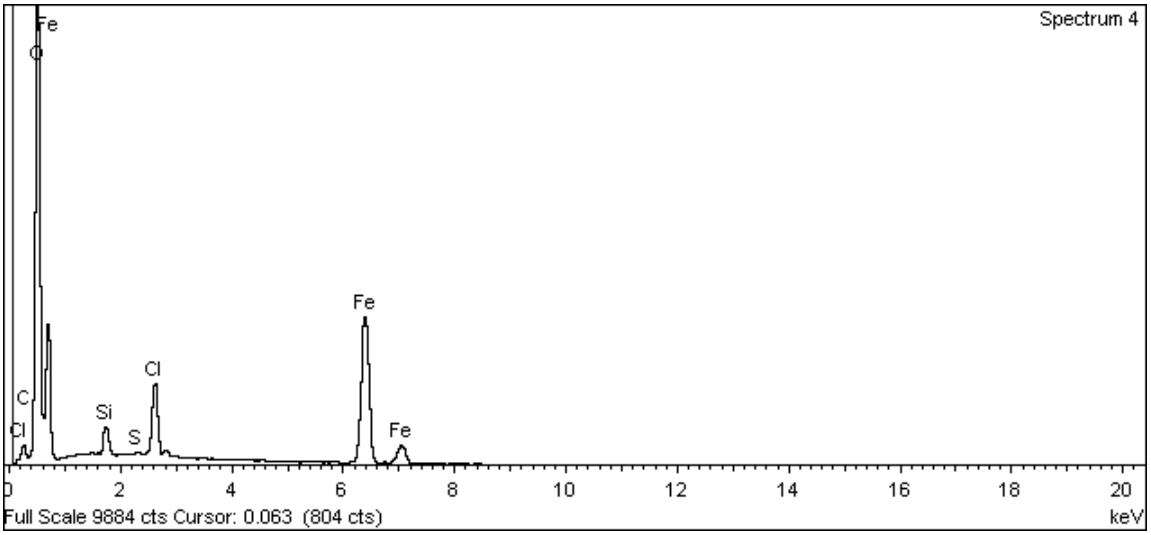

Figure A-327. Surface of cast iron insert and EDX analysis at position of Spectrum 4

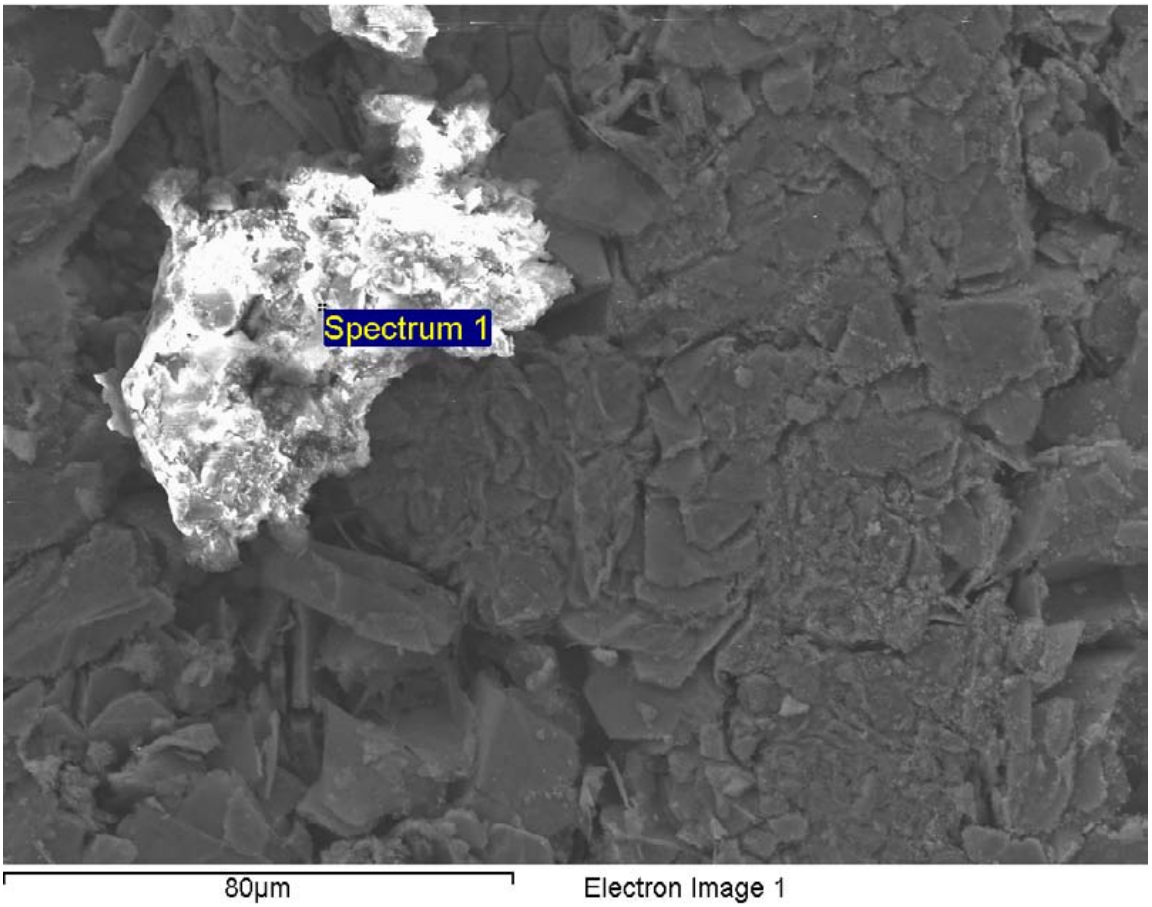

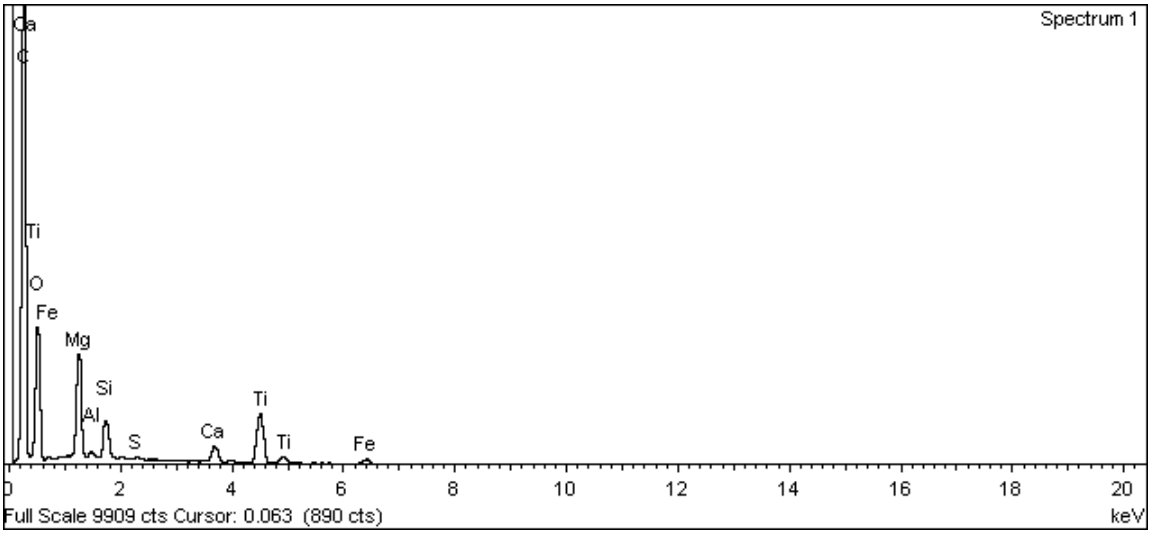

Figure A-328. Surface of cast iron insert and EDX analysis at position of Spectrum 1

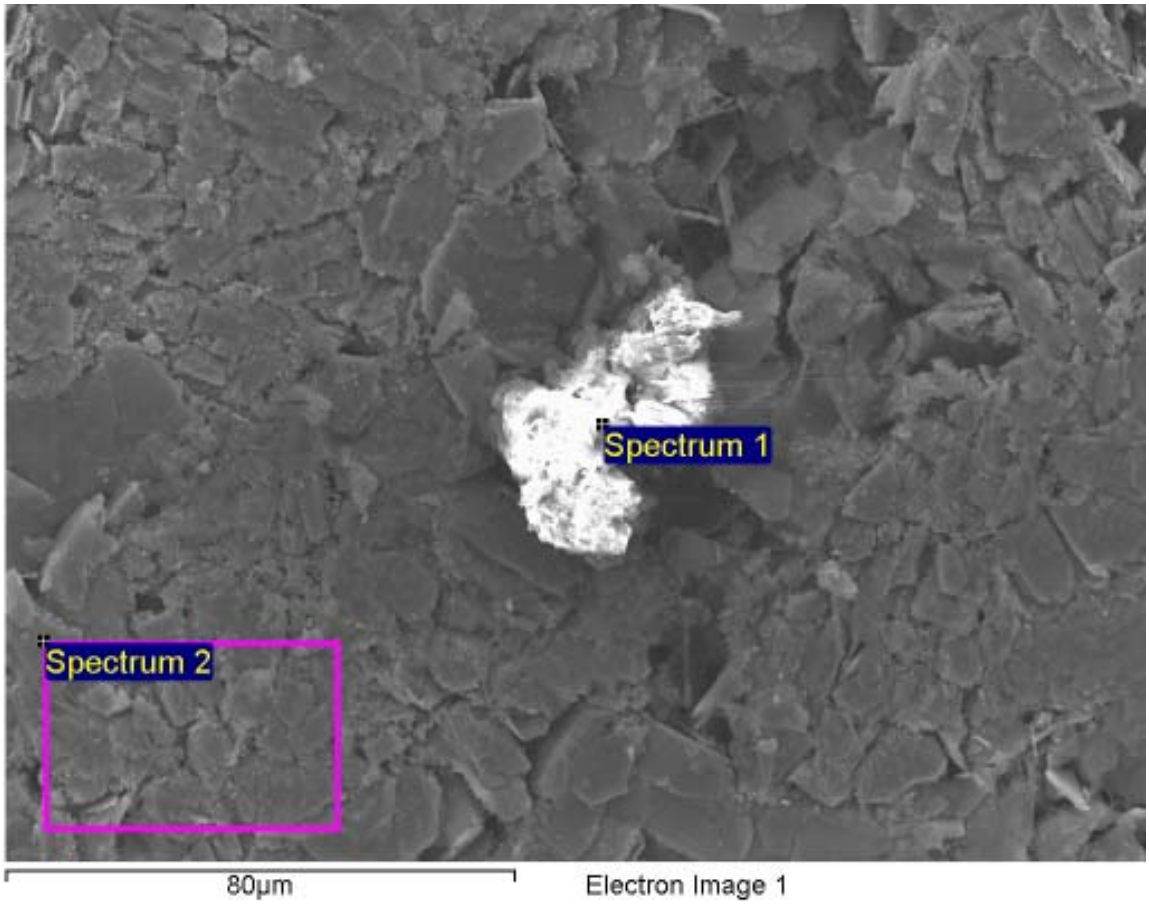

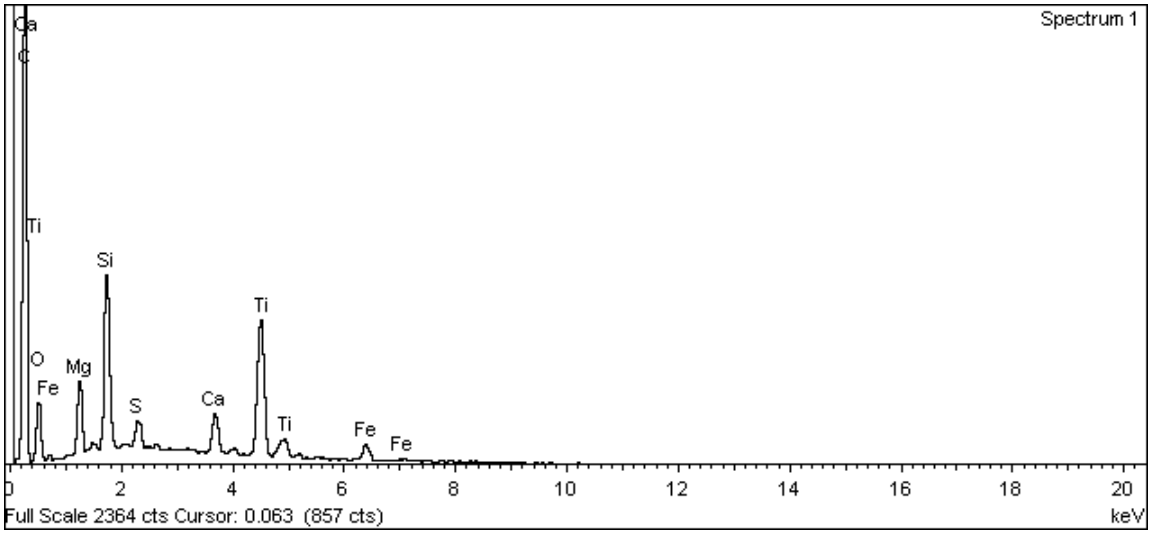

Figure A-329. Surface of cast iron insert and EDX analysis at position of Spectrum 1

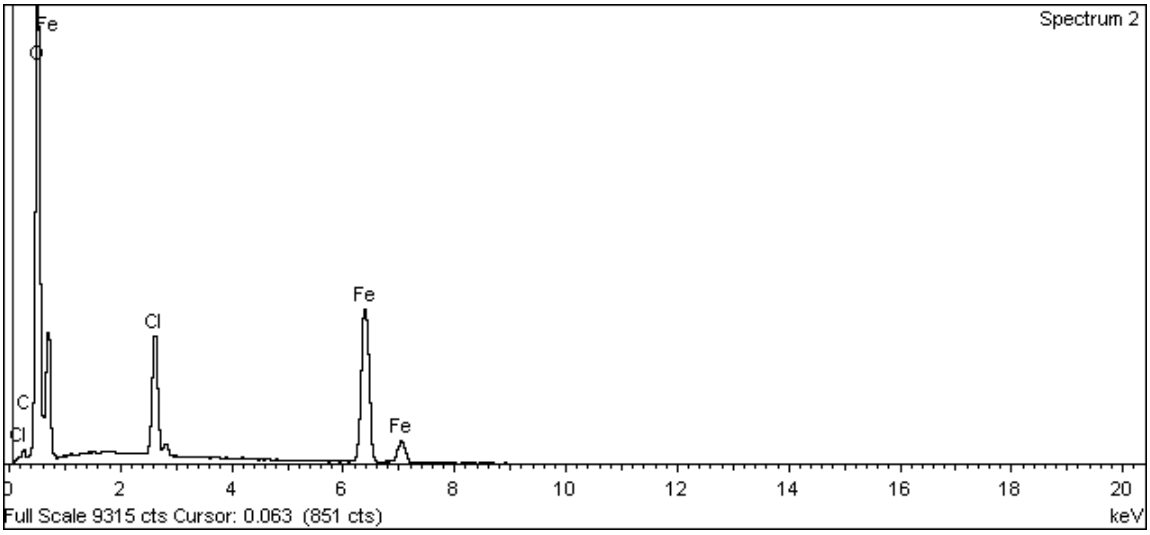

Figure A-330. Surface of cast iron insert and EDX analysis at position of Spectrum 2

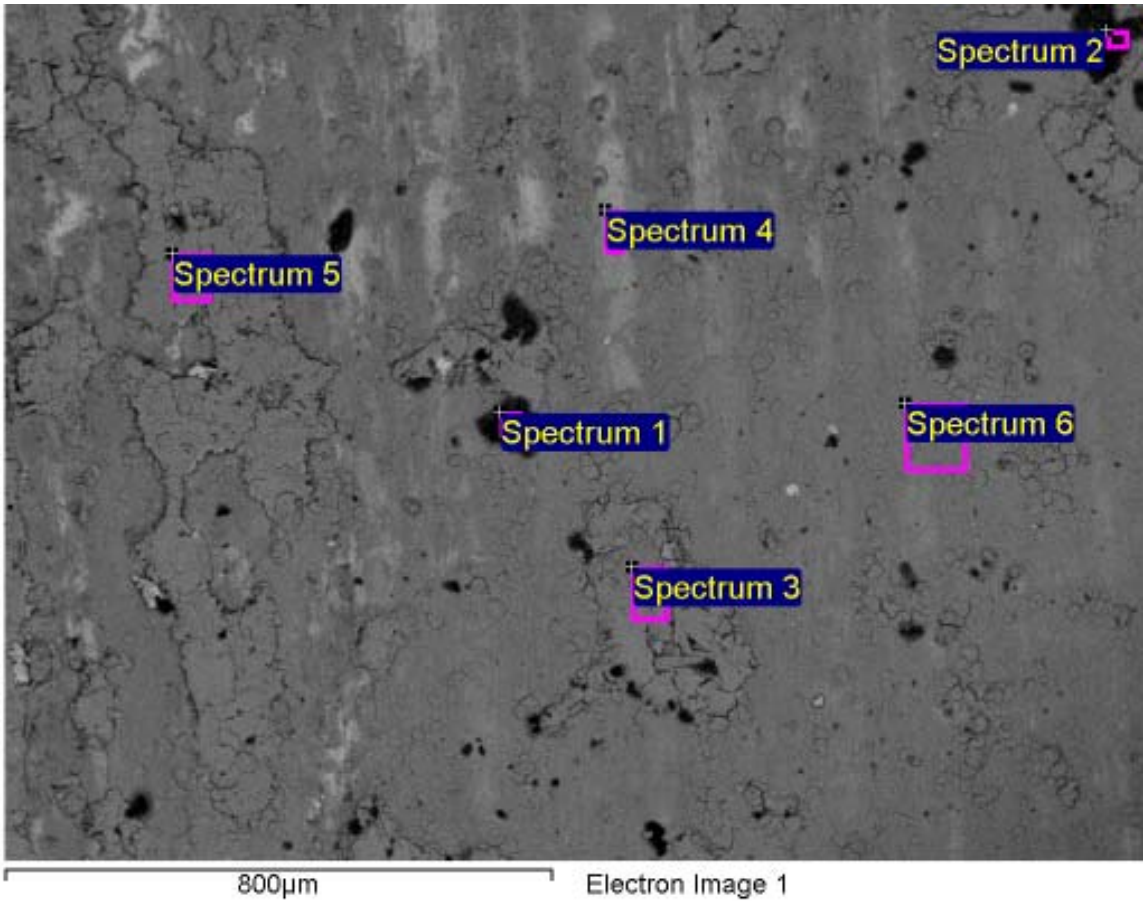

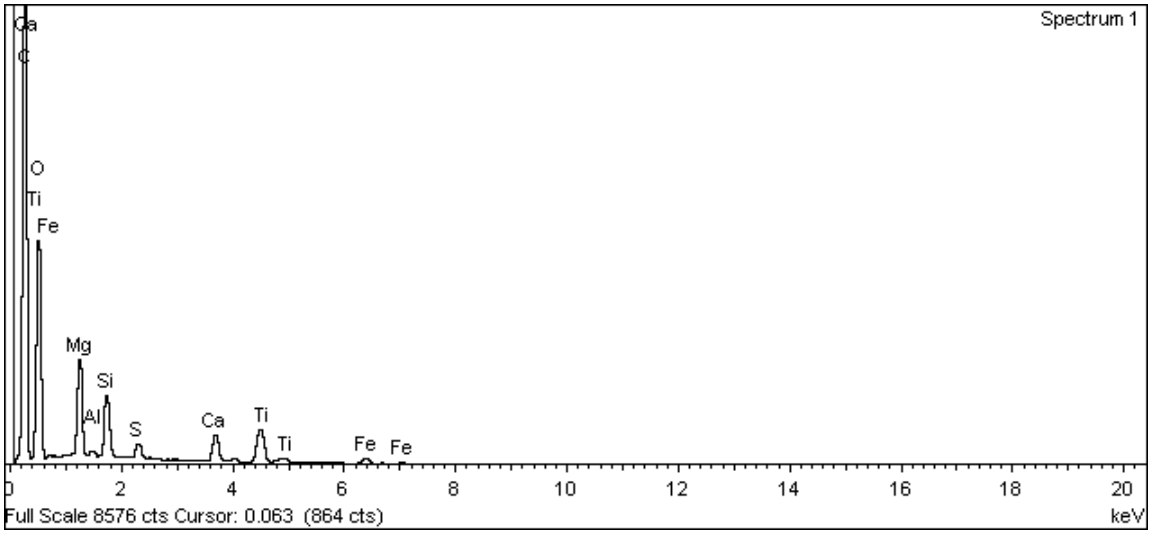

Figure A-331. Surface of cast iron insert and EDX analysis at position of Spectrum 1

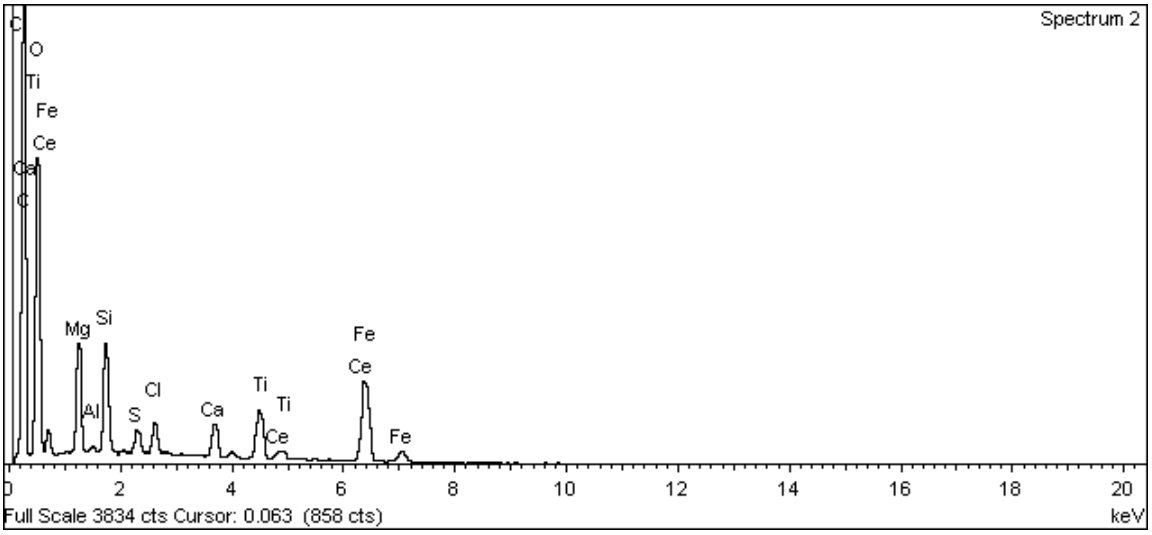

Figure A-332. Surface of cast iron insert and EDX analysis at position of Spectrum 2

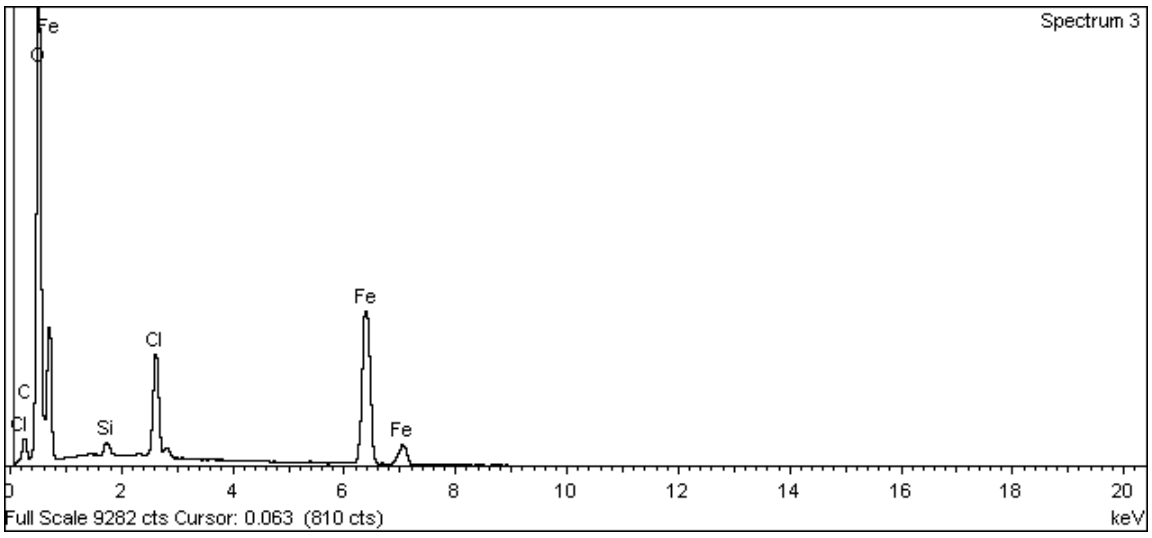

Figure A-333. Surface of cast iron insert and EDX analysis at position of Spectrum 3

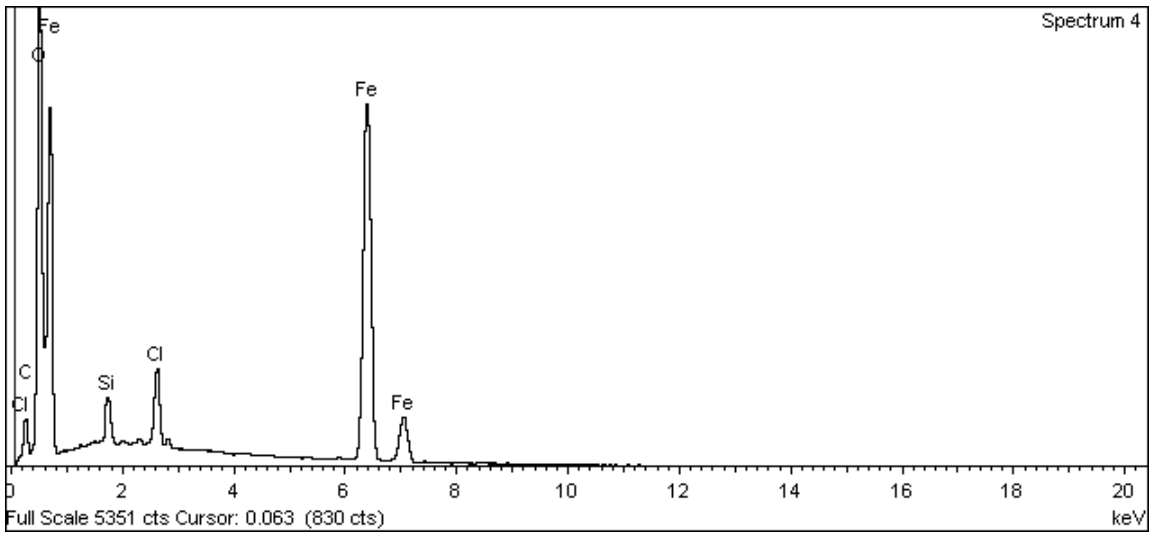

Figure A-334. Surface of cast iron insert and EDX analysis at position of Spectrum 4

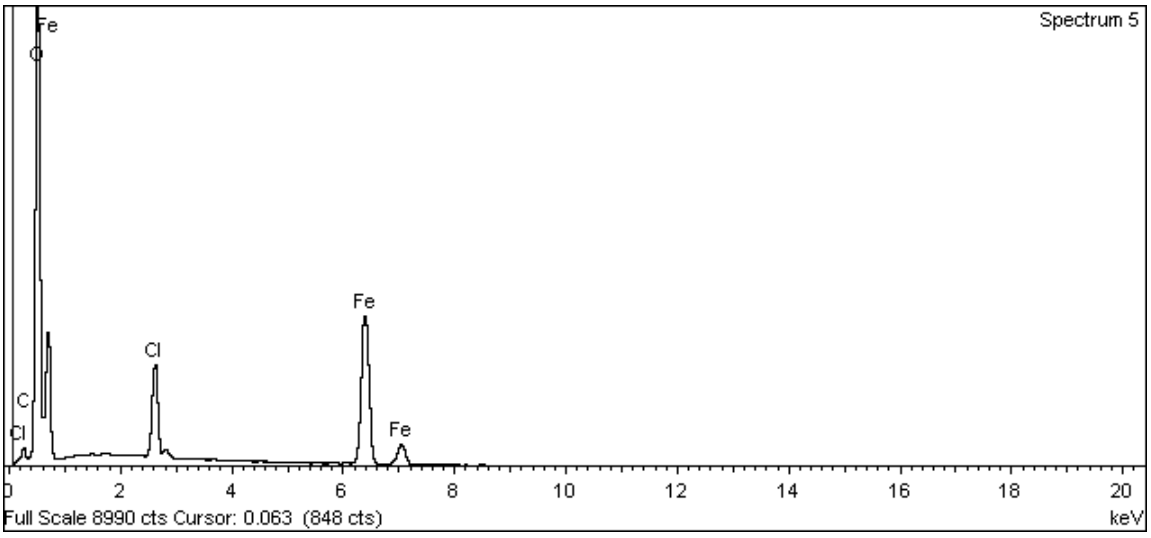

Figure A-335. Surface of cast iron insert and EDX analysis at position of Spectrum 5

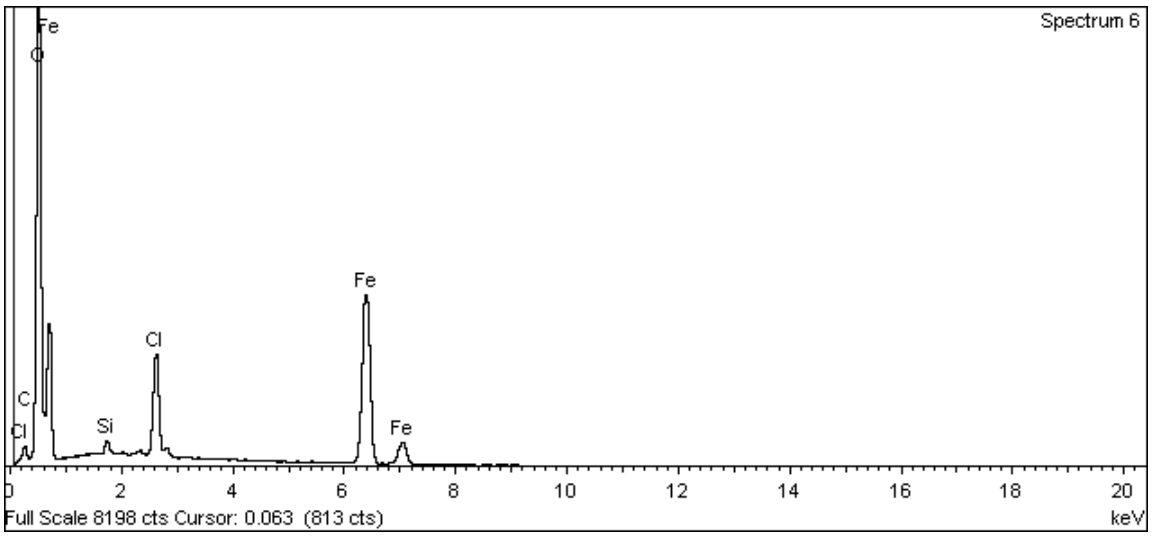

Figure A-336. Surface of cast iron insert and EDX analysis at position of Spectrum 6

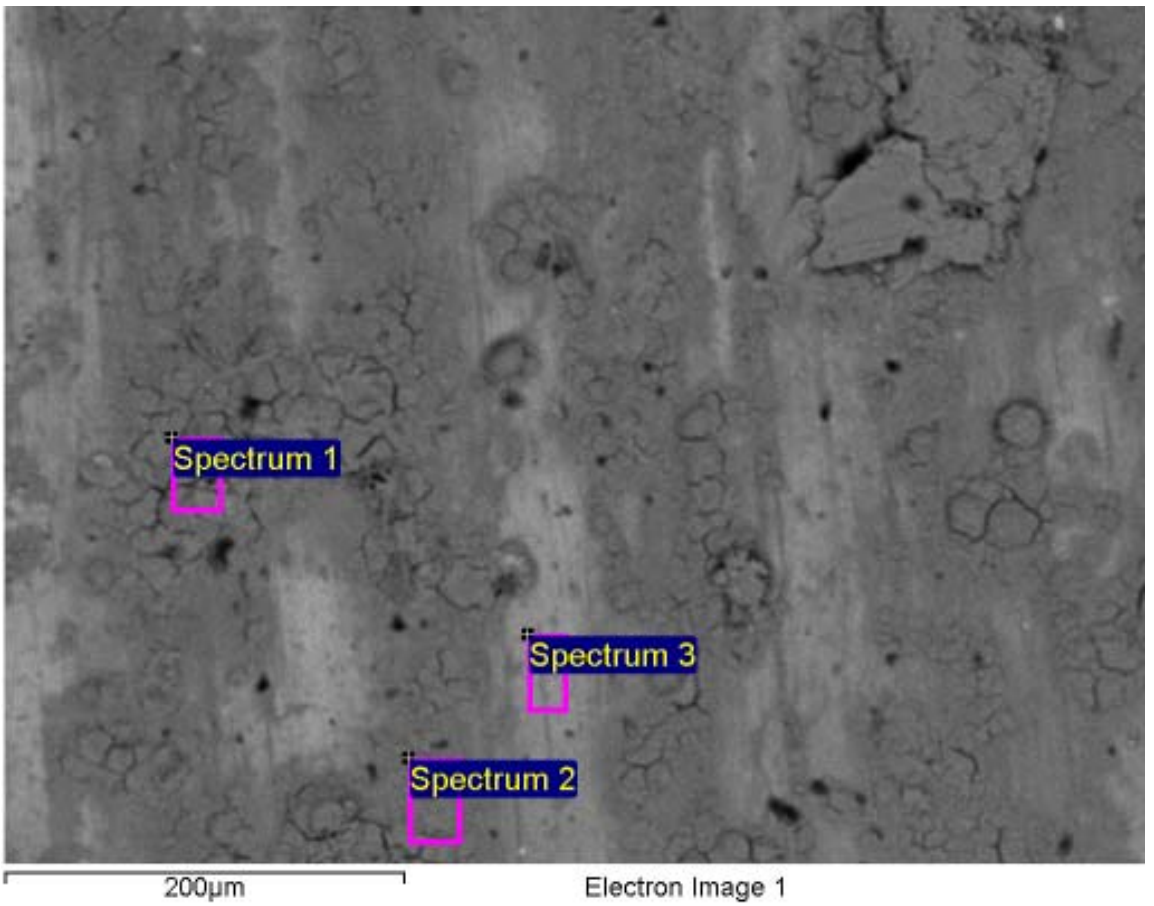

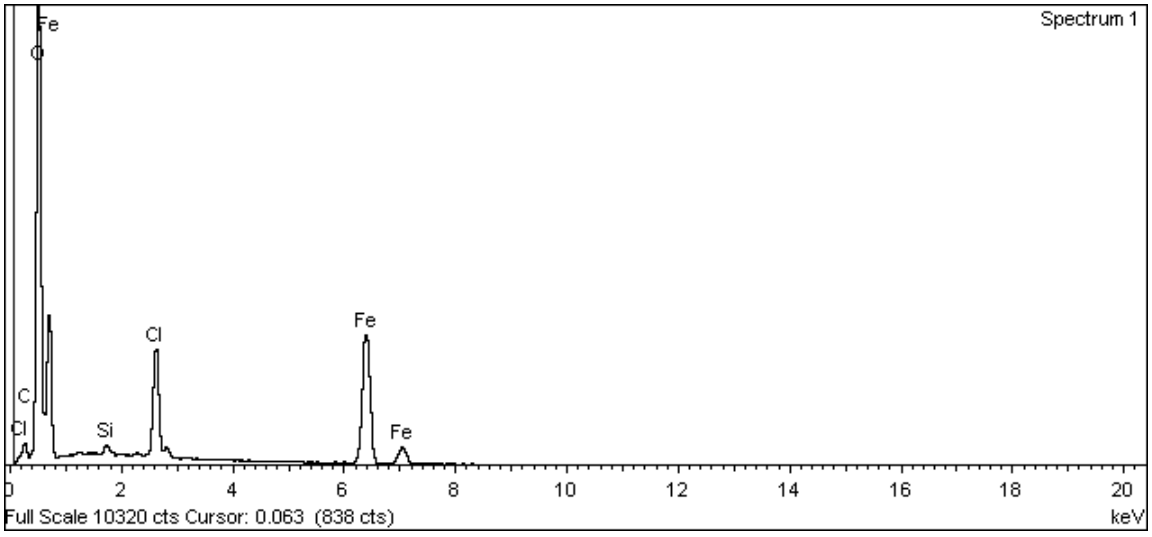

Figure A-337. Surface of cast iron insert and EDX analysis at position of Spectrum 1

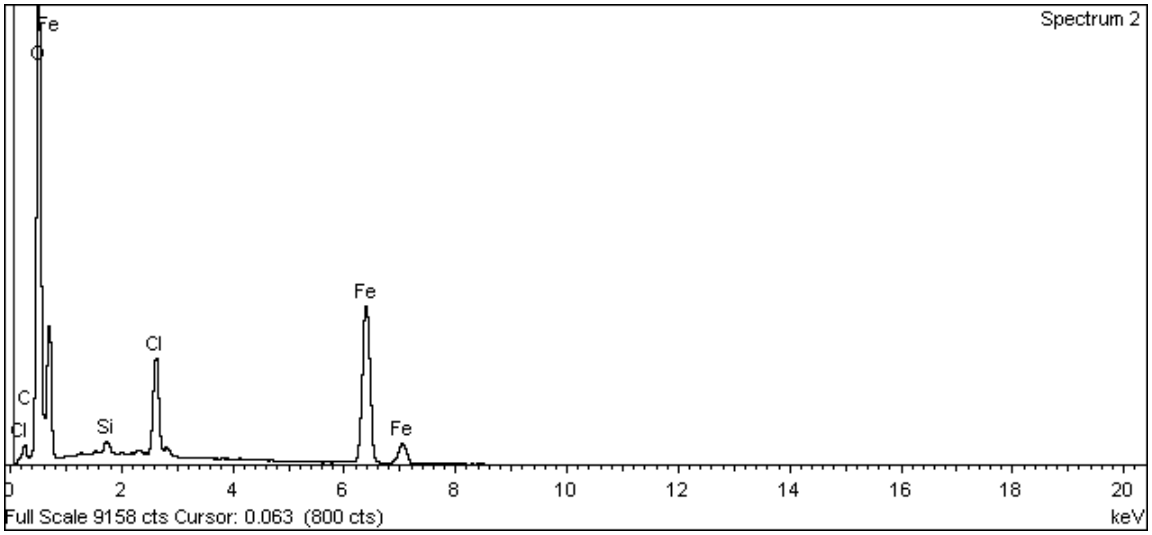

Figure A-338. Surface of cast iron insert and EDX analysis at position of Spectrum 2

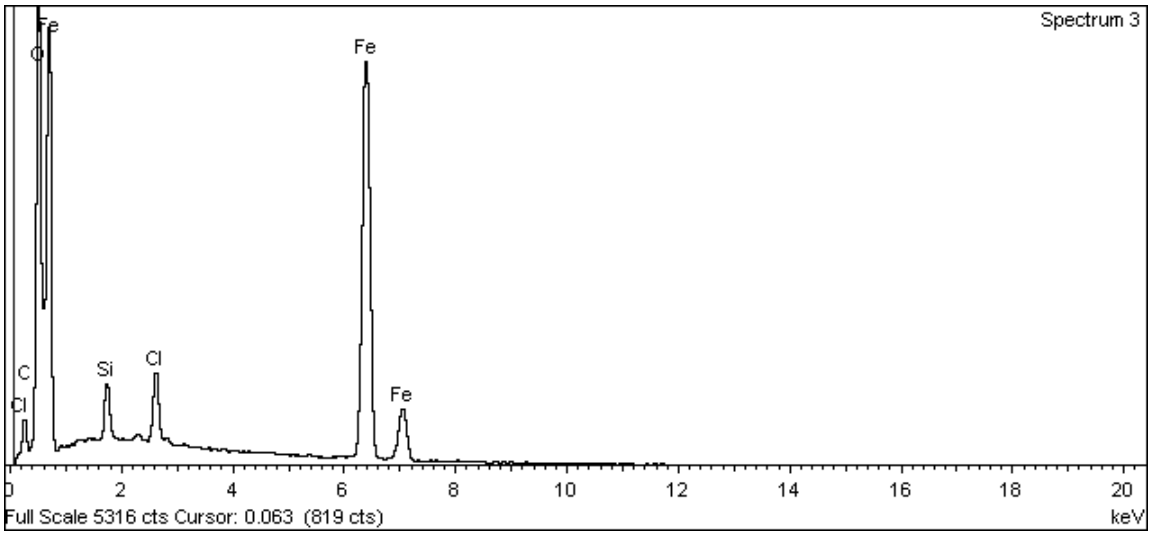

Figure A-339. Surface of cast iron insert and EDX analysis at position of Spectrum 3

Pit in Cast Iron Insert opposite hole in can

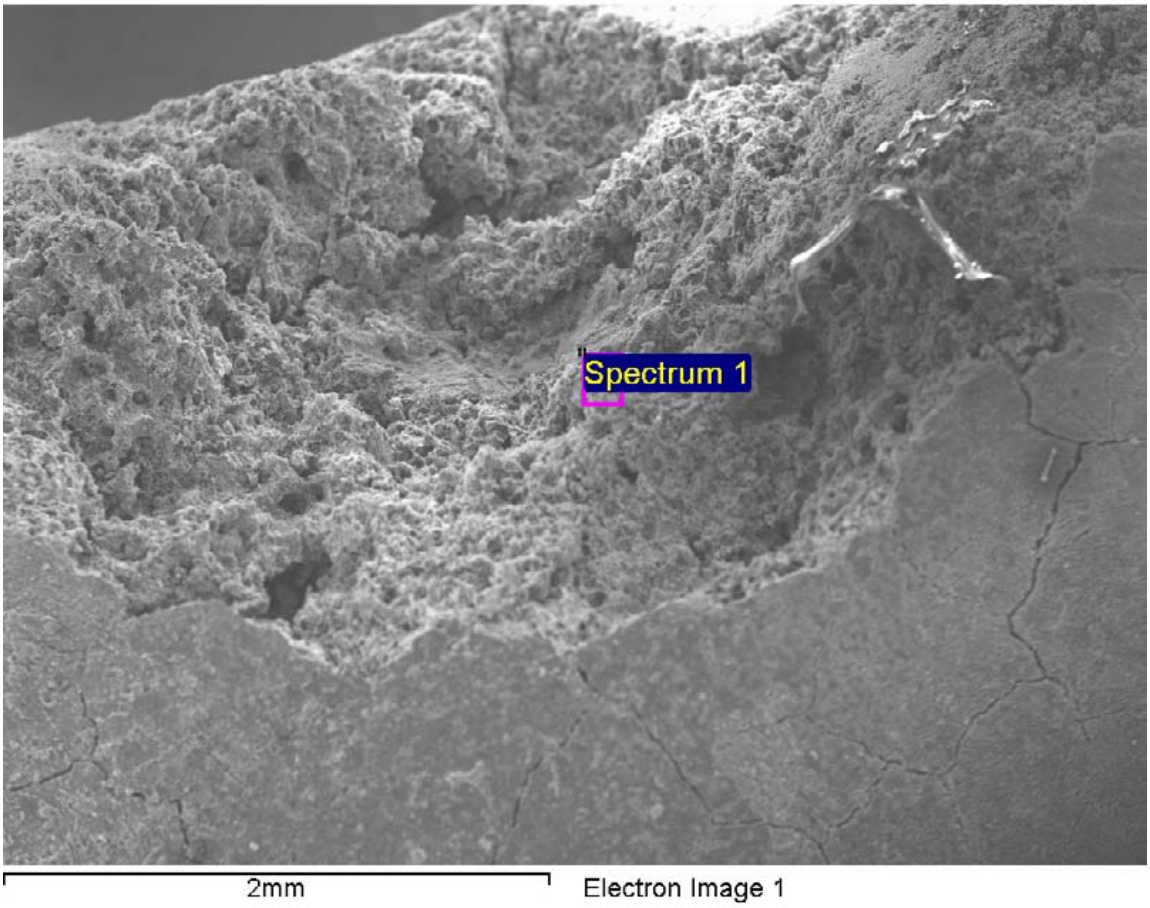

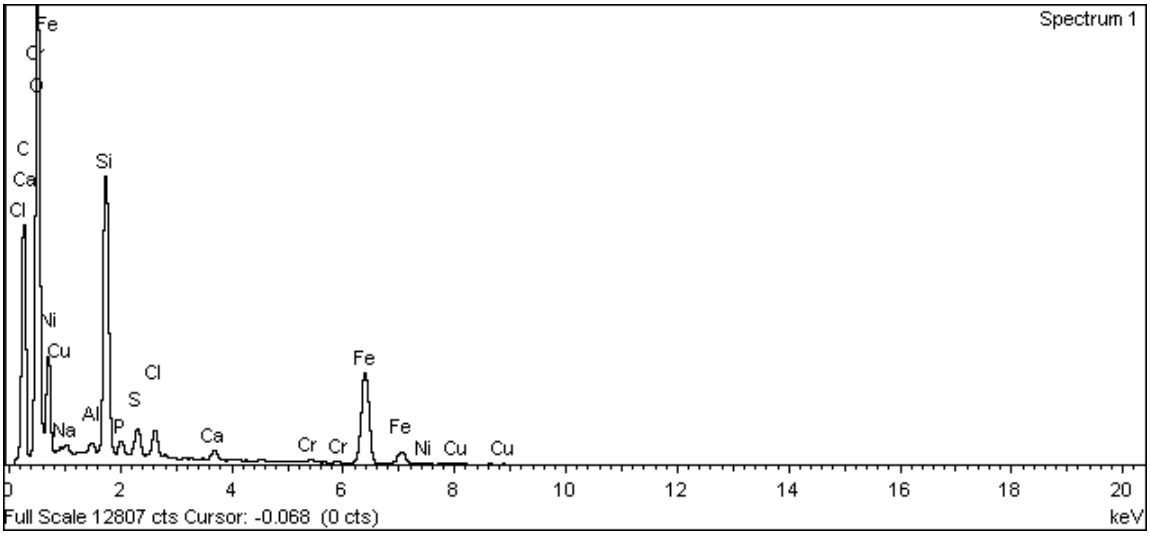

Figure A-340. Surface of pit in cast iron insert opposite hole in canister and EDX analysis at position of Spectrum 1

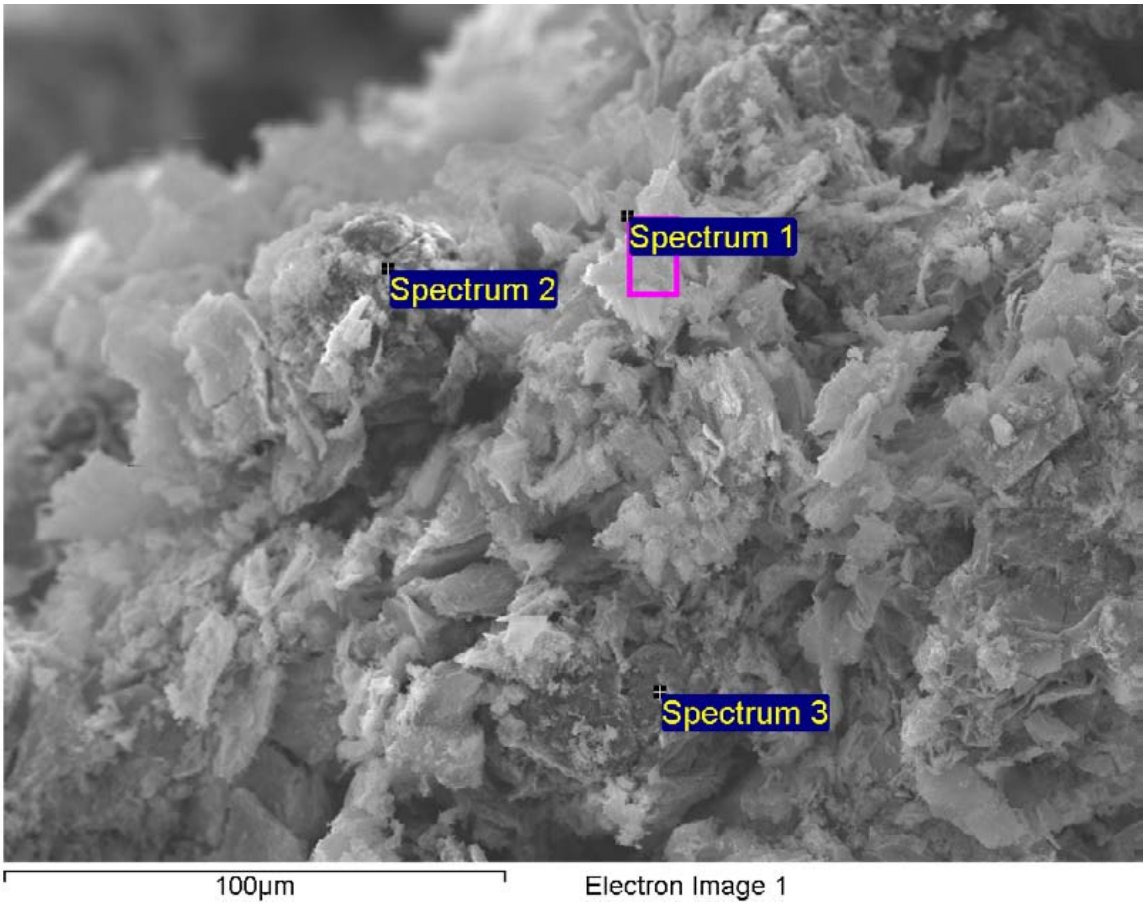

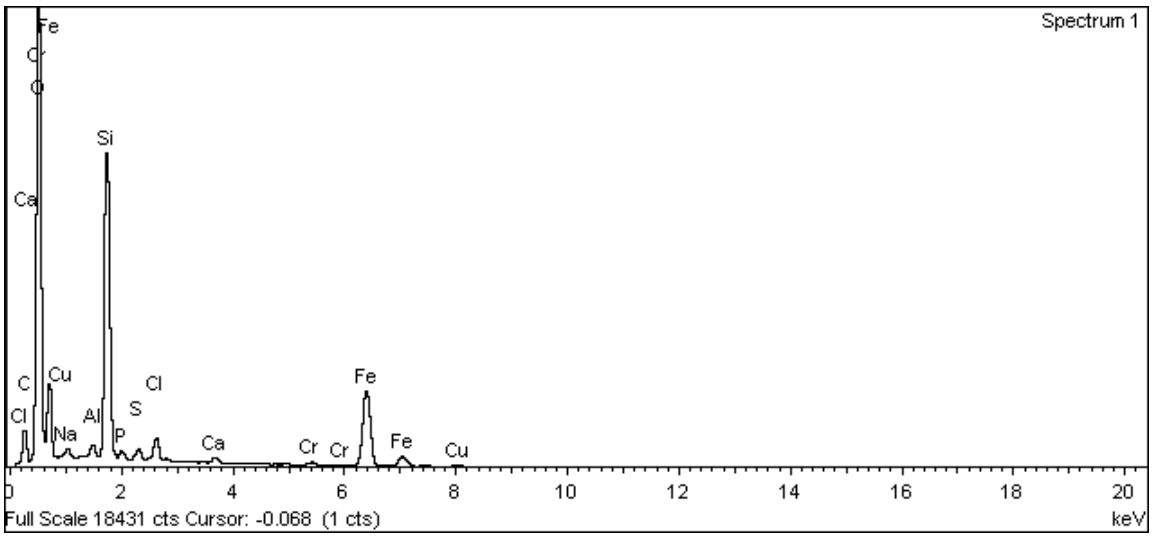

Figure A-341. Surface of pit in cast iron insert opposite hole in canister and EDX analysis at position of Spectrum 1

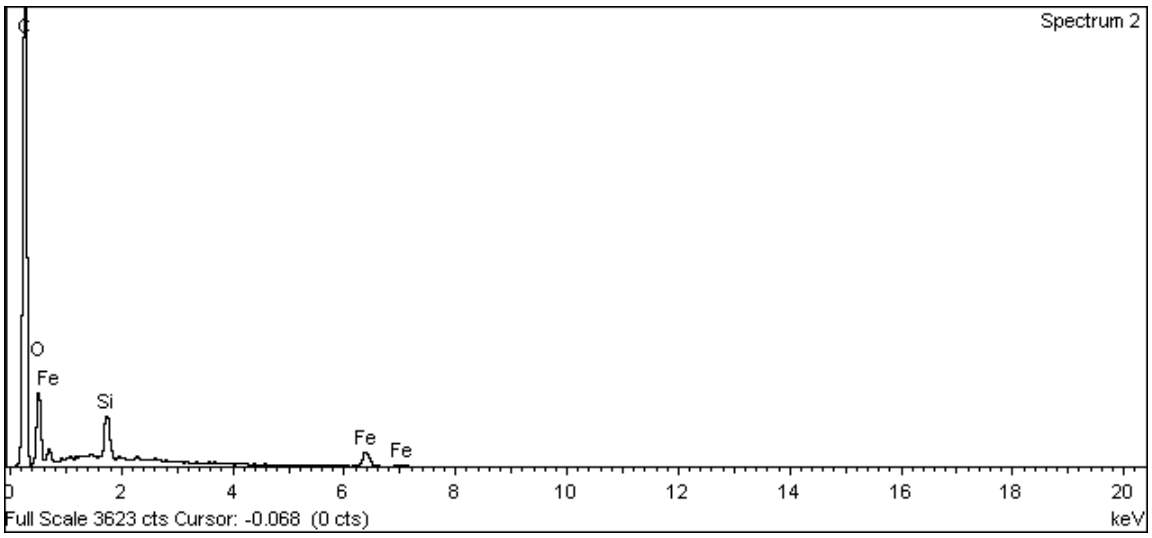

Figure A-342. Surface of pit in cast iron insert opposite hole in canister and EDX analysis at position of Spectrum 2

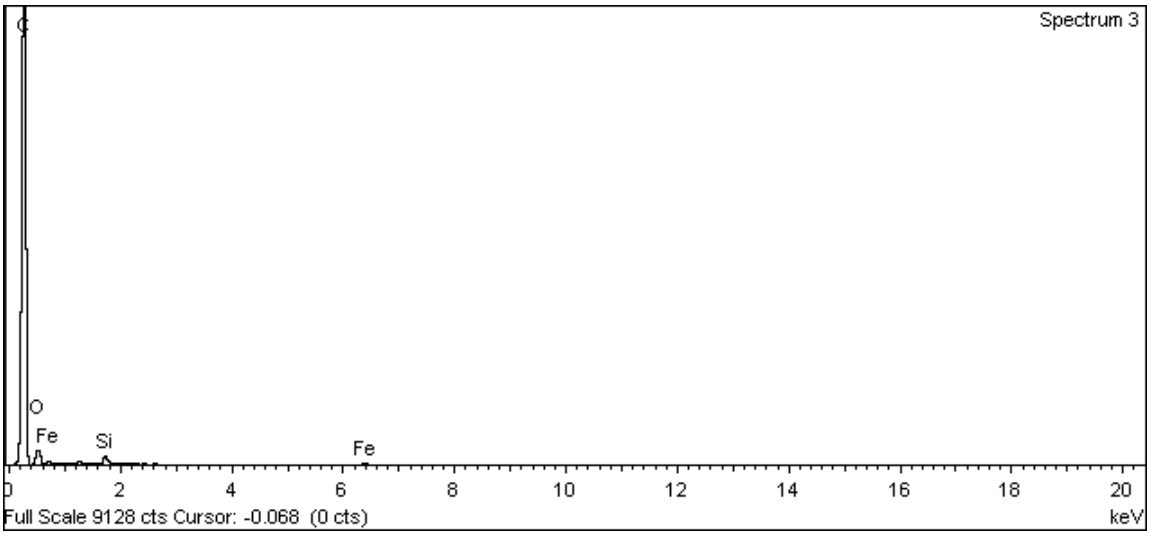

Figure A-343. Surface of pit in cast iron insert opposite hole in canister and EDX analysis at position of Spectrum 3

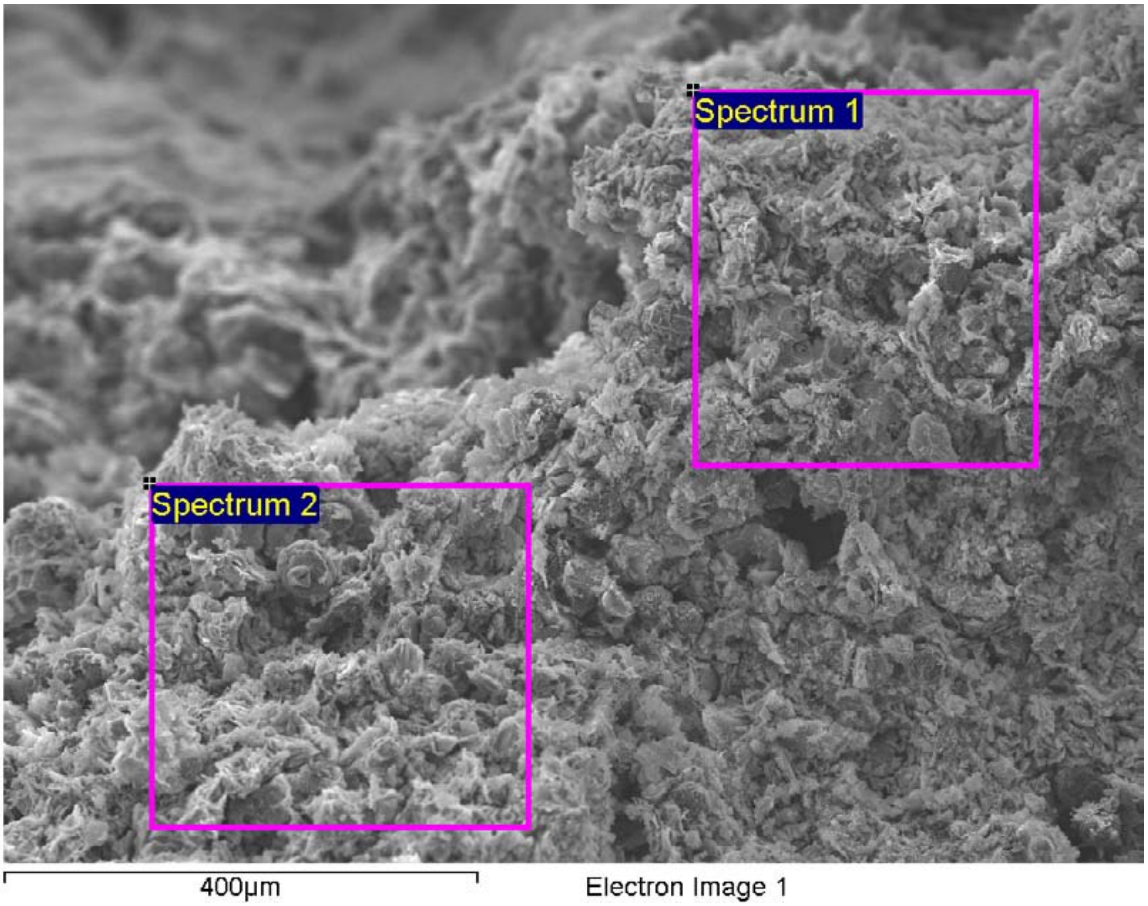

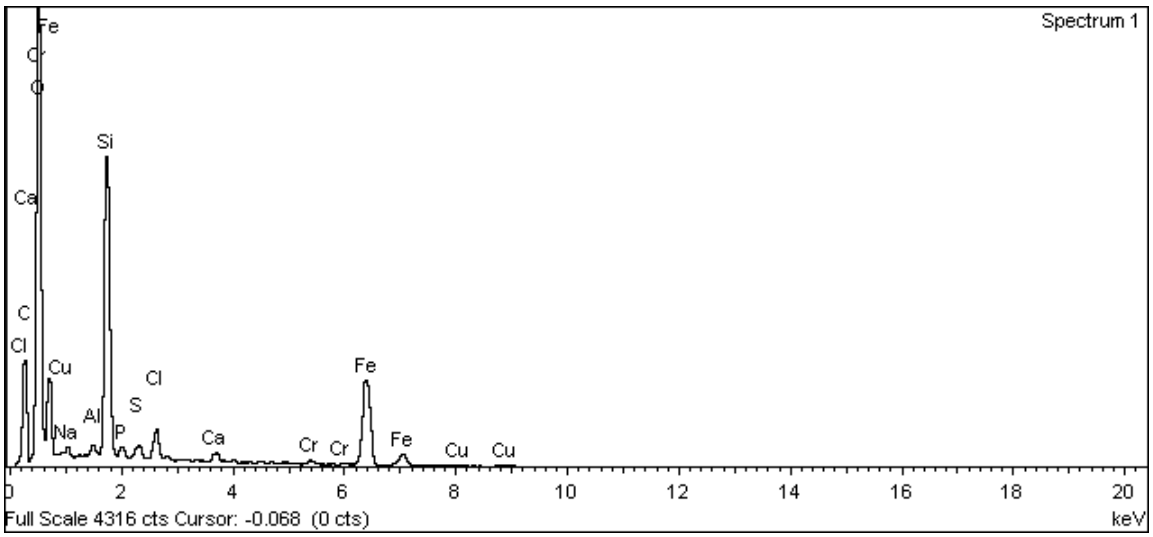

Figure A-344. Surface of pit in cast iron insert opposite hole in canister and EDX analysis at position of Spectrum 1

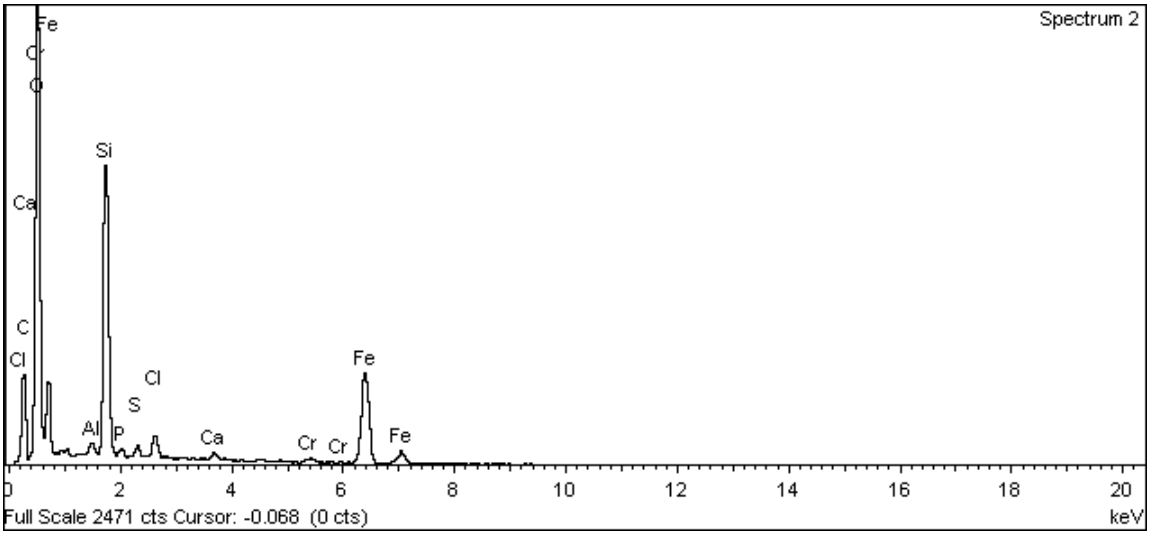

Figure A-345. Surface of pit in cast iron insert opposite hole in canister and EDX analysis at position of Spectrum 2

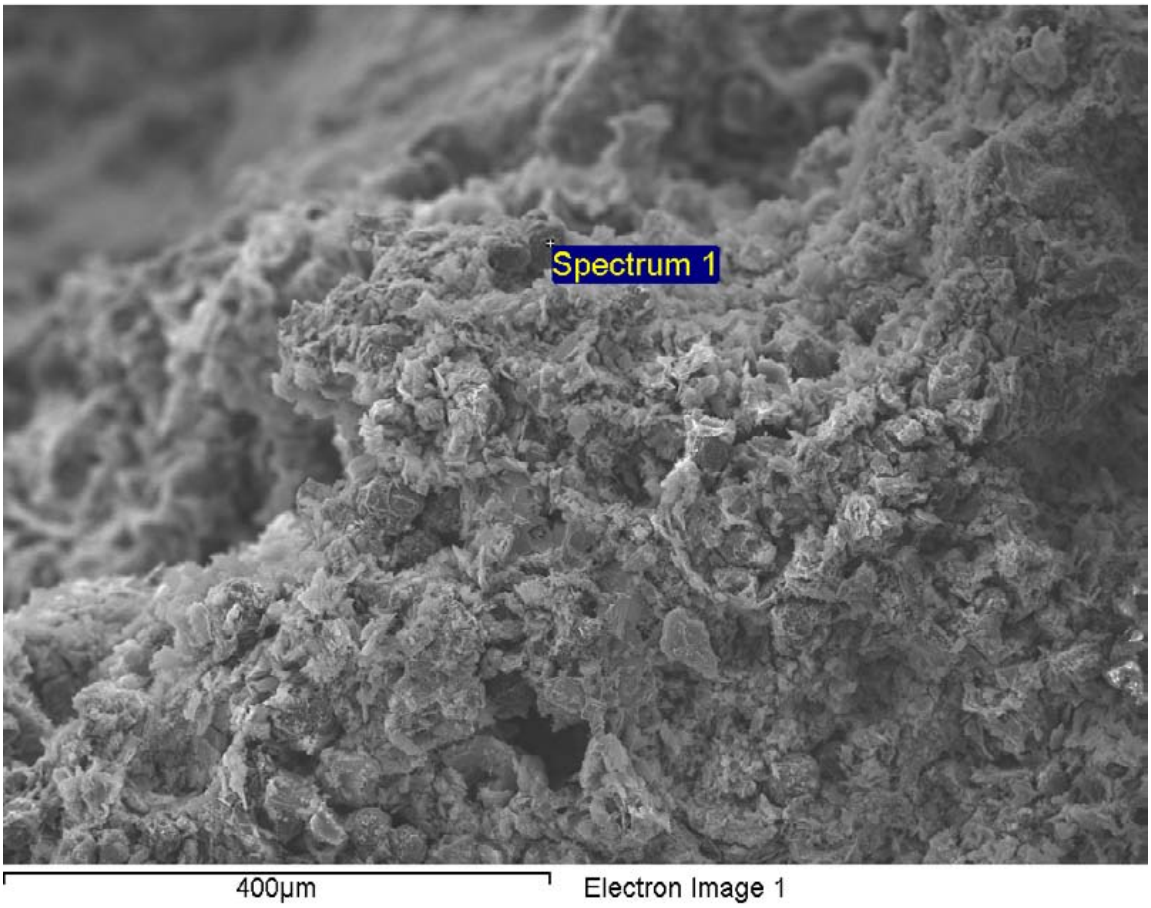

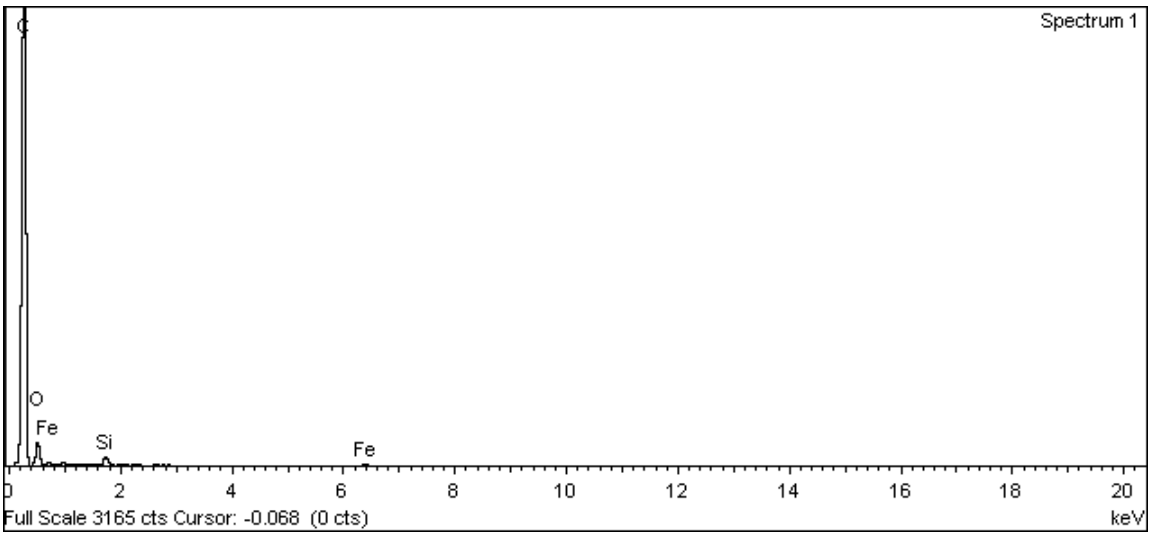

Figure A-346. Surface of pit in cast iron insert opposite hole in canister and EDX analysis at position of Spectrum 1

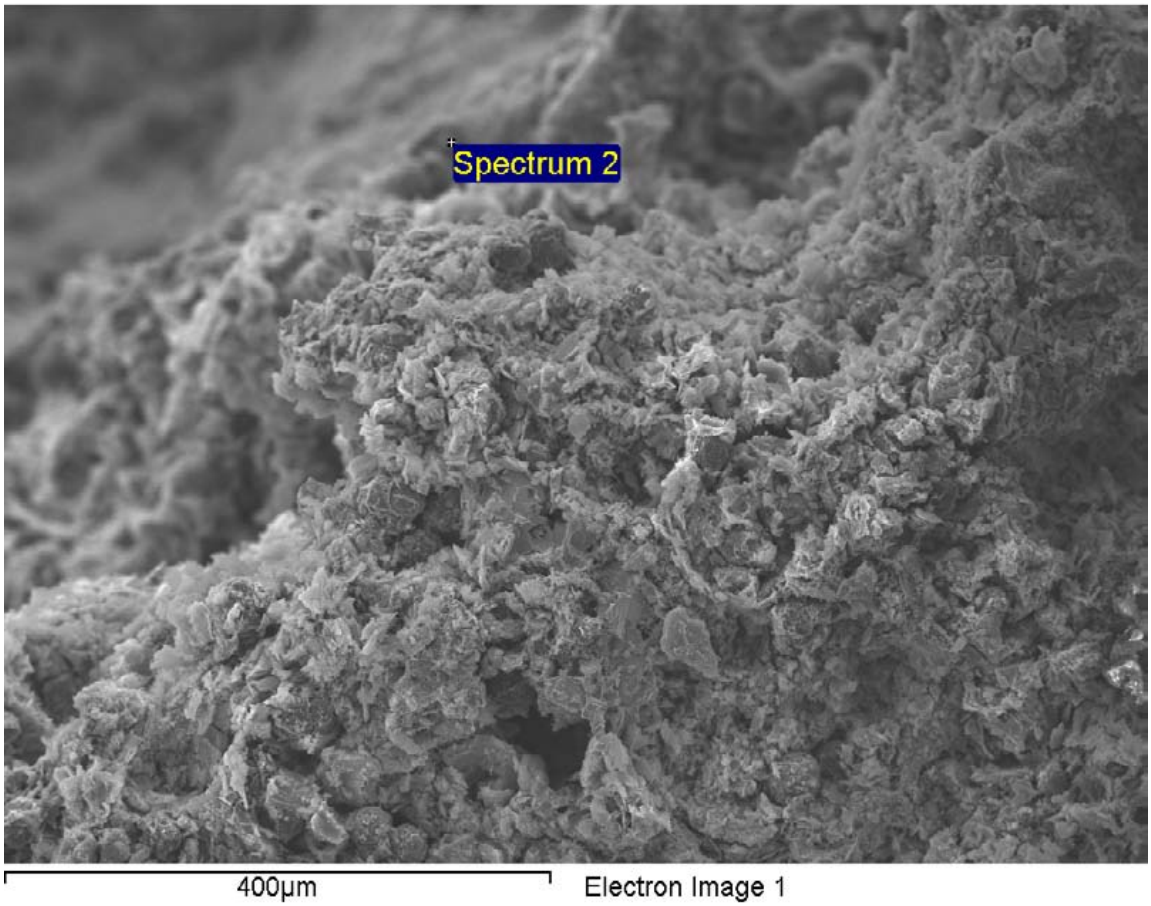

Figure A-347. Surface of pit in cast iron insert opposite hole in canister and EDX analysis at position of Spectrum 2

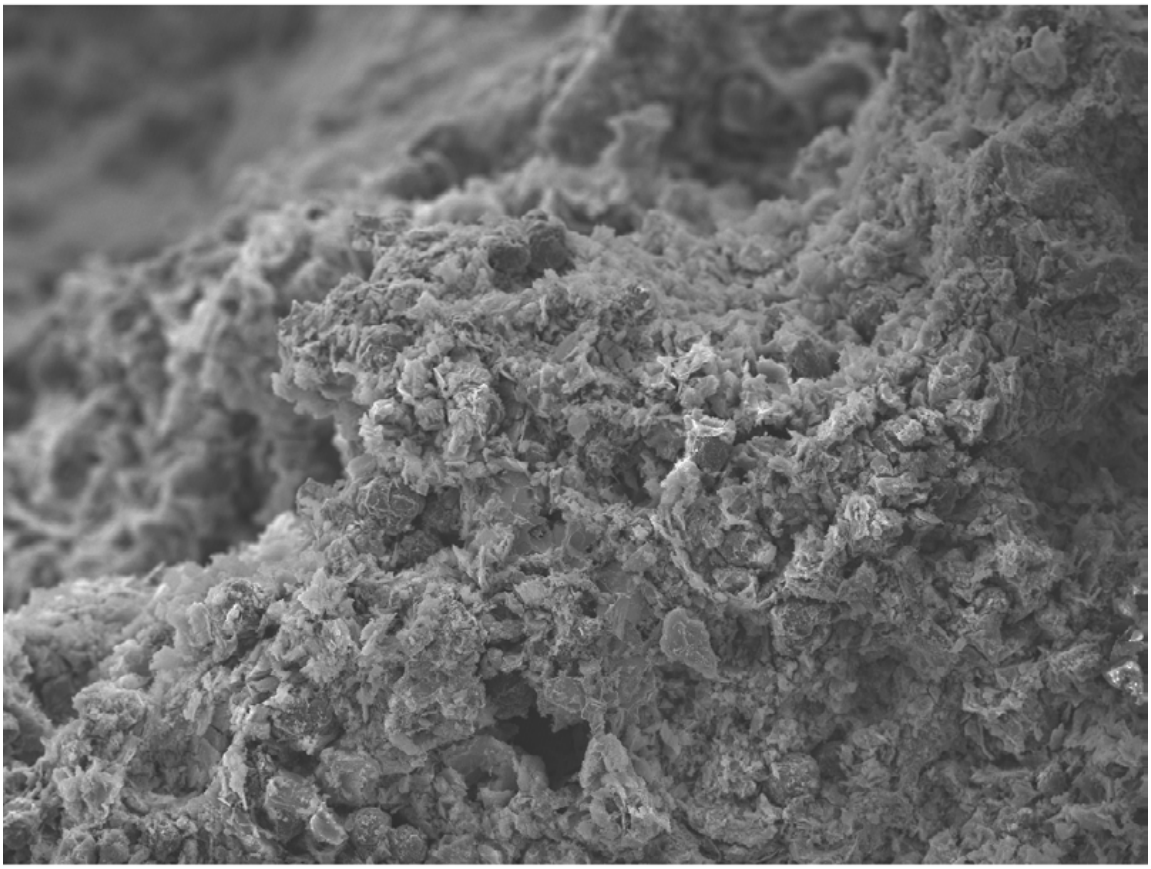

Figure A-348. Surface of pit in cast iron insert opposite hole in canister and EDX analysis – Sum Spectrum

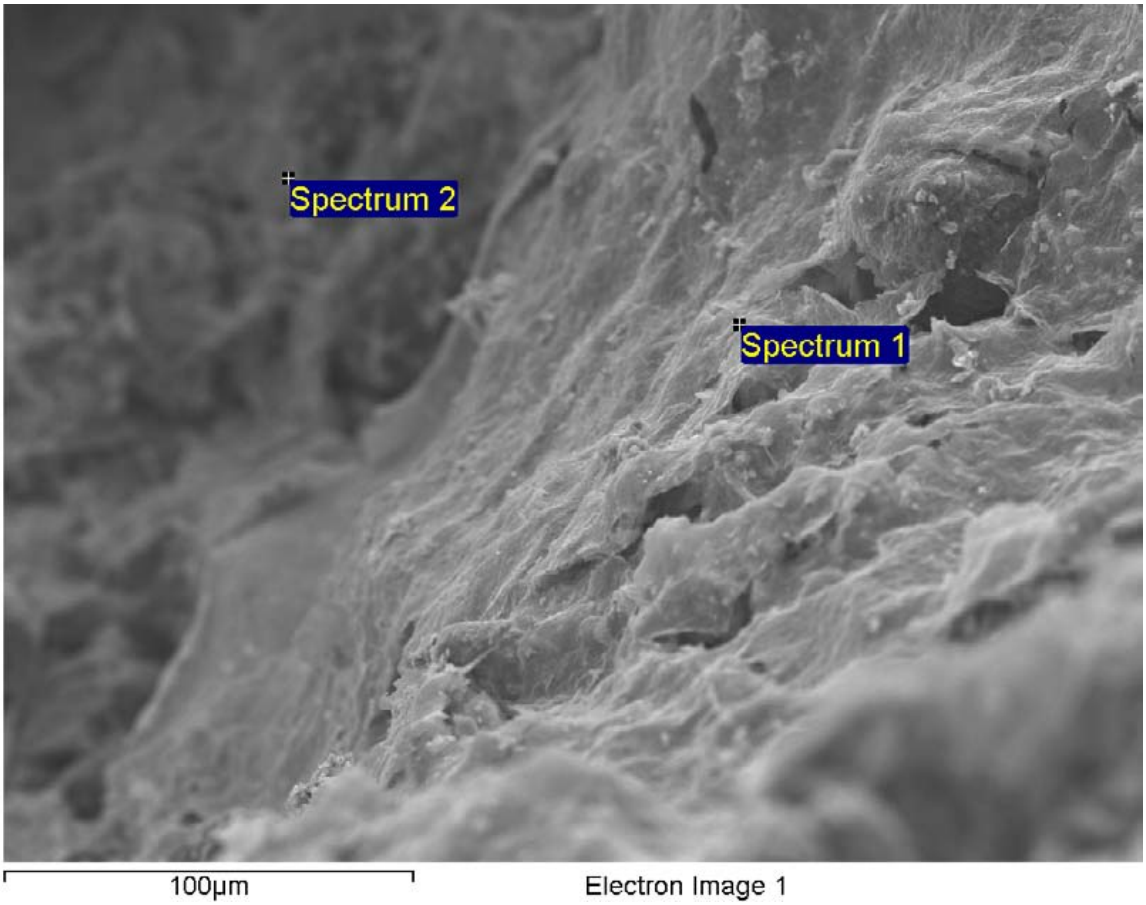

Figure A-349. Surface of pit in cast iron insert opposite hole in canister and EDX analysis at position of Spectrum 1

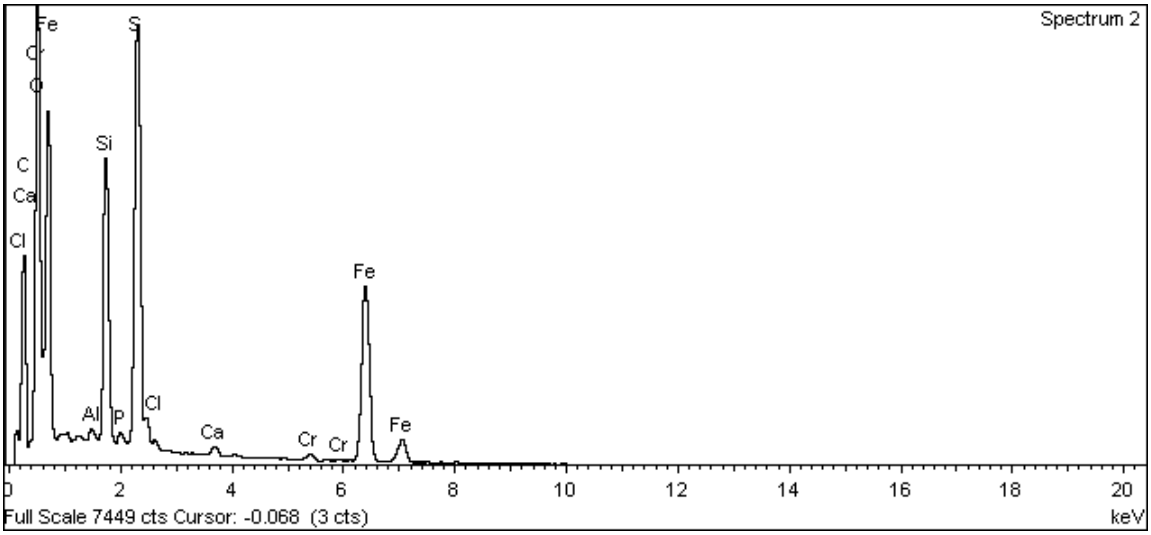

Figure A-350. Surface of pit in cast iron insert opposite hole in canister and EDX analysis at position of Spectrum 2

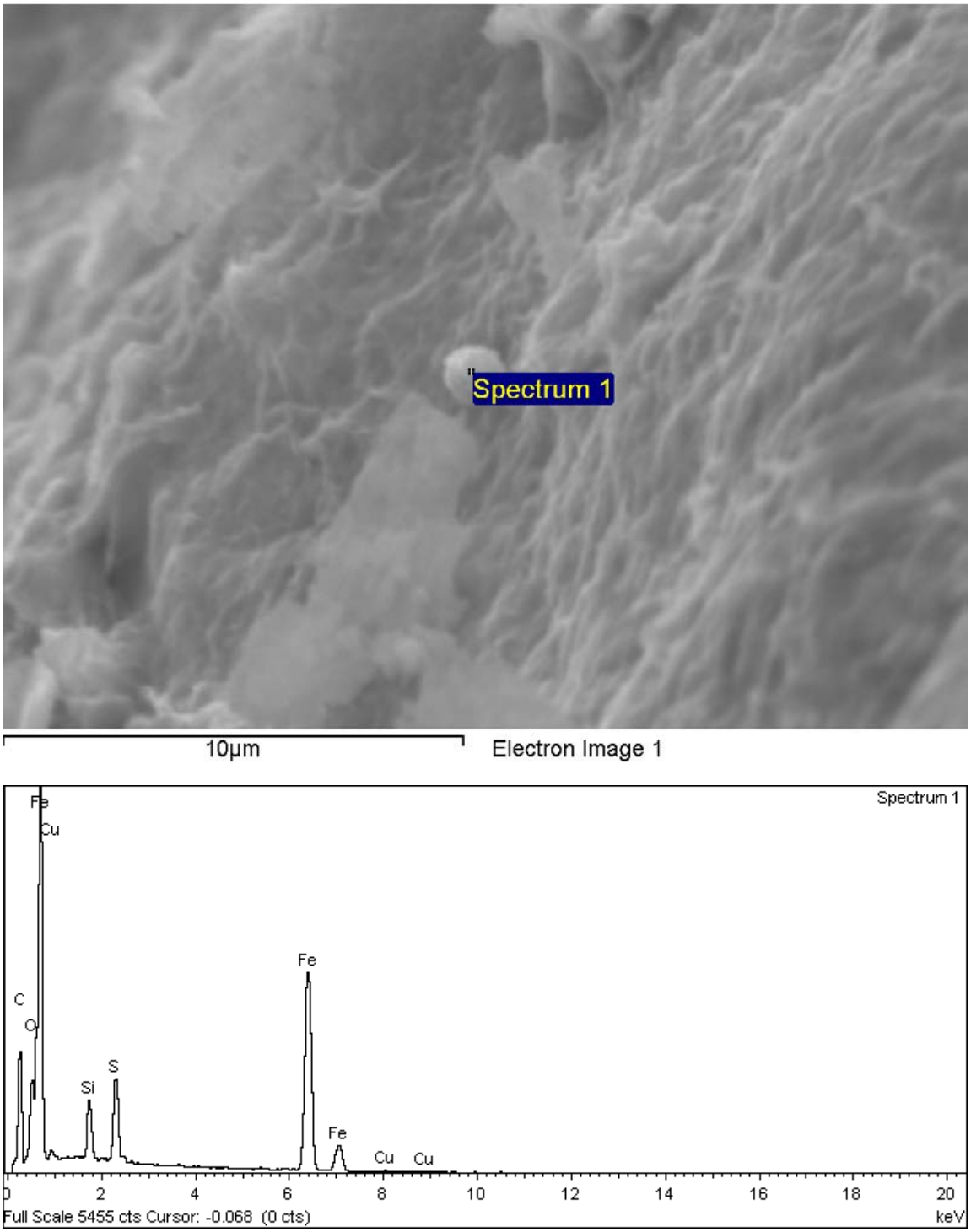

Figure A-351. Surface of pit in cast iron insert opposite hole in canister and EDX analysis at position of Spectrum 1

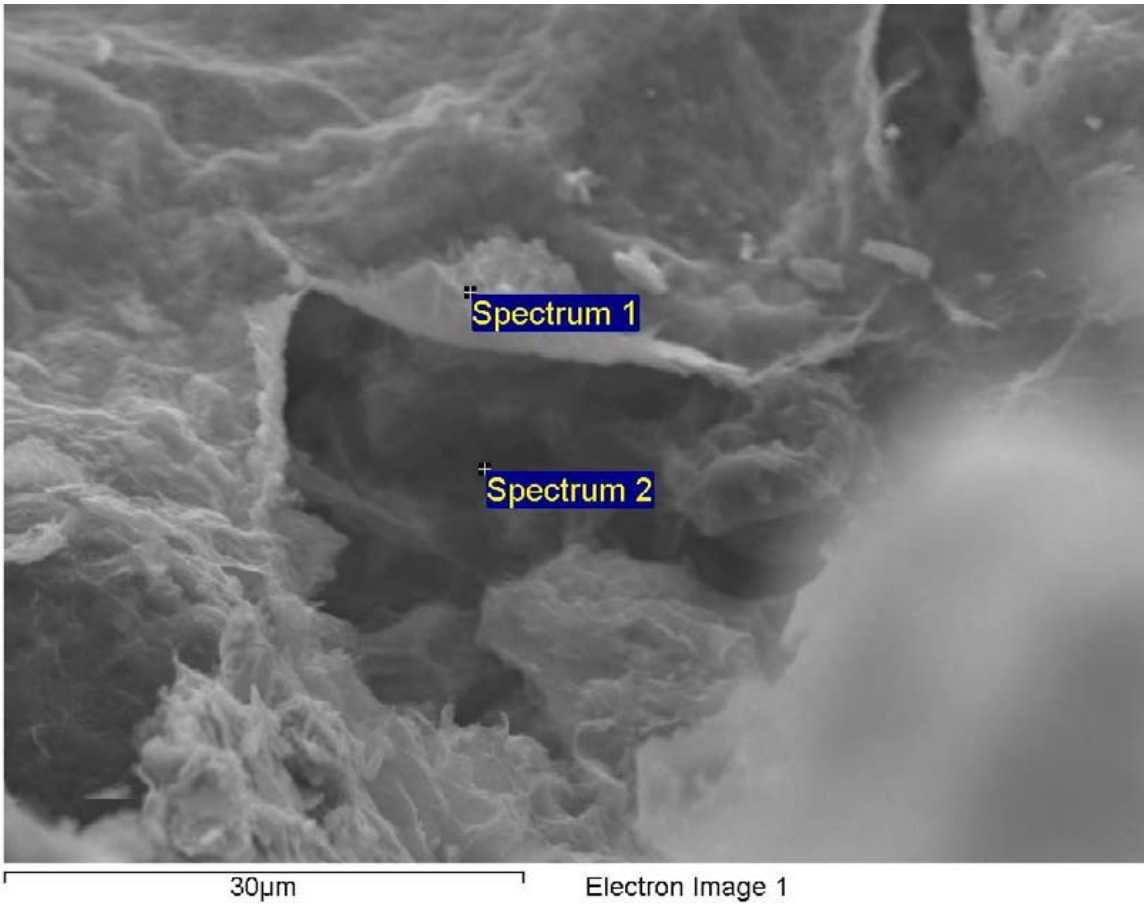

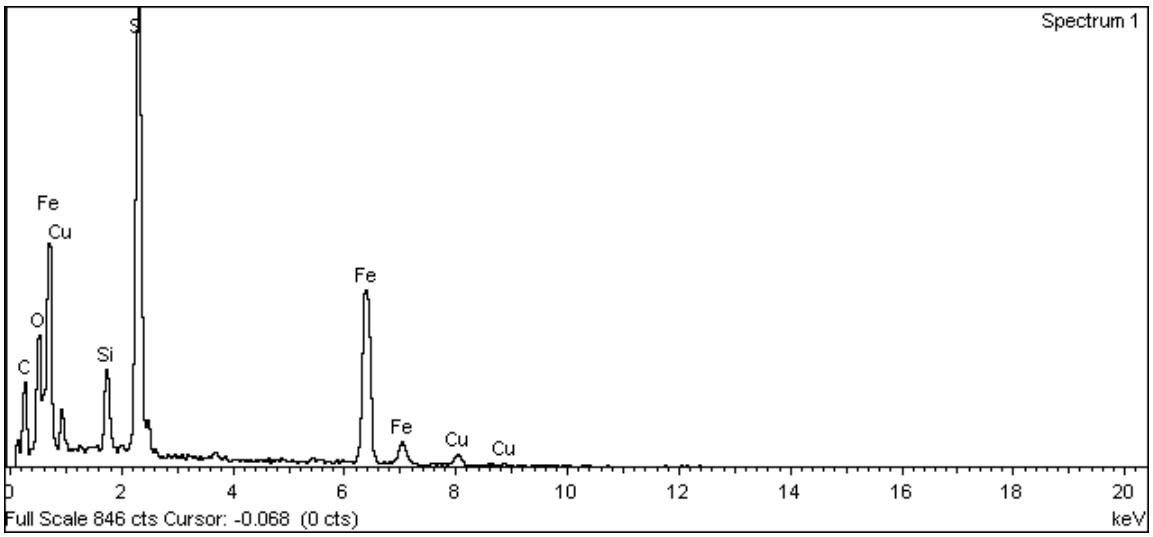

Figure A-352. Surface of pit in cast iron insert opposite hole in canister and EDX analysis at position of Spectrum 1

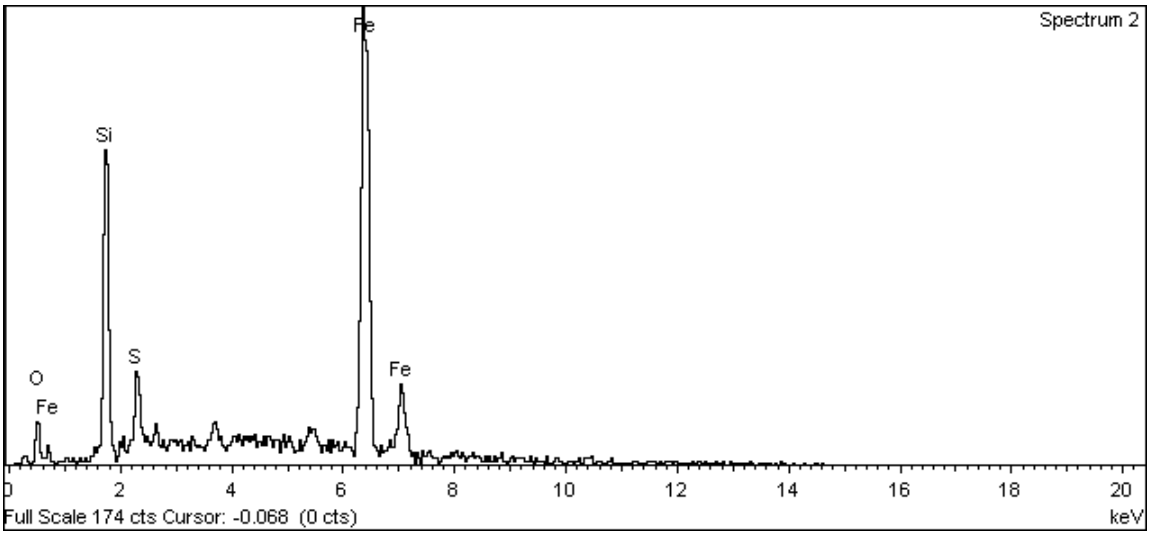

Figure A-353. Surface of pit in cast iron insert opposite hole in canister and EDX analysis at position of Spectrum 2

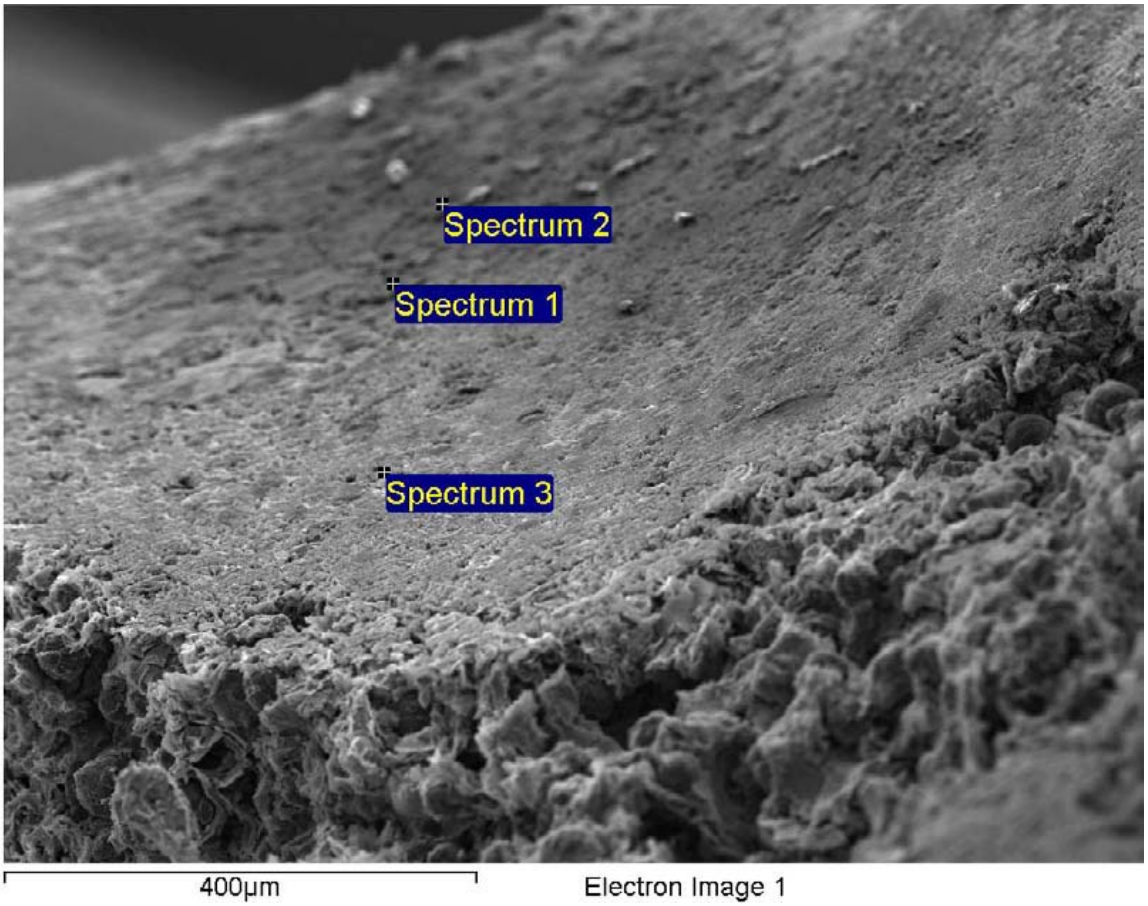

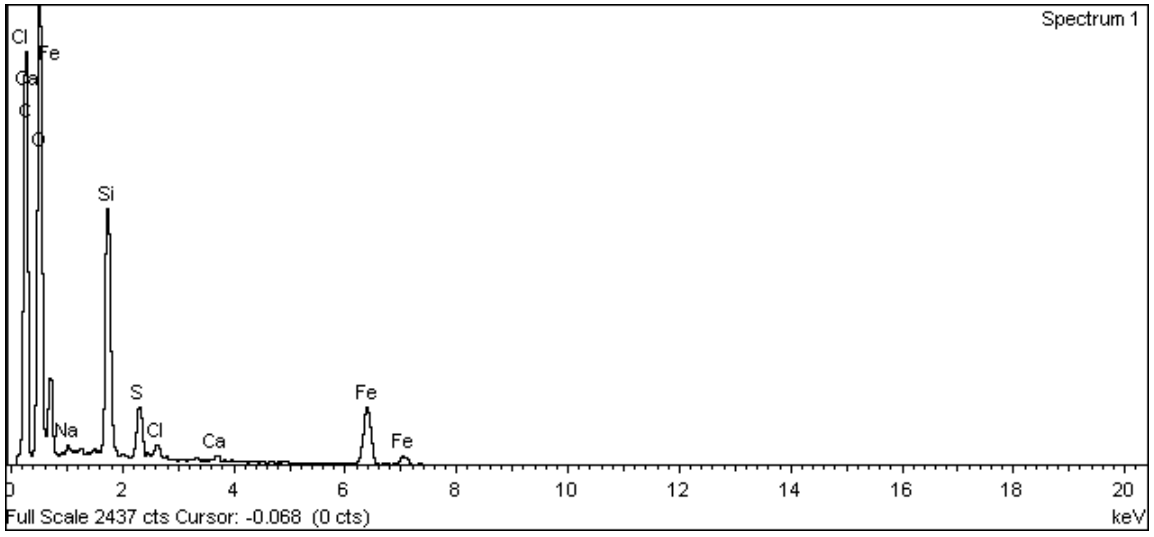

Figure A-354. Surface of pit in cast iron insert opposite hole in canister and EDX analysis at position of Spectrum 1

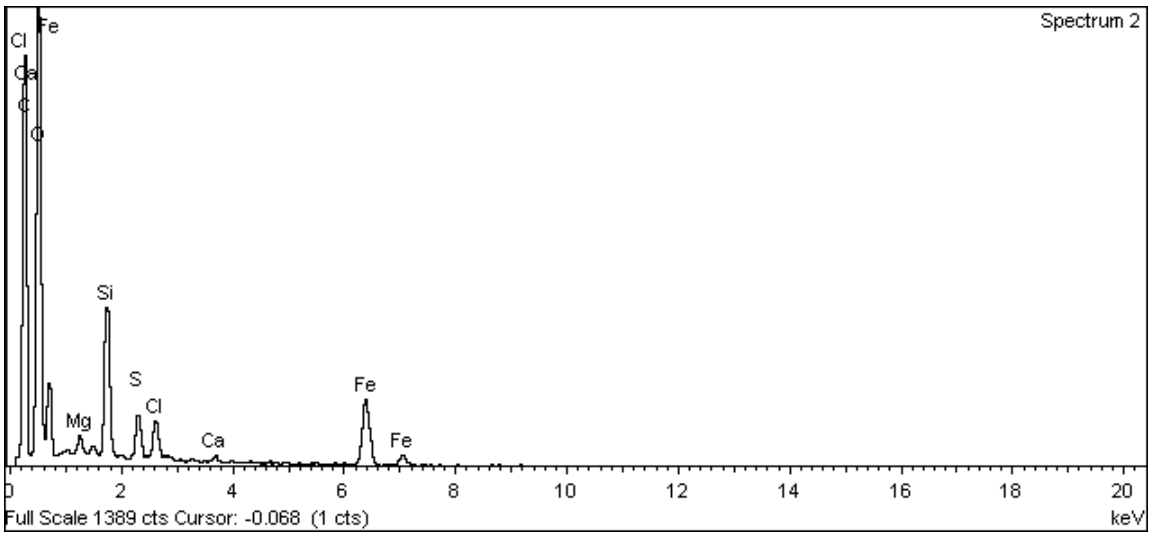

Figure A-355. Surface of pit in cast iron insert opposite hole in canister and EDX analysis at position of Spectrum 2

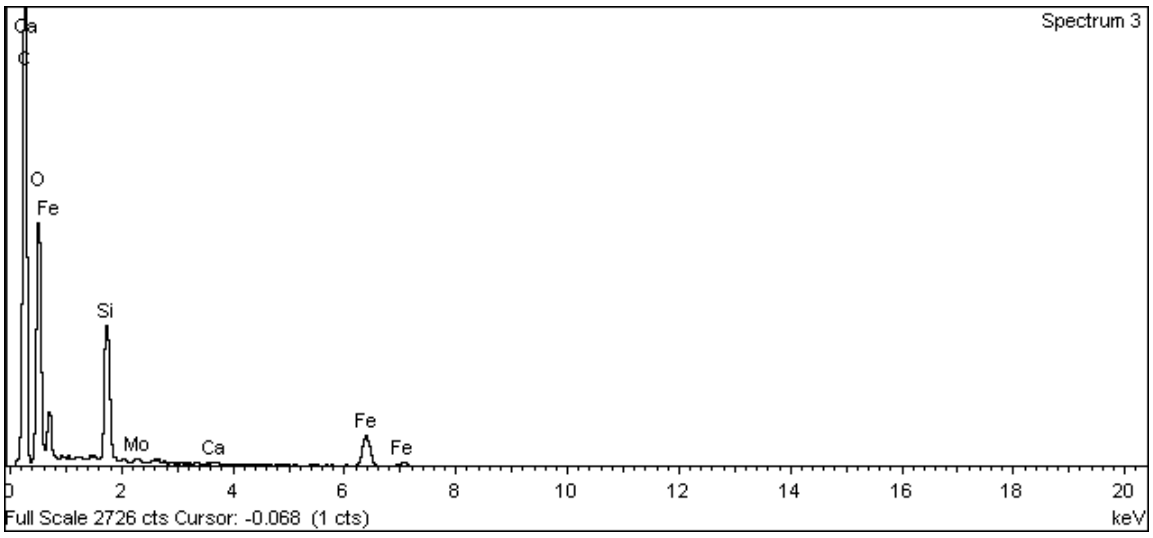

Figure A-356. Surface of pit in cast iron insert opposite hole in canister and EDX analysis at position of Spectrum 3

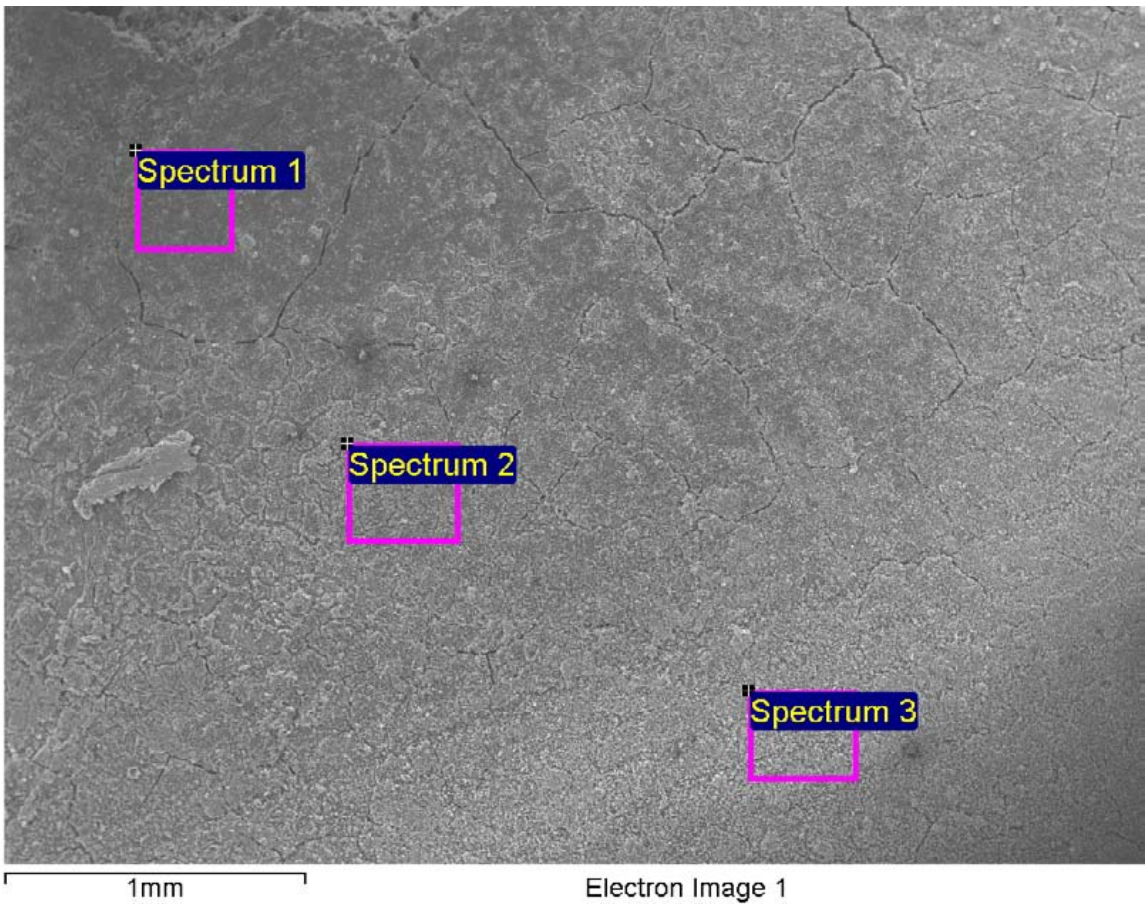

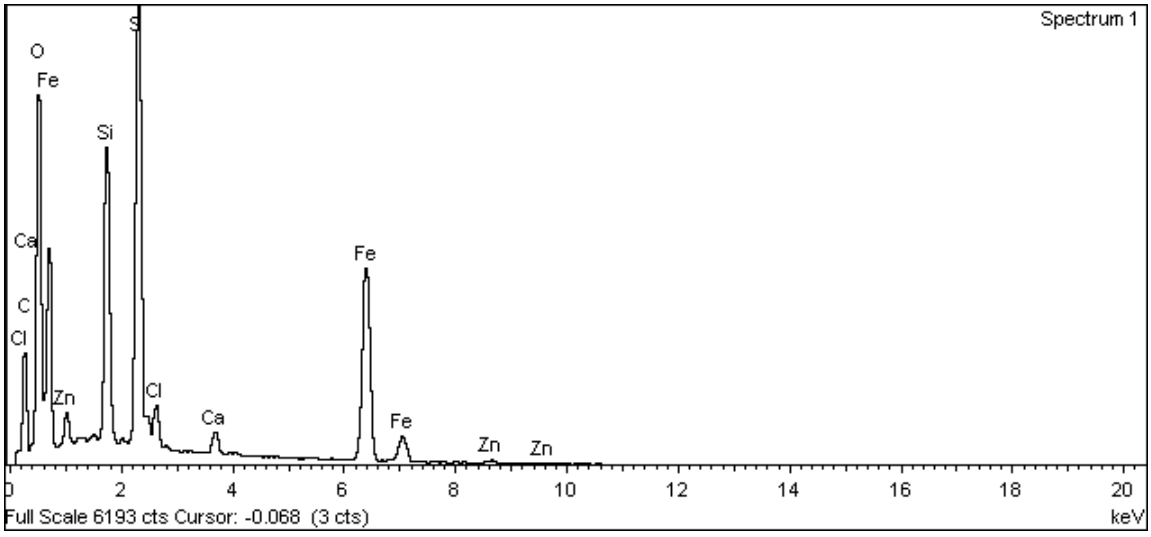

Figure A-357. Surface of pit in cast iron insert opposite hole in canister and EDX analysis at position of Spectrum 1

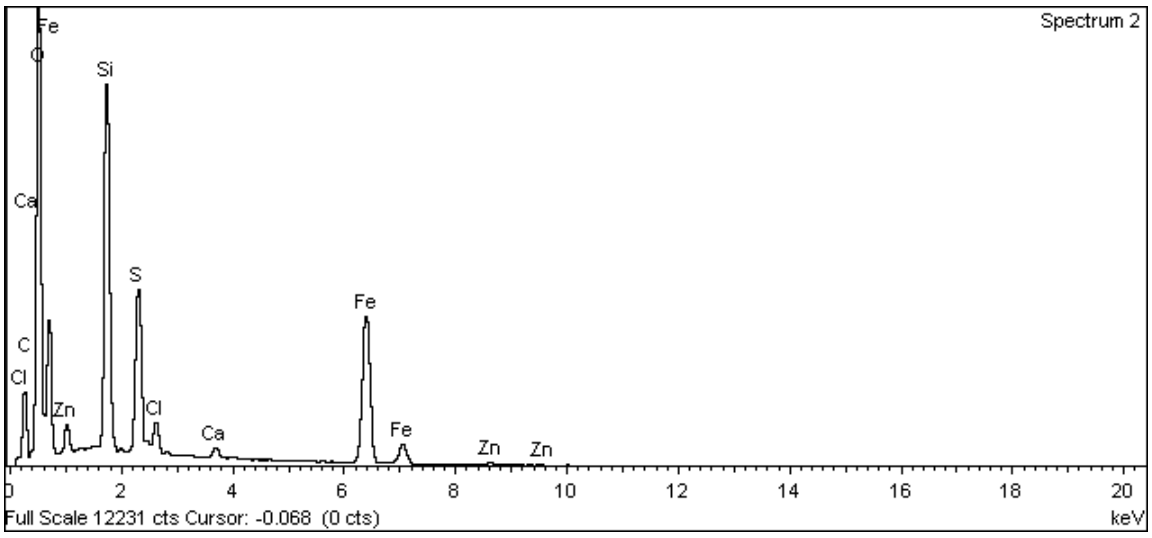

Figure A-358. Surface of pit in cast iron insert opposite hole in canister and EDX analysis at position of Spectrum 2

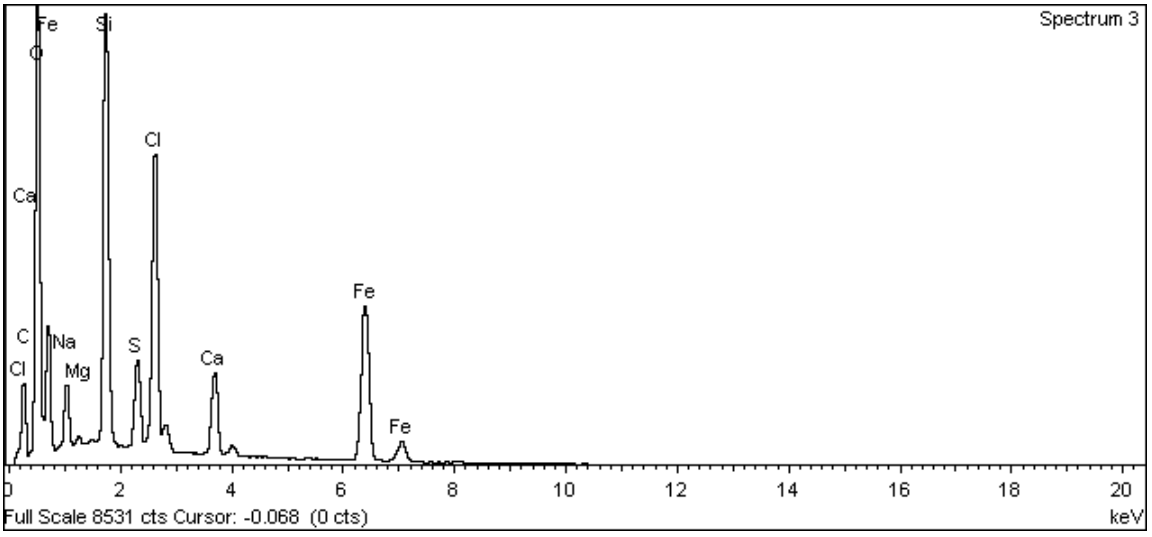

Figure A-359. Surface of pit in cast iron insert opposite hole in canister and EDX analysis at position of Spectrum 3

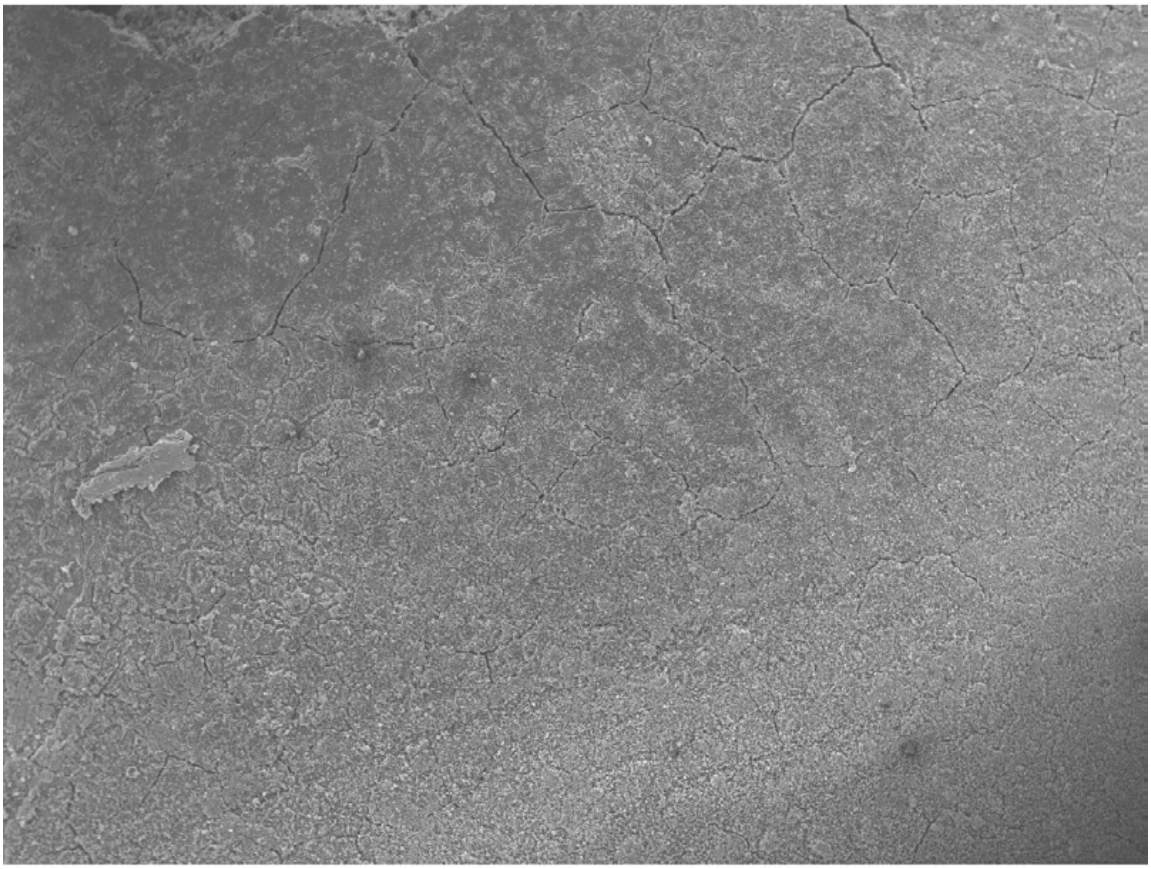

Figure A-360. Surface of pit in cast iron insert opposite hole in canister and EDX analysis – Sum Spectrum

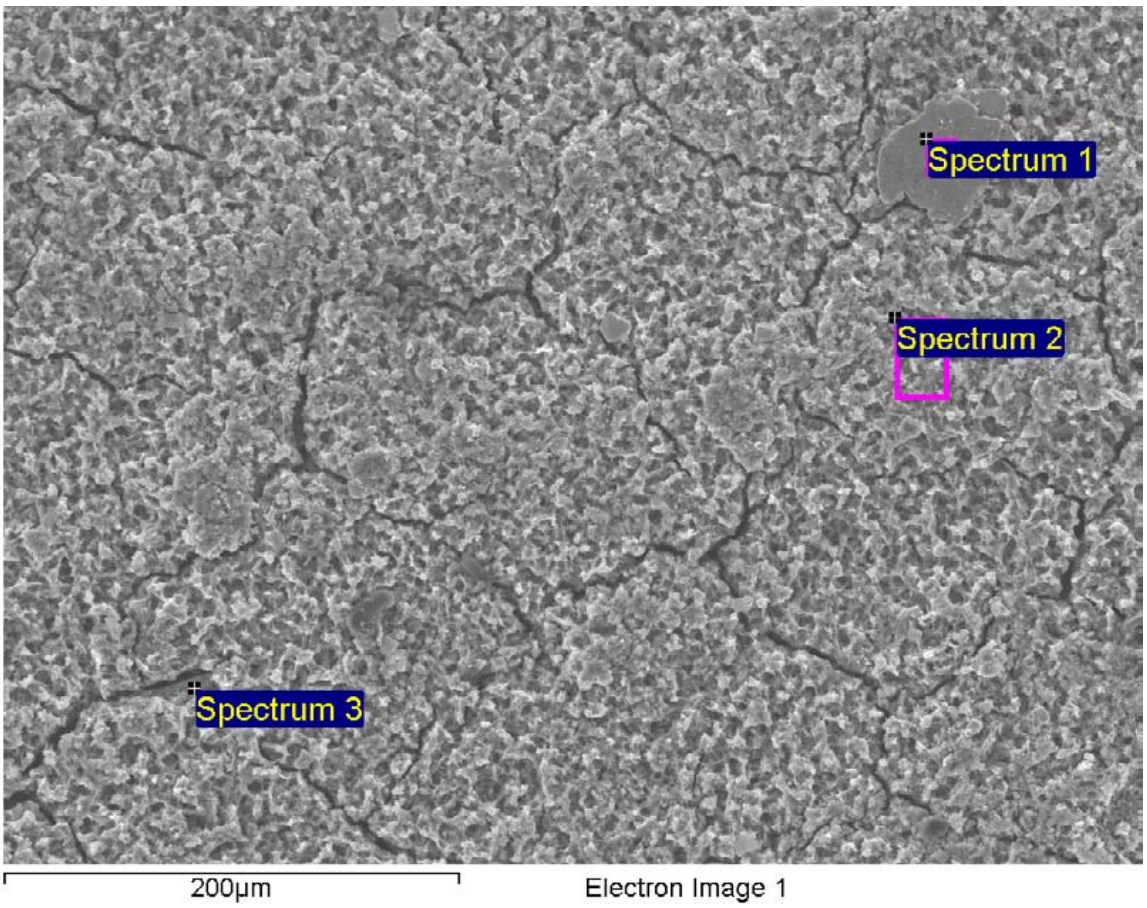

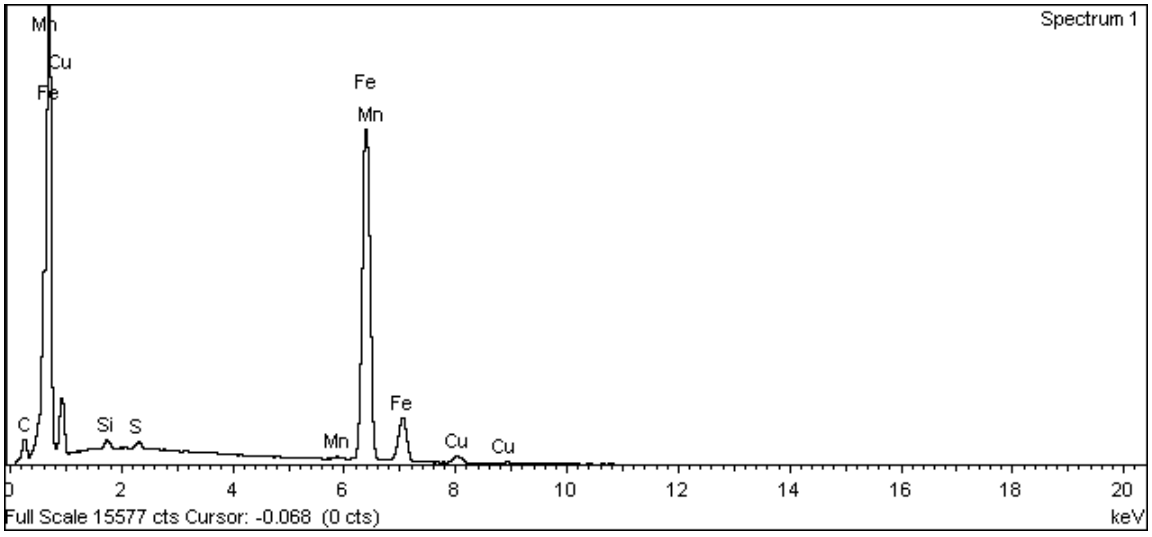

Figure A-361. Surface of pit in cast iron insert opposite hole in canister and EDX analysis at position of Spectrum 1

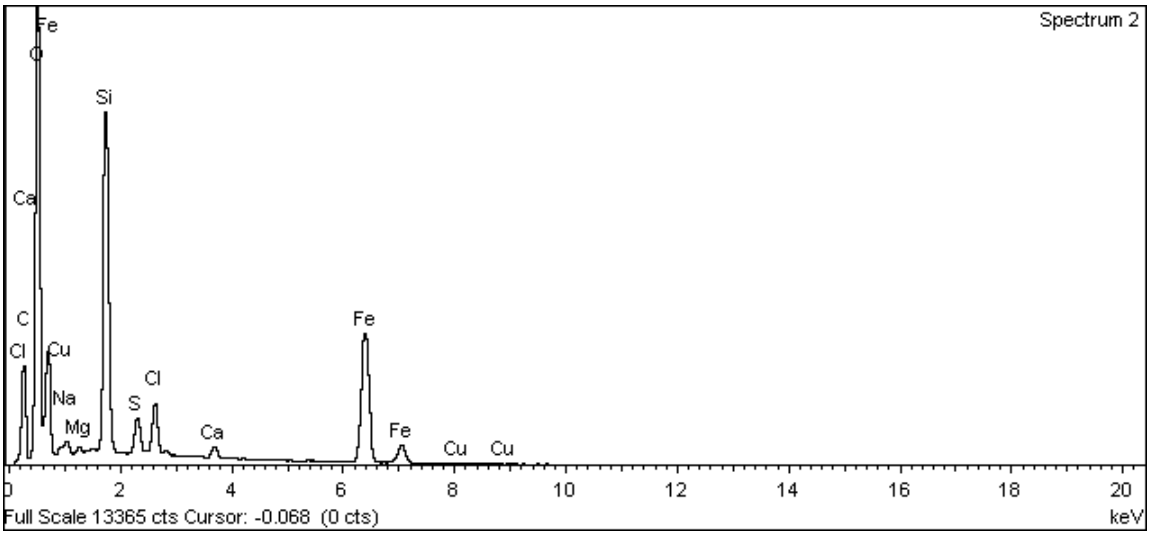

Figure A-362. Surface of pit in cast iron insert opposite hole in canister and EDX analysis at position of Spectrum 2

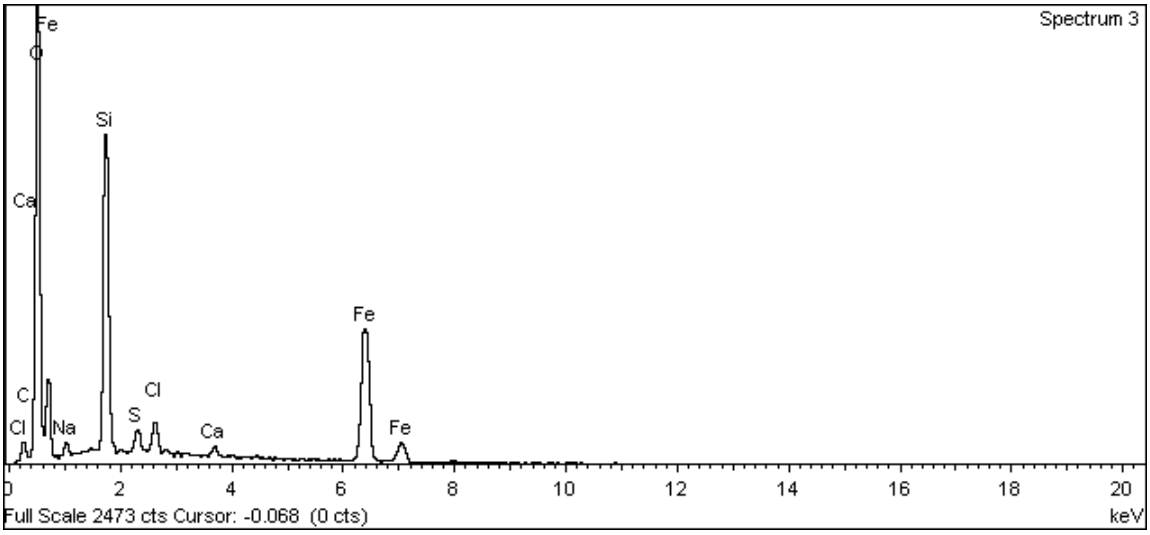

Figure A-363. Surface of pit in cast iron insert opposite hole in canister and EDX analysis at position of Spectrum 3

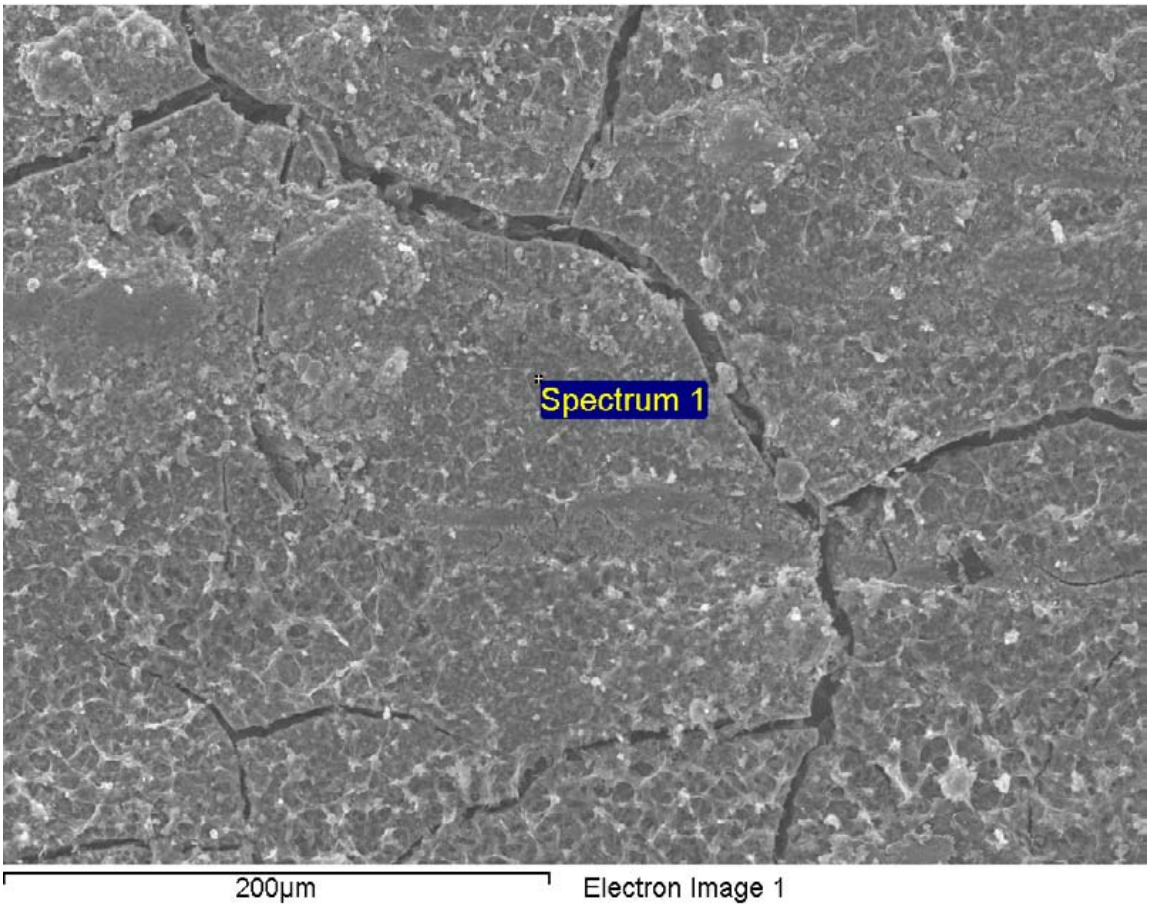

Figure A-364. Surface of pit in cast iron insert opposite hole in canister and EDX analysis at position of Spectrum 1

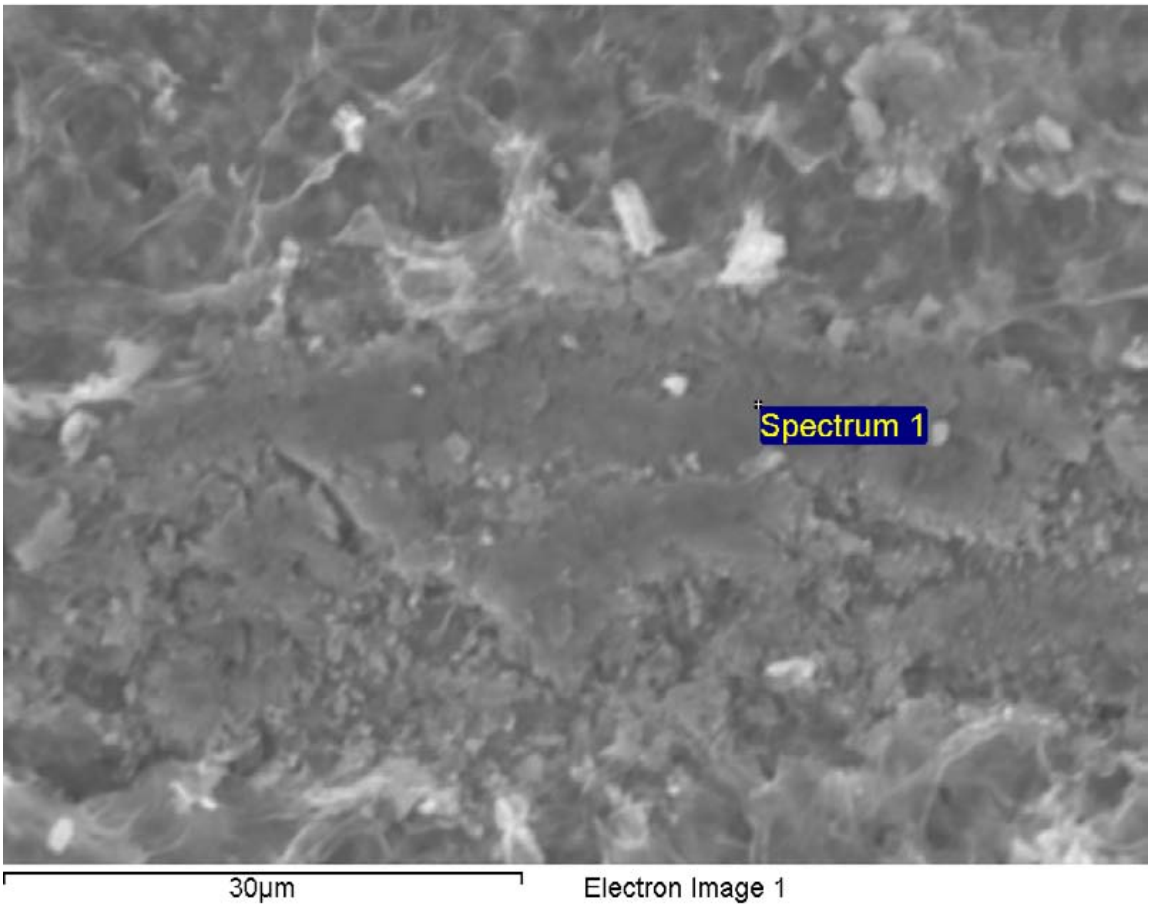

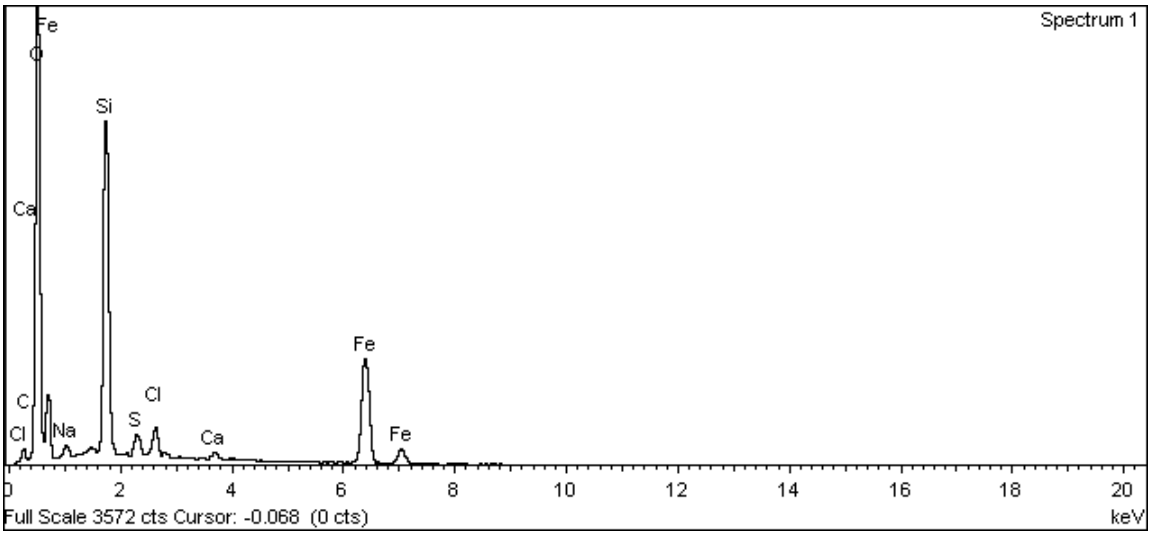

Figure A-365. Surface of pit in cast iron insert opposite hole in canister and EDX analysis at position of Spectrum 1

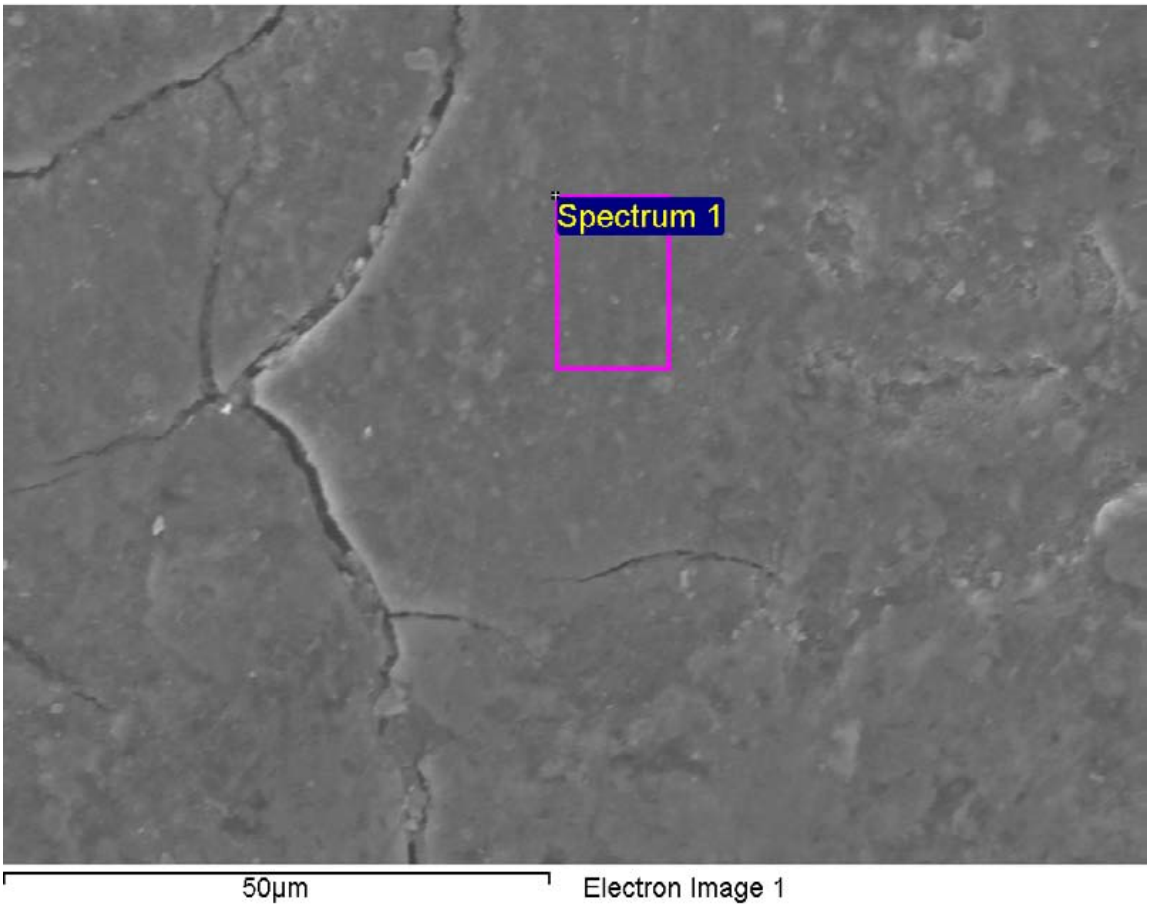

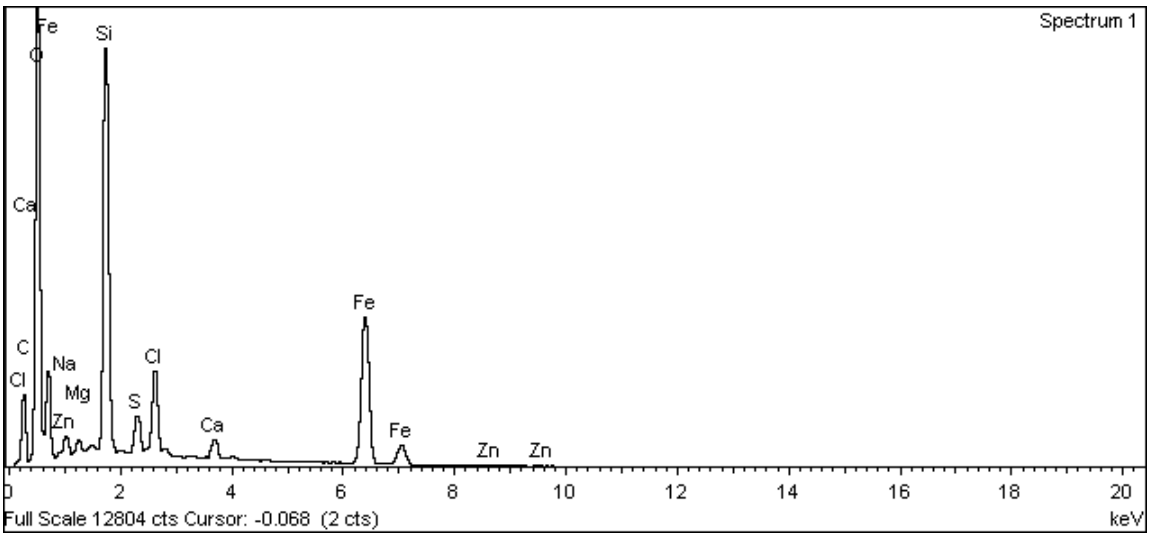

Figure A-366. Surface of pit in cast iron insert opposite hole in canister and EDX analysis at position of Spectrum 1